
Cancer
Cell
Volume 22
Number 5
November 13, 2012
www.cellpress.com
TGFβ
TGFβ-Activated Stroma
Promotes Metastasis

Cancer Cell
Article

Dependency of Colorectal Cancer on a TGF-β-Driven Program in Stromal Cells for Metastasis Initiation

Alexandre Calon,[1,11] Elisa Espinet,[1,11] Sergio Palomo-Ponce,[1] Daniele V.F. Tauriello,[1] Mar Iglesias,[4] María Virtudes Céspedes,[5] Marta Sevillano,[1] Cristina Nadal,[6] Peter Jung,[1] Xiang H.-F. Zhang,[7] Daniel Byrom,[2] Antoni Riera,[2,8] David Rossell,[3] Ramón Mangues,[5] Joan Massagué,[7,9] Elena Sancho,[1,*] and Eduard Batlle[1,10,*]
[1]Oncology Programme
[2]Chemistry and Molecular Pharmacology Programme
[3]Biostatistics and Bioinformatics Unit
Institute for Research in Biomedicine, 08028 Barcelona, Spain
[4]Pathology Department, Hospital del Mar, Institut Hospital del Mar d'Investigacions Mèdiques and Autonomous University of Barcelona, 08004 Barcelona, Spain
[5]Biomedical Research Institute Sant Pau, Hospital de la Santa Creu i Sant Pau and CIBER de Bioingeniería, Biomateriales y Nanomedicina, 08025 Barcelona, Spain
[6]Institut de Malalties Hemato-Oncològiques, Hospital Clínic-CIBERehd, 08036 Barcelona, Spain
[7]Cancer Biology and Genetics Program, Memorial Sloan-Kettering Cancer Center, New York, NY 10021, USA
[8]Departament de Quimica Organica, Universitat de Barcelona, 08028 Barcelona, Spain
[9]Howard Hughes Medical Institute, Chevy Chase, MD 20185, USA
[10]Institució Catalana de Recerca i Estudis Avançats (ICREA), 08010 Barcelona, Spain
[11]These authors contributed equally to this work
*Correspondence: elena.sancho@irbbarcelona.org (E.S.), eduard.batlle@irbbarcelona.org (E.B.)
http://dx.doi.org/10.1016/j.ccr.2012.08.013

SUMMARY

A large proportion of colorectal cancers (CRCs) display mutational inactivation of the TGF-β pathway, yet, paradoxically, they are characterized by elevated TGF-β production. Here, we unveil a prometastatic program induced by TGF-β in the microenvironment that associates with a high risk of CRC relapse upon treatment. The activity of TGF-β on stromal cells increases the efficiency of organ colonization by CRC cells, whereas mice treated with a pharmacological inhibitor of TGFBR1 are resilient to metastasis formation. Secretion of IL11 by TGF-β-stimulated cancer-associated fibroblasts (CAFs) triggers GP130/STAT3 signaling in tumor cells. This crosstalk confers a survival advantage to metastatic cells. The dependency on the TGF-β stromal program for metastasis initiation could be exploited to improve the diagnosis and treatment of CRC.

INTRODUCTION

Most colorectal cancers (CRCs) originate from the intestinal epithelium as premalignant lesions called adenomas. Over time, a small fraction of adenomas are transformed to CRCs because of the accumulation of genetic alterations in a small set of driver genes, including *KRAS*, *TP53*, *SMAD4*, or *PIK3CA* (Markowitz and Bertagnolli, 2009). Alterations in these and other cancer-causing genes have been associated with the different stages of the progression of the tumor (i.e., transition from normal intestinal mucosa to adenoma and further progression to CRC). In contrast, metastases that are either present at the time of diagnosis or develop as distant relapses after therapy are not strongly associated with alterations in any of these key

Significance

About 40%–50% of all patients with colorectal cancer will present with metastasis either at the time of diagnosis or as recurrent disease upon intended curative therapy. In the absence of genetic alterations that explicate these processes, it remains a major challenge to predict which patients will develop metastatic disease or to design targeted therapies. Here, we show that metastasis depends on a gene program expressed by the tumor microenvironment upon TGF-β stimulation. Low stromal TGF-β signaling is a robust predictor of disease-free survival after therapy, which improves on the current AJCC staging system. Furthermore, colonization of foreign organs requires TGF-β signaling in stromal cells and therefore may be a target for therapeutic intervention at early time points of the metastatic process.

genes (Walther et al., 2009). In addition, global genome sequencing of metastatic lesions and primary CRCs revealed hardly any metastasis-specific mutation (Jones et al., 2008). This drawback has hampered the development of metastasis-specific therapies, as well as the identification of patients with CRC at risk of suffering metastatic disease.

Mutational inactivation of the TGF-β signaling pathway is key during CRC progression. Alterations in TGF-β pathway components are first detected in advanced adenomas and affect 40%–50% of all CRCs (Markowitz et al., 1995; Markowitz and Bertagnolli, 2009). In mouse models, mutations in the tumor suppressor *Apc* combined with inactivation of TGF-β signaling components in epithelial intestinal cells trigger the development of invasive adenocarcinomas (Muñoz et al., 2006; Takaku et al., 1998). Restoration of a functional TGF-β pathway in human CRC cells abrogates proliferation and tumorigenicity (Wang et al., 1995), implying that TGF-β signaling exerts tumor-suppressive effects. Hence, it has been proposed that TGF-β imposes a selective pressure during CRC progression, which tumors avert by genetic inactivation of the TGF-β receptors (*TGFBR1* and *TGFBR2*) or of the SMAD intracellular mediators (*SMAD4*, *SMAD2*, and *SMAD3*) (Grady and Markowitz, 2002; Markowitz et al., 1995; Markowitz and Bertagnolli, 2009).

In addition to its tumor suppressor role in epithelial cells, TGF-β signaling also acts as a negative regulator of tumor formation by conditioning mucosa-resident stromal cells. Mice with a deletion of *Smad4* in T cells develop gastrointestinal tumors (Hahn et al., 2011; Kim et al., 2006). Similarly, transgenic expression of a dominant negative TGFBR2 in T cells accelerates azoxymethane-induced colon carcinogenesis (Becker et al., 2004). In both cases, T cells lacking TGF-β signals exacerbate the production of proinflammatory cytokines that spark off the transformation of the colonic epithelium (Becker et al., 2004; Kim et al., 2006).

Although the above genetic and mutational data support a tumor suppressor role for TGF-β signaling in intestinal carcinogenesis, high levels of TGFB1 in the serum of patients with CRC are associated with poor outcome in the clinical setting (Tsushima et al., 2001). The relevance of TGF-β signaling for disease progression has been widely recognized in tumors where cancer cells retain a functional TGF-β pathway, such as breast or prostate cancer (Massagué, 2008). In these tumor cells, TGF-β induces a variety of prometastatic programs that range from induction of epithelial-to-mesenchymal transition to expression of genes that allow colonization of foreign organs (Massagué, 2008). It is less clear, however, what CRC cells can gain from high TGF-β levels once the pathway is fully inactivated by mutations and how this phenomenon links to an adverse outcome. To address this apparent paradox, we investigated whether TGF-β may activate the tumor microenvironment to assist CRC cells in the metastatic process.

RESULTS

TGF-β Levels in CRC Are a Robust Predictor of Disease Relapse

We first investigated whether differences in TGF-β levels in primary tumors were associated with clinical disease progression in CRC. To this end, we interrogated a representative pooled cohort of 345 cases treated at three different hospitals for which transcriptomic profiles and clinical follow-up were publicly available. In this metacohort, overall TGF-β levels were low in patients with American Joint Cancer Committee (AJCC) stage I cancer, compared to cancer at more advanced stages (Figure 1A; see Tables S1 and S2 available online). The AJCC staging system has limited power to predict disease relapse, because 10%–20% of patients with stage II CRC and 30%–50% of patients with stage III CRC will develop recurrent cancer after therapeutic intervention. We found that, for every increase in overall TGF-β (*TGFB*) expression, the risk of cancer recurrence augmented by 83% (Figure 1B). As a consequence, we observed large differences in the frequency of disease relapse after therapy in patients bearing tumors with high, medium, or low *TGFB* (Figure 1C) or individual TGF-β isoform levels (Figures S1A and S1B). During 10 years of follow-up, only patients with medium or high *TGFB* expression in the primary tumor (53 of 220 patients) suffered cancer recurrence. Remarkably, all patients bearing *TGFB*-low tumors remained disease-free (Figure 1C, blue group). High *TGFB* levels were robustly associated with relapse in patients with stage II and III cancer, whereas low *TGFB* characterized a small set of patients with no observed recurrences in both stages (Figure 1D; 17% and 11% of patients with cancer at these stages, respectively). The rare relapses occurring in stage I CRCs (2 of 35 patients in this group) also expressed high *TGFB* levels (Figure 1D), although this comparison did not reach statistical significance, probably because of the low incidence of recurrences in this stage. Cox proportional hazards multivariate analysis demonstrated that *TGFB* expression is an independent predictor of cancer recurrence that outperforms AJCC staging system in the identification of patients with CRC who remained disease free upon therapy (Figure 1E). The predictive power of *TGFB* levels also compared favorably to that of other genes that have been repeatedly associated with disease relapse in CRC (Table S3).

TGF-β Response Signatures in Tumor-Associated Stromal Cells Predict Disease Relapse in CRC

An increase in TGF-β isoform levels was evident at the adenoma-CRC transition, as shown by expression profiling of a small cohort of colon tumors (Figure S1C). Nuclear p-SMAD3, a marker for TGF-β signaling, stained predominantly the stromal compartment in most CRCs (Figure S1D). In the majority of samples, epithelial CRC cells were markedly less stained compared to adjacent stromal cells or to the epithelial compartment of adenomas (Figures S1D–S1F). We characterized the stromal cell types stained by p-SMAD3 in CRCs but could not discriminate any obvious cell-type specificity. Rather, p-SMAD3 indiscriminately labeled all major types of stromal cells in CRCs, including T cells, macrophages, endothelial cells, and fibroblasts (Figures S2A–S2H). We thus quantified the association of TGF-β-activated stromal cell populations with disease progression. To this end, we used as surrogates the gene expression programs induced by the addition of TGF-β (TGF-β response signatures or TBRS) in cultures of normal-tissue-derived T cells (T-), macrophages (Ma-), endothelial cells (End-), or fibroblasts (F-). To avoid biases, we used the full set of genes upregulated by TGF-β signaling in these cell cultures (>2 fold, $p < 0.05$) without additional filtering or refinement (Table S4). By Gene

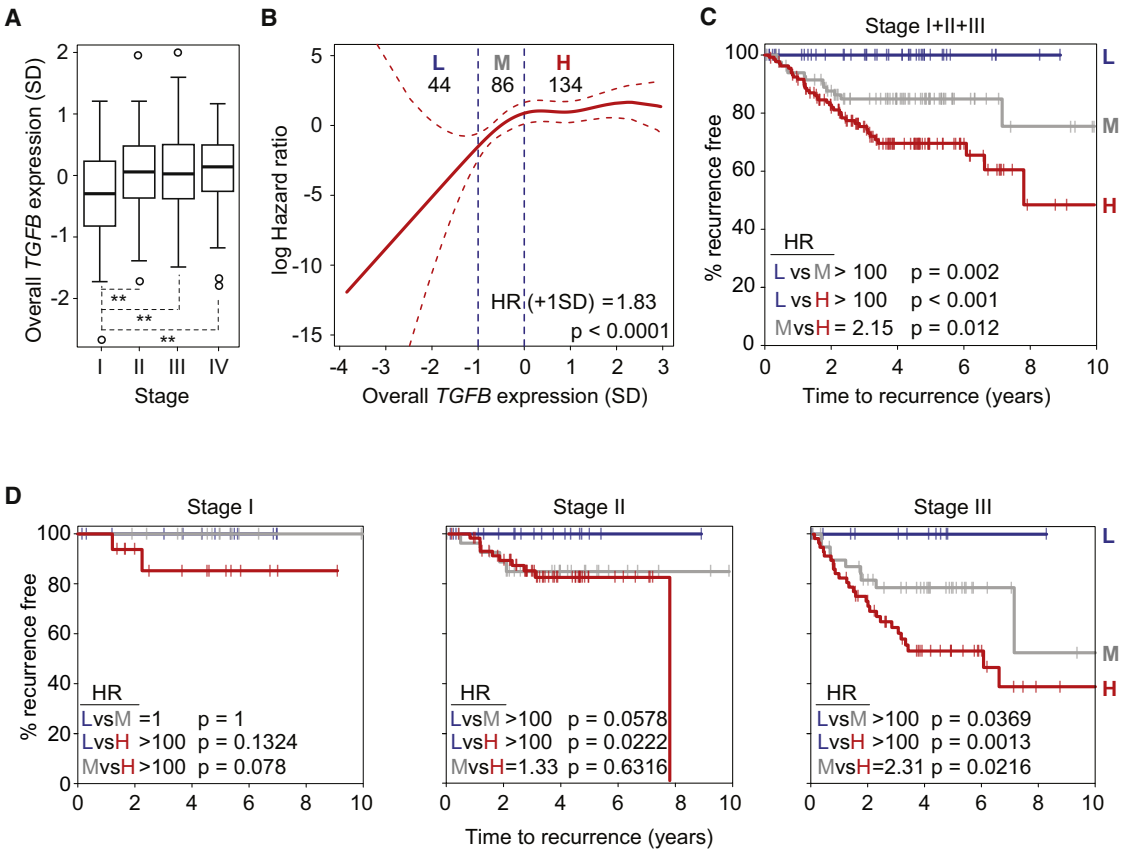

E

Overall *TGFB*	HR	CI. low	CI. up	p value
+1SD increase	1.68	1.28	2.21	0.0002
High *vs* Low	>100	NA	NA	<0.0001
Medium *vs* Low	>100	NA	NA	0.0043
High *vs* Medium	2.00	1.07	3.76	0.0231
AJCC stage	NA	NA	NA	0.0002
Stage II *vs* I	2.56	-1.74	11.40	0.1685
Stage III *vs* I	6.84	1.62	28.84	0.0006
Stage III *vs* II	2.67	1.43	4.98	0.0011
study	NA	NA	NA	0.0011

Figure 1. High TGF-β Expression Predicts CRC Relapse

(A) Overall *TGFB* mRNA expression in CRC stages I–IV. Values are z-scores with standard deviation (SD) from the mean (**p < 0.01, two-tailed Student's t test).

(B) Smooth function correlates overall *TGFB* mRNA expression with relative risk of recurrence. Patients with stage IV cancer were excluded from this analysis. Red dashed lines: 95% confidence interval (CI). Blue dashed lines: thresholds for patient selection into groups with low (L; blue, 44 patients), medium (M; gray, 86 patients), and high (H; red, 134 patients) *TGFB* expression; p values and increase in HR per each increase in standard deviation of expression (+1 SD) are shown.

(C and D) Kaplan-Meier plots display recurrence-free survival (RFS) over time (C) and grouped by AJCC stage (D) for groups defined in (B) . HR and p values compare RFS over time for patients grouped according to *TGFB* levels (L versus M, L versus H, and M versus H).

(E) Cox proportional hazards multivariate analysis of TGF-β expression and AJCC staging in identifying patients who remained disease-free upon therapy.

See also Figure S1.

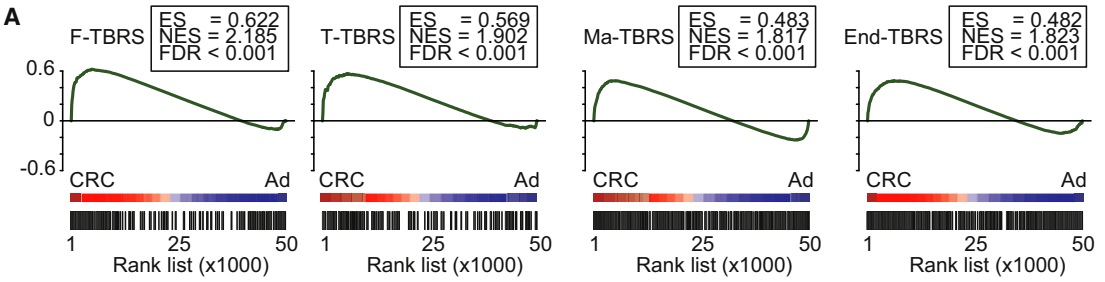

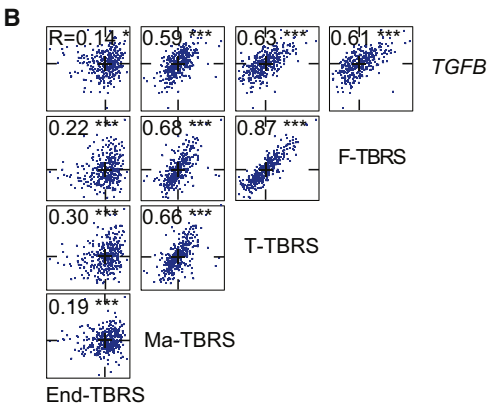

C

	TGF-β Response Signature			
	Fibro	T-cell	Ma	End
HR (+1SD)	1.56	1.89	1.91	1.50
(p=)	(0.0002)	(0.0005)	(0.001)	(0.46)

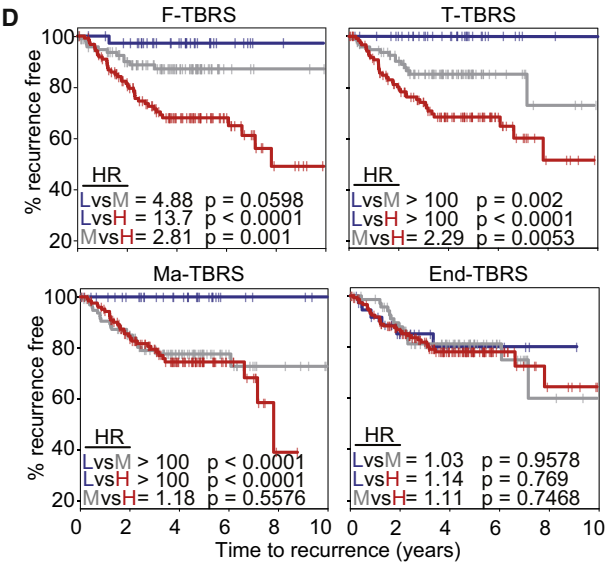

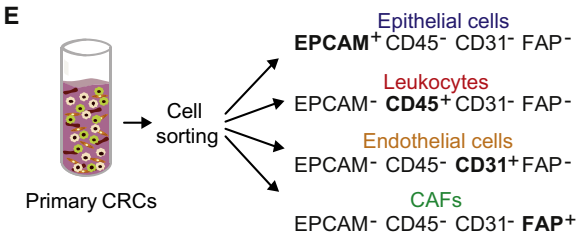

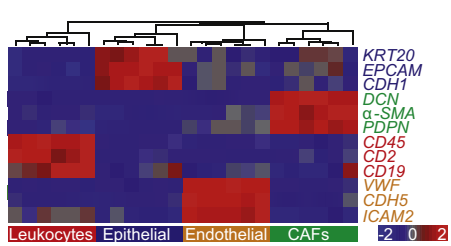

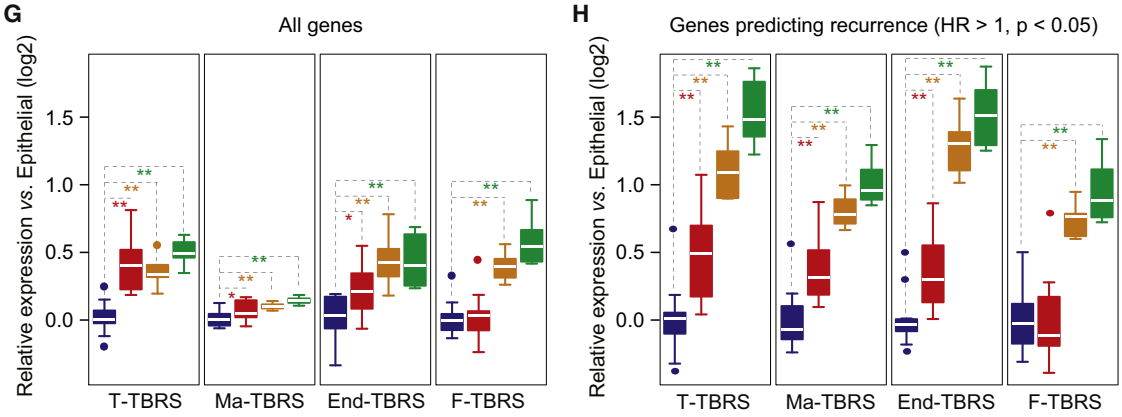

Set Enrichment Analysis (GSEA) (Subramanian et al., 2005), we determined that all stromal TBRSs were highly enriched in CRCs compared to adenomas (Figure 2A). Importantly, the expression levels of *TGFB*, F-TBRS, T-TBRS, and Ma-TBRS showed robust direct correlations in the cohort of patients with CRC (Figure 2B), implying that they are, to a large extent, concurrently expressed in CRC. Significantly, these three signatures were excellent predictors of disease relapse in patients with stage I, II, and III CRC and segregated a low-expression patient group with virtually no risk of developing recurrent cancer after therapy (Figures 2C and 2D, blue group). This result paralleled that obtained with *TGFB* levels (Figure 1). In patients with stage IV CRC who underwent potential curative therapy, high *TGFB* and stromal TBRS expression levels also correlated with higher risk of relapse (Figures S2I–S2L). However, a large proportion of these patients with stage IV disease eventually experienced relapse, likely because of the lack of effective therapies to eliminate an overt metastatic disease. Consistent with their ability to predict disease progression, the stromal TBRS included several well-known prometastatic genes, such as *ANGPTL4* (Padua et al., 2008), *PTHLH* (Yin et al., 1999), *HBEGF* (Bos et al., 2009), *CTGF* (Kang et al., 2003), *TNC* (Oskarsson et al., 2011), or *JAG1* (Sethi et al., 2011; Sonoshita et al., 2011), all of which encode for secreted or membrane-bound factors (Table S4).

To further analyze the cell-type-specific expression of each stromal TBRS in vivo, we purified by FACS various cell populations from fresh CRC samples and assessed their gene expression profiles (Figures 2E and 2F). Relative levels of cell-type-specific marker genes confirmed the purification of epithelial tumor cells ($EPCAM^+$), leukocytes ($CD45^+$), endothelial cells ($CD31^+$), and fibroblasts (FAP^+) (Figure 2F). A global comparative analysis revealed a trend toward high levels of all stromal TBRS in FAP^+ CAFs. Conversely, epithelial tumor cells expressed the lowest levels of each stromal TBRS (Figure 2G). Remarkably, these trends became very significant for those genes within the T-TBRS, Ma-TBRS, or End-TBRS that associated positively with cancer relapse ($HR > 1$, $p < 0.05$; Figure 2H). Although the in vitro derived End-TBRS did not predict disease progression (Figures 2C and 2D), we observed elevated expression of recurrence-associated TGF-β target genes in endothelial cells directly purified from tumors (Figure 2H). This observation may suggest that the response of in vitro cultured endothelial cells to TGF-β signaling deviates significantly from that occurring in the tumor microenvironment. Altogether, these data highlight that the response of stromal cells to TGF-β is an accurate predictor of disease relapse in patients with CRC. Although high *TGFB* levels activate gene programs in a wide range of tumor-associated stromal cell types, our in vivo data indicate that CAFs and, to a lesser extent, endothelial cells are the main contributors to the association of stromal TGF-β-driven programs with poor outcome after therapy.

TGF-β Signaling in the Stroma Promotes Tumor Initiation

The above data suggest the possibility that elevated *TGFB* levels in CRC influence disease progression by acting on stromal cells. To functionally dissect this effect without the interference of TGF-β signaling in epithelial cancer cells, we took advantage of the fact that virtually all late-stage CRC-derived cell lines display mutational inactivation of the TGF-β pathway. These CRC cell lines, however, did not induce robust stromal TGF-β responses when injected into nude mice, as shown by the lack of p-SMAD2 accumulation in tumor-associated stromal cells (arrows in Figures 3A and 3B; data not shown). To enforce high TGF-β signaling in xenografts, we engineered CRC cell lines to secrete active TGFB1. Subcutaneous tumors obtained from $HT29\text{-}M6^{TGF\text{-}\beta}$, $KM12L4a^{TGF\text{-}\beta}$ and $SW48^{TGF\text{-}\beta}$ cells contained abundant $p\text{-}SMAD2^+$ stromal cells (arrowheads in Figures 3A and 3B; data not shown) and increased expression levels of stromal TBRS genes (Figure 3C; data not shown). Importantly, secretion of TGF-β did not induce autocrine responses in these CRC cells (i.e., SMAD reporter activity, proliferation, or EMT induction; Figures S3A–S3D), owing to homozygous mutations in *TGFBR2* in KM12L4a and in SW48. HT29-M6 cells carry homozygous inactivation of the *SMAD4* locus, which rendered this cell line unresponsive to TGF-β (Figures S3A–S3D). Yet, this genetic alteration did not impede the nuclear accumulation of p-SMADs (Figure 3B), as previously reported for other *SMAD4* mutant cell lines (Alarcón et al., 2009; Liu et al., 1997). Therefore, the xenografts derived from these cells combine a TGF-β response in tumor stromal cells with lack of TGF-β signaling in cancer cells, the scenario characteristic of advanced CRC. We inoculated CRC cells subcutaneously into nude mice in quantities that generated suboptimal engraftment in control conditions (see Experimental Procedures). Elevated levels of

Figure 2. Stromal TGF-β Gene Signatures Predict Recurrence

(A) Gene set enrichment analyses (GSEA) of TGF-β response signatures (TBRS) of Fibroblasts (F-TBRS), T cells (T-TBRS), macrophages (Ma-TBRS), or endothelial cells (End-TBRS) in carcinoma versus adenoma samples. ES, enrichment score; NES, normalized enrichment score; FDR, false discovery rate.

(B) Cross-correlations between *TGFB*, F-TBRS, T-TBRS, Ma-TBRS, and End-TBRS in the patient cohort. Blue dots, patients. R, correlation coefficients. Values are Z scores (*$p < 0.05$, ***$p < 0.001$).

(C) The p values and increase in HR per each increase in expression (+1SD) in F-TBRS, T-TBRS, Ma-TBRS, and End-TBRS were obtained via Cox proportional Hazards model.

(D) Kaplan-Meier plots display RFS of patients with low (blue), medium (gray), or high (red) F-TBRS, T-TBRS, Ma-TBRS, or End-TBRS expression levels.

(E) FACS-purification of cell populations from primary CRC samples, enriched in the indicated cell types.

(F) Heat map shows relative expression levels of marker genes for epithelial (blue), leukocyte (red), endothelial (orange) cells, and cancer-associated fibroblasts (green) in each cell population. Values are normalized intensities, log2.

(G) Relative expression of each TBRS in cell populations from (F). Whiskers represent minimum (Vmin) and maximum (Vmax) values, truncated at 1.5 times the interquartile range (log2; *$p < 0.05$, **$p < 0.01$, Student's t test).

(H) Relative expression in each cell population of genes within the T-TBRS, Ma-TBRS, End-TBRS, or F-TBRS associating positively with relapse. Whiskers: Vmin, Vmax (log2; *$p < 0.05$, **$p < 0.01$, Student's t test).

See also Figure S2.

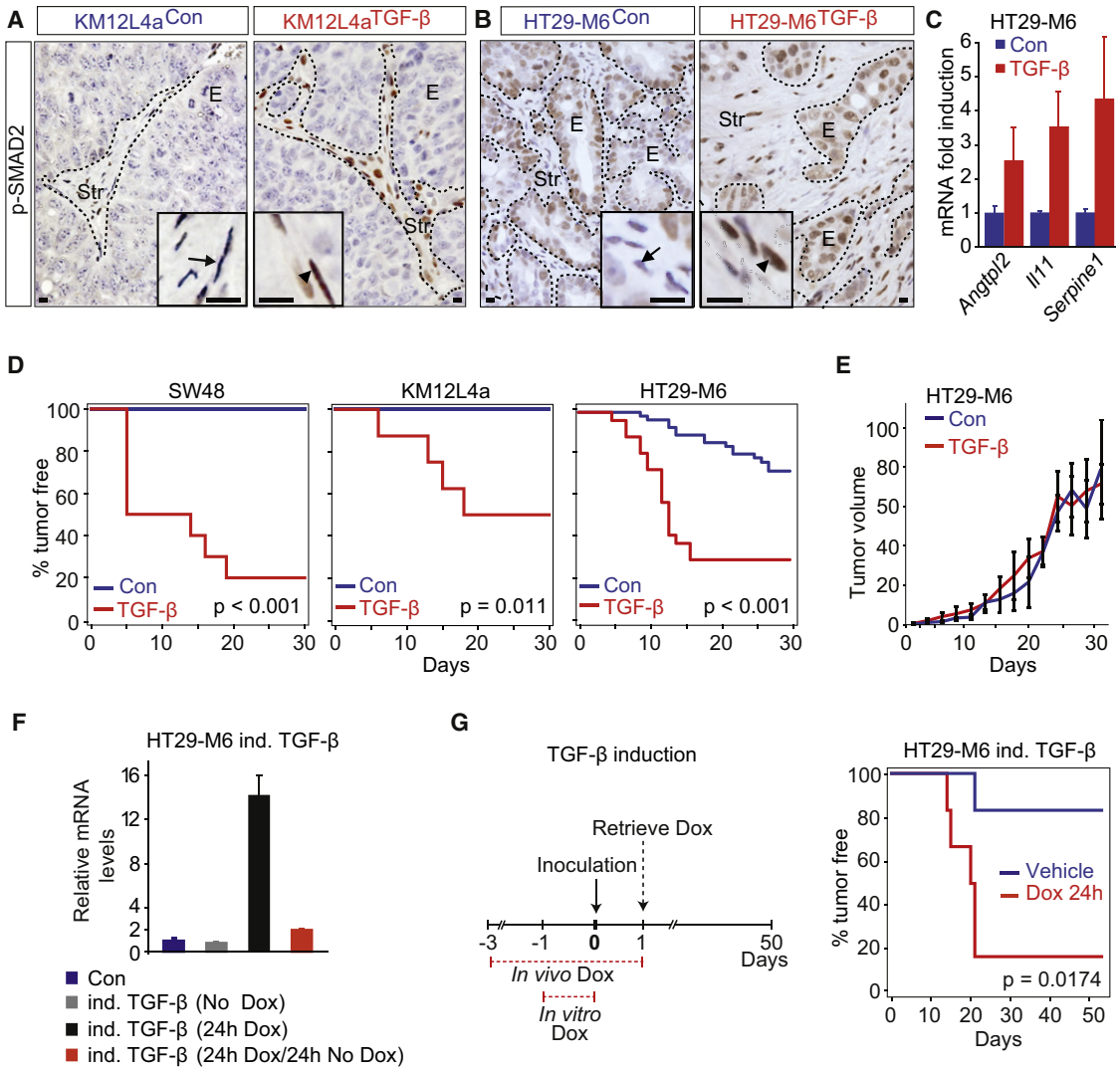

Figure 3. TGF-β Activated Stroma Induces Tumor Initiation

(A and B) Nuclear p-SMAD2 reactivity (arrowheads) in subcutaneous (s.c.) tumors derived from TGF-β-secreting KM12L4a (A) or HT-29M6 (B) CRC cells and control cells. E, epithelial cells; Str, stromal cells. Scale bars = 10 μm.

(C) Relative expression of some stromal TBRS genes in tumors from (B). Values are mean ± SEM (n = 3).

(D) Kaplan-Meier plots display tumor-free survival (TFS) for mice injected s.c. with 3×10^4 TGF-β-secreting (red) or control cell lines (blue); SW48 (n = 8); KM12L4a (n = 8); HT29-M6 cells (n = 25 (red), n = 39 (blue).

(E) Growth over time for HT29-M6$^{TGF-\beta}$ (red; n = 13) and HT29-M6^{Con} (blue; n = 16) derived tumors. Day 1: day of first detection. Values are mean ± SEM.

(F) Relative *TGFB* mRNA levels in HT29-M6 cells expressing active TGF-β through a doxycycline (Dox)-inducible promoter (HT29-M6 ind. TGF-β) compared to control cells (Con, blue). Inducible TGF-β cells were nontreated (gray), treated with Dox for 24 hr (black), or treated with Dox for 24 hr followed by 24 hr of Dox withdrawal prior to qRT-PCR (red). Values are mean ± SD (n = 3).

(G) Inducible TGF-β cells were either untreated (blue) or pretreated with Dox in vitro 24 hr before s.c. inoculation (3×10^4 cells; n = 6). Recipient mice received either Dox (red) or vehicle (blue) in drinking water ad libitum during 3 days prior to injection. Kaplan-Meier curves show TFS when TGF-β secretion is induced in vivo for 24 hr (red) compared to control cells (blue).

See also Figure S3.

TGF-β dramatically increased the frequency of tumor formation and reduced the latency period in all cell lines (Figure 3D). Yet, after tumor initiation, the TGF-β-activated microenvironment had no effect on xenograft growth rates (Figure 3E; data not shown). We further tested this early requirement by controlling the timing of TGF-β production in HT29-M6 CRC cells via a doxycycline-inducible promoter (Figures 3F and 3G). Secretion of TGF-β during the first 24 hr following inoculation of tumor cells was sufficient to enhance tumor initiation (Figure 3G). Given the well-established role of TGF-β in the polarization and suppression of the immune system in tumors (Flavell et al., 2010), we tested whether the enhancement of tumor initiation by TGF-β signaling could be explained by modulation of the immune system. To this end, we injected CRC cells in severely

immunocompromised mice of the NOD/SCID interleukin-2 receptor gamma chain null strain (NSG) (Shultz et al., 2007). In these NSG mice, high TGF-β levels were also capable of enhancing tumor initiation, although fewer cancer cells were required to form tumors in this strain (Figure S3E).

Stromal TGF-β Signaling Is Required for Efficient Metastasis Initiation

CRCs at stages I, II, and III displaying low stromal TGF-β signaling fail to form recurrences, which, in most patients with CRC, occur in the form of metastasis. To study whether stromal TGF-β signaling may influence metastasis formation, we inoculated KM12L4a^{Con} and KM12L4a$^{TGF\text{-}\beta}$ cells in the cecum of nude mice. Both cell lines gave rise to aggressive colorectal tumors, which killed mice by obstruction of the intestinal lumen. At death, KM12L4a^{Con} and KM12L4a$^{TGF\text{-}\beta}$ had generated colon tumors of equivalent size (data not shown) with no significant differences in their degree of invasion, spread to local lymph nodes, or major histological features (Figure 4A; Figures S4A and S4B). Yet, two thirds of mice bearing KM12L4a^{Con} colon tumors remained metastasis free, whereas 10 of 11 mice inoculated with KM12L4a$^{TGF\text{-}\beta}$ cells developed lung and/or liver metastasis ($p < 0.01$, Figure 4B). These data imply that stromal TGF-β signaling promotes metastasis formation. We further explored this phenomenon by using intrasplenic inoculation of CRC cells (Morikawa et al., 1988). Secretion of TGF-β by KM12L4a cells increased the liver metastases burden in mice (Figure 4C). We also observed a large increase in the number of liver metastases generated by HT29-M6 secreting TGF-β (Figure 4D). In addition, a significant fraction of mice inoculated with KM12L4a$^{TGF\text{-}\beta}$ or HT29-M6$^{TGF\text{-}\beta}$ developed lung metastases, implying that TGF-β signaling also facilitated secondary organ colonization (Figure 4E). The kinetics of liver metastasis revealed that control or TGF-β secreting cells expanded with similar rates once tumor cells had taken root and resumed growth (from day 7 in Figure 4F). However, during the first few days following inoculation, most KM12L4a^{Con} cells that reached the liver were progressively lost, and by 7 days, tumor cells were barely detectable (Figure 4F). A virtually complete loss of control metastatic cells was noticed during the first 24 hr upon inoculation of lower tumor cell numbers (Figure S4C). Secretion of TGF-β significantly increased the amounts of KM12L4a cells detected at these early time points (Figure 4F; Figure S4C). To further test this early requirement, we used CRC cells that expressed TGF-β from a doxycycline-inducible promoter. A short pulse of TGF-β (24 hr) at the moment of intrasplenic inoculation was sufficient to increase metastasis burden by facilitating metastasis initiation without affecting subsequent tumor growth (Figures 4G and 4H; Figure S4D; $p < 0.05$). Thus, high levels of TGF-β specifically act to enhance the colonization capability of CRC cells at the initial phase of metastasis. Because KM12L4a and HT29-M6 cells harbor an inactivated TGF-β pathway, enhanced metastasis initiation by TGF-β secretion must be the consequence of changes in the tumor microenvironment. Indeed, metastasis derived by both TGF-β secreting cell lines displayed enhanced desmoplastic reaction (Figures S4E–S4L) with abundant p-SMAD2 accumulation in stromal cells (Figures 4I and 4J; Figures S4M and S4N) and elevated expression of stromal TBRS genes (Figure 4K; data not shown).

Pharmacological Inhibition of Stromal TGF-β Signaling Blocks Metastasis Initiation

We have recently described the purification of Colon Cancer Stem Cells (CoCSCs) from CRC biopsies via surface expression of the receptor tyrosine kinase EPHB2 (Merlos-Suárez et al., 2011). We isolated EPHB2-high CoCSCs from the primary tumor of a patient with stage IV CRC and cultured them in conditions similar to those used for expansion of normal colon stem cells (Jung et al., 2011; Sato et al., 2011). EPHB2-high tumor cells embedded in matrigel expanded as epithelial tumor organoids (Figure 5A), which retained high expression levels of colon stem cell marker genes such as *LGR5* and *ASCL2* (data not shown). Genomic analysis of the tumor organoids revealed that the two *TGFBR2* alleles were inactivated by mutations in this patient (data not shown). Indeed, treatment with TGFBR1-specific inhibitor LY2157299 (Bueno et al., 2008) or the addition of active TGF-β did not modify in vitro growth rates, morphology, or organoid forming activity of this CoCSC-derived culture (Figures 5A–5C). Primary CoCSCs expressed higher *TGFB* levels than did CRC cells lines (Figure 5D). When injected in immunodeficient mice, they generated tumors with abundant p-SMAD2^{+} stromal cells (Figure 5E, left panel), implying that this primary CoCSCs elicited a TGF-β response in the tumor microenvironment. Feeding mice bearing macroscopic tumors from CoCSCs-derived cultures with LY2157299 blocked TGF-β signaling in the tumor stroma as shown by reduced stromal p-SMAD2 positivity (Figure 5E, right panel) and downregulated levels of stromal TBRS genes (Figure 5F). Importantly, treatment with LY2157299 conferred resistance to the formation of subcutaneous tumors by primary CoCSC-derived cells (Figures 5G and 5H). Remarkably, this TGF-β inhibitor regime also reduced formation of liver metastasis by CoCSCs inoculated via the spleen (Figures 5I and 5J). Kinetics of metastatic colonization showed that LY2157299 reduced the number of cells that engrafted the liver immediately after inoculation (Figure 5I, inset), the opposite behavior of that induced by secretion of high TGF-β levels in CRC cell lines. Of note, these experiments were performed in NSG mice, which rules out that LY2157299 blocked metastasis through changes in the function of the immune system. Altogether, the clinical and functional data described so far indicate that a TGF-β program activated in the tumor microenvironment confers CRC cell competence to overcome the initial phase of metastasis.

Metastasis Initiation by TGF-β-Stimulated Stromal Cells Depends on GP130/STAT3 Signaling in Tumor Epithelial Cells

We next sought to understand the mechanisms behind the potent effect of stromal TGF-β program on the capacity of CRC cells to initiate metastasis. We discovered that subcutaneous tumors and metastases generated in the context of a TGF-β activated microenvironment displayed prominent accumulation of p-STAT3 in CRC cells compared with those derived from control cells (Figure 6A; Figures S5A–S5H). STAT3 signaling depended on GP130 as shown by strong reduction of epithelial p-STAT3 levels upon GP130 shRNA-mediated knockdown in CRC cells (Figure 6A; Figures S5I and S5J). These results suggest that TGF-β induces the expression of GP130-binding cytokines in the tumor microenvironment, which in turn

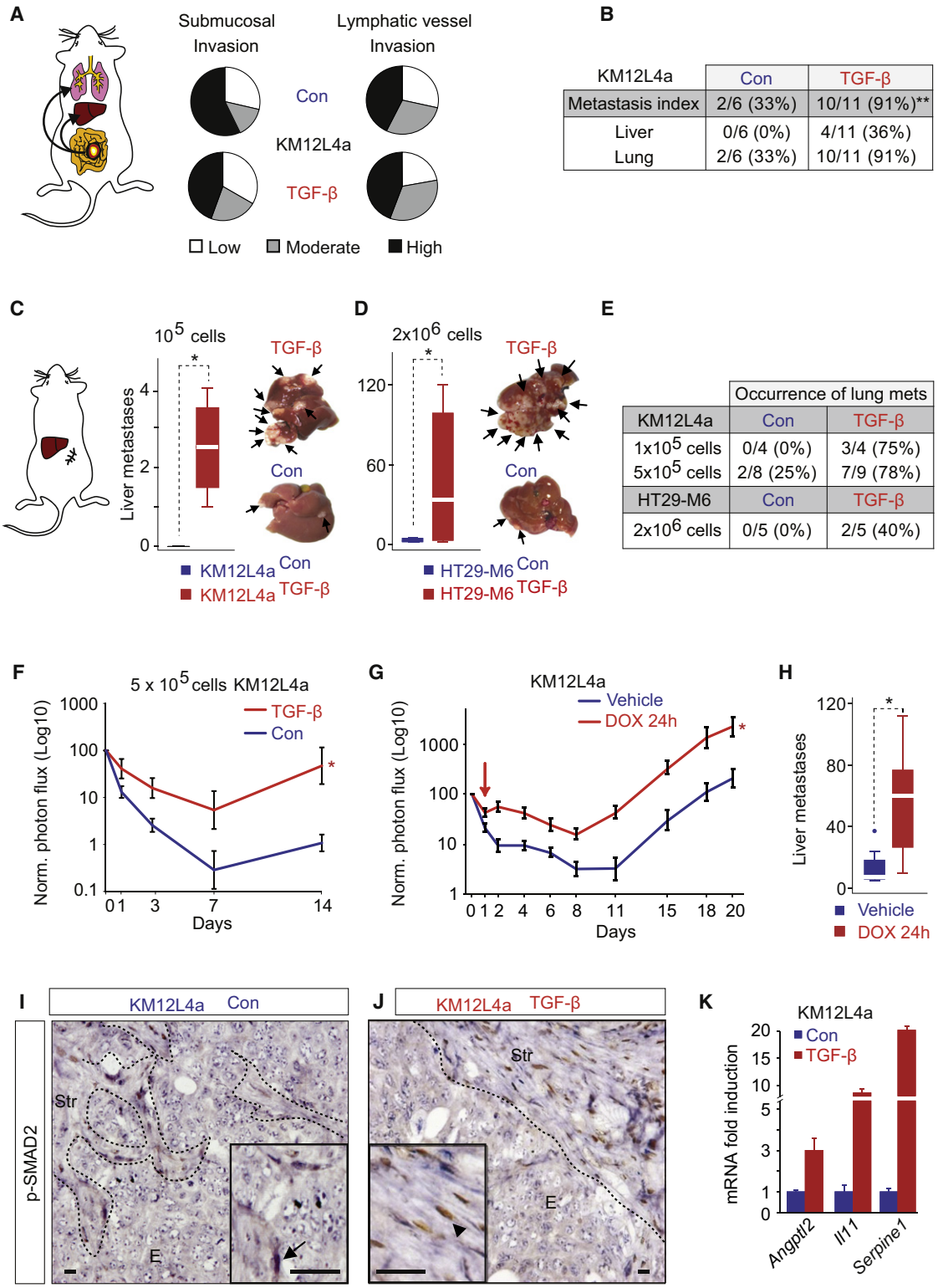

KM12L4a	Con	TGF-β
Metastasis index	2/6 (33%)	10/11 (91%)**
Liver	0/6 (0%)	4/11 (36%)
Lung	2/6 (33%)	10/11 (91%)

	Occurrence of lung mets	
KM12L4a	Con	TGF-β
$1x10^5$ cells	0/4 (0%)	3/4 (75%)
$5x10^5$ cells	2/8 (25%)	7/9 (78%)
HT29-M6	Con	TGF-β
$2x10^6$ cells	0/5 (0%)	2/5 (40%)

Figure 4. TGF-β Activated Stroma Induces CRC Metastasis

(A) Pie charts for submucosal or lymphatic vessel invasion in KM12L4a^{con}- and KM12L4a$^{TGF-β}$-derived cecum tumors.

(B) Incidence of metastases in mice from (A) (**$p < 0.01$; Fisher's exact test).

(C and D) Number of liver metastases after intrasplenic (IS) injection with 10^5 KM12L4a^{Con} or KM12L4a$^{TGF-β}$ cells (C) or 2×10^6 HT29-M6^{Con} or HT29-M6^{TGF-b} cells (D) (*$p < 0.05$, two-tailed Student's t test). Whiskers: Vmin, Vmax. Representative livers are shown from injections with 5×10^5 cells (C) or 2×10^6 cells (D). Arrows denote metastatic nodules.

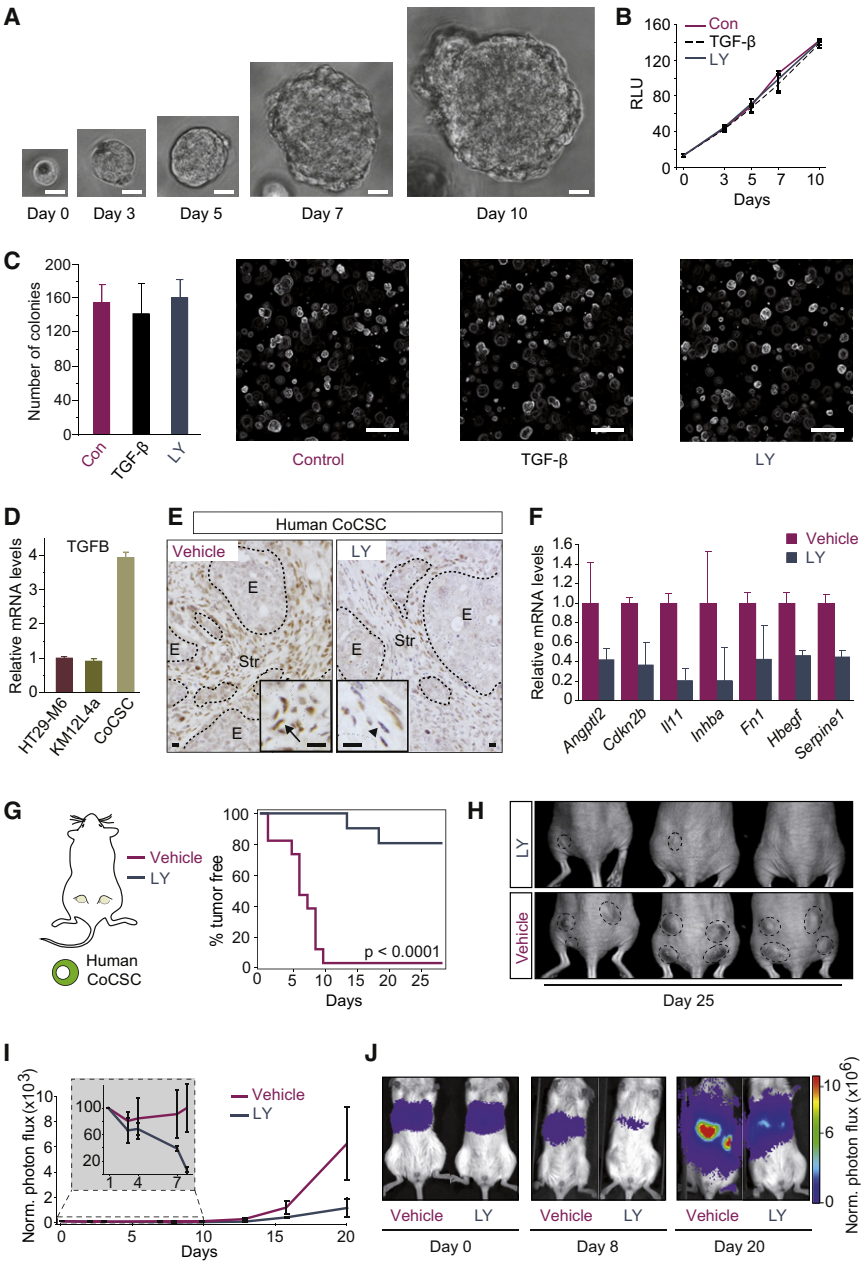

Figure 5. Inhibition of TGF-β Response in the Stroma Blocks Tumor Initiation

(A) In vitro expansion of a CoCSC. Scale bars = 10 μm.

(B) In vitro growth of human CoCSCs upon addition of TGF-β or LY2157299 (LY). Values are mean relative absorbance (RLU) over time ± SD (n = 3).

(C) Number of organoids from human CoCSCs treated with TGF-β or LY2157299. Values are mean ± SD (n = 3). Representative images are shown. Scale bars = 200 μm.

(D) qRT-PCR for *TGFB* in the indicated CRC cells. Values are mean ± SEM.

(E) p-SMAD2 staining in s.c. tumors derived from CoCSCs injected in NSG mice treated with LY2157299 for 3 days (LY; right panel, arrowhead) or untreated (left panel; arrow). E, epithelial cells; Str, stromal cells. Scale bars = 10 μm.

(F) Relative expression of some stromal TBRS genes in tumors from (E). Values are mean ± SEM (n = 2).

(G) Kaplan–Meier curves show TFS for mice injected s.c. with 10^6 CoCSCs. Mice received LY2157299 (blue) or vehicle (purple) from 3 days prior to inoculation until sacrifice (n = 12).

(H) Representative images from (G).

(I) Bioluminescence over time after IS inoculation of 5×10^5 CoCSCs cells in NSG mice treated as in (G). Values, normalized as in Figure 4F, are mean ± SEM.

(J) Representative images from (I).

switches on STAT3 signaling in tumor epithelial cells. To study the relevance of this signaling cycle for tumorigenesis, we inoculated subcutaneously into nude mice HT29-M6 cells that secreted active TGFB1 and at the same time were knockdown for GP130 (HT29-M6$^{shGP130/TGF-\beta}$). These experiments revealed that GP130/STAT3 signaling in cancer cells participated in the enhancement of tumor initiation mediated by stromal TGF-β signaling (Figure 6B), but it was not important for the growth of tumors once established (Figure 6C). HT29-M6^{shCon} or HT29-M6^{shGP130} cells grew with identical kinetics in vitro (Figure S5K) and, in the absence of a source of TGF-β, formed tumors in immunodeficient mice with equivalent latency and frequency (Figure S5L).

Importantly, these GP130-knockdown HT29-M6 cells secreting TGF-β displayed decreased liver take rates during the first hours following intrasplenic inoculation (Figures 6D and 6E) compared to control cells. After the initial phase, the number of tumor cells detected in the liver progressively decreased and, after two weeks, both HT29-M6$^{shCon/TGF-\beta}$ and HT29-M6$^{shGP130/TGF-\beta}$ cells reinitiated expansion with similar kinetics

(E) Incidence of metastasis induced in (C), (D), and (F).

(F) Normalized bioluminescence over time after injection of 5×10^5 KM12L4a^{Con} or KM12L4a$^{TGF-\beta}$ cells. Intensities were normalized to day 0 and arbitrarily set to 100. Values are mean ± SEM (*p < 0.05).

(G and H) Inducible TGF-β cells and recipient mice were treated as in Figure 3G. (G) Bioluminescence over time after injection with 5×10^5 cells. Values, normalized as in (F), are mean ± SEM (*p < 0.05). (H) Number of liver metastases at time of sacrifice. Whiskers: Vmin, Vmax (*p < 0.05, two-tailed Student's t test).

(I and J) p-SMAD2 staining in liver metastasis generated from KM12L4a^{Con} (I) or KM12L4a$^{TGF-\beta}$ cells (J). E, epithelial cells; Str, stromal cells. Scale bars = 10 μm.

(K) Relative expression levels of some stromal TBRS genes in dissected metastatic nodules. Values are mean ± SEM (n = 3).

See also Figure S4.

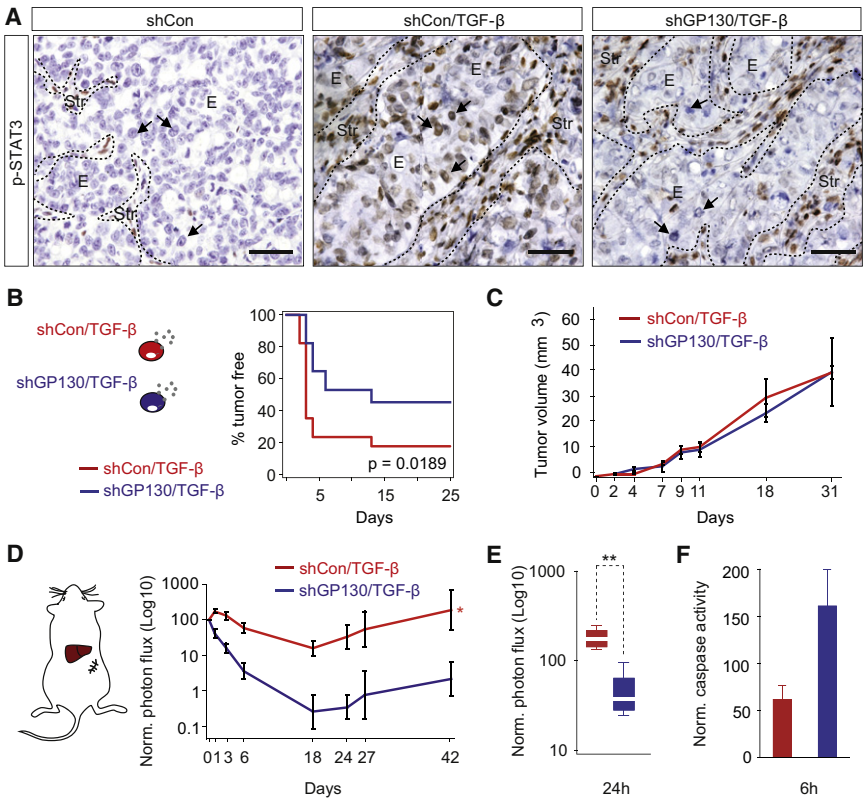

Figure 6. Metastasis Initiation Driven by Stromal TGF-β Signaling Requires GP130/STAT3 in Tumor Cells

(A) p-STAT3 staining in s.c. tumors derived from control (HT29-M6^{shCon}, left panel) cells, HT29-M6 cells that secrete TGF-β (HT29-M6$^{shCon/TGF-β}$, middle panel), or HT29-M6 shGP130 cells that also secrete TGF-β (HT29-M6$^{shGP130/TGF-β}$, right panel). Arrows point to epithelial tumor cell nuclei. E, epithelial cells; Str, stromal cells. Scale bars = 50 μm.

(B) Kaplan-Meier curves for mice injected with 3 × 10^4 HT29-M6$^{shGP130/TGF-β}$ (blue) or HT29-M6$^{shCon/TGF-β}$ cells (red; n = 16).

(C) Growth kinetics of HT29-M6$^{shGP130/TGF-β}$ (blue) and HT29-M6$^{shCon/TGF-β}$ (red) s.c. xenografts (n = 5). Day 1: day of first detection. Values are mean ± SEM.

(D) Bioluminescence over time after IS inoculation of 2 × 10^6 HT29-M6$^{shCon/TGF-β}$ (red) or HT29-M6$^{shGP130/TGF-β}$ (blue) cells. Values, normalized as in Figure 4F, are mean ± SEM (n = 4; *p < 0.05).

(E) Bioluminescence from (D) 24 hr after IS injection. Whiskers: Vmin, Vmax (**p < 0.01, two-tailed Student's t test).

(F) In vivo measurement of caspase 3/7 activity in CRC cells 6 hr after IS injection. Values are mean ratios between caspase activity and total cellular bioluminescence ± SEM (n = 3).

See also Figure S5.

(Figure 6D). The initial clearance of tumor cells is concurrent with apoptosis, as shown by measurement of in vivo caspase activity few hours after inoculation (Figure 6F). In the absence of GP130/STAT3 signaling, apoptosis levels were increased, suggesting that this pathway promotes survival in the context of liver colonization.

Interleukin-11, a TGF-β Target Gene in CAFs, Enhances Metastasis Initiation

Interleukin-11 (IL11), a GP130-binding cytokine, was among the genes highly upregulated by TGF-β in colon fibroblast cultures (F-TBRS, Table S4), although microarray measurements of *IL11* mRNA levels did not associate with cancer recurrence in the cohort of patients with CRC (Table S4). HT29-M6 CRC cells responded to recombinant IL11 by activating the GP130/STAT-3 pathway (Figure 7A). Genes upregulated by IL11 in this cell line constituted an IL11-response signature (IL11RS, Table S4). We found that IL11RS expression correlates tightly with both *TGFB* and FTBRS levels in CRC samples (Figure 7B) and predicts disease relapse (Figures 7C and 7D). Purification of stromal populations from primary human CRC samples showed that CAFs were the only source of IL11 in tumors (Figure 7E). Experimental metastasis generated from TGF-β secreting KM12L4a cells showed a marked upregulation of *IL11* (Figure 7F). Importantly, *IL11* mRNA was reduced to control levels upon LY2157299 treatment of mice bearing CRC stem cell-derived tumors (Figure 7F).

We tested the contribution of IL11 to metastasis by engineering CRC cells to autonomously produce this cytokine. Upon implantation in the cecum of mice, we observed no significant differences in the size (not shown), degree of invasion (Figure 7G), or histological appearance of primary tumors developed by control or study groups (Figures S6A–S6C). Yet, KM12L4a^{IL11} cells effectively colonized liver, lungs, distant lymph nodes, and brain, whereas control cells displayed limited metastatic capacity (Figure 7G, inset table). In the same set of experiments, KM12L4a cells expressing IL6, a cytokine closely related to IL11, displayed a marginal increase in metastatic capacity (Figures S6D and S6E). Intrasplenic inoculation of HT29-M6^{IL11} tumor cells confirmed that IL11 enhanced the liver metastatic potential of CRC cells (Figures 7H–7K). The initial kinetics of metastasis upon intrasplenic inoculation demonstrated that IL11-expressing cells were more proficient at colonizing livers than were control cells (Figures 7I and 7J), an effect that was evident as early as 24 hr after inoculation (Figure 7K). IL11 rescued apoptosis of tumor cells during the first hours of liver colonization (Figure 7L). This behavior paralleled that induced by stromal TGF-β through GP130 signaling in CRC cells shown in Figures 6D–6F.

DISCUSSION

Metastasis involves the regeneration of a full-blown tumor from few disseminated cancer cells. This process is intrinsically inefficient, mainly because of the inability of isolated tumor cells to colonize host tissues and reinitiate tumor growth in a different environment (Luzzi et al., 1998; Valastyan and Weinberg, 2011). The most accepted view is that competences to overcome this initial bottleneck result from Darwinian selection of appropriate genetic alterations in CRC cells. It is not clear, however, how

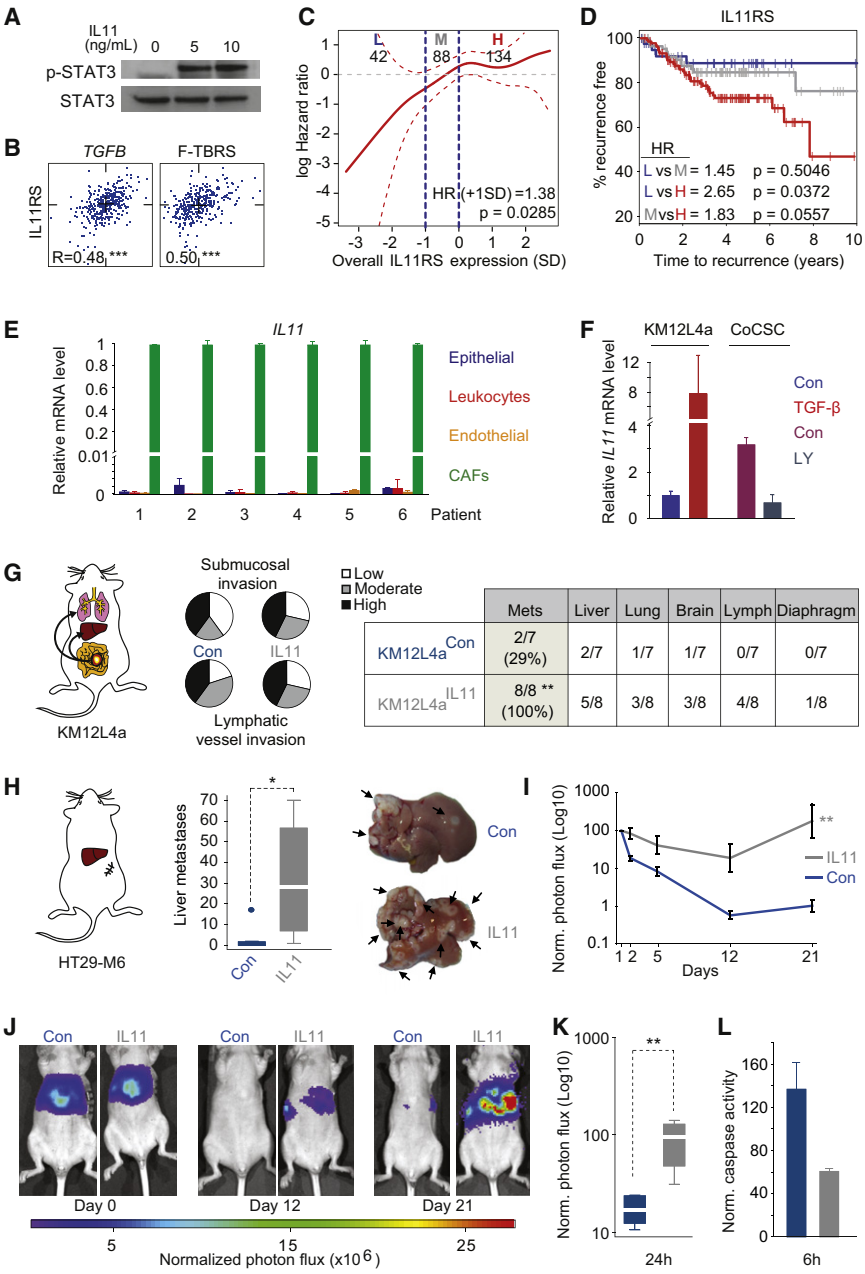

Figure 7. Stromal TGF-β-Induced *IL11* Increases Metastasis Initiation by CRC Cells

(A) Western blot of p-STAT3 and total STAT3 in CRC epithelial cells upon addition of rhIL11.

(B) Cross-correlation analysis between expression of IL11 response signature (IL11RS) and *TGFB* or F-TBRS in the cohort of patients with CRC. Blue dots, patients. R values are indicated (***p < 0.001).

(C) Smooth function correlates IL11RS expression with relative risk of recurrence, patients with stage IV disease excluded. Red dashed lines: 95% CI. Blue dashed lines: thresholds for selection into groups with low (L; blue, 42 patients), medium (M; gray, 88 patients), and high (H; red, 134 patients) IL11RS expression levels. HR (+1SD) and p values are indicated.

(D) Kaplan-Meier plots with RFS for groups defined in (C).

(E) *IL11* mRNA levels in the indicated tumor cell populations from six patients. qRT-PCR values are mean ± SD.

(F) Relative expression levels of *IL11* mRNA in liver metastasis from IS injection with KM12L4a^{Con} (blue) or KM12L4a$^{TGF-\beta}$ (red) (n = 3) and from s.c. tumors generated by CoCSCs treated with either vehicle (Con, purple) or LY2157299 (dark blue) (n = 2). Values are mean ± SEM.

(G) Pie charts evaluate submucosal or lymphatic vessel invasion in KM12L4a^{con}-derived (n = 7) and KM12L4a^{IL11}-derived (n = 8) cecum tumors. Table shows incidence of metastasis in mice (**p < 0.01, Fisher's exact test).

(H–L) Mice inoculated IS with 2 × 10^6 HT29-M6^{Con} cells (blue; n = 7) or HT29-M6^{IL11} cells (gray; n = 4).

(H) Quantification and representative pictures of liver metastases (arrows) at time of sacrifice (*p < 0.05, two-tailed Student's t test). Whiskers: Vmin, Vmax, truncated at 1.5 times the interquartile range. (I) Bioluminescence over time after IS inoculation. Values, normalized as in Figure 4F, are mean ± SEM (**p < 0.01). (J) Representative images from (I). (K) Bioluminescence 24 hr after injection in mice from (I). Whiskers: Vmin, Vmax (**p < 0.01, two-tailed Student's t test). (L) In vivo caspase 3/7 activity 6 hr after IS injection of HT29-M6^{con} or HT29-M6^{IL11} cells. Values are mean ± SEM.

See also Figure S6.

functions required for colonizing a foreign organ could be selected in the primary tumor where the specific constraints imposed by a different tissue environment are not present (Luzzi et al., 1998; Valastyan and Weinberg, 2011). Additionally, metastatic traits could be acquired after cancer cells have reached the metastatic site, yet this event would necessarily require that tumor cells gain extravasation capacity and survive in the host environment. Our data argue that key functions required to overcome the initial phase of metastasis are provided by the TGF-β-activated microenvironment. Without the activity of this stromal program, fully aggressive CRC cells fail to colonize the host organ. We speculate that those tumor cells capable of initiating metastasis with high efficiency would possess the capacity to raise such TGF-β response in the environment. During metastatic colonization, tumor cells may instruct the stroma of the host organ by either secreting TGF-β or recruiting TGF-β-producing cells such macrophages, CAFs, or platelets. An alternative hypothesis is that a TGF-β-driven premetastatic niche could be specified by the primary tumor in foreign tissues through secretion of systemic cytokines, including TGF-β itself.

Among the benefits that CRCs obtain via crosstalk with the TGF-β-subverted microenvironment is GP130/STAT3 signaling, which suppresses apoptotic stimuli encountered during the colonization of the metastatic site. Fitting these observations, it has been shown that p-STAT3 accumulation in primary CRC samples associates to advanced disease and poor outcome (Kusaba et al., 2006; Morikawa et al., 2011). Indeed, the GP130-binding cytokine IL11, which is secreted by TGF-β

stimulated CAFs, confers robust metastatic capacity to CRC cells. On a side note, IL11 is also a megakaryopoietic cytokine that stimulates platelet production (Musashi et al., 1991; Teramura et al., 1992), and recombinant IL11 is an efficient supportive therapy in patients with malignancies who develop thrombocytopenia as a side effect of chemotherapeutic treatment (Bhatia et al., 2007). Therefore, the prometastatic effect of IL11 described here calls for a reassessment of the use of this cytokine in an adjuvant setting. On the other hand, correlations between elevated platelet counts, referred to as thrombocytosis, and poor prognosis have been reported for many solid cancers, including gastrointestinal tumors (Ikeda et al., 2002; Nouso et al., 2008). Platelets protect circulating tumor cells from immune system, as well as assist them during extravasation (Gay and Felding-Habermann, 2011). In addition, platelets are a rich source of TGF-β (Labelle et al., 2011). It is thus possible that tumor-derived TGF-β may promote IL11 production from stromal cells to increase platelet activation, which may further enhance stromal TGF-β response.

Besides IL11, the TGF-β response signatures include some previously described prometastatic factors in other tumor types, such as ANGPTL4 (Padua et al., 2008), PTHLH (Yin et al., 1999), HBEGF (Bos et al., 2009), CTGF (Kang et al., 2003), TNC (Oskarsson et al., 2011), and JAG1 (Sethi et al., 2011; Sonoshita et al., 2011). For instance, *ANGPTL4* mRNA levels are induced by TGF-β in fibroblasts (Table S4). This secreted factor has been previously shown to mediate intravasation of breast cancer cells into lungs (Padua et al., 2008). Consistent with this observation, our assays show enhancement of lung metastatic capacity by CRC cells upon activation of stromal TGF-β program. JAG1 participates in breast cancer metastasis to the bone (Sethi et al., 2011), and activation of Notch signaling in CRC cells by endothelial cell-expressed JAG1 promotes transendothelial migration during liver and lung metastasis (Sonoshita et al., 2011). Indeed, we found that *JAG1* is a TGF-β response gene in endothelial cells (Table S4). Therefore, besides survival during the colonization phase of metastasis, the program activated by TGF-β in the microenvironment likely influences additional functions required to complete the metastasic process. Importantly, in contrast to CRC, the expression of *ANGPTL4*, *PTHLH*, *CTGF*, or *JAG1* is induced autonomously in breast cancer cells activated by TGF-β (Kang et al., 2003; Padua et al., 2008; Yin et al., 1999). *IL11* itself is a TGF-β target gene in breast cancer cells, with an important role during bone metastasis formation (Kang et al., 2005; Kang et al., 2003). It thus appears that, in the context of a lack of response to TGF-β, CRC cells instead achieve similar abilities by engaging the microenvironment in a TGF-β-dependent manner. It would be interesting to analyze whether this may be a general response in other cancer types that bear inactivating mutations in TGF-β pathway components, such as pancreatic cancer.

The invasive adenocarcinomas developed in mouse models bearing compound mutations in *Smad4* and *Apc* course with a prominent accumulation of reactive stroma (Kitamura et al., 2009; Takaku et al., 1998). Although it is not clear whether this effect depends on increased levels of TGF-β signaling in the microenvironment, *Tgfbr2* deletion in an *Apc* mutant background raises production of TGFB1 in tumors (Muñoz et al., 2006). It is thus plausible that CRCs evolve toward a favorable scenario for metastasis by combining an increase of TGF-β signaling in stromal cells with the acquisition of inactivating mutations in TGF-β pathway components in the cancer cells. The majority of CRCs display moderate-to-high TGF-β expression levels, which may help explain the high rates of CRC metastasis. Importantly, we discovered a subgroup of tumors (10%–20% of all CRCs) displaying invasion and/or local dissemination (i.e., AJCC stage II and III) yet with low TGF-β production that did not relapse after surgical intervention. Therefore, besides AJCC staging, our findings call for the assessment of TGF-β pathway activation in stromal cells as a central criterion for patient stratification. Several targeted therapies against TGF-β signaling, including LY2157299, are currently being evaluated for treatment of different cancer types (Tan et al., 2009; Yingling et al., 2004). Although their efficacy is not yet known, our observations predict that pharmacological inhibition of TGF-β signaling may prevent CRC relapse and metastasis when treating patients at early time point of the process.

EXPERIMENTAL PROCEDURES

Profile Data Sets

We defined overall TGF-β levels (*TGFB*) as the average expression of *TGFB1*, *TGFB2*, and *TGFB3* mRNAs in a given sample (see Supplemental Information). Data sets corresponding to human colon adenomas and carcinomas have been previously described (Sabates-Bellver et al., 2007; Van der Flier et al., 2007). To correlate *TGFB* and TBRS expression with clinical disease progression, we pooled two publicly available sets of Affymetrix transcriptomic profiles (GSE17537 and GSE14333) corresponding to primary CRCs for which clinical follow-up was available. GSE17537 (Smith et al., 2010) is composed of 55 patients with colon cancer treated at Vanderbilt University Medical Center (Nashville, TN, USA). GSE14333 (Jorissen et al., 2009) contains a pool of 290 patients with CRC treated at two different hospitals: Peter MacCallum Cancer Center (Australia) and H. Lee Moffitt Cancer Center (USA). The representation of tumor samples at different AJCC stages in these cohorts follows the natural distribution of patients with CRC receiving standard treatment in the aforementioned hospitals. Descriptive statistics (Table S1) as well as univariate analysis of clinical progression parameters (Table S2) in this metacohort are included as Supplemental Information. The TGF-β response signatures used in this study are detailed in Table S4.

Orthotopic Mouse Studies

All experiments with mouse models were approved by the animal care and use committee of the Barcelona Science Park (CEEA-PCB) and the Catalan Government. Cells were injected subcutaneously in 5–6–week-old Swiss nude or NSG mice (Jackson Laboratories), which were followed for the periods described. Tumor appearance was assessed by palpation. Five-to-six-week-old Balb/c nude or NSG mice (Jackson Laboratories) were used to perform metastasis experiments by intrasplenic injection (Warren et al., 1995) or intracecum injection (Céspedes et al., 2007).

Clinical Material

Biological samples were obtained from individuals treated at the Hospital del Mar (Barcelona, Spain) or from Hospital Clinic (Barcelona, Spain) under informed consent and approval of the Bank Tumor Committees of each hospital according to Spanish Ethical regulations. The study followed the guidelines of the Declaration of Helsinki and patient's identity of pathological specimens remained anonymous in the context of this study. Experiments were approved by the ethics committee of IRB/Hospital Clinic (project ERC-208488/CRCprogramme).

ACCESSION NUMBERS

The transcriptomic data sets generated for this study have been deposited in GEO with accession number GSE39397. This SuperSeries contains the

subset series GSE39394, GSE39395, and GSE39396 as detailed in Supplemental Experimental Procedures.

SUPPLEMENTAL INFORMATION

Supplemental Information includes six figures, four tables, and Supplemental Experimental Procedures and can be found with this article online at http://dx.doi.org/10.1016/j.ccr.2012.08.013.

ACKNOWLEDGMENTS

We thank the Institute for Research in Biomedicine Functional Genomics Core Facility for technical assistance in microarray hybridization experiments, Jonathan Cheng (Fox Chase Cancer Center) for the anti-FAP antibody, Mark Taketo (Kyoto University) for mouse tumor samples, Elisabeth Calderón and Azucena Salas (IDIBAPS, Barcelona) for support with tumor samples, Xavier Hernando for assistance in the animal facility, Jacob Sabates and Giancarlo Marra (IMZR, Zurich) for sharing the Ad-CRC Affymetrix patient data set, Jaume Comas and Ricard Álvarez, (UB, Barcelona) for expert technical assistance with the FACS, Iris Joval for assistance in mounting figures, and all members of the Batlle laboratory for support and discussions. A.C. and D.V.F.T each hold a Juan de la Cierva postdoctoral fellowship, and E.E. has an FPI PhD fellowship (both from Spanish Ministry of Science and Innovation). J.M. is an Investigator of the Howard Hughes Medical Institute. This work has been supported by grants from Instituto de Salud Carlos III FEDER (RD09/0076/00036) and the "Xarxa de Bancs de tumors" sponsored by Pla Director d'Oncologia de Catalunya (XBTC), the European Research Council (Starting Grant no. 208488) and Consolider programmes (MICINN) (both to E.B.), the Spanish Ministry of Science and Innovation (Grants SAF2006-02170 and SAF2009-11757 to E.S.), the National Institutes of Health (Grant CA34610 to J.M.), Fundación BBVA (grant to IRB Barcelona and the Metlab), and Grants PS09/00965 (MICINN) and NanoCoMets (CIBERBBN) (both to R.M.).

Received: February 14, 2012
Revised: June 18, 2012
Accepted: August 17, 2012
Published: November 12, 2012

REFERENCES

Alarcón, C., Zaromytidou, A.I., Xi, Q., Gao, S., Yu, J., Fujisawa, S., Barlas, A., Miller, A.N., Manova-Todorova, K., Macias, M.J., et al. (2009). Nuclear CDKs drive Smad transcriptional activation and turnover in BMP and TGF-beta pathways. Cell *139*, 757–769.

Becker, C., Fantini, M.C., Schramm, C., Lehr, H.A., Wirtz, S., Nikolaev, A., Burg, J., Strand, S., Kiesslich, R., Huber, S., et al. (2004). TGF-beta suppresses tumor progression in colon cancer by inhibition of IL-6 trans-signaling. Immunity *21*, 491–501.

Bhatia, M., Davenport, V., and Cairo, M.S. (2007). The role of interleukin-11 to prevent chemotherapy-induced thrombocytopenia in patients with solid tumors, lymphoma, acute myeloid leukemia and bone marrow failure syndromes. Leuk. Lymphoma *48*, 9–15.

Bos, P.D., Zhang, X.H., Nadal, C., Shu, W., Gomis, R.R., Nguyen, D.X., Minn, A.J., van de Vijver, M.J., Gerald, W.L., Foekens, J.A., and Massagué, J. (2009). Genes that mediate breast cancer metastasis to the brain. Nature *459*, 1005–1009.

Bueno, L., de Alwis, D.P., Pitou, C., Yingling, J., Lahn, M., Glatt, S., and Trocóniz, I.F. (2008). Semi-mechanistic modelling of the tumour growth inhibitory effects of LY2157299, a new type I receptor TGF-beta kinase antagonist, in mice. Eur. J. Cancer *44*, 142–150.

Céspedes, M.V., Espina, C., García-Cabezas, M.A., Trias, M., Boluda, A., Gómez del Pulgar, M.T., Sancho, F.J., Nistal, M., Lacal, J.C., and Mangues, R. (2007). Orthotopic microinjection of human colon cancer cells in nude mice induces tumor foci in all clinically relevant metastatic sites. Am. J. Pathol. *170*, 1077–1085.

Flavell, R.A., Sanjabi, S., Wrzesinski, S.H., and Licona-Limón, P. (2010). The polarization of immune cells in the tumour environment by TGFbeta. Nat. Rev. Immunol. *10*, 554–567.

Gay, L.J., and Felding-Habermann, B. (2011). Contribution of platelets to tumour metastasis. Nat. Rev. Cancer *11*, 123–134.

Grady, W.M., and Markowitz, S.D. (2002). Genetic and epigenetic alterations in colon cancer. Annu. Rev. Genomics Hum. Genet. *3*, 101–128.

Hahn, J.N., Falck, V.G., and Jirik, F.R. (2011). Smad4 deficiency in T cells leads to the Th17-associated development of premalignant gastroduodenal lesions in mice. J. Clin. Invest. *121*, 4030–4042.

Ikeda, M., Furukawa, H., Imamura, H., Shimizu, J., Ishida, H., Masutani, S., Tatsuta, M., and Satomi, T. (2002). Poor prognosis associated with thrombocytosis in patients with gastric cancer. Ann. Surg. Oncol. *9*, 287–291.

Jones, S., Chen, W.D., Parmigiani, G., Diehl, F., Beerenwinkel, N., Antal, T., Traulsen, A., Nowak, M.A., Siegel, C., Velculescu, V.E., et al. (2008). Comparative lesion sequencing provides insights into tumor evolution. Proc. Natl. Acad. Sci. USA *105*, 4283–4288.

Jorissen, R.N., Gibbs, P., Christie, M., Prakash, S., Lipton, L., Desai, J., Kerr, D., Aaltonen, L.A., Arango, D., Kruhøffer, M., et al. (2009). Metastasis-associated gene expression changes predict poor outcomes in patients with Dukes stage B and C colorectal cancer. Clin. Cancer Res. *15*, 7642–7651.

Jung, P., Sato, T., Merlos-Suárez, A., Barriga, F.M., Iglesias, M., Rossell, D., Auer, H., Gallardo, M., Blasco, M.A., Sancho, E., et al. (2011). Isolation and in vitro expansion of human colonic stem cells. Nat. Med. *17*, 1225–1227.

Kang, Y., Siegel, P.M., Shu, W., Drobnjak, M., Kakonen, S.M., Cordón-Cardo, C., Guise, T.A., and Massagué, J. (2003). A multigenic program mediating breast cancer metastasis to bone. Cancer Cell *3*, 537–549.

Kang, Y., He, W., Tulley, S., Gupta, G.P., Serganova, I., Chen, C.R., Manova-Todorova, K., Blasberg, R., Gerald, W.L., and Massagué, J. (2005). Breast cancer bone metastasis mediated by the Smad tumor suppressor pathway. Proc. Natl. Acad. Sci. USA *102*, 13909–13914.

Kim, B.G., Li, C., Qiao, W., Mamura, M., Kasprzak, B., Anver, M., Wolfraim, L., Hong, S., Mushinski, E., Potter, M., et al. (2006). Smad4 signalling in T cells is required for suppression of gastrointestinal cancer. Nature *441*, 1015–1019.

Kitamura, T., Biyajima, K., Aoki, M., Oshima, M., and Taketo, M.M. (2009). Matrix metalloproteinase 7 is required for tumor formation, but dispensable for invasion and fibrosis in SMAD4-deficient intestinal adenocarcinomas. Lab. Invest. *89*, 98–105.

Kusaba, T., Nakayama, T., Yamazumi, K., Yakata, Y., Yoshizaki, A., Inoue, K., Nagayasu, T., and Sekine, I. (2006). Activation of STAT3 is a marker of poor prognosis in human colorectal cancer. Oncol. Rep. *15*, 1445–1451.

Labelle, M., Begum, S., and Hynes, R.O. (2011). Direct signaling between platelets and cancer cells induces an epithelial-mesenchymal-like transition and promotes metastasis. Cancer Cell *20*, 576–590.

Liu, F., Pouponnot, C., and Massagué, J. (1997). Dual role of the Smad4/DPC4 tumor suppressor in TGFbeta-inducible transcriptional complexes. Genes Dev. *11*, 3157–3167.

Luzzi, K.J., MacDonald, I.C., Schmidt, E.E., Kerkvliet, N., Morris, V.L., Chambers, A.F., and Groom, A.C. (1998). Multistep nature of metastatic inefficiency: dormancy of solitary cells after successful extravasation and limited survival of early micrometastases. Am. J. Pathol. *153*, 865–873.

Markowitz, S.D., and Bertagnolli, M.M. (2009). Molecular origins of cancer: molecular basis of colorectal cancer. N. Engl. J. Med. *361*, 2449–2460.

Markowitz, S., Wang, J., Myeroff, L., Parsons, R., Sun, L., Lutterbaugh, J., Fan, R.S., Zborowska, E., Kinzler, K.W., Vogelstein, B., et al. (1995). Inactivation of the type II TGF-beta receptor in colon cancer cells with microsatellite instability. Science *268*, 1336–1338.

Massagué, J. (2008). TGFbeta in Cancer. Cell *134*, 215–230.

Merlos-Suárez, A., Barriga, F.M., Jung, P., Iglesias, M., Céspedes, M.V., Rossell, D., Sevillano, M., Hernando-Momblona, X., da Silva-Diz, V., Muñoz, P., et al. (2011). The intestinal stem cell signature identifies colorectal cancer stem cells and predicts disease relapse. Cell Stem Cell *8*, 511–524.

Morikawa, K., Walker, S.M., Nakajima, M., Pathak, S., Jessup, J.M., and Fidler, I.J. (1988). Influence of organ environment on the growth, selection,

and metastasis of human colon carcinoma cells in nude mice. Cancer Res. *48*, 6863–6871.

Morikawa, T., Baba, Y., Yamauchi, M., Kuchiba, A., Nosho, K., Shima, K., Tanaka, N., Huttenhower, C., Frank, D.A., Fuchs, C.S., and Ogino, S. (2011). STAT3 expression, molecular features, inflammation patterns, and prognosis in a database of 724 colorectal cancers. Clin. Cancer Res. *17*, 1452–1462.

Muñoz, N.M., Upton, M., Rojas, A., Washington, M.K., Lin, L., Chytil, A., Sozmen, E.G., Madison, B.B., Pozzi, A., Moon, R.T., et al. (2006). Transforming growth factor beta receptor type II inactivation induces the malignant transformation of intestinal neoplasms initiated by Apc mutation. Cancer Res. *66*, 9837–9844.

Musashi, M., Yang, Y.C., Paul, S.R., Clark, S.C., Sudo, T., and Ogawa, M. (1991). Direct and synergistic effects of interleukin 11 on murine hemopoiesis in culture. Proc. Natl. Acad. Sci. USA *88*, 765–769.

Nouso, K., Ito, Y., Kuwaki, K., Kobayashi, Y., Nakamura, S., Ohashi, Y., and Yamamoto, K. (2008). Prognostic factors and treatment effects for hepatocellular carcinoma in Child C cirrhosis. Br. J. Cancer *98*, 1161–1165.

Oskarsson, T., Acharyya, S., Zhang, X.H., Vanharanta, S., Tavazoie, S.F., Morris, P.G., Downey, R.J., Manova-Todorova, K., Brogi, E., and Massagué, J. (2011). Breast cancer cells produce tenascin C as a metastatic niche component to colonize the lungs. Nat. Med. *17*, 867–874.

Padua, D., Zhang, X.H., Wang, Q., Nadal, C., Gerald, W.L., Gomis, R.R., and Massagué, J. (2008). TGFbeta primes breast tumors for lung metastasis seeding through angiopoietin-like 4. Cell *133*, 66–77.

Sabates-Bellver, J., Van der Flier, L.G., de Palo, M., Cattaneo, E., Maake, C., Rehrauer, H., Laczko, E., Kurowski, M.A., Bujnicki, J.M., Menigatti, M., et al. (2007). Transcriptome profile of human colorectal adenomas. Mol. Cancer Res. *5*, 1263–1275.

Sato, T., Stange, D.E., Ferrante, M., Vries, R.G., Van Es, J.H., Van den Brink, S., Van Houdt, W.J., Pronk, A., Van Gorp, J., Siersema, P.D., and Clevers, H. (2011). Long-term expansion of epithelial organoids from human colon, adenoma, adenocarcinoma, and Barrett's epithelium. Gastroenterology *141*, 1762–1772.

Sethi, N., Dai, X., Winter, C.G., and Kang, Y. (2011). Tumor-derived JAGGED1 promotes osteolytic bone metastasis of breast cancer by engaging notch signaling in bone cells. Cancer Cell *19*, 192–205.

Shultz, L.D., Ishikawa, F., and Greiner, D.L. (2007). Humanized mice in translational biomedical research. Nat. Rev. Immunol. *7*, 118–130.

Smith, J.J., Deane, N.G., Wu, F., Merchant, N.B., Zhang, B., Jiang, A., Lu, P., Johnson, J.C., Schmidt, C., Bailey, C.E., et al. (2010). Experimentally derived metastasis gene expression profile predicts recurrence and death in patients with colon cancer. Gastroenterology *138*, 958–968.

Sonoshita, M., Aoki, M., Fuwa, H., Aoki, K., Hosogi, H., Sakai, Y., Hashida, H., Takabayashi, A., Sasaki, M., Robine, S., et al. (2011). Suppression of colon cancer metastasis by Aes through inhibition of Notch signaling. Cancer Cell *19*, 125–137.

Subramanian, A., Tamayo, P., Mootha, V.K., Mukherjee, S., Ebert, B.L., Gillette, M.A., Paulovich, A., Pomeroy, S.L., Golub, T.R., Lander, E.S., and Mesirov, J.P. (2005). Gene set enrichment analysis: a knowledge-based approach for interpreting genome-wide expression profiles. Proc. Natl. Acad. Sci. USA *102*, 15545–15550.

Takaku, K., Oshima, M., Miyoshi, H., Matsui, M., Seldin, M.F., and Taketo, M.M. (1998). Intestinal tumorigenesis in compound mutant mice of both Dpc4 (Smad4) and Apc genes. Cell *92*, 645–656.

Tan, A.R., Alexe, G., and Reiss, M. (2009). Transforming growth factor-beta signaling: emerging stem cell target in metastatic breast cancer? Breast Cancer Res. Treat. *115*, 453–495.

Teramura, M., Kobayashi, S., Hoshino, S., Oshimi, K., and Mizoguchi, H. (1992). Interleukin-11 enhances human megakaryocytopoiesis in vitro. Blood *79*, 327–331.

Tsushima, H., Ito, N., Tamura, S., Matsuda, Y., Inada, M., Yabuuchi, I., Imai, Y., Nagashima, R., Misawa, H., Takeda, H., et al. (2001). Circulating transforming growth factor beta 1 as a predictor of liver metastasis after resection in colorectal cancer. Clin. Cancer Res. *7*, 1258–1262.

Valastyan, S., and Weinberg, R.A. (2011). Tumor metastasis: molecular insights and evolving paradigms. Cell *147*, 275–292.

Van der Flier, L.G., Sabates-Bellver, J., Oving, I., Haegebarth, A., De Palo, M., Anti, M., Van Gijn, M.E., Suijkerbuijk, S., Van de Wetering, M., Marra, G., and Clevers, H. (2007). The intestinal Wnt/TCF signature. Gastroenterology *132*, 628–632.

Walther, A., Johnstone, E., Swanton, C., Midgley, R., Tomlinson, I., and Kerr, D. (2009). Genetic prognostic and predictive markers in colorectal cancer. Nat. Rev. Cancer *9*, 489–499.

Wang, J., Sun, L., Myeroff, L., Wang, X., Gentry, L.E., Yang, J., Liang, J., Zborowska, E., Markowitz, S., Willson, J.K., et al. (1995). Demonstration that mutation of the type II transforming growth factor beta receptor inactivates its tumor suppressor activity in replication error-positive colon carcinoma cells. J. Biol. Chem. *270*, 22044–22049.

Warren, R.S., Yuan, H., Matli, M.R., Gillett, N.A., and Ferrara, N. (1995). Regulation by vascular endothelial growth factor of human colon cancer tumorigenesis in a mouse model of experimental liver metastasis. J. Clin. Invest. *95*, 1789–1797.

Yin, J.J., Selander, K., Chirgwin, J.M., Dallas, M., Grubbs, B.G., Wieser, R., Massagué, J., Mundy, G.R., and Guise, T.A. (1999). TGF-beta signaling blockade inhibits PTHrP secretion by breast cancer cells and bone metastases development. J. Clin. Invest. *103*, 197–206.

Yingling, J.M., Blanchard, K.L., and Sawyer, J.S. (2004). Development of TGF-beta signalling inhibitors for cancer therapy. Nat. Rev. Drug Discov. *3*, 1011–1022.

Cancer Cell
Article

Crosstalk between ROR1 and the Pre-B Cell Receptor Promotes Survival of t(1;19) Acute Lymphoblastic Leukemia

Vincent T. Bicocca,[1,5] Bill H. Chang,[2,5] Behzad Kharabi Masouleh,[6] Markus Muschen,[6,7] Marc M. Loriaux,[3,5] Brian J. Druker,[1,5,8] and Jeffrey W. Tyner[4,5,*]
[1]Division of Hematology and Medical Oncology
[2]Division of Pediatric Hematology and Oncology, Department of Pediatrics
[3]Department of Pathology
[4]Department of Cell and Developmental Biology
Oregon Health & Science University, Portland, OR 97239, USA
[5]Knight Cancer Institute, Portland, OR 97239, USA
[6]Childrens Hospital Los Angeles and Leukemia and Lymphoma Program, Norris Comprehensive Cancer Center, University of Southern California, Los Angeles, CA 90027, USA
[7]Department of Laboratory Medicine, University of California San Francisco, San Francisco, CA 94143, USA
[8]Howard Hughes Medical Institute, Portland, OR 97239, USA
*Correspondence: tynerj@ohsu.edu
http://dx.doi.org/10.1016/j.ccr.2012.08.027

SUMMARY

We report that t(1;19) ALL cells universally exhibit expression of and dependence on the cell surface receptor ROR1. We further identify t(1;19) ALL cell sensitivity to the kinase inhibitor dasatinib due to its inhibition of the pre-B cell receptor (pre-BCR) signaling complex. These phenotypes are a consequence of developmental arrest at an intermediate/late stage of B-lineage maturation. Additionally, inhibition of pre-BCR signaling induces further ROR1 upregulation, and we identify distinct ROR1 and pre-BCR downstream signaling pathways that are modulated in a counterbalancing manner—both leading to AKT phosphorylation. Consistent with this, AKT phosphorylation is transiently eliminated after dasatinib treatment, but is partially restored following dasatinib potentiation of ROR1 expression. Consequently, ROR1 silencing accentuates dasatinib killing of t(1;19) ALL cells.

INTRODUCTION

Acute lymphoblastic leukemia (ALL) is the most common form of childhood malignancy, accounting for 25% of all childhood cancers. Although great strides have been made in the treatment of childhood leukemia, close to 20% of patients will have resistant disease eventually leading to death. To improve outcomes for these patients, it is critical to develop new therapeutic strategies that specifically target the cellular processes causing malignancy. This necessitates a comprehensive knowledge of the gene targets driving oncogenesis in each patient. From both a biological and clinical standpoint, tyrosine kinases represent an important gene family for interrogation because tyrosine kinases have been implicated in the genesis of a wide variety of malignancies, including certain subsets of ALL, and tyrosine kinase inhibitors are already in clinical use with remarkable outcomes (Krause and Van Etten, 2005). Unfortunately, most patients with ALL still present without knowledge of the specific tyrosine kinases that are operationally important in disease pathogenesis. As such, we have performed functional profiling to identify tyrosine kinase targets in patients with ALL.

Significance

The 1;19 translocation is one of the most common recurring chromosomal abnormalities in acute lymphoblastic leukemia (ALL). We have identified a therapeutic gene target, ROR1, for t(1;19) ALL. We have also identified a kinase inhibitor, dasatinib, with universal efficacy against t(1;19) ALL cells due to inhibition of the pre-B cell receptor (pre-BCR)—another oncorequisite pathway for t(1;19) ALL. These phenotypes are recapitulated in other ALL cells of intermediate developmental stage, such as t(17;19) ALL, as well as mature B cell malignancies, such as t(8;14) Burkitt's. Finally, we have identified signaling pathways downstream of ROR1, which cooperate with pre-BCR signaling. Our findings highlight a functional link between the pre-BCR and ROR1 and the importance of inhibiting both pathways to augment tumor cell killing.

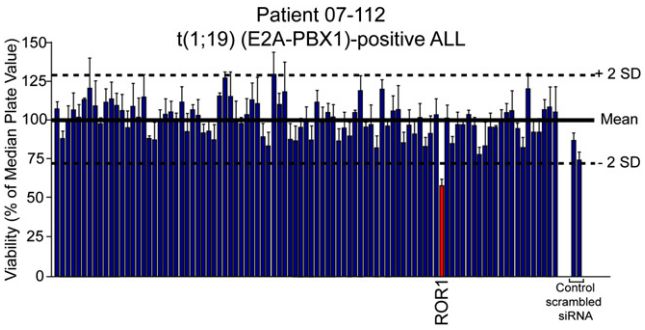

Figure 1. ROR1 Is a Functional Target in t(1;19) ALL

White blood cells (2.25×10^7) from a t(1;19)-positive patient with ALL (07-112) were suspended in siPORT buffer and incubated with 1 μM siRNA from an siRNA library individually targeting each member of the tyrosine kinase family as well as N-RAS, K-RAS, and single and pooled nonspecific siRNA controls. Cells were electroporated on a 96-well electroporation plate at 1110 V (equivalent of 150 V), 200 μs, and 2 pulses. Cells were replated into culture media, and cell viability was determined by addition of a tetrazolium salt (MTS assay) at day 4 after electroporation. Values represent percentage mean (normalized to the median value on the plate) ± SEM (n = 3).
See also Figure S1.

One of the most common, recurring translocations found in patients with ALL is t(1;19)(q23;p13), which is observed in approximately 5% of all pediatric ALL cases as well as 1%–2% of adult ALL cases. Greater than 90% of patients with t(1;19) exhibit blasts with expression of cytoplasmic immunoglobulin heavy-chain μ (Igμ) and an absence of CD34 on the cell surface, indicating that t(1;19) blasts are typically arrested at a later stage of B cell differentiation (large/small pre-BII) compared with most other ALL subsets (Hunger, 1996; Williams et al., 1984). The 1;19 translocation results in the fusion transcription factor complex *E2A-PBX1* (Hunger et al., 1991; Kamps et al., 1991), which has been shown to induce myeloid, T-lymphoid, and B-lymphoid malignancies in mouse models (Bijl et al., 2005; Dedera et al., 1993; Kamps and Baltimore, 1993; Kamps et al., 1991).

RESULTS

ROR1 Is a Therapeutic Gene Target in t(1;19) ALL

To identify tyrosine kinase gene targets in patients with ALL, we tested clinical specimens from pediatric patients with ALL by gene-silencing with an siRNA library that collectively targets the tyrosine kinome. Cells were electroporated with prevalidated siRNAs that individually target each tyrosine kinase, as well as nonspecific control siRNA (Tyner et al., 2008, 2009). After 4 days in culture, cells were subjected to an MTS assay for assessment of cell viability. Evaluation of the t(1;19)-positive sample 07-112 revealed hypersensitivity to siRNA targeting the receptor tyrosine kinase ROR1 (Figure 1; see Figure S1A available online). Other ALL cases with normal karyotype (sample 08-026 is used as an example), did not exhibit sensitivity to ROR1 silencing (Figure S1B). Further evaluation by RT-PCR revealed overexpression of ROR1 in sample 07-112 at levels comparable to artificial ROR1 overexpression in Ba/F3 cells, whereas sample 08-026 did not exhibit detectable ROR1 expression (Figure S1C).

ROR1 Expression and Functional Dependence Is Universal in t(1;19) ALL

To test whether the ectopic expression of ROR1 observed in t(1;19) patient 07-112 was uniformly detectable in all t(1;19) ALL samples, we obtained ten pediatric ALL samples (generously provided by the Children's Oncology Group ALL Biology Laboratory) and two cell lines that are positive for t(1;19) and compared them with five pediatric ALL samples and two cell lines that are t(1;19) negative. We observed that all t(1;19)-positive samples exhibited ROR1 overexpression, whereas none of the t(1;19)-negative samples or normal white blood cells displayed the same phenotype (Figure 2A; Figure S2A). Overexpression of ROR1 protein was also observed by immunoblot and FACS analysis on t(1;19)-positive cells (Figures 2B and 2C).

To assess the extent and exclusivity of ROR1 expression in a larger cohort of patient samples, we examined microarray meta-analysis data generated from pediatric patients with ALL and normal B cell progenitors (Trageser et al., 2009). We compared t(1;19) patients with ALL with those carrying t(9;22) (*BCR-ABL*), t(12;21) (*ETV6-RUNX1*), or patients with *MLL* (11q23) gene rearrangements. In addition, we evaluated ROR1 levels in distinct, normal B-lineage progenitor populations ($CD34^+$ Lin^-, pro-B, pre-BI, pre-BII large, pre-BII small, and immature B cells). We observed higher levels of ROR1 expression on every t(1;19) patient compared with all patients from each of the other leukemic subsets. Similarly, t(1;19) patients showed higher levels of ROR1 expression compared with normal B cell progenitor populations at the earliest stages of B-lineage development ($CD34^+$ Lin^-, pro-B, and pre-BI). However, when compared with normal B-lineage cells at an intermediate stage of B cell development (large/small pre-BII and immature B), we observed high levels of ROR1, similar to those seen on t(1;19) cells (Figure 2D). These results support recent findings showing ROR1 cell surface expression on intermediate stages of normal B cell development (Broome et al., 2011; Hudecek et al., 2010). Importantly, these and other studies did not observe ROR1 expression on normal, mature B cells or plasma cells (Baskar et al., 2008; Fukuda et al., 2008; Hudecek et al., 2010). Hence, in nonmalignant B-lineage cells, ROR1 expression appears to be absent at the earliest stages of development, becomes highly expressed at intermediate/late stages, and is then downregulated in normal, mature B cells. Interestingly, the vast majority of blasts from t(1;19) patients are arrested at this intermediate/late stage of B-lineage development (large/small pre-BII). Hence, these data suggest that high ROR1 expression in t(1;19) may be a product of the comparatively mature differentiation state of these malignant blasts and may not be due to aberrant transcription profiles of the chimeric transcription factor E2A-PBX1. Subsequent examination of the E2A-PBX1 transcription factor in t(1;19) cell lines supports this hypothesis, because siRNA-mediated knockdown of E2A-PBX1 in the t(1;19) cell line RCH-ACV showed a corresponding knockdown of the E2A-PBX1 transcriptional target WNT16B (McWhirter et al., 1999), but had no effect on expression of ROR1 (Figure S2B).

Because the two t(1;19) cell lines, RCH-ACV and Kasumi-2, recapitulated the ROR1 expression profile observed in t(1;19)-positive primary specimens, we next tested whether these cell

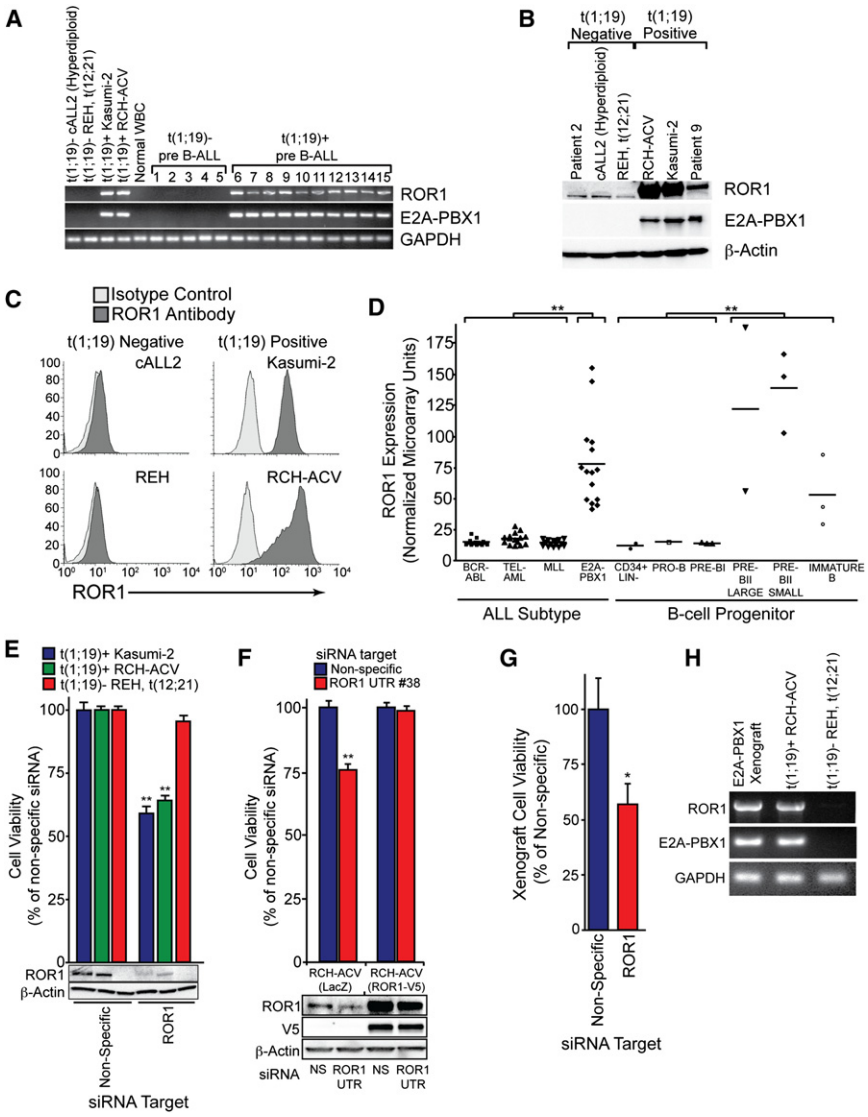

Figure 2. ROR1 Is Universally Expressed and a Therapeutic Target in t(1;19) ALL

(A) cDNA derived from t(1;19)-positive and -negative cell lines and primary patient samples was amplified using primers specific for ROR1, E2A-PBX1, or GAPDH, and PCR products were analyzed by gel electrophoresis.

(B) Whole-cell extracts derived from t(1;19)-positive and -negative cell lines and primary patient samples were subjected to immunoblot analysis using antibodies specific for ROR1, E2A-PBX1, or β-Actin.

(C) Flow cytometric analysis of t(1;19)-positive and -negative cell lines was performed using specific polyclonal antihuman ROR1 antibodies (dark gray histogram) versus isotype control (light gray histogram).

(D) Gene expression microarray data for pediatric patients with ALL and normal B cell progenitor populations were compiled into a meta-analysis. Patients with *MLL* gene rearrangements t(9;22) (BCR-ABL), t(12;21) (TEL-AML), or t(1;19) (E2A-PBX1) (n = 15 for each subset) and nonmalignant B cell progenitor populations ($CD34^+$ Lin^-, pro-B, pre-B, pre-BII large, pre-BII small, and immature B) (n = 15 total) were examined, and Affymetrix intensity values for ROR1 are plotted for each individual patient sample (**$p < 0.01$).

(E) RCH-ACV or Kasumi-2 cells (both t(1;19)-positive) as well as REH cells (t(12;21)-positive) were electroporated in the presence of nonspecific or ROR1-targeting siRNA and plated into culture media. After 3 days, a sample of cells was harvested for immunoblot analysis using antibodies specific for ROR1 or β-Actin. After 4 days, cells were subjected to an MTS assay to measure cell viability. Values represent percentage mean (normalized to nonspecific control wells) ± SEM (n = 10) (**$p < 0.01$).

(F) RCH-ACV cells stably expressing ROR1-V5 or LacZ control were electroporated in the presence of nonspecific or ROR1 UTR-targeting siRNA and plated into culture media. After 3 days, a sample of cells was harvested for immunoblot analysis using antibodies specific for ROR1, V5, or β-Actin. After 4 days, cells were subjected to an MTS assay to measure cell viability. Values represent percentage mean (normalized to nonspecific control wells) ± SEM (n = 6) (**$p < 0.01$).

(G) Primary cells from a t(1;19) patient with ALL were propagated in NOD-SCID mice lacking the IL-2 receptor γ chain. Xenograft cells were harvested from bone marrow and spleen of overtly leukemic mice and electroporated with nonspecific or ROR1-targeting siRNA. After 4 days, cells were subjected to an MTS assay to measure cell viability. Values represent percentage mean (normalized to nonspecific control wells) ± SEM (n = 4) (*$p < 0.05$).

(H) Primary cells from a t(1;19) patient with ALL were propagated in a xenograft mouse model as above, and RNA was harvested from cell extracts. PCR was performed on cDNA with primers specific for ROR1, E2A-PBX1, or GAPDH. The t(1;19) positive (RCH-ACV) and negative (REH) cell lines were included for comparison.

See also Figure S2.

lines were also sensitive to ROR1 silencing, as we observed with sample 07-112. We treated both cell lines as well as the control t(1;19)-negative cell line REH with siRNA specific for ROR1. Consistent with the results from sample 07-112, both RCH-ACV and Kasumi-2 cells were sensitive to ROR1 silencing (Figure 2E). Loss of ROR1 resulted in reduced cell growth and increased apoptosis (Figure S2C). In addition, treatment of RCH-ACV cells with three individual siRNA duplexes that target different portions of the ROR1 open reading frame (ORF), as well as three individual siRNA duplexes that target different portions of the ROR1 3′-untranslated region (UTR), resulted in reductions of RCH-ACV cell viability that were always proportional to the respective silencing capacity of each siRNA duplex (Figures S2D and S2E). Similarly, stable overexpression of an ORF-only ROR1 construct in RCH-ACV cells rescued cell viability when treated with an siRNA duplex targeting the ROR1 3′-UTR (Figure 2F), confirming that the siRNA-mediated killing of t(1;19) cells is due to a ROR1-specific phenomenon. We next confirmed that this finding was reproducible in early passage t(1;19) cells propagated by xenograft into NOD/SCID mice. Xenograft cells derived from four t(1;19) patients were tested for ROR1 overexpression as well as for sensitivity to ROR1 siRNA. We found that

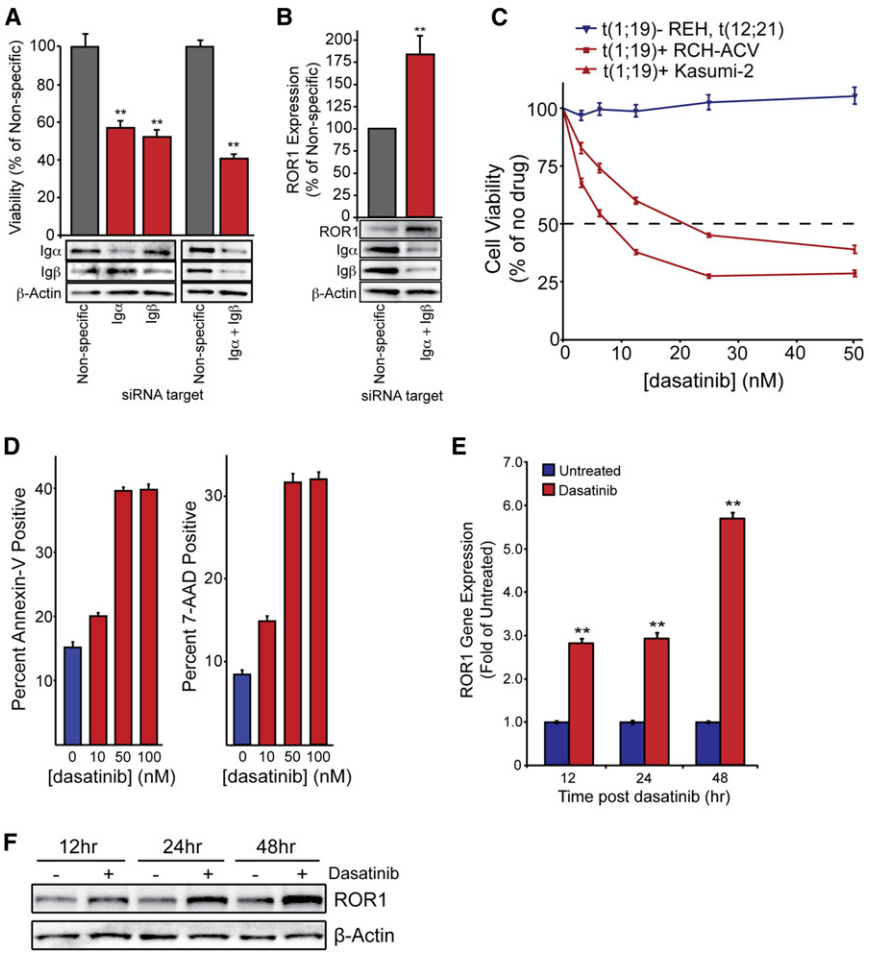

Figure 3. Pre-BCR Signaling Inhibition Impairs t(1;19) Cell Viability and Activates ROR1 Expression

(A) RCH-ACV cells were electroporated in the presence of nonspecific siRNA or siRNA targeting Igα, Igβ, or both and then plated in culture media. After 3 days, a sample of cells was harvested for immunoblot analysis using antibodies specific for Igα, Igβ, or β-Actin. After 4 days, cells were subjected to an MTS assay to measure cell viability. Values represent percentage mean (normalized to nonspecific control wells) ± SEM (n = 6) (**p < .01).

(B) RCH-ACV cells were electroporated in the presence of nonspecific or Igα and Igβ-targeting siRNA and then were plated in culture media. After 3 days, cells were harvested for immunoblot analysis using antibodies specific for ROR1, Igα, Igβ, or β-Actin. One representative blot is included. Densitometry was performed to quantitate ROR1 expression. Values represent percentage mean (normalized to nonspecific control) ± SEM (n = 3) (**p < .01).

(C) RCH-ACV, Kasumi-2, and REH cells were cultured in graded concentrations of the kinase inhibitor dasatinib for 3 days, at which time cells were subjected to an MTS assay for measurement of cell viability. Values represent percentage mean (normalized to no-drug control wells) ± SEM (n = 6).

(D) RCH-ACV cells were cultured in graded concentrations of dasatinib for 96 hr before being stained with Annexin-V PE and 7-AAD and were analyzed by flow cytometry to determine induction of apoptosis. Values represent the percentage of total positive cells ± SEM (n = 3) (*p < .05; **p < .01).

(E and F) RCH-ACV cells were cultured in the presence of 100 nM dasatinib for 12, 24, and 48 hr. Cells were collected for RNA harvest and quantitative PCR analysis (E) or were lysed for immunoblot analysis (F). PCR was performed on cDNA with primers specific for ROR1 and GAPDH to determine relative ROR1 mRNA expression levels. Values represent the fold change (normalized to untreated control cells) ± SEM (n = 6) (**p < .01). Immunoblotting was performed with antibodies specific for ROR1 or β-Actin to determine relative ROR1 protein expression.

See also Figure S3.

both features were recapitulated in these early passage t(1;19) xenograft cells (data for one representative cell line are shown in Figures 2G and 2H).

ROR1 Expression Is Regulated By Pre-BCR Signaling

We next wanted to investigate the functional role for ROR1 in t(1;19) ALL cells. Because upregulation of ROR1 in both malignant and normal B cell precursors occurs at the pre-BII stage, we first examined a possible connection with other biological events known to occur at this same stage of B-lineage maturation. One of the hallmarks of the pre-BII stage is the assembly and expression of the pre-BCR complex (Figure S3A). As such, we next examined the possibility of a functional connection between ROR1 and the pre-BCR. We tested two possibilities: (1) ROR1 directly interacts with the pre-BCR complex or (2) pre-BCR signaling may drive ROR1 expression. We began by examining ROR1 immunoprecipitates from t(1;19) ALL cells but found no evidence for interaction of ROR1 with Igμ or other constituents of the pre-BCR (Figure S3B). Next, we examined whether disruption of the pre-BCR would result in decreased ROR1 expression. To disrupt pre-BCR signaling, we utilized siRNA against the immunoglobulin alpha and beta (Igα and Igβ) components of the pre-BCR complex, which have previously been shown to be necessary for pre-BCR activity (Papavasiliou et al., 1995; Teh and Neuberger, 1997). As expected, knockdown of Igα or Igβ resulted in significantly impaired t(1;19) ALL cell viability, which was amplified with simultaneous silencing of both proteins (Figure 3A). We then analyzed ROR1 expression following inhibition of the pre-BCR by knockdown of Igα/β. Paradoxically, knockdown of Igα and Igβ did not inhibit ROR1 expression and instead resulted in significant ROR1 upregulation (Figure 3B).

The unexpected upregulation of ROR1 after pre-BCR silencing suggested a functional connection between ROR1 and the pre-BCR, with ROR1 upregulation after pre-BCR inhibition potentially representing an intrinsic response mechanism to perturbation of the pre-BCR pathway. We next examined a pharmacological approach to inhibition of pre-BCR signaling, employing the inhibitor dasatinib, which has been previously described to block mature-BCR signaling (McCaig et al.,

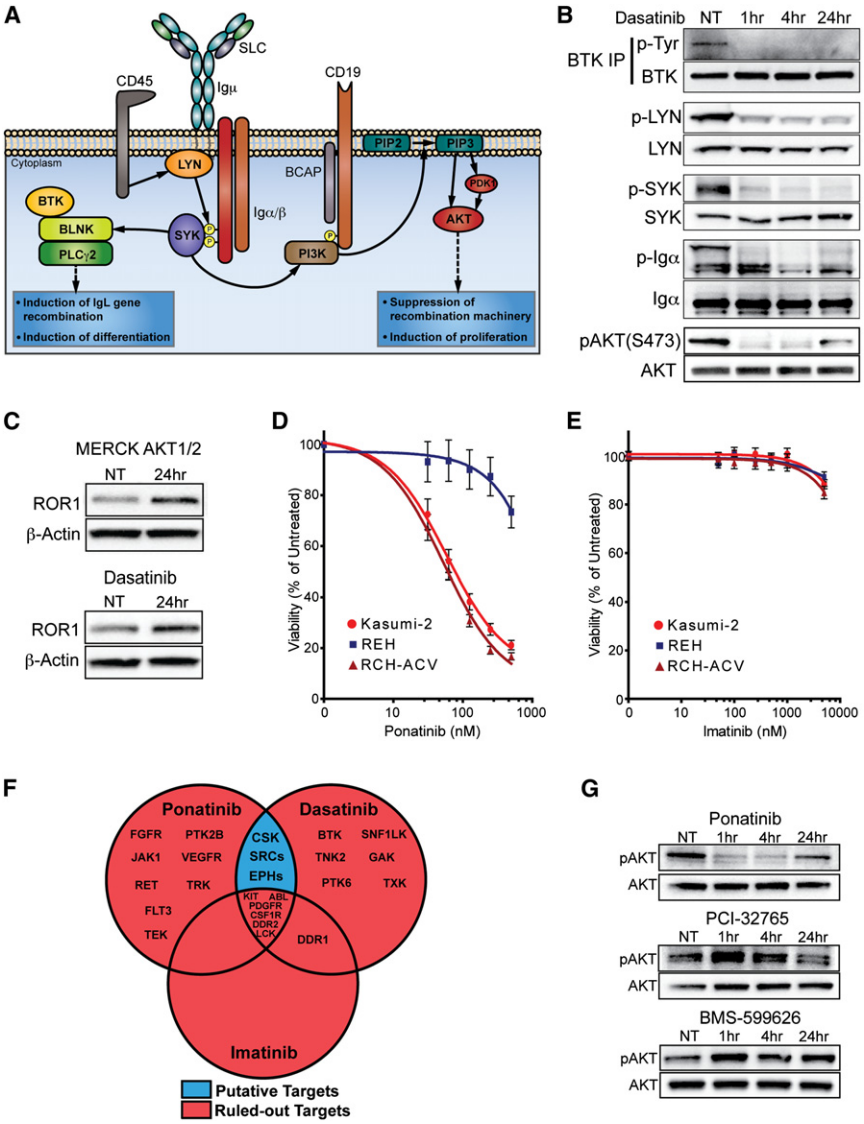

Figure 4. Dasatinib Inhibits Pre-BCR/SRC/AKT Signaling and Upregulates ROR1 in t(1;19) ALL

(A) Schematic of pre-BCR signaling and function during pre-B development. Adapted from (Herzog et al., 2009; Monroe, 2006).

(B) RCH-ACV cells were treated with dasatinib (50 nM) over a time course, and whole-cell extracts were subjected to immunoblot analysis for total or phospho-LYN, SYK, Igα, and AKT. In addition, BTK was immunoprecipitated from the same cellular lysates, and immunoprecipitates were immunoblotted for total or phospho-BTK.

(C) RCH-ACV cells were treated with an allosteric inhibitor of AKT (1 μM) or dasatinib (100 nM) for 24 hr and whole cell extracts were subjected to immunoblot analysis for ROR1 and β-Actin.

(D and E) RCH-ACV, Kasumi-2, and REH cells were cultured in graded concentrations of the kinase inhibitors ponatinib (D) or imatinib (E) for 3 days, at which time cells were subjected to an MTS assay for measurement of cell viability. Values represent percentage mean (normalized to no-drug control wells) ± SEM (n = 6).

(F) Venn-diagram identifies potential phenotype-mediated targets of dasatinib (CSK, SRC-family kinases, and EPH receptors). Binding constants were dasatinib (<10 nM), ponatinib (<25 nM), and imatinib (<500 nM) (O'Hare et al., 2009; Karaman et al., 2008).

(G) RCH-ACV cells were treated with ponatinib (50 nM), PCI-32765 (50 nM), or BMS-599626 (500 nM) over a time course, and whole-cell extracts were subjected to immunoblot analysis for total or phospho-AKT.

See also Figure S4.

Dasatinib-Inhibited Pre-BCR Signaling Disrupts AKT in t(1;19) ALL

The observation that dasatinib recapitulated the phenotype of pre-BCR silencing (reduction of t(1;19) ALL cell viability and ROR1 upregulation) suggested that dasatinib could be a useful tool to study functional interactions between ROR1 and the pre-BCR. First, however, we wanted to validate that dasatinib was operating via inhibition of pre-BCR signaling and also identify the specific kinase targets of dasatinib in this setting. As previously described, the pre-BCR is noted for regulation of both proproliferation and prodifferentiation signaling required for normal B cell differentiation, and a variety of kinases play a prominent role in this signaling complex (Figure 4A). We began by examining putative dasatinib targets that are known to participate in this pre-BCR signaling complex. BTK and SRC-family kinases are established targets of dasatinib (Hantschel et al., 2007; Karaman et al., 2008) and critical components of the pre-BCR and mature BCR signaling complexes (Hsueh and Scheuermann, 2000). Indeed, phosphorylation of BTK and the SRC-family kinase, LYN, were inhibited after dasatinib exposure. The additional loss of phosphorylation of pre-BCR complex components SYK, Igα, and AKT (which are not direct targets of dasatinib) indicated complete disruption of the pre-BCR

2011). Similar to siRNA-mediated disruption of the pre-BCR, inhibition of pre-BCR signaling with dasatinib resulted in impaired viability and increased apoptosis of the pre-BCR-positive t(1;19) ALL cell lines RCH-ACV and Kasumi-2, whereas the pre-BCR-negative t(12;21) ALL cell line REH was insensitive (Figures 3C and 3D). As with knockdown of Igα/β, dasatinib-mediated pre-BCR inhibition resulted in further upregulation of ROR1 mRNA and protein (Figures 3E and 3F; Figure S3C). To confirm that ROR1 upregulation is not a general response to all apoptotic stimuli in t(1;19) cells, we treated RCH-ACV cells with doxorubicin, which induces apoptosis through the p53 pathway and is a therapeutic agent used in the setting of ALL. We observed robust induction of apoptosis in response to doxorubicin (Figure S3D); however, ROR1 was not upregulated and, in fact, exhibited reduced expression (Figure S3E). This stands in marked contrast to the robust upregulation of ROR1 observed after inhibition of the pre-BCR with dasatinib or silencing of the pre-BCR with siRNA directed against Igα/β (Figures 3B and 3F; Figures S3C and S3E).

Table 1. ROR1-Associated Proteins Identified by IP-Mass Spectrometry in t(1;19) ALL

		Isotype Control			ROR1 Antibody		
Gene	Accession No.	Kasumi-2	697	RCH-ACV	Kasumi-2	697	RCH-ACV
ROR1	Q01973	0	0	0	30	28	19
TRIM21	P19474	0	0	0	12	0	12
MORC3	Q14149	0	0	0	7	17	18
TBC1D1	Q86TI0	0	0	0	9	1	3
TBC1D4	O60343	0	0	0	9	0	2
ACTB	P60709	15	23	26	8	47	26

Lysates from the t(1;19)-positive ALL cell lines (Kasumi-2, 697, and RCH-ACV) were subjected to immunoprecipitation with ROR1-specific antibody or an isotype matched control. Immunoprecipitates were then analyzed by mass spectrometry (MS). All proteins that were identified at a similar frequency in isotype controls as ROR1-specific antibody samples were considered to be nonspecific interactions and eliminated. Only proteins that were identified with ROR1 antibody and not with isotype control were considered as candidate ROR1-interacting proteins. Genes name, UniProt accession number, and corrected MS/MS spectral counts are shown for each identified protein as well as β-Actin control.
See also Figure S6.

signaling complex by dasatinib (Figure 4B). In addition, direct inhibition of AKT with an allosteric inhibitor of AKT (MERCK AKT1/2; published as drug #17 in Table 2 of Bilodeau et al., 2008) resulted in ROR1 upregulation, as was also observed with dasatinib and pre-BCR silencing (Figure 4C). These results suggested that t(1;19) ALL dasatinib sensitivity occurs as a result of inhibition of pre-BCR-initiated BTK and/or SRC kinases that subsequently activate AKT. However, dasatinib has the capacity to inhibit many other kinases, so we wanted to further validate this hypothesis. Accordingly, we treated t(1;19) ALL cells with the SRC kinase inhibitor ponatinib (which lacks activity against BTK; O'Hare et al., 2009) and observed a phenotype identical to dasatinib—selective sensitivity of t(1;19) ALL cells and potent reduction of AKT phosphorylation (Figures 4D and 4G). In contrast, a third kinase inhibitor, imatinib, exhibited no effect on t(1;19) ALL cells (Figure 4E). Examination of these three drugs to understand target genes inhibited by both dasatinib and ponatinib but not by imatinib revealed that the only candidate gene targets to explain the dasatinib/ponatinib phenotype are SRC kinases, EPH receptor kinases, and CSK (Figure 4F). Treatment of these cells with a CSK inhibitor (BMS-599626) or a BTK inhibitor (PCI-32765) did not recapitulate the dasatinib/ponatinib phenotype, indicating that dasatinib/ponatinib sensitivity is due to SRC kinases or EPH receptor kinases (Figure 4G). Examination of EPH receptor expression revealed that EPHA3 is upregulated in t(1;19) ALL cells (Figure S4A). However, silencing of EPHA3 did not yield any discernible effect on t(1;19) ALL cell viability. No other EPH receptors exhibited aberrant expression in the t(1;19) setting, indicating that EPH receptors are likely not underlying this dasatinib/ponatinib cell viability response and suggesting SRC-family kinases as the operationally important target underlying t(1;19) ALL dasatinib sensitivity (Figure S4B).

Finally, we closely examined downstream pre-BCR signaling in the context dasatinib exposure. The pre-BCR is known to stimulate a prodifferentiation pathway (BTK/BLNK/PLCγ2) as well as a prosurvival/proliferation, antidifferentiation pathway (PI3K/AKT) (Hashimoto et al., 1999; Herzog et al., 2009). We observed no effects on phosphorylation of BLNK/PLCγ2 after dasatinib treatment (Figure S4C), which is consistent with our conclusion that BTK is dispensable for dasatinib-mediated t(1;19) ALL cell killing. In contrast, analysis of downstream AKT substrates revealed activation (reduced phosphorylation) of FOXO-family transcription factors, upregulation of RAG1 protein, loss of expression of the prosurvival gene BCL6, and activation (reduced phosphorylation) of proapoptotic BAD—all of which lead to arrested proliferation and apoptosis (Figure 3D; Figures S4D–S4F) (Brunet et al., 1999; Datta et al., 1997; Hideshima et al., 2010).

ROR1 Drives Signaling Pathways that Are Compensatory with Pre-BCR Signaling

The increase of ROR1 expression after inhibition of the pre-BCR signaling complex led us to hypothesize the existence of counterbalancing pools of signaling proteins that function downstream of ROR1 or the pre-BCR in a compensatory manner to influence cell growth and viability. To evaluate this possibility, we needed to first determine the mechanism by which ROR1 influences downstream signaling pathways. We first examined the potential tyrosine kinase function of ROR1. However, we found no evidence of endogenous ROR1 tyrosine phosphorylation (Figure S5A). Likewise, in vitro kinase activity assays revealed no significant ROR1 kinase activity, a finding consistent with a recent study showing absence of intrinsic ROR1 kinase activity (Gentile et al., 2011). Hence, to identify alternative modalities for activation of signaling cascades by ROR1, we performed a mass spectrometry-based proteomic screen of proteins associating with endogenous ROR1 in t(1;19) ALL. Using three t(1;19) ALL cell lines (Kasumi-2, 697, and RCH-ACV), we prepared ROR1 or isotype control immunoprecipitates. We analyzed these samples with mass spectrometry to identify proteins that specifically and consistently coimmunoprecipitated with ROR1 and not with isotype control. This approach successfully identified four candidate ROR1 interacting proteins (Table 1; Figure S6). Two of these proteins (TBC1D1 and TBC1D4) have been reported to function as RAB GTPase-activating proteins (Park et al., 2011; Sano et al., 2003), suggesting regulation of small GTPase signaling as a possible avenue for ROR1 signaling.

Though this work presented a potential mechanism by which ROR1 can activate downstream signaling pathways, the specific signaling pathways regulated by ROR1 as well as the manner by which these pathways interact with the pre-BCR signaling

complex remained unclear. To address these questions, we examined protein phosphorylation patterns after treatment of cells with ROR1 siRNA or with dasatinib. We observed three categories of phosphorylation changes following these treatments: (1) phosphorylation decreased by dasatinib but increased or not changed by ROR1 siRNA, (2) phosphorylation increased by dasatinib but decreased or not changed by ROR1 siRNA, or (3) phosphorylation reduced by both dasatinib and ROR1 siRNA (Figure 5A). Notably, the MAP kinase family members, MEK and ERK, which are regulated downstream of small GTPases such as RAS (Mendoza et al., 2011), RAB (Bhuin and Roy, 2010), and RAC (Wang et al., 2010), exhibited reduced phosphorylation following ROR1 silencing and increased phosphorylation following dasatinib treatment. In addition, phosphorylation of AKT at serine 473 was among the phosphorylation events that were reduced by both dasatinib and ROR1 siRNA. Independent immunoblotting successfully validated reduction in phosphorylation of MEK, ERK, and AKT following ROR1 silencing (Figure 5B). Because AKT was regulated by both dasatinib and ROR1, this represented a potential signaling node for functional interaction between ROR1 and the pre-BCR. Consistent with this model, phosphorylation of AKT at serine 473 is almost completely abrogated after short time points with dasatinib treatment (1 and 4 hr); however, phosphorylation is partially restored at 24 hr once ROR1 expression has been further induced (Figure 5C). In addition, ROR1 exhibited the capacity to regulate the MEK/ERK cascade, so we hypothesized that crosstalk between AKT and MEK/ERK enables ROR1 to regulate AKT and thereby cooperate with the pre-BCR signaling complex. To test this hypothesis, we simultaneously treated cells with dasatinib and a MEK inhibitor, PD98059. This combination treatment resulted in sustained reduction of AKT phosphorylation, suggesting the 24 hr partial AKT recovery may, indeed, be mediated by crosstalk between MEK/ERK and AKT (Figure 5C). Finally, because STAT3 was recently described as a regulator of ROR1 expression in CLL (Li et al., 2010) and we observed increases in STAT3 phosphorylation after dasatinib exposure in t(1;19) ALL cells (Figure 5A; Figure S5B), we cotreated RCH-ACV cells with dasatinib and the STAT3 inhibitor S31-201 and we observed prevention of ROR1 upregulation in response to this drug combination (Figure S5C).

On the basis of the observed upregulation of ROR1 in response to pre-BCR inhibition by dasatinib and the compensatory signaling pathway driven by ROR1, we hypothesized that ROR1 may partially rescue cell survival after inhibition of the pre-BCR. If this were the case, then targeting of ROR1 in the context of dasatinib exposure would potentiate dasatinib killing of t(1;19) cells. To test this hypothesis, we treated t(1;19) ALL cell lines with nonspecific-, ROR1-, or Igα-targeting siRNA and subsequently exposed these cells to graded concentrations of dasatinib. As predicted, cells subjected to ROR1 silencing were more sensitive to dasatinib compared with cells treated with nonspecific siRNA, suggesting that ROR1 can function as a rescue pathway for cell survival in the context of pre-BCR inhibition (Figure 5D). Importantly, knockdown of Igα did not increase the level of killing when combined with dasatinib, indicating that the ROR1/dasatinib phenotype cannot be achieved by nonspecific combination of any two cellular insults.

Clinical Significance of Dasatinib Sensitivity in B Cell Malignancies

To determine the clinical significance of dasatinib sensitivity in t(1;19) ALL, we asked whether primary cells taken directly from patients with ALL were similarly sensitive to dasatinib exposure. We tested leukemia cells from ten patients with ALL of varying disease subsets over graded concentrations of dasatinib. Two of these ten patient samples were obtained from t(1;19)-positive patients, and both samples tested were highly sensitive to dasatinib, with IC_{50} values of approximately 2 and 12 nM, whereas the eight other ALL samples did not achieve IC_{50} values even at the highest tested concentration (1000 nM) (Figure 6A). Importantly, examination of ROR1 levels in these two t(1;19) patients confirmed ROR1 overexpression, similar to levels observed on all other t(1;19) samples previously tested (Figure 6B).

We next utilized a xenograft model of t(1;19) ALL to examine dasatinib sensitivity in vivo. The early passage t(1;19) ALL xenograft line ICN12 showed dasatinib sensitivity in vitro at concentrations similar to those observed in patient-derived cell lines and primary samples (Figure 6C). These ICN12, t(1;19)-ALL cells were then injected into NOD/SCID mice. Following engraftment, mice were treated with a dose-escalating regimen of dasatinib or vehicle control, starting with dosages already described for Ph^+ ALL (Boulos et al., 2011) and monitored for 60 days. Mice receiving dasatinib exhibited significantly prolonged survival compared with vehicle-treated control mice (Figure 6D).

Finally, because t(1;19) ALL does not represent the only B-lineage malignancy arrested at an intermediate/late stage of B cell development, we analyzed ROR1 status and dasatinib sensitivity in additional primary cells from B cell malignancies arrested at both the intermediate and mature stages of B cell development. Specifically, we examined primary samples from patients diagnosed with pre-BCR-positive t(17;19) ALL (as indicated by CD34-negativity and Igμ expression; Figures S7A and S7B), as well as a mature BCR-positive Burkitt's sample. Both showed high ROR1 expression levels, similar to those observed in t(1;19) ALL samples (Figure 6E). As expected, these samples were also sensitive to dasatinib treatment, with IC_{50} values comparable to those of t(1;19) ALL (Figure 6F). These results support the idea that ROR1 expression and dasatinib sensitivity are conserved characteristics of B cell malignancies exhibiting both pre-BCR and mature BCR expression.

DISCUSSION

In agreement with other recent work (Broome et al., 2011; Hudecek et al., 2010), we show that ROR1 upregulation in t(1;19) ALL is a product of B-lineage development arrest at the pre-BII stage of B cell development and not a result of aberrant regulation by the E2A-PBX1 transcription factor generated by the 1;19 translocation. Our studies also show that ROR1 is upregulated in t(17;19) ALL and Burkitt's leukemia/lymphoma, suggesting that ROR1 may be expressed in most B cell malignancies arrested at an intermediate or mature stage of development. This hypothesis is supported by findings showing ROR1 expression in cell lines and primary samples derived from patients with Mantle cell lymphoma (MCL) and chronic lymphocytic leukemia (CLL) (Baskar et al., 2008; Fukuda et al., 2008; Hudecek et al., 2010). Importantly, the expression of ROR1 on cells from the mature

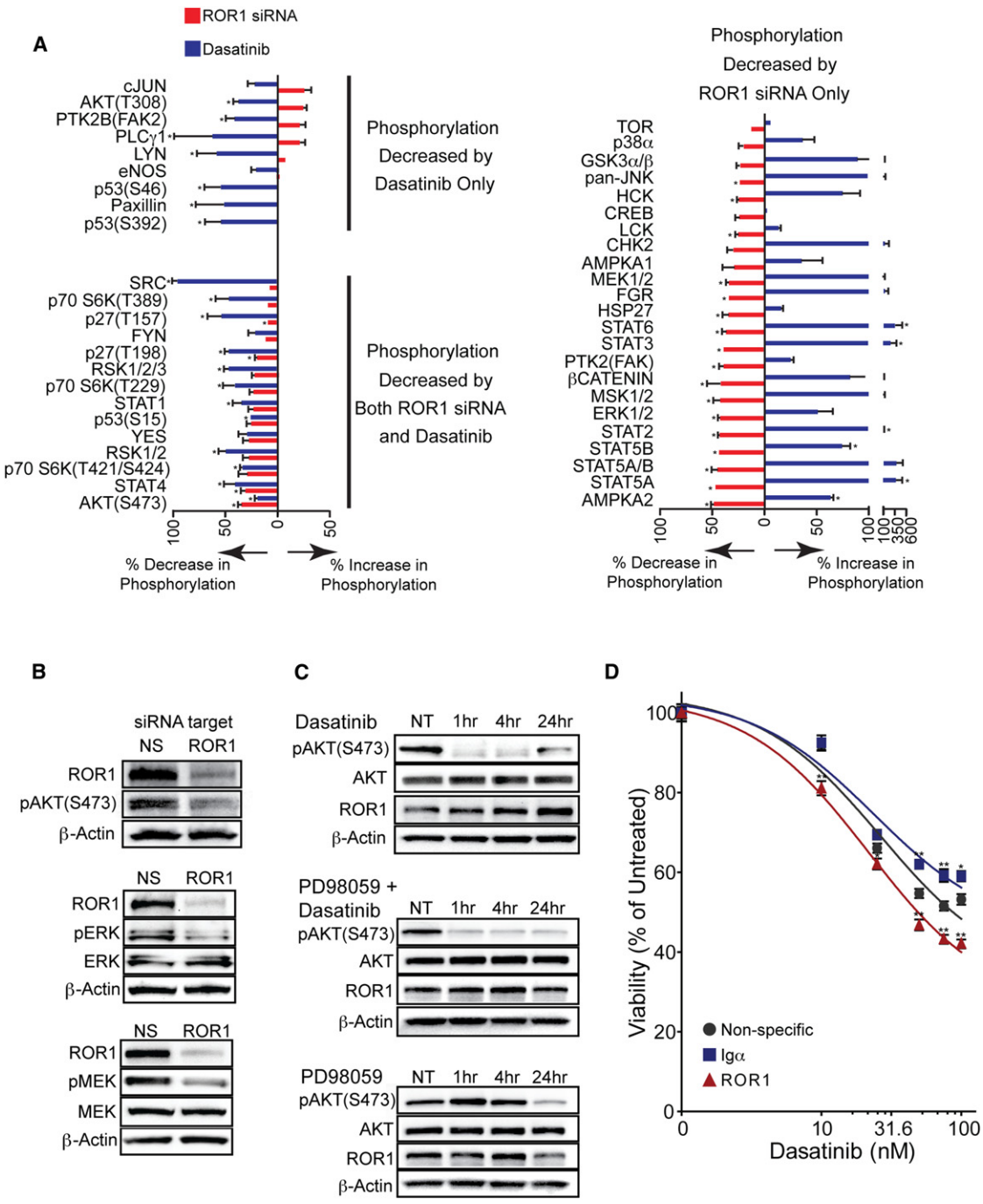

Figure 5. Inhibition of Pre-BCR or ROR1 Result in Counterbalancing Effects on Signaling

(A) RCH-ACV cells were treated with dasatinib for 24 hr or ROR1 siRNA for 72 hr, and whole-cell extracts were analyzed by phospho-proteomic array. Values on the graph represent percentage phosphorylation change ± SEM (n = 3) (*p < .05) of a total of 46 phospho-proteins for dasatinib relative to cells in the absence of any drug and for ROR1 siRNA relative to cells transfected with nonspecific siRNA.

(B) RCH-ACV cells were transfected with ROR1 or nonspecific siRNA for 72 hr, and whole-cell extracts were subjected to immunoblot analysis for ROR1, phospho-AKT at residue Serine 473, and β-Actin; ROR1, total and phospho-ERK, and β-Actin; and ROR1, total and phospho-MEK, and β-Actin for validation of ROR1 modulation observed by the phospho-proteomics screen in (A).

(C) RCH-ACV cells were treated with dasatinib (50 nM), PD98059 (50 μM), or both over a time course, and whole-cell extracts were subjected to immunoblot analysis for total or phospho-AKT at residue Serine 473, ROR1, and β-Actin.

(D) RCH-ACV cells were electroporated in the presence of nonspecific, ROR1-targeting, or Igα-targeting siRNA and then were plated in culture media. After 2 days, graded concentrations of dasatinib were added. Cells were allowed to culture an additional 2 days before they were subjected to an MTS assay for measurement of cell viability. Values represent percentage mean (normalized to no-drug control wells) ± SEM (n = 5) (*p < .05; **p < .01).

See also Figure S5.

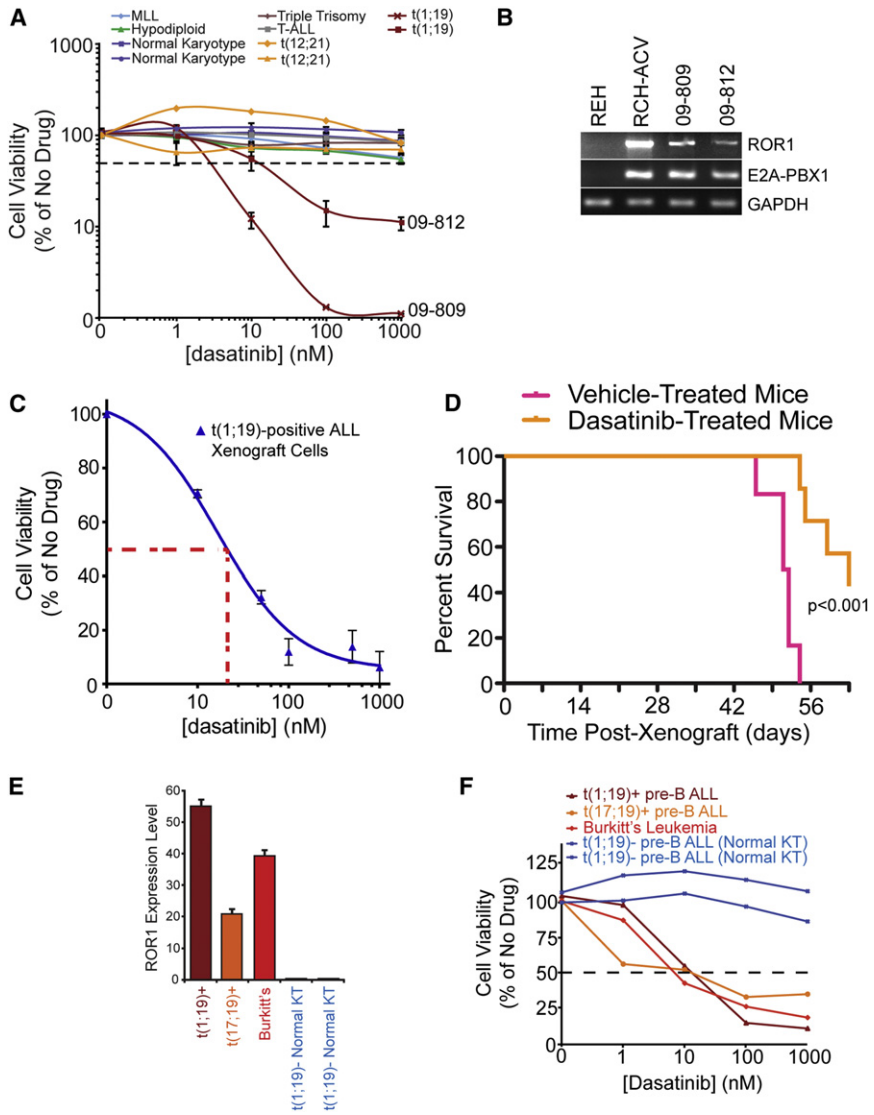

Figure 6. Clinical Significance of Dasatinib Sensitivity in Pre-BCR/BCR-Positive Malignancies

(A) Malignant cells from 10 pediatric patients with ALL exhibiting a variety of chromosomal translocations (2 positive for t(1;19)) were cultured in graded concentrations of the kinase inhibitor dasatinib for 3 days, at which time cells were subjected to an MTS assay for measurement of cell viability. Values represent percentage mean (normalized to no-drug control wells) ± SEM (n = 3).

(B) cDNA derived from primary samples of t(1;19) patients with ALL 09-809 and 09-812 was amplified using primers specific for ROR1, E2A-PBX1, or GAPDH. The t(1;19)-positive (RCH-ACV) and -negative (REH) cell lines were included for comparison.

(C) Early passage t(1;19) ALL xenograft cells (ICN12) were cultured in graded concentrations of the kinase inhibitor dasatinib for 3 days, at which time cells were subjected to an MTS assay for measurement of cell viability. Values represent percentage mean (normalized to no-drug control wells) ± SEM (n = 4).

(D) Early passage t(1;19) ALL xenograft cells (ICN12) were injected intravenously into NOD/SCID mice. Mice were left untreated for 8 days to allow engraftment of cells and subdivided into two groups, one treated with dasatinib and the other with vehicle control. An initial dose-escalating round of treatment commenced with 10 mg/kg dasatinib for 6 days, followed by 50 mg/kg dasatinib for 4 days. Mice were untreated for the following 24 days, and this was followed by 12 additional days of dasatinib or vehicle treatment. Mouse survival was monitored over the course of the treatment.

(E) cDNA derived from t(1;19) ALL, t(17;19) ALL, Burkitt's lymphoma, and normal karyotype ALL primary samples was analyzed for relative ROR1 mRNA expression using quantitative PCR. cDNA was amplified using primers specific for ROR1 and GAPDH, and ROR1 levels were normalized to GAPDH. Values represent mean arbitrary quantitative PCR units ± SEM (n = 3).

(F) t(1;19) ALL, t(17;19) ALL, Burkitt's lymphoma, and normal karyotype primary samples were cultured in the presence of graded concentrations of dasatinib. After 3 days, cells were subjected to an MTS assay for measurement of cell viability. Values represent percentage mean, normalized to no-drug control wells. See also Figure S7.

B-lineage malignancies, CLL, MCL, and Burkitt's, demonstrates a deviation from the normal distribution of ROR1 expression observed in B cell development. Although ROR1 expression is observed only in the intermediate stage of normal B cell development, it is observed in both intermediate and mature B cell malignancies. This important distinction suggests that retention or reactivation of ROR1 expression plays a role in maintenance of cell viability of these mature, malignant B cell clones.

We also show that the cytoplasmic pre-BCR, which is present in pre-BII progenitor equivalent t(1;19) ALL, is actively stimulating the PI3K/AKT pathway, and this pathway is inhibited following pre-BCR inhibition with dasatinib. Interestingly, we find that the PI3K/AKT component of the pre-BCR pathway can also be stimulated by ROR1, and inhibition of pre-BCR signaling results in rapid upregulation of ROR1 and subsequent reactivation of AKT via ROR1/MEK/ERK signaling. Indeed, cooperation between AKT and MEK/ERK has been demonstrated during B-lineage development; likewise, crosstalk between these signaling pathways is well documented in a variety of settings (Mendoza et al., 2011). This observation raises interesting questions about a potential cooperative role for ROR1 and MEK/ERK signaling in regulating B cell development with the pre-BCR. Supporting this idea is work that shows MEK/ERK signaling in pre-B cells can both cooperate with AKT signaling to coordinate RAG gene expression and drive prosurvival signaling (Novak et al., 2010; Taguchi et al., 2003). A prosurvival function for ROR1/MEK/ERK signaling supports our observation of impaired cell viability following ROR1 silencing in t(1;19) ALL cells and is consistent with the idea that ROR1 is being upregulated following pre-BCR/AKT inhibition in an attempt to rescue cell

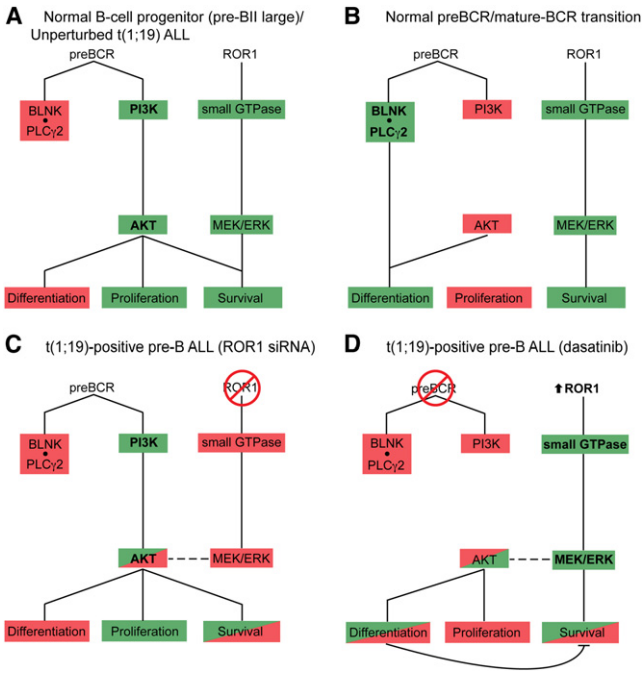

Figure 7. Model for ROR1 Supported B Cell Development and Cross-talk between ROR1 and the pre-BCR during Therapeutic Modulation of t(1;19) ALL

(A–D) Schematic of ROR1 and pre-BCR signaling network and function during normal B cell development and t(1;19)-positive pre-B ALL. Green indicates active signaling; red indicates inhibited signaling.

viability. The potentiated effect on cell viability we observe with simultaneous ROR1 silencing and pre-BCR inhibition supports this model.

Taken together, our findings support a model in which normal B cell progenitors upregulate ROR1 expression in coordination with assembly and signaling from the pre-BCR complex at the pre-BII large stage of development. Here, the pre-BCR drives AKT activation, which inhibits differentiation, drives proliferation and promotes survival. ROR1-activated MEK/ERK signaling cooperates with AKT to support convergent prosurvival pathways (Figure 7A) (Novak et al., 2010). As normal pre-B cells transition to immature B cells, the pre-BCR is internalized and light-chain is recombined, allowing assembly of the mature BCR. Here, the BLNK/PLCγ2 complex inhibits AKT activation and promotes differentiation. Although loss of AKT activity allows cell differentiation to proceed, it also represents loss of an important prosurvival signal. Our model would suggest that transient expression of ROR1 at this stage of B-lineage differentiation offers an alternative mechanism for prosurvival signaling through activation of MEK/ERK (Figure 7B) (Taguchi et al., 2003). In the case of t(1;19) ALL, the t(1;19) lesion generates the E2A-PBX1 fusion product that contributes to the developmental arrest of B cell progenitors at the pre-BII small stage of development. Expression and signaling of ROR1 and the pre-BCR complex are now retained in the malignant progenitor and provide onco-requisite signaling stimuli critical for the viability of these malignant cells. Abrogation of ROR1 signaling (with siRNA) results in inhibition of MEK/ERK activity leading to attenuation of AKT activity and impairment of cell viability (Figure 7C). Alternatively, inhibition of pre-BCR activity with dasatinib results in rapid inhibition of the PI3K/AKT pathway and results in loss of differentiation repression, abrogation of proproliferative signals, and subsequent impairment of viability. However, inhibition of the pre-BCR signaling complex also induces feedback activation of ROR1 expression and further activation of MEK/ERK signaling. In addition to partially supporting prosurvival signaling through MEK/ERK, ROR1 upregulation drives partial reactivation of AKT signaling, resulting in rescue of cell viability (Figure 7D). As such, modulation of only ROR1 or only the pre-BCR is not as effective at killing t(1;19) cells as simultaneous antagonism of both pathways.

The optimal strategy for therapeutic targeting of ROR1 remains unclear. Immunological-based therapies present a promising therapeutic strategy for specifically targeting ROR1-positive malignancies. Chimeric antigen receptor (CAR)-modified T cells targeting B cell lineage-specific surface markers, such as CD19 and CD20, are actively being investigated in clinical trials for B cell malignancies (Porter et al., 2011; Till et al., 2008). Our data suggest that a similar strategy targeting ROR1 could prove valuable in treating most intermediate and mature B cell malignancies. In fact, this strategy is already in development and showing promising results against CLL and MCL samples (Hudecek et al., 2010). Further study addressing the potential toxicity of targeting ROR1 surface expression will be critical for advancing ROR1 targeting as a viable therapeutic option.

In conclusion, our work provides important evidence of the biological function of ROR1 in normal B cell development and B cell malignancy. It expands the pool of patients who could potentially benefit from ROR1-targeted therapy and has further suggested a high rate of overlap between the overexpression of ROR1 and sensitivity to the targeted kinase inhibitor dasatinib. The addition of t(1;19) and t(17;19) ALL as well as Burkitt's leukemia/lymphoma to the growing list of B cell malignancies that exhibit ROR1 surface expression provides impetus for further study of ROR1 biology and ROR1-targeted therapies. Furthermore, although dasatinib does not directly target ROR1, it does effectively reduce the viability of many ROR1-positive B cell malignancies due to expression of the pre- or mature-BCR in these cells. Hence, our work would suggest further studies that may lead to implementation of dasatinib therapy for B cell malignancies expressing the pre- or mature-BCR, which could also be supplemented with ROR1-directed therapies for enhanced efficacy.

EXPERIMENTAL PROCEDURES

Patient Samples

All clinical samples were obtained with informed consent with approval by the Institutional Review Board of Oregon Health & Science University and the Children's Oncology Group. Bone marrow mononuclear cells were separated on a Ficoll gradient. Cells were cultured in RPMI-1640 medium with 20% FBS (Atlanta Biologicals), L-glutamine, insulin/transferrin/sodium selenite, penicillin/streptomycin, fungizone (Invitrogen), and 10^{-4} M 2-mercaptoethanol (Sigma).

Primary Leukemia Cell Xenograft

Cells (1×10^6) from a t(1;19) ALL patient bone marrow were inoculated via intra femoral injection into sublethally irradiated (250 cGy) NOD/SCID mice. When

the mice became terminally ill due to overt leukemia, they were sacrificed, and leukemia cells were harvested from bone marrow and spleen. Leukemic infiltration was confirmed by flow cytometry and cells were suspended in culture media (MEM-Alpha medium supplemented with 20% FBS, 1% penicillin/streptomycin, and 1% sodium-pyruvate). For in vivo dasatinib treatment, 14 mice were injected with t(1;19)-positive ALL cells and left untreated for 8 days to allow cell engraftment. Mice were then divided into two groups and treated by oral gavage with dasatinib or vehicle control according to a dose-escalating protocol, starting with 10 mg/kg daily for 6 days, 50 mg/kg once daily for 4 days, no treatment for 24 days, and 50 mg/kg twice daily thereafter. Mouse survival was monitored for 63 days. All mouse experiments were performed with approval by the Children's Hospital Los Angeles Institutional Animal Care and Use Committee.

Gene Expression Microarray

A meta-analysis was performed for gene expression microarray analyses of samples from pediatric patients with ALL and normal B cell progenitor populations as previously described (Trageser et al., 2009). Data sets were processed and normalized using the RMA algorithm, and normalization was validated on the basis of even expression levels for a set of seven reference genes (HPRT, COX6B, GUSB, GAPDH, PGK, ACTB, and B2M) among all tissue samples studied. Gene expression values for the ROR1 probesets (211057_at and 205805_s_at) and the IGHM probeset (212827_at) were studied.

siRNA and Kinase Inhibitors

The RAPID assay and other siRNA experiments were performed as previously described (Tyner et al., 2008, 2009). All siRNAs were from Thermo Fisher Scientific Dharmacon RNAi Technologies. Dasatinib and PD98059 were purchased from LC Labs; PCI-32765, BMS-599626, and ponatinib were purchased from Selleck; doxorubicin was from Sigma; and the allosteric AKT inhibitor (published as drug #17 in Table 2 of Bilodeau et al., 2008) was provided by Merck Pharmaceuticals.

Immunoblotting

All immunoblotting was performed using standard protocols. For phosphoproteomic arrays, Proteome Profiler Human Phospho-Kinase Array assays (R&D Systems) were used and analyzed according to the manufacturer's protocol. Data was analyzed with ImageJ.

Statistical Analyses

For RAPID screens, the mean and standard deviation of all data points on the plate were computed, and any data points exceeding two standard deviations of the mean plate value were considered significant. For cell viability, expression level, and phosphorylation state assays, a Student's t test was carried out for each drug dose or siRNA treatment compared with no drug control or nonspecific siRNA, respectively. Xenograft mouse survival curves were analyzed using Log-rank (Mantel-Cox) test.

For further experimental details, see Supplemental Experimental Procedures.

SUPPLEMENTAL INFORMATION

Supplemental Information includes seven figures and Supplemental Experimental Procedures and can be found with this article online at http://dx.doi.org/10.1016/j.ccr.2012.08.027.

ACKNOWLEDGMENTS

We thank Cristina Tognon for helpful review of this manuscript. Patient samples from the Children's Oncology Group were obtained through a collaboration with the COG ALL Cell Bank (Proposal #2008-08) J.W.T. is supported by grants from the William Lawrence and Blanche Hughes Fund, the Leukemia & Lymphoma Society, the National Cancer Institute (Grant 4R00CA151457-03), and the Oregon Clinical and Translational Research Institute (Grant UL1 RR024140 from the National Center for Research Resources, a component of the NIH, and NIH Roadmap for Medical Research). B.H.C. is supported by grants from the Oregon Child Health Research Center and by St. Baldricks Foundation. B.J.D. is an investigator of the Howard Hughes Medical Institute.

Received: July 6, 2011
Revised: March 22, 2012
Accepted: August 28, 2012
Published: November 12, 2012

REFERENCES

Baskar, S., Kwong, K.Y., Hofer, T., Levy, J.M., Kennedy, M.G., Lee, E., Staudt, L.M., Wilson, W.H., Wiestner, A., and Rader, C. (2008). Unique cell surface expression of receptor tyrosine kinase ROR1 in human B-cell chronic lymphocytic leukemia. Clin. Cancer Res. *14*, 396–404.

Bhuin, T., and Roy, J.K. (2010). Rab11 regulates JNK and Raf/MAPK-ERK signalling pathways during *Drosophila* wing development. Cell Biol. Int. *34*, 1113–1118.

Bijl, J., Sauvageau, M., Thompson, A., and Sauvageau, G. (2005). High incidence of proviral integrations in the Hoxa locus in a new model of E2a-PBX1-induced B-cell leukemia. Genes Dev. *19*, 224–233.

Bilodeau, M.T., Balitza, A.E., Hoffman, J.M., Manley, P.J., Barnett, S.F., Defeo-Jones, D., Haskell, K., Jones, R.E., Leander, K., Robinson, R.G., et al. (2008). Allosteric inhibitors of Akt1 and Akt2: a naphthyridinone with efficacy in an A2780 tumor xenograft model. Bioorg. Med. Chem. Lett. *18*, 3178–3182.

Boulos, N., Mulder, H.L., Calabrese, C.R., Morrison, J.B., Rehg, J.E., Relling, M.V., Sherr, C.J., and Williams, R.T. (2011). Chemotherapeutic agents circumvent emergence of dasatinib-resistant BCR-ABL kinase mutations in a precise mouse model of Philadelphia chromosome-positive acute lymphoblastic leukemia. Blood *117*, 3585–3595.

Broome, H.E., Rassenti, L.Z., Wang, H.Y., Meyer, L.M., and Kipps, T.J. (2011). ROR1 is expressed on hematogones (non-neoplastic human B-lymphocyte precursors) and a minority of precursor-B acute lymphoblastic leukemia. Leuk. Res. *35*, 1390–1394.

Brunet, A., Bonni, A., Zigmond, M.J., Lin, M.Z., Juo, P., Hu, L.S., Anderson, M.J., Arden, K.C., Blenis, J., and Greenberg, M.E. (1999). Akt promotes cell survival by phosphorylating and inhibiting a Forkhead transcription factor. Cell *96*, 857–868.

Datta, S.R., Dudek, H., Tao, X., Masters, S., Fu, H., Gotoh, Y., and Greenberg, M.E. (1997). Akt phosphorylation of BAD couples survival signals to the cell-intrinsic death machinery. Cell *91*, 231–241.

Dedera, D.A., Waller, E.K., LeBrun, D.P., Sen-Majumdar, A., Stevens, M.E., Barsh, G.S., and Cleary, M.L. (1993). Chimeric homeobox gene E2A-PBX1 induces proliferation, apoptosis, and malignant lymphomas in transgenic mice. Cell *74*, 833–843.

Fukuda, T., Chen, L., Endo, T., Tang, L., Lu, D., Castro, J.E., Widhopf, G.F., 2nd, Rassenti, L.Z., Cantwell, M.J., Prussak, C.E., et al. (2008). Antisera induced by infusions of autologous Ad-CD154-leukemia B cells identify ROR1 as an oncofetal antigen and receptor for Wnt5a. Proc. Natl. Acad. Sci. USA *105*, 3047–3052.

Gentile, A., Lazzari, L., Benvenuti, S., Trusolino, L., and Comoglio, P.M. (2011). Ror1 is a pseudokinase that is crucial for Met-driven tumorigenesis. Cancer Res. *71*, 3132–3141.

Hantschel, O., Rix, U., Schmidt, U., Bürckstümmer, T., Kneidinger, M., Schütze, G., Colinge, J., Bennett, K.L., Ellmeier, W., Valent, P., and Superti-Furga, G. (2007). The Btk tyrosine kinase is a major target of the Bcr-Abl inhibitor dasatinib. Proc. Natl. Acad. Sci. USA *104*, 13283–13288.

Hashimoto, S., Iwamatsu, A., Ishiai, M., Okawa, K., Yamadori, T., Matsushita, M., Baba, Y., Kishimoto, T., Kurosaki, T., and Tsukada, S. (1999). Identification of the SH2 domain binding protein of Bruton's tyrosine kinase as BLNK—functional significance of Btk-SH2 domain in B-cell antigen receptor-coupled calcium signaling. Blood *94*, 2357–2364.

Herzog, S., Reth, M., and Jumaa, H. (2009). Regulation of B-cell proliferation and differentiation by pre-B-cell receptor signalling. Nat. Rev. Immunol. *9*, 195–205.

Hideshima, T., Mitsiades, C., Ikeda, H., Chauhan, D., Raje, N., Gorgun, G., Hideshima, H., Munshi, N.C., Richardson, P.G., Carrasco, D.R., and Anderson, K.C. (2010). A proto-oncogene BCL6 is up-regulated in the bone marrow microenvironment in multiple myeloma cells. Blood *115*, 3772–3775.

Hsueh, R.C., and Scheuermann, R.H. (2000). Tyrosine kinase activation in the decision between growth, differentiation, and death responses initiated from the B cell antigen receptor. Adv. Immunol. *75*, 283–316.

Hudecek, M., Schmitt, T.M., Baskar, S., Lupo-Stanghellini, M.T., Nishida, T., Yamamoto, T.N., Bleakley, M., Turtle, C.J., Chang, W.C., Greisman, H.A., et al. (2010). The B-cell tumor-associated antigen ROR1 can be targeted with T cells modified to express a ROR1-specific chimeric antigen receptor. Blood *116*, 4532–4541.

Hunger, S.P. (1996). Chromosomal translocations involving the E2A gene in acute lymphoblastic leukemia: clinical features and molecular pathogenesis. Blood *87*, 1211–1224.

Hunger, S.P., Galili, N., Carroll, A.J., Crist, W.M., Link, M.P., and Cleary, M.L. (1991). The t(1;19)(q23;p13) results in consistent fusion of E2A and PBX1 coding sequences in acute lymphoblastic leukemias. Blood *77*, 687–693.

Kamps, M.P., and Baltimore, D. (1993). E2A-Pbx1, the t(1;19) translocation protein of human pre-B-cell acute lymphocytic leukemia, causes acute myeloid leukemia in mice. Mol. Cell. Biol. *13*, 351–357.

Kamps, M.P., Look, A.T., and Baltimore, D. (1991). The human t(1;19) translocation in pre-B ALL produces multiple nuclear E2A-Pbx1 fusion proteins with differing transforming potentials. Genes Dev. *5*, 358–368.

Karaman, M.W., Herrgard, S., Treiber, D.K., Gallant, P., Atteridge, C.E., Campbell, B.T., Chan, K.W., Ciceri, P., Davis, M.I., Edeen, P.T., et al. (2008). A quantitative analysis of kinase inhibitor selectivity. Nat. Biotechnol. *26*, 127–132.

Krause, D.S., and Van Etten, R.A. (2005). Tyrosine kinases as targets for cancer therapy. N. Engl. J. Med. *353*, 172–187.

Li, P., Harris, D., Liu, Z., Liu, J., Keating, M., and Estrov, Z. (2010). Stat3 activates the receptor tyrosine kinase like orphan receptor-1 gene in chronic lymphocytic leukemia cells. PLoS ONE *5*, e11859.

McCaig, A.M., Cosimo, E., Leach, M.T., and Michie, A.M. (2011). Dasatinib inhibits B cell receptor signalling in chronic lymphocytic leukaemia but novel combination approaches are required to overcome additional pro-survival microenvironmental signals. Br. J. Haematol. *153*, 199–211.

McWhirter, J.R., Neuteboom, S.T., Wancewicz, E.V., Monia, B.P., Downing, J.R., and Murre, C. (1999). Oncogenic homeodomain transcription factor E2A-Pbx1 activates a novel WNT gene in pre-B acute lymphoblastoid leukemia. Proc. Natl. Acad. Sci. USA *96*, 11464–11469.

Mendoza, M.C., Er, E.E., and Blenis, J. (2011). The Ras-ERK and PI3K-mTOR pathways: cross-talk and compensation. Trends Biochem. Sci. *36*, 320–328.

Monroe, J.G. (2006). ITAM-mediated tonic signalling through pre-BCR and BCR complexes. Nat. Rev. Immunol. *6*, 283–294.

Novak, R., Jacob, E., Haimovich, J., Avni, O., and Melamed, D. (2010). The MAPK/ERK and PI3K pathways additively coordinate the transcription of recombination-activating genes in B lineage cells. J. Immunol. *185*, 3239–3247.

O'Hare, T., Shakespeare, W.C., Zhu, X., Eide, C.A., Rivera, V.M., Wang, F., Adrian, L.T., Zhou, T., Huang, W.S., Xu, Q., et al. (2009). AP24534, a pan-BCR-ABL inhibitor for chronic myeloid leukemia, potently inhibits the T315I mutant and overcomes mutation-based resistance. Cancer Cell *16*, 401–412.

Papavasiliou, F., Jankovic, M., Suh, H., and Nussenzweig, M.C. (1995). The cytoplasmic domains of immunoglobulin (Ig) alpha and Ig beta can independently induce the precursor B cell transition and allelic exclusion. J. Exp. Med. *182*, 1389–1394.

Park, S.Y., Jin, W., Woo, J.R., and Shoelson, S.E. (2011). Crystal structures of human TBC1D1 and TBC1D4 (AS160) RabGTPase-activating protein (RabGAP) domains reveal critical elements for GLUT4 translocation. J. Biol. Chem. *286*, 18130–18138.

Porter, D.L., Levine, B.L., Kalos, M., Bagg, A., and June, C.H. (2011). Chimeric antigen receptor–modified T cells in chronic lymphoid leukemia. N. Engl. J. Med. *365*, 725–733.

Sano, H., Kane, S., Sano, E., Mîinea, C.P., Asara, J.M., Lane, W.S., Garner, C.W., and Lienhard, G.E. (2003). Insulin-stimulated phosphorylation of a Rab GTPase-activating protein regulates GLUT4 translocation. J. Biol. Chem. *278*, 14599–14602.

Taguchi, T., Kiyokawa, N., Mimori, K., Suzuki, T., Sekino, T., Nakajima, H., Saito, M., Katagiri, Y.U., Matsuo, N., Matsuo, Y., et al. (2003). Pre-B cell antigen receptor-mediated signal inhibits CD24-induced apoptosis in human pre-B cells. J. Immunol. *170*, 252–260.

Teh, Y.M., and Neuberger, M.S. (1997). The immunoglobulin (Ig)alpha and Igbeta cytoplasmic domains are independently sufficient to signal B cell maturation and activation in transgenic mice. J. Exp. Med. *185*, 1753–1758.

Till, B.G., Jensen, M.C., Wang, J., Chen, E.Y., Wood, B.L., Greisman, H.A., Qian, X., James, S.E., Raubitschek, A., Forman, S.J., et al. (2008). Adoptive immunotherapy for indolent non-Hodgkin lymphoma and mantle cell lymphoma using genetically modified autologous CD20-specific T cells. Blood *112*, 2261–2271.

Trageser, D., Iacobucci, I., Nahar, R., Duy, C., von Levetzow, G., Klemm, L., Park, E., Schuh, W., Gruber, T., Herzog, S., et al. (2009). Pre-B cell receptor-mediated cell cycle arrest in Philadelphia chromosome-positive acute lymphoblastic leukemia requires IKAROS function. J. Exp. Med. *206*, 1739–1753.

Tyner, J.W., Walters, D.K., Willis, S.G., Luttropp, M., Oost, J., Loriaux, M., Erickson, H., Corbin, A.S., O'Hare, T., Heinrich, M.C., et al. (2008). RNAi screening of the tyrosine kinome identifies therapeutic targets in acute myeloid leukemia. Blood *111*, 2238–2245.

Tyner, J.W., Deininger, M.W., Loriaux, M.M., Chang, B.H., Gotlib, J.R., Willis, S.G., Erickson, H., Kovacsovics, T., O'Hare, T., Heinrich, M.C., and Druker, B.J. (2009). RNAi screen for rapid therapeutic target identification in leukemia patients. Proc. Natl. Acad. Sci. USA *106*, 8695–8700.

Wang, Z., Pedersen, E., Basse, A., Lefever, T., Peyrollier, K., Kapoor, S., Mei, Q., Karlsson, R., Chrostek-Grashoff, A., and Brakebusch, C. (2010). Rac1 is crucial for Ras-dependent skin tumor formation by controlling Pak1-Mek-Erk hyperactivation and hyperproliferation in vivo. Oncogene *29*, 3362–3373.

Williams, D.L., Look, A.T., Melvin, S.L., Roberson, P.K., Dahl, G., Flake, T., and Stass, S. (1984). New chromosomal translocations correlate with specific immunophenotypes of childhood acute lymphoblastic leukemia. Cell *36*, 101–109.

Cancer Cell
Article

Aberrant Overexpression of IL-15 Initiates Large Granular Lymphocyte Leukemia through Chromosomal Instability and DNA Hypermethylation

Anjali Mishra,[1,2,9] Shujun Liu,[2] Gregory H. Sams,[1,2] Douglas P. Curphey,[1,2] Ramasamy Santhanam,[3] Laura J. Rush,[4] Deanna Schaefer,[4] Lauren G. Falkenberg,[1,2] Laura Sullivan,[1,2] Laura Jaroncyk,[1,2] Xiaojuan Yang,[7,9] Harold Fisk,[5] Lai-Chu Wu,[3] Christopher Hickey,[9] Jason C. Chandler,[2] Yue-Zhong Wu,[2] Nyla A. Heerema,[1,6] Kenneth K. Chan,[7,9] Danilo Perrotti,[1,9] Jianying Zhang,[8,9] Pierluigi Porcu,[2,9] Frederick K. Racke,[6] Ramiro Garzon,[2,9] Robert J. Lee,[7,9] Guido Marcucci,[1,2,9,10,*] and Michael A. Caligiuri[1,2,4,9,10,*]
[1]Department of Molecular Virology, Immunology, and Medical Genetics
[2]Division of Hematology, Department of Internal Medicine
[3]Department of Molecular and Cellular Biochemistry
[4]College of Veterinary Medicine
[5]Department of Molecular Genetics
[6]Department of Pathology
[7]College of Pharmacy
[8]Center for Biostatistics
[9]The Comprehensive Cancer Center and The James Cancer Hospital and Solove Research Institute
The Ohio State University, Columbus, OH 43210, USA
[10]These authors contributed equally to this work
*Correspondence: guido.marcucci@osumc.edu (G.M.), michael.caligiuri@osumc.edu (M.A.C.)
http://dx.doi.org/10.1016/j.ccr.2012.09.009

SUMMARY

How inflammation causes cancer is unclear. Interleukin-15 (IL-15) is a pro-inflammatory cytokine elevated in human large granular lymphocyte (LGL) leukemia. Mice overexpressing IL-15 develop LGL leukemia. Here, we show that prolonged in vitro exposure of wild-type (WT) LGL to IL-15 results in Myc-mediated upregulation of aurora kinases, centrosome aberrancies, and aneuploidy. Simultaneously, IL-15 represses *miR-29b* via induction of Myc/NF-κBp65/Hdac-1, resulting in Dnmt3b overexpression and DNA hypermethylation. All this is validated in human LGL leukemia. Adoptive transfer of WT LGL cultured with IL-15 led to malignant transformation in vivo. Drug targeting that reverses *miR-29b* repression cures otherwise fatal LGL leukemia. We show how excessive IL-15 initiates cancer and demonstrate effective drug targeting for potential therapy of human LGL leukemia.

INTRODUCTION

There are strong epidemiologic data to support the notion that chronic inflammation can increase the risk for malignant transformation of otherwise normal host cells (Ames et al., 1995). Deregulated cytokine production in the context of persistent infections can stimulate cells expressing cognate cytokine receptors to alter cell growth, cell differentiation, and cell survival, putting a cell at increased risk for malignant transformation when exposed to DNA damaging agents (Dranoff, 2004). For example, overexpression of macrophage-migration inhibitory factor in the setting of chronic inflammation can lead to the functional inactivation of the tumor suppressor gene *p53* (Hudson et al., 1999), and overexpression of interleukin-1 (IL-1) is associated with an increased risk of developing gastric cancer (El-Omar et al., 2000). While the alteration of cytokine gene expression

Significance

Our best opportunity for curing cancer will come from a complete understanding of its causes. Inflammation has long been associated with the progression of cancer but few if any studies have shown how inflammation can initiate cancer. Here, we show how an excess of a single pro-inflammatory cytokine, IL-15, causes chromosomal instability and DNA hypermethylation, leading to an aggressive acute leukemia of large granular lymphocytes, a rare yet uniformly fatal form of cancer. We show how drug targeting of the aberrant pathways induced by excessive IL-15 can cure this cancer. Thus, elucidating the molecular mechanisms involved in the genesis of cancer that results from chronic inflammation has merit for curing such cancers.

has been shown to alter the risk of malignant transformation, cytokines have only rarely been directly implicated as a cause of cancer, and to date, mechanistic insights into this process have not been understood.

IL-15 is a proinflammatory cytokine that is required for the genesis and homeostasis of natural killer (NK) cells or large granular lymphocytes (LGL) (Caligiuri, 2008). IL-15 utilizes the β (CD122) and γ (CD132) chains of the IL-2 receptor to transmit its growth and activation signals in LGL, yet presents to the βγ receptor complex in trans via its binding to a high-affinity IL-15 receptor α chain (Dubois et al., 2002). IL-15 was first shown to be overexpressed in HTLV-1-associated human T cell leukemia, and interruption of its autocrine loop with an anti-CD122 mab prevented leukemic cell growth and induced leukemic cell death in vitro (Bamford et al., 1994; Grabstein et al., 1994) but not in vivo (Morris et al., 2006). Overexpression of murine IL-15 causes LGL leukemia with either a NK cell or TNK cell phenotype in IL-15 transgenic (Tg) mice (Fehniger et al., 2001), and mice overexpressing mutated HMGI-C express excessive IL-15 that causes NK lymphoma (Baldassarre et al., 2001). Interestingly, IL-15 has been reported to be overexpressed in human LGL leukemia and to date, most human cell lines isolated from patients with LGL leukemia are dependent on IL-2 or IL-15 for in vitro propagation (Zambello et al., 1997). Collectively, these experimental and clinical data suggest a central role for IL-15 in the genesis of LGL leukemia, a highly malignant and uniformly fatal disorder, yet the mechanism by which this cytokine induces malignant transformation of LGL is not known. In this study, we attempt to unravel the mechanism of IL-15-induced LGL leukemia in mouse and man.

RESULTS

Chronic In Vitro Exposure of Normal LGLs to IL-15 Results in Leukemic Transformation

Because overexpression of IL-15 as a single growth factor can initiate leukemic transformation of LGL in vivo (Fehniger et al., 2001) and the neoplastic cells isolated from patients with LGL leukemia have higher expression of IL-15 than their normal LGL counterparts (Figure 1A), we first assessed the effects of IL-15 on wild-type (WT) mouse LGL (>95% $CD3^-NK1.1^+$) to determine if this transformation could occur in vitro (Figure 1B). Culture of 1×10^5 WT LGL with IL-15 at a concentration sufficient to saturate its cognate dimeric receptor induced robust growth of the LGL, which has continued for over 18 months while maintaining the LGL phenotype (Figures 1C and 1D). At 6 months, a karyotype was performed demonstrating striking aneuploidy (Figure 1E). While withdrawal of IL-15 led to eventual apoptosis of LGL in vitro (data not shown), adoptive transfer into SCID mice without exogenous IL-15 resulted in a dramatic increase in white blood cell (WBC) count (4.2×10^7/ml), splenomegaly, and death from fatal leukemia in vivo (Figures 1B and 1F). Interphase fluorescence in situ hybridization (FISH) analysis of splenocytes from the leukemic mouse revealed multiple copies of chromosome 15 (Figure 1F) as was seen in the in vitro culture before adoptive transfer (Figure 1E), and in our original IL-15 Tg mice (Yokohama et al., 2010). Thus, chronic exposure of WT LGL to IL-15 alone contributes to robust growth and chromosomal instability (CIN) in vitro, and leukemic transformation in vivo.

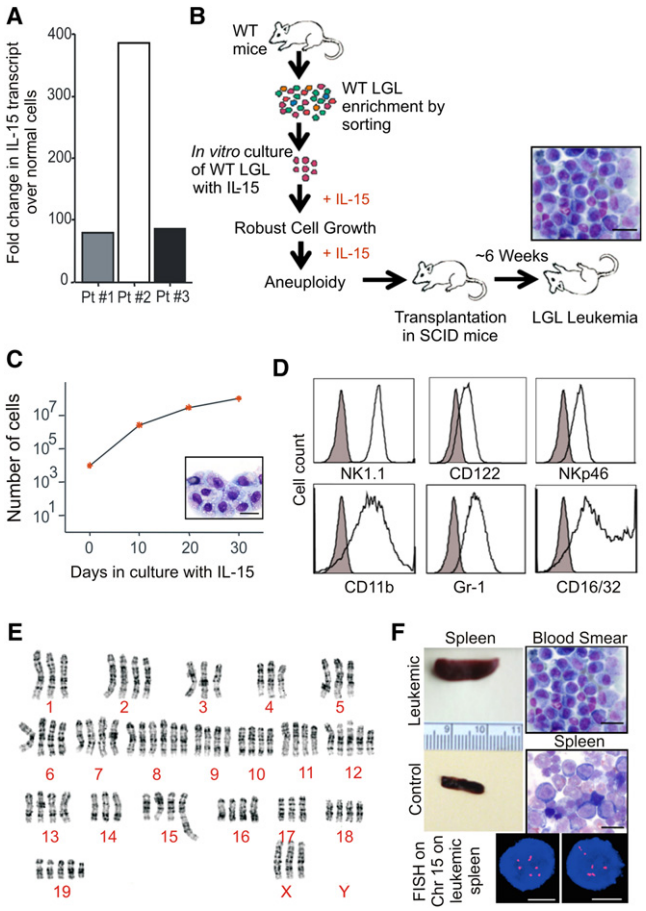

Figure 1. Chronic Exposure to IL-15 Initiates Robust Expansion and Chromosomal Instability in WT LGL

(A) Fold changes in expression of *IL-15* mRNA in human LGL leukemia samples from three patients (Pt), normalized to *18S* mRNA and then quantified relative to values of *IL-15* measured in normal donor cells that were enriched for either $CD56^+$ or $CD8^+$ (n = 4 each) and then arbitrarily set at 1.

(B) Schema for the generation of in vitro robust expansion of WT LGL during culture in IL-15 and adoptive transfer followed by malignant transformation in vivo in the absence of exogenous IL-15. Scale bars, 10 μm.

(C) WT splenic $NK1.1^+$ cells were sorted and incubated in triplicate with 100 ng/ml rhIL-15. Cell growth was quantified as absolute number of cells (mean ± SEM) using enumeration in trypan blue exclusion dye. Wright-Giemsa stain of the in vitro cultured cells. Scale bars, 10 μm.

(D) WT LGL were analyzed for their immuno-phenotype by FACS after 6 months of in vitro culture with IL-15.

(E) Karyotype analysis was performed on metaphase spreads from WT LGL cultured in IL-15 for approximately 6 months, demonstrating marked aneuploidy. Composite karyotype of the in vitro transformed WT LGL cells was: 76-79 < 4n > ,XXX,-X,-1,-3,del(4)(A1A2),-4,-5,+8,+8,+12,del(12)(A1.2B),-14, der(15)t(5;15)(B1;F2),-17,+19,+mar[cp7]/76 79,idem,+6[cp10]/76-79,idem,+ 19[cp3].

(F) ICR-SCID mice were intravenously injected with 1×10^7 WT LGL following approximately 8 months of in vitro culture with IL-15. Splenomegaly (compared to WT control as shown) and the presence of neoplastic LGL, both at the feathered edge of peripheral blood smear and on the spleen cytospin preparation, are shown. Scale bars, 10 μm. A representative FISH image illustrating gain of several copies chromosome 15 (red, chromosome 15 probe; blue, DAPI counter-stain) as seen in WT LGL cultured in vitro for months in IL-15 (E) is also shown. Scale bars, 5 μm.

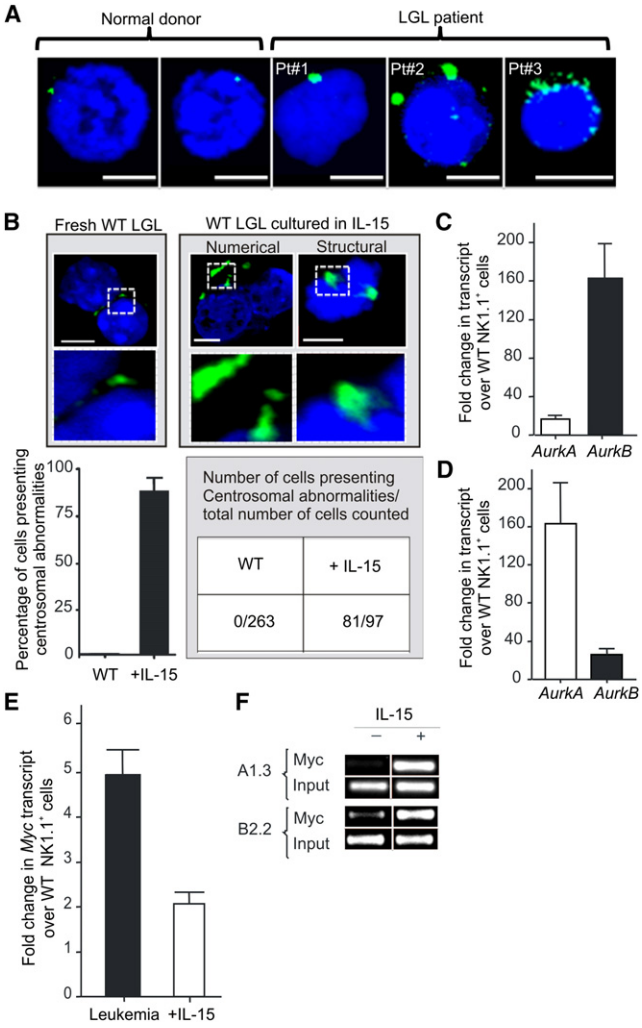

Figure 2. IL-15 Induces Centrosome Aberration in Normal LGLs

(A) The size, structure, and number of human centrosomes was determined by confocal microscopy and immunoflorescence staining with Pericentrin (green) in both freshly isolated normal human $CD56^+$ or $CD8^+$ LGL (top left) as well as in malignant cells from three patients with acute LGL leukemia. Cells were counterstained with DAPI (blue) for nuclear staining. Images shown are representative of slides with $\sim 10^5$ cells. Scale bars, 5 μm.

(B) The size, structure, and number of mouse centrosomes was determined by confocal microscopy and immunoflorescence staining with GTU88 (green) in both freshly isolated WT LGL (top left) as well as in WT LGL cultured in IL-15 for 6 months (top middle and right). Cells were counterstained with DAPI (blue) for nuclear staining. Images shown here are representative of three different slide preparation with $\sim 10^5$ cells. Graphical quantification of these centrosomal abnormalities is shown immediately below as percentage of cells (mean ± SEM) presenting centrosomal abnormalities from three independent slide preparations. Scale bars, 5 μm.

(C) Relative fold changes (mean ± SEM) in mRNA expression of *AurkA* and *AurkB* in splenocytes from LGL leukemic mice relative to values measured in fresh WT LGL. Quantification was by Real-time RT-PCR (n = 3 each). Each measurement was normalized against the level of *18S* mRNA, and then values for *AurkA* and *AurkB* in fresh WT LGL were arbitrarily set at 1.

(D) Relative fold changes (mean ± SEM) in mRNA expression of *AurkA* and *AurkB* for WT LGL cultured in IL-15 for 30 days, relative again to values measured in fresh WT LGL, which are arbitrarily set at 1 (n = 3 each).

(E) Relative fold changes (mean ± SEM) in mRNA expression of *Myc* in splenotyces from LGL leukemic mice (n = 3), and in WT mouse LGL cultured in IL-15 for 30 days. Both measurements are relative to values of *Myc* measured in fresh WT LGL that are arbitrarily set at 1.

(F) WT LGL were grown in vitro with IL-15 for approximately 6 months, and then harvested and starved for 24 hr and then divided up to be restimulated with either IL-15 or PBS for 4 hr. ChIP assay was performed using an anti-Myc antibody and PCR primers amplifying the *AurkA* and *AurkB* promoter 5′ regulatory regions.

See also Figure S1.

IL-15 Induces Centrosome Aberrations in Normal LGL

One proposed mechanism underlying CIN is centrosome-mediated asymmetric chromosome segregation resulting in aneuploidy (Ganem et al., 2009). Indeed we found numerical and structural centrosomal aberrations in primary cells obtained from patients with aggressive LGL leukemia (Figure 2A). We next assessed WT mouse LGL cultured for several months in IL-15 for centrosome aberrancies and compared them to fresh WT LGL. We found that the vast majority (81 of 97) of IL-15 cultured LGL counted had significant increases in centrosome numbers and/or size, while no such changes were noted in 263 fresh WT LGL (Figure 2B). Since altered regulation of centrosome replication can be caused by excessive aurora kinases encoded by *AurkA* and *AurkB* (Giet et al., 2005), we assessed the expression of these transcripts in LGL leukemic blasts from IL-15 Tg leukemic mice and found each to be significantly elevated in comparison to WT LGL from age-matched WT mice, although *AurkB* was significantly higher than *AurkA* (Figure 2C). Similarly, WT LGL exposed to IL-15 for only 30 consecutive days also showed higher transcript levels of *AurkA* and *AurkB* compared to the fresh LGL, although *AurkA* was significantly higher than *AurkB* (Figure 2D). Interestingly, overexpression of *AurkA* can transform rodent fibroblasts while *AurkB* cannot (Bischoff et al., 1998; Kanda et al., 2005; Zhou et al., 1998). This may explain the relative abundance of *AurkA* earlier in this process. Indeed, we show that forced overexpression of *AurkA* in WT mouse LGL exposed to IL-15 in a short-term culture resulted in quantitative and qualitative centrosome abnormalities as well as enhanced transformation in vitro (Figures S1A and S1B available online).

Because *AurkA* and *AurkB* are regulated by Myc (den Hollander et al., 2010), we measured and found increased transcript levels of *Myc* in both leukemic blasts as well as in the WT LGL cultured with IL-15 for 12 hr and for 30 days, and confirmed this at the protein level for both WT mouse and normal human LGL (Figures 2E, S1C and, S1D). This elevation of *AURKA, AURKB*, and *MYC* expression was confirmed in primary human LGL leukemia samples (Figure S1E). Chromatin immmuo-precipitation (ChIP) assays performed on WT mouse LGL that had been cultured in IL-15 for 6 months and then starved of IL-15 for 24 hr followed by re-stimulation with IL-15 or PBS for 4 hr demonstrated an increased binding of Myc within promoter regions of *AurkA* and *AurkB* (Figure 2F). Specific reduction of Myc by shRNA in IL-15-activated WT mouse LGL drastically reduced *AurkA* and *AurkB* expression (not shown). These data suggest that IL-15-mediated induction of Myc can lead to CIN in part via overexpression of *AurkA* and *AurkB*.

Using a luciferase construct, we next demonstrated that IL-15 induces Myc at least in part via activation of NF-κBp65

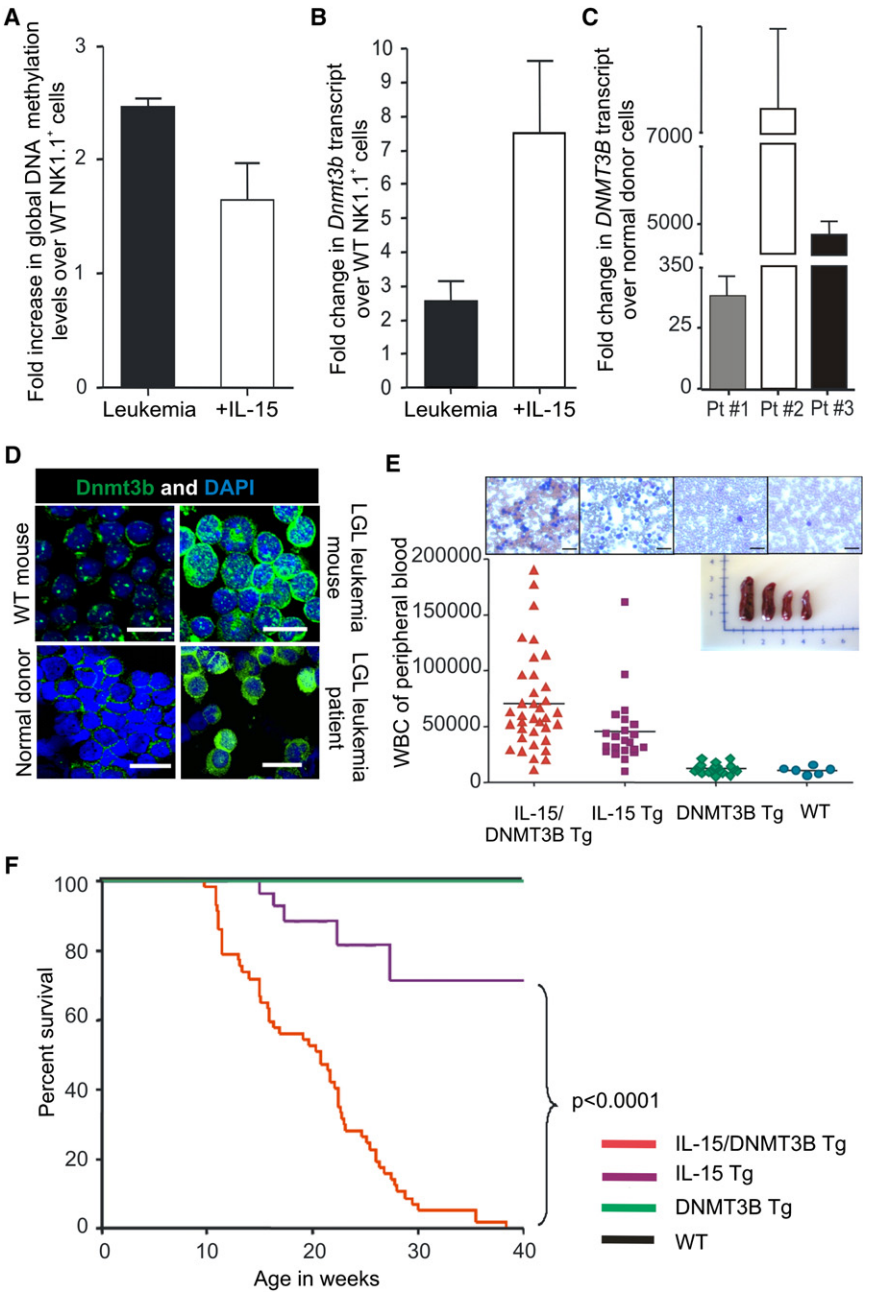

Figure 3. Aberrant DNA Methylation and Methytransferase Activity Contribute to IL-15-Induced LGL Leukemia

(A) Relative fold increase in GDM levels in splenocytes from LGL leukemic mice (n = 4) and in WT LGL cultured in IL-15 (n = 3) for 30 days relative to values of GDM measured in fresh WT LGL (n = 4), which is arbitrarily set at 1. Quantification was done by mass spectrophotometry and shown as mean ± SEM.

(B) Relative fold changes in mRNA expression of *Dnmt3b*, in splenocytes from LGL leukemic mice (n = 3) and in WT LGL cultured in IL-15 (n = 3) for 30 days relative to values of *Dnmt3b* measured in fresh WT LGL (n = 3). Quantification was by real-time RT-PCR and shown as the mean ± SEM. Each measurement was normalized against the level of *18S* mRNA, and then values of *Dnmt3b* for fresh WT LGL were arbitrarily set at 1.

(C) Fold changes (mean ± SEM) in mRNA expression of *DNMT3B* in three human LGL leukemia patient (Pt) samples, relative to values of *DNMT3B* measured in normal donors cells that were enriched for either $CD56^+$ or $CD8^+$ (n = 4 each) and arbitrarily set at 1. Each sample was normalized to *18S* mRNA.

(D) Confocal analysis of Dnmt3b protein expression in mouse and human LGL leukemia relative to normal LGL. Assay was done by immuno-labeling the cells with anti-Dnmt3b antibody. Data are representative of at least four independent mice, patients and normal donors. Cells were counterstained with DAPI (blue) for nuclear staining. Scale bars, 10 μm.

(E) WBC counts of different genotypes of adult mice generated from mating IL-15 Tg and DNMT3B Tg parents. The horizontal bar in each lane indicates the mean WBC count for 6-36 mice per group. Also included are four representative images from Wright-Giemsa staining of blood smears for each of the four genotypes, and an image of four whole spleens obtained from mice of each genotype.

(F) Comparative survival of DNMT3B Tg and WT mice (both 100%), IL-15 Tg, and IL-15/DNMT3B Tg mice.

See also Figure S2.

(Figure S1F). By EMSA, we showed binding at the putative NF-κB binding sites within the *Myc* promoter after 1 hr and 12 hr of exposure to IL-15 in both mouse (Figure S1G, left) and human LGL (Figure S1H, left). Supershift assay documented NF-κBp65 and p50 binding to the *Myc* promoter following LGL cell stimulation by IL-15 for 12 hr in both mouse (Figure S1G, right) and human LGL (Figure S1H, right). Finally, utilizing a ChIP assay, we demonstrated an enrichment of NF-κBp65 at the consensus binding site of the mouse *Myc* and human *MYC* promoter following LGL cell stimulation by IL-15 for 4 hr (Figures S1I and S1J). Thus, IL-15-mediated induction of Myc in normal LGL occurs, at least in part, via the activation of NF-κB.

IL-15 Increases Global DNA Methylation Levels in LGL

Hypermethylation of tumor suppressor and "stability" genes can also contribute to CIN (Esteller, 2006; Esteller, 2007), so we also pursued this in our mouse model. We previously showed that leukemic blasts from IL-15 Tg mice have an increase in methylation within the 5′ regulatory region of genes (Yu et al., 2005). We confirmed an increase in global DNA methylation (GDM) within LGL leukemic blasts from IL-15 Tg mice compared to age-matched WT LGL controls. We also measured a GDM increase in WT mouse LGL cultured with IL-15 for 30 days, suggesting that IL-15 is inducing methylation before leukemic transformation (Figure 3A). A similar increase in GDM was seen in our primary human LGL leukemia samples (Figure S2A). We investigated

whether changes in the DNA methyltransferase level is a cause for IL-15-mediated hypermethylation by measuring the mRNA levels of *Dnmt1*, *Dnmt3a*, and *Dnmt3b* in LGL leukemic blasts from IL-15 Tg mice and in WT LGL cultured with IL-15. Only *Dnmt3b* (mRNA and protein) was consistently elevated in both populations (Figure 3B and top row of Figure 3D). Further, only the expression of *DNMT3B* was consistently elevated in primary leukemic blasts from patients with LGL leukemia (Figure 3C and bottom row of Figure 3D), and was abundant in the nucleus of normal human LGL stimulated with IL-15 (Figure S2B). These data suggest that IL-15 may mediate hypermethylation of DNA in LGL at least in part via an induction of *DNMT3B*.

De Novo Overexpression of DNMT3B Augments the Incidence of LGL Leukemia In Vivo

We created DNMT3B Tg mice driven by the *Vav1* promoter (Figure S2C). In vitro, we demonstrated that LGL from these mice show enhanced transformation in the presence of IL-15, when compared to WT mouse LGL in the presence of IL-15 (Figure S2D). In contrast, mouse LGL with reduced expression of *Dnmt3b* showed a decrease in transformation in the presence of IL-15 when compared to WT mouse LGL in the same assay (Figure S2E). DNMT3B Tg mice were found to have a normal phenotype and life expectancy similar to their WT littermates (not shown). Mating IL-15 Tg and DNMT3B Tg parents generated four different genotypes: IL-15 Tg, DNMT3B Tg, IL-15/DNMT3B Tg, and WT mice. IL-15/DNMT3B Tg mice showed an increase in WBC count significantly earlier than their IL-15 Tg counterparts, while DNMT3B Tg mice and WT mice had normal WBC counts (Figure 3E). IL-15/DNMT3B Tg mice showed a significantly shorter latency and 100% incidence of fatal LGL leukemia compared with IL-15 Tg mice (Figures 3F and S2F). The immunophenotype of IL-15/DNMT3B Tg leukemia was similar to that of IL-15 Tg leukemia (Yokohama et al., 2010) (not shown) but IL-15/DNMT3B Tg mice had lymphadenopathy (Figure S2G). Thus, excess expression of DNMT3B does not initiate leukemia but contributes to its progression upon chronic exposure with IL-15.

Both the IL-15 Tg and the IL-15/DNMT3B Tg mice had significantly greater CpG methylation, as measured by LINE-1 hypomethylation (Estécio et al., 2007; Ogino et al., 2008), when compared to the DNMT3B Tg and WT mice (Figure S2H). While the differences in these measurements as well as those seen in Figure S2A appear modest, they measure methylation across the entire genome, rather than methylation of specific tumor suppressor genes. We previously documented promoter methylation and silencing of the tumor suppressor *Idb4* in leukemia from IL-15 Tg mice (Yu et al., 2005). Notably, *Idb4* promoter methylation was more pronounced in LGL leukemia from IL-15/DNMT3B Tg mice compared to that of IL-15 Tg mice (Figure S2I). Culture of WT LGL with IL-15 for 30 days also resulted in methylation of the *Idb4* promoter, albeit not as striking as seen in primary LGL leukemia samples from IL-15 Tg mice (Figure S2I). In contrast, LGL from DNMT3B Tg mice did not show any methylation at the *Idb4* promoter, similar to WT LGL (Figure S2I). Thus, overexpression of DNMT3B without IL-15 overexpression was insufficient to cause *Idb4* promoter methylation. Collectively, these results indicate that the overexpression of DNMT3B is likely necessary but without overexpression of IL-15 is insufficient for the hypermethylation of DNA noted in LGL chronically exposed to this cytokine.

IL-15 Regulates Expression of DNMT3B via Repression of MicroRNA (*miR)-29b*

We have reported that Dnmt3b is a direct, negatively regulated target of *miR-29b* and repression of *miR-29b* is induced by binding of Myc, Hdac-1, and NF-κBp65 to its promoter (Chang et al., 2008; Garzon et al., 2009b; Liu et al., 2010). We showed that short-term culture of WT mouse LGL with IL-15 induces Myc protein via NF-κB (Figures S1F–S1I). Similar data were obtained for Myc and NF-κB for both long-term cultures of WT mouse LGL in IL-15 (Figure 4A) as well as in mouse and human LGL leukemia (Figures 4B and 4C). Finally, we used a ChIP assay to show increased binding of Myc, Hdac-1, and NF-κBp65 repressors to the *miR-29b* 5′ regulatory region in WT mouse LGL first starved and then re-exposed to IL-15 (Figure 4D). Similar results were obtained in splenocytes from LGL leukemia in IL-15 Tg mice when compared to WT mouse splenocytes (Figure S3). As a result of these experiments, we postulated that IL-15 stimulation of WT LGL represses *miR-29b* via Myc, Hdac-1, and NF-κBp65.

Indeed, when compared to fresh WT LGL, *miR-29b* expression was significantly decreased in LGL leukemia from IL-15 Tg mice ($p < 0.02$) as well as in WT mouse LGL stimulated with IL-15 for 12 hr (Figure 4E). We found similar striking results in human LGL leukemia ($p < 0.0009$) and in normal human LGL incubated with IL-15 ($p < 0.003$) (Figures 4F and 4G). Further, forced overexpression of *miR-29b* by 40- to 60-fold in IL-15-activated WT mouse LGL was associated with a proportional decrease in *Dnmt3b* expression (Figures 5A and 5B), while the reduction of Myc expression by shRNA in IL-15-activated WT mouse LGL significantly increased *miR-29b* expression and decreased *Dnmt3b* expression (not shown). Thus, the IL-15-mediated induction of Myc, NF-κB, and Hdac-1 repressors in WT mouse LGL results in a decrease in *miR-29b* expression that in turn increases *Dnmt3b* expression.

To further confirm the role of *miR-29b* in IL-15-mediated LGL leukemia, we overexpressed *miR-29b* in fresh WT LGL cells, which were then cultured in IL-15 for 8–10 days prior to assessment for early evidence of transformation in vitro. We noted that overexpression of *miR-29b* was inversely associated with IL-15-mediated LGL transformation compared to control transfected cells, i.e., WT LGL with overexpression of *miR-29b* showed significantly less IL-15-mediated transformation (Figure 5C). Furthermore, a significant decrease of *miR-29b* expression in WT LGL cells transfected with *miR-29b* antagomir and cultured in IL-15 for 8–10 days resulted in a significant increase in their transformation compared with the same LGL transfected with a scrambled control (Figures 5D and 5E). Thus, collectively, we provide evidence in WT LGL for a mechanistic link between IL-15-mediated downregulation of *miR-29b*, increased *Dnmt3b*, and enhanced transformation in short-term cultures with IL-15, as well as increased methylation of the genome, including the tumor suppressor *Idb4*, in WT LGL cells chronically exposed to IL-15.

A Formulation of a Proteasomal Inhibitor Provides Long-Term Disease-free Survival in Leukemic Mice

Because our previous data reveal that it is possible to reverse *miR-29b* repression in leukemia cells by targeting the

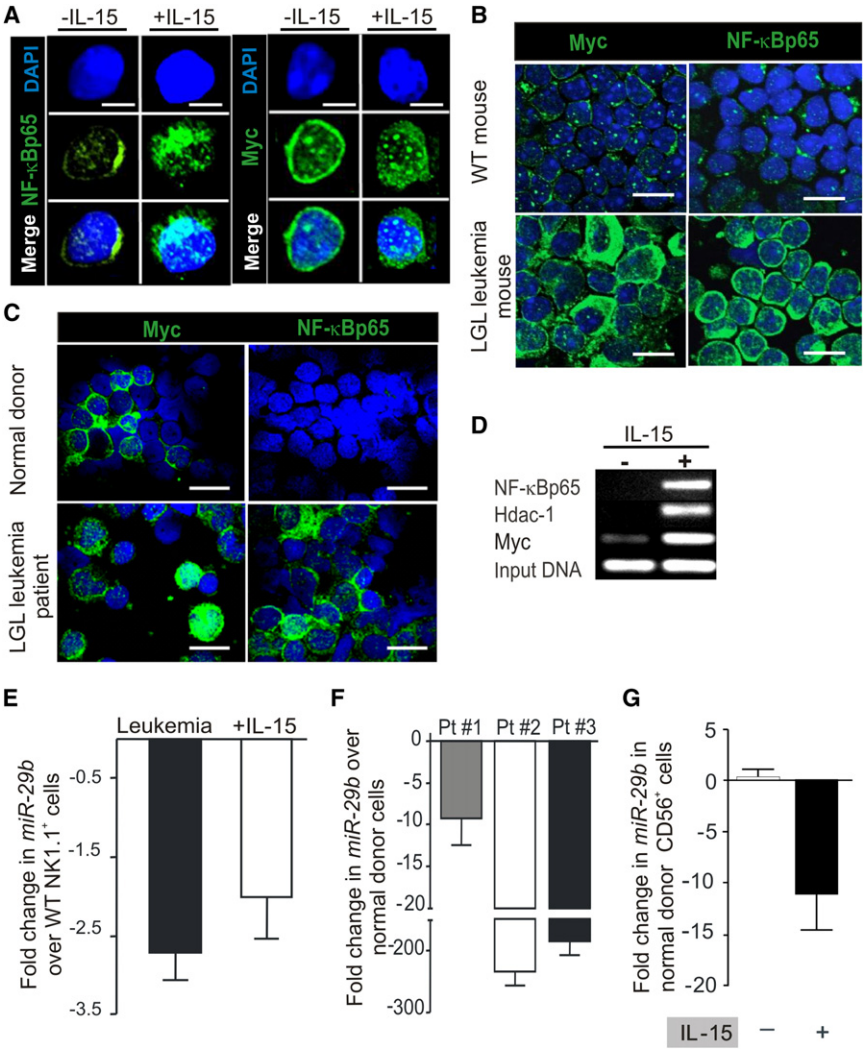

Figure 4. Alteration of Gene Expression by IL-15 and in LGL Leukemia

(A) Confocal analysis of fresh WT mouse LGL and WT mouse LGL cultured in IL-15 for 30 days was performed by immunolabeling the cells with anti-Myc and anti-NF-κBp65 as above. Scale bars, 5 μm.

(B) Confocal analysis of spleen samples from LGL leukemic mice and fresh WT LGL for Myc and NF-κB was performed by immuno-labeling of the cells with the respective antibody. Cells were counterstained with DAPI (blue) for nuclear staining. Data are representative of at least five independent mice evaluated for protein expression. Scale bars, 10 μm.

(C) Confocal analysis of enriched LGL from normal human donor blood samples compared with LGL leukemia samples from patients. Immuno-staining was done by incubating the cells with anti-MYC and an anti-NF-κBp65 antibody. Data are representative of at least four independent normal donors and LGL leukemia patients evaluated for protein expression. Scale bars, 10 μm.

(D) In vitro cultured WT LGL were grown with IL-15 for approximately 8 months, then harvested and starved for 24 hr and then divided up to be re-stimulated with either IL-15 or PBS for 4 hr. A ChIP assay was performed using the indicated antibody. The gel image shows the PCR product of the indicated gene performed on ChIP DNA with primers designed for amplification along the *miR-29b* promoter/enhancer region. The data are representative of three independent experiments.

(E) Fold decrease (mean ± SEM) in *miR-29b* transcript levels in splenocytes from LGL leukemic mice (n = 4) and in WT LGL cultured in IL-15 (n = 4) for 12 hr relative to value of *miR-29b* measured in fresh WT LGL (n = 4) which is arbitrarily set at 1. Each sample was normalized to *U6*.

(F) Fold changes (mean ± SEM) in expression of *miR-29b* transcript levels in human LGL leukemia samples, normalized to *U6* and then quantified relative to values of *miR-29b* measured in normal donor cells that were enriched for either $CD56^+$ or $CD8^+$ (n = 4 each) and then arbitrarily set at 1.

(G) Fold changes (mean ± SEM, n = 3) in expression of *miR-29b* in $CD3^-CD56^+$ normal human donor LGL from IL-15 stimulated and PBS treated control for 12 hr relative to values of *miR-29b* measured in unstimulated normal donor LGL and arbitrarily set at 1. Each measurement was normalized against the level of *U6*. See also Figure S3.

transcriptional repression of Myc, Hdac-1, and NF-κBp65 using pharmacologic proteasome inhibitors (Garzon et al., 2009b; Liu et al., 2010), we exposed LGL leukemia blasts from IL-15 Tg mice to the proteasome inhibitor bortezomib for 2 hr, and observed a 13,000-fold upregulation of *miR-29b* when compared to blasts treated with PBS (n = 3, p = .02; Figure 6A). This resurgence in *miR-29b* expression within 2 hr of treatment is followed by its return to levels seen in WT cells, suggestive of a block in the binding of Myc, Hdac-1, and NF-κBp65 to the *miR-29b* promoter. We also noted a significant (~50-fold) decrease in *Dnmt3b* transcript in bortezomib-treated LGL leukemic blasts at 48 and 72 hr, compared to PBS-treated blasts (Figure 6B), which was validated at the protein level (Figure 6C). Targeting the transcriptional repressors of *miR-29b* also led to a significant re-expression of the tumor suppressor gene *Idb4* compared to PBS-treated blasts (Figure 6D). COBRA analysis confirmed this was due to reduction in *Idb4* promoter methylation (Figure 6E). Notably, this in vitro treatment with bortezomib not only resulted in downregulation of *Dnmt3b*, but also reduced expression of *AurkA* and *AurkB* transcript in leukemic blasts compared to PBS treated blasts (Figures S4A and S4B). Marked apoptosis of WT LGL in the presence of IL-15 as well of LGL leukemia was noted with the in vitro treatment with bortezomib, which may also be secondary to the drug's effect on the induction of pro-apoptotic Bid, as previously reported (Hodge et al., 2009).

We reported that in vivo treatment of ICR-SCID mice engrafted with primary LGL leukemia from IL-15 Tg mice with a DNA hypomethylating agent that targets Dnmt1 (i.e., decitabine) or in combination with a HDAC inhibitor (i.e., depsipeptide) was either ineffective or highly toxic, respectively (Yu et al., 2009). To test the efficacy of bortezomib, we needed to first improve the in vivo pharmacodynamics of the drug because the naked

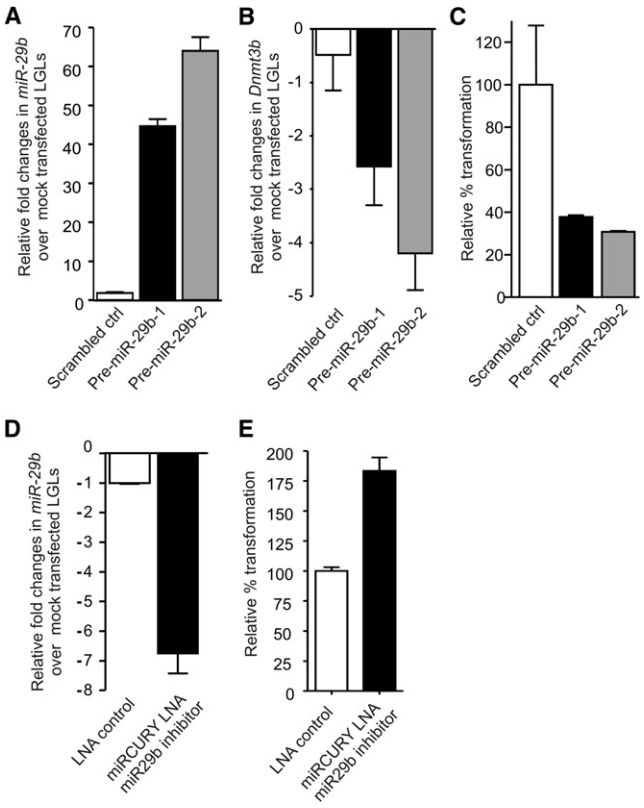

Figure 5. *Mir-29b* Overexpression or Repression Alters LGL Transformation

(A) Relative fold overexpression (mean ± SEM) of *miR-29b* in WT mouse LGL transfected with scrambled control or pre-*miR-29b*, relative to the value measured in mock transfected LGL (not shown), which is arbitrarily set at 1. Each sample was normalized to *U6*.

(B) Relative fold changes (mean ± SEM, n = 3) in mRNA expression of *Dnmt3b* in LGL shown in (A). Each measurement was normalized against the level of *18S* mRNA, and then values of *Dnmt3b* for mock transfected LGL cells were arbitrarily set at 1.

(C) LGL similarly transfected with scrambled control or pre-*miR-29b* as shown in (A) were then plated at 1 × 10^5/well in triplicate and cultured with IL-15 in a semisolid agar medium for 8–10 days after which CFU are detected and quantified in a cell transformation assay using a microtiter plate reader as described in Experimental Procedures. Percent transformation of pre-*miR-29b* transfected LGL relative to control (scrambled transfected LGL, arbitrarily set at 100%) is shown as mean ± SEM, n = 3 each.

(D) In vitro cultured mouse LGL were transfected with 50 pmole solution of LNA control or LNA *miR-29b* inhibitor oligonuleotide per manufacturer's instruction by electroporation. Cells were measured for *miR-29b* expression levels 24 hr post transfection.

(E) WT mouse LGL were plated at 1x10^5/well in triplicate and cultured with IL-15 in a semisolid agar medium for 8–10 days after which CFU are detected and quantified in a cell transformation assay using a microtiter plate reader as described in Experimental Procedures. Percent transformation of cells relative to LNA control (arbitrarily set at 100%) is shown as mean ± SEM, n = 3 each.

compound was toxic and ineffective. We therefore developed a liposomal preparation (Figure S4C). Four weeks after ICR-SCID mice were engrafted with a lethal dose of LGL leukemic blasts from IL-15 Tg mice, a twice-weekly treatment with the liposomal bortezomib was initiated at the dose of 1.0 mg/kg/mouse for the first week, which was continued at the dose of 2.0 mg/kg/mouse for next 2 weeks while monitoring for any clinical signs of toxicity or leukemia-related distress. In a randomized trial, control mice treated with a preparation of empty liposomes first succumbed to fatal LGL leukemia within 60–80 days following infusion of the LGL leukemic blasts, and mice treated with free bortezomib at a similar dose and schedule as liposomal bortezomib all died from leukemia generally within the same time. However, the mice engrafted with LGL leukemia and treated with liposomal bortezomib showed 100% survival 130 days following infusion of the LGL leukemic blasts, without any evidence of toxicity (Figure 6F). Spleens from mice treated with liposomal bortezomib were significantly reduced in weight (Figure S4D) and histologic examination showed a clearance of leukemic blasts from liver and spleen (not shown).

DISCUSSION

There are previous reports documenting the increased risk of cancer in association with aberrant cytokine signaling, and a few murine models where their overexpression of cytokines (i.e., IL-9 or IL-15) induces malignant transformation (Fehniger et al., 2001; Renauld et al., 1994; Waldmann and Tagaya, 1999), yet mechanistic data regarding the latter remains incomplete (Hodge et al., 2009; Yu et al., 2005). The crucial role of IL-15 in the survival and proliferation of LGL leukemia has also been well documented in both humans and mice (Fehniger et al., 2001; Yokohama et al., 2010; Zambello et al., 1997). Abnormal expression of IL-15 has been described in patients with other lymphoid malignancies and autoimmune diseases including rheumatoid arthritis, multiple sclerosis, psoriasis, inflammatory bowel disease, and also in diseases associated with human T cell lymphotropic virus I (HTLV-I) (Asadullah et al., 2000; Azimi et al., 1998, 1999; Carroll et al., 2008; D'Auria et al., 1999; Trentin et al., 1997). Zambello et al. previously showed that membrane-bound IL-15 is expressed on proliferating blast cells in LGL leukemia patients (Zambello et al., 1997), and most if not all human LGL leukemia cell lines require activation via the IL-15Rβγ for propagation in vitro, suggesting that IL-15 is required for initiation and maintenance of leukemogenesis in vivo.

Here, we provide the evidence that IL-15 alone can immortalize WT LGL in vitro that, upon adoptive transfer in vivo, undergoes fulminant leukemic transformation in the absence of exogenous IL-15. This oncogenic effect is the result of two distinct pathways by which IL-15 contributes to malignant transformation: first via the induction of CIN and marked aneuploidy; and second via an induction of DNA hypermethylation, which can contribute both to CIN (Esteller, 2006, 2007; Ganem et al., 2009) and to silencing of tumor suppressor genes (Figure 7). We show that IL-15 induces Myc, Hdac-1, and NF-κBp65, which mediate downregulation of *miR-29b* and consequent overexpression of *Dnmt3b*, thereby hastening the onset of LGL leukemia. Concurrent upregulation of IL-15, MYC, AURKA, AURKB, NF-κBp65, and downregulation of *miR-29* followed by upregulation of DNMT3B and increased GDM, as well as centrosome aberrancies were also demonstrated in primary patient LGL leukemic blasts compared with normal controls.

There is currently no curative treatment for LGL leukemia and the disease is fatal in most circumstances. Treatment options include methotrexate, cyclosporine A, or cyclophosphamide and

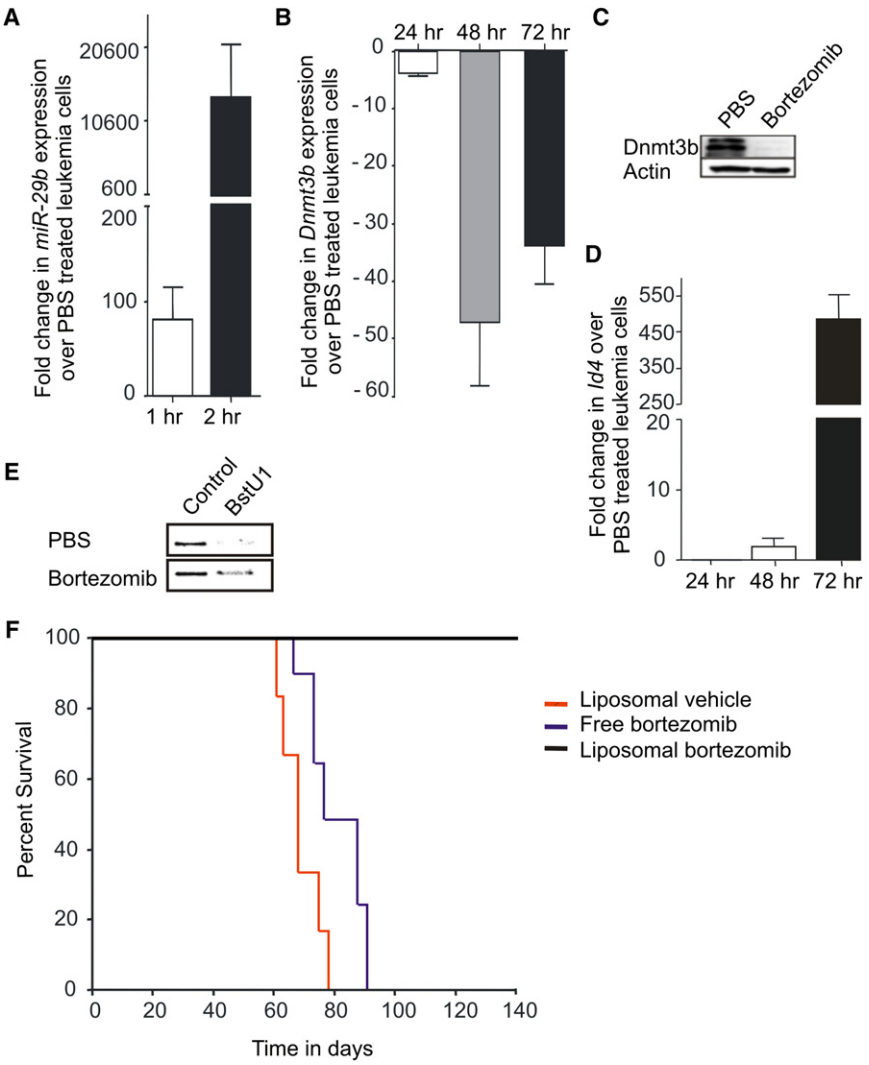

Figure 6. In Vitro and In Vivo Targeting of *miR-29b* Transcriptional Repression

(A) Fold increase in *miR-29b* transcript at 1 (white) and 2 (black) hr post in vitro bortezomib treatment (20 μM). Both measurements normalized to *U6* and then set relative to values of *miR-29b* measured in PBS treated LGL leukemia cells, which are arbitrarily set at 1.

(B) Relative fold changes in mRNA expression of *Dnmt3b* in bortezomib (20 nM) treated LGL leukemia samples at 24, 48, and 72 hr, normalized to *18S* mRNA and then quantified relative to values of *Dnmt3b* in PBS-treated LGL leukemia samples that are arbitrarily set at 1. Data for (A) and (B) are mean ± SEM (n = 3).

(C) Splenocytes from LGL leukemic mice were treated in vitro with either control (PBS) or bortezomib (20 nM) for 24 hr and then immunoblotted for Dnmt3b and actin that was used as an internal control.

(D) Relative fold changes (mean ± SEM) in mRNA expression of *Idb4* in mouse LGL leukemia cells treated in vitro with bortezomib (20 μM) at 24, 48, and 72 hr, normalized to *18S* mRNA, and then quantified relative to values of *Idb4* in PBS-treated LGL leukemia samples that are arbitrarily set at 1.

(E) COBRA analysis for *Idb4* promoter methylation in splenocytes from LGL leukemic mice that were treated in vitro for 72 hr with either control (PBS) or bortezomib (20 nM). Amplification of the *Idb4* promoter region and sequential COBRA analysis with a methylation sensitive restriction enzyme (*BstU1*) reveals only a partial loss of methylation at the *Idb4* promoter in LGL leukemia cells treated with bortezomib (20 μM), but not PBS.

(F) Kaplan–Meier survival plot for ICR-SCID mice (n = 6–8/group) after intravenous injection of splenocytes from LGL leukemia mice. Disease-free survival in mice treated with empty liposomes, free bortezomib, and liposomal bortezomib.

See also Figure S4.

monotherapy with corticosteroids (Sokol and Loughran, 2006; Utecht and Kolesar, 2008), and are often associated with significant hematologic and other toxicities (Sokol and Loughran, 2006). Relatively little data exist on effective alternative therapies for LGL leukemia. Targeting IL-15 or the β chain component of its receptor as a means of immunotherapy has been suggested, but has thus far not been successful in clinical trials for LGL leukemia patients (Morris et al., 2006). Furthermore, our experimental therapy with the Dnmt inhibitor decitabine targeting the aberrant epigenetic changes observed in our preclinical model of LGL leukemia resulted in only transient responses and associated hematologic toxicity, and the combination of decitabine with a histone deacetylase inhibitor resulted in fatal toxicity (Yu et al., 2009). These data therefore emphasize the need for approaches aimed at the pathogenic mechanisms responsible for initiation and maintenance of LGL leukemia. To pursue this goal, we designed a therapeutic strategy that used liposomal bortezomib to concurrently and effectively target upregulation of Myc, activation of AurkA, AurkB, and NF-κBp65; and downregulation of *miR-29*, which were shown to play a pivotal role in inducing CIN and aberrant *Dnmt* expression and in turn leukemia. Garzon et al. have previously shown that decreased *miR-29b* expression can also contribute to cancer progression by a concomitant increased expression of the anti-apoptotic Mcl-1 (Garzon et al., 2009a), and Hodge et al. have shown that IL-15 can lower the pro-apoptotic Bid protein in LGL leukemia via proteasome-mediated degradation (Hodge et al., 2009). STAT3 also lies downstream of IL-15 receptor activation, and LGL leukemia from our IL-15 Tg mice display constitutive activation if STAT3 (our data, not shown). The latter has been shown to induce anti-apoptotic Mcl-1 expression in patients with LGL leukemia (Epling-Burnette et al., 2001), and a recent study has uncovered activating STAT3 mutations in a subset of patients with chronic LGL leukemia (Johnston et al., 1995; Koskela et al., 2012). Hence it is possible that some of the effects shown to result from excessive IL-15 signaling in this report, as well as other unknown effects, are mediated at least in part by an activated STAT3. Extending and integrating these findings, therapeutic strategies for IL-15-mediated cancers could be also provided through the use of aurora kinase inhibitors, NF-κB inhibitors, STAT3 inhibitors, and/or synthetic miRNAs that target DNA methyltransferases (Chan et al., 2010).

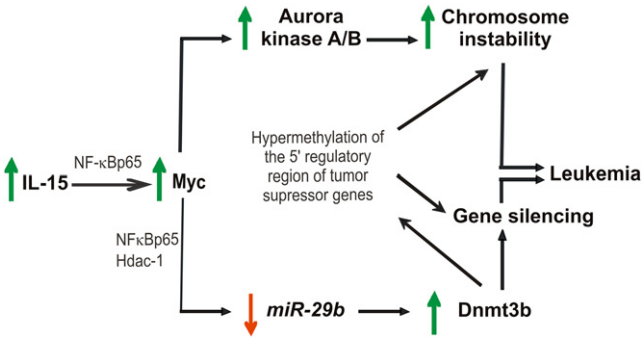

Figure 7. Schematic of the Proposed Network of IL-15-Mediated Transformation of WT LGL to LGL Leukemia

Our therapeutic effectively targets the proteasomal degradation pathway and transcriptional repressors/activators in vivo, thereby inducing a long-term disease-free remission as a single agent in this otherwise fatal and refractory malignancy. The correlative data we provide from human LGL leukemia samples document their overexpression of IL-15 as well as the two aberrant pathways that emanate from chronic stimulation by IL-15. Collectively this offers a strong rationale for a therapeutic intervention with liposomal bortezomib in patients with LGL leukemia.

EXPERIMENTAL PROCEDURES

Generation of Transgenic Mice

The Institutional Animal Care and Use Committee (IACUC) of The Ohio State University (OSU) approved all procedures involving animals. Expression of the human *DNMT3B* in Tg mouse is driven by the *Vav* promoter, which restricts expression to cells of hematopoietic lineage. The *Vav*-transgenic system is well established for mouse models of hematopoietic disease (Ogilvy et al., 1998). The transgenic construct, including a HA-tag, was injected into mouse pronuclei and multiple offspring were obtained with variable numbers of the transgene (Figure S2C) but with normal survival (Figure 3F). IL-15 Tg mice were generated and maintained as described previously (Fehniger et al., 2001).

In Vitro Culture of LGL Cells

To expand LGL cells in vitro, approximately 1 × 10^5 FACS sorted splenic NK1.1$^+$ cells were cultured in 96-well plates at a density of 1 × 10^5/100 μl RPMI medium supplemented with β-mercaptoethanol, antibiotics, and 100 ng/ml of rhIL-15. Typically culture medium was refreshed every 48–72 hr, and cells then transferred to six well plates and split back to original density in culture when they reached a density of 1.6 × 10^6/100 μl.

Antibody Staining and Flow Cytometry

Spleen, bone marrow, and peripheral blood samples were harvested from moribund mice following sacrifice and single cell suspensions were prepared as described previously (Fehniger et al., 2001). The experiments were performed according to the IACUC guidelines. The following fluorochrome-conjugated monoclonal antibodies (mAb) were purchased from BD PharMingen, San Jose, CA and used for flow cytometry: anti-CD3 (clone 145-2C11), anti-NK1.1 (clone PK136), anti-CD4 (clone RM4-5), and anti-CD8a (clone 53-6.7). Human LGL enrichment antibodies, anti-CD56 (clone N901), and anti-CD3 (clone UCHT-1) were purchased from Beckman Coulter (Beckman Coulter, Brea CA).

Enrichment of LGL

Normal human peripheral blood LGLs were enriched from leukopacks purchased from the American Red Cross (Columbus, OH) to >70% cell purity utilizing methods previously described (Park et al., 2009). Briefly, mononuclear cells were obtained using Ficoll-Paque Plus (GE Healthcare, Little Chalfont, United Kingdom) and CD56$^+$ cells were enriched using a Rosette separation cocktail (StemCell Technologies, Vancouver, BC) following the manufacturer's instructions. Enriched LGLs were then sorted with BD FACSAria cell sorter using anti-CD56 and anti-CD3. Sorted cells were >95% pure for CD56$^+$CD3$^-$ population. Patient samples were obtained from the OSU Leukemia Tissue Bank following informed consent. The OSU Institutional Review Board approved all experiments performed with human materials.

Total RNA and DNA Isolation

Single cell suspension was spun down and the cell pellet was resuspended in TRIzol Lysis reagent (Invitrogen, Carlsbad, CA) processed further using miRNeasy Mini Kit and Reagents (QIAGEN, Valencia, CA). On-column DNA digestion was performed to eliminate any residual DNA. Total RNA was eluted using RNase-free water, and was quantified by NanoDrop 1000 Spectrophotometer (Thermo Scientific, Wilmington, DE). DNA isolations were performed using QIAamp DNA Micro Kit (QIAGEN), according to manufacturer's protocols with the exception of the elution step, which was done with water instead of Buffer AE.

First Strand Synthesis for RT-PCR and Quantitative *Taqman* PCR

cDNA was generated from approximately 100–500 ng of total RNA, using the SuperScript First Strand Synthesis kit for RT-PCR (Invitrogen), according to the manufacturer's protocol. RT reaction was performed in a DNA Engine Dyad Peltier Thermal Cycler (Bio Rad, Hercules, CA) using the following program: 25°C for 10 min (min), 42°C for 50 min, and 70°C for 10 min. For first strand synthesis of *miR-29b* and *U6*, approximately 100 ng of RNA was processed using the Applied Biosystems mir-RT kit (Applied Biosystems, Austin, TX). Total RNA was added to a mix of dNTP mix, RT enzyme, 10× RT buffer, RNase inhibitor, and each desired Taqman 5× RT primer. RT reaction was performed using the following temperature conditions: 16°C for 30 min, 42°C for 45 min, and 85°C for 5 min and stored at 4°C until needed for quantitative PCR. Quantitative RT-PCR was performed using either 1μl of cDNA or its dilutions. Briefly, 1 μl of sample was added to a 20 μl total reaction volume containing 20× RT Taqman Assay for desired gene or miRs, 2× Taqman Universal Fast PCR Master Mix (Applied Biosystems). Reaction was performed in 96 well Fast Optic Plates, and run using the 7900HT Fast Real-Time PCR System (Applied Biosystems). Taqman probe ID for the genes can be provided upon request.

Chromatin Immunoprecipitation Assays and Quantitative ChIP PCR for *miR-29b* and the *AurkA* and *AurkB* Promoters

Approximately 2 × 10^7 cells were harvested from leukemic and WT mice and the chromatin immunoprecipitation (ChIP) assay were performed as described previously (Liu et al., 2010). For IL-15 stimulation experiments, WT LGL cultured with IL-15 were first starved of IL-15 for 24 hr, washed twice with cold RPMI medium, and then re-exposed to either PBS or IL-15 for 4 hr. The following antibodies were purchased from AbCam (Cambridge, England) and used for ChIP: anti-HDAC-1 (Ab7028) and anti-NF-κB p65 (Ab7970). Anti-c-Myc antibody was purchased from Santa Cruz Biotechnology. ChIP PCR was performed using Power SYBR PCR mix (Applied Biosystems) or AmpliTaq Gold 360 PCR Master Mix using ChIP DNA, which was added to 25 μl total reaction volume containing 2× PCR mix, and 10 μM of *miR-29b* forward and reverse primers (Sigma-Aldrich, St. Louis, MO). Primer sequence can be provided upon request. Fold change in binding was compared using input DNA as control. PCR for *AurkA* and *AurkB* was performed as described previously (den Hollander et al., 2010).

Immunofluorescence Staining and Confocal Microscopy

Approximately 1–2 × 10^5 freshly harvested cells were spun onto a microscope slide using Shandon Cytospin 4 cytofuge (Thermo Fisher Scientific, Waltham, MA). The slides were fixed immediately with ice-cold acetone for 10 min and washed twice with PBS and 20% FBS. Blocking was performed by incubating the cells in protein-free blocking solution (Dako Denmark A/S, Glostrup, Denmark) for 30 min. Cells were then stained with a 1:100 dilution of goat polyclonal to rabbit IgG anti-c-Myc, anti-Dnmt3b (Santa Cruz Biotechnology, Santa Cruz, CA), or anti-NF-κBp65 (AbCam) at room temperature for 60 min. Slides were washed twice with PBS containing 20% FBS before incubating the cells with 1:40 dilution of Texas Red-X goat anti-rabbit IgG (Invitrogen,

Carlsbad, CA) at room temperature for 60 min in dark. Cells were than washed with PBS containing 20% FBS and mounted with VECTASHIELD Mounting Medium with DAPI. Pericentrin (Abcam) and GTU-88 (Vector Laboratories, Burlingame, CA) antibodies were used to perform centrosomal staining in acetone fixed cells. Briefly, cells were mounted on Poly-L-Lysine coated slides and fixed in ice-cold acetone for 5 min. Cells were incubated with either Pericentrin (for human samples) or GTU88 (for mouse samples) antibody for 1 hr at room temperature followed by incubation with secondary antibody. Images were acquired using Olympus FV1000-Filter Confocal microscope (Olympus, Center Valley, PA) and analyzed with Olympus Fluoview software (version 2.0).

In Vitro Drug Studies

Cells were harvested from the spleens of leukemic mice. Cells were cultured in RPMI 1640 containing 10% FBS, at 37°C with 5% CO_2 and 100 units/ml of rhIL-2. Leukemic cells were incubated with 20 nM bortezomib or PBS for an incubation time that varied with the experiment performed. Viable cells were measured by trypan blue exclusion. Cells were harvested and washed with PBS prior to DNA and RNA isolation.

Bisulphite Conversion and COBRA Analysis of *Idb4* Promoter

Bisulphite conversion and COBRA Analysis of *Idb4* promoter was performed as described (Yu et al., 2005).

Transfection of Primary Murine LGL Cells

Transfections were performed using murine *Dnmt3b* and *AurkA* SureSilencing shRNA plasmids purchased from SABiosciences' (QIAGEN, Valencia, CA). Overexpression plasmids were purchased from Origene (Origene, Rockville, MD). Single cell suspension of LGL cells were transfected using the Amaxa Nucleofection system (Lonza Cologne GmbH, Cologne, Germany). Briefly, approximately 5×10^6 cells were transfected according to the manufacturer's protocol for Amaxa Mouse Macrophage Nucleofector Kit. Cells were assessed for the expression of GFP 12–24 hr after transfection.

In Vitro Transformation Assay

Normal activated T cells can form microscopically visible colonies in semisolid medium as early as 4–6 days following exposure to the transforming T cell leukemia virus, HTLV1. These lymphocytes proved to be transformed in that their proliferation subsequently became independent of growth factor. In the absence of infection by HTLV1, normal activated T cells do not transform and do not form colonies in semisolid medium (Aboud et al., 1987). We used a slightly modified colony forming unit (CFU) assay to assess for transformation of WT mouse LGL exposed to IL-15 and forced overexpression of *AurkA* or *Dnmt3b* or underexpression of *miR-29b*.

WT NK1.1$^+$CD3$^-$ LGL were activated and expanded in vitro with IL-15 and transfected by electroporation with 5 μg of GFP-plasmid DNA control construct or a GFP-experimental vector construct as indicated in the figure legends. Twenty-four hr after transfection, cells were sorted for GFP expression (~95% purity) and seeded at the density of 0.5×10^5–1×10^5 cells/well in 96 well plates in a semisolid agar medium without or with a supplement of IL-15 (100 ng/ml). The semisolid agar colony formation assay was performed per manufacturer's instruction using the Cytoselect 96-Well Cell Transformation Assay Kit (Cell Biolabs Inc, San Diego, CA). Briefly, following an 8–10 day incubation period, cell colonies are solubilized, lysed, detected, and quantified by the provided MTT solution (Invitrogen, Carlsbad CA) in a microtiter plate reader.

CFUs was absent from wells seeded with WT mouse LGL transfected with the GFP-plasmid DNA control construct but without IL-15. CFUs quantified in wells seeded with IL-15 and WT mouse LGL transfected with the GFP-plasmid DNA control construct were labeled the control group and arbitrarily assigned a transformation score of 100%. CFU quantified in wells seeded with IL-15 and WT mouse LGL transfected with GFP plus the experimental vector construct were labeled the experimental group and were scored as a percent transformation relative to the control group.

In Vivo Drug Studies

Age and sex matched ICR-SCID mice were used to study in vivo transplantability of the leukemia cells. Approximately 2×10^6 splenocytes obtained from IL-15 Tg leukemic mice were intravenously injected into recipient mice. Upon engraftment of leukemia (measured by increased peripheral WBC count), mice were given two doses of either bortezomib or liposomal bortezomib at the concentration of 1.0 mg/week/kg of body weight, followed by two doses of 2.0 mg/week/kg of body weight for next 2 weeks. Empty liposomes were injected as control. All the experimental mice were given drug or placebo via tail vein injection for 3 consecutive weeks.

SUPPLEMENTAL INFORMATION

Supplemental Information includes four figures and Supplemental Experimental Procedures and can be found with this article online at http://dx.doi.org/10.1016/j.ccr.2012.09.009.

ACKNOWLEDGMENTS

This work is supported by National Cancer Institute Grants CA16058, CA95426, CA68458, CA09338 (to M.A.C.); CA140158 (to M.A.C. and G.M.); CA102031 (to G.M.); CA149623 (to S.L.); and NSF EEC-0914790 (to R.J.L.). The authors wish to thank Kathleen McConnell for technical assistance; we thank Mr. and Mrs. Thomas Lauber and Greif, Inc. for their support.

Received: July 25, 2011
Revised: July 2, 2012
Accepted: September 14, 2012
Published: November 12, 2012

REFERENCES

Aboud, M., Golde, D.W., Bersch, N., Rosenblatt, J.D., and Chen, I.S. (1987). A colony assay for in vitro transformation by human T cell leukemia viruses type I and type II. Blood *70*, 432–436.

Ames, B.N., Gold, L.S., and Willett, W.C. (1995). The causes and prevention of cancer. Proc. Natl. Acad. Sci. USA *92*, 5258–5265.

Asadullah, K., Haeussler-Quade, A., Gellrich, S., Hanneken, S., Hansen-Hagge, T.E., Döcke, W.D., Volk, H.D., and Sterry, W. (2000). IL-15 and IL-16 overexpression in cutaneous T-cell lymphomas: stage-dependent increase in mycosis fungoides progression. Exp. Dermatol. *9*, 248–251.

Azimi, N., Brown, K., Bamford, R.N., Tagaya, Y., Siebenlist, U., and Waldmann, T.A. (1998). Human T cell lymphotropic virus type I Tax protein trans-activates interleukin 15 gene transcription through an NF-kappaB site. Proc. Natl. Acad. Sci. USA *95*, 2452–2457.

Azimi, N., Jacobson, S., Leist, T., and Waldmann, T.A. (1999). Involvement of IL-15 in the pathogenesis of human T lymphotropic virus type I-associated myelopathy/tropical spastic paraparesis: implications for therapy with a monoclonal antibody directed to the IL-2/15R beta receptor. J. Immunol. *163*, 4064–4072.

Baldassarre, G., Fedele, M., Battista, S., Vecchione, A., Klein-Szanto, A.J., Santoro, M., Waldmann, T.A., Azimi, N., Croce, C.M., and Fusco, A. (2001). Onset of natural killer cell lymphomas in transgenic mice carrying a truncated HMGI-C gene by the chronic stimulation of the IL-2 and IL-15 pathway. Proc. Natl. Acad. Sci. USA *98*, 7970–7975.

Bamford, R.N., Grant, A.J., Burton, J.D., Peters, C., Kurys, G., Goldman, C.K., Brennan, J., Roessler, E., and Waldmann, T.A. (1994). The interleukin (IL) 2 receptor beta chain is shared by IL-2 and a cytokine, provisionally designated IL-T, that stimulates T-cell proliferation and the induction of lymphokine-activated killer cells. Proc. Natl. Acad. Sci. USA *91*, 4940–4944.

Bischoff, J.R., Anderson, L., Zhu, Y., Mossie, K., Ng, L., Souza, B., Schryver, B., Flanagan, P., Clairvoyant, F., Ginther, C., et al. (1998). A homologue of Drosophila aurora kinase is oncogenic and amplified in human colorectal cancers. EMBO J. *17*, 3052–3065.

Caligiuri, M.A. (2008). Human natural killer cells. Blood *112*, 461–469.

Carroll, H.P., Paunovic, V., and Gadina, M. (2008). Signalling, inflammation and arthritis: Crossed signals: the role of interleukin-15 and -18 in autoimmunity. Rheumatology (Oxford) *47*, 1269–1277.

Chan, K.K., Liu, Z., Xie, Z., Chiu, M., Wang, H., Chen, P., Dunkerson, S., Chiu, M., Liu, S., Triantafillou, G., et al. (2010). A novel ultrasensitive

hybridization-based ELISA method for 2-methoxyphosphorothiolate microRNAs and its in vitro and in vivo application. AAPS J. *12*, 556–568.

Chang, T.C., Yu, D., Lee, Y.S., Wentzel, E.A., Arking, D.E., West, K.M., Dang, C.V., Thomas-Tikhonenko, A., and Mendell, J.T. (2008). Widespread microRNA repression by Myc contributes to tumorigenesis. Nat. Genet. *40*, 43–50.

D'Auria, L., Bonifati, C., Cordiali-Fei, P., Leone, G., Picardo, M., Pietravalle, M., Giacalone, B., and Ameglio, F. (1999). Increased serum interleukin-15 levels in bullous skin diseases: correlation with disease intensity. Arch. Dermatol. Res. *291*, 354–356.

den Hollander, J., Rimpi, S., Doherty, J.R., Rudelius, M., Buck, A., Hoellein, A., Kremer, M., Graf, N., Scheerer, M., Hall, M.A., et al. (2010). Aurora kinases A and B are up-regulated by Myc and are essential for maintenance of the malignant state. Blood *116*, 1498–1505.

Dranoff, G. (2004). Cytokines in cancer pathogenesis and cancer therapy. Nat. Rev. Cancer *4*, 11–22.

Dubois, S., Mariner, J., Waldmann, T.A., and Tagaya, Y. (2002). IL-15Ralpha recycles and presents IL-15 In trans to neighboring cells. Immunity *17*, 537–547.

El-Omar, E.M., Carrington, M., Chow, W.H., McColl, K.E., Bream, J.H., Young, H.A., Herrera, J., Lissowska, J., Yuan, C.C., Rothman, N., et al. (2000). Interleukin-1 polymorphisms associated with increased risk of gastric cancer. Nature *404*, 398–402.

Epling-Burnette, P.K., Liu, J.H., Catlett-Falcone, R., Turkson, J., Oshiro, M., Kothapalli, R., Li, Y., Wang, J.-M., Yang-Yen, H.-F., Karras, J., et al. (2001). Inhibition of STAT3 signaling leads to apoptosis of leukemic large granular lymphocytes and decreased Mcl-1 expression. J. Clin. Invest. *107*, 351–362.

Estécio, M.R., Gharibyan, V., Shen, L., Ibrahim, A.E., Doshi, K., He, R., Jelinek, J., Yang, A.S., Yan, P.S., Huang, T.H., et al. (2007). LINE-1 hypomethylation in cancer is highly variable and inversely correlated with microsatellite instability. PLoS ONE *2*, e399.

Esteller, M. (2006). Epigenetics provides a new generation of oncogenes and tumour-suppressor genes. Br. J. Cancer *94*, 179–183.

Esteller, M. (2007). Cancer epigenomics: DNA methylomes and histone-modification maps. Nat. Rev. Genet. *8*, 286–298.

Fehniger, T.A., Suzuki, K., Ponnappan, A., VanDeusen, J.B., Cooper, M.A., Florea, S.M., Freud, A.G., Robinson, M.L., Durbin, J., and Caligiuri, M.A. (2001). Fatal leukemia in interleukin 15 transgenic mice follows early expansions in natural killer and memory phenotype CD8+ T cells. J. Exp. Med. *193*, 219–231.

Ganem, N.J., Godinho, S.A., and Pellman, D. (2009). A mechanism linking extra centrosomes to chromosomal instability. Nature *460*, 278–282.

Garzon, R., Heaphy, C.E., Havelange, V., Fabbri, M., Volinia, S., Tsao, T., Zanesi, N., Kornblau, S.M., Marcucci, G., Calin, G.A., et al. (2009a). MicroRNA 29b functions in acute myeloid leukemia. Blood *114*, 5331–5341.

Garzon, R., Liu, S., Fabbri, M., Liu, Z., Heaphy, C.E., Callegari, E., Schwind, S., Pang, J., Yu, J., Muthusamy, N., et al. (2009b). MicroRNA-29b induces global DNA hypomethylation and tumor suppressor gene reexpression in acute myeloid leukemia by targeting directly DNMT3A and 3B and indirectly DNMT1. Blood *113*, 6411–6418.

Giet, R., Petretti, C., and Prigent, C. (2005). Aurora kinases, aneuploidy and cancer, a coincidence or a real link? Trends Cell Biol. *15*, 241–250.

Grabstein, K.H., Eisenman, J., Shanebeck, K., Rauch, C., Srinivasan, S., Fung, V., Beers, C., Richardson, J., Schoenborn, M.A., Ahdieh, M., et al. (1994). Cloning of a T cell growth factor that interacts with the beta chain of the interleukin-2 receptor. Science *264*, 965–968.

Hodge, D.L., Yang, J., Buschman, M.D., Schaughency, P.M., Dang, H., Bere, W., Yang, Y., Savan, R., Subleski, J.J., Yin, X.M., et al. (2009). Interleukin-15 enhances proteasomal degradation of bid in normal lymphocytes: implications for large granular lymphocyte leukemias. Cancer Res. *69*, 3986–3994.

Hudson, J.D., Shoaibi, M.A., Maestro, R., Carnero, A., Hannon, G.J., and Beach, D.H. (1999). A proinflammatory cytokine inhibits p53 tumor suppressor activity. J. Exp. Med. *190*, 1375–1382.

Johnston, J.A., Bacon, C.M., Finbloom, D.S., Rees, R.C., Kaplan, D., Shibuya, K., Ortaldo, J.R., Gupta, S., Chen, Y.Q., Giri, J.D., et al. (1995). Tyrosine phosphorylation and activation of STAT5, STAT3, and Janus kinases by interleukins 2 and 15. Proc. Natl. Acad. Sci. USA *92*, 8705–8709.

Kanda, A., Kawai, H., Suto, S., Kitajima, S., Sato, S., Takata, T., and Tatsuka, M. (2005). Aurora-B/AIM-1 kinase activity is involved in Ras-mediated cell transformation. Oncogene *24*, 7266–7272.

Koskela, H.L., Eldfors, S., Ellonen, P., van Adrichem, A.J., Kuusanmäki, H., Andersson, E.I., Lagström, S., Clemente, M.J., Olson, T., Jalkanen, S.E., et al. (2012). Somatic STAT3 mutations in large granular lymphocytic leukemia. N. Engl. J. Med. *366*, 1905–1913.

Liu, S., Wu, L.C., Pang, J., Santhanam, R., Schwind, S., Wu, Y.Z., Hickey, C.J., Yu, J., Becker, H., Maharry, K., et al. (2010). Sp1/NFkappaB/HDAC/miR-29b regulatory network in KIT-driven myeloid leukemia. Cancer Cell *17*, 333–347.

Morris, J.C., Janik, J.E., White, J.D., Fleisher, T.A., Brown, M., Tsudo, M., Goldman, C.K., Bryant, B., Petrus, M., Top, L., et al. (2006). Preclinical and phase I clinical trial of blockade of IL-15 using Mikbeta1 monoclonal antibody in T cell large granular lymphocyte leukemia. Proc. Natl. Acad. Sci. USA *103*, 401–406.

Ogilvy, S., Elefanty, A.G., Visvader, J., Bath, M.L., Harris, A.W., and Adams, J.M. (1998). Transcriptional regulation of vav, a gene expressed throughout the hematopoietic compartment. Blood *91*, 419–430.

Ogino, S., Kawasaki, T., Nosho, K., Ohnishi, M., Suemoto, Y., Kirkner, G.J., and Fuchs, C.S. (2008). LINE-1 hypomethylation is inversely associated with microsatellite instability and CpG island methylator phenotype in colorectal cancer. Int. J. Cancer *122*, 2767–2773.

Park, I.K., Giovenzana, C., Hughes, T.L., Yu, J., Trotta, R., and Caligiuri, M.A. (2009). The Axl/Gas6 pathway is required for optimal cytokine signaling during human natural killer cell development. Blood *113*, 2470–2477.

Renauld, J.C., van der Lugt, N., Vink, A., van Roon, M., Godfraind, C., Warnier, G., Merz, H., Feller, A., Berns, A., and Van Snick, J. (1994). Thymic lymphomas in interleukin 9 transgenic mice. Oncogene *9*, 1327–1332.

Sokol, L., and Loughran, T.P., Jr. (2006). Large granular lymphocyte leukemia. Oncologist *11*, 263–273.

Trentin, L., Zambello, R., Facco, M., Sancetta, R., Agostini, C., and Semenzato, G. (1997). Interleukin-15: a novel cytokine with regulatory properties on normal and neoplastic B lymphocytes. Leuk. Lymphoma *27*, 35–42.

Utecht, K.N., and Kolesar, J. (2008). Bortezomib: a novel chemotherapeutic agent for hematologic malignancies. Am. J. Health Syst. Pharm. *65*, 1221–1231.

Waldmann, T.A., and Tagaya, Y. (1999). The multifaceted regulation of interleukin-15 expression and the role of this cytokine in NK cell differentiation and host response to intracellular pathogens. Annu. Rev. Immunol. *17*, 19–49.

Yokohama, A., Mishra, A., Mitsui, T., Becknell, B., Johns, J., Curphey, D., Blaser, B.W., Vandeusen, J.B., Mao, H., Yu, J., and Caligiuri, M.A. (2010). A novel mouse model for the aggressive variant of NK cell and T cell large granular lymphocyte leukemia. Leuk. Res. *34*, 203–209.

Yu, L., Liu, C., Vandeusen, J., Becknell, B., Dai, Z., Wu, Y.Z., Raval, A., Liu, T.H., Ding, W., Mao, C., et al. (2005). Global assessment of promoter methylation in a mouse model of cancer identifies ID4 as a putative tumor-suppressor gene in human leukemia. Nat. Genet. *37*, 265–274.

Yu, J., Ershler, M., Yu, L., Wei, M., Hackanson, B., Yokohama, A., Mitsui, T., Liu, C., Mao, H., Liu, S., et al. (2009). TSC-22 contributes to hematopoietic precursor cell proliferation and repopulation and is epigenetically silenced in large granular lymphocyte leukemia. Blood *113*, 5558–5567.

Zambello, R., Facco, M., Trentin, L., Sancetta, R., Tassinari, C., Perin, A., Milani, A., Pizzolo, G., Rodeghiero, F., Agostini, C., et al. (1997). Interleukin-15 triggers the proliferation and cytotoxicity of granular lymphocytes in patients with lymphoproliferative disease of granular lymphocytes. Blood *89*, 201–211.

Zhou, H., Kuang, J., Zhong, L., Kuo, W.L., Gray, J.W., Sahin, A., Brinkley, B.R., and Sen, S. (1998). Tumour amplified kinase STK15/BTAK induces centrosome amplification, aneuploidy and transformation. Nat. Genet. *20*, 189–193.

Cancer Cell
Article

Phosphoglycerate Mutase 1 Coordinates Glycolysis and Biosynthesis to Promote Tumor Growth

Taro Hitosugi,[1,12] Lu Zhou,[4,11,12] Shannon Elf,[1] Jun Fan,[1] Hee-Bum Kang,[1] Jae Ho Seo,[1] Changliang Shan,[1] Qing Dai,[4] Liang Zhang,[4] Jianxin Xie,[5] Ting-Lei Gu,[5] Peng Jin,[2] Masa Alečković,[6] Gary LeRoy,[6] Yibin Kang,[6] Jessica A. Sudderth,[7] Ralph J. DeBerardinis,[7] Chi-Hao Luan,[8] Georgia Z. Chen,[1] Susan Muller,[3] Dong M. Shin,[1] Taofeek K. Owonikoko,[1] Sagar Lonial,[1] Martha L. Arellano,[1] Hanna J. Khoury,[1] Fadlo R. Khuri,[1] Benjamin H. Lee,[9] Keqiang Ye,[3] Titus J. Boggon,[10] Sumin Kang,[1] Chuan He,[4,*] and Jing Chen[1,*]

[1]Department of Hematology and Medical Oncology, Winship Cancer Institute
[2]Department of Human Genetics
[3]Department of Pathology and Laboratory Medicine
Emory University School of Medicine, Atlanta, GA 30322, USA
[4]Department of Chemistry and Institute for Biophysical Dynamics, University of Chicago, Chicago, IL 60637, USA
[5]Cell Signaling Technology, Inc. (CST), Danvers, MA 01923, USA
[6]Department of Molecular Biology, Princeton University, Princeton, NJ 08544, USA
[7]UT Southwestern Medical Center, Dallas, TX 75390, USA
[8]Department of Molecular BioSciences, Northwestern University, Evanston, IL 60208, USA
[9]Novartis Institutes for BioMedical Research, Cambridge, MA 02139, USA
[10]Department of Pharmacology, Yale University School of Medicine, New Haven, CT 06520, USA
[11]Current address: School of Pharmacy, Fudan University, Shanghai 201203, China
[12]These authors contributed equally to this work
*Correspondence: chuanhe@uchicago.edu (C.H.), jchen@emory.edu (J.C.)
http://dx.doi.org/10.1016/j.ccr.2012.09.020

SUMMARY

It is unclear how cancer cells coordinate glycolysis and biosynthesis to support rapidly growing tumors. We found that the glycolytic enzyme phosphoglycerate mutase 1 (PGAM1), commonly upregulated in human cancers due to loss of *TP53*, contributes to biosynthesis regulation in part by controlling intracellular levels of its substrate, 3-phosphoglycerate (3-PG), and product, 2-phosphoglycerate (2-PG). 3-PG binds to and inhibits 6-phosphogluconate dehydrogenase in the oxidative pentose phosphate pathway (PPP), while 2-PG activates 3-phosphoglycerate dehydrogenase to provide feedback control of 3-PG levels. Inhibition of PGAM1 by shRNA or a small molecule inhibitor PGMI-004A results in increased 3-PG and decreased 2-PG levels in cancer cells, leading to significantly decreased glycolysis, PPP flux and biosynthesis, as well as attenuated cell proliferation and tumor growth.

INTRODUCTION

The Warburg effect in cancer cells consists of an increase in aerobic glycolysis and enhanced lactate production, which generates more ATPs more quickly than in normal cells that overwhelmingly rely on oxidative phosphorylation (Kroemer and Pouyssegur, 2008). In addition, tumor tissue traps more glucose than normal tissue does because cancer cells use elevated amounts of glucose as a carbon source for anabolic biosynthesis of macromolecules. These include nucleotides, amino acids, and fatty acids, to produce RNA/DNA, proteins, and lipids, respectively, which are necessary for cell proliferation and to accommodate the rapidly growing tumors (Kroemer and Pouyssegur, 2008). Interestingly, leukemia cells are also highly glycolytic (Elstrom et al., 2004; Gottschalk et al., 2004), despite the fact that such cells reside within the bloodstream at higher oxygen tensions than cells in most normal tissues.

Significance

The current understanding of the Warburg effect consists of an increase in aerobic glycolysis in cancer cells. The connection between glycolysis and PPP/biosynthesis is based on a model in which glycolytic intermediates can be diverted into PPP and biosynthesis pathways as precursors. Our findings demonstrate that PGAM1 regulates the concentrations of glycolytic metabolites 3-PG and 2-PG, which function as signaling molecules to directly affect the catalytic activity of enzymes involved in PPP and biosynthesis, representing an additional link between glycolysis, PPP, and biosynthesis. PGAM1 inhibitor PGMI-004A exhibits promising efficacy and minimal toxicity in treatment of xenograft nude mice and human primary leukemia cells, providing "proof of principle" for the development of PGAM1 inhibitors as anticancer agents.

During glycolysis, glycolytic intermediates including glucose-6-phosphate (G6P) can be diverted into the pentose phosphate pathway (PPP), which contributes to macromolecular biosynthesis by producing reducing potential in the form of reduced nicotinamide adenine dinucleotide phosphate (NADPH) and/or ribose-5-phosphate (R5P), the building blocks for nucleotide synthesis. NADPH is the most crucial metabolite produced by the PPP, because NADPH not only fuels macromolecular biosynthesis such as lipogenesis, but also functions as a crucial antioxidant, quenching the reactive oxygen species (ROS) produced during rapid proliferation of cancer cells. Glycolysis and glutaminolysis supply the carbon input required for the tricarboxylic acid cycle to function as a biosynthetic "hub" and permit the production of other macromolecules including amino acids and fatty acids (Cairns et al., 2011). Thus, cancer cells appear to coordinate glycolysis and anabolism to provide an overall metabolic advantage to cancer cell proliferation and disease development. However, the detailed mechanisms underlying this coordination remain largely unknown.

Phosphoglycerate mutase 1 (PGAM1) catalyzes the conversion of 3-phosphoglycerate (3-PG) to 2-phosphoglycerate (2-PG) during glycolysis. PGAM1 regulates a unique step in glycolysis, and most of the glycolytic intermediates that are used as precursors for anabolic biosynthesis are upstream of this step. In many cancers, including hepatocellular carcinoma and colorectal cancer, PGAM1 activity is increased compared to that in the normal tissues (Liu et al., 2008; Ren et al., 2010). PGAM1 gene expression is believed to be upregulated due to loss of *TP53* in cancer cells because *TP53* negatively regulates PGAM1 gene expression (Corcoran et al., 2006; Tennant et al., 2009, 2010). Here, we study the role of PGAM1 in the coordination of glycolysis and anabolic biosynthesis, as well as the mechanism by which PGAM1 promotes cancer cell proliferation and tumor growth.

RESULTS

PGAM1 Controls Intracellular 3-PG and 2-PG Levels and Is Important for Cancer Cell Glycolysis, Anabolic Biosynthesis, Proliferation, and Tumor Growth

To better understand how cancer cells coordinate glycolysis and anabolic biosynthesis, we examined the effects of targeted downregulation of the glycolytic enzyme PGAM1. Stable knockdown of PGAM1 in lung cancer H1299, breast cancer MDA-MB231, acute myeloid leukemia Molm14, and head and neck cancer 212LN cells resulted in decreased PGAM1 activity (Figure S1 available online). We next performed Global Metabolic Profiling (Metabolon) using cell lysate samples of parental H1299 cells and cells with stable knockdown of PGAM1. The results indicate that PGAM1 knockdown results in altered intracellular concentrations of 118 biochemicals (61 upregulated and 57 downregulated) with $p < 0.05$ using Welch's t-tests. Among these biochemicals, we observed that the PGAM1 substrate 3-PG levels are increased in PGAM1 knockdown compared to control cells (Tables S1 and S2). In consonance with this observation, we found that attenuation of PGAM1 by shRNA in diverse cancer cells leads not only to increased 3-PG (Figure 1A), but also decreased 2-PG (Figure 1B) levels compared to corresponding control cells harboring an empty vector (detailed data are shown in Table S3). The intracellular levels of 3-PG and 2-PG determined using different methods are comparable (Figures S1B and S1C). In addition, stable overexpression of PGAM1 in 3T3 cells results in increased 2-PG and decreased 3-PG levels, compared to control parental 3T3 cells (Figure S1D). These results suggest a crucial role for PGAM1 controlling the metabolite levels of its substrate 3-PG and product 2-PG in cancer cells.

We next examined the role of PGAM1 in cancer cell metabolism. We found that, compared to vector control cells, stable knockdown of PGAM1 results in a decreased glycolytic rate (Figure 1C) and lactate production (Figure 1D), as well as reduced glucose-dependent biosynthesis of RNA and lipids, accompanied by reduced NADPH/$NADP^+$ ratio (Figures 1E–1G, respectively). Because the PPP produces NADPH and R5P to contribute to macromolecular biosynthesis, we next examined whether PGAM1 contributes to PPP flux. Indeed, we found that oxidative PPP flux is reduced in PGAM1 knockdown compared to control vector cells (Figure 1H). Interestingly, attenuation of PGAM1 in cancer cells does not affect glucose uptake rate (Figure S1E), intracellular ATP levels (Figure 1I), or O_2 consumption rate (Figure 1J) in either the presence or absence of ATP synthase inhibitor oligomycin. These results suggest that downregulation of PGAM1 attenuates glycolysis, PPP and biosynthesis, but does not significantly affect glucose uptake or intracellular ATP levels.

In addition, we found that stable knockdown of PGAM1 results in decreased cell proliferation in diverse human cancer and leukemia cells (Figure 1K). Moreover, we performed a xenograft experiment in which nude mice were subcutaneously injected with control H1299 cells harboring an empty vector on the left flank and PGAM1 knockdown H1299 cells on the right flank (Figure 1L, left). The mice were monitored for tumor growth over 6 weeks. The masses of tumors derived from PGAM1 knockdown H1299 cells were significantly reduced compared to those of tumors formed by vector control cells (Figure 1L, right).

PGAM1 Knockdown Results in Elevated Levels of 3-PG, which Binds to and Inhibits 6PGD by Competing with Its Substrate, 6-PG

We next explored the molecular mechanism by which PGAM1 regulates the PPP. Our data suggest that the abnormally high levels of 3-PG in PGAM1 knockdown cells may be accounted for inhibition of oxidative PPP flux (Figure 1). To test this hypothesis, we examined the effect of 3-PG on glucose-6-phosphate dehydrogenase (G6PD), the first and most important enzyme of the oxidative PPP, which produces NADPH, and 6-phosphogluconate dehydrogenase (6PGD), an enzyme that also produces NADPH while converting 6-phosphogluconate into ribulose 5-phosphate in the presence of $NADP^+$. We performed in vitro 6PGD and G6PD assays in the presence of increasing concentrations of 3-PG. Physiologic concentrations of 3-PG in human cells are reported to be approximately 50–80 μM (Feig et al., 1971; Minakami et al., 1964; Mulquiney and Kuchel, 1999). As shown in Table S3, we determined that, in H1299, MDA-MB231, and Molm14 cells, the 3-PG levels are approximately 60–80 μM in control vector cells and 200–300 μM in PGAM1 knockdown cells, while the 3-PG concentrations are approximately 160 μM and 310 μM in 212LN control

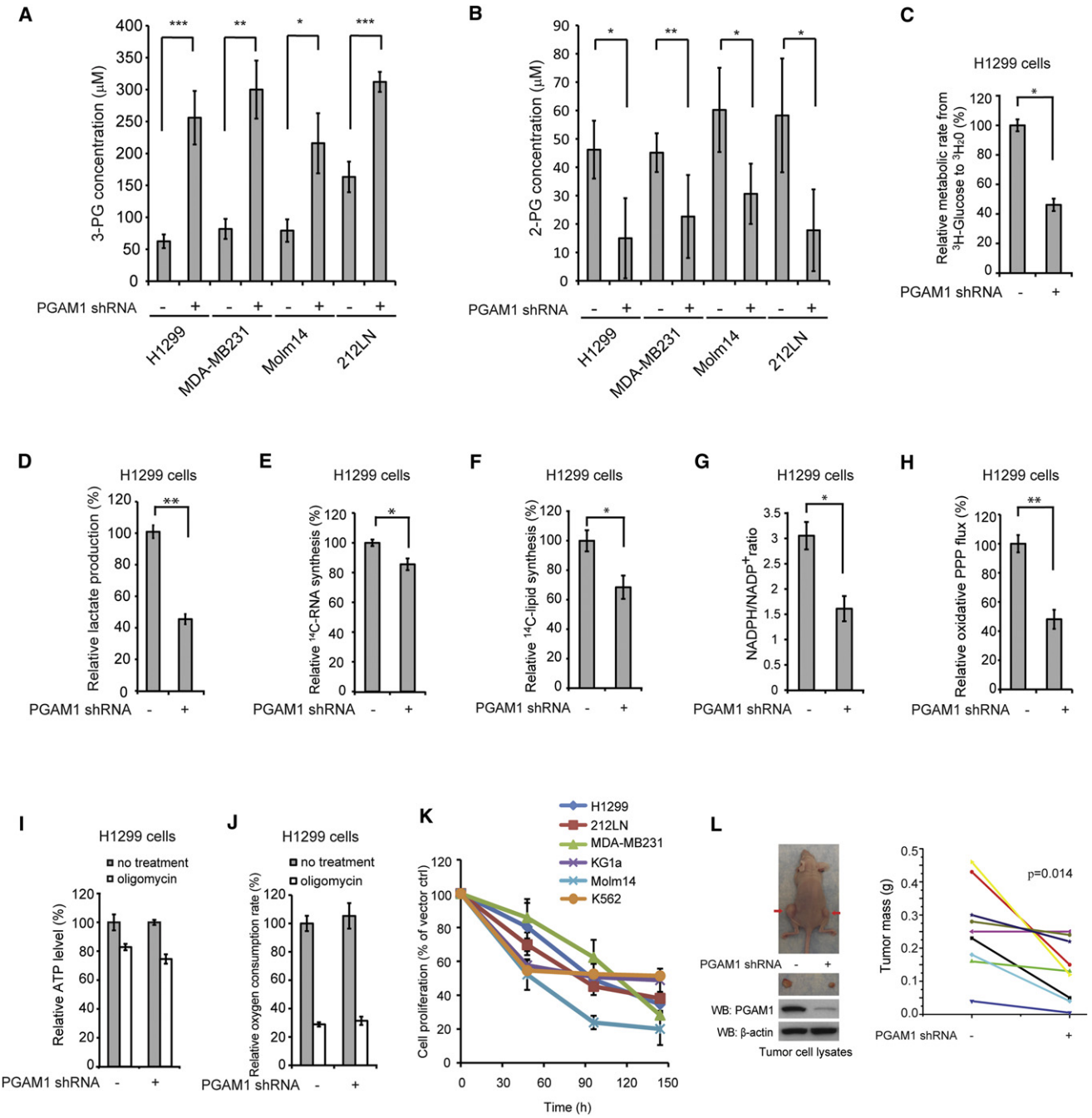

Figure 1. PGAM1 Controls Intracellular 3-PG and 2-PG Levels in Cancer Cells and Is Important for Glycolysis, Anabolic Biosynthesis, Cell Proliferation, and Tumor Growth

(A and B) Intracellular concentrations of 3-PG and 2-PG were determined in diverse PGAM1 knockdown cancer cells and compared to control cells. Detailed concentrations are listed in Table S3.

(C–J) H1299 cells with stable knockdown of PGAM1 and control cells harboring an empty vector were tested for glycolytic rate (C), lactate production (D), RNA biosynthesis (E), lipogenesis (F), NADPH/NADP$^+$ ratio (G), and oxidative PPP flux (H). The intracellular ATP levels (I) and oxygen consumption rate (J) in the presence or absence of 100 nM oligomycin (ATP synthase inhibitor) were also tested.

(K) Cell proliferation rates were determined by cell counting in diverse human cancer (H1299, 212LN, and MDA-MB231) and leukemia (KG1a, Molm14, and K562) cells with stable knockdown of PGAM1, which were normalized to the corresponding control cells harboring an empty vector.

(L) Stable knockdown of PGAM1 by shRNA attenuates tumor growth potential of H1299 cells in xenograft nude mice. Left: Dissected tumors (indicated by red arrows) in a representative nude mouse and expression of PGAM1 in tumor lysates are shown. Right: PGAM1 knockdown cells show significantly reduced tumor formation in xenograft nude mice compared to cells harboring empty vector control (p values were determined by a two-tailed paired Student's t test).

The error bars represent mean values ± SD from three replicates of each sample (*0.01 < p < 0.05; **0.001 < p < 0.01; ***p < 0.001). See also Figure S1 and Tables S1–S3.

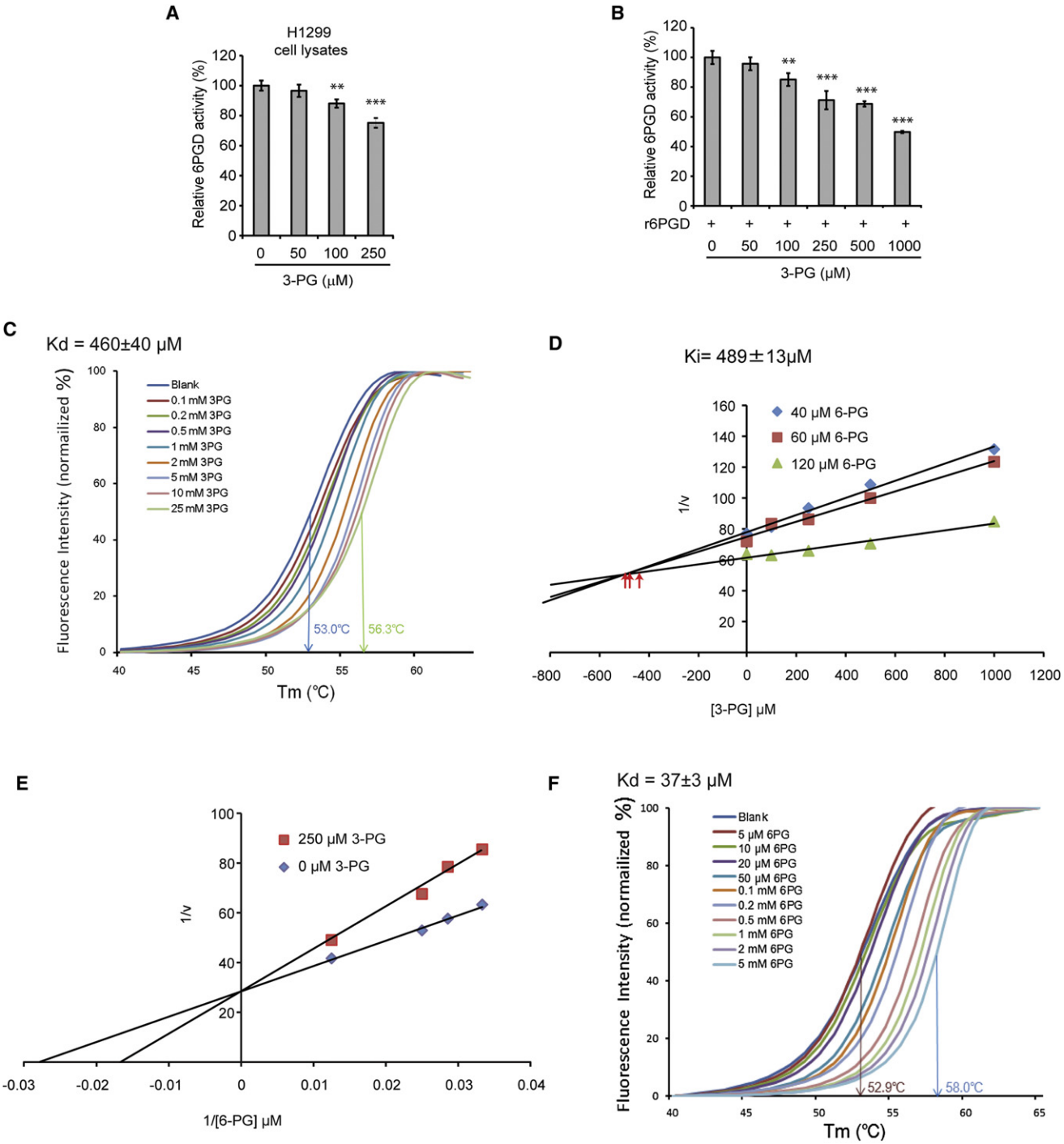

Figure 2. Attenuation of PGAM1 Results in Increased Intracellular Levels of 3-PG, which Binds to and Inhibits 6PGD by Competing with Its Substrate 6-PG

(A and B) Enzyme activity of 6PGD in H1299 cell lysates (A) or recombinant 6PGD (r6PGD) (B) was determined in the presence of increasing concentrations of 3-PG. Relative 6PGD activity was normalized to the control samples without 3-PG treatment. 3-PG levels in control H1299 cells with empty vector and PGAM1 knockdown are 62.5 ± 10.8 μM and 256 ± 41.9 μM, respectively. The error bars represent mean values ± SD from three replicates of each sample (**0.001 < p < 0.01; ***p < 0.001).

(C) Thermal shift melting curves of 6PGD and 3PG. Thermal shift assay was performed to examine the protein (6PGD) and "ligand" (3PG) interaction. Change of melting temperature (Tm) in a dose-dependent manner at concentrations from 100 μM to 25 mM demonstrates that 3-PG directly binds to the protein. Kd for 6PGD-3-PG interaction was determined to be 460 ± 40 μM.

(D) The Dixon plot shows that 3-PG inhibits 6PGD and the dissociation constant (Ki) was determined.

(E) The Lineweaver-Burk plot shows that 3-PG functions as a competitive inhibitor of 6PGD.

and PGAM1 knockdown cells, respectively. Thus, we next examined the effects of increasing concentrations of 3-PG on G6PD and 6PGD enzyme activities according to the aforementioned physiologic 3-PG levels in tumor cells.

We found that treatment with 3-PG concentrations analogous to those in PGAM1 knockdown H1299 cells (~250 μM) results in decreased enzyme activity of 6PGD (Figure 2A) in H1299 cell lysates or recombinant 6PGD (r6PGD) (Figure 2B), whereas the physiologic 3-PG concentrations determined in control H1299 cells (~60 μM) do not significantly affect 6PGD enzyme activity in both experiments. In control experiments, treatment with increasing concentrations of 3-PG did not significantly affect G6PD activity in H1299 cell lysates or rG6PD activity (Figure S2A). In addition, 2-PG did not affect 6PGD enzyme activity in H1299 cell lysates or r6PGD activity (Figure S2B). These results suggest that abnormally high levels of 3-PG, as in PGAM1 knockdown cells, may selectively and directly inhibit 6PGD but not G6PD.

To examine whether 3-PG binds to and inhibits 6PGD, we performed a thermal melt shift assay to examine the interaction of protein (6PGD) and "ligand" (3-PG). Incubation of increasing concentrations of 3-PG raises 6PGD melting temperature (Tm) in a dose-dependent manner, suggesting that 3-PG directly binds to the protein (Figure 2C). The Kd value for protein-"ligand" interaction was calculated to be 460 ± 40 μM. Moreover, we performed kinetics studies on the inhibition of 6PGD by 3-PG. As shown in Figure 2D, the Dixon plot indicates that 3-PG binds and inhibits 6PGD. The inhibition constant (Ki) was determined to be 489 ± 13 μM, in agreement with the Kd determined.

We next determined the intracellular concentration of 6-PG in H1299, MDA-MB231, and 212LN cells to be 34.9 ± 2.1 μM, 37.6 ± 0.7 μM, and 24.9 ± 0.4 μM, respectively. We performed additional enzyme kinetics assays to test whether 3-PG at a concentration analogous to that in PGAM1 knockdown H1299 cells (~250 μM) functions as a competitive or noncompetitive inhibitor of 6PGD in the presence of physiologic concentrations of 6-PG (~35 μM). As shown in Figure 2E, the Lineweaver-Burk plot demonstrates that 3-PG functions as a competitive inhibitor of 6PGD. Because the Kd value for protein (6PGD)-ligand (6-PG) interaction was calculated to be 37 ± 3 μM in a thermal melt shift assay (Figure 2F), these combined data suggest that at physiologic concentrations, 3-PG (~60–80 μM) cannot effectively compete with 6-PG (~35 μM) to inhibit 6PGD in cancer cells; however, upon attenuation of PGAM1, elevated cellular 3-PG levels (~250–300 μM) result in reduced 6PGD enzyme activity.

To further understand the structural properties of 3-PG-mediated inhibition of 6PGD, we crystallized the apo-form of 6PGD (1.39 Å), which was also soaked with 3-PG to obtain the 3-PG-bound form of 6PGD (1.53 Å) (Table S4). The Fo-Fc density analysis revealed that the electron density of 3-PG was located in the active site of the 3-PG-bound 6PGD structure (Figure 3A) but not in the apo-6PGD structure (Figure 3B). 3-PG interacts with several residues (Y191, T262, R287, R446) in the active site of 6PGD that are important for substrate binding and enzymatic activity of 6PGD (Li et al., 2006) (Figure 3A). Different conformations were observed for Arg 446 and His 452 in the 3-PG-bound 6PGD structure compared to the apo-form 6PGD structure (Figure 3C). An alignment of three different 6PGD structures with bound NADP, 6-PG, and 3-PG shows an overlap of 3-PG and 6-PG in the active site (Figure 3D). Together, these results demonstrate that 3-PG directly binds to 6PGD and inhibits 6PGD enzyme activity by competing with the cognate substrate 6-PG, representing a molecular mechanism to explain how PGAM1, as a glycolytic enzyme, contributes to the regulation of the oxidative PPP and consequently anabolic biosynthesis.

Rescue of Reduced 2-PG Levels in PGAM1 Knockdown Cells Results in Decreased 3-PG Levels by Activating 3-PG Dehydrogenase

To examine the effect of decreased 2-PG levels on cancer cell metabolism, we treated the aforementioned PGAM1 knockdown cancer cells with a cell permeable agent, methyl-2-PG, which converts to 2-PG in cells. We verified that in diverse PGAM1 knockdown cancer cells, treatment with methyl-2-PG results in increased 2-PG cellular levels comparable to those in the corresponding control vector cells (Figure 4A). We also observed that methyl-2-PG treatment rescues the reduced lactate production (Figure 4B) but has no significant effect on intracellular ATP levels (Figure S3A) in H1299 cells with stable knockdown of PGAM1 compared to control vector cells. This result suggests that rescuing cellular 2-PG levels reverses the inhibitory effect of PGAM1 knockdown on glycolysis and allows downstream glycolytic reactions to resume and ultimately produce lactate. However, such rescued glycolytic activity does not affect ATP levels, which is consistent with our previous observation (Figures 1I and 1J).

Surprisingly, we also found that methyl-2-PG treatment rescues the decreased oxidative PPP flux and biosynthesis of RNA and lipids, as well as partially restores the reduced cell proliferation in H1299 PGAM1 knockdown cancer cells compared to the corresponding control vector cells (Figures 4C–4F). Similar results were obtained using MDA-MB231 vector and PGAM1 knockdown cells (Figures S3B–S3E). These data suggest that the increased 2-PG levels in PGAM1 knockdown cells provide a feedback mechanism to rescue the abrogated PPP and anabolic biosynthesis upstream of PGAM1.

We tested this hypothesis by examining the effect of rescued 2-PG levels on 3-PG concentrations in PGAM1 knockdown cells. We found that treatment with methyl-2-PG results in decreased 3-PG concentrations in diverse PGAM1 knockdown cells to levels that are comparable to the 3-PG concentrations in the corresponding control vector cells (Figure 5A). These results further suggest that PGAM1 controls 2-PG levels in cancer cells, which contributes to PGAM1-dependent coordination of glycolysis and anabolic biosynthesis by adjusting 3-PG levels.

We next determined the molecular mechanism underlying 2-PG-dependent feedback regulation of intracellular 3-PG levels.

(F) Thermal shift melting curves of 6PGD and 6PG. Thermal shift assay was performed to examine the protein (6PGD) and ligand (6PG) interaction. Change of melting temperature (Tm) in a dose-dependent manner at concentrations from 5 μM to 5 mM demonstrates that 6-PG directly binds to the protein. Kd for 6PGD-6PG interaction was determined to be 37 ± 3 μM.
See also Figure S2.

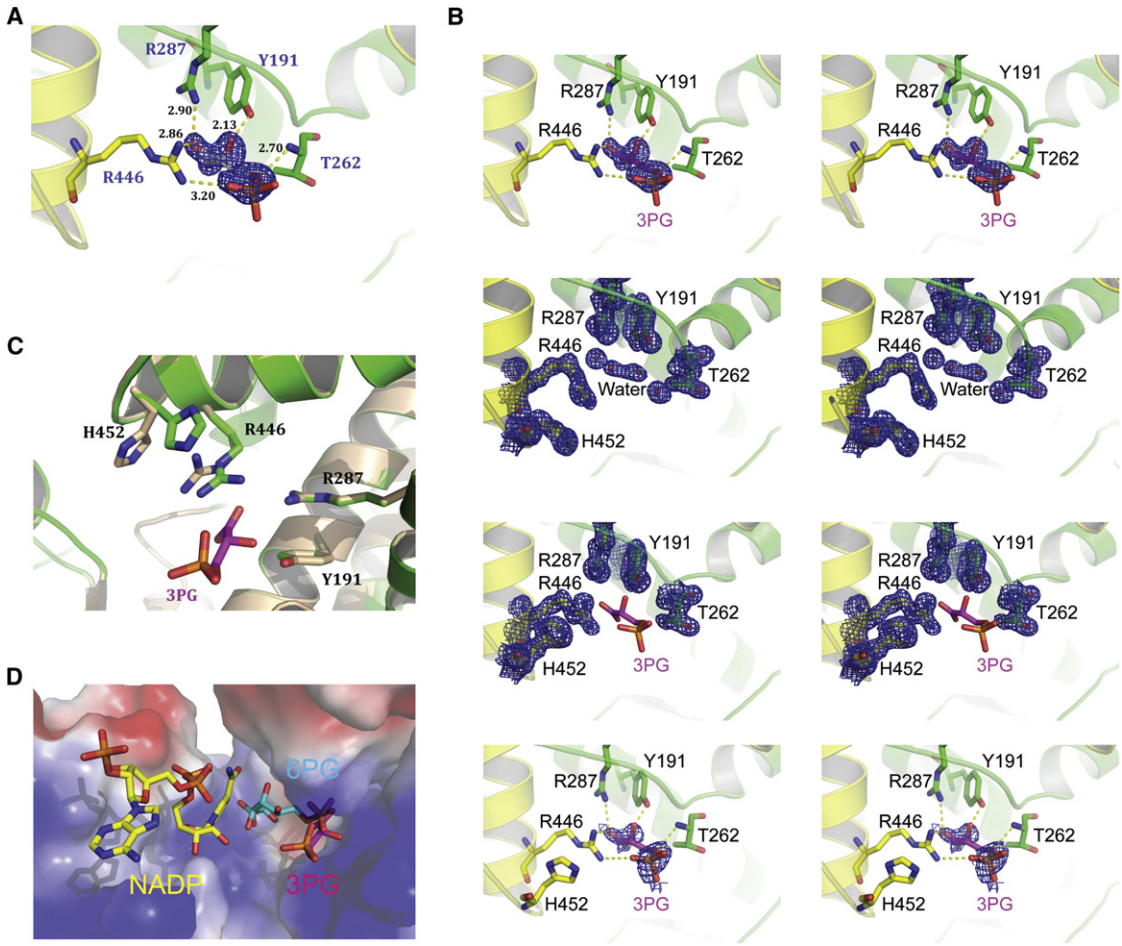

Figure 3. Co-Crystallization Analysis of 3-PG-Mediated Inhibition of 6PGD

(A) Stereo view of the Fo-Fc electron density map contoured at 3.0 σ around 3-PG. The Fo-Fc density map is shown as blue mesh. Residues of 6PGD interact with 3-PG are shown in stick.

(B) Upper top: Stereo view of the unbiased Fo-Fc electron density map contoured at 3.0 σ around 3PG. The Fo-Fc density map is shown as blue mesh. Residues interacting with 3-PG are shown in stick. Lower top: Stereo view of the 2Fo-Fc electron density map of 6PGD apo-form contoured at 1.2 σ at 3-PG binding pocket in the same orientation as in Figure 3A. The 2Fo-Fc density map is shown as blue mesh. Upper bottom: Stereo view of the 2Fo-Fc electron density map of 6PGD-3-PG complex contoured at 1.2 σ at 3-PG binding pocket in the same orientation as in Figure 3A. The 2Fo-Fc density map is shown as blue mesh. Lower bottom: Stereo view of simulated-annealing omit map contoured at 0.8 σ around 3-PG. The omit density map is shown as blue mesh.

(C) Structure comparison of the 6PGD apo-form (wheat) and the 6PGD-3-PG complex (green). Arg 446 and His 452 in the 6PGD-3-PG complex structure show different conformation.

(D) Surface electrostatic potential of the substrate binding pocket of 6PGD. The bound 3-PG (pink) competes with 6-PG (blue) but not NADP (yellow) in the active site. The model was built by aligning structures of 6PGD-NADP (PDB number: 2JKV), 6PGD-6-PG (PDB number: 3FWN), and 6PGD-3PG.

See also Table S4.

Besides conversion to 2-PG catalyzed by PGAM1 in glycolysis, 3-PG also serves as a precursor for serine synthesis and can be converted to 3-phosphohydroxypyruvate (pPYR) by 3-PG dehydrogenase (PHGDH). Because PGAM1 activity is attenuated in PGAM1 knockdown cells, it is possible that the rescued cellular 2-PG levels by methyl-2-PG treatment decreases 3-PG levels by activating PHGDH. We tested this hypothesis by examining the effect of 2-PG on PHGDH activity and we used PGAM1 knockdown cells to exclude the endogenous PGAM1 effect on 3-PG and 2-PG in the PHGDH enzyme activity reactions. Indeed, we found that treatment with 2-PG concentrations equivalent to those determined in control H1299 cells (~45 μM) or methyl-2-PG treated PGAM1 knockdown cells (~60 μM) results in higher PHGDH enzyme activity in H1299 PGAM1 knockdown cell lysates (Figure 5B, left). Similar results were obtained by treating 212LN PGAM1 knockdown cell lysates with increasing concentrations of 2-PG (Figure 5B, right). Moreover, treatment with increasing concentrations of 2-PG results in increased enzyme activity of recombinant PHGDH (rPHGDH) (Figure 5C). In contrast, 2-PG concentrations that correspond to those determined in PGAM1 knockdown cells (~15 μM) did not significantly affect PHGDH activity. Together, these studies reveal a feedback mechanism by which cellular 2-PG levels contribute to control of 3-PG levels in cells through regulation of PHGDH.

In addition, we found that stable knockdown of PGAM1 results in significantly decreased serine biosynthesis, while treatment

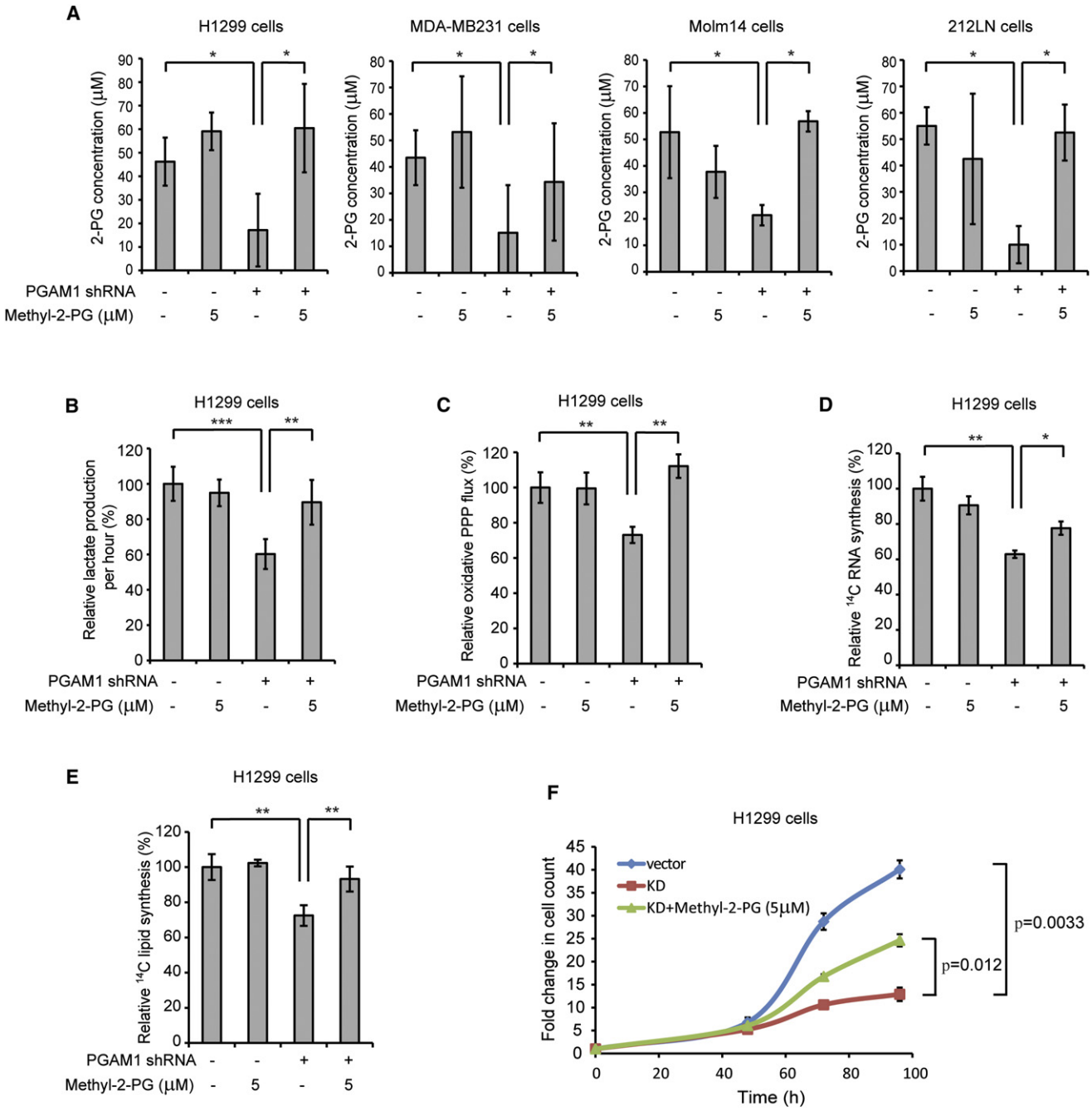

Figure 4. Rescue of Reduced 2-PG Levels in PGAM1 Knockdown Cells Reverses the Phenotypes due to Attenuation of PGAM1

(A) 2-PG levels in diverse cancer cells with stable knockdown of PGAM1 were determined in the presence and absence of cell-permeable methyl-2-PG.

(B–F) H1299 cells with stable knockdown of PGAM1 were tested for lactate production (B), oxidative PPP flux (C), biosynthesis of RNA (D) and lipids (E), and proliferation (F) in the presence and absence of methyl-2-PG.

The error bars represent mean values ± SD from three replicates of each sample (*0.01 < p < 0.05; **0.001 < p < 0.01; ***p < 0.001). See also Figure S3.

with methyl-2-PG rescues the phenotype (Figure 5D). Moreover, shRNA-mediated knockdown of PHGDH (Figure 5E) does not affect rescued 2-PG levels in PGAM1 knockdown cells upon treatment with methyl-2-PG, while PHGDH knockdown abolishes the methyl-2-PG-dependent decrease of the elevated 3-PG levels in H1299 PGAM1 knockdown cells (Figure 5F; left and right, respectively). These data support our hypothesis that PGAM1 controls 2-PG levels to regulate PHGDH, which consequently regulates 3-PG levels by diverting 3-PG in serine biosynthesis. Furthermore, knockdown of PHGDH in PGAM1 stable knockdown cells reverses the methyl-2-PG treatment dependent rescue of oxidative PPP flux as well as biosynthesis

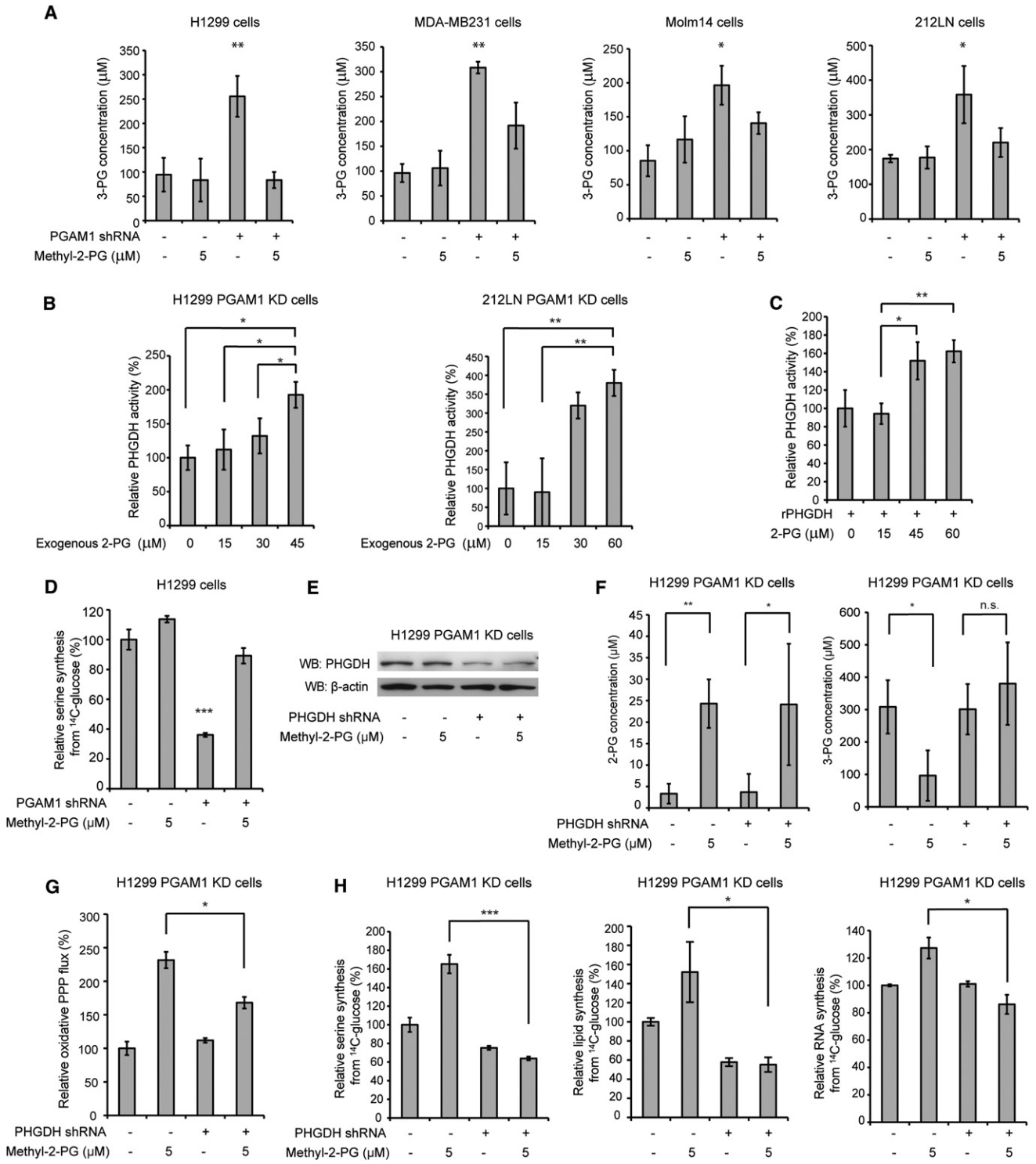

Figure 5. Rescue of Reduced 2-PG Levels due to PGAM1 Attenuation Results in Decreased 3-PG Levels by Activating PHGDH

(A) 3-PG levels in diverse cancer cells with stable knockdown of PGAM1 were determined in the presence and absence of methyl-2-PG.

(B and C) Enzyme activity of PHGDH in PGAM1 knockdown H1299 (B; left) or 212LN (B; right) cell lysates and recombinant PHGDH (rPHGDH) (C) were determined in the presence of increasing concentrations of 2-PG. Relative enzyme activity was normalized to the control samples without 2-PG treatment. 2-PG levels in control H1299 cells with empty vector and PGAM1 knockdown cells are 46.2 ± 10.2 μM and 15.0 ± 14.1 μM, respectively, while 2-PG levels in 212LN cells with empty vector and stable knockdown of PGAM1 are 58.3 ± 20.1 μM and 17.8 ± 14.4 μM, respectively.

(D) Serine biosynthesis rate of H1299 cells with stable knockdown of PGAM1 was determined by measuring ^{14}C incorporation into serine from ^{14}C-glucose in the presence and absence of methyl-2-PG. Relative serine biosynthesis was normalized to control cells harboring an empty vector without methyl-2-PG treatment.

of serine, lipids, and RNA (Figures 5G and 5H, respectively). These data together suggest that, besides being a glycolytic metabolite, 2-PG may also signal through PHGDH to provide regulation of PPP flux and anabolic biosynthesis, at least in part by regulating 3-PG levels.

PGAM1 Enzyme Activity Strikes a Balance between 3-PG and 2-PG Levels, which Coordinates Glycolysis and Biosynthesis to Promote Cancer Cell Proliferation

To study the role of PGAM1 enzyme activity in cancer metabolism and tumor development, we screened and developed a small molecule inhibitor of PGAM1. Currently the only reported PGAM1 inhibitor is MJE3, which specifically inhibits PGAM1 activity exclusively in intact cells, probably by targeting the active site of PGAM1 with certain modifications in vivo (Evans et al., 2005, 2007). We designed a screening strategy using coupled PGAM1 and enolase assays and identified three lead small molecule compounds, including alizarin, as PGAM1 inhibitors from a library of 2,000 US Food and Drug Adminstration-approved small molecule compounds (Figures 6A, S4A, and S4B). We focused on 1,2-dihydroxyanthraquinone, a.k.a. alizarin ($C_{14}H_8O_4$) (Figure 6B, top), which is an organic compound that is historically important as a prominent dye, originally derived from the roots of plants of the *Madder* genus. Treatment with alizarin results in decreased proliferation of human leukemia KG1a cells in a dose-dependent manner (Figures S4C and S4D).

We next identified Alizarin Red S (Figure 6B, middle) as a more potent PGAM1 inhibitor from a group of alizarin derivatives (Figures S4E and S4F). We designed a group of Alizarin Red S derivatives by adding hydrophobic groups through a sulfonamide bond (Figure S5A). Among these compounds, we focused on PGAM1 inhibitor 004A (PGMI-004A) (Figure 6B, bottom), which, although less potent than Red S in vitro, demonstrates enhanced potency to inhibit PGAM1 in leukemia KG1a cells compared to its parental compounds (Figures S5B and S5C). This may be due to the fact that PGMI-004A is more hydrophobic than alizarin and alizarin red S, which confers better cell permeability.

PGMI-004A inhibits PGAM1 with an IC_{50} of ~13.1 μM (Figure 6C) and the Kd value of the PGMI-004A-PGAM1 interaction was determined to be 7.2 ± 0.7 μM from fluorescence-based binding assay (Figure 6D). In a competitive binding assay where PGMI-004A was incubated with recombinant PGAM1 proteins in the presence of different concentrations of PGAM1 substrate 3-PG, we found that increasing concentrations of 3-PG caused an increase in the fluorescence intensity from PGMI-004A-unbound form of PGAM1 in the presence of different concentrations of PGMI-004A, but not in the absence of PGMI-004A (Figure 6E). This suggests that PGMI-004A may allosterically modulate the enzyme activity of PGAM1. The Ki value was determined to be 3.91 ± 2.50 μM using Dixon plot analysis (Figure 6F). In addition, we performed a thermal melt shift assay to examine the interaction of protein (PGAM1) and ligand (PGMI-004A). Incubation of increasing concentrations of PGMI-004A raises PGAM1 melting temperature (Tm) in a dose-dependent manner, suggesting that PGMI-004A directly binds to the protein (Figure 6G). The Kd value for protein-ligand interaction was calculated to be 9.4 ± 2.0 μM. Together, these results suggest that PGMI-004A directly binds to PGAM1 and inhibits its enzyme activity.

We found that inhibition of PGAM1 activity by PGMI-004A treatment results in decreased 2-PG and increased 3-PG levels in H1299 cells, which could be rescued by treatment with methyl-2-PG (Figure 7A). Moreover, treatment with PGMI-004A results in significantly reduced lactate production that was rescued by methyl-2-PG treatment (Figure 7B), but has no significant effect on intracellular ATP levels (Figure 7C). In consonance with these observations, the rescued lactate production due to methyl-2-PG treatment was abolished when enolase was knocked down or inhibited by specific inhibitor NaF in PGMI-004A treated cells (Figure S5D). These results also suggest that rescued 2-PG derived from methyl-2-PG is metabolized by cells to restore the decreased glycolysis due to PGAM1 inhibition in cancer cells. We also found that PGMI-004A treatment results in decreased oxidative PPP flux (Figure 7D) and NADPH/$NADP^+$ ratio (Figure 7E), as well as reduced biosynthesis of lipids and RNA (Figures 7F and 7G, respectively) and cell proliferation (Figure 7H) in H1299 cells. These phenotypes are similar to those observed in PGAM1 knockdown cells, which could be significantly rescued by treatment with methyl-2-PG, suggesting that PGMI-004A targets PGAM1 to inhibit cancer cell metabolism and proliferation.

In addition, we observed that PGMI-004A treatment results in decreased cell proliferation of diverse human cancer and leukemia cells (Figures 7I and 7J and S5E–S5H), but not control human dermal fibroblasts (HDF), human foreskin fibroblasts (HFF), human HaCaT keratinocyte cells and human melanocyte PIG1 cells (Figures 7K and S5I), suggesting minimal non-specific toxicity of PGMI-004A in normal, proliferating human cells.

Targeting PGAM1 by PGMI-004A Treatment Inhibits Cancer Cell Proliferation and Tumor Growth and Alters 3-PG and 2-PG Levels in Primary Leukemia Cells from Patients, Leading to Attenuated Leukemia Cell Proliferation

We next performed an in vivo drug treatment experiment. Initial toxicity studies by chronic injection of PGMI-004A to nude mice for 4 weeks revealed that 100 mg/kg/day administered intraperitoneally is a well-tolerated dose. In addition, continuous treatment with PGMI-004A (100 mg/kg/day) for 7 days did not result in significant alteration in body weight, complete blood cell counts, or hematopoietic properties of nude mice (Table S5). Histopathologic analyses revealed that no notable differences between the vehicle-treated and PGMI-004A-treated groups were evident (Figures S6A–S6D). We performed

(E) Western blot result shows shRNA-mediated knockdown of PHGDH in H1299 cells with stable knockdown of PGAM1 in the presence or absence of methyl-2-PG treatment.

(F) 2-PG (left) and 3-PG (right) levels in PGAM1 knockdown cells upon PHGDH knockdown were determined in the presence and absence of methyl-2-PG.

(G and H) PGAM1 stable knockdown cells treated with or without shRNA targeting PHGDH were tested for PPP flux (G) as well as biosynthesis of serine, lipids and RNA (H; left, middle, and right, respectively) in the presence and absence of methyl-2-PG.

The error bars represent mean values ± SD from three replicates of each sample (*0.01 < p < 0.05; **0.001 < p < 0.01; ***p < 0.001; n.s., not significant).

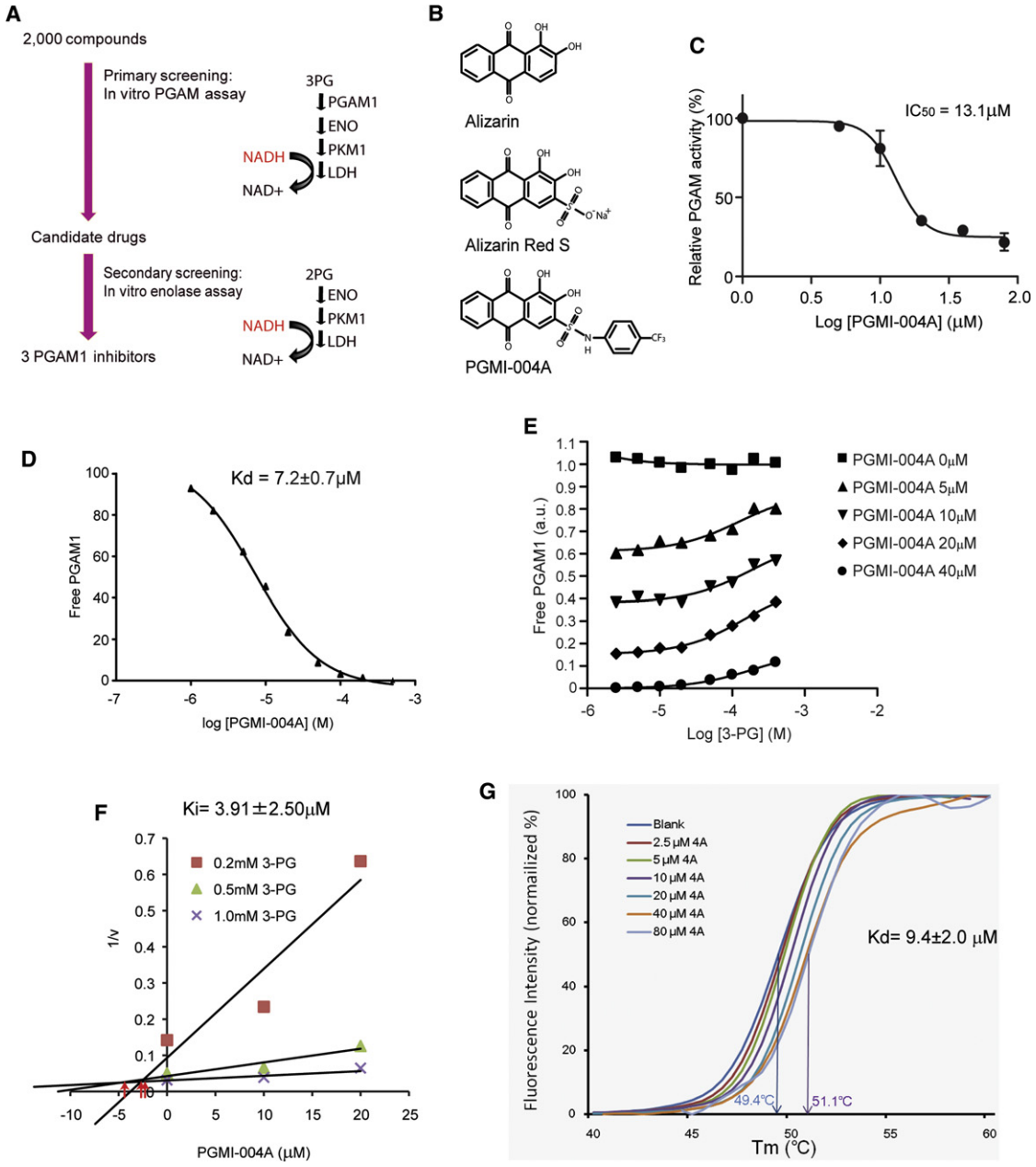

Figure 6. Identification and Characterization of a Small Molecule PGAM1 Inhibitor, PGMI-004A

(A) Schematic representation of the primary and secondary screening strategies to identify lead compounds as PGAM1 inhibitors.

(B) Structure of alizarin and its derivatives alizarin red S and PGAM1 inhibitor (PGMI)-004A.

(C) PGMI-004A inhibits PGAM1 with an IC_{50} of 13.1 μM, which was determined by incubating purified human PGAM1 proteins with increasing concentrations of PGMI-004A. The error bars represent mean values ± SD from three replicates of each sample.

(D) Kd value was determined as 7.2 ± 0.7 μM by incubating purified human PGAM1 proteins with increasing concentrations of PGMI-004A. The fluorescence intensity (Ex: 280 nm, Em: 350 nm) from tryptophan was measured (Schauerte and Gafni, 1989).

(E) Competitive binding assay of PGMI-004A with recombinant PGAM1 protein in the presence of increasing concentrations of PGAM1 substrate 3-PG. Increased free PGAM1 was determined by an increase in fluorescence intensity.

(F) Dixon plot analysis of PGAM1 enzyme assay in the presence of different concentrations of PGMI-004A and 3-PG. The reaction velocity (v) was determined by the rate of the decrease in fluorescence (ex: 340 nm, em: 460 nm) by NADH oxidation. Ki was determined to be 3.91 ± 2.50 μM.

(G) Thermal shift melting curves of PGAM1 and PGMI-004A. Thermal shift assay was performed to examine the protein (PGAM1) and "ligand" (inhibitor PGMI-004A) interaction. Change of melting temperature (Tm) in a dose-dependent manner at concentrations from 2.5 μM to 80 μM demonstrates that PGMI-004A directly binds to the protein. Kd for PGAM1-PGMI-004A interaction was determined to be 9.4 ± 2.0 μM.

See also Figure S4.

xenograft experiments by injecting H1299 cells into nude mice as described (Hitosugi et al., 2009). Six days postinjection, mice were divided into two groups (n = 8/group) and treated with either PGMI-004A (100 mg/kg/day) or vehicle for 21 days. We found that PGMI-004A treatment results in significantly decreased tumor growth and size in treated mice compared with mice receiving vehicle control (Figures 8A and 8B, respectively; Figures S6E and S6F). Moreover, treatment with PGMI-004A effectively inhibits PGAM1 enzyme activity in tumors in vivo in resected tumors from xenograft nude mice (Figure S6G). These combined data suggest that targeting PGAM1 by PGMI-004A inhibits PGAM1 in vivo, and that this inhibition causes specific toxicity to tumor cells.

We found that PGAM1 protein expression and enzyme activity levels are commonly upregulated in primary leukemia cells from diverse patients with acute myeloid leukemia (AML), chronic myelogenous leukemia (CML), or acute B lymphoblastic leukemia (B-ALL; n = 12), compared to control peripheral blood cells from healthy donors (n = 4) (Figure 8C). We next found that, consistent with our observations in cancer cell lines, inhibiting PGAM1 by PGMI-004A treatment results in increased 3-PG and decreased 2-PG levels in primary leukemia cells from a representative patient with AML (Figure 8D). PGMI-004A treatment also results in decreased cell viability and reduced PGAM1 activity and lactate production in the samples from seven (one CML and six AML) out of eight patients with leukemia. Figures 8E, S6H, and S6I show results using samples from patients with CML or AML as representatives, respectively. Moreover, methyl-2-PG treatment rescues the decreased cell viability (Figures 8F and 8G, left) and lactate production (Figure 8G, right) in primary leukemia cells from representative patients with AML. In addition, PGMI-004A treatment did not affect cell viability of mononucleocytes in peripheral blood samples from two healthy human donors (Figures 8H and S6J) and CD34+ cells isolated from bone marrow samples from four healthy donors (Figures 8I and S6K), suggesting promising anticancer potential of PGMI-004A with minimal toxicity to human blood cells. These combined results of translational studies suggest that PGAM1 is a promising therapeutic target in the treatment of human malignancies.

DISCUSSION

Our findings suggest that upregulation of PGAM1 by increased gene expression in cancer cells provides a metabolic advantage to cancer cell proliferation and tumor growth; PGAM1 coordinates glycolysis and anabolic biosynthesis, at least in part by controlling intracellular levels of its substrate 3-PG and product 2-PG (Figure 8J). Our results revealed a molecular mechanism by which 3-PG inhibits 6PGD by directly binding to the active site of 6PGD and competing with its substrate 6-PG. Attenuation of PGAM1 results in abnormal accumulation of 3-PG, which in turn inhibits 6PGD and consequently the oxidative PPP and anabolic biosynthesis. Moreover, our findings suggest that PGAM1 controls the intracellular levels of its substrate 3-PG not only directly through substrate consumption, but also indirectly by controlling levels of its product 2-PG. Physiologic concentrations of 2-PG promote the enzyme activity of PHGDH, which converts 3-PG to pPYR, reducing the cellular 3-PG levels. Upon attenuation of PGAM1, 2-PG is decreased to levels below the physiologic concentrations, leading to decreased PHGDH activity, which facilitates 3-PG accumulation. This represents a regulatory mechanism by which 2-PG activates PHGDH to provide feedback control of 3-PG levels. Thus, we suggest that PGAM1 activity is upregulated in cancer cells to promote glycolysis and keep the intracellular 3-PG levels low, which in turn permits high levels of the PPP and biosynthesis to fulfill the request of rapidly growing tumors. This is consistent with previous report that expression of TP53 suppresses oxidative PPP in cancer cells (Jiang et al., 2011). In addition, PGAM1 may also be responsible for maintaining the physiological levels of 2-PG to sustain PHGDH activity, which diverts 3-PG from glycolysis to serine synthesis and contributes to maintaining relatively low levels of 3-PG in cancer cells.

Inhibition of PGAM1 by shRNA or treatment with a small molecule inhibitor PGMI-004A results in altered glycolysis and anabolic biosynthesis, and reduced cancer cell proliferation and tumor growth. Interestingly, targeting PGAM1 does not significantly affect intracellular ATP levels. Decreased ATP production due to attenuated glycolysis in PGAM1 knockdown cells may be compensated by alternative mechanisms other than mitochondrial oxidative phosphorylation, or perhaps the ATP consumption in PGAM1 knockdown cells is decreased accordingly. Methyl-2-PG treatment rescues most of the aforementioned phenotypes. Rescued 2-PG levels in cells with attenuated PGAM1 reversed decreased lactate production by rescuing the glycolytic process downstream of PGAM1, as well as reduced oxidative PPP flux and biosynthesis of RNA and lipids, at least in part by decreasing elevated 3-PG levels. However, methyl-2-PG treatment only partially rescues the attenuated cell proliferation in PGAM1 knockdown cells or cells treated with PGMI-004A. This result suggests that PGAM1 may contribute to cell proliferation in both 2-PG-dependent and -independent manners.

The current understanding of the connection between glycolysis and PPP/biosynthesis is based on a model in which glycolytic intermediates can be diverted into PPP and biosynthesis pathways as precursors. Our results show that the concentrations of glycolytic metabolites such as 3-PG and 2-PG can directly affect the catalytic activity of enzymes involved in PPP and biosynthesis, which represents an additional link between glycolysis, PPP, and biosynthesis. Metabolites have been suggested to function as signaling molecules in the past. Examples include AMP, which is an allosteric activator for AMP-activated protein kinase (AMPK), a kinase that senses intracellular energy levels (ATP/AMP ratio) (Shackelford and Shaw, 2009), and glutamine, which activates leucine uptake, leading to mTOR activation (Nicklin et al., 2009). We found that the cellular levels of 3-PG and 2-PG, two key intermediates in glycolysis, have additional regulatory impact on metabolic enzymes to affect cell metabolism and consequently proliferation, which provides an example to suggest that glycolytic metabolites could also serve as signaling molecules to control cell metabolism and cellular responses. Moreover, our findings also describe a feedback mechanism by which the product levels (2-PG) of a metabolic enzyme (PGAM1) can regulate its substrate levels (3-PG) by affecting an alternative enzyme (PHGDH) that is involved in production of this substrate. Thus, this study showcases the

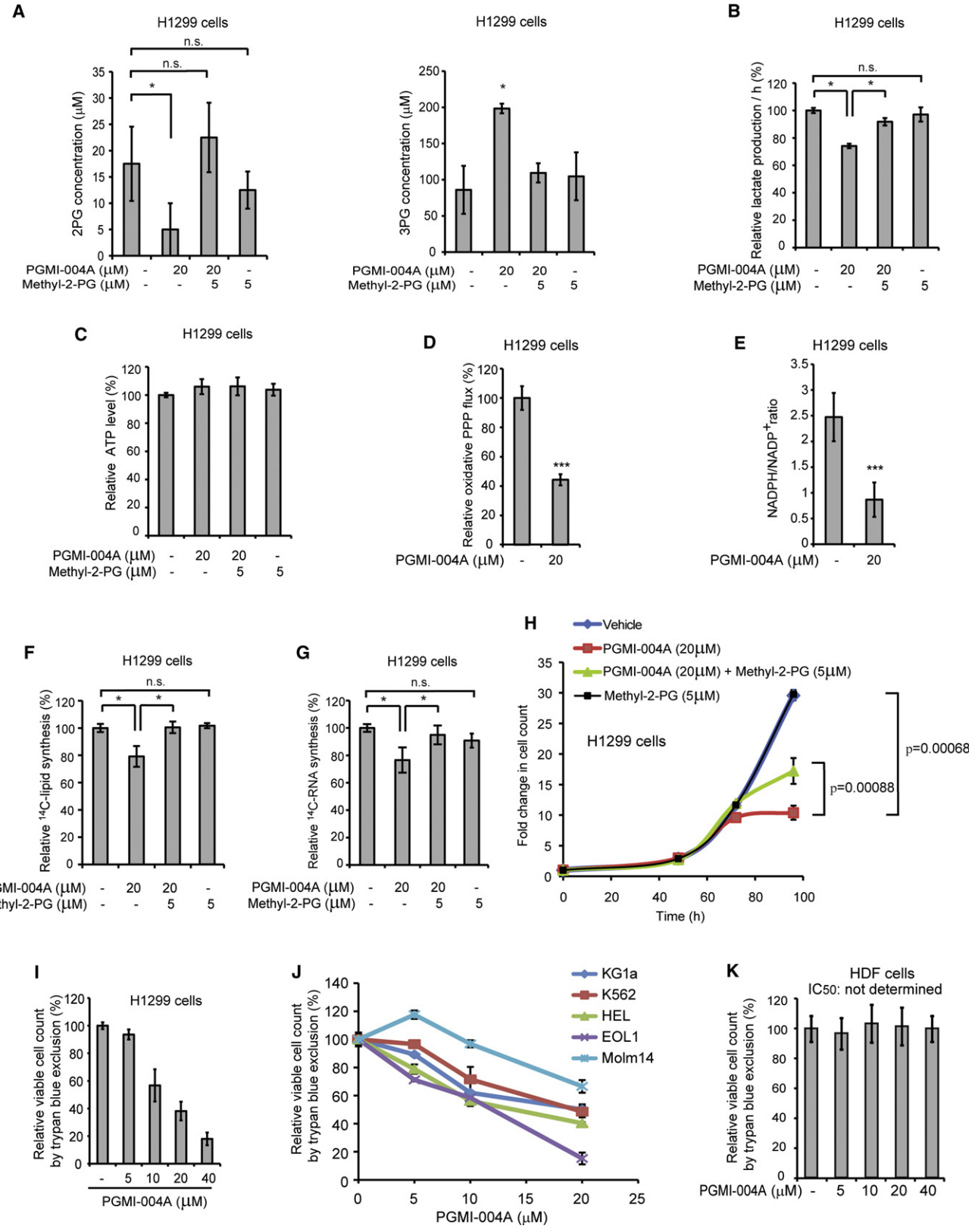
A
H1299 cells
2PG concentration (μM)
n.s.
n.s.
*
PGMI-004A (μM) - 20 20 -
Methyl-2-PG (μM) - - 5 5
H1299 cells
3PG concentration (μM)
*
PGMI-004A (μM) - 20 20 -
Methyl-2-PG (μM) - - 5 5
B
H1299 cells
Relative lactate production / h (%)
n.s.
* *
PGMI-004A (μM) - 20 20 -
Methyl-2-PG (μM) - - 5 5
C
H1299 cells
Relative ATP level (%)
PGMI-004A (μM) - 20 20 -
Methyl-2-PG (μM) - - 5 5
D
H1299 cells
Relative oxidative PPP flux (%)
***
PGMI-004A (μM) - 20
E
H1299 cells
NADPH/NADP+ratio
***
PGMI-004A (μM) - 20
F
H1299 cells
Relative 14C-lipid synthesis (%)
n.s.
* *
PGMI-004A (μM) - 20 20 -
Methyl-2-PG (μM) - - 5 5
G
H1299 cells
Relative 14C-RNA synthesis (%)
n.s.
* *
PGMI-004A (μM) - 20 20 -
Methyl-2-PG (μM) - - 5 5
H
Vehicle
PGMI-004A (20μM)
PGMI-004A (20μM) + Methyl-2-PG (5μM)
Methyl-2-PG (5μM)
H1299 cells
Fold change in cell count
p=0.00068
p=0.00088
Time (h)
I
H1299 cells
Relative viable cell count by trypan blue exclusion (%)
PGMI-004A (μM)
J
KG1a
K562
HEL
EOL1
Molm14
Relative viable cell count by trypan blue exclusion (%)
PGMI-004A (μM)
K
HDF cells
IC50: not determined
Relative viable cell count by trypan blue exclusion (%)
PGMI-004A (μM) - 5 10 20 40

complexity of cellular metabolism, demonstrating that control of the intracellular levels of a particular metabolite may involve diverse enzymes in different metabolic reactions, such that the balance of the intracellular levels of various metabolites may exert regulatory functions on enzymes in different pathways to control cellular metabolism. Such a mechanism can be explored for anticancer therapies.

Previous reports describe that targeting PGAM1 by a PGAM1-derived inhibitory peptide or PGAM inhibitor MJE3 attenuates cancer cell proliferation (Engel et al., 2004; Evans et al., 2005). In consonance with these observations, our studies suggest that protein expression and enzyme activity levels of PGAM1 are important for cancer cell proliferation and tumor growth. Our compound PGMI-004A exhibits promising efficacy in the treatment of xenograft nude mice in vivo with minimal toxicity, as well as in diverse human cancer cells and primary leukemia cells from human patients in vitro with no obvious off-target effect and minimal toxicity to human cells. These translational studies provide "proof of principle" to suggest anti-PGAM1 as a promising therapy in clinical treatment of tumors that heavily rely on the Warburg effect. However, the potential toxicity of PGAM inhibitors in vivo to normal postmitotic, metabolically active organs such as brain, liver, skeletal muscle, and heart, all of which are glycolytic, remains undetermined. This warrants further detailed toxicity and pharmacokinetics studies to improve the proposed anti-PGAM1 therapy in cancer treatment.

EXPERIMENTAL PROCEDURES

Cellular Metabolites Extraction and Measurement

Cellular metabolites were extracted and spectrophotometrically measured as described previously (Kauffman et al., 1969; Minakami et al., 1965) with some modifications. To determine cellular concentration of 2-PG and 3-PG, 100 μl of packed cell pellets were homogenized in 1.5 ml of hypotonic lysis buffer (20 mM HEPES (pH 7.0), 5 mM KCl, 1 mM $MgCl_2$, 5 mM DTT, and protease inhibitor cocktail). The homogenates were centrifuged in a cold room at 4°C for 10 min at maximum speed, and the supernatants were applied to Amicon Ultra tubes with 10KDa cut off filter (Millipore). The flow through containing the metabolites was used for the measurement. NADH, ADP, and $MgCl_2$ were added to the flow through to final concentrations of 0.14 mM, 1 mM, and 50 mM, respectively. Recombinant LDH and PKM1 proteins were added to final concentrations of 5 μg/ml and 10 μg/ml, respectively. Recombinant enolase protein was added to a final concentration of 50 μg/ml to measure cellular 2-PG. Once the reaction was initiated by enolase, a decrease in absorbance at 340 nm from NADH oxidation was measured by a DU800 spectrophotometer (Beckman). After termination of the enolase reaction, recombinant PGAM1 protein was added to a final concentration of 25 μg/ml and the decrease in absorbance at 340 nm was immediately monitored to measure cellular 3-PG. One hundred microliters of 2-PG and 3-PG (Sigma) diluted with 1.5 ml of hypotonic lysis buffer were used as the standards.

Protein Crystallization, Data Collection, and Structure Determination

For protein crystallization, 6PGD was crystallized by using the hanging drop vapor diffusion method. To soak in 3-PG, 0.2 μl of 5 mM 3-phosphoglycerate acid were added into the mixture and incubated for 2 hr. The crystals were then flash-frozen in liquid nitrogen with the same cryoprotectant solution. Because a high concentration of 3-PG causes the crystal to crack, a final 3-PG concentration of 833 μM was applied and an occupancy of 50% was obtained after refinement. For data collection, the crystal diffraction data of 6PGD apo-form and 6PGD-3-PG complex were collected at the macromolecular crystallography for life science beamline GM/CA-CAT (23-ID-F) and NE-CAT (24-ID-E) respectively at the Advanced Photon Source, Argonne National Laboratory. The data were processed with HKL2000 and the scaled data were used for molecular replacement. For phasing, model building and refinement, the structure of 6PGD apo-form was determined by molecular replacement using Molrep in the CCP4 suite, with the protein portion of the solved structure of 6PGD-6-PG as the search model (Protein Data Bank [pdb] number: 3FWN) (Chen et al., 2010). The structure was then refined by using Phenix (Haddadian et al., 2011). Manual rebuilding of the model was carried out using the molecular graphics program COOT based on electron density interpretation. Water molecules were incorporated into the model if they gave rise to peaks exceeding 3σ in Fo-Fc density maps. The structure of the 6PGD-3-PG complex was also determined by molecular replacement using Molrep with the solved structure of 6PGD apo-form as the search model, and then refined by using Phenix. Manual rebuilding of the model was carried out using the molecular graphics programs COOT. The final structures of apo-form and 6PGD-3-PG complex were visualized by using PyMol software.

Xenograft Studies

Approval of use of mice and designed experiments was given by the Institutional Animal Care and Use Committee of Emory University. Nude mice (Athymic Nude-Foxn1nu, female 6- to 8-week-old, Harlan) were subcutaneously injected with 10×10^6 H1299 cells harboring empty vector on the left flank, and cells with stable knockdown of endogenous hPGAM1 on the right flank, respectively. The tumors were harvested and weighed at the experimental endpoint, and the masses of tumors (g) derived from cells with and without stable knockdown of endogenous hPGAM1 in both flanks of each mouse were compared. Statistical analyses were performed by comparison in relation to the control group with a two-tailed paired Student's t test. For drug evaluation of PGMI-004A using xenograft mice, the drug was administered by daily intraperitoneal injection at a dose of 100 mg/kg from 6 days after subcutaneous injection of H1299 cells on right flank of each mouse. Tumor growth was recorded by measurement of two perpendicular diameters of the tumors over a 3 week course using the formula $4\pi/3 \times (\text{width}/2)^2 \times (\text{length}/2)$. The tumors were harvested and weighed at the experimental endpoint. The masses of tumors (g) treated with vehicle control (DMSO: PEG400:PBS at a ratio of 4:3:3) and PGMI-004A were compared and p values were determined by a two-tailed Student's t test.

Primary Tissue Samples from Patients with Leukemia and Healthy Donors

Approval of use of human specimens was given by the Institutional Review Board of Emory University School of Medicine. All clinical samples were

Figure 7. Inhibition of PGAM1 by PGMI-004A Reveals that PGAM1 Enzyme Activity Is Important for Regulation of 3-PG and 2-PG Levels and Coordination of Glycolysis and Biosynthesis to Promote Cancer Cell Proliferation

(A) 2-PG (left) and 3-PG (right) levels in H1299 cells treated with or without PGMI-004A were determined in the presence and absence of methyl-2-PG.

(B and C) Lactate production (B) and intracellular ATP levels (C) in H1299 cells treated with or without PGMI-004A were determined in the presence and absence of methyl-2-PG.

(D and E) H1299 cells treated with or without PGMI-004A were tested for oxidative PPP flux (D) and NADPH/$NADP^+$ ratio (E).

(F–H) H1299 cells treated with or without PGMI-004A were tested for biosynthesis of lipids (F) and RNA (G), as well as cell proliferation (H) in the presence and absence of methyl-2-PG.

(I–K) Cell viability of H1299 cells (I), diverse human leukemia cells (J) and control HDF cells (K) in the presence of increasing concentrations of PGMI-004A. Cell viability was determined by trypan blue exclusion.

The error bars represent mean values ± SD from three replicates of each sample (*$0.01 < p < 0.05$; ***$p < 0.001$; n.s., not significant).

See also Figure S5.

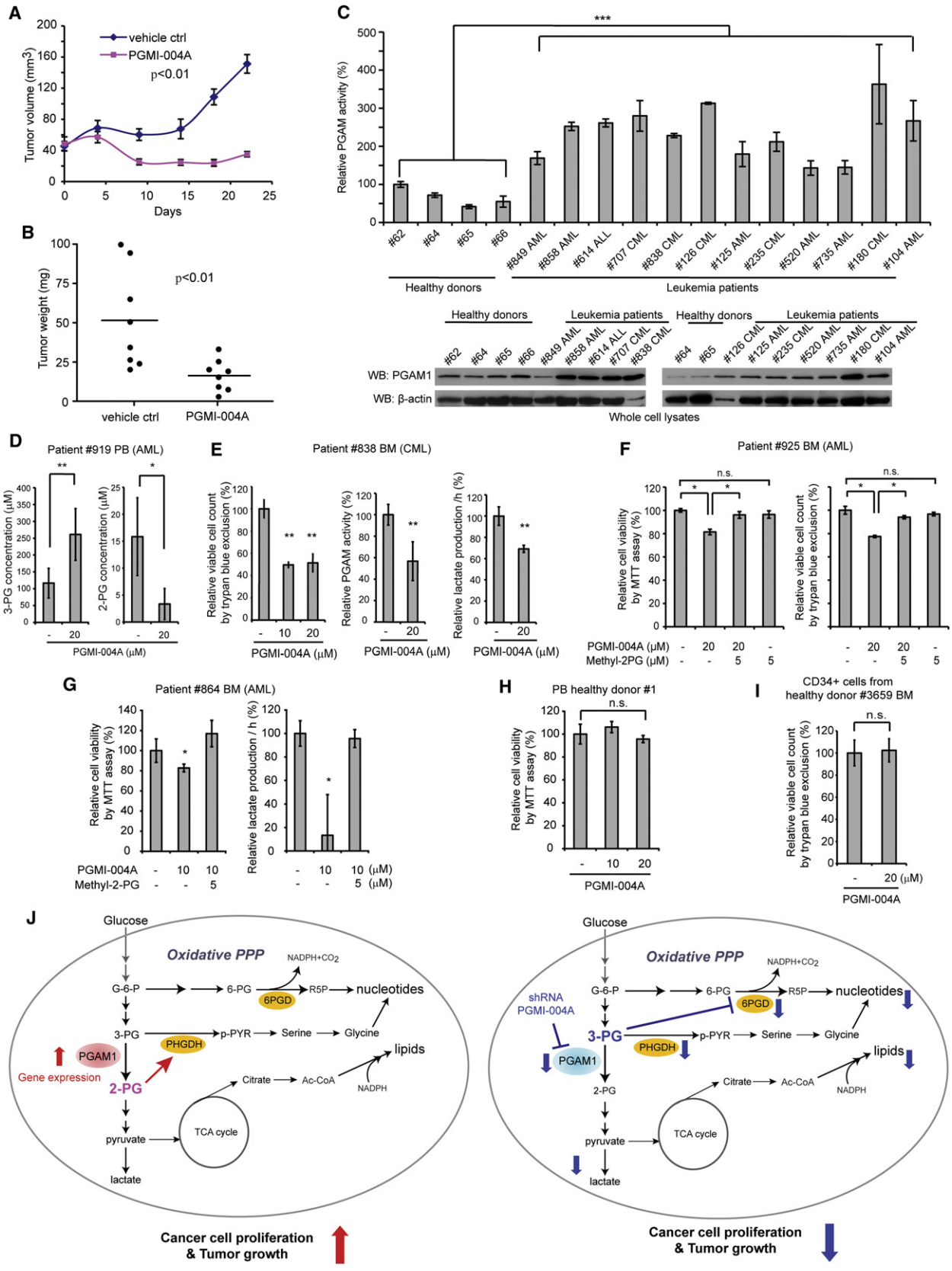
A
vehicle ctrl
PGMI-004A
p<0.01
Tumor volume (mm3)
Days
B
Tumor weight (mg)
p<0.01
vehicle ctrl
PGMI-004A
C
Relative PGAM activity (%)
***
Healthy donors
Leukemia patients
WB: PGAM1
WB: β-actin
Whole cell lysates
D
Patient #919 PB (AML)
3-PG concentration (μM)
2-PG concentration (μM)
PGMI-004A (μM)
E
Patient #838 BM (CML)
Relative viable cell count by trypan blue exclusion (%)
Relative PGAM activity (%)
Relative lactate production /h (%)
PGMI-004A (μM)
F
Patient #925 BM (AML)
Relative cell viability by MTT assay (%)
Relative viable cell count by trypan blue exclusion (%)
n.s.
PGMI-004A (μM)
Methyl-2PG (μM)
G
Patient #864 BM (AML)
Relative cell viability by MTT assay (%)
Relative lactate production / h (%)
PGMI-004A
Methyl-2-PG
H
PB healthy donor #1
Relative cell viability by MTT assay (%)
n.s.
PGMI-004A
I
CD34+ cells from healthy donor #3659 BM
Relative viable cell count by trypan blue exclusion (%)
n.s.
PGMI-004A
J
Glucose
Oxidative PPP
NADPH+CO2
G-6-P
6-PG
6PGD
R5P
nucleotides
3-PG
PHGDH
p-PYR
Serine
Glycine
PGAM1
Gene expression
2-PG
Citrate
Ac-CoA
lipids
NADPH
pyruvate
TCA cycle
lactate
shRNA PGMI-004A
Cancer cell proliferation & Tumor growth

obtained with informed consent with approval by the Emory University Institutional Review Board. Clinical information for the patients was obtained from the pathologic files at Emory University Hospital under the guidelines and with approval from the Institutional Review Board of Emory University School of Medicine and according to the Health Insurance Portability and Accountability Act. Only samples from patients that were not previously treated with chemotherapy or radiation therapy were used. Mononuclear cells were isolated from peripheral blood and bone marrow samples from patients with leukemia or peripheral blood samples from healthy donors using lymphocyte separation medium (Cellgro). Cells were cultured in RPMI 1640 medium supplemented with 10% fetal bovine serum and penicillin/streptomycin and incubated with increasing concentrations of PGMI-004A for up to 72 or 120 hr.

SUPPLEMENTAL INFORMATION

Supplemental Information includes six figures, five tables, and Supplemental Experimental Procedures and can be found with this article online at http://dx.doi.org/10.1016/j.ccr.2012.09.020.

ACKNOWLEDGMENTS

We thank Susan Sunay at the Hematology Division Tissue Bank, Winship Cancer Institute of Emory, for providing primary tissue samples from patients with leukemia, Drs. Sagar Lonial and Lawrence Boise for providing peripheral blood samples from healthy donors, and Dr. Yoke Wah Kow for human HaCaT and PIG1 cell lines. This work was supported in part by NIH Grants CA120272 (to J.C.), CA140515 (to J.C.), GM071440 (to C.H.), and the Pharmacological Sciences Training Grant T32 GM008602 (to S.E.). J.X. and T.-L.G. are employees of Cell Signaling Technology, Inc. T.H. is a Fellow Scholar of the American Society of Hematology. S.E. is an NIH pre-doctoral fellow and an ARCS Foundation Scholar. G.Z.C., D.M.S., F.R.K., S.K., and J.C. are Georgia Cancer Coalition Distinguished Cancer Scholars. S.K. is a Robbins Scholar. S.K. and J.C. are American Cancer Society Basic Research Scholars. J.C. is a Scholar of the Leukemia and Lymphoma Society.

Received: March 29, 2012
Revised: July 23, 2012
Accepted: September 12, 2012
Published: November 12, 2012

REFERENCES

Cairns, R.A., Harris, I.S., and Mak, T.W. (2011). Regulation of cancer cell metabolism. Nat. Rev. Cancer *11*, 85–95.

Chen, Y.Y., Ko, T.P., Chen, W.H., Lo, L.P., Lin, C.H., and Wang, A.H. (2010). Conformational changes associated with cofactor/substrate binding of 6-phosphogluconate dehydrogenase from Escherichia coli and Klebsiella pneumoniae: Implications for enzyme mechanism. J. Struct. Biol. *169*, 25–35.

Corcoran, C.A., Huang, Y., and Sheikh, M.S. (2006). The regulation of energy generating metabolic pathways by p53. Cancer Biol. Ther. *5*, 1610–1613.

Elstrom, R.L., Bauer, D.E., Buzzai, M., Karnauskas, R., Harris, M.H., Plas, D.R., Zhuang, H., Cinalli, R.M., Alavi, A., Rudin, C.M., and Thompson, C.B. (2004). Akt stimulates aerobic glycolysis in cancer cells. Cancer Res. *64*, 3892–3899.

Engel, M., Mazurek, S., Eigenbrodt, E., and Welter, C. (2004). Phosphoglycerate mutase-derived polypeptide inhibits glycolytic flux and induces cell growth arrest in tumor cell lines. J. Biol. Chem. *279*, 35803–35812.

Evans, M.J., Saghatelian, A., Sorensen, E.J., and Cravatt, B.F. (2005). Target discovery in small-molecule cell-based screens by in situ proteome reactivity profiling. Nat. Biotechnol. *23*, 1303–1307.

Evans, M.J., Morris, G.M., Wu, J., Olson, A.J., Sorensen, E.J., and Cravatt, B.F. (2007). Mechanistic and structural requirements for active site labeling of phosphoglycerate mutase by spiroepoxides. Mol. Biosyst. *3*, 495–506.

Feig, S.A., Shohet, S.B., and Nathan, D.G. (1971). Energy metabolism in human erythrocytes. I. Effects of sodium fluoride. J. Clin. Invest. *50*, 1731–1737.

Gottschalk, S., Anderson, N., Hainz, C., Eckhardt, S.G., and Serkova, N.J. (2004). Imatinib (STI571)-mediated changes in glucose metabolism in human leukemia BCR-ABL-positive cells. Clin. Cancer Res. *10*, 6661–6668.

Haddadian, E.J., Gong, H., Jha, A.K., Yang, X., Debartolo, J., Hinshaw, J.R., Rice, P.A., Sosnick, T.R., and Freed, K.F. (2011). Automated real-space refinement of protein structures using a realistic backbone move set. Biophys. J. *101*, 899–909.

Hitosugi, T., Kang, S., Vander Heiden, M.G., Chung, T.W., Elf, S., Lythgoe, K., Dong, S., Lonial, S., Wang, X., Chen, G.Z., et al. (2009). Tyrosine phosphorylation inhibits PKM2 to promote the Warburg effect and tumor growth. Sci. Signal. *2*, ra73.

Jiang, P., Du, W., Wang, X., Mancuso, A., Gao, X., Wu, M., and Yang, X. (2011). p53 regulates biosynthesis through direct inactivation of glucose-6-phosphate dehydrogenase. Nat. Cell Biol. *13*, 310–316.

Figure 8. PGMI-004A Treatment Results in Increased 3-PG and Decreased 2-PG Levels, and Reduced Cell Proliferation of Primary Leukemia Cells from Patients, and Attenuated Tumor Growth in Xenograft Nude Mice In Vivo

(A and B) Tumor growth (A) and tumor size (B) in xenograft nude mice injected with H1299 cells were compared between the group of mice treated with PGMI-004A and the control group treated with vehicle control. p values were determined by a two-tailed Student's t test.

(C) PGAM1 protein expression (lower) and enzyme activity (upper) levels were examined using primary leukemia cells from diverse human patients with AML, CML, or B-ALL and compared to control peripheral blood cells from healthy donors.

(D) Effect of PGMI-004A treatment on 3-PG (left) and 2-PG (right) levels in human primary leukemia cells isolated from peripheral blood samples from a representative patient with AML.

(E) Effect of PGMI-004A treatment on cell viability (left), PGAM1 activity (middle), and lactate production (right) in human primary leukemia cells from a representative patient with CML.

(F and G) Effect of methyl-2-PG treatment on decreased cell viability (F; G left) and lactate production (G right) in PGMI-004A-treated human primary leukemia cells from patients with AML.

(H and I) PGMI-004A shows no toxicity in treatment (120 hr) of peripheral blood cells (H) and CD34+ cells isolated from bone marrow samples (I) from representative healthy human donors.

(J) Proposed model: role of PGAM1 in cancer cell metabolism.

Left: PGAM1 activity is upregulated in cancer cells to promote glycolysis and keep the intracellular 3-PG levels low, which in turn permits high levels of the PPP and biosynthesis to fulfill the request of rapidly growing tumors. PGAM1 also maintains the physiologic levels of 2-PG to sustain PHGDH activity, which diverts 3-PG from glycolysis to serine synthesis and contributes to maintaining relatively low levels of 3-PG in cancer cells. These effects in concert provide a metabolic advantage to cancer cell proliferation and tumor growth.

Right: When PGAM1 is inhibited, 3-PG levels are elevated, which in turn inhibit 6PGD and consequently the oxidative PPP and anabolic biosynthesis. At the same time, 2-PG is decreased to levels below the physiologic concentrations, leading to decreased PHGDH activity, which facilitates 3-PG accumulation. Such metabolic changes result in attenuated cell proliferation and tumor development.

The error bars represent mean values ± SD from three replicates of each sample (*$0.01 < p < 0.05$; **$0.001 < p < 0.01$; ***$p < 0.001$; n.s., not significant). See also Figure S6 and Table S5.

Kauffman, F.C., Brown, J.G., Passonneau, J.V., and Lowry, O.H. (1969). Effects of changes in brain metabolism on levels of pentose phosphate pathway intermediates. J. Biol. Chem. *244*, 3647–3653.

Kroemer, G., and Pouyssegur, J. (2008). Tumor cell metabolism: cancer's Achilles' heel. Cancer Cell *13*, 472–482.

Li, L., Dworkowski, F.S., and Cook, P.F. (2006). Importance in catalysis of the 6-phosphate-binding site of 6-phosphogluconate in sheep liver 6-phosphogluconate dehydrogenase. J. Biol. Chem. *281*, 25568–25576.

Liu, L., Wang, S., Zhang, Q., and Ding, Y. (2008). Identification of potential genes/proteins regulated by Tiam1 in colorectal cancer by microarray analysis and proteome analysis. Cell Biol. Int. *32*, 1215–1222.

Minakami, S., Takayasu, S., Suzuki, C., and Yoshikawa, H. (1964). The hydrogen ion concentrations and erythrocyte glycolysis. Biochem. Biophys. Res. Commun. *17*, 748–751.

Minakami, S., Suzuki, C., Saito, T., and Yoshikawa, H. (1965). Studies on erythrocyte glycolysis. I. Determination of the glycolytic intermediates in human erythrocytes. J. Biochem. *58*, 543–550.

Mulquiney, P.J., and Kuchel, P.W. (1999). Model of 2,3-bisphosphoglycerate metabolism in the human erythrocyte based on detailed enzyme kinetic equations: equations and parameter refinement. Biochem. J. *342*, 581–596.

Nicklin, P., Bergman, P., Zhang, B., Triantafellow, E., Wang, H., Nyfeler, B., Yang, H., Hild, M., Kung, C., Wilson, C., et al. (2009). Bidirectional transport of amino acids regulates mTOR and autophagy. Cell *136*, 521–534.

Ren, F., Wu, H., Lei, Y., Zhang, H., Liu, R., Zhao, Y., Chen, X., Zeng, D., Tong, A., Chen, L., et al. (2010). Quantitative proteomics identification of phosphoglycerate mutase 1 as a novel therapeutic target in hepatocellular carcinoma. Mol. Cancer *9*, 81.

Schauerte, J.A., and Gafni, A. (1989). Long-lived tryptophan fluorescence in phosphoglycerate mutase. Biochemistry *28*, 3948–3954.

Shackelford, D.B., and Shaw, R.J. (2009). The LKB1-AMPK pathway: metabolism and growth control in tumour suppression. Nat. Rev. Cancer *9*, 563–575.

Tennant, D.A., Durán, R.V., Boulahbel, H., and Gottlieb, E. (2009). Metabolic transformation in cancer. Carcinogenesis *30*, 1269–1280.

Tennant, D.A., Durán, R.V., and Gottlieb, E. (2010). Targeting metabolic transformation for cancer therapy. Nat. Rev. Cancer *10*, 267–277.

Cancer Cell
Article

ATF4 Regulates *MYC*-Mediated Neuroblastoma Cell Death upon Glutamine Deprivation

Guoliang Qing,[1,3,4,5] Bo Li,[1,4] Annette Vu,[2] Nicolas Skuli,[1,3] Zandra E. Walton,[1] Xueyuan Liu,[2] Patrick A. Mayes,[2] David R. Wise,[1] Craig B. Thompson,[1,6] John M. Maris,[1,2] Michael D. Hogarty,[2] and M. Celeste Simon[1,3,*]
[1]Abramson Family Cancer Research Institute
[2]Division of Oncology and Center for Childhood Cancer Research, Children's Hospital of Philadelphia, Department of Pediatrics Perelman School of Medicine at the University of Pennsylvania, Philadelphia, PA 19104, USA
[3]Howard Hughes Medical Institute, 421 Curie Boulevard, Philadelphia, PA 19104, USA
[4]These authors contributed equally to this work
[5]Present address: Provincial Key Laboratory of Drug Target Research and Pharmacodynamic Evaluation, Tongji Medical College, Huazhong University of Science and Technology, 13 Hangkong Road, Wuhan, Hubei Province 430030, China
[6]Present address: Memorial Sloan-Kettering Cancer Center, 1275 York Avenue, New York, NY 10065, USA
*Correspondence: celeste2@mail.med.upenn.edu
http://dx.doi.org/10.1016/j.ccr.2012.09.021

SUMMARY

Oncogenic Myc alters mitochondrial metabolism, making it dependent on exogenous glutamine (Gln) for cell survival. Accordingly, Gln deprivation selectively induces apoptosis in *MYC*-overexpressing cells via unknown mechanisms. Using *MYCN*-amplified neuroblastoma as a model, we identify *PUMA*, *NOXA*, and *TRB3* as executors of Gln-starved cells. Gln depletion in *MYC*-transformed cells induces apoptosis through ATF4-dependent, but p53-independent, *PUMA* and *NOXA* induction. *MYC*-transformed cells depend on both glutamate-oxaloacetate transaminase and glutamate dehydrogenase to maintain Gln homeostasis and suppress apoptosis. Consequently, either ATF4 agonists or glutaminolysis inhibitors potently induce apoptosis in vitro and inhibit tumor growth in vivo. These results reveal mechanisms whereby Myc sensitizes cells to apoptosis, and validate ATF4 agonists and inhibitors of Gln metabolism as potential Myc-selective cancer therapeutics.

INTRODUCTION

Neuroblastoma is one of the most frequent solid tumors detected in childhood, accounting for ~10%–15% of all pediatric oncology deaths (Maris, 2010). Risk factors indicative of poor prognosis include age > 18 months at diagnosis, advanced stage, unfavorable histologic grade, and *MYCN* amplification (Maris, 2010). Recent studies demonstrated that mutations in the anaplastic lymphoma kinase (*ALK*) gene are causal for most familial neuroblastomas and occur in ~10% of sporadic neuroblastomas, and that polymorphisms in genes encoding BRCA1-associated RING Domain-1 (BARD1) and LIM domain only 1 (LMO1) influence disease susceptibility (Capasso et al., 2009; Mossé et al., 2008; Wang et al., 2011). Nevertheless, *MYCN* amplification remains the most important oncogenic driver and reliable prognostic factor, and is highly correlated with advanced disease stage and a poor survival rate. *MYCN* amplification occurs in 20%–25% of neuroblastomas overall and 40% of high-risk cases (Maris, 2010). Alternatively, elevated *c-MYC* expression correlates with poor prognosis in *MYCN*-nonamplified neuroblastoma (Liu et al., 2008). High levels of Myc activity likely contribute to aggressive phenotypes by regulating and/or cooperating with other oncogenic pathways.

Neuroblastomas, like other solid tumors, require specific metabolic alterations to fuel their deregulated growth and invasion into surrounding tissues. The regulation and dynamics of

Significance

Myc-transformed cells depend on elevated glutaminolysis for survival, but little is known about the molecular pathways that trigger apoptosis upon glutamine (Gln) withdrawal. Here we describe a regulatory mechanism whereby ATF4 induces expression of the proapoptotic proteins PUMA, NOXA, and TRB3 to promote apoptosis in Gln-deprived, Myc-overexpressing neuroblastoma cells. Moreover, xenograft and autochthonous murine neuroblastoma tumor growth is inhibited by small molecules that either enhance ATF4 activity or block glutaminolysis. Importantly, we demonstrate that *MYCN*-amplified human neuroblastomas selectively overexpress high-affinity Gln transporters and other glutaminolytic enzymes that correlate with poor prognosis. These data suggest that drugs that inhibit glutaminolysis or elevate ATF4 function may be effective therapeutic strategies for treating the ≥40% of human cancers that overexpress Myc.

the central metabolic pathways and energy production differ between normal and malignant cells. Fast-growing, poorly differentiated tumor cells typically exhibit increased aerobic glycolysis, a phenomenon known as the Warburg effect (Vander Heiden et al., 2009). Cancer cells also depend on sustained mitochondrial activity, and provide biosynthetic substrates to support enhanced proliferation and survival. Glucose and glutamine (Gln) are two of the most abundant nutrients consumed by neoplastic cells (DeBerardinis et al., 2008). In most human cancers, >80% of the absorbed glucose is catabolized into lactate. While glycolytic ATP generation maintains the cellular bioenergetics, the remaining glucose enters the tricarboxylic acid cycle (TCA) cycle, where it is converted to citrate. Citrate is then preferentially exported into the cytosol to support lipid synthesis. However, increased citrate efflux from mitochondria can deplete TCA cycle metabolites. To prevent this, Gln (another major substrate oxidized by tumor cells) replenishes a truncated TCA cycle through a process termed anaplerosis (DeBerardinis et al., 2008). Moreover, Gln metabolism maintains mitochondrial integrity and nicotinamide adenine dinucleotide phosphate (NADPH) levels needed for redox homeostasis and macromolecular synthesis (DeBerardinis et al., 2008; Metallo et al., 2012; Mullen et al., 2012; Wise et al., 2011).

MYC oncogenes regulate multiple aspects of tumor metabolism, enabling cancer cells to avidly uptake both glucose and Gln (Dang, 2012). The *MYC* family consists of three members: *c-MYC*, *MYCN*, and *MYCL*. Whereas *c-MYC* is broadly deregulated in many human tumors, *MYCN* expression is more restricted to neural tumors and *MYCL* is predominantly found in small cell lung cancer. Both c-Myc and N-Myc have been documented to enhance aerobic glycolysis by directly activating the transcription of glycolytic genes (Dang, 2012; Qing et al., 2010). Oncogenic c-Myc has been linked to increased glutaminolysis through coordinated transcriptional and post-transcriptional programs (Gao et al., 2009; Wise et al., 2008). For instance, c-Myc directly activates the transcription of *SLC1A5* (solute carrier family 1, member 5, also known as *ASCT2*) and *SLC38A5* (solute carrier family 38, member 5, also known as *SN2*), which encode two highly efficient Gln transporters (Wise et al., 2008). Furthermore, c-Myc indirectly stimulates glutaminase (encoded by *GLS*) expression through suppression of microRNAs miR-23a/b, which specifically target the *GLS* 3′ untranslated region and inhibit *GLS* messenger RNA (mRNA) translation (Gao et al., 2009). Thus, c-Myc coordinates the expression of multiple genes that are necessary for Gln metabolism, replenishing the TCA cycle and supplying essential intermediates for nucleic acid, amino acid, and glutathione biosynthesis.

MYCN amplification is strongly correlated with advanced-stage neuroblastoma (Maris, 2010) and is used worldwide for patient-risk classification. *MYCN*-amplified neuroblastomas are frequently resistant to conventional therapeutic drugs, due in part to defects in death-inducing signaling complex (DISC) components such as Caspase 8 (encoded by *CASP8*; Teitz et al., 2000) and altered ABC transporter expression (Porro et al., 2010). Therefore, it is critical to identify effective druggable targets in neuroblastoma. By achieving systemic inhibition in a Ras-mediated lung adenocarcinoma mouse model, Soucek et al. (2008) demonstrated the benefit of targeting MYC (a recipient of multiple oncogenic signals) as an efficient and tumor-specific cancer therapy. Thus far, however, no small molecules targeting nonkinase oncoproteins such as MYC have been developed. *MYCN*-amplified neuroblastomas are highly vascular (Maris, 2010), which makes the use of antiangiogenic agents (e.g., agents that target vascular endothelial growth factor) a promising therapeutic approach. However, recent studies demonstrated that antiangiogenics significantly increase invasion and metastasis in multiple tumor models (Ebos et al., 2009; Pàez-Ribes et al., 2009), which has somewhat decreased enthusiasm for this treatment in cancers such as neuroblastoma.

Myc-mediated metabolic reprogramming triggers cellular dependency on exogenous Gln to sustain viability. Consequently, Gln depletion kills transformed cells in a Myc-dependent manner (Le et al., 2012; Wise et al., 2008; Yuneva et al., 2007). However, whether genes involved in Gln metabolism are deregulated in primary human tumors, and the mechanisms responsible for Gln deprivation-mediated cell death remain largely unknown. We therefore sought to determine whether these cell-death pathway(s) and/or alterations of Gln metabolism can be therapeutically exploited.

RESULTS

Gln Depletion Induces Neuroblastoma Cell Death in an N-Myc Dependent Manner

To evaluate the impact of *MYC* on cell death upon Gln starvation, we analyzed human tumor cell lines overexpressing N-Myc (Kelly, from *MYCN*-amplified neuroblastoma) or c-Myc (SF188, from glioma). SHEP cells (from *MYCN* nonamplified neuroblastoma) with low N- or c-Myc levels were used for comparison (Figure 1A). We then subjected these cells to Gln deprivation for 48 hr. As expected, Gln starvation induced significant cell death in Kelly and SF188 cells associated with Myc overexpression (Figures 1B and 1C), whereas SHEP cells exhibited minimal cell death under similar conditions (Figures 1B and 1C). Furthermore, direct N-Myc inhibition by specific small interfering RNAs (siRNAs) in Kelly cells alleviated cell death upon Gln loss (Figures S1A and S1B available online), confirming the essential role of Myc in this process. When tested in cultured cell lines, elevated c-Myc was shown to enhance the transcription of genes involved in glutaminolysis (Wise et al., 2008). However, whether this in vitro observation is representative of what occurs in human tumors remained unknown. To address this issue, we evaluated 80 primary neuroblastomas of diverse risk classes with and without *MYCN* amplification. Of note, *ASCT2*, *LAT1* (or *SLC7A5*, solute carrier family 7, member 5), *LAT2* (or *SLC7A6*, solute carrier family 7, member 6), *GLS2* (glutaminase 2), *GOT2* (glutamate-oxaloacetate transaminase 2), and *SLC1A7* (solute carrier family 1 glutamate transporter, member 7) mRNAs were significantly elevated in *MYCN*-amplified tumors when compared with nonamplified tumors (Figures 1D and S1C; data not shown). In contrast, *GLS* (also known as *GLS1*, glutaminase 1), *GLUD1* (glutamate dehydrogenase), and *SN1* (solute carrier family 38, member 3) expression was largely unchanged or even reduced (Figure S1C; data not shown), suggesting that they are not N-Myc targets. Taken together, these results suggest that ASCT2, LAT1, LAT2, GLS2, GOT2,

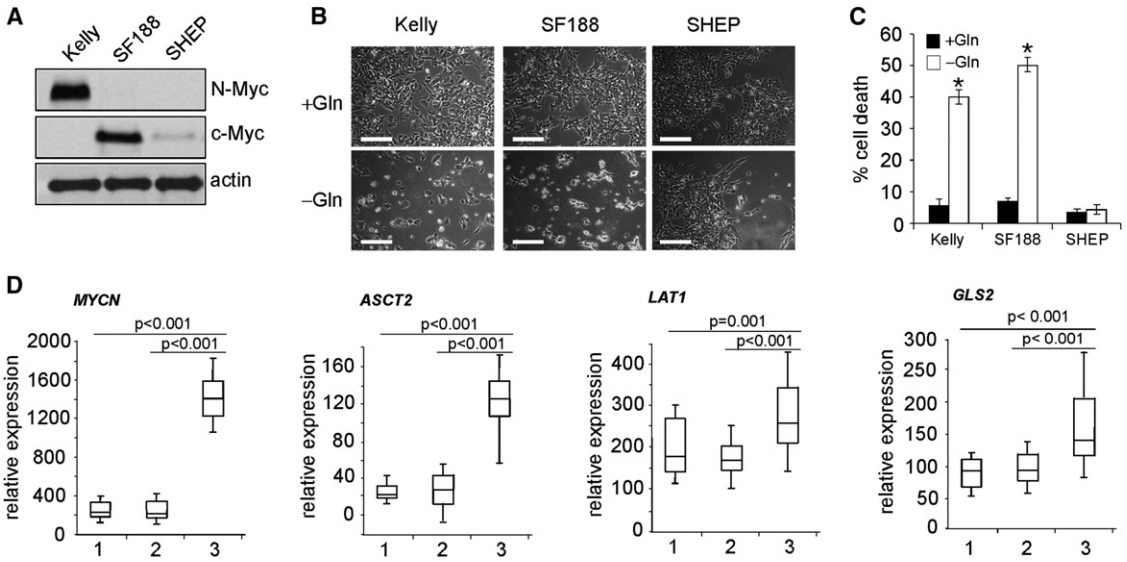

Figure 1. Gln Starvation Triggers Tumor Cell Death in a *MYC*-Dependent Manner

(A) Western blot analysis of Myc (N-Myc and c-Myc) expression in Kelly, SF188, and SHEP cells. β-actin was used as a loading control.

(B) Representative images of Kelly, SF188, and SHEP cells in the presence or absence of Gln for 48 hr. Scale bars represent 50 μm.

(C) Quantification of cell death by PI-Annexin V staining. Data are presented as an average of triplicates. Error bars represent the standard deviation (SD). *$p < 0.001$.

(D) Relative expression of *MYCN*, *ASCT2*, *LAT1*, and *GLS2* in primary neuroblastoma tumors. 1, Low-risk group (28 tumors); 2, *MYCN*-nonamplified, high-risk group (32 tumors); and 3, *MYCN*-amplified, high-risk group (20 tumors); defined according to International Neuroblastoma Risk Group criteria (Maris, 2010). Data are presented as box plots; the box represents the 25th through 75th percentiles (the line through the box denotes the median), and the whiskers above and below extend to the 90th and 10th percentiles, respectively.

See also Figure S1.

and SLC1A7 play a critical role in the regulation of Gln metabolism in *MYCN*-amplified neuroblastomas.

Gln Depletion Induces Tumor Cell Death Depending Largely on Bax and Caspase Activities

Studies using gene-targeted mice revealed that cellular apoptosis is frequently governed by two proapoptotic Bcl-2 family proteins: Bax and Bak (Wei et al., 2001). Bax and Bak exert similar function in most stress-induced apoptotic pathways and can functionally substitute for each other. To determine whether Gln deprivation induces apoptosis via Bax and/or Bak, we first examined Bax and Bak activation in Kelly cells using conformation-specific antibodies. Gln starvation activated both Bax and, to a lesser extent, Bak, as the 6A7 antibody for Bax and Ab1 antibody for Bak efficiently immunoprecipitated these proteins in comparison with nonstarved cells (Figure 2A). Subsequently, Bax and Bak were each depleted by two distinct siRNAs (Figure 2B) and the cells were subjected to Gln starvation. Surprisingly, inhibition of Bax, but not Bak, significantly decreased the death of N-Myc-overexpressing Kelly cells upon Gln deprivation (Figure 2C). This was recapitulated in c-Myc-overexpressing SF188 cells (Figure 2D), suggesting a general mechanism that depends predominantly on Bax for Myc-mediated cell death during Gln limitation. Of note, previous data demonstrated that Bax depletion cooperates with c-Myc during murine lymphomagenesis (Eischen et al., 2001). Because Bax activates downstream caspase-dependent and/or -independent pathways, we treated Kelly cells with escalating doses of z-VAD-fmk (z-VAD), a broad-spectrum caspase inhibitor, and found that 50 μM of z-VAD completely inhibited Caspase 3 activation and Kelly cell death (data not shown). Therefore, a caspase-dependent pathway regulates Myc-mediated cell death during Gln starvation. Consistent with this finding, blocking Bax mitochondrial translocation using the cell membrane-permeable V5 peptide inhibitor (Sawada et al., 2007; Figure 2E) partially rescued Gln deprivation-induced cell death (Figure 2F). Therefore, *MYCN*-amplified neuroblastomas provide an attractive model for studying the molecular mechanisms that underlie the connection between Myc overexpression and Gln addiction.

PUMA, NOXA, and TRB3 Promote Gln Deprivation-Mediated Cell Death

Unlike Bak, Bax can be sequestered in the cytosol by specific interaction with the non-Bcl2 family protein Ku70 in an acetylation-dependent fashion (Figure S2A). Cellular stress causes Ku70 acetylation by CBP and PCAF, leading to subsequent Bax dissociation, Bax activation, and apoptosis (Sawada et al., 2007). We examined whether Gln deprivation affects Ku70 acetylation and Bax association. Kelly cell starvation did not result in detectable changes in either Ku70 acetylation or Ku70-Bax interaction, whereas treatment with the broad deacetylase inhibitor TSA increased Ku70 acetylation and disrupted Ku70-Bax binding (Figure S2B). Therefore, we concluded that Ku70 is not involved in Bax activation upon Gln withdrawal.

We then investigated expression of multiple factors inducing apoptosis upstream of Bax, and observed in Gln-starved Kelly cells a significant increase in *PUMA*, *NOXA*, and *TRB3* (tribbles homolog 3) mRNA (Figure 3A) and protein (Figure 3B). TRB3 is

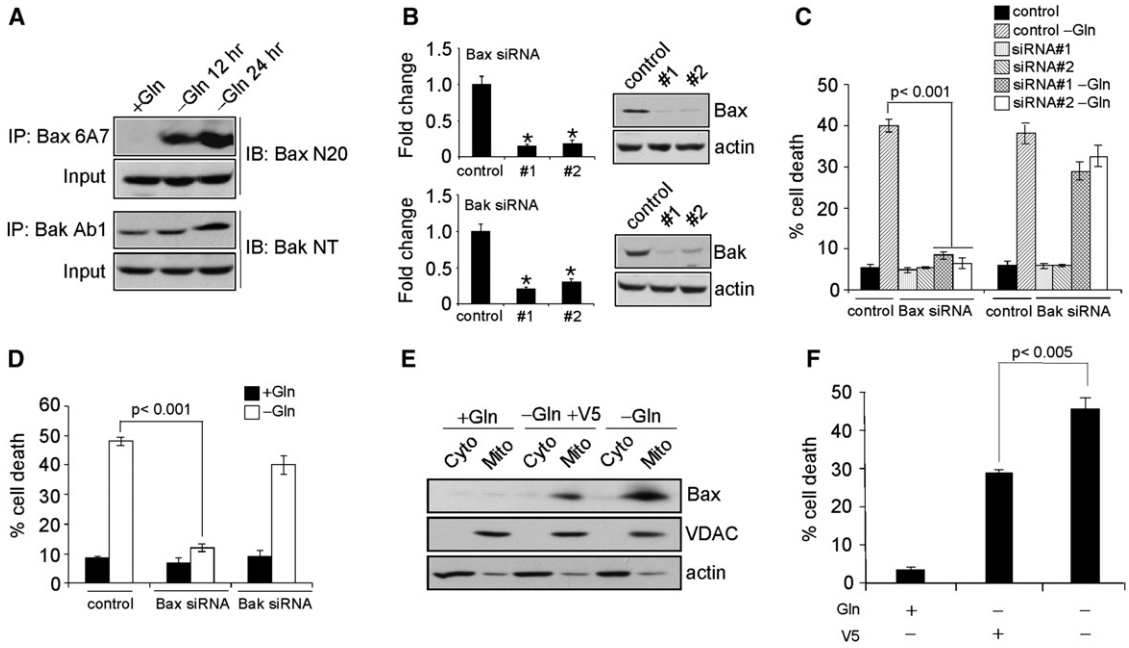

Figure 2. Gln Depletion Triggers Bax-Dependent but Bak-Independent Cell Death

(A) Immunoprecipitation of active Bax and Bak using conformation-specific antibodies in Kelly cells subjected to Gln starvation at indicated time points.

(B) Protein levels of Bax and Bak upon siRNA knockdown in Kelly cells. Bar graphs show the quantification results. *p < 0.001.

(C and D) Viability of Kelly cells (C) and SF188 cells (D) upon indicated siRNA knockdown were examined by PI-Annexin V staining after 48 hr of Gln starvation. Data are shown as an average of triplicates.

(E) Immunoblotting of Bax in the cytosolic (Cyto) and mitochondrial (Mito) fraction of NLF cells treated with V5 peptide in the presence or absence of Gln. VDAC and actin antibodies were used as controls for mitochondrial and cytosolic protein purification.

(F) Gln-starvation-induced cell death with or without V5 peptide treatment was examined by PI-Annexin V staining. Shown are average results from three experiments.

All error bars represent SD.

a mammalian homolog of the *Drosophila* protein tribbles, a pseudo-kinase protein that is frequently induced by endoplasmic reticulum (ER) stress (Ohoka et al., 2005). Of note, TRB3 is activated by the ATF4/CHOP pathway and in turn represses CHOP, possibly via direct CHOP interaction, blocking CHOP coactivator recruitment. Depletion of PUMA alone by specific siRNAs significantly inhibited Myc-mediated Kelly cell death upon Gln deprivation, and a triple depletion of PUMA, NOXA, and TRB3 further reduced apoptosis (Figure 3C). We then extended our study to a number of additional neuroblastoma cell lines. A total of 17 neuroblastoma lines, including nine *MYCN*-amplified and eight *MYCN*-nonamplified lines were subjected to Gln starvation. Of note, six of nine *MYCN*-amplified lines, but only one *MYCN*-nonamplified line exhibited Gln dependence (Figure 3D and data not shown). The single outlier for Gln dependence absent *MYCN* amplification was NBL-S, a cell line with markedly deregulated N-Myc activity through protein stabilization (Liu et al., 2008). We examined N-Myc expression in two *MYCN*-amplified lines (NLF and IMR32) and NBL-S, and corroborated similar levels of deregulated protein (Figure S2C; Qing et al., 2010), underscoring the association between deregulated *MYCN* and Gln dependence. Moreover, significant *PUMA*, *NOXA*, and *TRB3* induction was observed in all three cell lines when Gln was absent (Figure S2D), and a combined inhibition of PUMA, NOXA, and TRB3 reversed IMR32 and NLF cell death upon Gln removal (Figure 3E). Efficient siRNA-mediated depletion of PUMA, NOXA, and TRB3 protein in both Kelly and NLF cells was confirmed by western blot (Figure 3F). Taken together, these results demonstrate that PUMA, NOXA, and TRB3 work in concert to regulate Gln-deprivation-mediated cell death in *MYCN*-amplified neuroblastomas.

PUMA, NOXA, and TRB3 Are Regulated by a p53-Independent, ATF4-Dependent Mechanism

PUMA potently induces apoptosis, and its overexpression is sufficient to cause cell death in numerous cell types because it directly binds and antagonizes many antiapoptotic Bcl2 family members, resulting in mitochondrial dysfunction and Bax activation (Letai et al., 2002). *PUMA* is normally expressed at low levels but is rapidly induced by p53 and other factors (Yu and Zhang, 2008). Because Gln loss in Kelly cells specifically activates *PUMA* and *NOXA* (both well-known p53 targets), we inhibited p53 by siRNA (Figure 4A) in Kelly cells and then subjected the cells to Gln starvation. Interestingly, p53 inhibition had no effect on *PUMA*, *NOXA*, and *TRB3* induction (Figure 4B), whereas the expression of another p53 target, *TIGAR* (p53-induced glycolysis and apoptosis regulator; Bensaad et al., 2006), was significantly inhibited under the same conditions (Figure 4B). In addition to p53, other transcription factors have been implicated in context-dependent *PUMA* and/or *NOXA*

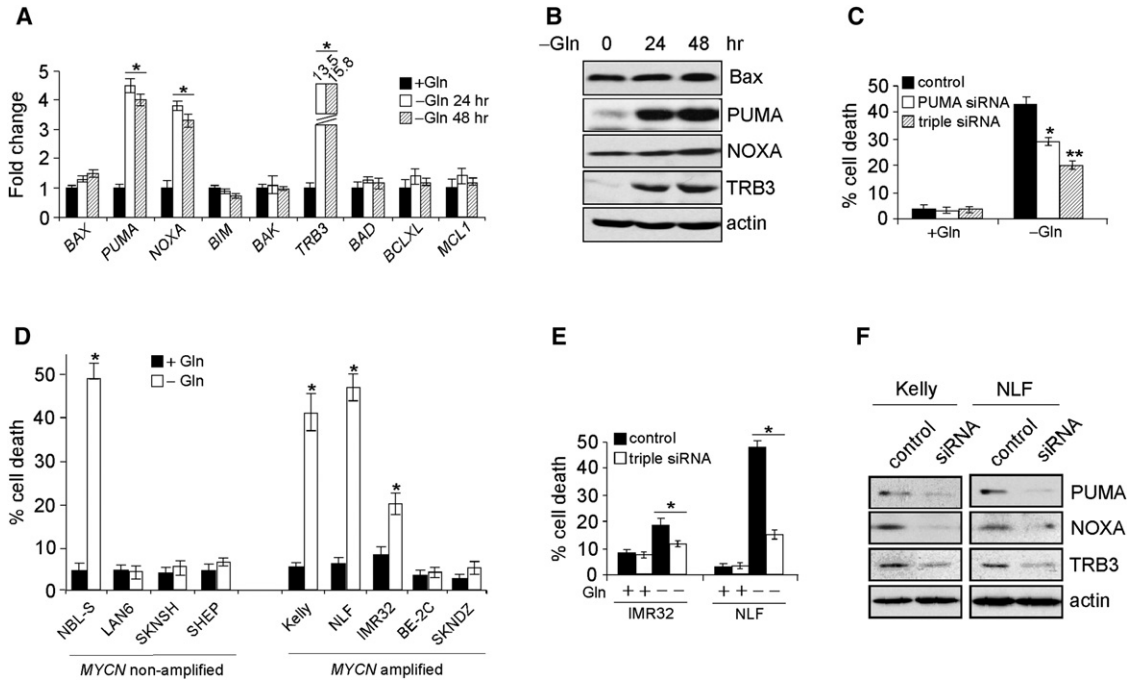

Figure 3. PUMA, NOXA, and TRB3, but Not Ku70, Are Involved in Gln-Deprivation-Mediated Cell Death

(A) RT-PCR analysis of genes involved in apoptosis. Data are shown as an average of triplicates.

(B) Western blot analysis of indicated protein levels in Gln-starved Kelly cells.

(C) The viability of Kelly cells transfected with the indicated siRNAs in the presence or absence of Gln was analyzed by AnnexinV-PI staining. Data are shown as an average of triplicates.

(D) Examination of Gln-starvation-induced cell death in five *MYCN*-amplified and four *MYCN*-nonamplified neuroblastoma cell lines. Cell death was measured by Annexin V-PI staining.

(E) The viability of IMR32 and NLF cells transfected with siRNAs targeting PUMA, NOXA, and TRB3 in the presence or absence of Gln was analyzed by AnnexinV-PI staining. Data are shown as an average of triplicates.

(F) Western blots confirming the effect of siRNA knockdown.

All error bars represent the SD; *$p < 0.01$, **$p < 0.005$. See also Figure S2.

induction, including Myc, FOXO3, SP1, and E2F1. Each factor was inhibited by specific siRNAs without a detectable effect on *PUMA* and *NOXA* activation (data not shown).

To identify *PUMA* regulatory factor(s), we performed bioinformatic analyses, and identified a conserved ATF4-binding site within the *PUMA* promoter region (Figure S3A). ATF4 knockdown (Figure 4C) potently inhibited *PUMA*, *NOXA*, and *TRB3* activation in Gln-starved Kelly, IMR32, and NLF neuroblastoma cells (Figures 4D and S3B). A chromatin immunoprecipitation (ChIP) analysis demonstrated that significant ATF4 pools were recruited to the *PUMA* promoter along with enhanced RNA polymerase II (Pol II) occupancy in Gln-starved Kelly cells (Figure 4E). We created a luciferase reporter construct using a pGL3 plasmid containing the putative ATF4-binding site (in triplicate) 5′ of the SV40 promoter (ATF4-RE/luc; Figure 4F). As a control, we generated an additional construct harboring mutations in the ATF4-binding motif (ATF4-REmut/luc; Figure 4F). Compared with empty pGL3 vector and ATF4-REmut/luc, ATF4-RE luciferase activity was significantly increased by exogenous ATF4 or Gln starvation (Figure 4G). Interestingly, we identified a different ATF4 response element within the *NOXA* promoter (Figure S3C). Both ChIP and luciferase assays confirmed that ATF4 directly activated *NOXA* transcription through binding to this site (Figures S3D–S3F). Furthermore, two distinct ATF4 siRNAs significantly reduced Gln starvation-induced death in Kelly and NLF cells (Figures 4H and 4I), which was further alleviated by combinatorial inhibition of PUMA, NOXA, and TRB3 (Figures 4I and 4J). To control for off-target effects, independent siRNAs for PUMA, NOXA, and TRB3 were used in these assays (compare Figures 4I and 4J with Figures 3C, 3E, and 3F). In contrast, ATF4 depletion in SF188 glioma cells had little effect on Gln-starvation-induced cell death (Figures S3G and S3H), possibly due to a different tumorigenic background. A recent study indicated that ATF4 directly activates *CHOP* expression, which subsequently stimulates *PUMA* and apoptosis (Galehdar et al., 2010). However, CHOP inhibition in Gln-starved Kelly cells failed to affect *PUMA* and *NOXA* activation (Figure S3I) or concomitant cell death (Figure S3J), suggesting that CHOP was not involved in this process. Taken together, these results indicate that ATF4 functions as a transcription factor in directly regulating *PUMA*, *NOXA*, and *TRB3* expression in *MYCN*-transformed cells.

Gln can be converted by two deamination reactions into α-ketoglutarate (α-KG) to replenish a functional TCA cycle (Figure 4K). Because the TCA cycle provides a "hub" for multiple metabolic pathways, loss of cycle intermediates could have

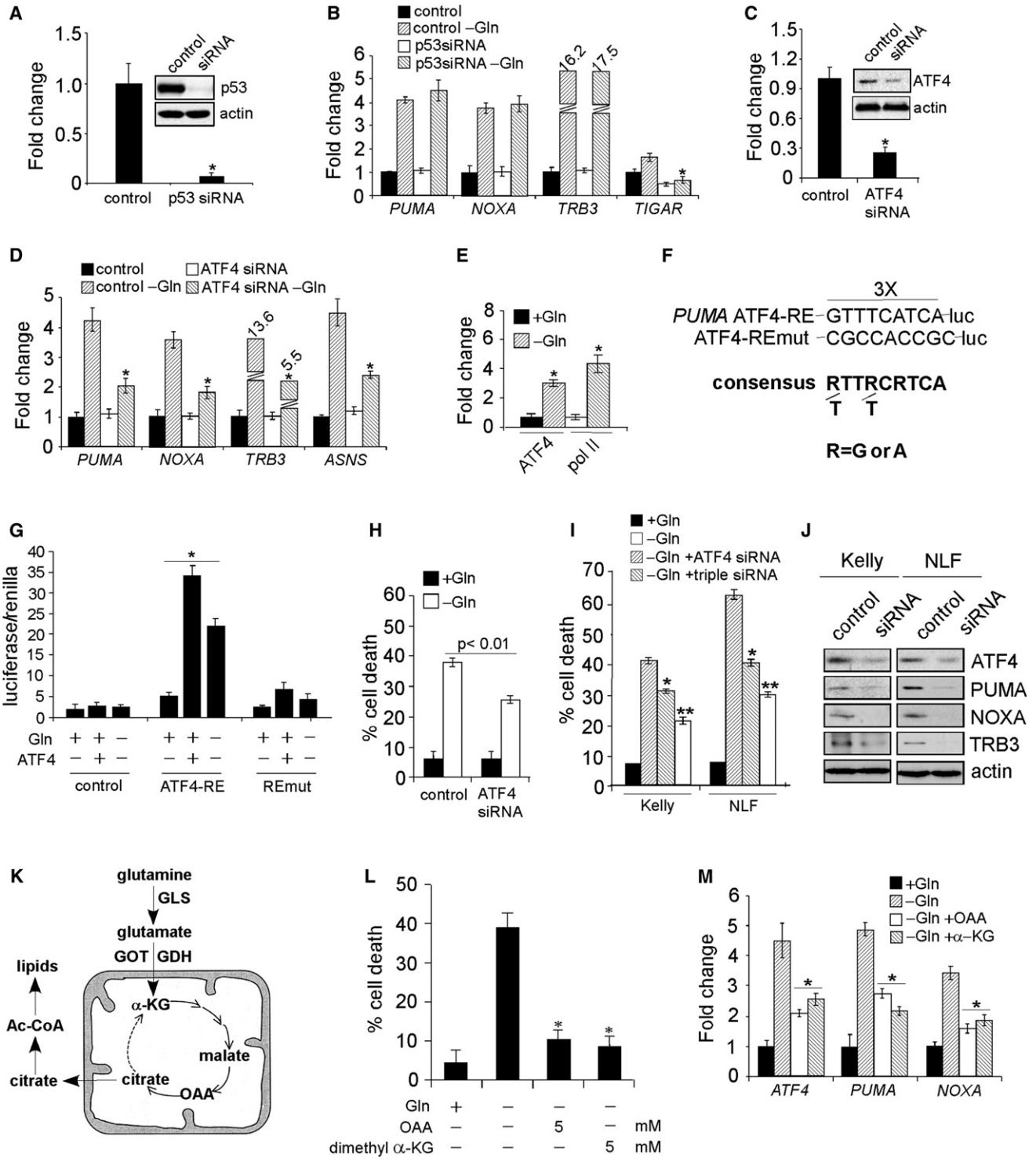

Figure 4. ATF4, but Not p53, Is Responsible for *PUMA*, *NOXA*, and *TRB3* Activation

(A) Protein levels of p53 with or without siRNA knockdown.

(B) The mRNA expression of indicated genes was examined by RT-PCR in Kelly cells transfected with a control siRNA or p53 siRNA in the presence or absence of Gln. Data are shown as an average of triplicates.

(C) Protein levels of ATF4 in Kelly cells with or without siRNA knockdown.

(D) The indicated gene expression was quantitated by RT-PCR in Kelly cells transfected with a control or ATF4 siRNA in the presence or absence of Gln. Data are shown as an average of triplicates.

(E) Specific chromatin binding of ATF4 evaluated by ChIP assay. Recruitment of Pol II was also assessed.

various consequences, including cell death (DeBerardinis et al., 2008). Indeed, oxaloacetate (OAA), a cell-membrane-permeable TCA-cycle intermediate, or dimethyl α-KG, a cell-membrane-permeable α-KG analog, prevented apoptosis of Gln-starved cells (Figure 4L). We reasoned that if ATF4-mediated *PUMA* stimulation is critical for cell death, then OAA or α-KG should decrease *PUMA* and *NOXA* expression when Gln is absent. As expected, supplementation of OAA or α-KG (4 mM) efficiently inhibited *PUMA* and *NOXA* induction (Figure 4M). Of note, inhibition of both *PUMA* and *NOXA* correlated with that of *ATF4* (Figure 4M), raising the possibility that enhanced *ATF4* transcription occurs following Gln withdrawal. Moreover, Kelly cell treatment with actinomycin D, which abrogates *ATF4* transcriptional induction, significantly reduced ATF4 protein levels when Gln was absent (Figure S3K). *ATF4* transcriptional control is largely unknown, except for stress-regulated transcription factor p8, which induces *ATF4* during cannabinoid-mediated apoptosis (Carracedo et al., 2006). Although p8 expression was significantly increased at both the mRNA and protein levels in Gln-starved cells, p8 inhibition had no detectable effect on *ATF4* (Figure S3L). Because *ATF4* is activated by Gln starvation, we investigated whether *ATF4* is regulated by signaling pathways that promote Gln metabolism, such as AMPK-mTOR (Nicklin et al., 2009) and Myc (Gao et al., 2009; Wise et al., 2008; Yuneva et al., 2007). However, siRNA knockdown of AMPKα1 and α2 catalytic subunits or N-Myc had no significant impact on *ATF4* mRNA levels (Figure S3M). Finally, a bioinformatic analysis of *ATF4* regulatory regions identified ten potential transcription factors involved in *ATF4* induction. However, their RNAi-mediated inhibition failed to decrease *ATF4* induction in Gln-starved cells (data not shown), suggesting that other unidentified factor(s) are involved in this process.

ATF4 Translation Depends on the GCN2 Kinase, but Not PERK, in the Absence of Gln

Translation of *ATF4* mRNA is also regulated by stress signals (Kilberg et al., 2009), transduced by multiple eIF2α kinases, including GCN2 (general control nonrepressed-2), PERK (protein kinase-like ER kinase), and PKR (double-strand RNA activated protein kinase). Amino acid deprivation (usually essential ones like leucine and lysine) triggers the amino acid response (AAR) signal transduction pathway via GCN2, while ER disruption and viral infection activate PERK and PKR, respectively. Mechanistically, these kinases promote eIF2α phosphorylation at Ser 51. Phospho-eIF2α then binds eIF2B in a nonfunctional complex that suppresses global protein synthesis, while promoting increased translation of select mRNAs, including *ATF4* (Figure 5A). We first examined eIF2α phosphorylation in Kelly cells at different time points. As expected, Gln starvation gradually elevated eIF2α phosphorylation concomitantly with a dramatic increase in total ATF4 protein (Figure 5B), suggesting that *ATF4* translation is also enhanced in Gln-starved Kelly cells. Of note, this stress response is tightly linked to *MYC* overexpression. Although *ATF4*, *PUMA*, *NOXA*, and *TRB3* transcripts were somewhat increased in three *MYCN*-nonamplified cell lines (SHEP, SKNAS, and EBC1) upon Gln depletion (Figure S4A), their protein levels did not change in all cell lines tested (Figure S4B). Consistent with this result, *MYCN*-nonamplified neuroblastoma cells failed to engage the eIF2α-ATF4 pathway, as shown by similar levels of p-eIF2α in both conditions (Figure S4B).

One highly conserved function of *MYC* family members across species is to activate ribosome biogenesis and mRNA translation, which are essential for cell growth (Dang, 2012). Gln is utilized in O-linked β-N-acetylglucosamine (O-GlcNAc) modification of nascent polypeptides, a posttranslational modification that is critical for transcription factor function (Butkinaree et al., 2010). Theoretically, Gln deprivation results in protein misfolding and ER accumulation, leading to ER stress pathway activation. In addition, oncogenic Myc converts the nonessential amino acid Gln into an essential one, triggering cellular addiction to Gln (Wise et al., 2008; Yuneva et al., 2007) and AAR stress pathway activation. Indeed, the mRNA levels of ER stress-inducing genes *ASNS* (asparagine synthetase), *GRP78* (glucose-regulated protein 78), and *XBP-1* (X-box binding protein 1) were significantly increased in Gln-starved Kelly cells (data not shown). Whereas glucose starvation in mouse embryonic fibroblasts (MEFs) induces *ATF4* translation via both GCN2 and PERK, Gln depletion affects ATF4 levels in a GCN2-dependent but PERK-independent manner (Ye et al., 2010). To confirm this result, we examined wild-type (WT), *Gcn2*$^{-/-}$, and *Perk*$^{-/-}$ MEFs. Indeed, lack of GCN2, but not PERK, abolished *ATF4* translation in response to Gln depletion, as increased ATF4 abundance was selectively lost in *Gcn2*$^{-/-}$ but not *Perk*$^{-/-}$ cells (Figure 5C). In parallel, eIF2α phosphorylation was exclusively abrogated in *Gcn2*$^{-/-}$ fibroblasts (Figure 5C). We then depleted GCN2 and PERK in Kelly cells (Figure 5D), and demonstrated that GCN2 inhibition selectively abrogated eIF2α phosphorylation in association with decreased *ATF4* translation (Figure 5E).

(F) Schematic representation of the consensus ATF4-binding site, the ATF4 response element (ATF4-RE) within the *PUMA* promoter and its mutant (ATF4-REmut).
(G) Luciferase assay was performed using control, ATF4-RE, and ATF4-REmut constructs with or without exogenous ATF4 expression or Gln starvation. Data are shown as an average of triplicates.
(H) Viability of Kelly cells transfected with a control or ATF4 siRNA in the presence or absence of Gln was examined by PI-Annexin V staining. Data are shown as an average of triplicates.
(I) Evaluation of Kelly and NLF cell death upon siRNA knockdown of ATF4 (using independent siRNAs from [C] and [H]), or a combination of PUMA, NOXA, and TRB3 in the absence of Gln.
(J) Western blots confirming the effect of siRNA knockdown in (I).
(K) Diagram depicting Gln metabolism in the TCA cycle. See text for more details.
(L) Evaluation of Gln-starved Kelly cell death upon the addition of OAA or α-KG.
(M) RT-PCR analysis of the indicated genes in Kelly cells cultured in Gln-free or -replete medium, or Gln-free medium supplemented with OAA or α-KG. Data are shown as an average of triplicates.
All error bars represent SD; *$p < 0.01$, **$p < 0.005$. See also Figure S3.

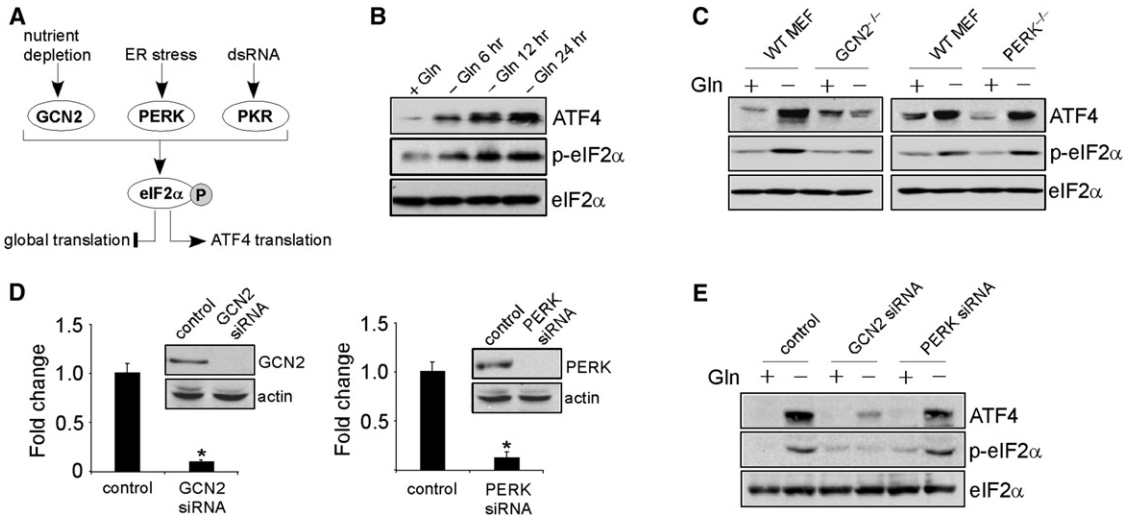

Figure 5. The GCN2-eIF2α Pathway Activates *ATF4* Translation in the Absence of Gln

(A) Diagram depicting pathways involved in selective *ATF4* translation. See text for more details.

(B) Western blot analysis of ATF4 and phosphorylated eIF2α (p-eIF2α) in Kelly cells in the presence or absence of Gln. Total eIF2α was used as a loading control.

(C) Immunoblotting of ATF4 and phosphorylated eIF2α (p-eIF2α) in WT MEFs and GCN2- or PERK-deficient (KO) MEFs with or without Gln starvation.

(D) Protein levels of GCN2 and PERK upon the indicated siRNA knockdown in Kelly cells. Error bars represent the SD; *$p < 0.005$.

(E) Protein levels of ATF4 and phosphorylated eIF2α (p-eIF2α) were detected in Kelly cells transfected with a control or GCN2 or PERK siRNA in the presence or absence of Gln.

See also Figure S4.

Either Pharmacological Intervention of Gln Metabolism or ATF4 Stimulation Induces Cell Death In Vitro and Inhibits Tumorigenesis In Vivo

Because Gln is critical for maintaining TCA-cycle homeostasis and providing precursors for protein, nucleotide, and lipid synthesis, we tested whether pharmacological inhibition of Gln metabolism induces apoptosis. Gln is metabolized to α-KG, a critical TCA-cycle intermediate, through two deamination steps: glutaminase converts Gln to glutamate, and then glutamate dehydrogenase (GDH) or transaminases transfer the amino group to α-keto acids to generate amino acids such as alanine and aspartate (Figure 6A). Both amino oxyacetate (AOA), a chemical inhibitor of glutamate-dependent transaminases (Wise et al., 2008), and epigallocatechin gallate (EGCG), which inhibits GDH (Li et al., 2007), induced cell death in a dose-dependent manner in Kelly cells (Figure 6B). Both AOA and EGCG effectively induced apoptosis at levels comparable to that resulting from Gln depletion. The effect of AOA and EGCG was specific to Gln metabolism, as supplementation of OAA or cell-permeable pyruvate significantly inhibited the toxic effects of both chemical inhibitors (Figure 6B). To highlight the importance of enzymes involved in glutaminolysis in maintaining cell viability, GDH inhibition was also achieved by siRNA knockdown (Figure S5A). Indeed, *GLUD1* (encoding GDH) mRNA degradation (Figure S5A) triggered dramatic cell death independently of Gln status, whereas control cells underwent apoptosis only in the absence of Gln (Figure S5B).

Because Gln starvation resulted in ATF4 accumulation, *PUMA/NOXA/TRB3* induction, and apoptosis, we evaluated the effect of ATF4 agonists. We chose fenretinide (FRT, also known as 4-hydroxyphenyl-retinamide), a chemotherapeutic agent, for the following reasons: (1) preliminary data obtained from clinical trials demonstrated that FRT is well tolerated in humans (Villablanca et al., 2006), and (2) FRT induces a signaling cascade that activates ATF4 and cell death (Corazzari et al., 2007). Indeed, when incubated with FRT, both Kelly and NLF cells exhibited increased eIF2α phosphorylation (Figure S5C), indicating that FRT treatment leads to ER stress in neuroblastoma cells, promoting *ATF4* translation. In addition, FRT administration mimics the effect of Gln withdrawal in a number of other ways, including resistance to Bak inhibition (Figure S5D) and partial rescue by ATF4 knockdown (Figure 6C), reinforcing the idea that FRT functions through the ATF4 pathway to induce cell death in neuroblastoma.

To confirm whether the effects of EGCG and FRT are dependent on N-Myc overexpression, we stably expressed MYCN-ER in SHEP, a *MYCN*-nonamplified cell line with undetectable N-Myc expression (Figure 1A). Induction of MYCN-ER by 4-hydroxytamoxifen in SHEP cells significantly increased the expression of genes involved in Gln metabolism (Figure 6D) and sensitized these cells to Gln deprivation (Figure 6E). More importantly, both EGCG and FRT induced dramatic cell death in N-Myc-overexpressing SHEP cells (SHEP MYCN-ER) while causing minimal cell death in control SHEP cells (Figure 6F), suggesting that both chemicals constitute a synthetic lethal interaction with *MYC* transformation in the context of neuroblastoma.

In addition, administration of either EGCG or FRT to Kelly cells significantly elevated *ATF4*, *PUMA*, and *NOXA* expression (Figure 6G), suggesting that either direct inhibition of Gln metabolism or activation of upstream signaling achieved a phenotype similar to that obtained by Gln starvation. When combined with

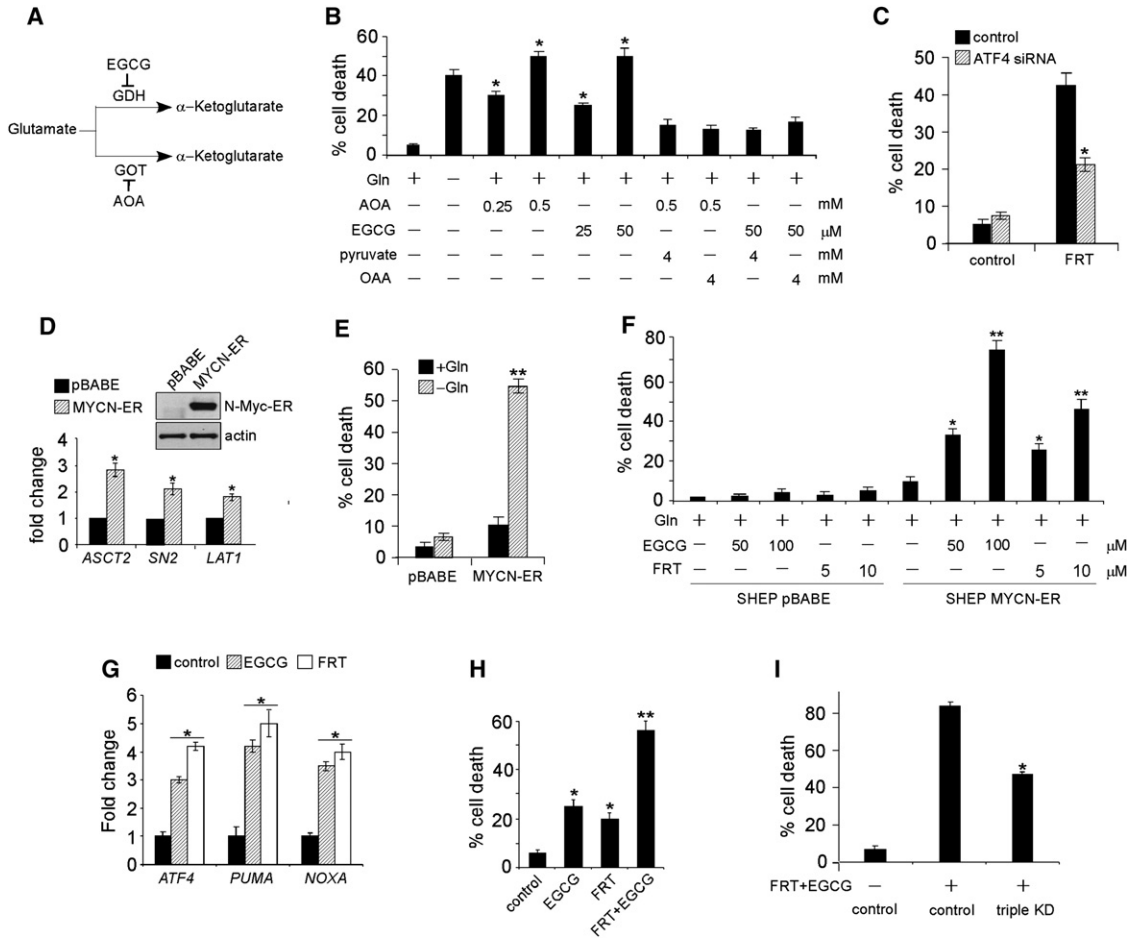

Figure 6. Pharmacological Inhibition of Gln Metabolism or ATF4 Hyperactivation Triggers Dramatic Cell Death In Vitro

(A) Diagram showing enzymes involved in glutamate metabolism. See text for details.

(B) Kelly cell death was examined by PI-Annexin V staining upon EGCG or AOA treatment in the presence of Gln. Where indicated, various metabolites were also supplemented.

(C) Kelly cell death was measured upon fenretinide treatment with or without ATF4 knockdown.

(D) Induction of *MYCN-ER* and its target genes in SHEP cells. Data are shown as an average of triplicates.

(E) SHEP cell death with or without *MYCN-ER* induction was quantified by PI-Annexin V staining in the presence or absence of Gln.

(F) SHEP cells with or without *MYCN-ER* induction were cultured in Gln-replete medium, and their viability was measured upon the indicated drug treatments. Data are shown as an average of triplicates.

(G) RT-PCR analysis of *ATF4*, *PUMA*, and *NOXA* mRNAs in Kelly cells treated without or with EGCG (50 μM) or fenretinide (5 μM). Data are shown as an average of triplicates.

(H) Kelly cell death was quantitated by Annexin V-PI staining upon different drug treatments. Where indicated, 25 μM EGCG and/or 3 μM fenretinide was used, and data are shown as an average of triplicates.

(I) Evaluation of Kelly cell death upon PUMA/NOXA/TRB3 triple knockdown in the presence or absence of fenretinide/EGCG. Experiments were repeated three times.

All error bars represent SD; *$p < 0.01$, **$p < 0.005$. See also Figure S5.

EGCG, FRT treatment resulted in enhanced cell death (Figure 6H), indicating that their combination could achieve antitumor activity without significant toxicity. Interestingly, other glutaminolysis enzymes, especially those upregulated in high-risk neuroblastomas (Figures 1D and S1C), may also become feasible drug targets, given that they underlie neuroblastoma Gln addiction (Figures S5E and S5F). Finally, to highlight the importance of PUMA, NOXA, and TRB3 as the major cell-death mediators upon drug treatment, we constructed a *PUMA/NOXA/TRB3* stable knockdown variant of the NLF cell line. In contrast to control cells, NLF cells with *PUMA*, *NOXA*, and *TRB3* triple inhibition exhibited strong resistance to Gln starvation or FRT/EGCG treatment (Figures 6I, S5G, and S5H).

Together, these in vitro results suggested a functional interplay among Gln metabolism, ATF4 activity, and the Myc-driven oncogenic phenotype of *MYCN*-amplified neuroblastomas that can be pharmacologically targeted by FRT and/or EGCG. However, it remained to be determined whether these signaling events occur in vivo, and whether similar therapeutic approaches can be applied to other tumors. To investigate this

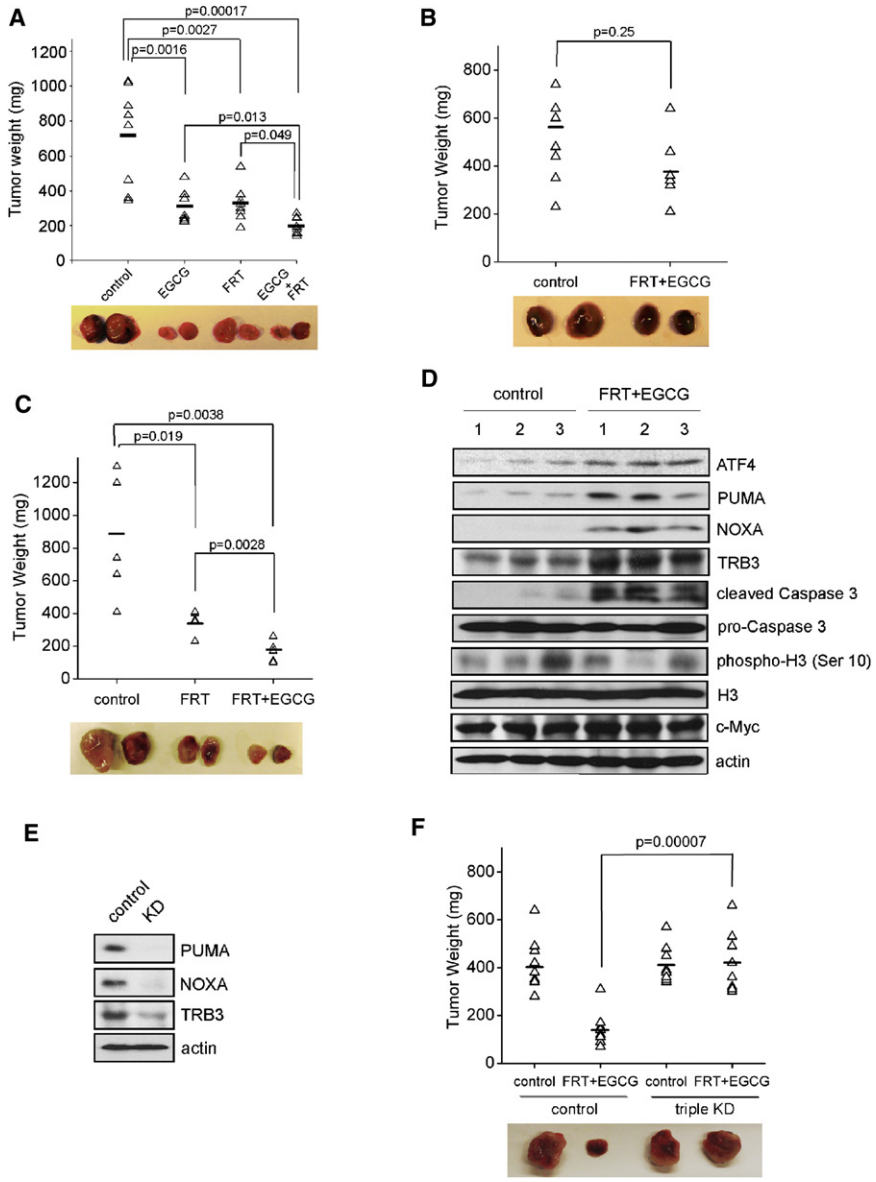

Figure 7. Pharmacological Intervention of Gln Metabolism or ATF4 Stimulation Significantly Inhibits *MYC*-Mediated Xenograft Tumor Growth

(A) A xenograft tumor growth assay was performed using Kelly cells with EGCG and/or fenretinide administration. Representative pictures of subcutaneous tumors under different treatments are shown.

(B and C) SKNAS cells (B) and P493B lymphoma cells overexpressing c-Myc (C) were subjected to the same xenograft experiments as performed in (A).

(D) Western blot analysis of P493B-inititated xenograft tumor lysates for the indicated proteins.

(E) ShRNA viruses targeting PUMA, NOXA, and TRB3 were transduced into P493B cells, and knockdown efficiencies were evaluated by means of western blots.

(F) Xenografts of P493B cells with or without PUMA/NOXA/TRB3 triple knockdown in the presence or absence of fenretinide/EGCG.

The horizontal lines in (A)–(C) and (F) represent the average tumor weights for each group. See also Figure S6.

issue, we established subcutaneous xenografts in nude mice using Kelly cells. Mice with palpable tumors were randomized into four groups, each receiving different drug treatments. Consistent with the in vitro findings, administration of EGCG or FRT significantly suppressed tumor progression, and combined treatment resulted in more marked tumor inhibition (Figure 7A). SKNAS, a *MYCN*-nonamplified neuroblastoma cell line, was found to be highly resistant to FRT and EGCG (Figure 7B). We performed xenograft assays using P493B Burkitt's lymphoma cells, which overexpress c-Myc and are addicted to Gln (Figures S6A and S6B). P493B tumors were also sensitive to FRT and/or EGCG administration to a similar extent as Kelly xenografts (Figure 7C). Importantly, P493B tumors treated with FRT/EGCG exhibited increased expression of ATF4, PUMA, NOXA, and TRB3 (Figure 7D), indicating that the ATF4-PUMA/NOXA/TRB3 pathway was activated by these drugs in xenograft lymphomas. In addition, we generated PUMA/NOXA/TRB3 triple knockdown P493B cells (Figure 7E), and found that P493 cells with PUMA/NOXA/TRB3 depletion exhibited substantial resistance to FRT/EGCG treatments in vivo (Figure 7F), as did PUMA/NOXA/TRB3-depleted NLF cells (Figure S6C). We also probed responses to FRT, AOA, EGCG, or Gln deprivation in A549 lung cancer cells driven by an oncogenic *KRAS* mutation. Interestingly, A549 cells were resistant to all of these conditions (Figure S6D), and no significant increases in ATF4, PUMA, NOXA, or TRB3 protein levels were observed (Figure S6E). Moreover, FRT/EGCG treatment failed to inhibit A549-initiated xenograft tumor growth (Figure S6F), further demonstrating that ATF4-regulated Gln dependence is tightly linked to *MYC* overexpression.

Finally, we tested this approach using the TH-*MYCN* transgenic mouse model, in which spontaneous neuroblastomas arise in autochthonous tumor sites due to enforced *MYCN* expression in neural crest tissues. Homozygous TH-*MYCN* mice were treated with AOA or vehicle control at the time a palpable tumor was documented. As a result, AOA therapy led to inhibition of tumor growth in comparison with control mice (Figure 8A), and tumors treated with AOA exhibited induction of ATF4, PUMA, NOXA, and TRB3 (Figure 8B). The antitumor effects of these drugs (AOA/FRT/EGCG) are not due to decreased tumor cell proliferation [as evaluated by phosphorylated H3 immunoblotting (Figure 7D), Ki-67 staining (Figures 8C and 8D), or *MYC* expression (Figures 7D, 8B, and S7A–S7C)],

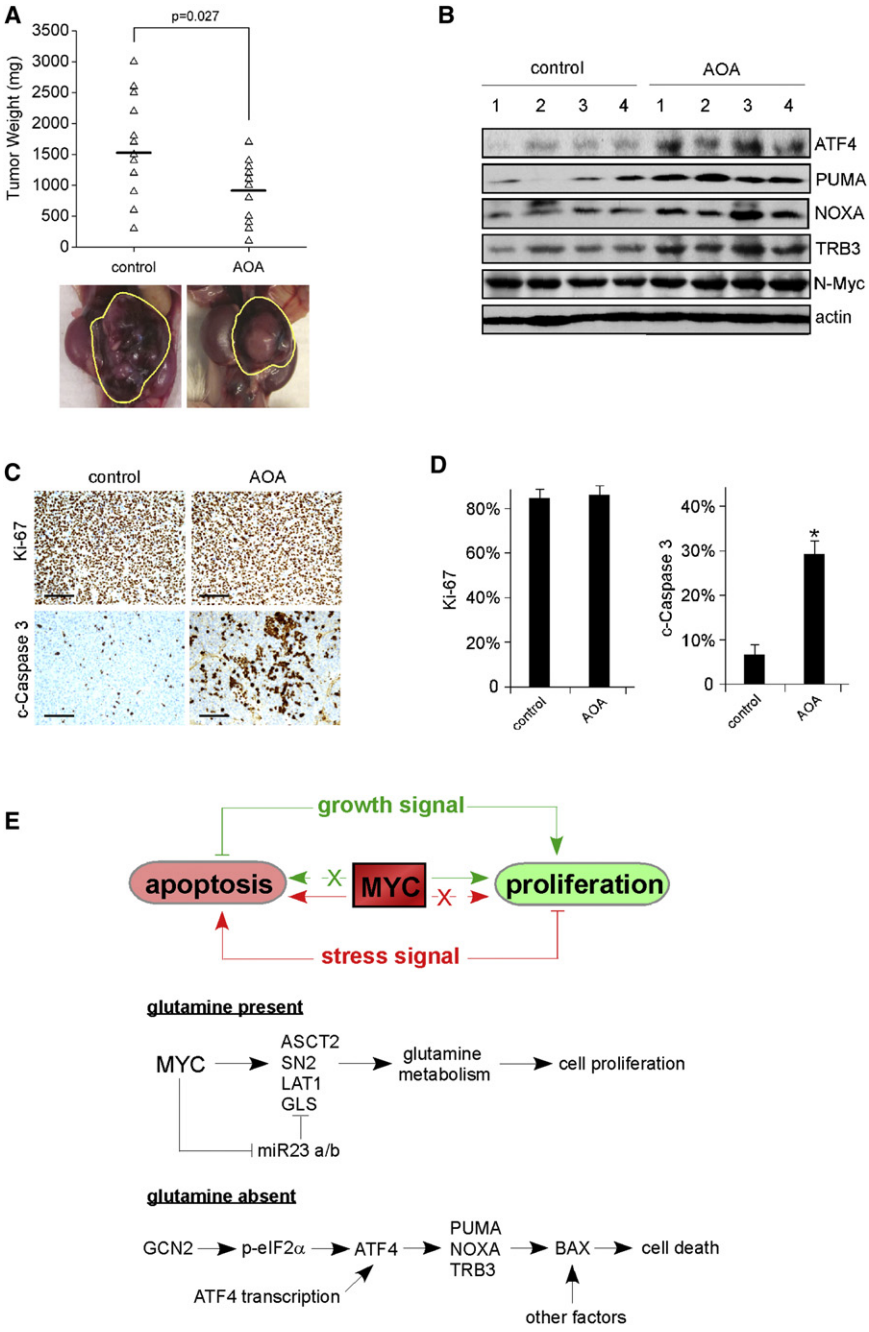

Figure 8. The Transaminase Inhibitor AOA Reduces Autochthonous Neuroblastoma Growth in the TH-*MYCN* Transgenic Mouse Model

(A) Tumor-bearing homozygous TH-*MYCN* mice were i.p. injected daily with PBS or 10 mg/kg AOA as described in Experimental Procedures, and 8 days later the tumors were isolated and weighed. The horizontal lines represent the average tumor weights for each group. The pictures shown are of representative neuroblastomas.

(B) Tumors harvested from homozygous TH-*MYCN* mice as described in (A) were lysed and subjected to western blot analysis using the indicated antibodies.

(C) Ki-67 and c-Caspase 3 staining were performed on paraffin-embedded tumor tissue sections derived from (A). Representative staining micrographs are shown. Scale bars represent 100 μm.

(D) Quantification of the results in (C); n = 8, *p < 0.001. Error bars represent SD.

(E) Model depicting the action of Gln in *MYC*-overexpressing tumors. See text for additional details.

See also Figure S7.

but to significantly increased intratumoral apoptosis as quantified by cleaved Caspase 3 (c-Caspase 3) levels (Figures 7D, 8C, and 8D). All of these results support the clinical potential of glutaminolysis inhibitors as cancer therapeutics against *MYC*-driven tumors.

DISCUSSION

Cancer cells exhibit increased metabolic autonomy in comparison with normal cells, importing and metabolizing nutrients required to support their growth and proliferation (Vander Heiden et al., 2009). The important role played by bioenergetics and cellular metabolism in the process of cancer development is receiving renewed attention. In order to achieve rampant proliferation, tumor cells must duplicate their entire biomass, including nucleic acids, proteins, and lipids, and assemble these components in daughter cells (DeBerardinis et al., 2008). Therefore, in addition to enhanced energy generation, tumors alter their metabolism to generate macromolecules more efficiently. In these processes, Gln plays an important role. Recently, oncogenic *MYC* was shown to reprogram glutaminolysis to support biosynthetic activities through transcriptional and posttranscriptional stimulation of genes involved in Gln metabolism (Gao et al., 2009; Le et al., 2012; Wise et al., 2008). However, precisely how Gln deprivation leads to apoptosis in *MYC*-transformed cells was unknown. Using neuroblastoma as a model system, we were able to identify a pathway that links ATF4 to *PUMA/NOXA/TRB3* activation and cell death upon Gln starvation, and propose the model shown in Figure 8E. Our results are highly consistent with the notion that Myc functions as a double-edged sword in regulating cellular activities, that is, oncogenic Myc promotes proliferation or apoptosis depending on upstream signals and enforced dependencies. In Gln-replete conditions, Myc induces genes (e.g., *ASCT2*, *GLS1*, and *LAT1*) involved in Gln metabolism to support increased biosynthetic activities. It should be noted that Myc also regulates gene networks that activate glucose metabolism, mitochondrial biogenesis, and

ribosome biogenesis (Dang, 2012). In concert, these processes lead to a robust growth phenotype. When Gln is depleted, cells initiate a distinct network that includes ATF4 activation. Mechanistically, two pathways mediate *ATF4* stimulation upon Gln deprivation: increased transcription through a currently unknown mechanism, and enhanced translation via GCN2-eIF2α. ATF4 then activates *PUMA* and other genes (e.g., *NOXA* and *TRB3*) involved in the execution of cell death, sensitizing tumor cells to Myc-mediated apoptosis.

Like Myc, ATF4 also plays a dual role in regulating cellular activities. ATF4's typical role as a protective factor is well documented (Ameri and Harris, 2008). Genome-wide profiling in ATF4 WT and deficient MEFs revealed that ATF4 regulates amino acid metabolism and resistance to oxidative stress (Ameri and Harris, 2008). Indeed, *Atf4*$^{-/-}$ fibroblasts are prone to death in response to stress, including oxidative stress and amino acid deprivation. Nevertheless, numerous reports have also described a prodeath role for ATF4 in neurons (Carracedo et al., 2006; Lange et al., 2008; Ohoka et al., 2005). In contrast to fibroblasts, ATF4 is a proapoptotic factor in neurons both in vitro and in vivo (Lange et al., 2008). A subset of ATF4-regulated genes, including *TRB3* (Ohoka et al., 2005), promote neuronal apoptosis, suggesting that context-dependent ATF4 regulation may account for the divergent phenotypes observed. ATF4 activation also results in tumor cell death under stress conditions (Ameri and Harris, 2008; Carracedo et al., 2006), suggesting that ATF4 agonists constitute a potential therapeutic strategy for inhibiting tumor growth. The different metabolic demands of *MYCN*-amplified and -nonamplified neuroblastomas may explain the distinct roles for ATF4 in divergent cell types. Given that ATF4 plays opposing roles (prosurvival versus prodeath) in different tumors, one must use caution when considering ATF4 agonists or antagonists as potential therapeutics for cancer treatment.

MYC deregulation occurs frequently in human cancers and has been estimated to contribute to at least 40% of all human cancers (Dang, 2012). In multiple models, *MYC* has been shown to be continuously required for tumor maintenance (Shachaf et al., 2004; Soucek et al., 2008), suggesting that direct targeting of Myc is an effective therapeutic strategy. However, attempts to chemically disrupt its function have met with limited success, possibly due to the inherent difficulty of inhibiting transcription factors with small molecules. Here, we demonstrate and validate an alternative, pharmacologic approach that exploits the enforced Gln addiction present in Myc-overexpressing tumor cells. Previous treatments that involved inducing Gln deficiency or interfering with its metabolism (e.g., administration of 6-diazo-5-oxo-l-norleucine [DON] and acivicin) showed great promise in animal models (Ahluwalia et al., 1990) but were unacceptably toxic in humans and eventually abandoned. In screens for compounds that suppress Rho GTPase activation by oncogenic Dbl (for diffuse B cell lymphoma), recent work identified a tetrahydrobenzo derivative (compound No. 968) that blocks Rho GTPase-mediated transformation and tumor growth via mitochondrial glutaminase inhibition (Wang et al., 2010). Consistent with this finding, administration of BPTES, another glutaminase inhibitor, significantly decreased xenograft tumor growth initiated by c-Myc-transformed lymphoma cells (Le et al., 2012). Nevertheless, the efficacy and toxicity of both compound 968 and BPTES for treating human patients remain largely unknown. Here we show that the combination of FRT (4-hydroxyphenyl-retinamide) and EGCG is effective for killing neuroblastoma and lymphoma cells when administered both in vitro and in vivo. Both drugs are well tolerated in humans (Khan and Mukhtar, 2008; Villablanca et al., 2006) and may have clinical utility for human cancers overexpressing the *MYC* oncogene. Although FRT alone may not elicit robust antitumor responses, it could be combined with EGCG as a strategy to move forward in patient care. Moreover, the development of drugs targeting Gln metabolism in neuroblastoma should occur with some urgency, as patients with *MYCN* amplifications are likely to respond.

EXPERIMENTAL PROCEDURES

Cell Culture

Cells were maintained in Dulbecco's modified Eagle's medium (DMEM) supplemented with 10% fetal bovine serum (FBS), 2 mM Gln, and 1× penicillin and streptomycin. To deplete Gln, cells were cultured in Gln-free DMEM supplemented with 10% dialyzed FBS. When indicated, Gln was added back at a final concentration of 2 mM.

siRNA Knockdown and RNA and Protein Analysis

All assays were performed as described in Qing et al. (2010). Details regarding the applied siRNAs, primers, and antibodies are provided in Supplemental Experimental Procedures.

Cell Death Assay

Cells were harvested by combining floating cells in the medium and adherent cells detached by 0.25% trypsin, and cell pellets were washed once with cold PBS. Apoptosis was analyzed using the Annexin V-FITC Apoptosis Kit (BioVision), and data are presented as an average of triplicates.

Luciferase Reporter Assay

Empty pGL3 luciferase vector (0.5 μg) or pGL3 expressing ATF4-RE (or indicated mutants) was transiently cotransfected in triplicate into HEK293T cells using Fugene 6 (Roche Molecular Biochemicals) with 0.1 μg Renilla luciferase reporter. When indicated, 0.5 μg pCMV-ATF4 plasmid was included. Luciferase activities were measured 16–20 hr later with a Dual Luciferase Kit (Promega). Firefly luciferase activities were normalized to Renilla luciferase control values and shown as an average of triplicates.

Human Subjects

Primary human neuroblastoma samples were collected and handled at the Children's Hospital of Philadelphia with the approval of its institutional review board committees. Related procedures were performed in accordance with ethical and legal standards regarding human subjects, and informed consent was obtained.

Animal Studies

All animal experiments were approved by the Animal Care and Use Committee at the University of Pennsylvania. For xenograft experiments, female BALB/C nude mice (Charles River) were injected subcutaneously in both flanks with three million Kelly, NLF, SKNAS, A549, or P493B cells diluted in 100 μl DMEM mixed with an equal volume of matrigel (BD Bioscience). Once palpable tumors were established, mice were randomly divided into several groups receiving different treatments. Fenretinide (1.5 mg/kg) was intravenously injected every 3 days, and EGCG (50 mg/kg) was intraperitoneally (i.p.) injected daily. Tumor weight was measured at the time of sacrifice. For experiments using the transgenic mouse model, 30 homozygous TH-*MYCN* mice bearing palpable intra-abdominal tumors (ultrasound verified) were randomly divided into two groups and i.p. injected daily with PBS or 10 mg/kg AOA, respectively. Eight days later, the mice were sacrificed and tumors were isolated and weighed. To prepare tumor lysates for western blot analysis, the tumors were snap-frozen in liquid nitrogen, ground with a mortar, and then lysed.

To prepare tumor tissue sections for Ki-67 and c-Caspase 3 staining, fresh tumors were fixed in 10% formalin or 4% formaldehyde, and then dehydrated with a series of ethanol solutions (75%, 95%, and 100%). Immunohistochemical analyses of Ki-67 and c-Caspase 3 were performed by the Pathology Core of the Children's Hospital of Philadelphia. ImageJ software was used to quantify the staining results.

SUPPLEMENTAL INFORMATION

Supplemental Information includes seven figures and Supplemental Experimental Procedures and can be found with this article online at http://dx.doi.org/10.1016/j.ccr.2012.09.021.

ACKNOWLEDGMENTS

We thank Dr. Chi Dang for providing the P493B lymphoma cells overexpressing c-Myc, and members of the Simon laboratory for helpful discussions. This work was supported by the Howard Hughes Medical Institute, the National Institutes of Health (Grants CA104838 to M.C.S., CA097323 to J.M.M., CA97323 to M.D.H., CA104838 and CA105463 to C.B.T., and NIH F32 Training Grant 1F32CA137988 to G.L.Q.), and the National Natural Science Foundation of China (Grant 81171928 to G.L.Q.). M.C.S. is an Investigator of the Howard Hughes Medical Institute. C.B.T. is a founder of and consultant for Agios Pharmaceuticals. C.B.T. also serves on the Board of Directors of Merck.

Received: August 15, 2011
Revised: May 11, 2012
Accepted: September 17, 2012
Published: November 12, 2012

REFERENCES

Ahluwalia, G.S., Grem, J.L., Hao, Z., and Cooney, D.A. (1990). Metabolism and action of amino acid analog anti-cancer agents. Pharmacol. Ther. *46*, 243–271.

Ameri, K., and Harris, A.L. (2008). Activating transcription factor 4. Int. J. Biochem. Cell Biol. *40*, 14–21.

Bensaad, K., Tsuruta, A., Selak, M.A., Vidal, M.N., Nakano, K., Bartrons, R., Gottlieb, E., and Vousden, K.H. (2006). TIGAR, a p53-inducible regulator of glycolysis and apoptosis. Cell *126*, 107–120.

Butkinaree, C., Park, K., and Hart, G.W. (2010). O-linked beta-N-acetylglucosamine (O-GlcNAc): Extensive crosstalk with phosphorylation to regulate signaling and transcription in response to nutrients and stress. Biochim. Biophys. Acta *1800*, 96–106.

Capasso, M., Devoto, M., Hou, C., Asgharzadeh, S., Glessner, J.T., Attiyeh, E.F., Mosse, Y.P., Kim, C., Diskin, S.J., Cole, K.A., et al. (2009). Common variations in BARD1 influence susceptibility to high-risk neuroblastoma. Nat. Genet. *41*, 718–723.

Carracedo, A., Lorente, M., Egia, A., Blázquez, C., García, S., Giroux, V., Malicet, C., Villuendas, R., Gironella, M., González-Feria, L., et al. (2006). The stress-regulated protein p8 mediates cannabinoid-induced apoptosis of tumor cells. Cancer Cell *9*, 301–312.

Corazzari, M., Lovat, P.E., Armstrong, J.L., Fimia, G.M., Hill, D.S., Birch-Machin, M., Redfern, C.P., and Piacentini, M. (2007). Targeting homeostatic mechanisms of endoplasmic reticulum stress to increase susceptibility of cancer cells to fenretinide-induced apoptosis: the role of stress proteins ERdj5 and ERp57. Br. J. Cancer *96*, 1062–1071.

Dang, C.V. (2012). MYC on the path to cancer. Cell *149*, 22–35.

DeBerardinis, R.J., Lum, J.J., Hatzivassiliou, G., and Thompson, C.B. (2008). The biology of cancer: metabolic reprogramming fuels cell growth and proliferation. Cell Metab. *7*, 11–20.

Ebos, J.M., Lee, C.R., Cruz-Munoz, W., Bjarnason, G.A., Christensen, J.G., and Kerbel, R.S. (2009). Accelerated metastasis after short-term treatment with a potent inhibitor of tumor angiogenesis. Cancer Cell *15*, 232–239.

Eischen, C.M., Roussel, M.F., Korsmeyer, S.J., and Cleveland, J.L. (2001). Bax loss impairs Myc-induced apoptosis and circumvents the selection of p53 mutations during Myc-mediated lymphomagenesis. Mol. Cell. Biol. *21*, 7653–7662.

Galehdar, Z., Swan, P., Fuerth, B., Callaghan, S.M., Park, D.S., and Cregan, S.P. (2010). Neuronal apoptosis induced by endoplasmic reticulum stress is regulated by ATF4-CHOP-mediated induction of the Bcl-2 homology 3-only member PUMA. J. Neurosci. *30*, 16938–16948.

Gao, P., Tchernyshyov, I., Chang, T.C., Lee, Y.S., Kita, K., Ochi, T., Zeller, K.I., De Marzo, A.M., Van Eyk, J.E., Mendell, J.T., and Dang, C.V. (2009). c-Myc suppression of miR-23a/b enhances mitochondrial glutaminase expression and glutamine metabolism. Nature *458*, 762–765.

Khan, N., and Mukhtar, H. (2008). Multitargeted therapy of cancer by green tea polyphenols. Cancer Lett. *269*, 269–280.

Kilberg, M.S., Shan, J., and Su, N. (2009). ATF4-dependent transcription mediates signaling of amino acid limitation. Trends Endocrinol. Metab. *20*, 436–443.

Lange, P.S., Chavez, J.C., Pinto, J.T., Coppola, G., Sun, C.W., Townes, T.M., Geschwind, D.H., and Ratan, R.R. (2008). ATF4 is an oxidative stress-inducible, prodeath transcription factor in neurons in vitro and in vivo. J. Exp. Med. *205*, 1227–1242.

Le, A., Lane, A.N., Hamaker, M., Bose, S., Gouw, A., Barbi, J., Tsukamoto, T., Rojas, C.J., Slusher, B.S., Zhang, H., et al. (2012). Glucose-independent glutamine metabolism via TCA cycling for proliferation and survival in B cells. Cell Metab. *15*, 110–121.

Letai, A., Bassik, M.C., Walensky, L.D., Sorcinelli, M.D., Weiler, S., and Korsmeyer, S.J. (2002). Distinct BH3 domains either sensitize or activate mitochondrial apoptosis, serving as prototype cancer therapeutics. Cancer Cell *2*, 183–192.

Li, M., Allen, A., and Smith, T.J. (2007). High throughput screening reveals several new classes of glutamate dehydrogenase inhibitors. Biochemistry *46*, 15089–15102.

Liu, X., Mazanek, P., Dam, V., Wang, Q., Zhao, H., Guo, R., Jagannathan, J., Cnaan, A., Maris, J.M., and Hogarty, M.D. (2008). Deregulated Wnt/beta-catenin program in high-risk neuroblastomas without MYCN amplification. Oncogene *27*, 1478–1488.

Maris, J.M. (2010). Recent advances in neuroblastoma. N. Engl. J. Med. *362*, 2202–2211.

Metallo, C.M., Gameiro, P.A., Bell, E.L., Mattaini, K.R., Yang, J., Hiller, K., Jewell, C.M., Johnson, Z.R., Irvine, D.J., Guarente, L., et al. (2012). Reductive glutamine metabolism by IDH1 mediates lipogenesis under hypoxia. Nature *481*, 380–384.

Mossé, Y.P., Laudenslager, M., Longo, L., Cole, K.A., Wood, A., Attiyeh, E.F., Laquaglia, M.J., Sennett, R., Lynch, J.E., Perri, P., et al. (2008). Identification of ALK as a major familial neuroblastoma predisposition gene. Nature *455*, 930–935.

Mullen, A.R., Wheaton, W.W., Jin, E.S., Chen, P.H., Sullivan, L.B., Cheng, T., Yang, Y., Linehan, W.M., Chandel, N.S., and DeBerardinis, R.J. (2012). Reductive carboxylation supports growth in tumour cells with defective mitochondria. Nature *481*, 385–388.

Nicklin, P., Bergman, P., Zhang, B., Triantafellow, E., Wang, H., Nyfeler, B., Yang, H., Hild, M., Kung, C., Wilson, C., et al. (2009). Bidirectional transport of amino acids regulates mTOR and autophagy. Cell *136*, 521–534.

Ohoka, N., Yoshii, S., Hattori, T., Onozaki, K., and Hayashi, H. (2005). TRB3, a novel ER stress-inducible gene, is induced via ATF4-CHOP pathway and is involved in cell death. EMBO J. *24*, 1243–1255.

Pàez-Ribes, M., Allen, E., Hudock, J., Takeda, T., Okuyama, H., Viñals, F., Inoue, M., Bergers, G., Hanahan, D., and Casanovas, O. (2009). Antiangiogenic therapy elicits malignant progression of tumors to increased local invasion and distant metastasis. Cancer Cell *15*, 220–231.

Porro, A., Haber, M., Diolaiti, D., Iraci, N., Henderson, M., Gherardi, S., Valli, E., Munoz, M.A., Xue, C., Flemming, C., et al. (2010). Direct and coordinate regulation of ATP-binding cassette transporter genes by Myc factors generates specific transcription signatures that significantly affect the chemoresistance phenotype of cancer cells. J. Biol. Chem. *285*, 19532–19543.

Qing, G., Skuli, N., Mayes, P.A., Pawel, B., Martinez, D., Maris, J.M., and Simon, M.C. (2010). Combinatorial regulation of neuroblastoma tumor

progression by N-Myc and hypoxia inducible factor HIF-1alpha. Cancer Res. *70*, 10351–10361.

Sawada, M., Sun, W., Hayes, P., Leskov, K., Boothman, D.A., and Matsuyama, S. (2007). Retraction. Nat. Cell Biol. *9*, 480.

Shachaf, C.M., Kopelman, A.M., Arvanitis, C., Karlsson, A., Beer, S., Mandl, S., Bachmann, M.H., Borowsky, A.D., Ruebner, B., Cardiff, R.D., et al. (2004). MYC inactivation uncovers pluripotent differentiation and tumour dormancy in hepatocellular cancer. Nature *431*, 1112–1117.

Soucek, L., Whitfield, J., Martins, C.P., Finch, A.J., Murphy, D.J., Sodir, N.M., Karnezis, A.N., Swigart, L.B., Nasi, S., and Evan, G.I. (2008). Modelling Myc inhibition as a cancer therapy. Nature *455*, 679–683.

Teitz, T., Wei, T., Valentine, M.B., Vanin, E.F., Grenet, J., Valentine, V.A., Behm, F.G., Look, A.T., Lahti, J.M., and Kidd, V.J. (2000). Caspase 8 is deleted or silenced preferentially in childhood neuroblastomas with amplification of MYCN. Nat. Med. *6*, 529–535.

Vander Heiden, M.G., Cantley, L.C., and Thompson, C.B. (2009). Understanding the Warburg effect: the metabolic requirements of cell proliferation. Science *324*, 1029–1033.

Villablanca, J.G., Krailo, M.D., Ames, M.M., Reid, J.M., Reaman, G.H., and Reynolds, C.P. (2006). Phase I trial of oral fenretinide in children with high-risk solid tumors: a report from the Children's Oncology Group (CCG 09709). J. Clin. Oncol. *24*, 3423–3430.

Wang, J.B., Erickson, J.W., Fuji, R., Ramachandran, S., Gao, P., Dinavahi, R., Wilson, K.F., Ambrosio, A.L., Dias, S.M., Dang, C.V., and Cerione, R.A. (2010). Targeting mitochondrial glutaminase activity inhibits oncogenic transformation. Cancer Cell *18*, 207–219.

Wang, K., Diskin, S.J., Zhang, H., Attiyeh, E.F., Winter, C., Hou, C., Schnepp, R.W., Diamond, M., Bosse, K., Mayes, P.A., et al. (2011). Integrative genomics identifies LMO1 as a neuroblastoma oncogene. Nature *469*, 216–220.

Wei, M.C., Zong, W.X., Cheng, E.H., Lindsten, T., Panoutsakopoulou, V., Ross, A.J., Roth, K.A., MacGregor, G.R., Thompson, C.B., and Korsmeyer, S.J. (2001). Proapoptotic BAX and BAK: a requisite gateway to mitochondrial dysfunction and death. Science *292*, 727–730.

Wise, D.R., DeBerardinis, R.J., Mancuso, A., Sayed, N., Zhang, X.Y., Pfeiffer, H.K., Nissim, I., Daikhin, E., Yudkoff, M., McMahon, S.B., and Thompson, C.B. (2008). Myc regulates a transcriptional program that stimulates mitochondrial glutaminolysis and leads to glutamine addiction. Proc. Natl. Acad. Sci. USA *105*, 18782–18787.

Wise, D.R., Ward, P.S., Shay, J.E., Cross, J.R., Gruber, J.J., Sachdeva, U.M., Platt, J.M., DeMatteo, R.G., Simon, M.C., and Thompson, C.B. (2011). Hypoxia promotes isocitrate dehydrogenase-dependent carboxylation of α-ketoglutarate to citrate to support cell growth and viability. Proc. Natl. Acad. Sci. USA *108*, 19611–19616.

Ye, J., Kumanova, M., Hart, L.S., Sloane, K., Zhang, H., De Panis, D.N., Bobrovnikova-Marjon, E., Diehl, J.A., Ron, D., and Koumenis, C. (2010). The GCN2-ATF4 pathway is critical for tumour cell survival and proliferation in response to nutrient deprivation. EMBO J. *29*, 2082–2096.

Yu, J., and Zhang, L. (2008). PUMA, a potent killer with or without p53. Oncogene *27*(*Suppl 1*), S71–S83.

Yuneva, M., Zamboni, N., Oefner, P., Sachidanandam, R., and Lazebnik, Y. (2007). Deficiency in glutamine but not glucose induces MYC-dependent apoptosis in human cells. J. Cell Biol. *178*, 93–105.

Cancer Cell
Article

Differential Remodeling of Actin Cytoskeleton Architecture by Profilin Isoforms Leads to Distinct Effects on Cell Migration and Invasion

Ghassan Mouneimne,[1] Scott D. Hansen,[3] Laura M. Selfors,[1] Lara Petrak,[1] Michele M. Hickey,[1] Lisa L. Gallegos,[1] Kaylene J. Simpson,[4,5] James Lim,[1] Frank B. Gertler,[6] John H. Hartwig,[2] R. Dyche Mullins,[3] and Joan S. Brugge[1,*]
[1]Department of Cell Biology
[2]Division of Translational Medicine at Brigham and Women's Hospital
Harvard Medical School, Boston, MA 02115, USA
[3]Department of Cellular and Molecular Pharmacology, University of California, San Francisco, CA 94158, USA
[4]Victorian Centre for Functional Genomics, Peter MacCallum Cancer Centre, East Melbourne 3002, Australia
[5]Sir Peter MacCallum Department of Oncology, University of Melbourne, Parkville 3050, Australia
[6]The Koch Institute for integrative Cancer Research at MIT, Massachusetts Institute of Technology, Cambridge, MA 02139, USA
*Correspondence: joan_brugge@hms.harvard.edu
http://dx.doi.org/10.1016/j.ccr.2012.09.027

SUMMARY

Dynamic actin cytoskeletal reorganization is integral to cell motility. Profilins are well-characterized regulators of actin polymerization; however, functional differences among coexpressed profilin isoforms are not well defined. Here, we demonstrate that profilin-1 and profilin-2 differentially regulate membrane protrusion, motility, and invasion; these processes are promoted by profilin-1 and suppressed by profilin-2. Compared to profilin-1, profilin-2 preferentially drives actin polymerization by the Ena/VASP protein, EVL. Profilin-2 and EVL suppress protrusive activity and cell motility by an actomyosin contractility-dependent mechanism. Importantly, EVL or profilin-2 downregulation enhances invasion in vitro and in vivo. In human breast cancer, lower EVL expression correlates with high invasiveness and poor patient outcome. We propose that profilin-2/EVL-mediated actin polymerization enhances actin bundling and suppresses breast cancer cell invasion.

INTRODUCTION

Cell motility requires precisely orchestrated regulation of multiple cellular processes that involve dynamic actin cytoskeletal reorganization. Reorganization of the actin cytoskeleton is controlled by actin-binding proteins that regulate nucleation, branching, elongation, bundling, severing, and capping of actin filaments (DesMarais et al., 2005; Insall and Machesky, 2009; Pollard and Borisy, 2003). In particular, profilins are key actin polymerization regulators that promote the conversion of ADP-actin to ATP-actin and interact with poly-L-proline domains (PPP[A/P]PPLP; abbreviated as "PLP") found in a variety of actin nucleation promotion factors, actin nucleators, and actin filament barbed end elongation factors. These include WASp/WAVE/SCAR, formins, and Ena/VASP proteins (Mena, VASP, and EVL) (Ferron et al., 2007; Gertler et al., 1996; Jockusch et al., 2007; Lambrechts et al., 2000; Mahoney et al., 1997; Reinhard et al., 1995). Orchestrated regulation of these actin polymerization factors leads to distinct changes in the actin cytoskeleton architecture. These cytoskeletal changes regulate cellular processes that impact cell motility, and can also promote or suppress invasive migration. Four profilin isoforms have been identified; while profilin-1 is ubiquitously expressed, other isoforms show more selective expression in specific

Significance

The actin cytoskeletal architecture impacts many cellular processes associated with cancer invasion. We show that changing the relative levels of two profilin paralogs alters actin cytoskeletal architecture and influences normal and cancer cell behavior. Our studies revealed functional divergence between profilin-1, which promotes membrane protrusion, motility, and invasion, and profilin-2, which suppresses these processes. These contrasting phenotypic effects involve distinct actin cytoskeletal remodeling by the two profilins. Profilin-2 exerts these previously unrecognized suppressive effects through selective interaction with the actin polymerization regulator, EVL, which promotes profilin-2-mediated actin cytoskeletal remodeling and suppresses migratory and invasive behaviors. Importantly, analyses of breast tumors revealed that lower EVL expression corresponds to high invasiveness and poor prognosis, making EVL a potential biomarker for patient outcome.

tissues. It is currently unclear whether profilin-2/3/4 isoforms have evolved to carry out distinct functional activities with respect to actin polymerization or to protect against loss of one isoform by genetic or epigenetic alterations.

Previously, in a siRNA high-throughput cell migration screen, we found that suppression of *PFN1,* the ubiquitously expressed profilin isoform, inhibited cell migration in MCF10A mammary epithelial cells whereas *PFN2* downregulation enhanced migration in these cells (Simpson et al., 2008). Although profilin-2 has been considered a neuronal-specific isoform (Honoré et al., 1993; Witke et al., 1998), it is expressed in many other tissues, including breast epithelium (EST Profile Viewer at http://www.ncbi.nlm.nih.gov/UniGene/ESTProfileViewer.cgi?uglist=Hs.91747). Despite structural similarities in their PLP binding sites (Kursula et al., 2008; Lambrechts et al., 1997; Witke, 2004), profilin-1 and profilin-2 show variation in surface charge distribution at these sites (Nodelman et al., 1999). Differences in ligand binding preferences have been reported using in vitro binding assays or mass spectrometry analysis of profilin-1 and profilin-2 binding proteins (Lambrechts et al., 2000; Miki et al., 1998; Nodelman et al., 1999; Veniere et al., 2009; Witke et al., 1998); however, the extent to which these binding differences affect actin-based cellular processes has not been explored mechanistically.

In this report, we demonstrate that altering profilin-1 or profilin-2 levels has dramatically different effects on actin cytoskeletal organization, affecting cell migration and invasion. Profilin-2 controls protrusive activity and migratory behavior of normal and tumor cells by promoting EVL-mediated polymerization of long actin filaments that assemble into contractile bundles. In addition, downregulation of profilin-2 or EVL markedly enhances invasion in vitro and in vivo, and the expression profiles of these actin regulators in human tumors is significantly correlated with tumor grade and invasiveness.

RESULTS

Profilin-1 and Profilin-2 Have Differential Effects on Cell Motility and Invasion

To investigate profilin-1 and profilin-2 contributions to cell motility, we depleted each isoform and analyzed changes in the motile behavior of MCF10A cells. SMARTpool siRNAs selectively downregulated profilin-1 and profilin-2 levels, and knockdown (KD) of one isoform did not affect the levels of the other (Figures 1A–1C). *PFN2* KD increased migration speed and scattering, whereas *PFN1* KD decreased migration speed and promoted cell clustering (Figures 1A–1D; Movie S1 available online). We confirmed the siRNA specificity using two shRNAs, targeting each isoform; these shRNAs displayed the same specificity and efficacy in knockdown, and induced the same migratory phenotypes (Figure S1A). Using these shRNAs, we evaluated the effects of profilin-1 and profilin-2 depletion in 3D cultures. MCF-10A cells form cyst-like acinar structures reminiscent of mammary gland alveoli (Muthuswamy et al., 2001; Petersen et al., 1992). *PFN2* KD induced the formation of dysmorphic 3D structures not observed in control cultures (Figures 1E); and about 5% of *PFN2* KD structures displayed an invasive phenotype exhibiting cell dissemination into the matrix (Figure 1E). This invasive behavior is noteworthy because overcoming structural restraints within acini is highly atypical; most genes that have been implicated in tumor progression fail to induce invasion in MCF-10A cells, requiring additional genetic or epigenetic alterations to promote this phenotype (Debnath and Brugge, 2005; Witt et al., 2006). *PFN2* KD also significantly induced MCF10A cell invasion through Matrigel in a Boyden chamber assay (Figure 1F).

To examine the contrasting functions of profilin-1 and profilin-2 in cancer cell migration, we screened a large number of breast tumor cell lines for expression of the two profilin isoforms; we chose SUM159 cells for analysis because they express levels of profilin-1 and profilin-2 comparable to MCF-10A cells (Figures 1G and S1B). Similarly to MCF10A cells (Simpson et al., 2008), *PFN2* KD enhanced SUM159 cell migration in a wound-healing assay and increased cell scattering at the wound edge, whereas *PFN1* KD suppressed wound closure (Figures 1H and S1C).

To determine the contribution of each profilin isoform to the total pool of profilin, we quantified profilin-1 and profilin-2 cellular concentrations in MCF10A and SUM159 cells. Profilin-1 concentration, approximately 13 μM, was about 15-fold higher than that of profilin-2, 0.8 μM (Figures 1G and S1B); this suggests that cell migration is sensitive to changes in profilin-2 levels specifically since altering profilin-2 alone would not significantly alter the combined concentration of both isoforms.

To examine whether alterations in profilin-1 and profilin-2 levels affect invasive behavior of SUM159 cells, we embedded them in Matrigel, in which they form 3D clusters with cells protruding into the surrounding matrix. *PFN2* KD enhanced migratory and invasive behavior of SUM159 cells in 3D cultures, exhibiting enhanced protrusive activity and cell dissemination into the matrix, whereas overexpression of *PFN2* (HA-profilin-2) resulted in the opposite phenotypes (Figures 2A and S2A–S2B); *PFN1* KD diminished protrusive activity and suppressed migration and invasion into the matrix, whereas *PFN1* overexpression enhanced them (Figures 2A and S2A–S2B). Consistent with these results, *PFN2* KD increased invasion in Boyden chambers, whereas *PFN1* KD significantly decreased it (Figure 2B).

To investigate whether profilin-1 and profilin-2 influence invasion of breast cancer cells in vivo, we injected control, *PFN1* KD, or *PFN2* KD SUM159 cells orthotopically into the mammary fat pad of NOD/SCID mice. While there were no discernable differences in tumor growth among *PFN1* KD, *PDN2* KD, and control tumors (Figure S2C), *PFN2* KD significantly increased the number of extratumoral invasive foci, particularly in the surrounding stroma and muscle tissue and occasionally in the sentinel lymph node (Figures 2C, 2D, and S2D). These studies indicate that profilin-2 downregulation enhances stromal infiltration in SUM159-derived tumors.

Profilin-2-Mediated Actin Polymerization Promotes Actin Bundling and Suppresses Protrusive Activity

Given its low cellular concentration, the significant effects of profilin-2 downregulation on migration and invasion suggest that its contribution to actin cytoskeletal reorganization is distinct from that of profilin-1. To characterize the contribution of each profilin to actin cytoskeletal remodeling, we examined *PFN1* KD and *PFN2* KD SUM159 cells microinjected with labeled

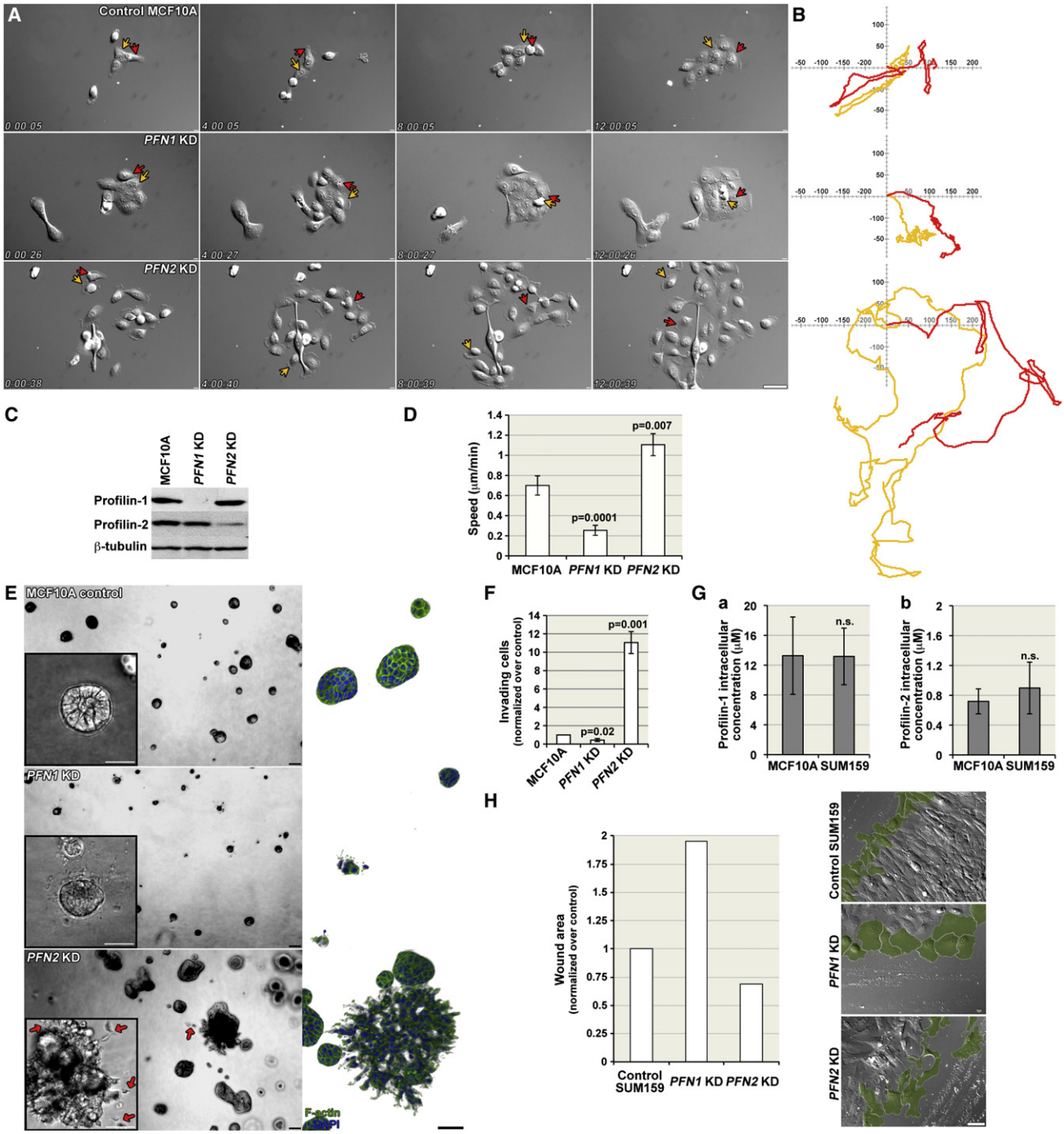

Figure 1. Profilin-1 and Profilin-2 Differentially Regulate Cell Migration and Invasion

(A) Montages of DIC from Movie S1. Time stamps are hr:min:s. Scale bar is 50 μm.

(B) Migration tracks of the cells indicated by red and yellow arrows in (A). Units are in μm.

(C) Western blot analysis of profilin-1 and profilin-2.

(D) Quantitation of migration speed; values are averages of mean speed from at least 30 cells ± SEM from three experiments.

(E) MCF10A 3D cultures. Left panels are phase-contrast images (arrows indicate cell invasion) and right panels are 3D reconstruction of confocal z-series. Scale bar is 50 μm.

(F) Boyden chamber invasion assays; values are averages of mean number of invading cells (normalized over control) from three independent experiments ± SEM.

(G) Quantitation of profilin-1 (a) and profilin-2 (b) intracellular concentrations. Values are means from three independent experiments ± SD.

(H) Wound-healing assay of SUM159 control, *PFN1* KD, and *PFN2* KD cells. Plot shows wound areas (normalized over control) from a representative experiment (of three experiments); and right panels show cells at the edge of the wound highlighted in green. Scale bar is 50 μm.

See also Figure S1 and Movie S1.

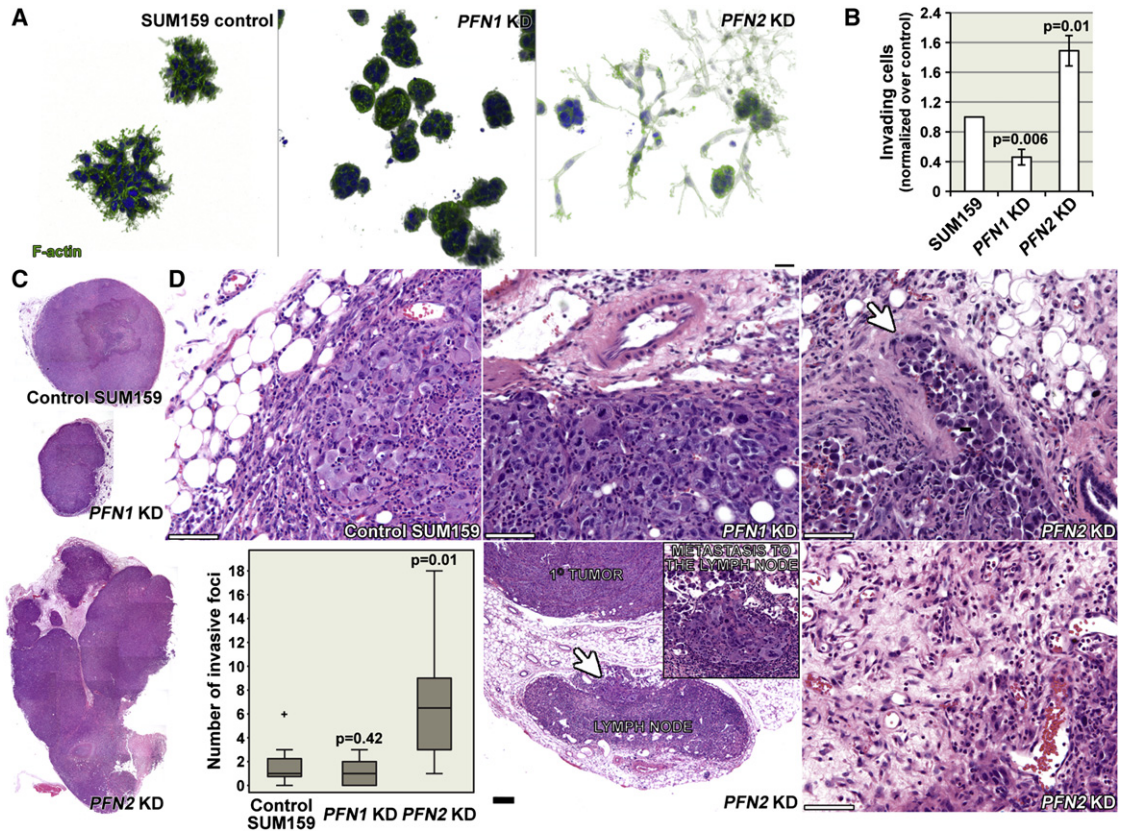

Figure 2. *PFN2* Knockdown Enhances Invasion of SUM159 Breast Tumor Cells

(A) Three-dimensional reconstruction of confocal z-series of 3D cultures. Scale bar is 40 μm.

(B) Boyden chamber invasion assays; values are averages of mean number of invading cells (normalized over control) from three independent experiments ± SEM.

(C) Macroscopic view of representative tumors from mammary fat pads injections.

(D) Top row: Hematoxylin and eosin staining of sections from control, *PFN1* KD, and *PFN2* KD SUM159 tumors. White arrow indicates local invasion. Bottom row: Left panel shows box plots of the quantitation of invasive foci in tumors from three experiments; middle panel shows an invasive focus at the sentinel lymph node in *PFN2* KD tumor (inset is a magnification of the region indicated by a white arrow); and right panel shows a tumor edge with dissociated invasive cells in a *PFN2* KD tumor. Scale bar is 50 μm.

See also Figure S2.

actin by time-lapse microscopy. *PFN1* KD increased F-actin bundling; *PFN2* KD, however, decreased bundling, especially at regions of the leading edge undergoing increased protrusive activity (Figure 3A; Movie S2).

To compare the ultrastructure of the actin cytoskeleton in control and KD cells, we examined metal cast cytoskeletons generated by rapid freezing and rotary shadowing. Consistent with the light microscopy data, *PFN1* KD cytoskeletons showed marked increase in actin filament bundles (Figure 3B). To quantify the change in actin bundling, we assessed the percentage of cells with prominent stress fibers by light microscopy; *PFN1* KD enhanced stress fiber formation in SUM159 cells, whereas *PFN2* KD diminished it (Figures 3C, 3D, and S3A). Importantly, *PFN2* KD in *PFN1* KD cells (double knockdown) resulted in dramatic reduction in actin polymerization and in collapse of the actin cytoskeleton (Figure S3B); these data suggest that profilin-1 and profilin-2 are the two major profilin isoforms regulating actin polymerization in SUM159 cells and that profilin-2 promotes actin bundling. Indeed, similarly to *PFN1* KD, overexpression of *PFN2* enhanced stress fiber formation, a phenotype that was reversed by the concomitant KD of *PFN2;* moreover, overexpression of a siRNA-resistant *PFN2* mutant prevented the reversal of the *PFN2* overexpression phenotype by *PFN2* KD, further validating the specificity of profilin-2 effects on actin bundling (Figures S3C and S3D).

Because these alterations in the actin cytoskeleton correlated with changes in protrusive activity, we examined protrusion and retraction dynamics after altering profilin-1 and profilin-2 levels. *PFN2* KD in SUM159 cells enhanced protrusion and retraction as compared to control cells, while *PFN1* KD suppressed these activities (Figure 4A; Movie S3). Changes in protrusive activity were quantified in kymographs generated from highly resolved time-lapse image series (3,600 frames at a rate of 1 frame/sec). *PFN2* KD increased speed and frequency of protrusion and retraction by 1.6-fold to 2-fold, and decreased protrusion persistence by 32% as compared to control ($p < 0.05$) (Figures 4B–4E and S4A–S4D; Movie S3); additionally, *PFN2* KD decreased the idle time between

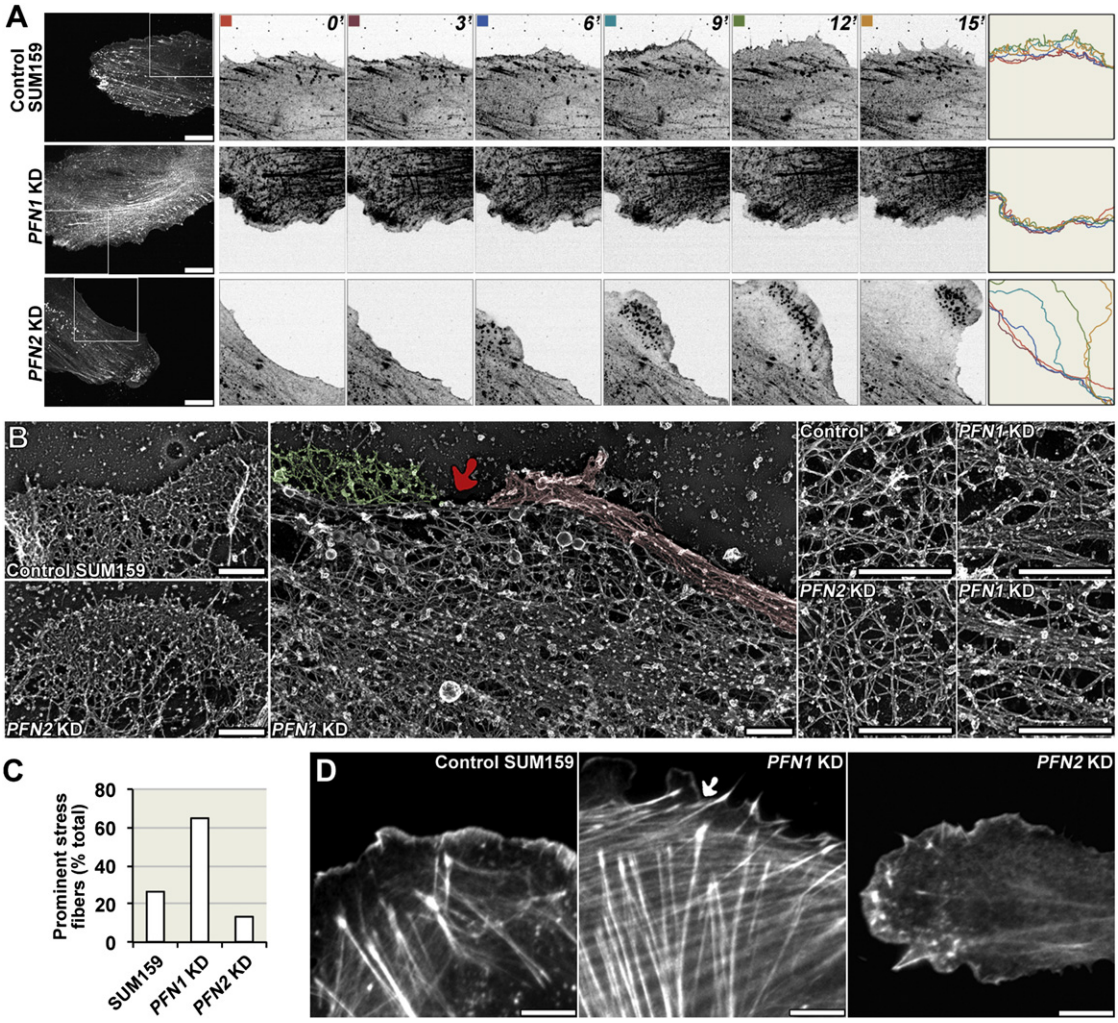

Figure 3. Profilin-2 Promotes Actin Bundling in SUM159 Cells

(A) Montage from time-lapse movies of cells microinjected with Alexa Fluor 568-conjugated actin (Movie S2); colored lines indicate the positions of the leading edge in the corresponding cells. Indicated time is in minutes. Scale bar is 10 μm.

(B) Electron micrographs of cortical F-actin cytoskeletons. Arrow indicates a small protrusion (green) next to an actin bundles (red). Insets are higher resolution images. Scale bar is 1 μm.

(C) Quantitation of cells with prominent stress fibers (~200 cells were analyzed per group).

(D) Representative images; arrow indicates small protrusion. Scale bar is 10 μm.

See also Figure S3 and Movie S2.

protrusion/retraction events, as compared to control (Figure S4C). In contrast, *PFN1* KD diminished protrusion speed, but did not affect persistence or frequency (Figures 4B–4D and S4A–S4D). To observe the direct effects of increased intracellular concentrations of profilin-1 or profilin-2, we microinjected the respective purified proteins into SUM159 cells (Figure 4F; Movie S4). Profilin-1 injection enhanced protrusion/retraction speed and frequency, whereas profilin-2 injection suppressed these activities (Figures 4G–4J and S4D–S4F; Movie S4); overexpression of *PFN2a* also suppressed protrusive activity significantly (Figures S4G and S4H). Together, these results suggest that profilin-2 suppresses protrusive activity in SUM159 cells, consistent with its suppressive effects on migration and invasion of these cells.

The Suppressive Effects of Profilin-2 Are Dependent on Myosin Contractility

To investigate the involvement of myosin motor activity in profilin-2-induced actin bundling, we examined myosin light chain (MLC) phosphorylation. In *PFN1* KD cells, phospho-MLC decorated F-actin bundles at the leading edge (Figure 5A); *PFN2* KD cells displayed reduced total phospho-MLC, consistent with reduced cortical actin bundling (Figures 5A, 5B, and S5A). Conversely, overexpression of *PFN2a* increased phospho-MLC levels (Figure S5A). Moreover, we examined the effects of overexpression of *PFN2b*; *PFN2b* is a *PFN2* splice isoform that does not bind to G-actin and has low affinity to poly-L-proline (Di Nardo et al., 2000), and was used as negative control lacking the capacity to promote actin polymerization.

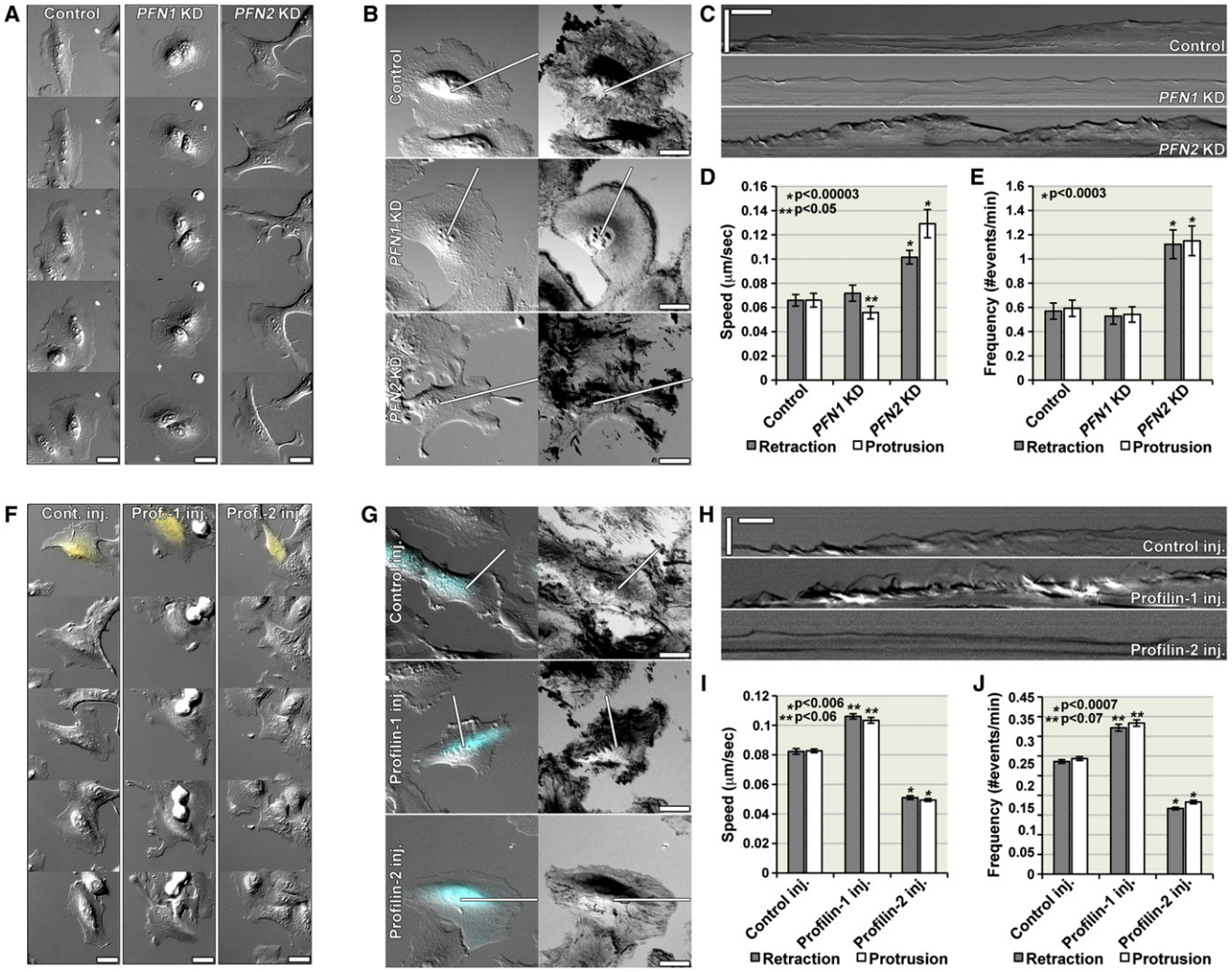

Figure 4. Profilin-2 Suppresses Protrusive Activity in SUM159 Cells

(A) Montages of DIC images selected from a segment of Movie S3 at 1-hr intervals. Scale bar is 20 μm.

(B) Kymography analysis. Left panel shows DIC images from Movie S3 at time 0. Right panel shows minimum projections (showing regions of protrusive activity) of entire time series (acquired at a rate of one frame/s). Lines indicate the position at which kymographs were registered. Scale bar is 20 μm.

(C) Kymographs from the corresponding movies in (B). Vertical scale bar is 20 μm. Horizontal scale bar is 2 min.

(D and E) Average retraction and protrusion speeds (D) and frequency (E). Values are averages of means from at least 30 cells (pooled from three different experiments) ± SEM.

(F) Montages of DIC images selected from a segment of Movie S4 at 1-hr intervals. Yellow dextran marks the injected cells. Scale bar is 20 μm.

(G) Kymography analysis. Left panel shows DIC images from Movie S4 at time 0. Right panel shows minimum projections of entire time series (acquired at a rate of one frame/s). Labeled dextran (cyan) was coinjected to identify microinjected cells. Lines indicate the position at which kymographs were registered. Scale bar is 20 μm.

(H) Kymographs from the corresponding movies in (E). Vertical scale bar is 10 μm. Horizontal scale bar is one minute.

(I and J) Average retraction and protrusion speed (I) and frequency (J). Values are averages of means from at least 30 cells (pooled from three different experiments) ± SEM.

See also Figure S4 and Movies S3 and S4.

Overexpression of *PFN2b* did not increase phospho-MLC levels, suggesting that profilin-2-mediated polymerization is required for the generation of the contractile actin bundles (Figure S5A).

To examine the connection between the generation of contractile actin bundles and the regulation of protrusive activity by profilin-2, we assessed the effect of altering myosin activity on profilin-2's suppressive effects. For that purpose, we used Y27632, a pharmacological inhibitor of ROCK-mediated MLC phosphorylation and myosin motor activity. ROCK inhibition reversed the suppressive effects of profilin-2 on protrusive activity, thus increasing the frequency and speed of protrusion and retraction (Figure 5C; Movie S5); this increase was significantly greater than baseline, suggesting that profilin-2 has a positive effect on protrusion in the absence of myosin activity. In a wound-healing assay, ROCK inhibition reversed the suppression of cell migration by *PFN1* KD (Figure S5B); not

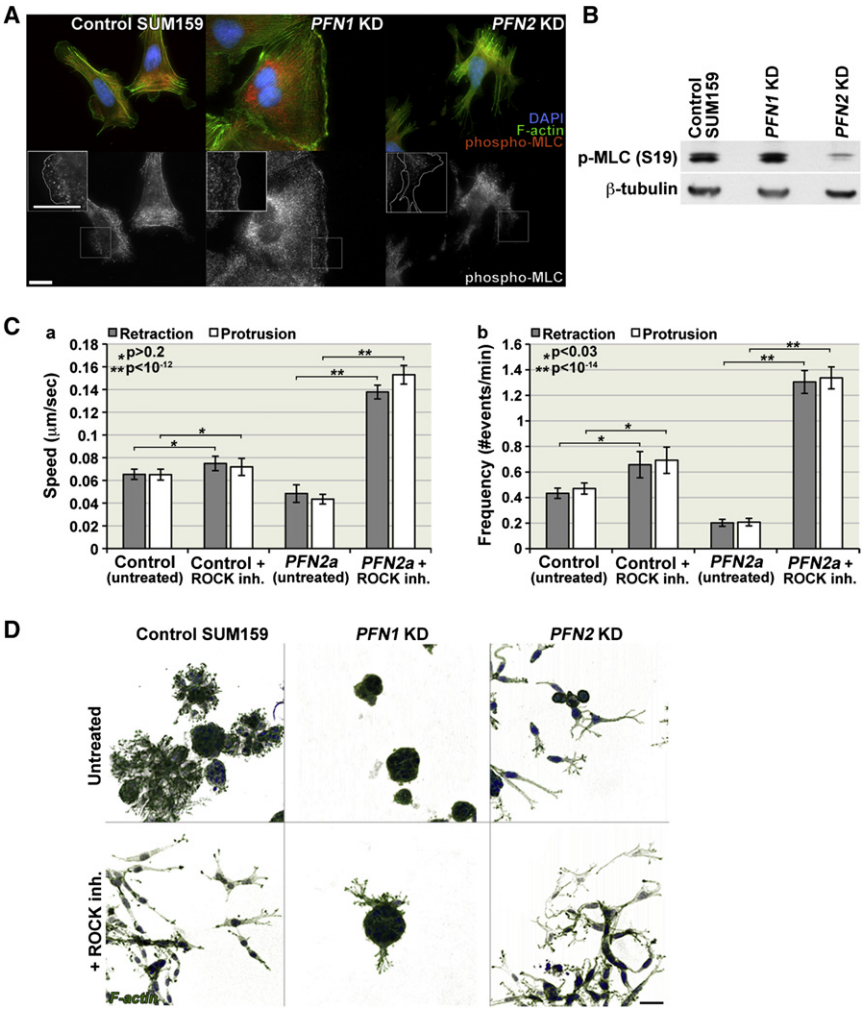

Figure 5. Profilin-2 Suppressive Effects Are Dependent on Acto-myosin Contractility in SUM159 Cells

(A) Phospho-MLC staining (phospho-Ser19). Insets are magnifications of the areas in the white boxes; white lines trace the cell edge. Scale bar is 10 μm.

(B) Phospho-MLC western blot analysis.

(C) Speed (a) and frequency (b) of retraction/protrusion in control and *PFN2a* overexpressing SUM159 cells with or without ROCK inhibition (Movie S5). Values are averages of means from at least 30 cells (pooled from three different experiments) ± SEM.

(D) Three-dimensional reconstruction of confocal z-series of SUM159 3D cultures. Scale bar is 40 μm.

See also Figure S5 and Movie S5.

surprisingly, this "rescue" was only partial since the KD cells are depleted of profilin-1, and the endogenous levels of profilin-2 are significantly lower than 1. In agreement with these data, ROCK inhibition increased protrusion and invasion into the surrounding matrix in 3D cultures, mimicking the effects of *PFN2* KD, and partially "rescued" protrusive activity in *PFN1* KD cell clusters (Figures 5D and S5C). Moreover, blebbistatin (an inhibitor of myosin ATPase activity) also increased protrusion and invasion into the matrix and partially reversed *PFN1* KD phenotype (Figure S5C). Collectively, these results suggest that suppression of protrusive activity, migration, and invasion of SUM159 cells by profilin-2 is dependent on the generation of contractile actomyosin bundles.

Profilin-2-Induced Contractile Actin Bundles Are Generated by EVL, which Suppresses Protrusive Activity, Migration, and Invasion

The structural differences in actin filaments generated by profilin-1 and profilin-2 (Figures 6A and S6A) suggest that they interact with distinct actin polymerization regulators. Using mass spectrometry, we identified high-confidence interactions between profilin-1/2 and Ena/VASP proteins; in particular, EVL was found to preferentially bind profilin-2 as compared to profilin-1 (L.L.G. and Mathew Sowa, unpublished data), consistent with previous studies (Ferron et al., 2007; Kursula et al., 2008; Lambrechts et al., 2000; Nodelman et al., 1999; Veniere et al., 2009).

To characterize the binding preferences of profilin-2 to the three ENA/VASP family members, we examined the relative binding capacity of Mena, EVL, and VASP to profilin-2 as compared to profilin-1 (Figures 6B, S6B, and S6C). Both EVL and VASP preferentially immunoprecipitated with profilin-2 (7-fold and 1.8-fold, respectively); Mena showed no preferential binding to either profilin isoform (data not shown). Direct measurement of profilin binding capacity with purified monomeric EVL and VASP using sedimentation equilibrium confirmed that both proteins show preferential binding to profilin-2 relative to profilin-1 (Figures 6C and S6D). In addition, both monomeric EVL and VASP had higher affinity and binding capacity for profilin-2 compared to profilin-1 (Figure S6D). Similarly, 10-fold more profilin-2 than profilin-1 immunoprecipitated with HA-EVL (Figure 6B) and, vice versa, 7-fold more EVL were immunoprecipitated with profilin-2 compared to profilin-1 (Figure S6B). Consistent with the mass spectrometry analysis, these results indicate that VASP and EVL interact preferentially with profilin-2 in vivo and in vitro.

Although VASP has been previously shown to enhance barbed end filament elongation in the presence of profilin-1 and cytoplasmic actin (Hansen and Mullins, 2010), the profilin isoform specificity for Ena/VASP proteins remains poorly understood. To compare the relative ability of EVL and VASP to enhance actin barbed end polymerization in the presence of profilin-1 and profilin-2, we visualized the assembly of single actin filaments in vitro using total internal reflection fluorescence (TIRF) microscopy. EVL-dependent barbed end polymerization was significantly faster in the presence of profilin-2, compared to

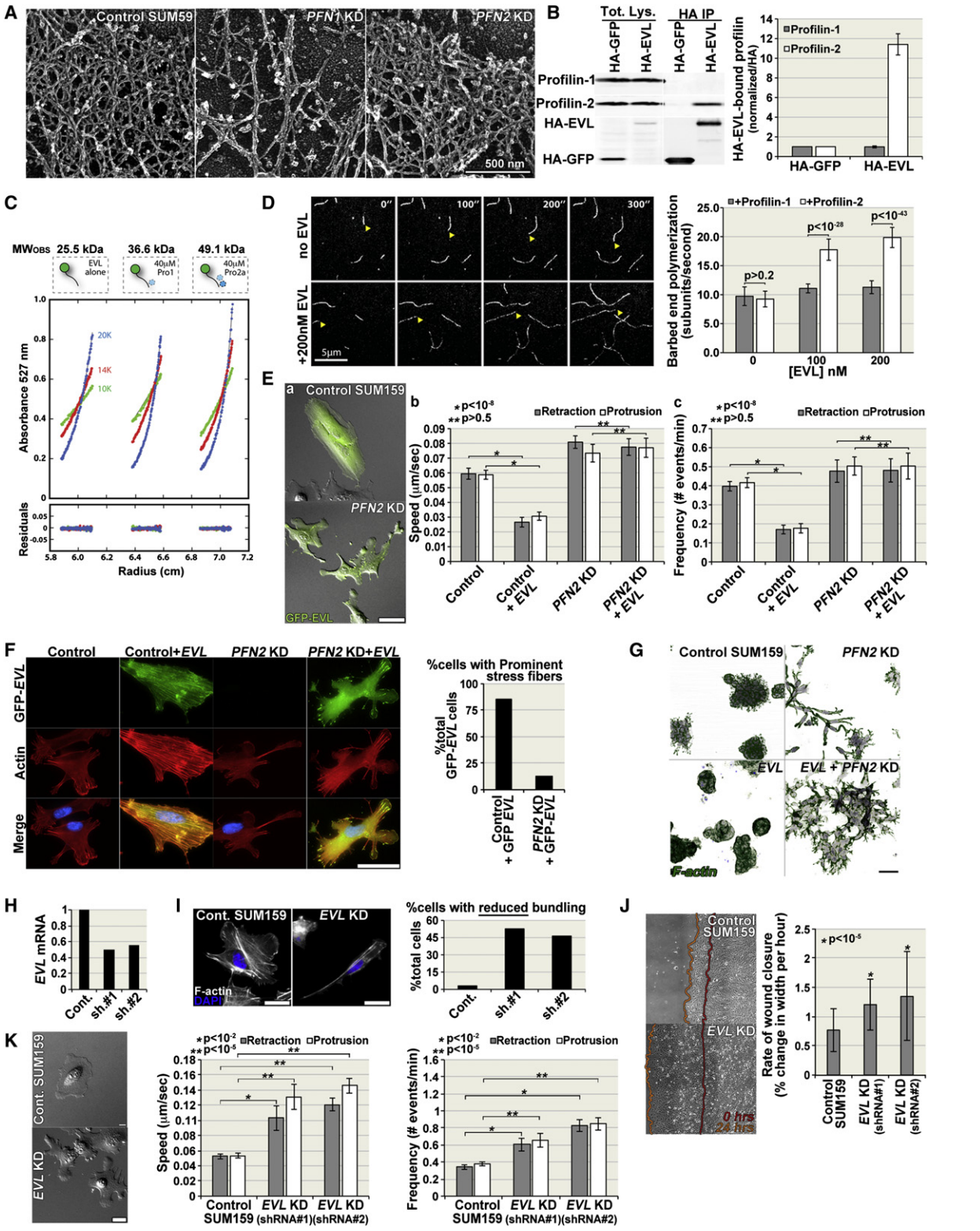

Figure 6. EVL Exhibits Preferential Binding to Profilin-2 and Suppresses Protrusive Activity by Generating Actin Bundles in a Profilin-2-Dependent Manner

(A) High-magnification micrographs of the cell edge actin of control, *PFN1* KD, and *PFN2* KD SUM159 cells. Scale bar is 500 nm.

(B) Left panel shows analysis of EVL binding to profilin-1 and profilin-2 in SUM159 cells: HA immunoprecipitation, followed by profilin-1 and profilin-2 western blot. HA-GFP was used as negative control, and HA western blot shows the expression levels of HA-GFP and HA-EVL. Right panel shows quantitation of the

profilin-1 (Figure 6D). Furthermore, although EVL could bind to profilin-1 in our sedimentation equilibrium experiments, elongation of actin filaments in the presence of profilin-1 was inefficient (Figure 6D). VASP exhibited a similar preference for profilin-2 binding in vitro; however, we observed only a marginal difference in the rate of VASP-mediated barbed end filament elongation in the presence of profilin-1 versus profilin-2 (Figure S6E). Based on observations reported by Breitsprecher et al. (2011), the rate of Ena/VASP-dependent barbed end elongation is directly related to the affinity for monomeric actin. Because profilin enhances actin monomer binding to Ena/VASP proteins (Ferron et al., 2007), the differences in filament elongation rates in the presence of the two profilin isoforms can be attributed to the different affinities and binding capacity of EVL and VASP. Based on these differences between profilin-1 and profilin-2, it is feasible that profilin-2 could compete effectively with profilin-1 for binding to EVL despite the 15-fold higher concentrations of profilin-1, because only the former would appreciably participate in generating EVL-mediated actin structures. This is supported by the immunoprecipitation of EVL with profilin-1 and profilin-2 from cell lysates.

To investigate the effect of EVL activity on membrane protrusion and the requirement of profilin-2 for this activity, we examined membrane dynamics in control and *PFN2* KD SUM159 cells overexpressing GFP-*EVL* (Figure 6E; Movie S6). Overexpression of GFP-*EVL* significantly inhibited protrusion and retraction in control but not in *PFN2* KD cells (Figure 6E). In addition, GFP-EVL increased the abundance of stress fibers in control cells in a profilin-2-dependent manner (Figures 6F and S6F); this EVL-induced increase in stress fibers correlated with suppression of protrusion and invasion in 3D cultures (Figure 6G).

In addition, *EVL* KD suppressed stress fiber formation in SUM159 cells (Figures 6H–6I and S6G). This decrease in stress fibers correlated with significantly weakened matrix adhesion, especially in cells strongly depleted of EVL (data not shown); moderate *EVL* depletion, which did not weaken adhesion to the same extent, increased wound closure rate (Figure 6J) and protrusion and retraction frequency and speed in SUM159 cells, similarly to *PFN2* KD (Figure 6K; Movie S6). In addition, *EVL* KD increased migration speed of MCF10A cells, which also exhibited compromised adhesion at high KD levels (Figures S6H–S6J and data not shown). These results suggest that EVL-induced actin polymerization is dependent on profilin-2, and that this polymerization mode promotes actin bundling leading to diminished protrusive activity.

VASP overexpression, on the other hand, increased stress fiber generation only weakly (Figures S6K–S6L). In addition, *VASP* KD did not have a significant effect on protrusive activity (Figures S6M–S6N). These data are consistent with VASP having only a marginal preference for binding to profilin-2 relative to profilin-1.

To investigate the effects of *EVL* KD on invasion, we established an inducible shRNA system in SUM159 cells, which made it feasible to achieve high knockdown levels—70%–80% depletion after 48 hr of induction (Figure S7A); this approach allowed us to circumvent any effect the KD might have on tumor initiation and growth due to altered adhesion properties. In 3D cultures, induction of *EVL* KD increased invasion, similarly to *PFN2* KD (Figure 7A). To examine invasion in vivo, we induced EVL KD in SUM159 tumors derived from orthotopic fat pad injections. *EVL* KD did not affect tumor volume over the course of 2-week induction, after which the tumors were harvested (Figure S7B). Induction of either of two different shRNAs targeting *EVL* increased in the number of extratumoral invasive foci significantly (Figure 7B). Moreover, staining for turboRFP, which is expressed as a cytoplasmic marker upon induction, allowed us to examine subcellular structures in tumor cells. Interestingly, *EVL* KD increased the number of protrusions per cell as compared to control (Figure 7C). Together, these studies

relative levels of profilin-1 and profilin-2 bound to HA-EVL in SUM159 cells. These data are representative of three independent experiments. Values are averages ± SEM.

(C) Sedimentation equilibrium analytical ultracentrifugation used to determine the solution molecular weight of monomeric EVL in the presence of profilin-1 or profilin-2a. The sedimentation profile of Cy3-mEVL1-235aa (5 μM) alone or combined with either profilin-1 or profilin-2a (40 μM) was determined by monitoring the absorbance at 527/550 nm. Global fitting of three equilibrium traces (at three different centrifugation speeds: 10,000, 14,000, and 20,000 rpm) for each condition was performed (see Experimental Procedures for more detail). An extinction coefficient of 79,982 $M^{-1}cm^{-1}$ (Cy3, 527 nm) was used to determine the protein concentration as a function of the radial position. A monomer-dimer model was used to determine the molecular weight for a single ideal species (top panels).

(D) Left panel shows image sequence of filaments polymerizing in vitro in the presence of 2 μM actin (10% Alexa488), plus 2 μM profilin-2a. Barbed end growth of actin filaments was visualized using TIRF microscopy. Top row, 0 nM EVL; bottom row, plus 200 nM EVL. Yellow arrowhead tracks the growth of a single actin filament barbed end. Scale bar is 5 μm. Right panel shows average barbed-end polymerization rates (subunits/s) for single actin filaments in the presence of profilin-1 or profilin-2, plus or minus EVL. In the presence of 1 μM actin (10% Alexa488) alone and 100 nM EVL, barbed ends elongated at a rate of 31.1 ± 2.9 subunits/s (S.D.H. and R.D.M., unpublished data). Values are averages of polymerization rates from at least 30 filaments pooled from two or three slides ± SEM.

(E) Control or *PFN2* KD SUM159 cells expressing GFP-*EVL*. (a) Still images from Movie S6, scale bar is 50 μm; speed (b) and frequency (c) of retraction/protrusion in control or *PFN2* KD cells with or without GFP-*EVL* expression as calculated from corresponding kymographs. Values are averages of means from at least 30 cells (pooled from three different experiments) ± SEM.

(F) (Right) F-actin staining in control and *PFN2* KD cells with or without *EVL* overexpression. Scale bar is 50 μm. Left panel shows percentage of *EVL* overexpressing (GFP positive) cells with prominent stress fibers.

(G) Three-dimensional reconstruction of confocal z-series of 3D cultures of control and *PFN2* KD cells with or without *EVL* overexpression. Scale bar is 50 μm.

(H) Quantitative real-time PCR showing decreased *EVL* expression after long-term selection in control cells and cells expressing the two shRNAs targeting *EVL*.

(I) F-actin staining and quantitation of reduced bundling. Scale bar is 20 μm.

(J) Representative wound-healing assay. Values are averages ± SD.

(K) Kymograph analyses (images are from Movie S6; scale bar is 20 μm); values are averages of means from at least 30 cells (pooled from three different experiments) ± SEM.

See also Figure S6 and Movie S6.

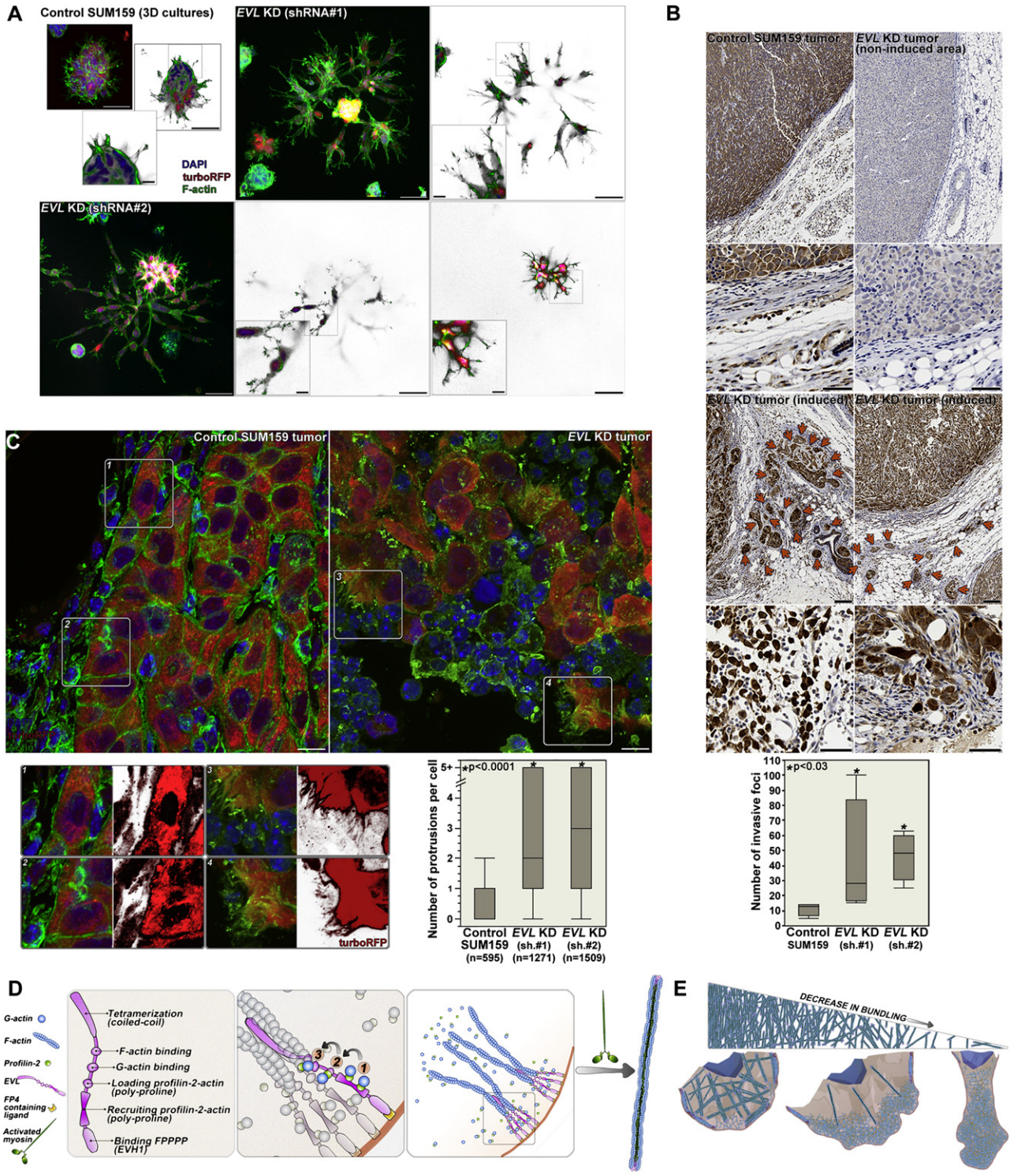

Figure 7. *EVL* Knockdown Enhances Invasion In Vitro and In Vivo

(A) Confocal microscopy (maximum projection images) of 3D cultures of SUM159 cells on day 8 and after 4 days of induction with doxycycline of control and *EVL* KD cells using two different inducible shRNA targeting *EVL* (scale bar is 50 μm). Large insets are single sections from the confocal z-series and small insets are magnification of the region in the box (scale bar is 10 μm).

(B) TurboRFP staining of sections from control, noninduced area of *EVL* KD SUM159 tumors; arrows indicate extratumoral invasive foci. Box-and-whisker plot shows quantitation of invasive foci in the corresponding tumors. Scale bar is 50 μm.

(C) Confocal microscopy (maximum projection images) of control and *EVL* KD tumors. Scale bar is 10 μm. Insets are magnified areas within the designated boxes. Red channels are shown separately to visualize tumor cell morphology. Box-and-whisker plot shows quantitation of the number of protrusions per cell.

indicate that EVL downregulation is associated with increased protrusion and invasion in vitro and in vivo.

To examine the effects of altering profilin-2/EVL-mediated actin polymerization on protrusive activity and cell migration in other cell lines, we examined the expression profile of *PFN2* and *EVL* in an array of cancer cell lines using published data sets (Neve et al., 2006). We chose MCF7 cells because they express relatively high levels of *PFN2* and *EVL* (Neve et al., 2006). Consistent with the results from SUM159 cells, *PFN2* KD or *EVL* KD enhanced MCF7 cell migration in wound-healing assays and increased protrusive activity as measured by kymography (Figures S7C–S7F; Movie S7). In addition, *PFN2* KD or *EVL* KD in colorectal adenocarcinoma Caco-2 cells also increased protrusive activity (Figure S7G; Movie S8).

Our findings support a model in which three elements are important for EVL-mediated suppression of protrusive activity (Figures 7D and 7E): (1) profilin-2 to specifically deliver polymerization-competent actin monomers to EVL, (2) EVL to assemble unbranched actin filaments, and (3) myosin contractility to generate actin bundles.

PFN2 and EVL Are Differentially Expressed in Human Breast Cancer

To examine whether the expression of *PFN2* and *EVL* is linked to clinical aspects of breast tumors, we examined the relationship between these markers and tumor grade. In five data sets (Desmedt et al., 2007; Ivshina et al., 2006; Loi et al., 2007; Lu et al., 2008; Minn et al., 2005), *EVL* transcript levels were significantly lower in grade II and III tumors as compared to grade I, whereas *PFN2* expression was higher in high-grade tumors (Figures 8A and S8A; data not shown). In addition, multiple logistic regression analyses of two large data sets (Ivshina et al., 2006 and Lu et al., 2008) determined that *EVL* is a significant predictor of tumor grade, independent of other known markers, namely *ESR1, PGR,* and *ERBB2; PFN2,* on the other hand, did not show a consistent pattern in both studies (Figures 8B and S8B).

To investigate the prognostic significance of *EVL* and *PFN2* expression, we examined the association of *EVL* and *PFN2* expression with the probability of survival in two large breast cancer patient cohorts with long-term follow up (Schmidt et al., 2008; van de Vijver et al., 2002). Patients who had tumors with low *EVL* expression exhibited a significantly lower probability of survival (Figure 8C). Moreover, when treated as a continuous variable, *EVL* expression proved to be a significant prognostic marker in both cohorts. On the other hand, patients whose tumors expressed either high or low *PFN2* expression had a significantly lower probability of survival (Figure S8C). Importantly, in both studies, the high-*PFN2* group of patients with poor outcome was significantly enriched in tumors with low *EVL* expression (Schmidt: 1.4-fold enriched, $p = 0.0318$; Vandevijver: 1.5-fold enriched, $p = 0.00134$).

To examine profilin-2 and EVL protein expression in tumors, we used an array of normal and tumor tissue samples donated by 65 breast cancer patients (spotted in triplicates). Consistent with mRNA levels, profilin-2 protein expression was higher in grade III tumors compared to other tumor grades (Figure 8D). EVL protein levels, on the other hand, were significantly lower in grade II and III tumors as compared to normal breast tissue (mammary ducts) and grade I tumors (Figure 8D); these results were validated using a second tissue array of samples from 48 patients (spotted in duplicates) (Figure S8D).

Moreover, we grouped tumors based on the extent of tumor infiltration into stroma using a visual score consisting of three categories: "non-inv," including normal breast tissue and DCIS tumors with no infiltrating tumor cells; "low-inv" with minimal tumor infiltration; and "high-inv," with extensive infiltration into the stroma as small clusters and single cells (Figure 8E). Profilin-2 levels were lower in the low-inv group compared to the non-inv group; however, as predicted based on the high percentage of grade III tumors in the high-inv group, the levels of profilin-2 were higher in this group compared to the low-inv group (Figure 8E). EVL expression, on the other hand, was strongly anticorrelated with invasion in all categories (Figure 8E); these results were confirmed in the second tissue array (Figure S8D). Consistent with the multivariate analyses, these results suggest that EVL is a potential biomarker for invasion, in addition to tumor grade.

In addition, we stained for actin (β and γ-1) in the same tumors in which we assessed profilin-2 and EVL levels. Grade II and III tumors exhibited significantly lower staining intensity as compared to normal ducts and grade I tumors (Figures 8F and 8G). Moreover, *EVL* expression significantly correlated with actin staining intensity regardless of tumor grade (Figure 8H). Importantly, tumors from different grades express equivalent levels of actin (ACTB and *ACTG1)* and, in tissue culture cells, *EVL* KD did not alter actin expression (Figure S8E); therefore, the observed differences in actin staining intensity are likely due to differences in actin density possibly caused by changes in the structure of the actin cytoskeleton, such as decreased actin bundling.

Together, these results suggest that *EVL* is an independent biomarker for tumor grade, and could serve as a potential predictor of prognosis in breast cancer.

DISCUSSION

Our results demonstrate that profilin-2 regulates actin-based cellular processes in a distinct manner compared to the ubiquitous and well-characterized profilin-1 isoform. Profilin-2 preferentially promotes the activity of the Ena/VASP protein EVL, generating unbranched filaments that, when bundled by myosin-dependent contractility, suppress protrusive activity. Downregulation of either profilin-2 or EVL enhances cell

(D) Model representing the generation of actin bundles by profilin-2/EVL-mediated linear actin polymerization and activated myosin: right panel illustrates the process of actin polymerization mediated by profilin-2, which is summarized in three major steps (middle panel): recruitment (1) and loading (2) of profilin-2:actin by interaction with the profilin-2 PLP binding site; followed by addition of one actin monomer (G-actin) to the barbed end (3). Left panel shows the domain structure of EVL.
(E) Model representing the correlation between protrusive activity and the level of actin bundling.
See also Figure S7 and Movies S7 and S8.

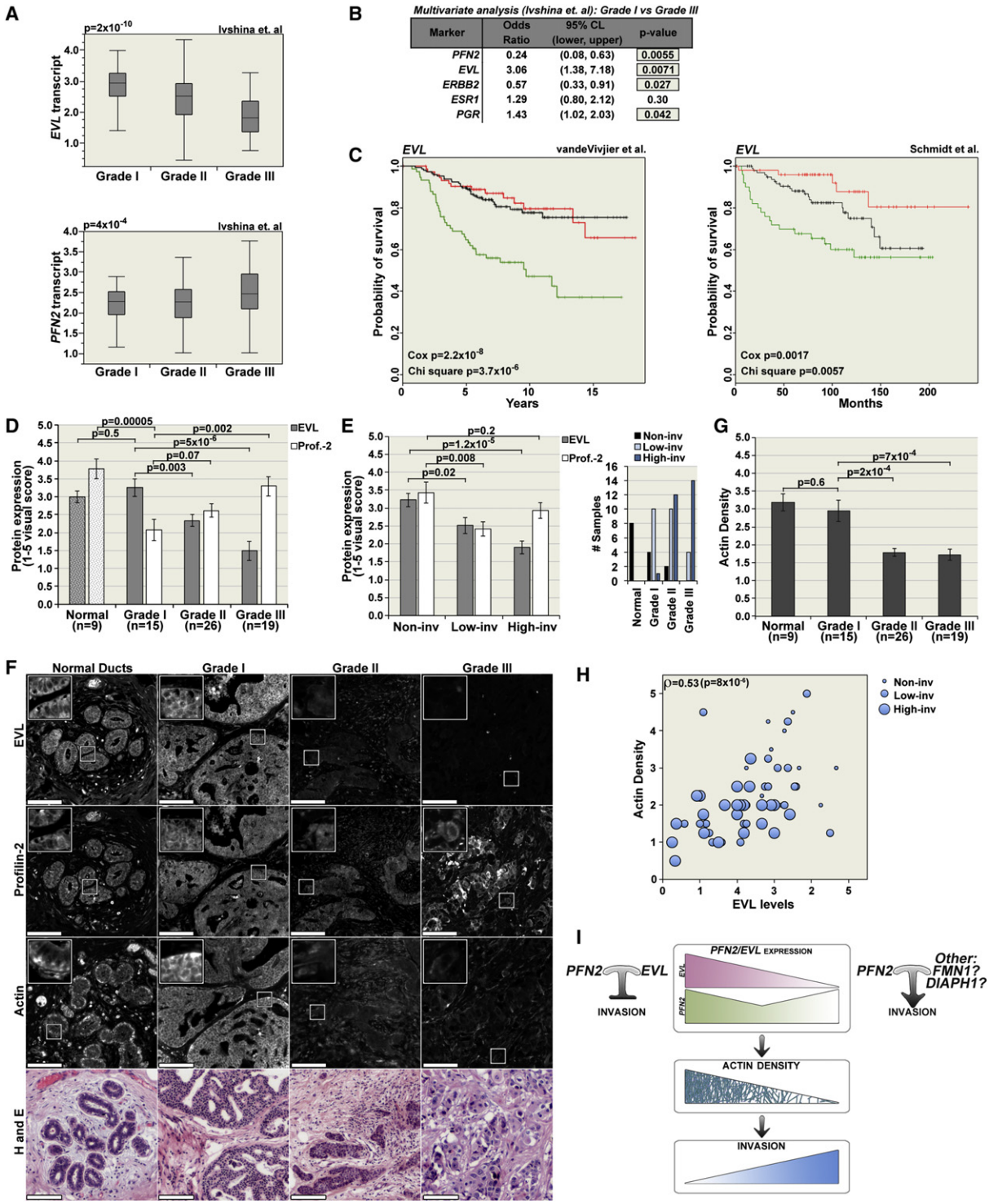

Figure 8. *PFN2* and *EVL* Are Differentially Expressed in Human Breast Tumors

(A) Box-and-whisker plots showing relative levels of *EVL* and *PFN2* transcript in grade I, II, and III; p values are from ANOVA analysis.

(B) Logistic regression analysis of the relationship between transcript level and tumor grade.

(C) Kaplan-Meier curves representing the probability of survival of breast cancer patients based on relative levels of *EVL* expression (green, tumors in the lowest quartile; red, tumors in the highest quartile; and black, the interquartile range). Chi square p values evaluate whether there are significant differences among any of the three groups. Cox p values evaluate the association of expression with survival by treating *EVL* levels as a continuous variable.

(D) Quantitation of EVL and profilin-2 protein expression in normal breast tissue, and in grade I, II, and III tumors (n is the number of patients per group; and triplicate sections from each patient were analyzed). Values are averages from visual scores (scale: 1–5) ± SEM.

migration and invasion in vitro and in vivo. In human tumors, relatively low levels of EVL correlate with low actin density and high invasive activity. Critically, *EVL* expression is an independent biomarker for tumor grade, and predictive of poor patient outcome.

Profilin Isoforms Regulate the Architecture of the Actin Cytoskeleton

Modulation of the actin cytoskeleton architecture by altering the relative levels of profilin-1 and profilin-2 is due, in part, to a shift in the dominant mode of actin polymerization. Our data suggest that decreasing the relative levels of profilin-1 and increasing those of profilin-2 result in a shift toward a less branched and more linear actin polymerization. Profilin-2 displays higher binding affinity for EVL (and to a lesser extent VASP) than profilin-1, making it more efficient in promoting EVL-mediated linear polymerization; this is in agreement with previous reports showing that EVL and VASP preferentially interact with profilin-2 as compared to profilin-1 (Kursula et al., 2008; Lambrechts et al., 2000; Nodelman et al., 1999; Veniere et al., 2009). Therefore, when profilin-2 is more abundant, EVL activity becomes more dominant in driving actin polymerization; the generation of long unbranched actin filaments by EVL, when coupled with myosin contractility, could suppress protrusive activity.

Moreover, previous reports suggest that profilin-1 binds with higher affinity than profilin-2 to WAVE-2, which promotes branched polymerization by Arp2/3 activation (Miki et al., 1998); this difference in binding affinity renders profilin-1 more critical for Arp2/3-mediated polymerization. Therefore, downregulation of profilin-1 could significantly suppress filament branching and make profilin-2/EVL-dependent polymerization the more dominant mode of polymerization. In addition, dominant EVL activity at the leading edge could directly reduce branched polymerization by suppressing Arp2/3 activity through anticapping and antibranching (Bear and Gertler, 2009). Conversely, downregulation of profilin-2 expression could increase filament branching by the Arp2/3 complex and decrease actin bundling, leading to highly dynamic protrusions.

In previous studies using the MDA-MB-231 breast tumor cell line, *PFN1* KD was reported to decrease speed of protrusion but increase persistence and enhance directionality of cell migration (Bae et al., 2009; Zou et al., 2007). However, *PFN1* KD in MDA-MB-231 cells used in our studies decreased the number of protrusions per cell and suppressed cell migration and invasion (data not shown). In these cells, the profilin-1 concentration (30 μM) was more than 100-fold higher than that of profilin-2 (0.27 μM), consistent with the correlation between highly dynamic cell migration and high profilin-1/low profilin-2 levels. Interestingly, the phenotypic changes to protrusive activity described in Bae et al. are similar to those induced by *PFN1* KD in SUM159 cells, which express higher levels of profilin-2 than MDA-MB-231 cells. We speculate that the discrepancy between our data and the published studies could be due to differences in the expression of profilin-2 between the MDA-MB-231 variants employed in these studies, or other experimental variables.

Actomyosin Contractility Is Important for the Suppression of Protrusive Activity by Profilin-2/EVL-Mediated Actin Polymerization

Our data revealed that the suppression of protrusive activity by profilin-2/EVL-mediated actin polymerization requires the aggregation of actin filaments into contractile bundles in a myosin-dependent mechanism. Inhibition of myosin contractility is sufficient to reverse the suppressive effects of profilin-2 and EVL. Interestingly, in the absence of myosin activation, *PFN2* overexpression enhances protrusive activity instead of suppressing it. In addition, downregulation of either *PFN2* or *EVL* dramatically decreases actin bundling and increases protrusive activity; this suggests that the polymerization events driven by profilin-2 and EVL are involved in the regulation of protrusion and cell migration by contractile activity.

Importantly, VASP do not exhibit the same capacity to generate profilin-2-mediated actin bundles capable of suppressing protrusive activity; this suggests that the generation of such actin bundles, which might represent a distinct subpopulation of stress fibers, could be unique to EVL. The specificity of EVL involvement in this type of actin cytoskeletal remodeling could be due to distinct set of binding partners that affect EVL function spatially and temporally; currently, we are analyzing the components of the EVL complex by mass spectrometry.

In addition to our data, the suppressive effects of cortical actomyosin bundling on protrusive activity and cell migration have been previously reported in endothelial cells (Fischer et al., 2009). However, other studies showed that some cancer cells are dependent on contractility for migration (Sanz-Moreno et al., 2011). We hypothesize that the effects of contractility vary depending on many factors, including the spatial organization of contractile actin filaments, the nature and strength of matrix adhesion, and the cortical actin organization and linkage to the membrane (Friedl and Wolf, 2010; Nakamura et al., 2011; Sheetz et al., 2006). In our model, EVL could play a role in the regulation of several of these factors, thus affecting the outcome of increased contractility.

Profilin-2/EVL-Mediated Regulation of Actin Assembly Influences Invasion In Vitro and In Vivo

Our data show that elevated levels of profilin-2 or EVL suppress invasion in 3D matrices in a manner dependent on myosin

(E) Representation of protein expression versus tumor invasion (invasion was assessed in a blinded fashion: Non-inv is the noninvasive group and low-inv and high inv are the low- and high-invasion groups, respectively). Right panel shows the distribution of each group in terms of tumor grade.
(F) Representative images of normal and tumor breast tissue. Scale bar is 100 μm. Insets are magnifications of the boxed areas.
(G) Analysis of actin density in normal and tumor breast tissue (actin density was assessed in a blinded fashion). Values are averages from visual scores (scale: 1–5) ± SEM.
(H) Correlation of *EVL* levels with actin density (Spearman's $\rho = 0.53$; $p < 8 \times 10^{-6}$); size of the circles represents the invasive activity in the corresponding tumors.
(I) Schematic representation of the correlation between EVL/profilin-2 expression, actin density and invasive behavior, and the potential effect of profilin-2 activity on invasion with or without EVL.
See also Figure S8.

contractility; and downregulation of profilin-2 or EVL or inhibition of contractility increases 3D invasion significantly. Moreover, in mammary fat-pad xenograft tumors, downregulation of *PFN2* or *EVL* increases the number of extratumoral invasive foci.

The increase in invasion associated with *EVL* KD correlates with increased protrusions and decreased contractility. Nonetheless, the mechanism by which EVL/profilin-2-mediated polymerization regulates invasion also involves alteration of other cellular processes, such as cell-cell and cell-matrix adhesion. In fact, we did observe that downregulation of *PFN2* or *EVL* decreases both types of adhesion in normal and cancer cells. The characteristic changes in cellular processes that contribute to promoting invasion vary based on genetic and epigenetic alterations within tumor cells, and on alterations in the tumor microenvironment; therefore, the mode of invasion could vary within the same tumor and over the course of tumor progression. In fact, some types of tumor cells are able to switch between different modes of single-cell invasion, such as amoeboid, characterized by round morphology, high contractility, weak matrix adhesion, decreased protrusive activity, and increased membrane blebbing; and mesenchymal, characterized by elongated morphology, low contractility, strong matrix adhesion, and increased protrusive activity (Sanz-Moreno et al., 2008; Friedl and Wolf, 2010).

In the model we present here, increased invasion is associated with increased protrusion, decreased contractility and also decreased adhesion. Therefore, the invasive phenotype that is induced by downregulation of EVL does not fit the characteristics of either mesenchymal or amoeboid modes of invasion. This suggests that invading cancer cells may display phenotypes along a continuum between the mesenchymal and amoeboid states, in which multiple cellular processes are continuously altered.

PFN2 and EVL Distinctive Expression Profiles Are Predictive of Invasiveness and Poor Prognosis in Human Breast Cancer

EVL expression is significantly lower in highly invasive human breast tumors, in particular high-grade tumors. Moreover, we discovered a strong correlation between *EVL* expression and actin density in human tumors; highly invasive tumors are characterized by low *EVL* expression and low actin density. More importantly, lower levels of *EVL* correlate with poor prognosis and higher mortality in patients. Our analyses demonstrate that *EVL* is a significant independent biomarker of invasiveness and tumor grade, and could be predictive of prognosis.

Downregulation of *EVL* has also been implicated in progression of other epithelial tumors. In two large-scale studies investigating genetic and epigenetic alterations in colon cancer, DNA methylation of *EVL* was frequently observed and correlated with poor prognosis (Grady et al., 2008; Yi et al., 2011). Consistent with these studies, we found that *PFN2* and *EVL* KD enhance protrusive activity in colorectal carcinoma Caco-2 cells. This suggests that downregulation of *EVL* might be a common feature of more aggressive tumors in multiple types of cancer. Paradoxically, a previous study has shown that *EVL* mRNA levels are correlated positively with clinical stage (Hu et al., 2008); however the number of tumors analyzed therein was very low (i.e., three stage III tumors) and neither invasiveness nor tumor grade were assessed in the context of *EVL* expression.

Low *PFN2* expression has been reported to be associated with poor prognosis in a study of 88 patients with oral squamous cell carcinomas (Ma et al., 2011). In breast adenocarcinomas, we found that both high and low levels of *PFN2* expression correlate with poor prognosis in two major clinical studies including data from 495 patients followed over the course of 15 years. This dichotomous correlation of profilin-2 expression with outcome may reflect differences in the phenotypic effects of profilin-2 interactions with distinct binding partners. For example, in tumors that express *EVL*, profilin-2 could suppress invasive activity, whereas in tumors with low *EVL* expression, profilin-2 could promote invasive behavior through interactions with other actin polymerization regulators, such as formins (Figure 8I). This may explain why profilin-2 alone does not serve as a significant biomarker of outcome, whereas EVL, which may have more specialized activities that suppress invasion, serves as a better biomarker. More generally, this highlights how differences in expression of a given protein in tumors can lead to distinct outcomes depending on the expression of collaborating proteins. Thus, the assessment of certain biomarkers of clinical outcome may require analysis of interacting proteins that together regulate a biological process.

EXPERIMENTAL PROCEDURES

Quantitation of Intracellular Concentration of Profilin-1 and Profilin-2

Total protein concentration was measured in MCF10A, SUM159, and MDA231 cells using purified profilin-1 and profilin-2 as standards (see Supplemental Experimental Procedures).

Kymography Analysis

Kymographs were generated in Nikon Elements along the axis of protrusion/retraction, perpendicular to the cell membrane. Minimum intensity projections were used to determine the areas of high membrane dynamics. Average velocity and frequency of retractions and protrusions, as well as the percent of time the membrane spent retracting, protruding, or resting, were calculated. Persistence (the average duration of protrusion) was also calculated for all conditions, but it was discussed in Results only when significant.

Analytical Ultracentrifugation

We determined the solution molecular weight of monomeric hVASP and EVL in the presence of human profilin-1 and mouse profilin-2a using sedimentation equilibrium analytical ultracentrifugation. Samples containing 5 μM Cy3-hVASP1-240aa or Cy3-mEVL1-235aa were combined with 20–40 μM human profilin-1 and/or mouse profilin-2a. A buffer composition of 10 mM HEPES (pH 7.5), 50 mM KCl, and 1 mM TCEP was used for all experiments. Proteins were centrifuged until they reached equilibrium at three different speeds (e.g., 10,000, 14,000, and, 20,000 rpm) in a Beckman Coulter XL-I ultracentrifuge. The sedimentation profile of Cy3-VASP and Cy3-EVL was determined by monitoring the absorbance at 550 nm (Cy3 fluorophore) every 2 hr. Global fitting of three equilibrium traces for each condition was performed using NIH Sedphit and Sedphat software. An extinction coefficient of 150,000 $M^{-1}cm^{-1}$ (Cy3, 550 nm) was used to determine the protein concentration as a function of the radial position. Using a monomer-dimer model, we determined the molecular weight for a single ideal species. Proteins were purified and characterized as previously described (Hansen and Mullins, 2010). See Supplemental Experimental Procedures for determination of equilibrium dissociation constants.

Single Actin Filament TIRF Assays

Biotin pegylated TIRF-M imaging chambers used for the visualization of single actin filament polymerization kinetics were generated as previously described by Hansen and Mullins (2010) and Bieling et al. (2010). See Supplemental Experimental Procedures for details.

SUM159 Tumor Model

A total of 10^6 SUM159 cells resuspended in 30 μl Matrigel were injected into the fat pad of 6- to 8 week-old female NOD/SCID Balb/C mice. Three independent experiments were performed; the first and the second experiment consisted of injections of five mice per group in each, and the third experiment consisted of injections of ten mice per group. For invasion analysis, tumors were collected at 8 to 10 weeks. Invasive foci were defined as clusters of tumor cells outside the margin of the tumor. Invasion was quantified in nine control, ten *PFN1* KD, and ten *PFN2* KD tumors, which account for all tumors of similar size and incubation time. (See Supplemental Experimental Procedures for the experimental procedure using to generate and induce the *EVL* KD tumors.) All experiments were performed according to the guidelines of the IACUC committee of Harvard Medical School.

Analysis Human Tumor Array

Tumor grade is obtained from the patient pathology report associated with each sample. Protein expression was assessed based on a visual scale ranging from 1 (lowest) to 5 (highest), in triplicate (array#1, 65 patients) or duplicate (array#2, 48 patients) sections from each patient; each analysis was performed in a blinded fashion by at least two different individuals. Human samples used in our studies are exempt from informed consent.

SUPPLEMENTAL INFORMATION

Supplemental Information includes eight figures, eight movies, and Supplemental Experimental Procedures and can be found with this article online at http://dx.doi.org/10.1016/j.ccr.2012.09.027.

ACKNOWLEDGMENTS

We thank James Bui and Wa Xian for technical assistance; Rachel Davidowitz, Taru Muranen, and Scott Valastyan for their blinded analysis of the human tumor tissue arrays; the Nikon Imaging Center, particularly Jennifer Waters and Wendy Salmon; and the Rodent Histopathology Core Facility, particularly Roderick Bronson. This work was funded by the Breast Cancer Research Foundation, the NIGMS Cell Migration Consortium, a gift from the Lee Jeans Foundation through the Entertainment Industry Foundation (to J.S.B.); NIH Grant P01 HL059561 (to J.H.H.); NIH Grant ROI #GM61010, UCSF/UC Berkeley Nanomedicine Development Center and the National Science Foundation (to R.D.M. and S.D.H.); and NIH #GM58801 (to F.B.G.).

Received: June 25, 2012
Revised: September 6, 2012
Accepted: September 28, 2012
Published: November 12, 2012

REFERENCES

Bae, Y.H., Ding, Z., Zou, L., Wells, A., Gertler, F., and Roy, P. (2009). Loss of profilin-1 expression enhances breast cancer cell motility by Ena/VASP proteins. J. Cell. Physiol. *219*, 354–364.

Bear, J.E., and Gertler, F.B. (2009). Ena/VASP: towards resolving a pointed controversy at the barbed end. J. Cell Sci. *122*, 1947–1953.

Bieling, P., Telley, I.A., Hentrich, J., Piehler, J., and Surrey, T. (2010). Fluorescence microscopy assays on chemically functionalized surfaces for quantitative imaging of microtubules, motors, and + TIP dynamics. Methods Cell Biol. *95*, 549–574.

Breitsprecher, D., Kiesewetter, A.K., Linkner, J., Vinzenz, M., Stradal, T.E., Small, J.V., Curth, U., Dickinson, R.B., and Faix, J. (2011). Molecular mechanism of Ena/VASP-mediated actin-filament elongation. EMBO J. *30*, 456–467.

Debnath, J., and Brugge, J.S. (2005). Modelling glandular epithelial cancers in three-dimensional cultures. Nat. Rev. Cancer *5*, 675–688.

DesMarais, V., Ghosh, M., Eddy, R., and Condeelis, J. (2005). Cofilin takes the lead. J. Cell Sci. *118*, 19–26.

Desmedt, C., Piette, F., Loi, S., Wang, Y., Lallemand, F., Haibe-Kains, B., Viale, G., Delorenzi, M., Zhang, Y., d'Assignies, M.S., et al; TRANSBIG Consortium. (2007). Strong time dependence of the 76-gene prognostic signature for node-negative breast cancer patients in the TRANSBIG multicenter independent validation series. Clin. Cancer Res. *13*, 3207–3214.

Di Nardo, A., Gareus, R., Kwiatkowski, D., and Witke, W. (2000). Alternative splicing of the mouse profilin II gene generates functionally different profilin isoforms. J. Cell Sci. *113*, 3795–3803.

Ferron, F., Rebowski, G., Lee, S.H., and Dominguez, R. (2007). Structural basis for the recruitment of profilin-actin complexes during filament elongation by Ena/VASP. EMBO J. *26*, 4597–4606.

Fischer, R.S., Gardel, M., Ma, X., Adelstein, R.S., and Waterman, C.M. (2009). Local cortical tension by myosin II guides 3D endothelial cell branching. Curr. Biol. *19*, 260–265.

Friedl, P., and Wolf, K. (2010). Plasticity of cell migration: a multiscale tuning model. J. Cell Biol. *188*, 11–19.

Gertler, F.B., Niebuhr, K., Reinhard, M., Wehland, J., and Soriano, P. (1996). Mena, a relative of VASP and Drosophila Enabled, is implicated in the control of microfilament dynamics. Cell *87*, 227–239.

Grady, W.M., Parkin, R.K., Mitchell, P.S., Lee, J.H., Kim, Y.H., Tsuchiya, K.D., Washington, M.K., Paraskeva, C., Willson, J.K., Kaz, A.M., et al. (2008). Epigenetic silencing of the intronic microRNA hsa-miR-342 and its host gene EVL in colorectal cancer. Oncogene *27*, 3880–3888.

Hansen, S.D., and Mullins, R.D. (2010). VASP is a processive actin polymerase that requires monomeric actin for barbed end association. J. Cell Biol. *191*, 571–584.

Honoré, B., Madsen, P., Andersen, A.H., and Leffers, H. (1993). Cloning and expression of a novel human profilin variant, profilin II. FEBS Lett. *330*, 151–155.

Hu, L.D., Zou, H.F., Zhan, S.X., and Cao, K.M. (2008). EVL (Ena/VASP-like) expression is up-regulated in human breast cancer and its relative expression level is correlated with clinical stages. Oncol. Rep. *19*, 1015–1020.

Insall, R.H., and Machesky, L.M. (2009). Actin dynamics at the leading edge: from simple machinery to complex networks. Dev. Cell *17*, 310–322.

Ivshina, A.V., George, J., Senko, O., Mow, B., Putti, T.C., Smeds, J., Lindahl, T., Pawitan, Y., Hall, P., Nordgren, H., et al. (2006). Genetic reclassification of histologic grade delineates new clinical subtypes of breast cancer. Cancer Res. *66*, 10292–10301.

Jockusch, B.M., Murk, K., and Rothkegel, M. (2007). The profile of profilins. Rev. Physiol. Biochem. Pharmacol. *159*, 131–149.

Kursula, P., Kursula, I., Massimi, M., Song, Y.H., Downer, J., Stanley, W.A., Witke, W., and Wilmanns, M. (2008). High-resolution structural analysis of mammalian profilin 2a complex formation with two physiological ligands: the formin homology 1 domain of mDia1 and the proline-rich domain of VASP. J. Mol. Biol. *375*, 270–290.

Lambrechts, A., Verschelde, J.L., Jonckheere, V., Goethals, M., Vandekerckhove, J., and Ampe, C. (1997). The mammalian profilin isoforms display complementary affinities for PIP2 and proline-rich sequences. EMBO J. *16*, 484–494.

Lambrechts, A., Kwiatkowski, A.V., Lanier, L.M., Bear, J.E., Vandekerckhove, J., Ampe, C., and Gertler, F.B. (2000). cAMP-dependent protein kinase phosphorylation of EVL, a Mena/VASP relative, regulates its interaction with actin and SH3 domains. J. Biol. Chem. *275*, 36143–36151.

Loi, S., Haibe-Kains, B., Desmedt, C., Lallemand, F., Tutt, A.M., Gillet, C., Ellis, P., Harris, A., Bergh, J., Foekens, J.A., et al. (2007). Definition of clinically distinct molecular subtypes in estrogen receptor-positive breast carcinomas through genomic grade. J. Clin. Oncol. *25*, 1239–1246.

Lu, X., Lu, X., Wang, Z.C., Iglehart, J.D., Zhang, X., and Richardson, A.L. (2008). Predicting features of breast cancer with gene expression patterns. Breast Cancer Res. Treat. *108*, 191–201.

Ma, C.Y., Zhang, C.P., Zhong, L.P., Pan, H.Y., Chen, W.T., Wang, L.Z., Andrew, O.W., Ji, T., and Han, W. (2011). Decreased expression of profilin-2 in oral squamous cell carcinoma and its clinicopathological implications. Oncol. Rep. *26*, 813–823.

Mahoney, N.M., Janmey, P.A., and Almo, S.C. (1997). Structure of the profilin-poly-L-proline complex involved in morphogenesis and cytoskeletal regulation. Nat. Struct. Biol. *4*, 953–960.

Miki, H., Suetsugu, S., and Takenawa, T. (1998). WAVE, a novel WASP-family protein involved in actin reorganization induced by Rac. EMBO J. *17*, 6932–6941.

Minn, A.J., Gupta, G.P., Siegel, P.M., Bos, P.D., Shu, W., Giri, D.D., Viale, A., Olshen, A.B., Gerald, W.L., and Massagué, J. (2005). Genes that mediate breast cancer metastasis to lung. Nature *436*, 518–524.

Muthuswamy, S.K., Li, D., Lelievre, S., Bissell, M.J., and Brugge, J.S. (2001). ErbB2, but not ErbB1, reinitiates proliferation and induces luminal repopulation in epithelial acini. Nat. Cell Biol. *3*, 785–792.

Nakamura, F., Stossel, T.P., and Hartwig, J.H. (2011). The filamins: organizers of cell structure and function. Cell Adhes. Migr. *5*, 160–169.

Neve, R.M., Chin, K., Fridlyand, J., Yeh, J., Baehner, F.L., Fevr, T., Clark, L., Bayani, N., Coppe, J.P., Tong, F., et al. (2006). A collection of breast cancer cell lines for the study of functionally distinct cancer subtypes. Cancer Cell *10*, 515–527.

Nodelman, I.M., Bowman, G.D., Lindberg, U., and Schutt, C.E. (1999). X-ray structure determination of human profilin II: A comparative structural analysis of human profilins. J. Mol. Biol. *294*, 1271–1285.

Petersen, O.W., Rønnov-Jessen, L., Howlett, A.R., and Bissell, M.J. (1992). Interaction with basement membrane serves to rapidly distinguish growth and differentiation pattern of normal and malignant human breast epithelial cells. Proc. Natl. Acad. Sci. USA *89*, 9064–9068.

Pollard, T.D., and Borisy, G.G. (2003). Cellular motility driven by assembly and disassembly of actin filaments. Cell *112*, 453–465.

Reinhard, M., Giehl, K., Abel, K., Haffner, C., Jarchau, T., Hoppe, V., Jockusch, B.M., and Walter, U. (1995). The proline-rich focal adhesion and microfilament protein VASP is a ligand for profilins. EMBO J. *14*, 1583–1589.

Schmidt, M., Böhm, D., von Törne, C., Steiner, E., Puhl, A., Pilch, H., Lehr, H.A., Hengstler, J.G., Kölbl, H., and Gehrmann, M. (2008). The humoral immune system has a key prognostic impact in node-negative breast cancer. Cancer Res. *68*, 5405–5413.

Sanz-Moreno, V., Gadea, G., Ahn, J., Paterson, H., Marra, P., Pinner, S., Sahai, E., and Marshall, C.J. (2008). Rac activation and inactivation control plasticity of tumor cell movement. Cell *135*, 510–523.

Sanz-Moreno, V., Gaggioli, C., Yeo, M., Albrengues, J., Wallberg, F., Viros, A., Hooper, S., Mitter, R., Féral, C.C., Cook, M., et al. (2011). ROCK and JAK1 signaling cooperate to control actomyosin contractility in tumor cells and stroma. Cancer Cell *20*, 229–245.

Sheetz, M.P., Sable, J.E., and Döbereiner, H.G. (2006). Continuous membrane-cytoskeleton adhesion requires continuous accommodation to lipid and cytoskeleton dynamics. Annu. Rev. Biophys. Biomol. Struct. *35*, 417–434.

Simpson, K.J., Selfors, L.M., Bui, J., Reynolds, A., Leake, D., Khvorova, A., and Brugge, J.S. (2008). Identification of genes that regulate epithelial cell migration using an siRNA screening approach. Nat. Cell Biol. *10*, 1027–1038.

van de Vijver, M.J., He, Y.D., van't Veer, L.J., Dai, H., Hart, A.A., Voskuil, D.W., Schreiber, G.J., Peterse, J.L., Roberts, C., Marton, M.J., et al. (2002). A gene-expression signature as a predictor of survival in breast cancer. N. Engl. J. Med. *347*, 1999–2009.

Veniere, S., Ampe, C., Vandekerckhove, J., and Lambrechts, A. (2009). The interaction of proline-rich ligands with profilin probed with an enzyme-linked immunosorbent assay. J. Biomol. Screen. *14*, 350–359.

Witke, W. (2004). The role of profilin complexes in cell motility and other cellular processes. Trends Cell Biol. *14*, 461–469.

Witke, W., Podtelejnikov, A.V., Di Nardo, A., Sutherland, J.D., Gurniak, C.B., Dotti, C., and Mann, M. (1998). In mouse brain profilin I and profilin II associate with regulators of the endocytic pathway and actin assembly. EMBO J. *17*, 967–976.

Witt, A.E., Hines, L.M., Collins, N.L., Hu, Y., Gunawardane, R.N., Moreira, D., Raphael, J., Jepson, D., Koundinya, M., Rolfs, A., et al. (2006). Functional proteomics approach to investigate the biological activities of cDNAs implicated in breast cancer. J. Proteome Res. *5*, 599–610.

Yi, J.M., Dhir, M., Van Neste, L., Downing, S.R., Jeschke, J., Glöckner, S.C., de Freitas Calmon, M., Hooker, C.M., Funes, J.M., Boshoff, C., et al. (2011). Genomic and epigenomic integration identifies a prognostic signature in colon cancer. Clin. Cancer Res. *17*, 1535–1545.

Zou, L., Jaramillo, M., Whaley, D., Wells, A., Panchapakesa, V., Das, T., and Roy, P. (2007). Profilin-1 is a negative regulator of mammary carcinoma aggressiveness. Br. J. Cancer *97*, 1361–1371.

Cancer Cell
Article

Loss of the Par3 Polarity Protein Promotes Breast Tumorigenesis and Metastasis

Luke Martin McCaffrey,[1,*] JoAnne Montalbano,[2] Constantina Mihai,[1] and Ian G. Macara[3]
[1]Rosalind and Morris Goodman Cancer Research Centre, Department of Oncology, McGill University, Montreal H3A 1A3, Canada
[2]Department of Microbiology, University of Virginia School of Medicine, University of Virginia, Charlottesville, VA 22908, USA
[3]Department of Cell and Developmental Biology, Vanderbilt University Medical Center, Nashville, TN 37232, USA
*Correspondence: luke.mccaffrey@mcgill.ca
http://dx.doi.org/10.1016/j.ccr.2012.10.003

SUMMARY

Loss of epithelial organization is a hallmark of carcinomas, but whether polarity regulates tumor growth and metastasis is poorly understood. To address this issue, we depleted the *Par3* polarity gene by RNAi in combination with oncogenic Notch or Ras^{61L} expression in the murine mammary gland. Par3 silencing dramatically reduced tumor latency in both models and produced invasive and metastatic tumors that retained epithelial marker expression. Par3 depletion was associated with induction of MMP9, destruction of the extracellular matrix, and invasion, all mediated by atypical PKC-dependant JAK/Stat3 activation. Importantly, Par3 expression is significantly reduced in human breast cancers, which correlates with active aPKC and Stat3. These data identify Par3 as a regulator of signaling pathways relevant to invasive breast cancer.

INTRODUCTION

Most solid tumors arise from epithelial cells that have acquired changes in proliferative and organizational capacity. Epithelial cells form characteristic intercellular adhesions and possess apical-basal polarity, which is lost in some invasive and metastatic cancers in a process related to the epithelial-mesenchymal transitions (EMTs) that occur during development (Thiery et al., 2009). However, in many cases, epithelial features are retained. How epithelial tissues establish their organization in a normal state and how this organization is disrupted during cancer progression are still not well understood. In particular, it is largely unknown if the cell polarity machinery is perturbed during tumorigenesis and if such disruptions promote metastasis.

Many of the polarity protein complexes localize to distinct domains within the plasma membrane. The Par genes (Par1, Par3, Par4, Par5, Par6, and atypical PKC [aPKC]) encode an evolutionarily conserved group of polarity proteins that play key roles in many aspects of cell polarization (Goldstein and Macara, 2007). To date and to our knowledge, only Par4, a protein kinase also known as LKB1, has been identified as a tumor suppressor (Jansen et al., 2009), and it remains uncertain if tumorigenesis in patients with mutant LKB1 is caused by loss of its polarity function.

We have focused on Par3, a multidomain scaffolding protein required for the spatial organization of several important signaling proteins (Goldstein and Macara, 2007). Par3 is essential for the delivery of aPKC to the apical surface (Harris and Peifer, 2005; McCaffrey and Macara, 2009), through binding of Par3 to the adaptor protein Par6, which forms a constitutive complex with aPKC. Furthermore, aPKC can interact directly with Par3, which is essential for apical aPKC localization and epithelial organization (Horikoshi et al., 2009; McCaffrey and Macara, 2009). Loss of aPKC from the apical cortex causes spindle pole orientation defects and epithelial mis-organization (Hao et al., 2010). Both the level of aPKC expression and mislocalization correlate with increased invasion and metastasis in breast cancer (Kojima et al., 2008). However, to our knowledge, whether loss of Par3 has a role in regulating aPKC during tumorigenesis is unknown.

Some proteins have oncogenic activity when overexpressed. The Notch receptor, an important transcriptional regulator of stem cell fate, is activated by proteolytic cleavage to release an intracellular domain (NICD), which is found at elevated levels

Significance

Although loss of cell polarity is often considered a hallmark of invasive cancers, there is little experimental evidence for any role of the polarity machinery in tumor suppression. Here, we demonstrate that Par3 polarity protein expression is frequently lost in human breast cancers. In the context of different oncogenes, loss of Par3 increases primary tumor growth and metastatic colonization of the lungs through the production of MMP9 downstream of Jak/Stat3 signaling, which is responsible for the invasive behavior of the tumors. We find that expression of Par3 is anticorrelated with phospho-aPKC, phospho-JAK, phospho-Stat3, and MMP9 expression in human breast cancers, establishing Par3 as a potent tumor growth and invasion suppressor.

in up to 50% of human breast cancers (Pece et al., 2004); and mammary-specific expression of NICD in mice induces breast tumors, though with no metastasis (Hu et al., 2006). Additionally, enhanced growth factor receptor signaling promotes breast cancer. A central effector of growth factor receptor signaling is the Ras oncogene, which, although rarely mutated in breast cancer, is frequently hyperactivated (Clark and Der, 1995). Elevated expression of Neu/ErbB2 or Met receptors is observed in 20%–30% and 15%–20% of breast cancers, respectively, and can inappropriately stimulate Ras-mediated signaling pathways (Reese and Slamon, 1997; Ponzo and Park, 2010).

Progression of in situ breast carcinomas to metastatic disease requires additional steps, and it is now established that inflammation is necessary for this process (Grivennikov and Karin, 2008). Stat3 has a central role in regulating inflammation in breast cancer through a cytokine loop involving IL-6 (Grivennikov and Karin, 2008; Schafer and Brugge, 2007). Stat3 is Tyr phosphorylated by Src or JAK kinases, which induces translocation to the nucleus. Stat3 can be hyperactivated in breast cancers, which promotes invasion and metastasis, although Stat3 activation alone is insufficient to induce tumorigenesis (Barbieri et al., 2010b; Ranger et al., 2009). Therefore, many of the processes that drive tumorigenesis and metastasis are separable, but how they relate to tissue organization is not well understood.

The goal of this study was to determine the role of the apical-basal cell polarity machinery in tumorigenesis, with a focus on the Par3 polarity protein. Using a mouse mammary transplant model coupled with lentiviral transduction, we silenced Par3 expression in the context of two different oncogenes and determined whether loss of Par3 drives tumor growth and/or metastasis. The expression of Par3 was also examined in human breast cancers.

RESULTS

Loss of Par3 Cooperates with NICD to Promote Tumorigenesis

We used lentiviral RNAi to deplete Par3 from primary mammary epithelial cells (MECs) and transplanted them orthotopically into the inguinal (#4) mammary fat pads of syngeneic mice. Previously, we reported that Par3-depleted mammary progenitor cells form disorganized ductal outgrowths that resemble early ductal carcinoma in situ (DCIS) (McCaffrey and Macara, 2009). However, over a period of 24–37 weeks post-transplantation, Par3 depletion did not lead to tumor formation (Figure 1A), suggesting that Par3 is not a classical tumor suppressor. Next, we asked whether loss of Par3 might enhance tumorigenesis in the context of an oncogene. We initially used NICD, which is upregulated in ~50% of human breast cancers (Pece et al., 2004) and drives tumor formation in mice after a latency of ~9 months (Hu et al., 2006). Primary MECs isolated from C3H mice were transduced with lentivirus that expresses active, myc-tagged NICD plus small hairpin RNAs (shRNAs) to either Luciferase (control) or murine Par3, using Par3 shRNA that we had validated previously (McCaffrey and Macara, 2009). We refer to the transduced MECs as NICD/shLuc and NICD/shPar3, respectively. For each animal, 10,000 NICD/shLuc or NICD/shPar3 MECs were injected into contralateral inguinal (#4) fat pads of the same mouse. Immunoblots of tissue lysates showed that myc-NICD was expressed in the tumors and that Par3 silencing was efficient (Figure 1B).

Strikingly, loss of Par3 caused a dramatic reduction in tumor latency for NICD-transduced MECs, with 50% of NICD/shPar3 animals developing tumors by 18 weeks (Figure 1A). We confirmed that tumors were derived from cells expressing both NICD and shPar3 by imaging the GFP marker for the RNAi lentivirus and by staining for myc-NICD (Figures 1C and 1D).

We transplanted NICD/shLuc and NICD/shPar3 MECs into opposite sides of the same mouse, and palpable NICD/shLuc tumors were rarely formed when mice were sacrificed due to the NICD/shPar3 tumor burden. However, in some cases, small NICD/shLuc tumors were found by microscopic examination of the mammary fat pads (Figure 1D). Consistently, all tumors were GFP positive, and tumors derived from NICD/shPar3 MECs were much larger than those from the NICD/shLuc MECs (Figure 1D). Moreover, whereas NICD/shLuc tumors possessed well-defined boundaries, the loss of Par3 induced a more invasive phenotype, with cells protruding into the surrounding fat pad (Figure 1E). Both types of tumors retained epithelial characteristics, including expression of cytokeratin 8, E-cadherin at intercellular junctions and the tight junction marker ZO1 at apicolateral boundaries surrounding microlumens (Figures 1E and 1F). We further examined cellular organization by staining tumor sections for cytokeratin 8 (K8) and cytokeratin 14 (K14). In normal murine mammary ducts, K14 is expressed in myoepithelial cells, whereas K8 is restricted to luminal cells (see Figure S1 available online). Loss of Par3 increased tumor cell heterogeneity in our NICD model (Figures 1E, 1F, and S1). NICD/shLuc tumors were homogeneous and predominantly $K8^{+}K14^{moderate}$, but the NICD/shPar3 tumors displayed a substantially greater degree of cellular diversity.

Loss of Par3 Cooperates with Oncogenic H-Ras to Promote Tumorigenesis

To determine if the promotion of tumor growth by loss of Par3 is specific to NICD or is of more general importance, we asked if Par3 depletion cooperates with a different oncogene, $H\text{-}Ras^{61L}$. Knockdown of Par3 in conjunction with oncogenic GFP-tagged Ras^{61L} significantly reduced tumor latency compared to GFP-Ras^{61L} alone (Figure 2A). Palpable Ras^{61L}/shPar3 tumors had an average latency of 114 ± 68 days compared to Ras^{61L}/shLuc, which had a latency of >230 days. By 37 weeks, 92% of Ras^{61L}/shLuc transplant mice remained tumor-free compared to 54% Ras^{61L}/shPar3 transplant mice (Figure 2A). We confirmed comparable Ras expression levels and efficient Par3 knockdown by immunoblotting tumor lysates (Figure 2B).

Although both Ras^{61L}/shLuc and Ras^{61L}/shPar3 tumors expressed GFP and were able to grow to comparable sizes (Figure 2C), Ras^{61L}/shPar3 tumors grew more rapidly and were consistently more aggressive than Ras^{61L}/shLuc tumors; they invaded through the peritoneum, with the bulk of the tumors growing inside the body cavity, and were not detected during palpation (Figure S2A). Additionally, ~30% of the Ras^{61L}/shPar3 tumors invaded through the skin (data not shown). Consistent with these differences in invasiveness, Ras^{61L}/shLuc tumors were more organized and retained regions that possessed a lobular organization with distinct boundaries, whereas Ras^{61L}/shPar3 tumors exhibited no discernable organization,

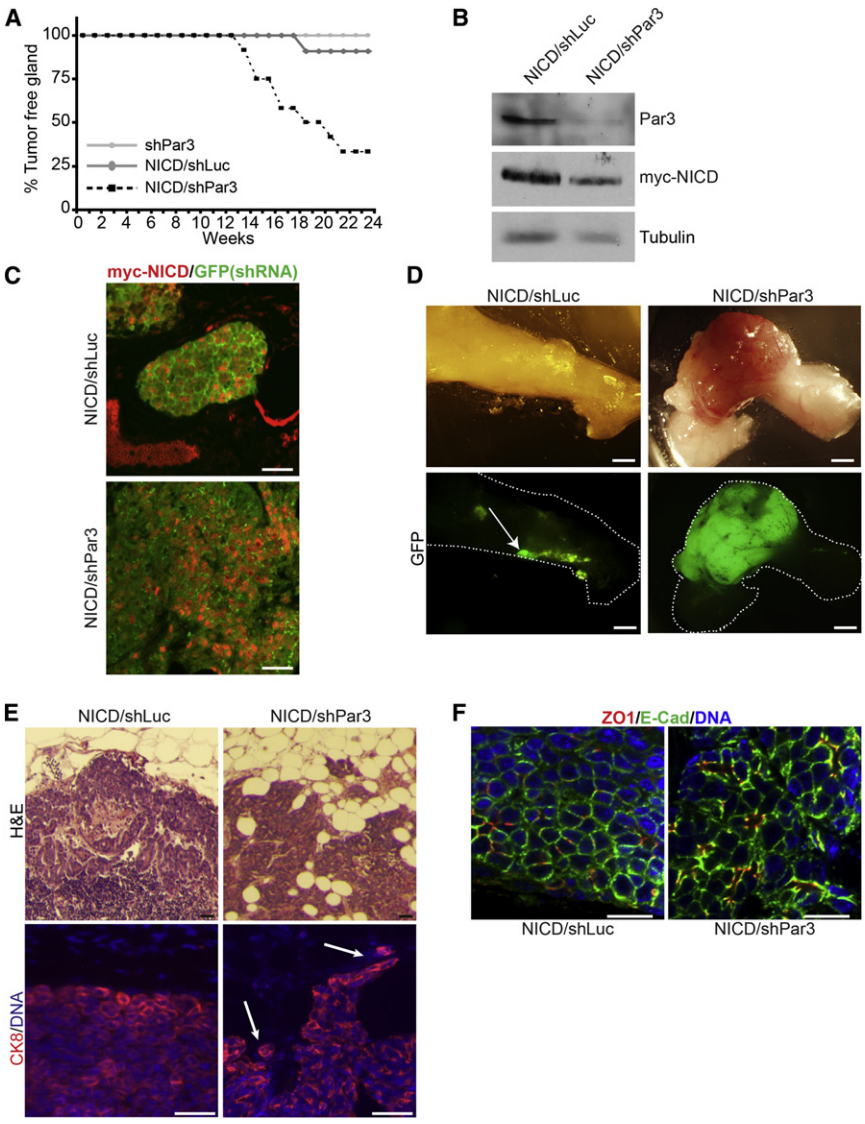

Figure 1. Loss of Par3 Cooperates with NICD to Promote Mammary Tumor Formation

(A) Kaplan-Meier (KM) curve of tumor-free status in mice transplanted with shPar3 (n = 17), NICD/shLuc (n = 11), or NICD/shPar3 (n = 12) MECs.

(B) Tumors arising from orthotopically transplanted myc-NICD/shLuc or myc-NICD/shPar3 MECs were immunoblotted for Par3, myc-NICD, and tubulin.

(C) Immunofluorescence staining of tumor sections for myc-NICD (red) and GFP (green), which marks cells expressing shRNA.

(D) Tumors arising from NICD/shLuc or NICD/shPar3-transduced MECs. GFP is coexpressed with the shRNA and is used as a marker for transduction. Arrow indicates small nonpalpable NICD/shLuc tumors, which were found in 7 of 11 fat pads.

(E) Upper panels show hematoxylin and eosin-stained (H&E) sections of the edges of NICD/shLuc and NICD/shPar3 tumors. Lower panels present tissue sections of the tumor edge stained with CK8 (red) and Hoechst 33258 (DNA, blue). Arrows show invading cells.

(F) Immunofluorescence staining of tumor sections for E-cadherin, ZO1, and Hoechst 33342 for DNA. Scale bars, 50 μm (C), 2 mm (D), 100 μm (E), and 20 μm (F).

See also Figure S1.

and cells appeared more spindle shaped (Figures 2D and 2E). In contrast, NICD/shPar3 tumors were restricted to the fat pad, with occasional invasion into the peritoneum.

Ras tumors depleted of Par3 retained expression of ZO1, which remained localized at sites of cell-cell contacts marking the boundaries of minilumens (Figure 2D). Unexpectedly, although Ras^{61L} is concentrated at intercellular junctions in the Ras^{61L}/shLuc tumors, loss of Par3 results in the partial redistribution of the oncoprotein into the cytoplasm (Figure 2D, insets), which might have consequences for downstream signaling. The tumors also retained expression of the luminal epithelial marker K8 (Figure 2E), demonstrating that, as with the NICD model, the Ras^{61L} tumor cells are disorganized but retain epithelial characteristics in the absence of Par3. The Ras^{61L}/shLuc tumors also expressed E-cadherin (Figure 2E). In contrast, however, E-cadherin (Figure 2E) and β-catenin (Figure S2B) were almost undetectable in Ras^{61L}/shPar3 tumors. The absence of staining reflects downregulation of expression rather than mislocalization (Figures 2F and S2C). Although Ras^{61L}/shPar3 tumor cells were more spindle shaped, there was no increase in vimentin, a mesenchymal marker (Figure 2F). Thus, loss of Par3, specifically in the context of the Ras oncogene, represses E-cadherin expression, though not the loss of other luminal epithelial markers.

Interestingly, Ras^{61L}/shLuc tumor cells were primarily $K8^+K14^-$, whereas the Ras^{61L}/shPar3 tumors were more heterogeneous, and included $K8^+K14^-$ and $K8^+K14^+$ dual-positive cells (Figure 2E). $K8^+K14^+$ dual-positive cells may be undifferentiated progenitors (Raouf et al., 2008; Shackleton et al., 2006; Villadsen et al., 2007). Together, these data are consistent with our previous identification of a role for Par3 in driving progenitor cell differentiation in the mammary gland (McCaffrey and Macara, 2009). They also indicate that loss of Par3 causes tissue mis-organization rather than a simple loss of apical-basal polarity.

Par3 Acts as an Invasion and Metastasis Suppressor

To determine if loss of Par3 promotes metastasis, we examined the lungs of mice after orthotopic injection of NICD/shLuc or NICD/shPar3 into mammary fat pads. None of the NICD/shLuc mice had lung metastases (n = 14), consistent with published data on NICD transgenic mice (Hu et al., 2006). However, >80% of NICD/shPar3 mice (n = 17) displayed extensive colonization, with an average of 32 colonies visible per lung (Figures 3A and 3B). These values are significantly different (p = 0.0001). Importantly, lung metastases from both NICD/shPar3 and

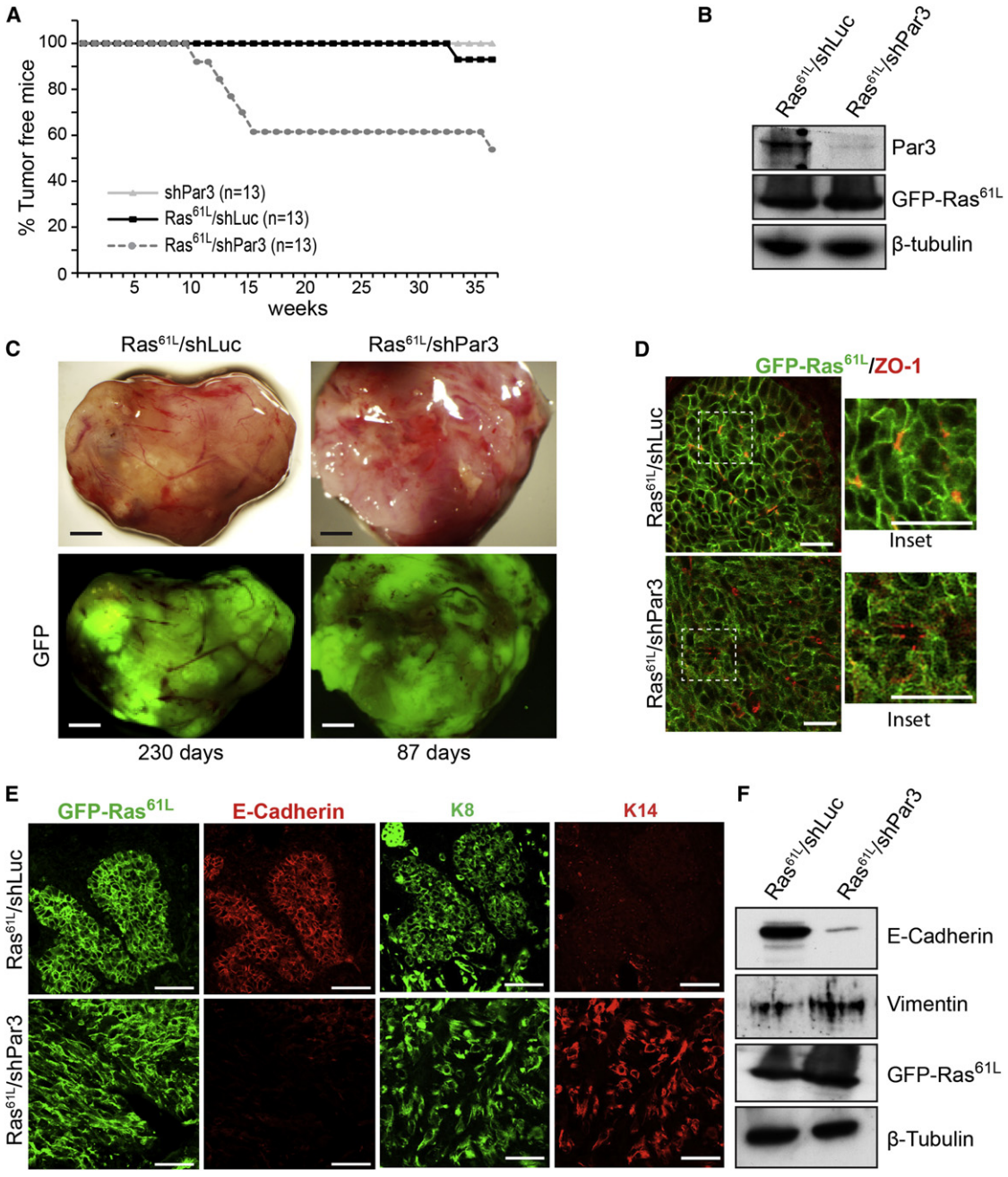

Figure 2. Loss of Par3 Cooperates with Ras^{61L} to Promote Mammary Tumor Formation

(A) KM curve for mice transplanted with MECs expressing GFP/shPar3 (n = 13), Ras^{61L}/shLuc (n = 13), or Ras^{61L}/shPar3 (n = 13).

(B) Immunoblot of primary Ras^{61L}/shLuc and Ras^{61L}/shPar3 tumor lysates.

(C) Micrographs of tumors from transplanted Ras^{61L}/shLuc or Ras^{61L}/shPar3 MECs. GFP indicates tumor cells are transduced with lentivirus.

(D) Immunofluorescence staining of tumor sections for GFP-Ras^{61L} (green) and ZO1 (red).

(E) Immunofluorescence staining of tumor sections for GFP-Ras^{61L} (green) and E-cadherin (red), or CK8 (green) and K14 (red).

(F) Western blot of primary Ras^{61L}/shLuc and Ras^{61L}/shPar3 tumor cell lysates.

Scale bars, 500 μm (C) and 50 μm (D and E).

See also Figure S2.

Ras^{61L}/shPar3 tumors were comprised of similar epithelial cell types as the primary tumors (Figures S3A and S3B). Although Ras^{61L} alone was sufficient to induce metastasis, loss of Par3 increased the number and size of the colonies (Figure S3C).

As a further test of metastatic potential, we injected equal numbers of NICD/shLuc or NICD/shPar3 mammary cells systemically via the tail veins (n = 10), and after 3 weeks, the lungs were sectioned and examined for metastases. In all cases,

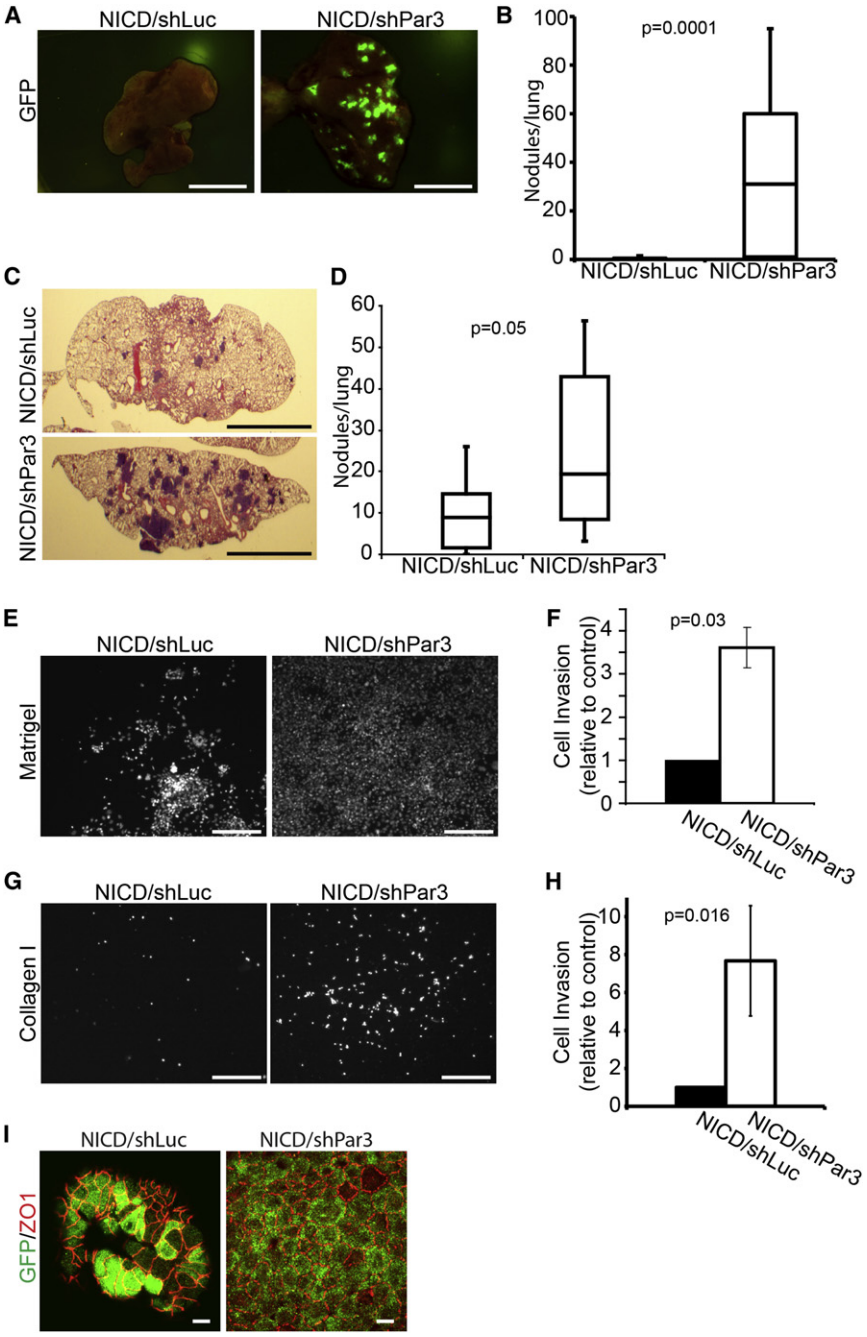

Figure 3. Suppression of Par3 Increases Tumor Invasion and Metastasis

(A) Whole-mount GFP fluorescent images of lung metastases from tumor-bearing mice following orthotopic mammary gland transplants of MECs transduced with NICD/shLuc (n = 14) and NICD/shPar3 (n = 17; p = 0.0001).

(B) Box plots showing the number of metastatic nodules in lungs from (A).

(C) H&E sections of lungs following tail vein injections of 3 × 10^5 MECs transduced with NICD/shLuc or NICD/shPar3.

(D) Box plots showing the number of metastatic nodules in lungs (n = 10) following systemic injections of transduced cells from (C).

(E) Hoechst-stained nuclei of NICD/shLuc or NICD/shPar3 MECs that invaded through the Matrigel pad and 8 μm filter inserts after 72 hr.

(F) Quantification of (E); results are average of three independent experiments. Error bars, 1 SEM.

(G) Same as (E), except invasion through collagen I gels.

(H) Quantification of (G); results are means of three independent experiments. Error bars, SEM.

(I) Immunofluorescence staining of NICD/shLuc or NICD/shPar3 MECs that migrated through the Matrigel for GFP (green) and ZO1 (red).

Scale bars, 1 cm (A and C), 100 μm (E and G), and 10 μm (I).

See also Figure S3.

colonization of the lungs was detected (Figure 3C), but metastases produced by NICD/shPar3 cells were significantly larger and more numerous compared to NICD/shLuc cells (Figure 3D). These results are consistent with increased efficiency of invasion, dissemination, and colonization and support the hypothesis that Par3 normally can suppress metastatic progression.

To further examine the potential for Par3 to suppress tumor invasion, we asked if MECs transduced with or without Par3 shRNA and an oncogene would show increased migration in vitro, using three-dimensional (3D) Matrigel or collagen I invasion assays (Figures 3E–3H, S3D, and S3E). Previously, loss of Par3 has been reported to inhibit cell migration in two-dimensional scratch wound assays (Schmoranzer et al., 2009). The nontransduced cells showed no detectable invasion through Matrigel pads over the time course of the experiment, and silencing of Par3 alone did not enable invasion (data not shown). Expression of either the NICD or Ras^{61L} oncogenes caused a significant number of cells to penetrate through the Matrigel. Strikingly, however, the silencing of Par3 in the context of either oncogene caused a substantial increase in invasion efficiency. Loss of Par3 caused a 3.5-fold (NICD) and 3.9-fold increase (Ras^{61L}) in cells that invaded through the 3D matrix, compared to controls (Figures 3E, 3F, S3D, and S3E). Invasion of NICD cells through collagen I was also stimulated more than 7-fold by loss of Par3 (Figures 3G and 3H).

Although most metastatic carcinomas retain epithelial characteristics, it has been proposed that tumor cells might undergo a transient EMT during dissemination then revert to an epithelial phenotype when they colonize an ectopic site (Guarino et al., 2007). We examined the expression of EMT markers in our cultures and found a modest increase in ZEB1 expression, but no overall changes in gene expression that would indicate a complete EMT (Figure S3F). Interestingly, the NICD/shPar3 cells that had migrated through the matrix to the filter retained

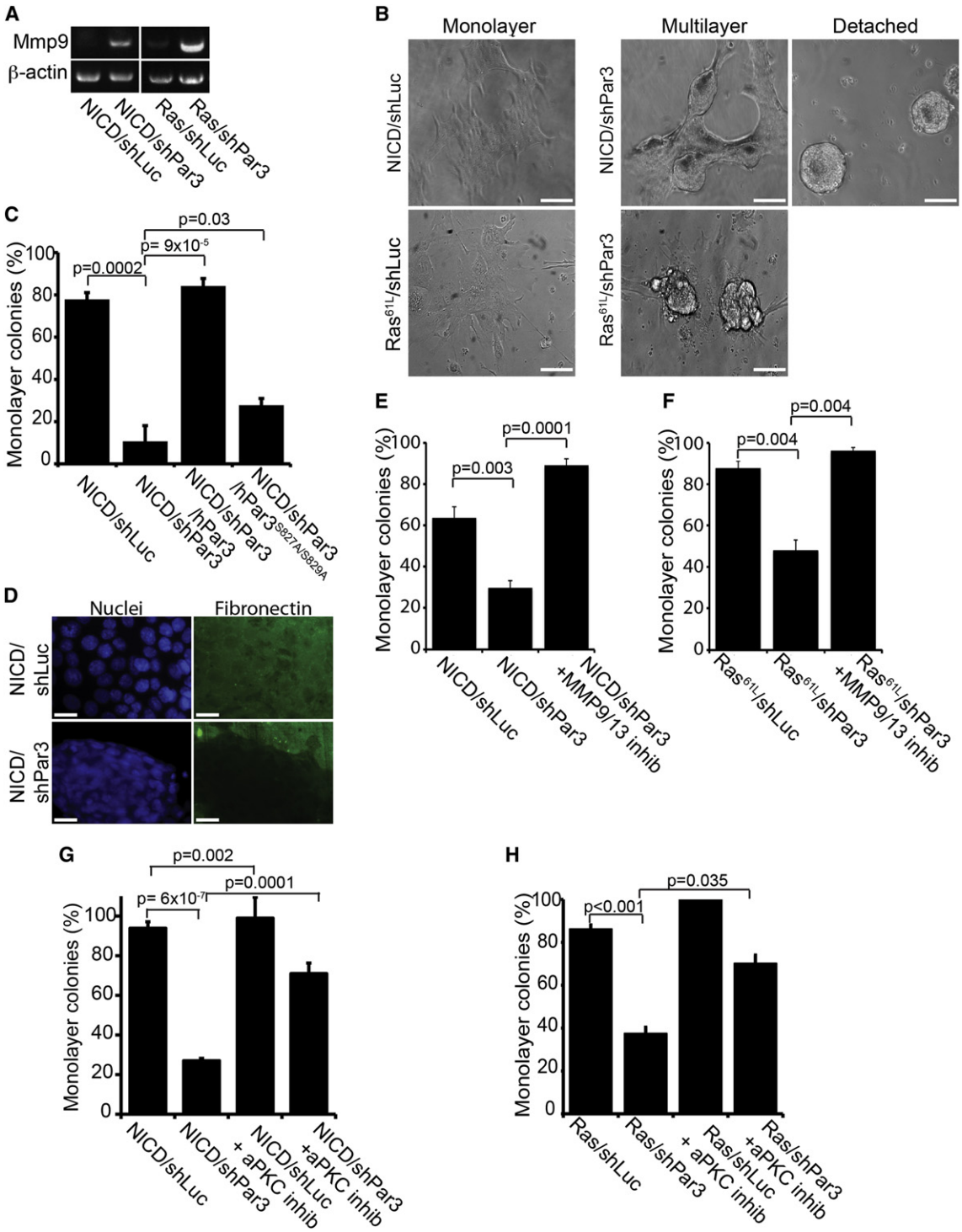

Figure 4. Loss of Par3 Induces MMP Expression and Cell Detachment in Transformed MECs through Activation of aPKC

(A) RT-PCR on total RNA from tumor tissues expressing either NICD or Ras^{61L} with or without shRNA against Par3, using primers for MMP9 and β-actin (control).

(B) Primary MECs stably expressing NICD/shLuc, NICD/shPar3, Ras^{61L}/shLuc, or Ras^{61L}/shPar3 were plated on fibronectin for 72 hr and imaged by DIC. Representative images of the various colony phenotypes are shown. Scale bars, 50 μm.

(C) Quantification of cell detachment by MECs expressing NICD/shLuc, NICD/shPar3, and NICD/shPar3 with RNAi-resistant full-length human Par3, or mutant $Par3^{S827A/S829A}$ that does not bind aPKC.

(D) Immunofluorescent staining of fibronectin under colonies of NICD/shLuc and NICD/shPar3 MECs. Scale bars, 10 μm.

(E) Quantification of cell detachment for NICD/shLuc and NICD/shPar3 MECs with or without 400 pM of MMP inhibitor I.

(F) Quantification of cell detachment for Ras^{61L}/shLuc and Ras^{61L}/shPar3 MECs grown with or without 400 pM MMP9/MMP13 inhibitor I.

expression of the epithelial marker ZO1 (Figure 3I). We conclude that in the context of an activated oncogene, loss of Par3 expression increases invasive behavior, and these cells retain the ability to express epithelial characteristics.

Loss of Par3 Induces MMP Expression and Cell Detachment in Transformed Mammary Cells

Migration through 3D matrices often requires expression of matrix metalloproteinases (MMPs), which degrade the ECM (Rørth, 2009). To test whether loss of Par3, in the context of an oncogene, might alter MMP expression, or expression of other adhesion-related genes, we performed quantitative RT-PCR array analysis of adhesion-related genes on primary NICD/shLuc and NICD/shPar3 MECs in vitro, in the absence of selection. In the context of NICD/shPar3, MMP9 showed the most robust increase in expression over NICD/shLuc, and MMP9 induction was second highest in the Ras model, of all genes analyzed (Tables S1–S4). Changes in MMP9 expression were confirmed by RT-PCR using different primers (Figure 4A). The expression of three other genes was upregulated, and ten genes were reduced in both models (Figure S4A). Expression of other genes differed between the two models, and the expression of some other MMPs was reduced (MMP1a, MMP12, and MMP14 for NICD; and MMP2 and MMP15 for Ras). NICD/shPar3 cells also showed significant decreases in the protease inhibitors, TIMP1 and TIMP2. Therefore, in both models, metalloproteinase expression was altered by Par3 depletion, with MMP9 being the most consistently upregulated gene.

Consistent with induction of MMPs, there was a dramatic change in colony morphology when Par3 expression was suppressed. Most NICD/shLuc cells grew as monolayers on fibronectin-coated dishes (~60%–80%; Figures 4B and 4C). In contrast, only ~10%–30% of NICD/shPar3 cells formed monolayers, with the rest detaching as spheroid colonies after several days' culture (Figure 4B). Importantly, all cultures adhered normally during the first 24–48 hr, demonstrating that maintenance rather than initial adhesive ability of the NICD/shPar3 cells is defective. Moreover, after trypsinization, detached cells were able to readhere to new plates, and again the cells began to detach after 24–48 hr. To determine if loss of Par3 causes defective attachment to specific types of ECM, we also plated cells on collagen I. Whereas ~67% of NICD/shLuc cells grew as monolayer colonies on collagen I, less than 1% of cells lacking Par3 remained as monolayer colonies on collagen I (Figure S4B).

Ras^{61L}-transduced MECs also grew as monolayers, and silencing of Par3 increased multiple layering, whereas detachment occurred as single cells, rather than as multicellular spheroids (Figures 4B, S4C, and S4D). The inability of Ras^{61L}/shPar3 to form spheroids may be due to reduced E-cadherin expression as noted above, which would prevent cells from maintaining intercellular adhesions.

Consistent with the idea that ECM degradation is responsible for cell detachment, staining for fibronectin showed that whereas the ECM was intact beneath cells that express NICD alone, it was absent from patches where clusters of detached NICD/shPar3 cells had formed (Figure 4D). Finally, we asked if MMP activity is required for cell detachment. A MMP inhibitor almost completely blocked detachment induced by Par3 depletion in the context of either NICD or Ras (Figures 4E and 4F). To confirm the involvement of MMP9 in the invasive behavior of the NICD/shPar3 cells, we used shRNA-lentivirus that target the murine MMP9 and transduced them together with the NICD and shPar3 viruses into primary MECs. The two most effective shRNAs (shMMP9-1 and shMMP9-3) significantly reduced invasion through Matrigel (Figures S4E and S4F). The MMP inhibitor also efficiently blocked invasion (Figure S4G). Together, these data identify a mechanism whereby loss of Par3 induces MMP9, which triggers degradation of ECM with consequent cell detachment and increased invasive migration.

Cell Detachment Is Mediated through Inappropriate Activation of aPKC

To confirm that the adhesion defects were caused by loss of Par3, we first performed rescue experiments using shRNA-resistant human Par3, which efficiently restored the ability of cells (85%) to remain attached to the ECM (Figure 4C). Notably, however, a mutant ($Par3^{S827A/S829A}$) that is unable to directly bind and be phosphorylated by aPKC could not rescue the adhesion defects, with only 28% of colonies growing as monolayers (Figure 4C). Next, to determine more directly whether aPKC activity is required for adhesion, we plated cells with or without an aPKC inhibitor. This myristoylated pseudosubstrate peptide penetrates cell membranes and specifically inhibits aPKC isoforms. Inhibition of aPKC completely restored cell-ECM adhesion to NICD/shPar3 and reduced Ras^{61L}/shPar3 multilayering (Figures 4G and 4H).

Our previous work showed that Par3 is required for normal localization of aPKC to the apical surface of luminal epithelial cells (McCaffrey and Macara, 2009). To determine if aPKC is also mislocalized in NICD/shPar3 cells, we stained for aPKC and ZO1. In the NICD/shLuc control, ZO1 and aPKC both formed a tight border around the cells (Figure S4H). Thus, expression of the NICD oncogene alone is not sufficient to disrupt tight junctions and aPKC localization. In contrast, aPKC was completely lost from the apical junctions of Par3-depleted NICD MECs. Cortical ZO1 persisted in Par3-depleted cells but was more punctate (Figure S4H). This result is consistent with our previous studies showing that loss of Par3 negatively affects tight junction formation (Chen and Macara, 2005).

Because inhibiting aPKC can reverse cell detachment, we asked whether aPKC activity was altered in NICD/shPar3 cells. Active aPKC is phosphorylated on T403/T410, and immunoblots of cell lysates for total and p-aPKC revealed a substantial increase in p-$aPKCT^{410}$ levels in NICD/shPar3 cells (Figure 5A, left panels). Thus, in these oncogene-transformed mammary cells, loss of Par3 induces aPKC activation. Notably, however, in normal epithelial cells, although loss of Par3 causes mislocalization of aPKC, it does not alter T410 phosphorylation (Hao et al., 2010).

(G) Quantification of cell detachment for NICD/shLuc and NICD/shPar3 MECs with or without 40 μg/ml of aPKC pseudosubstrate inhibitor.
(H) Detachment of Ras^{61L}/shLuc and Ras^{61L}/shPar3 MECs grown with or without 40 μg/ml aPKC inhibitor.
Results are means of at least three independent cultures. Error bars, ±1 SD.
See also Figure S4 and Tables S1–S4.

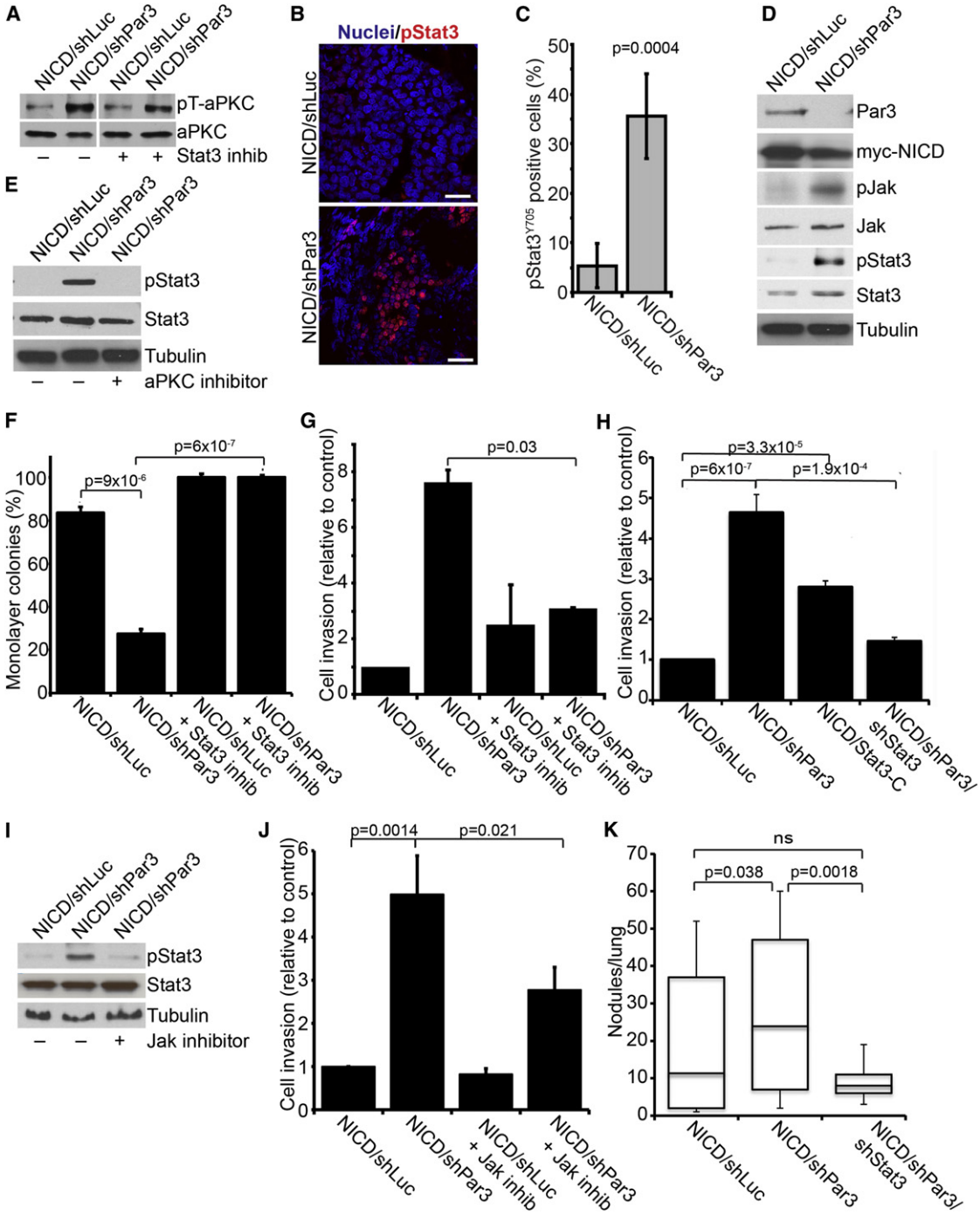

Figure 5. Loss of Par3 Activates Stat3 Signaling through aPKC

(A) Immunoblot of NICD/shLuc and NICD/shPar3 MEC lysates showing active phospho-aPKC$^{T410/403}$ (pT-aPKC) and total aPKC protein levels with or without 50 nM Stat3 inhibitor, Cucurbitacin I.

(B) Immunofluorescence staining of NICD/shLuc or NICD/shPar3 tumor sections for pStat3^{Y705} (red) and nuclei (blue). Scale bars, 50 μm.

(C) Quantification of pStat3^{Y705}-positive cells in tumor sections (n = 8).

(D) Immunoblots of lysates from NICD/shLuc or NICD/shPar3 primary MECs. Phospho-antibodies were used to detect pJAK$^{Y1007/8}$ and pStat3^{Y705}.

(E) Immunoblots of NICD/shLuc or NICD/shPar3 MEC lysates with or without 40 μg/ml aPKC inhibitor.

(F) Quantification of cell detachment for NICD/shLuc and NICD/shPar3 MECs grown with or without 50 nM Cucurbitacin I. Results are from two independent experiments.

(G) Quantification of invasion of NICD/shLuc and NICD/shPar3 MECs through Matrigel with or without 50 nM Cucurbitacin I.

(H) Quantification of invasion of NICD/shLuc, NICD/shPar3, constitutively active Stat3-C, and NICD/shPar3/shStat3 MECs through Matrigel.

(I) Immunoblots of NICD/shLuc or NICD/shPar3 MEC lysates with or without 10 nM JAK inhibitor, Pyridone 6.

Loss of Par3 Activates Stat3 Signaling through aPKC

To determine the mechanism by which Par3 controls adhesion and invasion, we examined potential downstream signaling pathways. Stat3 activation drives MMP expression in multiple cancer cells and promotes invasive behavior (Song et al., 2008; Xie et al., 2004). Active Stat3 is also frequently present at the invasive edge of tumors (Bromberg and Wang, 2009). Therefore, we stained sections from the NICD tumors for phospho-Stat3 (pStat3^{Y705}). Although few cells were pStat3^{Y705} positive in the NICD/shLuc tumors, silencing Par3 increased the number of pStat3^{Y705}-positive cells throughout the tumor mass (Figures 5B and 5C).

In many tumors, Stat3 activation can be induced indirectly through cytokine secretion by infiltrating hematopoietic cells (Yu et al., 2009). To test whether Stat3 activation is intrinsic to NICD/shPar3 epithelial cells, we examined transduced, unselected MECs. Only ~5% of NICD/shLuc cells expressed detectable (but weak) levels of pStat3^{Y705}. Significantly, however, pStat3^{Y705} was present in 18% of NICD/shPar3 MECs, with a higher intensity of staining compared to NICD/shLuc cells (Figures S5A and S5B). Silencing Par3 in Ras^{61L} MECs also caused a substantial increase in pStat3^{Y705}, as judged by immunofluorescence (Figures S5C and S5D). We confirmed that loss of Par3 caused a marked increase in pStat3^{Y705} levels, as determined by immunoblot (Figure 5D). Furthermore, conditioned medium from NICD/shPar3 cultures failed to induce Stat3 activation when added to NICD/shLuc cultures (data not shown). We conclude that Stat3 activation is cell autonomous and does not depend on paracrine cytokine signaling from immune cells.

To determine whether aPKC acts upstream or downstream of Stat3 activation, we inhibited Stat3 and examined aPKC activation by blotting for p-aPKC$^{T403/410}$. aPKC activity was independent of Stat3 activity (Figure 5A). In contrast, treatment of mammary NICD/shPar3 cells with the aPKCps inhibitor diminished pStat3^{Y705} to control levels (Figure 5E), demonstrating that aPKC acts upstream of Stat3 induction.

Because Stat3 can induce MMP expression in some cancer cells, we next tested the effect of a selective Stat3 inhibitor, Cucurbitacin-I (JSI-124), on mammary cell detachment. Cells were treated with 50 nM Cucurbitacin, 24 hr after being plated on ECM, and were examined 48 hr later. Cucurbitacin completely reversed the adhesion defect in NICD/shLuc, NICD/shPar3, Ras^{61L}/shLuc, and in ~80% of Ras^{61L}/shPar3 colonies (Figures 5F and S5E). Moreover, treatment of NICD/shLuc and NICD/shPar3 MECs with Cucurbitacin significantly reduced the invasive potential of the MECs through Matrigel (Figure 5G). In addition, we asked if reducing Stat3 expression could block the effects of Par3 depletion in the invasion of MECs through Matrigel. As shown in Figures 5H and S5F, knockdown of Stat3 significantly reduced the invasiveness of the oncogene-transduced cells that lack Par3. These data suggest that activation of Stat3 is required for the cell detachment and invasive phenotypes caused by loss of Par3.

As a direct test of this hypothesis, we expressed a constitutively active mutant, Stat3-C (Bromberg et al., 1999), in MECs together with NICD or Ras^{61L}. This mutant phenocopied the loss of Par3 by reducing cell attachment and increasing invasion (Figures 5H and S5F). Furthermore, we confirmed that in murine MECs, active Stat3-C also induces MMP9 (Figure S5G).

Jak phosphorylation was also substantially increased by loss of Par3 (Figure 5D). To test whether Jak is upstream of Stat3 activation in Par3-depleted cells, we used a specific Jak inhibitor, Pyridone 6 (Thompson et al., 2002). This inhibitor blocked shPar3-dependent Stat3 activation and significantly reduced invasion of the cells through Matrigel (Figures 5I and 5J).

Importantly, all of the effects on signaling caused by loss of Par3 in the context of oncogenic activation could be fully reversed by expression of a GFP fusion of human Par3 (Figure S5H). GFP-hPar3 did not induce re-expression of the endogenous Par3 but inhibited the phosphorylation of aPKC and Stat3 and blocked the induction of MMP9. Therefore, these signaling responses depend specifically on the loss of Par3 and are not off-target effects of the shRNA.

Finally, to determine whether the induction of Stat3-mediated invasive behavior is significant for shPar3-dependent metastasis in vivo, we measured lung colonization after tail vein injections of NICD-transformed cells with shRNAs against Par3 alone or Par3 and Stat3. As described above (Figure 3), loss of Par3 caused a significant increase in lung metastasis, which was completely suppressed by cosilencing Stat3 (Figure 5K). These data identify an unanticipated pathway in which loss of Par3 results in the aPKC-dependent activation of JAK/STAT signaling, which induces MMP9 expression and consequent destruction of the ECM, increased invasion, and lung metastasis by oncogene-activated mammary cells.

Par3 Expression Is Frequently Lost in Human Breast Cancers

To address the relevance of Par3 loss to human breast cancer, we explored the expression of the *PARD3* transcript in tumors from selected cohorts of patients. Significant reductions in *PARD3* gene expression were apparent in invasive ductal and lobular carcinomas compared to normal breast tissue (Figure 6A). Notably, *PARD3* expression was also reduced in other epithelial cancers (Figure S6A). We next analyzed a human tumor lysate array by immunoblot and found a significant reduction in PAR3 protein for 50% of the tumors as compared to matched samples of normal breast tissue from the same patients (Figure 6Ba). A second, independent matched group of 52 patient samples also showed significant reduction in PAR3 expression (Figure 6Bb). The same membranes were also probed for RanGTPase as a loading control, and the PAR3/RAN ratios were measured, to provide a corrected level of PAR3 (Figure 6C). To validate the specificity of the Par3 antibody, we probed breast cancer cell line lysates under similar buffer conditions to those used in generating the commercial membranes. The antibody

(J) Quantification of invasion of NICD/shLuc and NICD/shPar3 MECs through Matrigel with or without 10 nM Jak inhibitor, Pyridone 6.
(K) Quantification of lung nodules arising from NICD/shLuc, NICD/shPar3, and NICD/shPar3/shStat3-transformed MECs injected systemically. Five sections were examined from each lung of five mice for each treatment. Results are means of at least three independent cultures, unless otherwise noted. Error bars, ±1 SD. ns, not significant.
See also Figure S5.

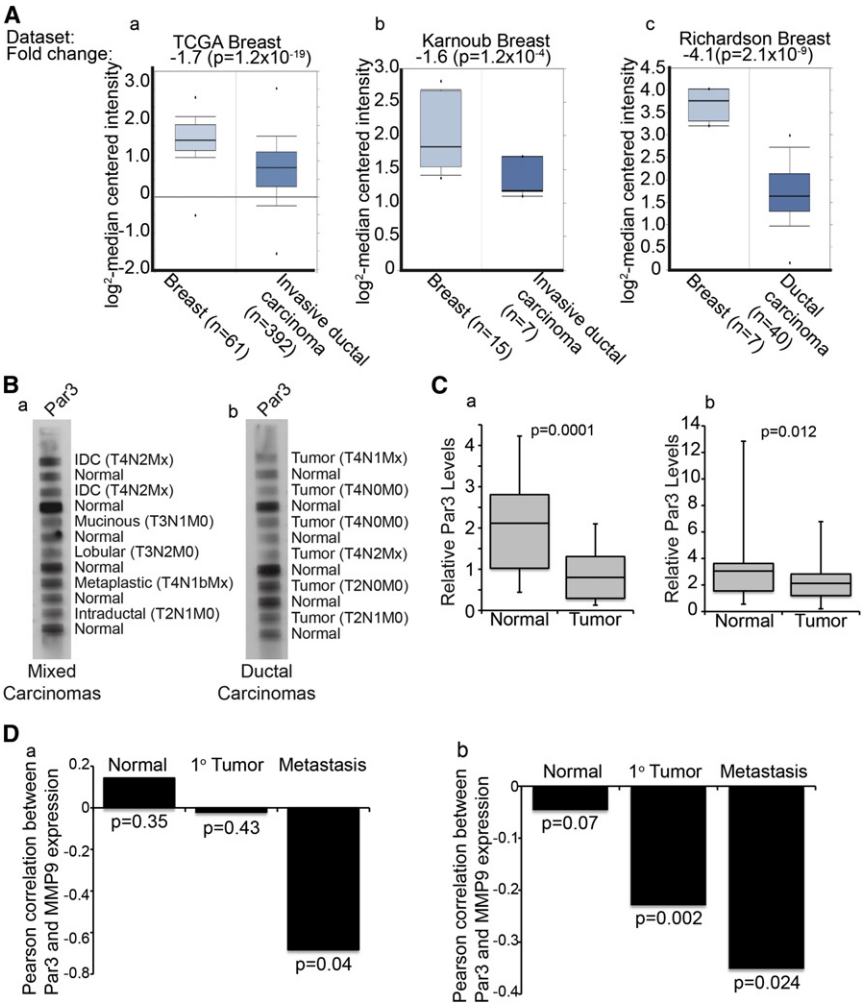

Figure 6. PAR3 Expression Is Reduced in Human Breast Cancer, Correlating with Elevated MMP9 Expression

(A) Microarray data showing relative levels of *PARD3* gene expression for invasive ductal carcinomas versus matched normal breast tissue from TCGA (a), Karnoub (b), and Richardson (c) data sets (see Supplemental Experimental Procedures for information on data sets).

(B) Human tumor protein array membranes of mixed carcinomas (a) and ductal carcinomas (b) with matched normal adjacent tissue were immunoblotted for PAR3. IDC, intraductal carcinoma. TNM classification values are given for each tumor sample.

(C) Box and whisker plots showing quantification of band intensities for PAR3 that were normalized to RAN expression levels in 52 matched human normal and breast tumor lysates from mixed carcinomas (a) and ductal carcinomas (b).

(D) Spearman's correlation coefficients between *PAR3* and *MMP9* expression in normal breast, primary breast tumor, and metastatic human breast cancers from two independent data sets (a, accession number GSE1477; b, accession number GSE7390).

See also Figure S6.

specifically detected PAR3, with low background and no nonspecific bands, indicating that the signal detected on the arrays is PAR3 specific (Figure S6B). In addition, we immunoblotted a limited number of freshly isolated normal and breast tumor samples including three invasive carcinomas (IDC) and one DCIS, which confirmed a decrease in PAR3 protein expression in the invasive breast cancer samples compared to normal tissue (Figure S6C).

To determine if *PARD3* expression is associated with any change in survival probability, we compared Kaplan-Meier plots for high and low expression of *PARD3* using a validated Jetset probe (Figure S6D). For a set of 2,324 patients with breast cancer, low *PARD3* correlated with a modest but statistically significant reduction in survival probability ($p = 9.8 \times 10^{-5}$) (Györffy et al., 2010). Our mouse models had revealed that loss of Par3 triggers the induction of MMP9 and invasion. Therefore, we compared the expression of *PARD3* and *MMP9* in cohorts of normal human breast, primary breast cancers, and metastases. Consistent with a role for loss of PAR3 in regulating metastasis through MMP9, a significant anticorrelation exists between *PARD3* and *MMP9* expression in metastases (Figure 6D). One data set also showed a significant anticorrelation in primary tumors, although to a lesser degree than in metastases (Figure 6Db).

Par3 protein is localized to tight junctions at the apical/lateral boundary in murine mammary epithelia (McCaffrey and Macara, 2009), and immunofluorescence of tissue arrays revealed a similar distribution for human mammary ducts (Figure 7A, a–c). Strikingly, however, PAR3 localization was completely lost in many of the human breast cancer samples (Figure 7A, d–i). From a total of 76 tumor samples examined, 63 lacked strong cortex-associated PAR3 staining. Importantly, costaining of tissue sections of 166 human invasive ductal carcinomas showed that p-aPKC and pSTAT3 were frequently prominent in regions with weak Par3 staining, whereas regions with more intense Par3 staining were negative for $pSTAT3^{Y705}$ and p-aPKC (Figures 7B and 7C). Furthermore, many regions were dual positive for p-aPKC and pJAK2 (Figure 7D), consistent with a role for PAR3 in regulating aPKC, JAK, and STAT3 activity in human breast cancers.

DISCUSSION

The apical-basal polarity of epithelial cells is controlled in part by the Par proteins together with a group of epithelial-specific proteins first identified in *Drosophila* (Crumbs, Scribble [Scrib], Lgl, Dlg). Loss of such proteins, or their misregulation, might therefore be expected to play a pivotal role in carcinogenesis, an idea that has been discussed in numerous reviews (Dow and Humbert, 2007; Feigin and Muthuswamy, 2009; Januschke and Gonzalez, 2008; St Johnston and Ahringer, 2010). Yet, there are surprisingly little published data to support this view. In *Drosophila*, Scrib, Lgl, and Dlg can behave as tumor suppressors

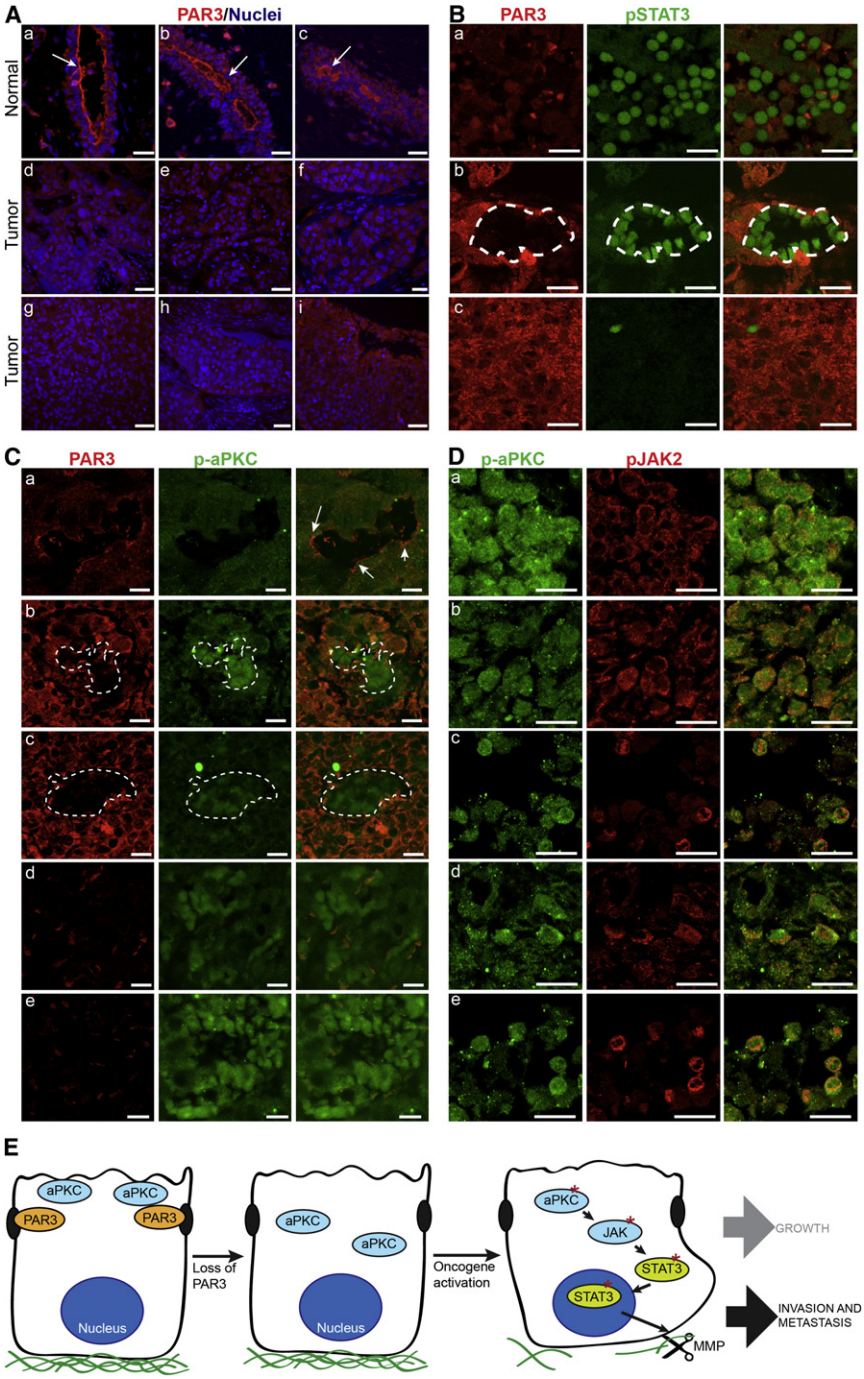

Figure 7. PAR3 Protein Expression Is Reduced and aPKC/STAT3 Signaling Is Activated in Human Breast Cancers

(A) Tissue sections of human normal and breast cancers stained for PAR3 (red) and nuclei (blue). Arrows show PAR3 enriched at the apical membrane. Images represent normal (a–c), infiltrating ductal carcinoma (d–f), and metastatic carcinoma (g–i). Scale bars, 100 μm.

(B) Tissue sections of human invasive breast cancers stained for PAR3 (red) and pSTAT3^{Y705} (green), representative of 166 stained tumor samples. Tumors with weak (top, 64% of tumors), mixed (middle, 28% of tumors), and intense (bottom, 8% of tumors) PAR3 staining.

(C) Tissue sections of human invasive breast cancers stained for PAR3 (red) and active phospho-aPKC^{T560} (green). Arrows show PAR3 enriched at apical membrane and weak p-aPKC staining. Images show representative weak (a, 69% of tumors), mixed (b and c, 25% of tumors), and intense (d and e, 6% of tumors) p-aPKC staining.

(D) Tissue sections of human invasive breast cancers costained for p-aPKC^{T560} (green) and pJAK2$^{Y1007/8}$ (red). Representative images are shown for five tumor samples (a–e).

(E) Model for cooperative effects of loss of Par3 in NICD or Ras^{61L} tumors. Loss of Par3 in the context of either oncogene results in the mislocalization and inappropriate activation of aPKC, which drives the induction and activation of Jak/Stat3 signaling, thereby causing increased MMP expression and ECM degradation.

Scale bars, 30 μm.

(Bilder et al., 2000; Brumby and Richardson, 2003) and can cooperate with oncogenes to drive metastasis (Pagliarini and Xu, 2003; Wu et al., 2010). Deletion of Scrib in prostate epithelium predisposed mice to neoplasia (Pearson et al., 2011). Silencing of Scrib in murine mammary cells stimulated tumor growth driven by c-*myc* but had no effect on tumor latency and did not induce metastasis (Zhan et al., 2008). Nor does silencing of Scrib disrupt apical-basal polarity in mammalian epithelial cells (Dow and Humbert, 2007; Qin et al., 2005). Additionally, increased aPKC activity or Par6 levels have been linked to TGF-β signaling and to breast cancer invasiveness (Viloria-Petit et al., 2009; Zhan et al., 2008). However, to date, and to our knowledge, the only bona fide tumor suppressor among the polarity proteins in humans is PAR4/LKB1 (Jansen et al., 2009), and we are not aware of evidence that other Par proteins function as invasion suppressors or that disruption of a polarity gene can induce tumorigenesis through loss of epithelial polarity.

To examine this issue, we used lentiviruses to deplete Par3 and express activated Notch or Ras in primary murine mammary cells, which were implanted orthotopically into normal immunocompetent mice. An advantage of this approach is that multiple changes in gene expression can be manipulated simultaneously, for instance to couple RNAi with ectopic expression. Additionally, the same cells can be used in vitro, without prior selection, to elucidate the molecular mechanisms underlying their phenotypes. This cancer model revealed several unexpected effects of silencing Par3. Most remarkably, despite the fact that the Ras and NICD oncogenes function through distinct mechanisms, the phenotypes induced by loss of Par3 are very similar. Loss of Par3 potently reduced tumor

latency in both contexts and increased lung colonization, consistent with in vitro increases in invasiveness and detachment from the ECM. These effects were independent of any consistent pattern of EMT. For example, both the NICD and Ras tumors and metastases retained K8 and ZO1 expression and did not express the classical mesenchymal markers vimentin or N-cadherin, consistent with a classification as luminal-type tumors. Moreover, loss of Par3 caused the activation of Stat3 and induction of MMP9 expression in both tumor models. Indeed, the only consistent difference was that Ras/shPar3 tumors had lost expression of E-cadherin, whereas cadherin expression was retained in the context of NICD.

What are the underlying mechanisms through which loss of Par3 triggers rapid tumor growth and invasion? We propose the following model (Figure 7E). First, Par3 spatially restricts aPKC at the apical membrane (McCaffrey and Macara, 2009), and apical localization requires the binding and phosphorylation of Par3 by aPKC. Notably, overexpression or mislocalization of aPKC is commonly found in invasive human breast tumors (Kojima et al., 2008; Regala et al., 2005). Loss of Par3 triggers both the mislocalization and—in the context of at least some oncogenes—the activation of aPKC, which, unexpectedly, triggers JAK-dependent activation of Stat3. Stat3 in turn induces MMP expression, resulting in degradation of the ECM and permitting escape from the primary tumor. Our results generally agree with previous data that aPKCs were necessary for STAT3 activity and MMP1/MMP13 expression in cytokine-stimulated chondrocytes (Litherland et al., 2010). However, Litherland et al. (2010) found a dependence on ERK phosphorylation, whereas we saw no changes in ERK activation in Par3-depleted cells (data not shown). Instead, loss of Par3 in an epithelial tumor context induces Stat3 activation through JAK by a cytokine-independent mechanism.

Stat3 is normally expressed only at low levels in the developing mammary gland and is upregulated during involution to regulate cell death. Nonetheless, active STAT3 is often found at the invasive edges of tumors (Bromberg and Wang, 2009) and is known to promote metastasis in breast cancer (Barbieri et al., 2010a). Brugge and colleagues found that NICD is sufficient to activate STAT3 in MCF10A cells (Mazzone et al., 2010). However, these cells cannot form normal tight junctions and do not exhibit cortical polarity (Fogg et al., 2005). Most likely, therefore, aPKC is not restricted to the apical surface, and NICD expression is sufficient to induce Stat3 activation.

The coupling between polarity proteins, oncogenes, and Stat3 is paralleled to a remarkable degree by *Drosophila*, in which clones of epithelial cells lacking the Scrib polarity protein become highly metastatic in the context of oncogenic Ras (Pagliarini and Xu, 2003; Wu et al., 2010). Loss of Scrib alone triggers a JNK-dependent apoptotic response through the cell competition pathway, by which neighboring wild-type cells eliminate the mutant cells; however, the expression of Ras^{V12} switches this response from apoptosis to uncontrolled proliferation, via a compensatory mechanism dependent on JAK/STAT activation. Tantalizingly, loss of a polarity protein in the mammary gland also stimulates apoptosis, just as in *Drosophila* (McCaffrey and Macara, 2009). An important question for the future is whether this response is mediated by cell competition and whether an aberrant compensatory mechanism drives tumor growth and dissemination when polarity proteins are lost from oncogene-transformed cells.

The striking effects of Par3 deficiency in the context of activated oncogenes suggest that polarity proteins might be suppressors of tumorigenesis in human carcinomas. PAR3 protein levels are significantly reduced in 50% of breast cancer samples compared with matched normal tissue, and a large majority of breast cancers lack normal PAR3 localization. Importantly, loss of Par3 was tightly correlated with increased p-aPKC and pSTAT3 across multiple breast tumor samples. Our data demonstrate that in addition to promoting metastasis through Stat3/MMPs, reduction of Par3 also reduces tumor latency, indicating that Par3 may suppress several steps in tumorigenesis. Microarray data support a broad decrease in *PARD3* gene expression across multiple epithelial cancers, including invasive ductal carcinoma of the breast. Deletions in the *PARD3* locus have also been identified. For human esophageal small-cell carcinoma, the *PARD3* gene was homozygously deleted in 15%, and expression was reduced in 90% of cell lines tested, compared to normal esophageal epithelial cells (Zen et al., 2009). Additionally, small deletions have been identified within the *PARD3* locus in a variety of cancer types (Rothenberg et al., 2010). Because Par3 functions in a polarity signaling network, mutations in other components of this network might also contribute to metastasis by human carcinomas. Together, our data establish that the Par3 polarity protein is an important suppressor of tumorigenesis and metastasis and that it may play a significant role in human breast cancer progression.

EXPERIMENTAL PROCEDURES

Culture Conditions, Antibodies, Immunostaining, and Inhibitors

See Supplemental Experimental Procedures.

Orthotopic Mammary Transplants

All animal procedures were performed in accordance with protocols approved by the Animal Use Committees at the University of Virginia and McGill University, Montreal. Freshly isolated mammary cells were transduced with lentivirus expressing myc-NICD, Ras^{61L}, and control shRNA (shLuc; against luciferase) or shRNA specific to murine Par3 (shPar3) (Zhang and Macara, 2006). Cells were transduced at an moi of 5 for oncogenes and 10 for shRNA. For in vivo tumorigenesis, 1×10^4 transduced MECs for NICD experiments or 1×10^5 MECs for Ras^{61L} were injected into cleared fat pads, as described previously (McCaffrey and Macara, 2009). For assessing tumor incidence and growth, cells expressing NICD/shLuc were injected in the contralateral side to NICD/shPar3 of each mouse. Mice were examined biweekly for palpable tumors. To assess metastasis, cells were transplanted into paired inguinal (#4) fat pads. Once palpable tumors were found, they were measured with calipers weekly. Mice were sacrificed when the calculated tumor volume reached 1 cm^3.

Invasion Assays

A total of 2.5×10^4 primary MECs/well was transduced with NICD/shLuc, or NICD/shPar3, Ras61L/shLuc or Ras61L/shPar3 lentivirus, and 2.5×10^4 Comma-D1 cells/well transduced with Ras^{61L}/shLuc or Ras^{61L}/shPar3 were plated in 8 μm pore Transwell inserts (Corning) in a 24-well plate format on top of 100 μl of 50% growth factor-reduced Matrigel or 100 μl of Collagen I gels (rat tail collagen I; GIBCO), prepared as described by Estecha et al. (2009). Culture medium was changed twice a day for 3 days. After 72 hr, cells that had migrated through the Matrigel to the filter were stained with Hoechst 33342 and counted.

Tumor Array

Commercially available membranes (ST2-6X-1 and ST2-6X-2) and SomaPlex Breast Cancer Tissue Lysate Protein Microarray (PMA2-001-L) from Protein Biotechnologies were probed according to the manufacturer's protocol (see Supplemental Experimental Procedures). Breast tissue was provided by the University of Virginia Biorepository and Tissue Research Facility. All human samples were deidentified and are exempt from informed consent.

Statistical Analyses

A Wilcoxon signed-rank test was used to determine the significance (p value) of tumor-free status in mice for the in vivo tumorigenesis. p Values were determined using unpaired, two-tailed Student's t tests for all assays except the tumor arrays, which used paired two-tailed Student's t tests.

SUPPLEMENTAL INFORMATION

Supplemental Information includes six figures, four tables, and Supplemental Experimental Procedures and can be found with this article online at http://dx.doi.org/10.1016/j.ccr.2012.10.003.

ACKNOWLEDGMENTS

We thank Didier Trono (Lausanne, Switzerland) for lentivectors, Shinya Yamanaka (Kyoto University) for Stat3-C, Connie Cepko (Harvard University) for myc-NICD, Jim Fawcett (Dalhousie University, Canada) for Par3 antibody, and Deborah Lannigan (University of Virginia) for breast tissue samples. We acknowledge support from NIH Grants GM070902 and CA132898 (to I.G.M.) and F32CA139950 (to J.M.), the Terry Fox Research Institute, Project #1009 (to L.M.M.), and CIHR 200602MFE-159430-14-900 (to L.M.M.).

Received: July 8, 2011
Revised: January 5, 2012
Accepted: October 1, 2012
Published: November 12, 2012

REFERENCES

Barbieri, I., Pensa, S., Pannellini, T., Quaglino, E., Maritano, D., Demaria, M., Voster, A., Turkson, J., Cavallo, F., Watson, C.J., et al. (2010a). Constitutively active Stat3 enhances neu-mediated migration and metastasis in mammary tumors via upregulation of Cten. Cancer Res. *70*, 2558–2567.

Barbieri, I., Quaglino, E., Maritano, D., Pannellini, T., Riera, L., Cavallo, F., Forni, G., Musiani, P., Chiarle, R., and Poli, V. (2010b). Stat3 is required for anchorage-independent growth and metastasis but not for mammary tumor development downstream of the ErbB-2 oncogene. Mol. Carcinog. *49*, 114–120.

Bilder, D., Li, M., and Perrimon, N. (2000). Cooperative regulation of cell polarity and growth by *Drosophila* tumor suppressors. Science *289*, 113–116.

Bromberg, J., and Wang, T.C. (2009). Inflammation and cancer: IL-6 and STAT3 complete the link. Cancer Cell *15*, 79–80.

Bromberg, J.F., Wrzeszczynska, M.H., Devgan, G., Zhao, Y., Pestell, R.G., Albanese, C., and Darnell, J.E., Jr. (1999). Stat3 as an oncogene. Cell *98*, 295–303.

Brumby, A.M., and Richardson, H.E. (2003). scribble mutants cooperate with oncogenic Ras or Notch to cause neoplastic overgrowth in *Drosophila*. EMBO J. *22*, 5769–5779.

Chen, X., and Macara, I.G. (2005). Par-3 controls tight junction assembly through the Rac exchange factor Tiam1. Nat. Cell Biol. *7*, 262–269.

Clark, G.J., and Der, C.J. (1995). Aberrant function of the Ras signal transduction pathway in human breast cancer. Breast Cancer Res. Treat. *35*, 133–144.

Dow, L.E., and Humbert, P.O. (2007). Polarity regulators and the control of epithelial architecture, cell migration, and tumorigenesis. Int. Rev. Cytol. *262*, 253–302.

Estecha, A., Sánchez-Martín, L., Puig-Kröger, A., Bartolomé, R.A., Teixidó, J., Samaniego, R., and Sánchez-Mateos, P. (2009). Moesin orchestrates cortical polarity of melanoma tumour cells to initiate 3D invasion. J. Cell Sci. *122*, 3492–3501.

Feigin, M.E., and Muthuswamy, S.K. (2009). Polarity proteins regulate mammalian cell-cell junctions and cancer pathogenesis. Curr. Opin. Cell Biol. *21*, 694–700.

Fogg, V.C., Liu, C.J., and Margolis, B. (2005). Multiple regions of Crumbs3 are required for tight junction formation in MCF10A cells. J. Cell Sci. *118*, 2859–2869.

Goldstein, B., and Macara, I.G. (2007). The PAR proteins: fundamental players in animal cell polarization. Dev. Cell *13*, 609–622.

Grivennikov, S., and Karin, M. (2008). Autocrine IL-6 signaling: a key event in tumorigenesis? Cancer Cell *13*, 7–9.

Guarino, M., Rubino, B., and Ballabio, G. (2007). The role of epithelial-mesenchymal transition in cancer pathology. Pathology *39*, 305–318.

Győrffy, B., Lanczky, A., Eklund, A.C., Denkert, C., Budczies, J., Li, Q., and Szallasi, Z. (2010). An online survival analysis tool to rapidly assess the effect of 22,277 genes on breast cancer prognosis using microarray data of 1,809 patients. Breast Cancer Res. Treat. *123*, 725–731.

Hao, Y., Du, Q., Chen, X., Zheng, Z., Balsbaugh, J.L., Maitra, S., Shabanowitz, J., Hunt, D.F., and Macara, I.G. (2010). Par3 controls epithelial spindle orientation by aPKC-mediated phosphorylation of apical Pins. Curr. Biol. *20*, 1809–1818.

Harris, T.J., and Peifer, M. (2005). The positioning and segregation of apical cues during epithelial polarity establishment in *Drosophila*. J. Cell Biol. *170*, 813–823.

Horikoshi, Y., Suzuki, A., Yamanaka, T., Sasaki, K., Mizuno, K., Sawada, H., Yonemura, S., and Ohno, S. (2009). Interaction between PAR-3 and the aPKC-PAR-6 complex is indispensable for apical domain development of epithelial cells. J. Cell Sci. *122*, 1595–1606.

Hu, C., Diévart, A., Lupien, M., Calvo, E., Tremblay, G., and Jolicoeur, P. (2006). Overexpression of activated murine Notch1 and Notch3 in transgenic mice blocks mammary gland development and induces mammary tumors. Am. J. Pathol. *168*, 973–990.

Jansen, M., Ten Klooster, J.P., Offerhaus, G.J., and Clevers, H. (2009). LKB1 and AMPK family signaling: the intimate link between cell polarity and energy metabolism. Physiol. Rev. *89*, 777–798.

Januschke, J., and Gonzalez, C. (2008). *Drosophila* asymmetric division, polarity and cancer. Oncogene *27*, 6994–7002.

Kojima, Y., Akimoto, K., Nagashima, Y., Ishiguro, H., Shirai, S., Chishima, T., Ichikawa, Y., Ishikawa, T., Sasaki, T., Kubota, Y., et al. (2008). The overexpression and altered localization of the atypical protein kinase C lambda/iota in breast cancer correlates with the pathologic type of these tumors. Hum. Pathol. *39*, 824–831.

Litherland, G.J., Elias, M.S., Hui, W., Macdonald, C.D., Catterall, J.B., Barter, M.J., Farren, M.J., Jefferson, M., and Rowan, A.D. (2010). Protein kinase C isoforms zeta and iota mediate collagenase expression and cartilage destruction via STAT3- and ERK-dependent c-fos induction. J. Biol. Chem. *285*, 22414–22425.

Mazzone, M., Selfors, L.M., Albeck, J., Overholtzer, M., Sale, S., Carroll, D.L., Pandya, D., Lu, Y., Mills, G.B., Aster, J.C., et al. (2010). Dose-dependent induction of distinct phenotypic responses to Notch pathway activation in mammary epithelial cells. Proc. Natl. Acad. Sci. USA *107*, 5012–5017.

McCaffrey, L.M., and Macara, I.G. (2009). The Par3/aPKC interaction is essential for end bud remodeling and progenitor differentiation during mammary gland morphogenesis. Genes Dev. *23*, 1450–1460.

Pagliarini, R.A., and Xu, T. (2003). A genetic screen in *Drosophila* for metastatic behavior. Science *302*, 1227–1231.

Pearson, H.B., Perez-Mancera, P.A., Dow, L.E., Ryan, A., Tennstedt, P., Bogani, D., Elsum, I., Greenfield, A., Tuveson, D.A., Simon, R., and Humbert, P.O. (2011). SCRIB expression is deregulated in human prostate cancer, and its deficiency in mice promotes prostate neoplasia. J. Clin. Invest. *121*, 4257–4267.

Pece, S., Serresi, M., Santolini, E., Capra, M., Hulleman, E., Galimberti, V., Zurrida, S., Maisonneuve, P., Viale, G., and Di Fiore, P.P. (2004). Loss of

negative regulation by Numb over Notch is relevant to human breast carcinogenesis. J. Cell Biol. *167*, 215–221.

Ponzo, M.G., and Park, M. (2010). The Met receptor tyrosine kinase and basal breast cancer. Cell Cycle *9*, 1043–1050.

Qin, Y., Capaldo, C., Gumbiner, B.M., and Macara, I.G. (2005). The mammalian Scribble polarity protein regulates epithelial cell adhesion and migration through E-cadherin. J. Cell Biol. *171*, 1061–1071.

Ranger, J.J., Levy, D.E., Shahalizadeh, S., Hallett, M., and Muller, W.J. (2009). Identification of a Stat3-dependent transcriptional regulatory network involved in metastatic progression. Cancer Res. *69*, 6823–6830.

Raouf, A., Zhao, Y., To, K., Stingl, J., Delaney, A., Barbara, M., Iscove, N., Jones, S., McKinney, S., Emerman, J., et al. (2008). Transcriptome analysis of the normal human mammary cell commitment and differentiation process. Cell Stem Cell *3*, 109–118.

Reese, D.M., and Slamon, D.J. (1997). HER-2/neu signal transduction in human breast and ovarian cancer. Stem Cells *15*, 1–8.

Regala, R.P., Weems, C., Jamieson, L., Khoor, A., Edell, E.S., Lohse, C.M., and Fields, A.P. (2005). Atypical protein kinase C iota is an oncogene in human non-small cell lung cancer. Cancer Res. *65*, 8905–8911.

Rørth, P. (2009). Collective cell migration. Annu. Rev. Cell Dev. Biol. *25*, 407–429.

Rothenberg, S.M., Mohapatra, G., Rivera, M.N., Winokur, D., Greninger, P., Nitta, M., Sadow, P.M., Sooriyakumar, G., Brannigan, B.W., Ulman, M.J., et al. (2010). A genome-wide screen for microdeletions reveals disruption of polarity complex genes in diverse human cancers. Cancer Res. *70*, 2158–2164.

Schafer, Z.T., and Brugge, J.S. (2007). IL-6 involvement in epithelial cancers. J. Clin. Invest. *117*, 3660–3663.

Schmoranzer, J., Fawcett, J.P., Segura, M., Tan, S., Vallee, R.B., Pawson, T., and Gundersen, G.G. (2009). Par3 and dynein associate to regulate local microtubule dynamics and centrosome orientation during migration. Curr. Biol. *19*, 1065–1074.

Shackleton, M., Vaillant, F., Simpson, K.J., Stingl, J., Smyth, G.K., Asselin-Labat, M.L., Wu, L., Lindeman, G.J., and Visvader, J.E. (2006). Generation of a functional mammary gland from a single stem cell. Nature *439*, 84–88.

Song, Y., Qian, L., Song, S., Chen, L., Zhang, Y., Yuan, G., Zhang, H., Xia, Q., Hu, M., Yu, M., et al. (2008). Fra-1 and Stat3 synergistically regulate activation of human MMP-9 gene. Mol. Immunol. *45*, 137–143.

St Johnston, D., and Ahringer, J. (2010). Cell polarity in eggs and epithelia: parallels and diversity. Cell *141*, 757–774.

Thiery, J.P., Acloque, H., Huang, R.Y., and Nieto, M.A. (2009). Epithelial-mesenchymal transitions in development and disease. Cell *139*, 871–890.

Thompson, J.E., Cubbon, R.M., Cummings, R.T., Wicker, L.S., Frankshun, R., Cunningham, B.R., Cameron, P.M., Meinke, P.T., Liverton, N., Weng, Y., and DeMartino, J.A. (2002). Photochemical preparation of a pyridone containing tetracycle: a Jak protein kinase inhibitor. Bioorg. Med. Chem. Lett. *12*, 1219–1223.

Villadsen, R., Fridriksdottir, A.J., Rønnov-Jessen, L., Gudjonsson, T., Rank, F., LaBarge, M.A., Bissell, M.J., and Petersen, O.W. (2007). Evidence for a stem cell hierarchy in the adult human breast. J. Cell Biol. *177*, 87–101.

Viloria-Petit, A.M., David, L., Jia, J.Y., Erdemir, T., Bane, A.L., Pinnaduwage, D., Roncari, L., Narimatsu, M., Bose, R., Moffat, J., et al. (2009). A role for the TGFbeta-Par6 polarity pathway in breast cancer progression. Proc. Natl. Acad. Sci. USA *106*, 14028–14033.

Wu, M., Pastor-Pareja, J.C., and Xu, T. (2010). Interaction between Ras(V12) and scribbled clones induces tumour growth and invasion. Nature *463*, 545–548.

Xie, T.X., Wei, D., Liu, M., Gao, A.C., Ali-Osman, F., Sawaya, R., and Huang, S. (2004). Stat3 activation regulates the expression of matrix metalloproteinase-2 and tumor invasion and metastasis. Oncogene *23*, 3550–3560.

Yu, H., Pardoll, D., and Jove, R. (2009). STATs in cancer inflammation and immunity: a leading role for STAT3. Nat. Rev. Cancer *9*, 798–809.

Zen, K., Yasui, K., Gen, Y., Dohi, O., Wakabayashi, N., Mitsufuji, S., Itoh, Y., Zen, Y., Nakanuma, Y., Taniwaki, M., et al. (2009). Defective expression of polarity protein PAR-3 gene (PARD3) in esophageal squamous cell carcinoma. Oncogene *28*, 2910–2918.

Zhan, L., Rosenberg, A., Bergami, K.C., Yu, M., Xuan, Z., Jaffe, A.B., Allred, C., and Muthuswamy, S.K. (2008). Deregulation of scribble promotes mammary tumorigenesis and reveals a role for cell polarity in carcinoma. Cell *135*, 865–878.

Zhang, H., and Macara, I.G. (2006). The polarity protein PAR-3 and TIAM1 cooperate in dendritic spine morphogenesis. Nat. Cell Biol. *8*, 227–237.

Cancer Cell
Article

An Inv(16)(p13.3q24.3)-Encoded *CBFA2T3-GLIS2* Fusion Protein Defines an Aggressive Subtype of Pediatric Acute Megakaryoblastic Leukemia

Tanja A. Gruber,[1,6,8] Amanda Larson Gedman,[6] Jinghui Zhang,[2,8] Cary S. Koss,[1] Suresh Marada,[3] Huy Q. Ta,[6] Shann-Ching Chen,[7] Xiaoping Su,[2,25] Stacey K. Ogden,[3] Jinjun Dang,[6] Gang Wu,[2] Vedant Gupta,[1] Anna K. Andersson,[6] Stanley Pounds,[5] Lei Shi,[5] John Easton,[8] Michael I. Barbato,[8] Heather L. Mulder,[8] Jayanthi Manne,[8] Jianmin Wang,[4,8] Michael Rusch,[2,8] Swati Ranade,[24] Ramapriya Ganti,[6] Matthew Parker,[2] Jing Ma,[7] Ina Radtke,[6] Li Ding,[8,11] Giovanni Cazzaniga,[13] Andrea Biondi,[14] Steven M. Kornblau,[9] Farhad Ravandi,[10] Hagop Kantarjian,[10] Stephen D. Nimer,[15] Konstanze Döhner,[16] Hartmut Döhner,[16] Timothy J. Ley,[8,11,12] Paola Ballerini,[17] Sheila Shurtleff,[6] Daisuke Tomizawa,[20] Souichi Adachi,[21] Yasuhide Hayashi,[22] Akio Tawa,[23] Lee-Yung Shih,[18] Der-Cherng Liang,[19] Jeffrey E. Rubnitz,[1] Ching-Hon Pui,[1] Elaine R. Mardis,[8,11,12] Richard K. Wilson,[8,11,12] and James R. Downing[6,8,*]

[1]Department of Oncology
[2]Department of Computational Biology
[3]Department of Biochemistry
[4]Information Sciences
[5]Department of Biostatistics
[6]Department of Pathology
[7]Hartwell Center for Biotechnology and Bioinformatics
[8]St. Jude Children's Research Hospital, Washington University Pediatric Cancer Genome Project
St. Jude Children's Research Hospital, Memphis, TN 38105, USA
[9]Department of Blood and Marrow Transplantation
[10]Department of Leukemia
University of Texas MD Anderson Cancer Center, Houston, TX 77030, USA
[11]The Genome Institute at Washington University
[12]Siteman Cancer Center
Washington University School of Medicine, St. Louis, MO 63110, USA
[13]Centro Ricerca Tettamanti, Pediatric Clinic, University of Milan-Bicocca, 20052 Monza, Italy
[14]Pediatric Unit, University of Milan-Bicocca, San Gerardo Hospital, 20900 Monza, Italy
[15]Molecular Pharmacology and Chemistry Program, Sloan Kettering Institute, New York, NY 10065, USA
[16]Department of Internal Medicine III, University of Ulm, 89081 Ulm, Germany
[17]Laboratoire d'Hématologie, Hôpital A. Trousseau, 75012 Paris, France
[18]Division of Hematology-Oncology, Department of Internal Medicine, Chang Gung Memorial Hospital, Chang Gung University, Taipei 105, Taiwan
[19]Division of Pediatric Hematology Oncology, Mackay Memorial Hospital, Taipei 104, Taiwan
[20]Department of Pediatrics, Tokyo Medical and Dental University, Tokyo 113-8510, Japan
[21]Human Health Sciences, Graduate School of Medicine, Kyoto University, Kyoto 606-8501, Japan
[22]Department of Haematology/Oncology, Gunma Children's Medical Center, Shibukawa 377-8577, Japan
[23]Department of Pediatrics, National Hospital Organization Osaka National Hospital, Osaka 540-0006, Japan
[24]Pacific Biosciences, Menlo Park, CA 94025, USA
[25]Present address: Department of Bioinformatics and Computational Biology, University of Texas MD Anderson Cancer Center, Houston, TX 77030, USA
*Correspondence: james.downing@stjude.org
http://dx.doi.org/10.1016/j.ccr.2012.10.007

SUMMARY

To define the mutation spectrum in non-Down syndrome acute megakaryoblastic leukemia (non-DS-AMKL), we performed transcriptome sequencing on diagnostic blasts from 14 pediatric patients and validated our

Significance

Acute megakaryoblastic leukemia (AMKL) accounts for 10% of childhood acute myeloid leukemia (AML). Although AMKL patients with Down syndrome (DS-AMKL) have an excellent survival, non-DS-AMKL patients have an extremely poor outcome with a 3 year survival of less than 40%. With the exception of the t(1;22) seen in the majority of infants with non-DS-AMKL, little is known about the molecular lesions that underlie this leukemia subtype. Our results identified a fusion gene, *CBFA2T3-GLIS2*, that functions as a driver mutation in a subset of these patients. Importantly, pediatric patients with *CBFA2T3-GLIS2* expressing AMKL had inferior outcomes (5 year survival 34.3% versus 88.9%; p = 0.03), demonstrating that this lesion is a prognostic factor in this leukemia population.

findings in a recurrency/validation cohort consisting of 34 pediatric and 28 adult AMKL samples. Our analysis identified a cryptic chromosome 16 inversion (inv(16)(p13.3q24.3)) in 27% of pediatric cases, which encodes a CBFA2T3-GLIS2 fusion protein. Expression of CBFA2T3-GLIS2 in *Drosophila* and murine hematopoietic cells induced bone morphogenic protein (BMP) signaling and resulted in a marked increase in the self-renewal capacity of hematopoietic progenitors. These data suggest that expression of CBFA2T3-GLIS2 directly contributes to leukemogenesis.

INTRODUCTION

Acute megakaryoblastic leukemia (AMKL) accounts for approximately 10% of pediatric acute myeloid leukemia (AML) and 1% of adult AML (Athale et al., 2001; Barnard et al., 2007; Oki et al., 2006; Tallman et al., 2000). AMKL is divided into two subgroups: AMKL arising in patients with Down syndrome (DS-AMKL), and leukemia arising in patients without Down syndrome (non-DS-AMKL). Although DS-AMKL patients have an excellent prognosis with an ~80% survival, non-DS-AMKL patients do not fare as well, with a reported survival of only 14%–34% despite high-intensity chemotherapy (Athale et al., 2001; Barnard et al., 2007; Creutzig et al., 2005). With the exception of the t(1;22) seen in infant non-DS-AMKL, little is known about the molecular lesions that underlie this leukemia subtype (Carroll et al., 1991; Lion et al., 1992; Ma et al., 2001; Mercher et al., 2001).

We recently reported data from a high-resolution study of DNA copy number abnormalities (CNAs) and loss of heterozygosity on pediatric de novo AML (Radtke et al., 2009). These analyses demonstrated a very low burden of genomic alterations in all pediatric AML subtypes except AMKL. AMKL cases were characterized by complex chromosomal rearrangements and a high number of CNAs. To define the functional consequences of the identified chromosomal rearrangements in non-DS-AMKL, the St. Jude Children's Research Hospital-Washington University Pediatric Cancer Genome Project performed transcriptome and exome sequencing on diagnostic leukemia samples.

RESULTS

AMKL Is Characterized by Chimeric Transcripts

Transcriptome sequencing was performed on diagnostic leukemia cells from 14 pediatric non-DS-AMKL patients (discovery cohort) (see Tables S1 and S2 available online). Our analysis identified structural variations (SVs) that resulted in the expression of chimeric transcripts encoding fusion proteins in 12 of 14 cases (Table S3). Remarkably, in 7 of 14 cases, a cryptic inversion on chromosome 16 (inv(16)(p13.3q24.3)) was detected that resulted in the joining of *CBFA2T3*, a member of the ETO family of nuclear corepressors, to *GLIS2*, a member of the GLI family of transcription factors (Figures 1, 2, and S1). In six of these cases, exon 10 of *CBFA2T3* was fused to exon 3 of *GLIS2*, whereas in the remaining one case, exon 11 of *CBFA2T3* was fused to exon 1 of *GLIS2*. Both encoded proteins retain the three CBFA2T3 N-terminal *nervy* homology regions that mediate protein interactions and the five GLIS2 C-terminal zinc finger domains that bind the *Glis* DNA consensus sequence (Figures 1A and 1B). Whole-genome sequence analysis of tumor and germline DNA from four cases demonstrated that the *CBFA2T3-GLIS2* chimeric gene resulted from simple balanced inversions in three cases and a complex rearrangement involving chromosomes 16 and 9 in the fourth case (Figures 2 and S1).

Chimeric transcripts were also detected in five of seven leukemia samples that lacked expression of *CBFA2T3-GLIS2*, including one case each expressing in-frame fusions of *GATA2-HOXA9*, *MN1-FLI1*, *NIPBL-HOXB9*, *NUP98-KDM5A*, *GRB10-SDK1*, and *C8orf76-HOXA11AS* (Figure 3; Table S3). Importantly, several of the genes involved in these translocations play a direct role in normal megakaryocytic differentiation (*GATA2* and *FLI1*), have been previously shown to be involved in leukemogenesis (*HOXA9*, *MN1*, *HOXB9*, *NUP98*, *KDM5A*), or are highly expressed in hematopoietic stem cells or myeloid/megakaryocytic progenitors (Figure S2) (Argiropoulos and Humphries, 2007; Buijs et al., 2000; Heuser et al., 2011; Kawada et al., 2001; Visvader et al., 1995; Wang et al., 2009). Analysis of a recurrency/validation cohort consisting of diagnostic leukemia cells from 62 AMKL cases (34 pediatric and 28 adult) revealed 6 additional pediatric samples carrying *CBFA2T3-GLIS2* for an overall frequency of 27% (13 of 48) in pediatric AMKL (Table S1). None of the adult AMKL cases contained this chimeric transcript, suggesting that this lesion is restricted to pediatric non-DS-AMKLs. *NUP98-KDM5A* was the only other chimeric transcript that was recurrent, being detected in 8.3% (4 of 48) of pediatric cases (Table S1). This chimeric transcript was also not detected in adult AMKLs.

Cooperating Lesions in AMKL

In addition to the described chimeric transcripts, exome sequence analysis on 10 of the 14 samples in the discovery cohort that had matched germline DNA, coupled with CNAs detected by Affymetrix SNP6 microarrays, revealed an average of 5 (range 1–14) somatic nonsilent sequence mutations and 5 (range 0–11) CNAs involving annotated genes per case. (Tables S4, S5, and S6; Figure S1). Despite the relative paucity of somatic mutations, recurrent lesions were identified in *JAK* kinase genes, *MPL* and *GATA1*, which have been previously shown to play a role in AMKL (Malinge et al., 2008). Sequence analysis of these genes in cases within the recurrency cohort that had available genomic DNA revealed activating mutations in *JAK* kinases (9 of 51, 17.6%) and *MPL* (2 of 51, 3.9%), as well as inactivating mutations in *GATA1* (5 of 51, 9.8%) (Tables S1 and S6). In addition, 7 of 14 cases with available copy number data contained amplification of chromosome 21 in the Down syndrome critical region (DSCR; chr21q22) that includes genes known to play a role in AML such as *RUNX1*, *ETS2*, and *ERG* (Table S4; Figure S1). Three of these cases carry the *CBFA2T3-GLIS2* chimeric gene. Importantly, the total burden of somatic mutations was significantly lower in the *CBFA2T3-GLIS2*-expressing cases (7.17 ± 3.60 versus 16.60 ± 5.13; $p = 0.009$; Table S5).

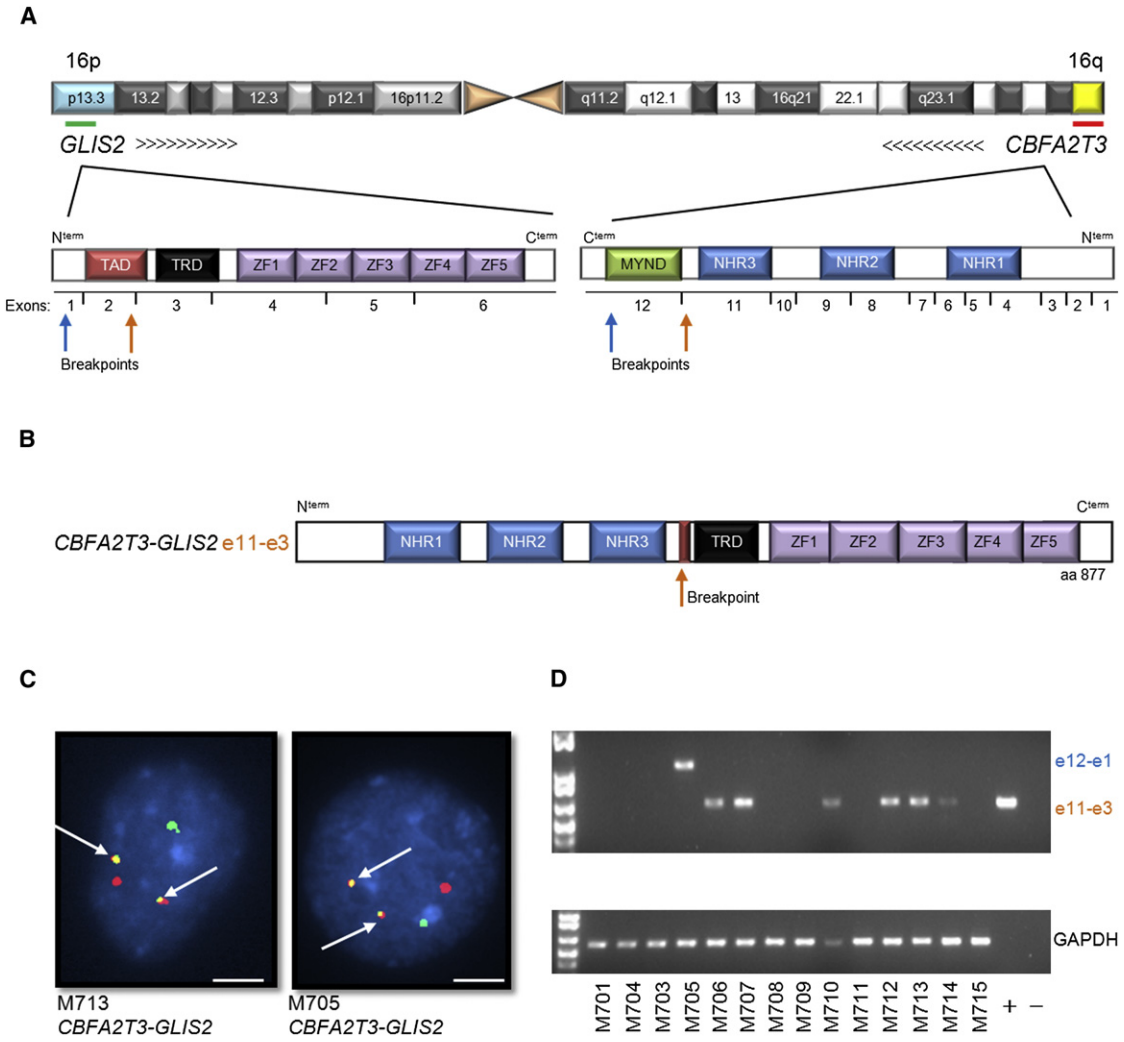

Figure 1. Inv(16)(p13.3;q24.3) Encodes a *CBFA2T3-GLIS2* Chimeric Transcript

(A) Schematic of chromosome 16 with locations of *GLIS2* and *CBFA2T3* shown. Arrows indicate orientation of the gene and the green and red lines the probes used for FISH. The protein structure of the genes is shown below chromosome 16 and is not drawn to scale. Breakpoints are indicated by arrows. TAD, transactivation domain; TRD, transcriptional regulatory domain; ZF, zinc finger; NHR, nervy homology region.

(B) Schematic of CBFA2T3-GLIS2 chimeric protein.

(C) Interphase FISH analysis of two representative patient samples carrying *CBFA2T3-GLIS2*. The *GLIS2* probe is green; the *CBFA2T3* probe is red. White arrows indicate the fusion event. Scale bars, 10 μm.

(D) RT-PCR for CBFA2T3-GLIS2 and GAPDH on the discovery cohort.

See also Figure S1 and Tables S1, S2, S3, S4, S5, and S6.

CBFA2T3-GLIS2 AMKL Is a Distinct Subtype of Pediatric AMKL with a Poor Prognosis

The gene expression profile of *CBFA2T3-GLIS2* AMKL was distinct from that of AMKL cells lacking this chimeric transcript and from other genetic subtypes of pediatric AML (Figures 4A and 4B). A detailed coexpression network analysis of the top 4,000 differentially expressed genes suggests that expression of *CBFA2T3-GLIS2* leads to marked upregulation of *BMP2*, a downstream target of Hedgehog signaling (Figures 4B and S3; Table S7). Moreover, gene set enrichment analysis based on KEGG pathway annotation of the top-scoring network module demonstrated Hedgehog and JAK-STAT pathways to be significantly upregulated in *CBFA2T3-GLIS2*-positive AMKL (Figure S3).

Given the historically poor outcomes seen in pediatric non-DS-AMKL, we next explored whether the presence of *CBFA2T3-GLIS2* identified a clinically distinct subset of cases. Outcome data were available on 40 pediatric patients. Although these patients were treated at a number of different centers using a variety of different therapeutic approaches, the presence of *CBFA2T3-GLIS2* identified a subgroup of patients with a significantly worse overall survival at 5 years as compared to patients with AMKL that lacked this chimeric transcript (28.1% versus 41.9%; p = 0.05; Figure 4C). Moreover, when this analysis was limited to patients treated at a single institution (St. Jude, n = 19), the adverse prognostic impact of *CBFA2T3-GLIS2* on survival was maintained (34.3% versus 88.9%; p = 0.03; Figure 4D).

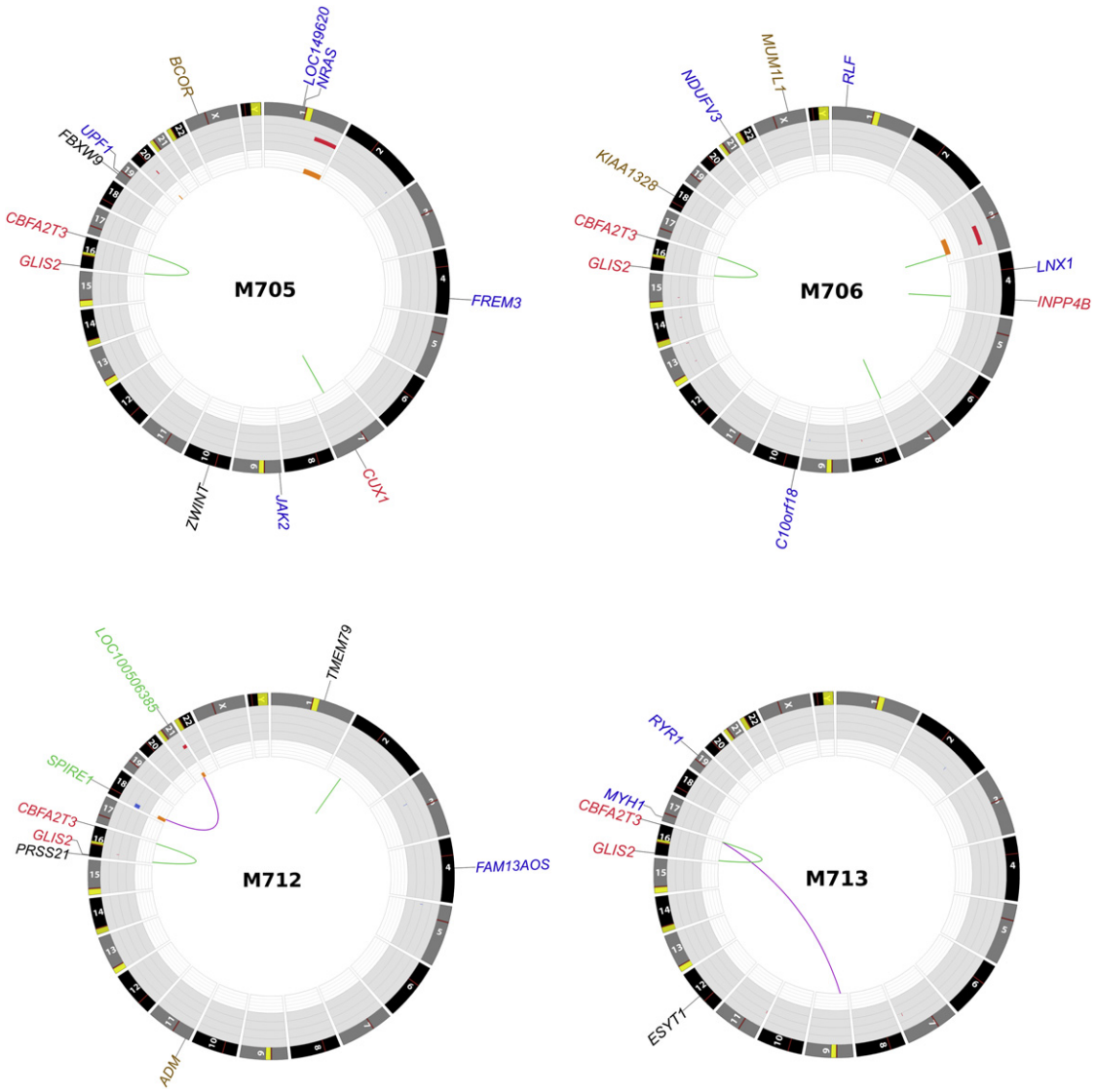

Figure 2. Somatic Mutations in Whole-Genome-Sequenced AMKL Cases

Plots depict structural genetic variants, including DNA copy number alterations, intra- and interchromosomal translocations, and sequence alterations (Krzywinski et al., 2009). DNA copy number alterations: loss of heterozygosity (LOH), orange; amplification, red; deletion, blue. Sequence mutations in Refseq genes: silent SNVs (SNVs), black; UTR, brown; nonsilent SNVs, blue. Genes at structural variant breakpoints: genes involved in in-frame fusions, red; others, green.

CBFA2T3-GLIS2-Modified Hematopoietic Cells Demonstrate Enhanced Self-Renewal

CBFA2T3 (also known as *MTG16*) was initially identified as a fusion partner with *RUNX1* in rare cases of therapy-related AML that contain a t(16;21)(q24;q22) (Gamou et al., 1998). More recently, CBFA2T3 has been implicated in the maintenance of hematopoietic stem cell quiescence (Chyla et al., 2008). By contrast, to our knowledge, GLIS2 has not been previously implicated in leukemogenesis. GLIS2 is a member of the GLI-similar (GLIS1-3) subfamily of Krüppel-like zinc finger transcription factors and is closely related to the GLI family of transcription factors that function as critical elements of the hedgehog signaling pathway (Kim et al., 2007; Lamar et al., 2001). GLIS2 is expressed in the kidney, and germline-inactivating mutations lead to nephronophthisis, an autosomal recessive cystic kidney disease (Attanasio et al., 2007). Although *GLIS2* is not normally expressed in the hematopoietic system, its fusion to *CBFA2T3* as a result of the inv(16)(p13.3q24.3) results in high-level expression of the C-terminal portion of the protein including its DNA-binding domain (Figure S1).

To explore the functional effects of the CBFA2T3-GLIS2 fusion protein, we transduced murine hematopoietic cells with a retrovirus expressing either *CBFA2T3-GLIS2* or *GLIS2* alone and assessed their effect on in vitro colony formation, differentiation, and replating efficiency as a surrogate measure of self-renewal (Figures 5A and 5B). On the initial plating, the expression of CBFA2T3-GLIS2 had no effect on colony numbers, size, or overall myeloid/erythroid differentiation when cells were grown in the presence of IL3, IL6, SCF, and EPO. However, hematopoietic cells transduced with the empty

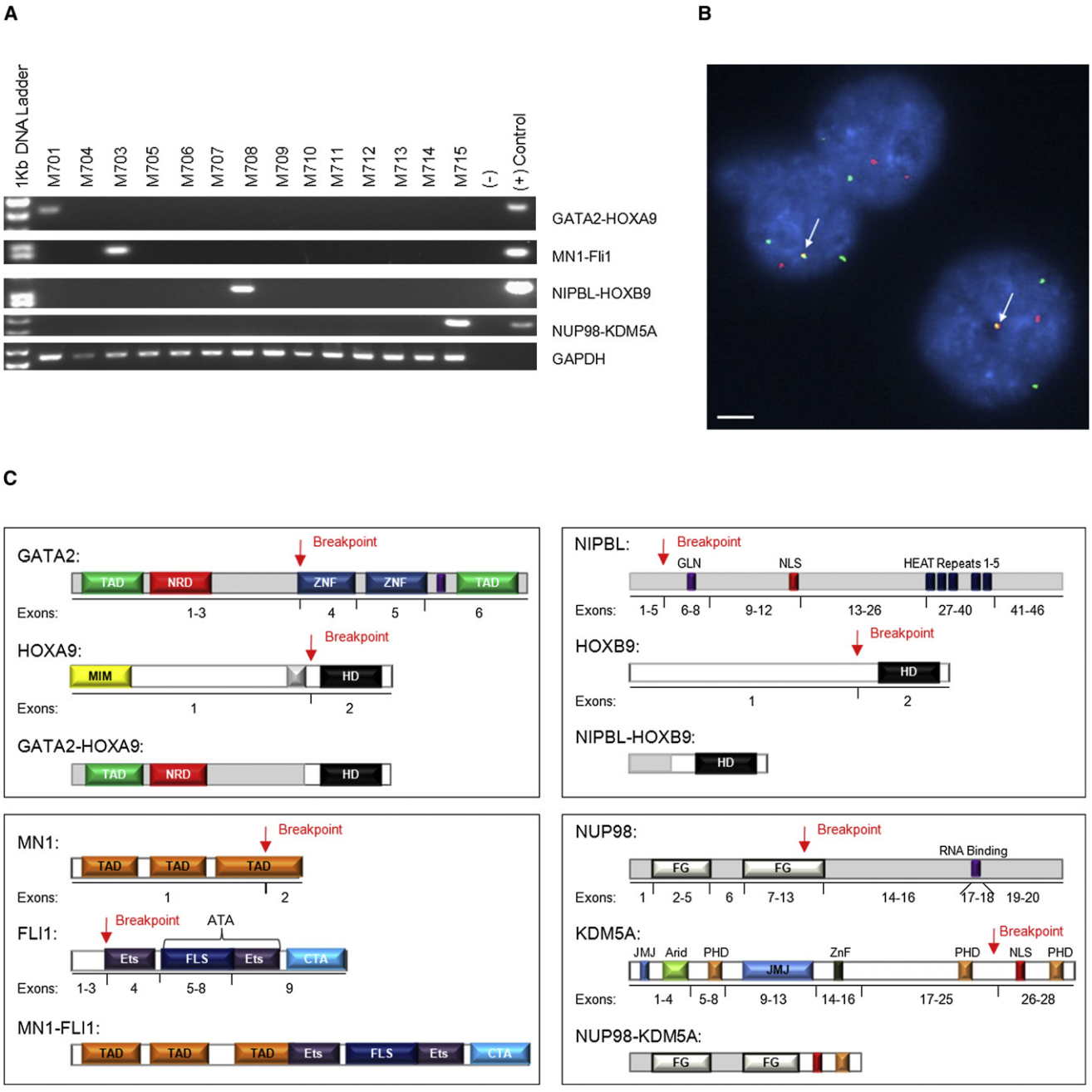

Figure 3. Low-Frequency Chimeric Transcripts in Pediatric AMKL

Four chimeric transcripts were identified in one case each of the discovery cohort and tested for in the recurrency cohort: *GATA2-HOXA9*, *MN1-FLI1*, *NIPBL-HOXB9*, and *NUP98-KDM5A*.

(A) RT-PCR validation of the discovery cohort. Primers and conditions are described in Supplemental Experimental Procedures.

(B) Interphase FISH analysis of M703 carrying the MN1-FLI1 chimeric protein. The *MN1* probe is red; the *FLI1* probe is green. White arrows indicate the fusion event. Scale bar, 10 μm.

(C) Schematic of chimeric proteins. Exons and domains are not drawn to scale. NRD, negative regulatory domain; ZNF, zinc finger; MIM, Meis interaction motif; HD, Hox domain; Ets, E-twenty six domain; FLS, Fli1-specific region; CTA, C-terminal transactivation domain; GLN, glutamine-rich domain; NLS, nuclear-localizing signal; HEAT, *H*untingtin/*E*F3/PP2*A*/*T*OR1 domain; FG, phenylalanine-glycine repeats; JMJ, jumonji domain; ARID, AT-rich interaction domain; PHD, plant homeodomain. See also Figure S2.

retrovirus (MSCV-IRES-mCherry [MIC]) failed to form colonies after the second replating, whereas expression of either CBFA2T3-GLIS2 or wild-type GLIS2 resulted in a marked increase in the self-renewal capacity, with colony formation persisting through ten replatings (Figure 5C). Upon serial replating, two colony types were detected: CFU-GM and CFU-Meg

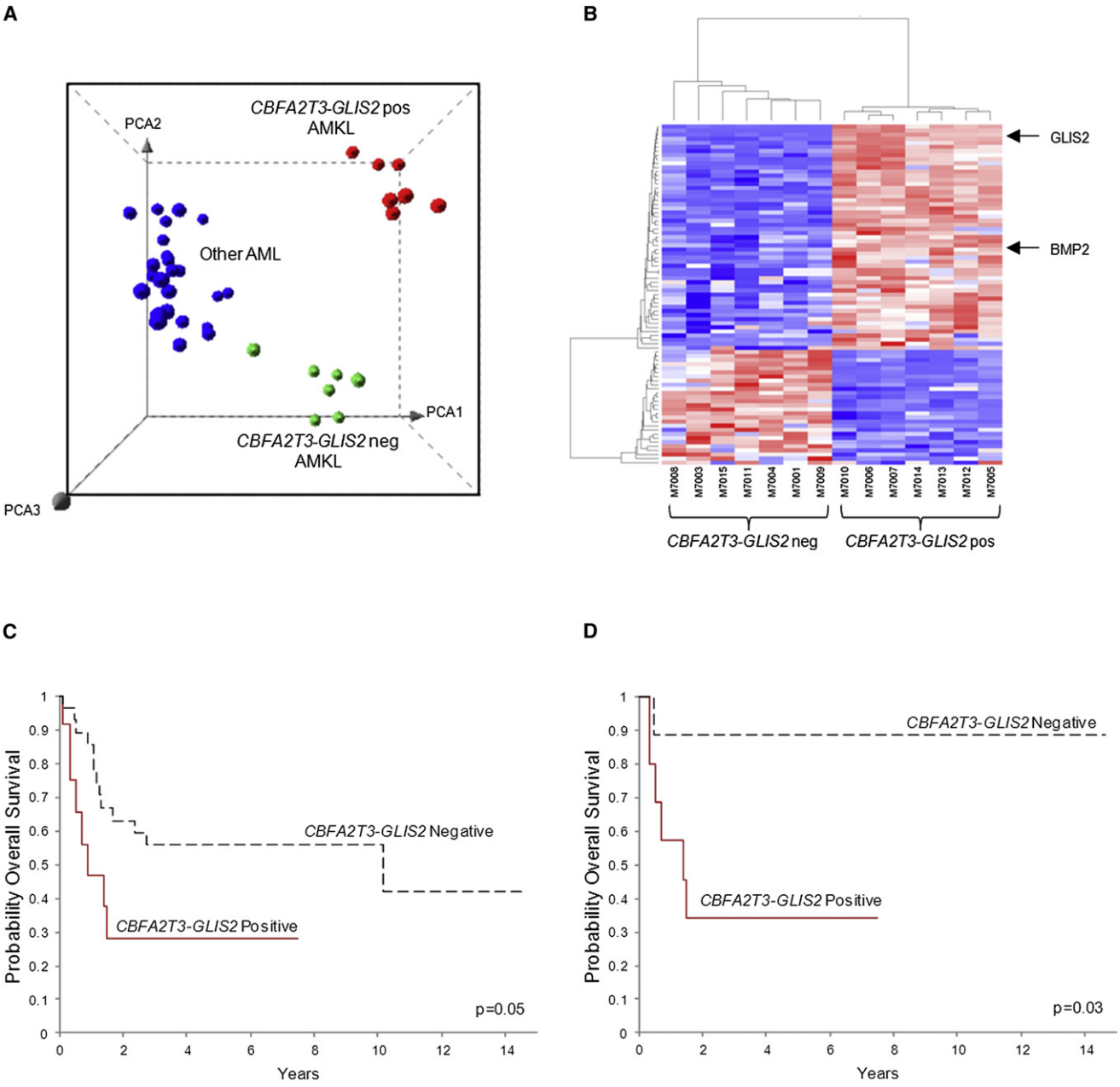

Figure 4. *CBFA2T3-GLIS2* Defines a Unique Subtype of AML with a Distinct Gene Expression Signature and Poor Outcomes

(A) Principal component analysis of the gene expression profiles of the AMKL discovery cohort and 32 other non-AMKL AML samples representing all other known genetic subtypes of pediatric AML. Clusters were generated using 1,000 genes selected by k-means algorithm. A detailed description of the samples included in this analysis can be found at NCBI Gene Expression Omnibus, accession GSE35203.

(B) Heatmap of differentially expressed genes in the top-scoring network module of CBFA2T3-GLIS2-positive (pos) and -negative (neg) AMKL patient samples. For gene relationships, please see Figure S3. For a detailed list of the top 500 differentially expressed genes (not limited to this network), please see Table S7.

(C) Overall survival of 40 pediatric non-DS AMKL cases treated at multiple institutions (*CBFA2T3-GLIS2*-negative cases n = 28, and *CBFA2T3-GLIS2*-expressing cases, n = 12). The curves for the two groups were tested by log rank method and exact test using permutation that yielded a p value of 0.05.

(D) Overall survival of 19 pediatric non-DS AMKL cases treated at St. Jude Children's Research Hospital (*CBFA2T3-GLIS2*-negative cases, n = 9, and *CBFA2T3-GLIS2*-expressing cases, n = 10). The curves for the two groups were tested by log rank method and exact test using permutation that yielded a p value of 0.03. See also Figure S3 and Table S7.

(Figure 5D). Immunophenotypic analysis at the third replating also revealed evidence of megakaryocytic differentiation with CD41/CD61 dual expression and the absence of cKIT and Sca1 expression in the majority of cells (Figure 5E). Importantly, CBFA2T3-GLIS2-expressing cells remained growth factor dependent, suggesting that cooperating mutations in growth factor

signaling pathways are likely required for full leukemic transformation (data not shown). Moreover, transplantation of *CBFA2T3-GLIS2*-transduced bone marrow cells into syngeneic recipients failed to induce overt leukemia at day 365 as demonstrated by normal blood counts and low-level reporter gene expression in peripheral blood (<5%) (data not shown), consistent with a requirement for cooperative mutations. Failure to induce leukemia in mice as a single lesion has been previously reported for other chimeric genes that confer the ability to serially replate in colony-forming assays, including *AML1-ETO* (Higuchi et al., 2002).

CBFA2T3-GLIS2 Induces BMP Signaling

GLIS2 can function as both a transcriptional activator and repressor depending on the cellular context and has been implicated in altered signaling through a number of pathways including sonic hedgehog-GLI1 (SHH) and WNT/β-catenin (Attanasio et al., 2007; Kim et al., 2007). Analysis of the gene expression signatures of *CBFA2T3-GLIS2* expressing AMKLs revealed altered expression of a number of genes in the SHH and WNT pathways, as well as genes in the bone morphogenic protein (BMP) pathway, which is directly influenced by SHH signaling (Figures 4B, 6A, and S3) (Dahn and Fallon, 2000; Ingham and McMahon, 2001; Vokes et al., 2007). When this analysis was limited to genes containing GLI consensus DNA-binding sites (Gli-BS) in their promoters or to genes known to be transcriptional targets of GLIS2, marked overexpression of *PTCH1*, *HHIP*, *BMP2*, and *BMP4* was observed (Figures 6B, S3, and S4; Table S7) (Attanasio et al., 2007). Consistent with this observation, although CBFA2T3-GLIS2 only weakly activated transcription of a reporter construct containing the Gli-BS (Figure S4), it strongly activated transcription of the Gli-BS-containing BMP4 promoter-driven luciferase construct and induced expression of BMP4 in murine hematopoietic cells (Figures 6C and S4). Moreover, CBFA2T3-GLIS2 strongly activated a BMP response element (BRE) containing luciferase reporter construct and induced expression of the BMP downstream transcriptional target, inhibitor of differentiation 1 (*ID1*) (Korchynskyi and ten Dijke, 2002), consistent with the induced expression of BMP2/BMP4 (Figure S4).

BMP signaling plays a critical role in the specification of hematopoiesis in developing embryos, and studies suggest that BMP4 stimulation can augment megakaryocytic output from CD34 progenitors (Jeanpierre et al., 2008; Söderberg et al., 2009). To determine if the observed CBFA2T3-GLIS2-induced BMP expression contributes to the enhanced replating capacity of murine hematopoietic cells, colony-replating assays were repeated in the presence of dorsomorphin, a selective small molecule inhibitor of the BMP type I receptors that blocks BMP-mediated phosphorylation of SMAD 1/5/8 (Yu et al., 2008). Importantly, CBFA2T3-GLIS2 as well as GLIS2-expressing hematopoietic cells were significantly more sensitive to dorsomorphin than wild-type cells in the first plating (Figure 6D). Continuous exposure to dorsomorphin inhibited colony formation in a dose-dependent manner on subsequent platings (data not shown). Interestingly, sublethal doses of dorsomorphin in *CBFA2T3-GLIS2*-positive cells led to an upregulation of *Bmp4* and *Id1* transcripts over time, with colony counts returning to untreated levels, suggesting that cells are able to overcome this inhibition by upregulating the BMP pathway (data not shown).

To further explore the downstream signaling of CBFA2T3-GLIS2 in human leukemia cell lines, we first assessed the expression level of *GLIS2* in human cancer cell lines using the recently published Broad-Novartis Cancer Cell Line Encyclopedia (Figure 7A) (Barretina et al., 2012). Interestingly, this analysis showed that GLIS2 expression levels are lowest in leukemia cell lines. Moreover, within the leukemias, the highest expressing cell line was the pediatric AMKL cell line M07e. To further explore AMKL cell lines, we performed RT-PCR for *CBFA2T3-GLIS2* on five human AMKL cell lines. Three of the five cell lines (RS1, WSU-AML, and M07e) expressed *CBFA2T3-GLIS2* (Figure 7B). The presence of the chimeric gene in these lines was validated by FISH analysis (Figure 7B). We went on to determine the relative expression of BMP genes by semiquantitative RT-PCR and found a trend toward upregulation of these genes in the CBFA2T3-GLIS2-positive cells (Figure 7C). We also assessed our AMKL cell lines for dorsomorphin sensitivity and found a trend toward increased sensitivity in cell lines expressing *CBFA2T3-GLIS2* as determined by a standard MTT assay (Figure 7D).

To determine if CBFA2T3-GLIS2 induces the upregulation of BMP signaling in vivo, we generated transgenic *Drosophila* expressing either *CBFA2T3-GLIS2* or full-length *GLIS2* using an epithelial promoter and examined their effect on fly development. During *Drosophila* development, the WNT, BMP, and SHH homologs (Wg, Dpp, and Hh, respectively) have distinct roles in patterning adult wing structures (Dahn and Fallon, 2000; Ingham and McMahon, 2001; Vokes et al., 2007). When altered, these signaling pathways trigger characteristic loss- and gain-of-function phenotypes (Tabata and Takei, 2004). Expression of CBFA2T3-GLIS2 and full-length GLIS2 in *Drosophila* resulted in ectopic expression of endogenous *dpp*, the fly homolog of *BMP4*, in wing imaginal discs (Figures 8A and S5). Immunofluorescence confirmed the nuclear localization of CBFA2T3-GLIS2 (Figure 8A). Both CBFA2T3-GLIS2 and GLIS2 overexpression induced lethality. However, a small number of escapers developed to pharate adults and demonstrated a morphologic *dpp* gain-of-function phenotype; wing hinges were converted to notum, and legs were shortened and broadened (Figure 8B) (Grieder et al., 2009). Rare *CBFA2T3-GLIS2* transgenic flies developed to adulthood and demonstrated mild ectopic venation throughout the wing blade, as well as wing blistering consistent with a *dpp* gain-of-function phenotype (Figure 8B) (Sander et al., 2010).

DISCUSSION

Sequence analysis of pediatric non-DS-AMKLs revealed the expression of an inv(16)-encoded *CBFA2T3-GLIS2* in almost 30% of pediatric non-DS-AMKL patients, and its presence defined a distinct subgroup of patients that had an exceptionally poor outcome when compared to patients with AMKL that lacked this lesion. In addition, five other chimeric transcripts (*GATA2-HOXA9*, *MN1-FLI1*, *NIPBL-HOXB9*, *GRB10-SDK1*, and *C8orf76-HOXA11AS*) were detected in single AMKL cases. Surprisingly, none of the identified chimeric transcripts was detected in adult AMKL cases, highlighting the significant

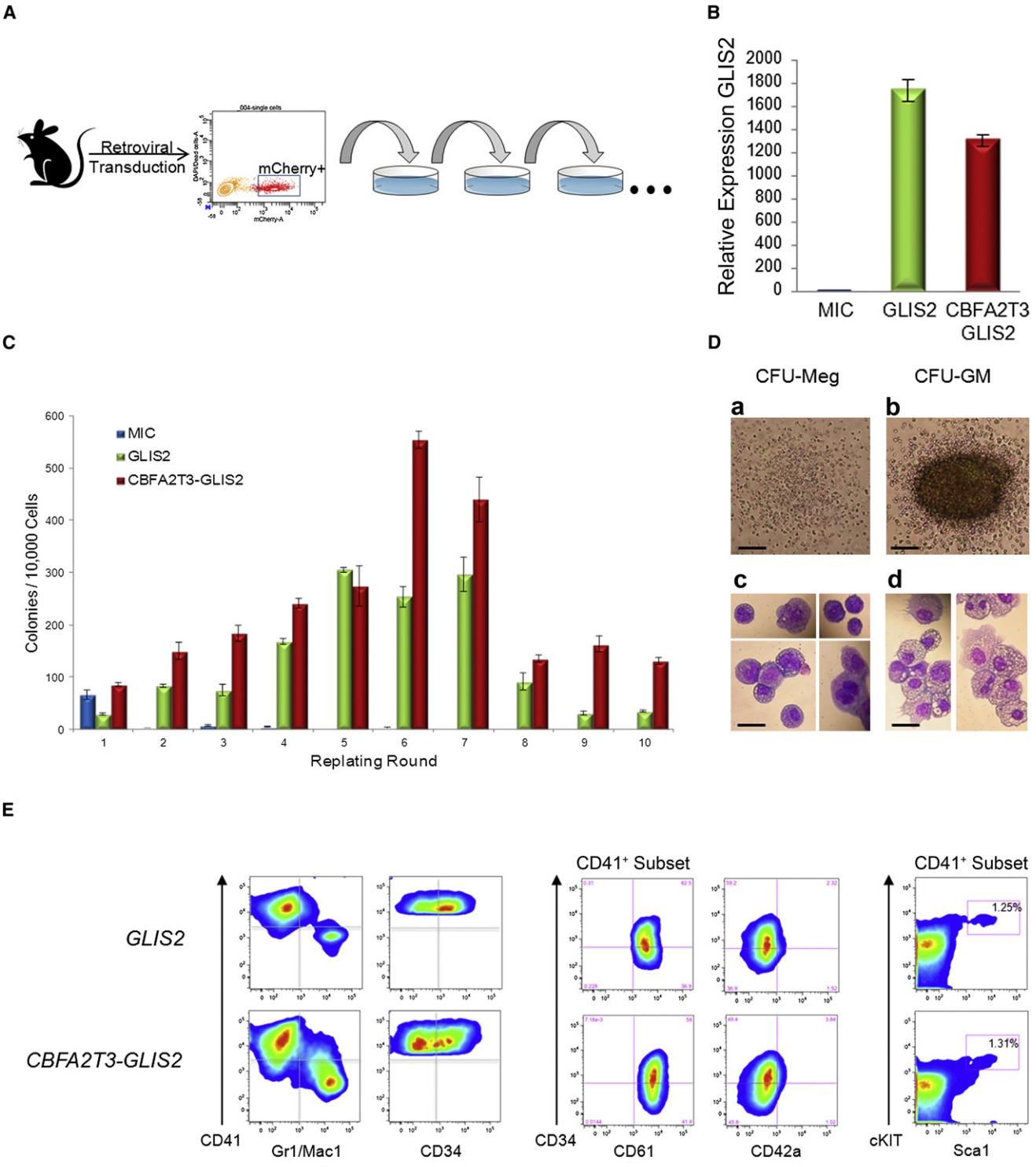

Figure 5. *CBFA2T3-GLIS2* Leads to Enhanced Replating of Hematopoietic Cells

(A) Experimental design. Murine bone marrow cells were transduced with retroviral vectors expressing mCherry alone (MIC), or mCherry along with *GLIS2*, or *CBFA2T3-GLIS2*. Transduced cells were purified by sorting mCherry-positive cells and plated onto methylcellulose containing IL3, IL6, SCF, and EPO. Colonies were counted after 7 days of growth and replated serially.

(B) Semiquantitative RT-PCR of GLIS2 utilizing cells harvested from first round of plating. *GLIS2* primers are specific for the 3′ half of the transcript and thus pick up both full-length GLIS2 as well as CBFA2T3-GLIS2. Expression in MIC cells was defined as one (1), and data are pooled from two separate experiments with similar results. $p \leq 0.0001$ as determined by one-way ANOVA. Error bars represent mean ± SEM of two independent experiments.

(C) Number of colonies detected at 7 days following each plating. Error bars represent mean ± SEM of two independent experiments.

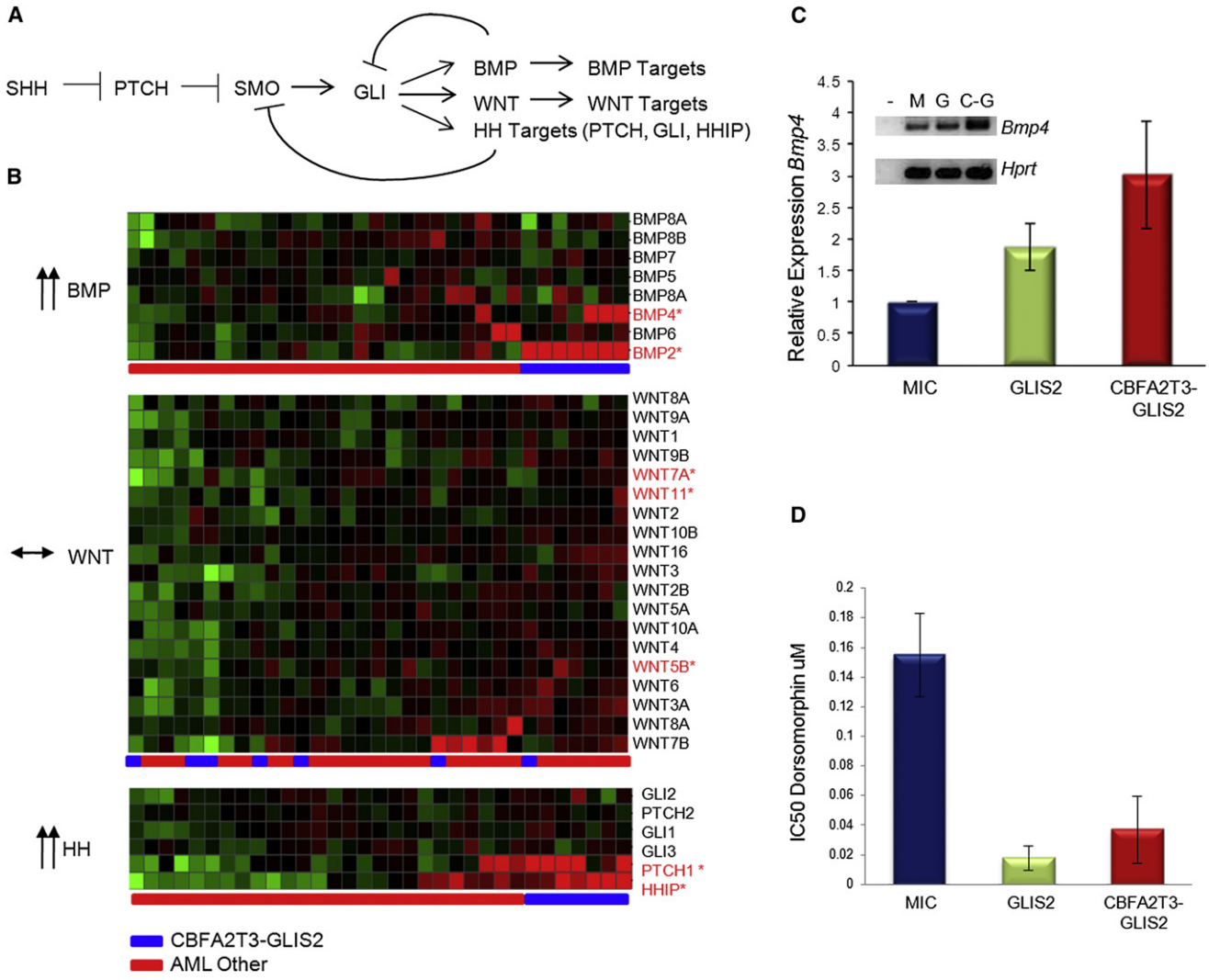

Figure 6. *CBFA2T3-GLIS2* Activates the BMP Pathway

(A) The Hedgehog (HH) signaling pathway. In addition to classic hedgehog targets such as *PTCH* and *HHIP*, *WNT* and *BMP* gene expression have been demonstrated to be affected by the GLI transcription factor in various models (Dahn and Fallon, 2000; Ingham and McMahon, 2001; Vokes et al., 2007).

(B) Gene expression profiles from *CBFA2T3-GLIS2* containing AMKL cases and other AML subtypes were evaluated for expression levels of *BMP*, *WNT*, and HH target genes. *CBFA2T3-GLIS2*-negative AMKL cases are not shown in this analysis. Significantly upregulated probe sets (FDR less than 0.05) are designated with red font: BMP2 FDR 1.06 × 10–17, BMP4 FDR 0.015976, PTCH1 FDR 2.05 × 10–6, and HHIP FDR 0.0038.

(C) Murine bone marrow cells were transduced with retroviral vectors carrying mCherry alone (MIC), mCherry plus *GLIS2*, or *CBFA2T3-GLIS2*. mCherry-positive cells were sorted and plated in methylcellulose containing IL3, IL6, SCF, and EPO. Following 1 week of growth, RNA was isolated, reverse transcribed, and amplified with *Bmp4* or *Hprt*-specific primers. Error bars represent mean ± SEM of four independent experiments. A representative gel is shown (–, neg; M, MIC; G, *GLIS2*; C-G, *CBFA2T3-GLIS2*). p = 0.047 as determined by one-way ANOVA.

(D) *GLIS2* and *CBFA2T3-GLIS2* sensitize murine hematopoietic cells to BMP receptor type I inhibition. Colony-formation assays were conducted in the presence or absence of dorsomorphin at the indicated concentrations (Yu et al., 2008). IC_{50} values were calculated as the amount of drug required to inhibit 50% of the colony formation as determined by colony counts. Error bars represent mean ± SEM of two independent experiments. p = 0.036 as determined by one-way ANOVA. See also Figure S4.

biological differences between pediatric and adult AMKL. Importantly, each of the detected chimeric transcripts is predicted to encode a fusion protein that would alter signaling pathways known to play a role in normal hematopoiesis, suggesting that these lesions are "driver" mutations that directly contribute to the development of leukemia. In addition to these somatic

(D) Colony morphology detected in *GLIS2* and *CBFA2T3-GLIS2*-modified cells from the second plating and beyond. a, CFU-Meg; b, CFU-GM. Scale bars, 500 μm. Representative cytospins and morphology of each colony type are shown. c, CFU-Meg; d, CFU-GM. Scale bars, 50 μm.

(E) Cells harvested from colony-forming assays after three or more replatings were subjected to flow cytometry. Cells were negative for acetylcholinesterase (data not shown).

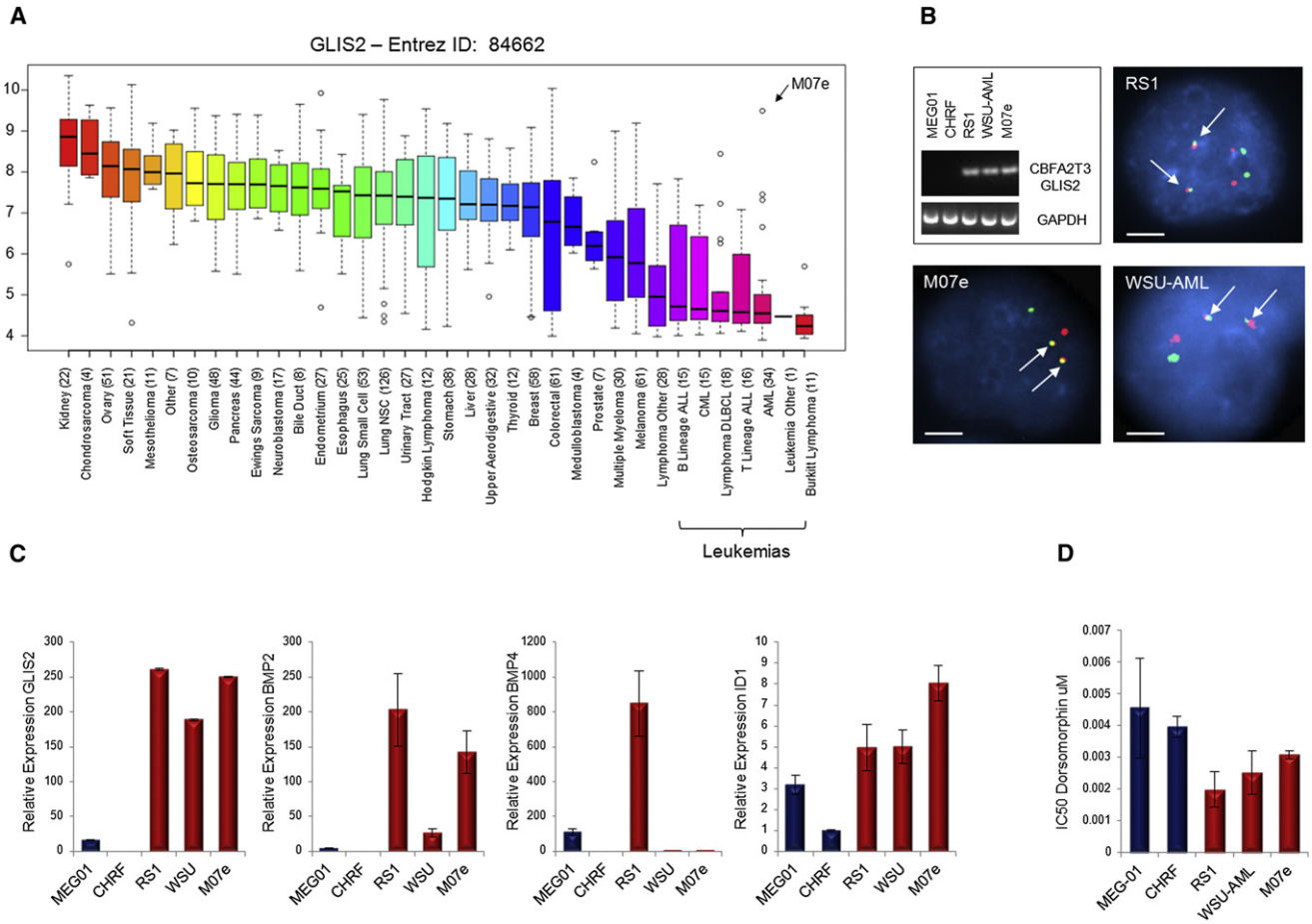

Figure 7. *CBFA2T3-GLIS2* Is Present in AMKL Cell Lines

(A) *GLIS2* expression as determined by gene expression arrays in 991 human cancer cell lines. Log_2-transformed expression levels are shown. Data were obtained from the Broad-Novartis Cancer Cell Line Encyclopedia (http://www.broadinstitute.org/ccle/home). A total of 34 AML cell lines are included; the extreme outlier of this subtype, M07e, is indicated. The *GLIS2* probe set recognizes the end of the transcript and thus does not distinguish between wild-type *GLIS2* and *CBFA2T3-GLIS2*. Median values are indicated by the band within the box plots; the ends of the whiskers indicate upper and lower adjacent values. Outliers are denoted by open circles.

(B) RT-PCR on five AMKL cell lines: MEG-01, CHRF-288-11, RS-1, WSU-AML, and M07e. The three cell lines carrying *CBFA2T3-GLIS2* were validated by FISH. Scale bars, 10 μm.

(C) Real-time semiquantitative RT-PCR of *GLIS2*, *BMP2*, *BMP4*, and *ID1* on the five AMKL cell lines. Expression levels relative to β-actin are shown. CHRF-288-11 expression levels were set to one (1) for comparison across cell lines. Error bars represent mean ± SEM of two independent experiments.

(D) Dorsomorphin sensitivity in the cell lines as determined by MTT assay. Error bars represent mean ± SEM of two independent experiments. For cell line information and MTT assay, please see Supplemental Experimental Procedures.

structural alterations, a variety of other somatic mutations were detected, including activating mutations in kinase signaling pathways in 21.6% of cases (*JAK* kinase family members and *MPL*), inactivating mutations in *GATA1* in 9.8% of cases, and amplification of chromosome 21 in the DSCR that includes genes known to play a role in AML such as *RUNX1*, *ETS2*, and *ERG* in 50% of the cases. How these mutations interact to not only induce overt leukemia but also to influence therapeutic responses remains to be determined.

As part of the St. Jude Children's Research Hospital-Washington University Pediatric Cancer Genome Project, we have sequenced 260 cases of pediatric cancers across multiple tumor types (Downing et al., 2012). The CBFA2T3-GLIS2 fusion was limited to AMKL cases. This specificity may exist for several reasons. The N-terminal portion of the fusion, CBFA2T3, is primarily expressed in the hematopoietic compartment, leading one to predict that expression of the inversion product, if it were to occur, would primarily be limited to hematopoietic cells. Although we do not know the exact target cell of transformation, induction of BMP4 signaling in human CD34+ progenitors has been demonstrated to increase the percentage of megakaryocyte and erythroid colonies in vitro (Fuchs et al., 2002; Jeanpierre et al., 2008). Thus, enhanced BMP signaling as a result of the expression of the inv(16)-encoded CBFA2T3-GLIS2 may directly contribute to the megakaryocytic differentiation of the leukemia cells.

The inv(16)-encoded *CBFA2T3-GLIS2* chimeric gene induced aberrant high-level expression of the DNA-binding domain of

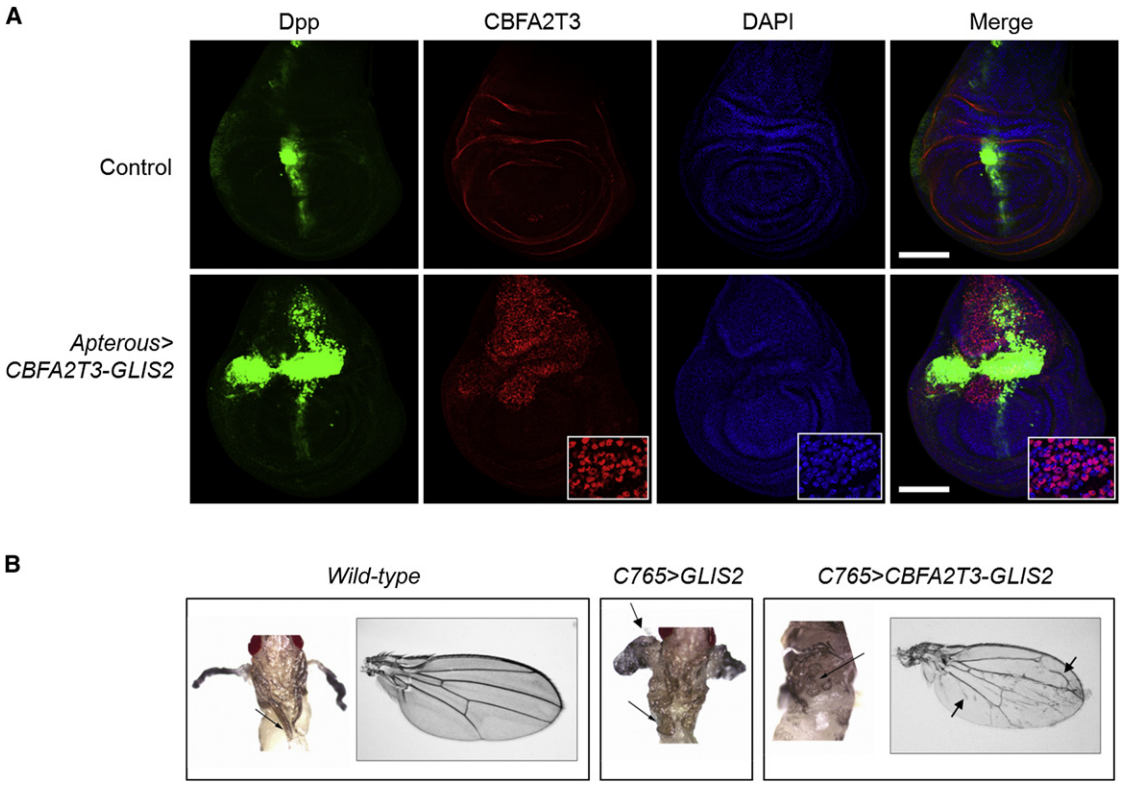

Figure 8. Transgenic *CBFA2T3-GLIS2 Drosophila* Ectopically Expresses Dpp

(A) *CBFA2T3-GLIS2* was expressed under control of *Apterous-Gal4* (strong epithelial dorsal driver). *dpp-lacZ* serves as a reporter for *dpp* induction. Wing imaginal discs were isolated at the late third instar, stained for β-gal as a readout for dpp (green), CBFA2T3 (red), and DAPI (blue), followed by immunofluorescence analysis. Nuclear localization of CBFA2T3-GLIS2 can be seen by the pink signal (inset). Scale bars, 100 μm.

(B) *CBFA2T3-GLIS2* was expressed under control of C765, a weak epithelial driver. Pharate adults were dissected from pupal casings and imaged. Arrows indicate ectopic notum, broadened and shortened legs. No *C765 > GLIS2 Drosophila* matured to adulthood. Arrows indicate ectopic veins in wings of rare *C765 > CBFA2T3-GLIS2* escapers.

See also Figure S5.

GLIS2 in hematopoietic cells, along with the disruption of one allele of *CBFA2T3*, a gene whose encoded protein has been shown to play a role in maintaining normal hematopoietic stem cell quiescence (Chyla et al., 2008). GLIS2 is a distant member of the GLI superfamily of transcriptional factors that function as critical transcriptional targets of the SHH signaling pathway (Hui and Angers, 2011). Although alterations in the SHH pathway have been directly implicated in a range of cancers (Barakat et al., 2010), the role of SHH signaling in normal hematopoiesis and leukemia remains poorly defined (Lim and Matsui, 2010). Our data suggest that aberrant expression of GLIS2 results in upregulation of the classic SHH-negative feedback inhibitors PTCH and HHIP, coupled with a marked increase in the expression of BMP 2 and 4, resulting in enhanced BMP signaling. These results indicate that CBFA2T3-GLIS2 functions, in part, as a gain-of-function GLIS2 allele. The exact mechanisms by which GLIS2 induced the upregulation of BMP2/BMP4 remains incompletely defined, although our data suggest that a direct transcription effect of GLIS2 on the BMP4 promoter is likely, although an indirect mechanism may also contribute.

Interestingly, BMP4 has been shown to expand and maintain human cord blood hematopoietic stem cells in vitro both directly, as well as indirectly via SHH signaling (Bhardwaj et al., 2001; Bhatia et al., 1999). Furthermore, *ID1*, a downstream BMP target previously implicated in leukemogenesis, was found to be upregulated in *CBFA2T3-GLIS2*-modified hematopoietic cells, demonstrating that this pathway is activated (Wang et al., 2011). Consistent with these findings, we demonstrated that activation of BMP signaling contributed to the marked increase in the replating capacity of myeloid/erythroid-committed progenitors. Accordingly, we found that murine hematopoietic cells carrying either full-length *GLIS2*, or *CBFA2T3-GLIS2*, demonstrated an increased sensitivity to BMP inhibition, suggesting that upregulation of this pathway contributes to the observed phenotype. In addition, BMP4 signaling has been shown to induce the differentiation of human CD34+ progenitors into megakaryocytes (Jeanpierre et al., 2008), suggesting that the upregulation of this pathway is also contributing to the megakaryocyte differentiation phenotype of these leukemias. Finally, BMP4, like thrombopoietin, appears to exert its effects on human megakaryopoiesis in part through the JAK/STAT pathways (Jeanpierre et al., 2008). Interestingly, functional pathway analysis of gene expression profiles in *CBFA2T3-GLIS2*-positive AMKL samples identified genes in the Jak-STAT signaling pathway to be significantly upregulated ($p = 0.0038$; FDR 0.022978; Figure S4). Combined with the identification in some cases of

activating mutations in either JAK family members or MPL in *CBFA2T3-GLIS2*-expressing leukemias, our data suggest that these lesions likely cooperate in leukemogenesis.

Taken together, these data define a poor prognostic subgroup of pediatric AMKL patients that are characterized by the inv(16)(p13.3q24.3)-encoded CBFA2T3-GLIS2 fusion protein. Expression of *CBFA2T3-GLIS2* induces an enhanced replating capacity of lineage-committed myeloid progenitors, along with megakaryocytic differentiation, in part through enhanced BMP2/BMP4 signaling. Whether altered SHH and CBFA2T3-induced signaling also contributes to leukemogenesis remains to be determined. Nevertheless, the presented data raise the important possibility that inhibition of the BMP pathway may have a therapeutic benefit in this aggressive form of pediatric AML.

EXPERIMENTAL PROCEDURES

Patients and Samples

Paired-end transcriptome sequencing on diagnostic leukemic blasts was performed on 14 pediatric non-DS-AMKL cases using the Illumina platform. Four of these cases underwent whole-genome sequencing (WGS) on diagnostic leukemia blasts and matched germline samples. All 14 cases underwent whole-exome sequencing for which 10 had matching germline samples. One additional diagnostic sample with matched germline DNA had whole-exome sequencing done that did not undergo transcriptome sequencing. All 15 of these patients were treated at St Jude Children's Research Hospital from 1990 to 2008. The recurrence cohort consisted of 61 additional cases including 33 pediatric specimens and 28 adult specimens . All samples were obtained with patient or parent/guardian-provided informed consent under protocols approved by the Institutional Review Board at each institution and St. Jude Children's Research Hospital.

Sequencing

RNA and DNA library construction for transcriptome and whole-genome DNA sequencing, respectively, has been described previously (Mardis et al., 2009; Zhang et al., 2012). Analysis of WGS data and whole-exome sequencing data that include mapping, coverage and quality assessment, single-nucleotide variant (SNV)/Indel detection, tier annotation for sequence mutations, prediction of deleterious effects of missense mutations, and identification of loss of heterozygosity was described previously (Zhang et al., 2012). Please see Supplemental Experimental Procedures for details.

Recurrency Screening for Sequence Variations and Fusions

We performed recurrence screening on a cohort of 61 AMKL samples. All 61 were screened by RT-PCR (see Supplemental Experimental Procedures for primers and conditions) for *CBFA2T3-GLIS2*, *GATA2-HOXA9*, *MN1-FLI1*, *NIPBL-HOXB9*, and *NUP98-KDM5A*. Whole-genome-amplified DNA (QIAGEN) from 38 cases underwent PCR and Sanger sequencing by Beckman Coulter Genomics for *JAK1*, *JAK2*, *JAK3*, and *MPL* mutations. In 8 of 38 cases, a paired matched germline was available. Putative SNVs and indel variants were detected by SNPdetector (Zhang et al., 2005).

Overall Survival Probabilities

Outcome data were available for 40 pediatric patients tested for *CBFA2T3-GLIS2*. *CBFA2T3-GLIS2* was found in 13 patients. Overall survival was defined as the date of diagnosis or study enrollment to the date of death with surviving patients censored at the date of last follow-up. Survival curves were estimated using the Kaplan-Meier method and compared using the exact log rank test based on 10,000 permutations.

Affymetrix SNP Array

Affymetrix SNP 6.0 array genotyping was performed for 14 of 15 AMKL cases in the discovery cohort, and array normalization and DNA copy number alterations were identified as previously described (Lin et al., 2004; Mullighan et al., 2007; Olshen et al., 2004; Pounds et al., 2009). To differentiate inherited copy number alterations from somatic events in leukemia blasts from patients lacking matched normal DNA, identified putative variants were filtered using public copy number polymorphism databases and a St. Jude database of SNP array data from several hundred samples (Iafrate et al., 2004; McCarroll et al., 2008).

Gene Expression Profiling

Gene expression profiling was performed using Affymetrix Human Exon 1.0 ST Arrays (Affymetrix) according to manufacturer's instructions. This cohort comprised 39 pediatric AML samples including AMKL (n = 14), *AML1-ETO* (n = 4), *CBFB-MYH11* (n = 2), *MLL* rearranged (n = 3), *PML-RARA* (n = 2), *NUP98-NSD1* (n = 2), *HLXB9-ETV6* (n = 1), and AML cases lacking chimeric genes (n = 11). Please see Supplemental Experimental Procedures for further details.

FISH

Dual-color FISH was performed on archived bone marrow cells and cell lines as described previously by Mullighan et al. (2007). Probes were derived from bacterial artificial chromosome (BAC) clones (Invitrogen). BACs used were RP11-830F9 (*CBFA2T3*), CTD-25555M20 (*GLIS2*), RP11-345E21 (*MN1*), and CTD-2542E23 (*FLI1*). BAC clone identity was verified by T7 and SP6 BAC-end sequencing and by hybridization of fluorescently labeled BAC DNA with normal human metaphase preparations.

Cloning of CBFA2T3-GLIS2 and GLIS2

Total RNA was extracted from leukemia blasts using RNeasy (QIAGEN) and reverse transcribed using Superscript III (Invitrogen) as per manufacturer's instructions. The coding region of *CBFA2T3-GLIS2* was PCR amplified from patient M712 and M707 using primers CBFA2T3_119F and GLIS2_1685R (see Supplemental Experimental Procedures for primers and conditions). *GLIS2* was PCR amplified from cDNA using primers GLIS2_21F and GLIS2_1685R (see Supplemental Experimental Procedures for primers and conditions). PCR products were subcloned into the pGEM-T Easy Vector (Promega) and sequenced. Clones containing the correct sequence were then subcloned into the MIC retroviral backbone (Volanakis et al., 2009).

Murine Bone Marrow Transduction and Colony-Forming Assays

All experiments involving mice were reviewed and approved by the Institutional Animal Care and Use Committee. Bone marrow from 4- to 6-week-old female C57/BL6 mice was harvested and cultured in the presence of recombinant murine SCF (rmSCF), IL3 (rmIL3), and IL6 (rmIL6) (Peprotech; all 50 ng/ml) for 24 hr prior to transduction on RetroNectin (Takara Bio)-coated plates. Ecotropic envelope-pseudotyped retroviral supernatant was produced by transient transfection of 293T cells as previously described by Soneoka et al. (1995). Forty-eight hours following transduction, cells were harvested, sorted for mCherry expression, and plated on methylcellulose containing IL3, IL6, SCF, and EPO (Stem Cell Technologies, Vancouver, British Columbia, Canada) as per manufacturer's instructions. Colonies were counted after 7 days of growth at 37°C, harvested, and replated. In a subset of experiments, dorsomorphin (Sigma-Aldrich) was added to the methylcellulose at the indicated concentrations.

Flow Cytometry

Cells were resuspended in PBS and preincubated with anti-CD16/CD32 Fc-block (BD PharMingen) if staining did not include conjugated anti-murine CD16/32. Aliquots were stained for 15 min at 4°C with conjugated antibodies. Cells were washed and resuspended in DAPI containing solution (1 μg/ml DAPI in PBS) for subsequent analysis using FACS LSR II D (BD Biosciences). For a list of antibodies used, please see Supplemental Experimental Procedures.

Luciferase Assays

The human BMP4 promoter-driven luciferase construct pSLA4.1EX (Van den Wijngaard et al., 1999) was kindly provided by E. Joop van Zoelen, Nijmegen, The Netherlands. The murine BMP response element (pBRE) (Korchynskyi and ten Dijke, 2002) was kindly provided by Peter ten Dijke, Leiden, The Netherlands. The 8 × 3′ Gli-BS luciferase reporter (pGli-BS) (Sasaki et al., 1997) has been previously described. TOPFlash and FOPFlash (Korinek et al., 1997) constructs were obtained from Addgene. For details on luciferase reporter assays, please see Supplemental Experimental Procedures.

ELISA

BMP4 protein levels in the supernatants from transduced murine hematopoietic cells were determined by ELISA. Briefly, mCherry-positive bone marrow cells transduced with empty (MIC), GLIS2, or CBFA2T3-GLIS2-containing retroviruses were placed in media containing IL3, IL6, and SCF for 48 hr, and supernatant was then harvested and the level of murine BMP4 determined using an ELISA kit purchased from TSZELISA (http://www.tszelisa.com). Measurements were done according to manufacturer's instructions.

Transgenic *Drosophila*

CBFA2T3-GLIS2 and *GLIS2* cDNAs were subcloned into the *pUAS-attB* plasmid (Bischof et al., 2007). Transgenic UAS-*CBFA2T3-GLIS2* and UAS-*GLIS2* flies were generated using site-specific ϕC31 integration system (Bischof et al., 2007). Embryo injections were performed by Best Gene. UAS constructs were targeted to chromosome 2R-51D in order to avoid differential positional effects on transgene expression. For wing imaginal disc staining, relevant crosses were performed to generate flies carrying all three transgenes: *Apterous-Gal4* (a strong epithelial dorsal compartment-specific GAL4 driver), UAS-*CBFA2T3-GLIS2*, and a *dpp-lacZ* enhancer trap reporter. Gal4 driver and *dpp-lacZ* reporter stocks were obtained from the Bloomington Stock Center. Wing imaginal discs were dissected from wandering third-instar larvae, fixed, and immunostained using anti-β-gal (Promega; Z378), anti-CBFA2T3 (Abcam; ab33072), and DAPI (Invitrogen; D3571) as previously described by Carroll et al. (2012). To assess the phenotypic effects of *CBFA2T3-GLIS2* and *GLIS2*, UAS transgenes were expressed under control of the epithelial driver *C765-Gal4*, and progeny was observed. Pharate adults were dissected from pupal casings and imaged.

ACCESSION NUMBERS

The sequence data and SNP microarray data have been deposited in the dbGaP database (http://www.ncbi.nlm.nih.gov/gap) under the accession number phs000413.v1.p1. Affymetrix gene expression data have been deposited in the NCBI Gene Expression Omnibus (http://www.ncbi.nlm.nih.gov/geo/) under GSE35203.

SUPPLEMENTAL INFORMATION

Supplemental Information includes five figures, seven tables, and Supplemental Experimental Procedures and can be found with this article online at http://dx.doi.org/10.1016/j.ccr.2012.10.007.

ACKNOWLEDGMENTS

The authors would like to specifically thank Joy Nakitandwe for critical input and discussions, Susana Raimondi for review of cytogenetics, Matt Stine for assistance with data deposition, Bill Pappas and Scott Malone for support of the information technology infrastructure, and the staff of Tissue Resources Laboratory, Flow Cytometry and Cell Sorting Core, the Hartwell Center for Biotechnology and Bioinformatics of St Jude Children's Research Hospital, and Emily Dolezale for assistance in sample procurement at Memorial Sloan Kettering Cancer Center. This work was supported by grants from the National Institutes of Health (Cancer Center Support Grant P30 CA021765), the Eric Trump Foundation, a Leukemia & Lymphoma Society Specialized Center of Research Grant LLS7015, and the American Lebanese Syrian Associated Charities (ALSAC) of St Jude Children's Research Hospital.

Received: June 21, 2012
Revised: September 5, 2012
Accepted: October 17, 2012
Published: November 12, 2012

REFERENCES

Argiropoulos, B., and Humphries, R.K. (2007). Hox genes in hematopoiesis and leukemogenesis. Oncogene *26*, 6766–6776.

Athale, U.H., Razzouk, B.I., Raimondi, S.C., Tong, X., Behm, F.G., Head, D.R., Srivastava, D.K., Rubnitz, J.E., Bowman, L., Pui, C.H., and Ribeiro, R.C. (2001). Biology and outcome of childhood acute megakaryoblastic leukemia: a single institution's experience. Blood *97*, 3727–3732.

Attanasio, M., Uhlenhaut, N.H., Sousa, V.H., O'Toole, J.F., Otto, E., Anlag, K., Klugmann, C., Treier, A.C., Helou, J., Sayer, J.A., et al. (2007). Loss of GLIS2 causes nephronophthisis in humans and mice by increased apoptosis and fibrosis. Nat. Genet. *39*, 1018–1024.

Barakat, M.T., Humke, E.W., and Scott, M.P. (2010). Learning from Jekyll to control Hyde: Hedgehog signaling in development and cancer. Trends Mol. Med. *16*, 337–348.

Barnard, D.R., Alonzo, T.A., Gerbing, R.B., Lange, B., and Woods, W.G.; Children's Oncology Group. (2007). Comparison of childhood myelodysplastic syndrome, AML FAB M6 or M7, CCG 2891: report from the Children's Oncology Group. Pediatr. Blood Cancer *49*, 17–22.

Barretina, J., Caponigro, G., Stransky, N., Venkatesan, K., Margolin, A.A., Kim, S., Wilson, C.J., Lehár, J., Kryukov, G.V., Sonkin, D., et al. (2012). The Cancer Cell Line Encyclopedia enables predictive modelling of anticancer drug sensitivity. Nature *483*, 603–607.

Bhardwaj, G., Murdoch, B., Wu, D., Baker, D.P., Williams, K.P., Chadwick, K., Ling, L.E., Karanu, F.N., and Bhatia, M. (2001). Sonic hedgehog induces the proliferation of primitive human hematopoietic cells via BMP regulation. Nat. Immunol. *2*, 172–180.

Bhatia, M., Bonnet, D., Wu, D., Murdoch, B., Wrana, J., Gallacher, L., and Dick, J.E. (1999). Bone morphogenetic proteins regulate the developmental program of human hematopoietic stem cells. J. Exp. Med. *189*, 1139–1148.

Bischof, J., Maeda, R.K., Hediger, M., Karch, F., and Basler, K. (2007). An optimized transgenesis system for *Drosophila* using germ-line-specific phiC31 integrases. Proc. Natl. Acad. Sci. USA *104*, 3312–3317.

Buijs, A., van Rompaey, L., Molijn, A.C., Davis, J.N., Vertegaal, A.C., Potter, M.D., Adams, C., van Baal, S., Zwarthoff, E.C., Roussel, M.F., and Grosveld, G.C. (2000). The MN1-TEL fusion protein, encoded by the translocation (12;22)(p13;q11) in myeloid leukemia, is a transcription factor with transforming activity. Mol. Cell. Biol. *20*, 9281–9293.

Carroll, A., Civin, C., Schneider, N., Dahl, G., Pappo, A., Bowman, P., Emami, A., Gross, S., Alvarado, C., Phillips, C., et al. (1991). The t(1;22) (p13;q13) is nonrandom and restricted to infants with acute megakaryoblastic leukemia: a Pediatric Oncology Group Study. Blood *78*, 748–752.

Carroll, C.E., Marada, S., Stewart, D.P., Ouyang, J.X., and Ogden, S.K. (2012). The extracellular loops of Smoothened play a regulatory role in control of Hedgehog pathway activation. Development *139*, 612–621.

Chyla, B.J., Moreno-Miralles, I., Steapleton, M.A., Thompson, M.A., Bhaskara, S., Engel, M., and Hiebert, S.W. (2008). Deletion of Mtg16, a target of t(16;21), alters hematopoietic progenitor cell proliferation and lineage allocation. Mol. Cell. Biol. *28*, 6234–6247.

Creutzig, U., Reinhardt, D., Diekamp, S., Dworzak, M., Stary, J., and Zimmermann, M. (2005). AML patients with Down syndrome have a high cure rate with AML-BFM therapy with reduced dose intensity. Leukemia *19*, 1355–1360.

Dahn, R.D., and Fallon, J.F. (2000). Interdigital regulation of digit identity and homeotic transformation by modulated BMP signaling. Science *289*, 438–441.

Downing, J.R., Wilson, R.K., Zhang, J., Mardis, E.R., Pui, C.-H., Ding, L., Ley, T.J., and Evans, W.E. (2012). The Pediatric Cancer Genome Project. Nat. Genet. *44*, 619–622.

Fuchs, O., Simakova, O., Klener, P., Cmejlova, J., Zivny, J., Zavadil, J., and Stopka, T. (2002). Inhibition of Smad5 in human hematopoietic progenitors blocks erythroid differentiation induced by BMP4. Blood Cells Mol. Dis. *28*, 221–233.

Gamou, T., Kitamura, E., Hosoda, F., Shimizu, K., Shinohara, K., Hayashi, Y., Nagase, T., Yokoyama, Y., and Ohki, M. (1998). The partner gene of AML1 in t(16;21) myeloid malignancies is a novel member of the MTG8(ETO) family. Blood *91*, 4028–4037.

Grieder, N.C., Morata, G., Affolter, M., and Gehring, W.J. (2009). Spalt major controls the development of the notum and of wing hinge primordia of the *Drosophila melanogaster* wing imaginal disc. Dev. Biol. *329*, 315–326.

Heuser, M., Yun, H., Berg, T., Yung, E., Argiropoulos, B., Kuchenbauer, F., Park, G., Hamwi, I., Palmqvist, L., Lai, C.K., et al. (2011). Cell of origin in AML: susceptibility to MN1-induced transformation is regulated by the MEIS1/AbdB-like HOX protein complex. Cancer Cell *20*, 39–52.

Higuchi, M., O'Brien, D., Kumaravelu, P., Lenny, N., Yeoh, E.J., and Downing, J.R. (2002). Expression of a conditional AML1-ETO oncogene bypasses embryonic lethality and establishes a murine model of human t(8;21) acute myeloid leukemia. Cancer Cell *1*, 63–74.

Hui, C.C., and Angers, S. (2011). Gli proteins in development and disease. Annu. Rev. Cell Dev. Biol. *27*, 513–537.

Iafrate, A.J., Feuk, L., Rivera, M.N., Listewnik, M.L., Donahoe, P.K., Qi, Y., Scherer, S.W., and Lee, C. (2004). Detection of large-scale variation in the human genome. Nat. Genet. *36*, 949–951.

Ingham, P.W., and McMahon, A.P. (2001). Hedgehog signaling in animal development: paradigms and principles. Genes Dev. *15*, 3059–3087.

Jeanpierre, S., Nicolini, F.E., Kaniewski, B., Dumontet, C., Rimokh, R., Puisieux, A., and Maguer-Satta, V. (2008). BMP4 regulation of human megakaryocytic differentiation is involved in thrombopoietin signaling. Blood *112*, 3154–3163.

Kawada, H., Ito, T., Pharr, P.N., Spyropoulos, D.D., Watson, D.K., and Ogawa, M. (2001). Defective megakaryopoiesis and abnormal erythroid development in Fli-1 gene-targeted mice. Int. J. Hematol. *73*, 463–468.

Kim, Y.S., Kang, H.S., and Jetten, A.M. (2007). The Krüppel-like zinc finger protein Glis2 functions as a negative modulator of the Wnt/beta-catenin signaling pathway. FEBS Lett. *581*, 858–864.

Korchynskyi, O., and ten Dijke, P. (2002). Identification and functional characterization of distinct critically important bone morphogenetic protein-specific response elements in the Id1 promoter. J. Biol. Chem. *277*, 4883–4891.

Korinek, V., Barker, N., Morin, P.J., van Wichen, D., de Weger, R., Kinzler, K.W., Vogelstein, B., and Clevers, H. (1997). Constitutive transcriptional activation by a beta-catenin-Tcf complex in APC-/- colon carcinoma. Science *275*, 1784–1787.

Krzywinski, M., Schein, J., Birol, I., Connors, J., Gascoyne, R., Horsman, D., Jones, S.J., and Marra, M.A. (2009). Circos: an information aesthetic for comparative genomics. Genome Res. *19*, 1639–1645.

Lamar, E., Kintner, C., and Goulding, M. (2001). Identification of NKL, a novel Gli-Kruppel zinc-finger protein that promotes neuronal differentiation. Development *128*, 1335–1346.

Lim, Y., and Matsui, W. (2010). Hedgehog signaling in hematopoiesis. Crit. Rev. Eukaryot. Gene Expr. *20*, 129–139.

Lin, M., Wei, L.J., Sellers, W.R., Lieberfarb, M., Wong, W.H., and Li, C. (2004). dChipSNP: significance curve and clustering of SNP-array-based loss-of-heterozygosity data. Bioinformatics *20*, 1233–1240.

Lion, T., Haas, O.A., Harbott, J., Bannier, E., Ritterbach, J., Jankovic, M., Fink, F.M., Stojimirovic, A., Herrmann, J., Riehm, H.J., et al. (1992). The translocation t(1;22)(p13;q13) is a nonrandom marker specifically associated with acute megakaryocytic leukemia in young children. Blood *79*, 3325–3330.

Ma, Z., Morris, S.W., Valentine, V., Li, M., Herbrick, J.A., Cui, X., Bouman, D., Li, Y., Mehta, P.K., Nizetic, D., et al. (2001). Fusion of two novel genes, RBM15 and MKL1, in the t(1;22)(p13;q13) of acute megakaryoblastic leukemia. Nat. Genet. *28*, 220–221.

Malinge, S., Ragu, C., Della-Valle, V., Pisani, D., Constantinescu, S.N., Perez, C., Villeval, J.L., Reinhardt, D., Landman-Parker, J., Michaux, L., et al. (2008). Activating mutations in human acute megakaryoblastic leukemia. Blood *112*, 4220–4226.

Mardis, E.R., Ding, L., Dooling, D.J., Larson, D.E., McLellan, M.D., Chen, K., Koboldt, D.C., Fulton, R.S., Delehaunty, K.D., McGrath, S.D., et al. (2009). Recurring mutations found by sequencing an acute myeloid leukemia genome. N. Engl. J. Med. *361*, 1058–1066.

McCarroll, S.A., Kuruvilla, F.G., Korn, J.M., Cawley, S., Nemesh, J., Wysoker, A., Shapero, M.H., de Bakker, P.I., Maller, J.B., Kirby, A., et al. (2008). Integrated detection and population-genetic analysis of SNPs and copy number variation. Nat. Genet. *40*, 1166–1174.

Mercher, T., Coniat, M.B., Monni, R., Mauchauffe, M., Nguyen Khac, F., Gressin, L., Mugneret, F., Leblanc, T., Dastugue, N., Berger, R., and Bernard, O.A. (2001). Involvement of a human gene related to the *Drosophila* spen gene in the recurrent t(1;22) translocation of acute megakaryocytic leukemia. Proc. Natl. Acad. Sci. USA *98*, 5776–5779.

Mullighan, C.G., Goorha, S., Radtke, I., Miller, C.B., Coustan-Smith, E., Dalton, J.D., Girtman, K., Mathew, S., Ma, J., Pounds, S.B., et al. (2007). Genome-wide analysis of genetic alterations in acute lymphoblastic leukaemia. Nature *446*, 758–764.

Oki, Y., Kantarjian, H.M., Zhou, X., Cortes, J., Faderl, S., Verstovsek, S., O'Brien, S., Koller, C., Beran, M., Bekele, B.N., et al. (2006). Adult acute megakaryocytic leukemia: an analysis of 37 patients treated at M.D. Anderson Cancer Center. Blood *107*, 880–884.

Olshen, A.B., Venkatraman, E.S., Lucito, R., and Wigler, M. (2004). Circular binary segmentation for the analysis of array-based DNA copy number data. Biostatistics *5*, 557–572.

Pounds, S., Cheng, C., Mullighan, C., Raimondi, S.C., Shurtleff, S., and Downing, J.R. (2009). Reference alignment of SNP microarray signals for copy number analysis of tumors. Bioinformatics *25*, 315–321.

Radtke, I., Mullighan, C.G., Ishii, M., Su, X., Cheng, J., Ma, J., Ganti, R., Cai, Z., Goorha, S., Pounds, S.B., et al. (2009). Genomic analysis reveals few genetic alterations in pediatric acute myeloid leukemia. Proc. Natl. Acad. Sci. USA *106*, 12944–12949.

Sander, V., Eivers, E., Choi, R.H., and De Robertis, E.M. (2010). *Drosophila* Smad2 opposes Mad signaling during wing vein development. PLoS One *5*, e10383.

Sasaki, H., Hui, C., Nakafuku, M., and Kondoh, H. (1997). A binding site for Gli proteins is essential for HNF-3beta floor plate enhancer activity in transgenics and can respond to Shh in vitro. Development *124*, 1313–1322.

Söderberg, S.S., Karlsson, G., and Karlsson, S. (2009). Complex and context dependent regulation of hematopoiesis by TGF-beta superfamily signaling. Ann. N Y Acad. Sci. *1176*, 55–69.

Soneoka, Y., Cannon, P.M., Ramsdale, E.E., Griffiths, J.C., Romano, G., Kingsman, S.M., and Kingsman, A.J. (1995). A transient three-plasmid expression system for the production of high titer retroviral vectors. Nucleic Acids Res. *23*, 628–633.

Tabata, T., and Takei, Y. (2004). Morphogens, their identification and regulation. Development *131*, 703–712.

Tallman, M.S., Neuberg, D., Bennett, J.M., Francois, C.J., Paietta, E., Wiernik, P.H., Dewald, G., Cassileth, P.A., Oken, M.M., and Rowe, J.M. (2000). Acute megakaryocytic leukemia: the Eastern Cooperative Oncology Group experience. Blood *96*, 2405–2411.

Van den Wijngaard, A., Pijpers, M.A., Joosten, P.H., Roelofs, J.M., Van zoelen, E.J., and Olijve, W. (1999). Functional characterization of two promoters in the human bone morphogenetic protein-4 gene. J. Bone Miner. Res. *14*, 1432–1441.

Visvader, J.E., Crossley, M., Hill, J., Orkin, S.H., and Adams, J.M. (1995). The C-terminal zinc finger of GATA-1 or GATA-2 is sufficient to induce megakaryocytic differentiation of an early myeloid cell line. Mol. Cell. Biol. *15*, 634–641.

Vokes, S.A., Ji, H., McCuine, S., Tenzen, T., Giles, S., Zhong, S., Longabaugh, W.J., Davidson, E.H., Wong, W.H., and McMahon, A.P. (2007). Genomic characterization of Gli-activator targets in sonic hedgehog-mediated neural patterning. Development *134*, 1977–1989.

Volanakis, E.J., Williams, R.T., and Sherr, C.J. (2009). Stage-specific Arf tumor suppression in Notch1-induced T-cell acute lymphoblastic leukemia. Blood *114*, 4451–4459.

Wang, G.G., Song, J., Wang, Z., Dormann, H.L., Casadio, F., Li, H., Luo, J.L., Patel, D.J., and Allis, C.D. (2009). Haematopoietic malignancies caused by dysregulation of a chromatin-binding PHD finger. Nature *459*, 847–851.

Wang, L., Gural, A., Sun, X.J., Zhao, X., Perna, F., Huang, G., Hatlen, M.A., Vu, L., Liu, F., Xu, H., et al. (2011). The leukemogenicity of AML1-ETO is dependent on site-specific lysine acetylation. Science *333*, 765–769.

Yu, P.B., Hong, C.C., Sachidanandan, C., Babitt, J.L., Deng, D.Y., Hoyng, S.A., Lin, H.Y., Bloch, K.D., and Peterson, R.T. (2008). Dorsomorphin inhibits BMP signals required for embryogenesis and iron metabolism. Nat. Chem. Biol. *4*, 33–41.

Zhang, J., Wheeler, D.A., Yakub, I., Wei, S., Sood, R., Rowe, W., Liu, P.P., Gibbs, R.A., and Buetow, K.H. (2005). SNPdetector: a software tool for sensitive and accurate SNP detection. PLoS Comput. Biol. *1*, e53.

Zhang, J., Ding, L., Holmfeldt, L., Wu, G., Heatley, S.L., Payne-Turner, D., Easton, J., Chen, X., Wang, J., Rusch, M., et al. (2012). The genetic basis of early T-cell precursor acute lymphoblastic leukaemia. Nature *481*, 157–163.

BMP Meets AML: Induction of BMP Signaling by a Novel Fusion Gene Promotes Pediatric Acute Leukemia

John D. Crispino[1,*] and Michelle M. Le Beau[2]
[1]Division of Hematology/Oncology, Northwestern University
[2]Section of Hematology/Oncology, and the Comprehensive Cancer Center
University of Chicago, Chicago, IL 60637, USA
*Correspondence: j-crispino@northwestern.edu
http://dx.doi.org/10.1016/j.ccr.2012.10.008

In this issue of *Cancer Cell*, Gruber et al. report that a significant proportion of children with acute megakaryoblastic leukemia acquire a translocation that confers enhanced BMP signaling and promotes self-renewal of hematopoietic progenitors. This study presents novel therapeutic targets that may lead to improved therapies for this aggressive leukemia.

Acute megakaryoblastic leukemia (AMKL) is a rare and deadly form of acute myeloid leukemia. There are three major subtypes of AMKL that differ from one another in their genetics and their prognosis: leukemia found in children with Down syndrome (DS), in children without DS, or in adults. Of these groups, the pathogenesis of DS-AMKL has the greatest clarity. Nearly 5% of children with DS-AMKL acquire *GATA1* mutations in mid-gestation that lead to abnormal megakaryocyte development. It is believed that the combination of a *GATA1* mutation and aberrant expression of *ERG* and *DYRK1A*, among other genes on chromosome 21, promotes a preleukemia named transient myeloproliferative disorder (TMD) (Malinge et al., 2012). Evolution of TMD to AMKL likely requires the acquisition of additional mutations in genes such as *MPL* and *JAK2*, which are associated with aberrant megakaryopoiesis in the myeloproliferative neoplasms (MPNs). It is also believed that *GATA1* mutations confer hypersensitivity to treatment with cytosine arabinoside, which leads to a favorable outcome (Ge et al., 2004). In sharp contrast, adults with AMKL face a dismal prognosis, with nearly all patients relapsing within one year of diagnosis (Tallman et al., 2000). Apart from sporadic mutations in *JAK2* and *MPL*, little is known about the genetic basis of adult AMKL.

Although there have been many revelations about pediatric AMKL in children with DS, much less is known about the etiology of other pediatric cases. One exception is the presence of a recurring (1;22) translocation, which creates the OTT-MAL (or RBM15-MKL1) fusion unique to pediatric AMKL. This fusion leads to altered expression of serum response factor target genes and aberrant Notch pathway activation (Cheng et al., 2009; Mercher et al., 2009). Additionally, rare findings of *JAK* and *MPL* mutations have also been observed in this group.

To identify new mutations and chromosomal aberrations that define pediatric AMKL, Gruber et al. (2012; this issue of *Cancer Cell*) took advantage of next-generation sequencing, a powerful tool that provides new insights into the genetics of cancer. Paired-end sequencing of a discovery cohort consisting of 14 pediatric non-DS AMKL patients revealed structural variations that led to novel chimeric transcripts in 12 of the cases. Of note, half of the AMKL cases harbored a cryptic inversion on chromosome 16 inv(16)(p13.3q24.3), which led to fusion of *CBFA2T3* and *GLIS2*. Two of these cases with the *CBFA2T3-GLIS2* fusion also had a gain of chromosomal arm 21q, a common abnormality in AMKL. Remarkably, after screening a larger validation cohort and other leukemia samples, the fusion was detected in 27% of pediatric non-DS AMKL cases. The *CBFA2T3-GLIS2* fusion was not observed in adult AMKL nor in any other form of myeloid leukemia. In addition, none of the samples with inv(16)(p13.3q24.3) had t(1;22), suggesting that these two recurring translocations are mutually exclusive. Surprisingly, seven cases, including three cases with the novel fusion, also contained amplification of the Down syndrome critical region, implying that dysregulation of Hsa21 genes contributes to more than just the DS subtype of AMKL (Gruber et al., 2012).

CBFA2T3 is a member of the ETO family of co-repressors that is expressed in hematopoietic cells and plays a role in regulating stem cell quiescence (Chyla et al., 2008). In contrast, the gene encoding GLIS2, which participates in the regulation of SHH signaling, is not expressed in hematopoietic cells. However, as a consequence of the fusion, the C-terminal zinc finger domain that binds the GLIS consensus sequence is fused to the N-terminal CBFA2T3 *nervy* domain that mediates protein-protein interactions and is expressed in blood cells. Gene expression studies comparing fusion-positive AMKLs against other forms of AML revealed that cases with the fusion showed altered expression of genes in the BMP, SHH, and WNT pathways. In particular, marked overexpression of BMP2 and BMP4 was observed (Figure 1). Of note, expression of CBFA2T3-GLIS2 or GLIS2 alone in *Drosophila* led to enhanced BMP signaling and the associated *dpp* gain-of-function phenotype, including shortened legs and wing blistering (Gruber et al., 2012).

The discovery of this novel recurring translocation raises a number of important questions. First, is the fusion a necessary and/or sufficient factor in leukemogenesis? Functional studies

demonstrated that expression of the fusion protein, or GLIS2 alone, led to enhanced self-renewal of hematopoietic progenitors in vitro. This phenotype was blocked by dorsomorphin, a small molecule that interferes with BMP signaling to Smad effectors, suggesting that the increased expression of BMP downstream of the fusion is essential for the phenotype. Expression of the *CBFA2T3-GLIS2* fusion transcript in mice, however, did not lead to leukemia, indicating that the fusion protein is not sufficient for leukemogenesis. It is likely that mutations, which confer cytokine independent growth, such as those in *MPL* or *JAK* family members, cooperate with the fusion to promote AMKL.

Second, is there a contribution by *CBFA2T3* apart from driving expression of *GLIS2* in hematopoietic cells? The finding that *GLIS2* transduced hematopoietic progenitors failed to re-plate to the same extent as progenitors transduced with the fusion strongly suggests that there is an additional, as yet undefined, contribution by CBFA2T3. Alternatively, it is possible that loss of the N-terminal amino acids of GLIS2 in the fusion may alter GLIS2 function.

Third, what is the natural history of the disease? *GATA1* mutations in DS-AMKL originate in the fetal liver and can be detected as early as 21 weeks of gestation (Taub et al., 2004). However, although *GATA1* mutations in DS are suspected to cause TMD, not all babies with *GATA1* mutations show an overt hematopoietic phenotype, and the majority do not go on to develop AMKL. This finding is reminiscent of classical studies by Greaves and Wiemels (2003), who showed that chromosomal translocations can be detected at birth even in children who do not go on to develop leukemia. The timing of the pediatric non-DS AMKL suggests that the fusion of *CBFA2T3* and *GLIS2* occurs in utero and within the fetal liver. Whether all instances of the fusion lead to leukemia remains to be determined, but the fact that expression of CBFA2T3-GLIS2 in mice does not confer leukemia suggests that additional events are required for full transformation. Similar to *GATA1* mutations, the fusion is not detected in adult AMKL, implying perhaps that necessary cooperating events are not possible in bone marrow progenitors.

Fourth, how does the translocation specifically lead to pediatric AMKL? Previous studies have shown that increased BMP signaling induces the differentiation of $CD34^+$ cells to megakaryocytes (Jeanpierre et al., 2008). This effect may be the result of upregulation of JAK/STAT signaling, as seen in MPNs and AMKL with activating mutations in *MPL* and *JAK* family members. However, the details of how activated BMP signaling, downstream of the CBFA2T3-GLIS2 fusion protein, imparts a megakaryocytic phenotype remains a mystery.

Finally, will BMP inhibitors prove to be effective new therapies for AMKL? Given the poor prognosis of AMKL and, in particular, cases with the CBFA2T3-GLIS2 fusion, development of novel therapies is essential. The observation that a BMP antagonist disrupts re-plating of hematopoietic progenitors suggests that inhibition of BMP signaling may provide therapeutic benefit. However, additional events that cooperate with the fusion to drive acute leukemia may circumvent anti-BMP therapy. Future preclinical and, if appropriate, clinical studies to determine the effectiveness of BMP inhibitors against human AMKL are needed.

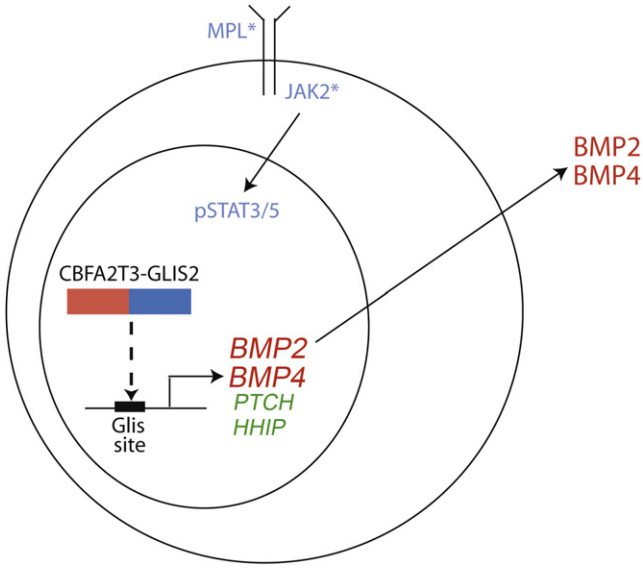

Figure 1. Model of the Activity of inv(16)(p13.3q24.3) Gene Fusion Product in AMKL

The CBFA2T3-GLIS2 fusion protein generated by inv(16)(p13.3q24.3) likely directly activates transcription of activators of BMP signaling *BMP2* and *BMP4* as well as inhibitors of SHH signaling *PTCH* and *HHIP*. BMP2/4 may act in an autocrine manner to foster growth of AMKL blasts or may alternatively signal in a paracrine manner to hematopoietic progenitors that, in turn, would promote the megakaryocytic lineage phenotype of the leukemia. In addition, mutations in *MPL* or *JAK* family members confer cytokine independence and likely cooperate with the fusion to promote AMKL.

REFERENCES

Cheng, E.C., Luo, Q., Bruscia, E.M., Renda, M.J., Troy, J.A., Massaro, S.A., Tuck, D., Schulz, V., Mane, S.M., Berliner, N., et al. (2009). Blood *113*, 2826–2834.

Chyla, B.J., Moreno-Miralles, I., Steapleton, M.A., Thompson, M.A., Bhaskara, S., Engel, M., and Hiebert, S.W. (2008). Mol. Cell. Biol. *28*, 6234–6247.

Ge, Y., Jensen, T.L., Stout, M.L., Flatley, R.M., Grohar, P.J., Ravindranath, Y., Matherly, L.H., and Taub, J.W. (2004). Cancer Res. *64*, 728–735.

Greaves, M.F., and Wiemels, J. (2003). Nat. Rev. Cancer *3*, 639–649.

Gruber, T.A., Gedman, A.L., Zhang, J., Koss, C.S., Marada, S., Ta, H.Q., Chen, S.-C., Su, X., Ogden, S.K., Dang, J., et al. (2012). Cancer Cell *22*, this issue, 683–697.

Jeanpierre, S., Nicolini, F.E., Kaniewski, B., Dumontet, C., Rimokh, R., Puisieux, A., and Maguer-Satta, V. (2008). Blood *112*, 3154–3163.

Malinge, S., Bliss-Moreau, M., Kirsammer, G., Diebold, L., Chlon, T., Gurbuxani, S., and Crispino, J.D. (2012). J. Clin. Invest. *122*, 948–962.

Mercher, T., Raffel, G.D., Moore, S.A., Cornejo, M.G., Baudry-Bluteau, D., Cagnard, N., Jesneck, J.L., Pikman, Y., Cullen, D., Williams, I.R., et al. (2009). J. Clin. Invest. *119*, 852–864.

Tallman, M.S., Neuberg, D., Bennett, J.M., Francois, C.J., Paietta, E., Wiernik, P.H., Dewald, G., Cassileth, P.A., Oken, M.M., and Rowe, J.M. (2000). Blood *96*, 2405–2411.

Taub, J.W., Mundschau, G., Ge, Y., Poulik, J.M., Qureshi, F., Jensen, T., James, S.J., Matherly, L.H., Wechsler, J., and Crispino, J.D. (2004). Blood *104*, 1588–1589.

Cancer Cell
Article

Relief of Profound Feedback Inhibition of Mitogenic Signaling by RAF Inhibitors Attenuates Their Activity in BRAFV600E Melanomas

Piro Lito,[1,2,7] Christine A. Pratilas,[1,3,7] Eric W. Joseph,[1,7] Madhavi Tadi,[1] Ensar Halilovic,[6] Matthew Zubrowski,[6] Alan Huang,[6] Wai Lin Wong,[1] Margaret K. Callahan,[2] Taha Merghoub,[2,4] Jedd D. Wolchok,[2,4] Elisa de Stanchina,[1] Sarat Chandarlapaty,[2,5] Poulikos I. Poulikakos,[1] James A. Fagin,[2,5] and Neal Rosen[1,2,*]
[1]Molecular Pharmacology and Chemistry Program
[2]Department of Medicine
[3]Department of Pediatrics
[4]Ludwig Center for Cancer Immunotherapy
[5]Human Oncology and Pathogenesis Program
Memorial Sloan-Kettering Cancer Center, New York, NY 10065, USA
[6]Novartis Institutes for BioMedical Research, Cambridge, MA 02139, USA
[7]These authors contributed equally to this work
*Correspondence: rosenn@mskcc.org
http://dx.doi.org/10.1016/j.ccr.2012.10.009

SUMMARY

BRAF^{V600E} drives tumors by dysregulating ERK signaling. In these tumors, we show that high levels of ERK-dependent negative feedback potently suppress ligand-dependent mitogenic signaling and Ras function. BRAF^{V600E} activation is Ras independent and it signals as a RAF-inhibitor-sensitive monomer. RAF inhibitors potently inhibit RAF monomers and ERK signaling, causing relief of ERK-dependent feedback, reactivation of ligand-dependent signal transduction, increased Ras-GTP, and generation of RAF-inhibitor-resistant RAF dimers. This results in a rebound in ERK activity and culminates in a new steady state, wherein ERK signaling is elevated compared to its initial nadir after RAF inhibition. In this state, ERK signaling is RAF inhibitor resistant, and MEK inhibitor sensitive, and combined inhibition results in enhancement of ERK pathway inhibition and antitumor activity.

INTRODUCTION

ERK signaling plays an important role in regulating pleiotypic cellular functions. Activation of receptor tyrosine kinases (RTKs) causes Ras to adopt an active, guanosine triphosphate (GTP)-bound conformation (Downward, 2003) in which it induces the dimerization and activation of members of the RAF kinase family (Wellbrock et al., 2004a). Activated RAF phosphorylates and activates MEK1/2; these phosphorylate and activate ERK1/2, which regulate cellular function by phosphorylating multiple substrates. A complex network of negative-feedback interactions limits the amplitude and duration of ERK signaling. Negative feedback is mediated directly by ERK-dependent inhibitory phosphorylation of components of the pathway, including epidermal growth factor receptor (EGFR), SOS, and RAF (Avraham and Yarden, 2011; Dougherty et al., 2005; Douville and Downward, 1997). In addition, ERK activation induces the expression of proteins that negatively regulate the pathway, including members of the Sprouty (Spry) and dual specificity phosphatase (DUSP) families (Eblaghie et al., 2003; Hanafusa et al., 2002).

ERK activation is a common feature of tumors with KRas, NRas, or BRAF mutation, or dysregulation of RTKs (Solit and Rosen, 2011). Tumors with BRAF mutation and some with RAS

Significance

The resistance of BRAF^{V600E} to ERK-dependent feedback is key to its transforming activity and for the effectiveness of RAF inhibitors. In BRAF^{V600E} melanomas, elevated ERK-dependent feedback suppresses signaling by growth factors; Ras activity is low and BRAF^{V600E} functions as a monomer. RAF inhibitors potently inhibit RAF monomers, but not dimers and thus are active in these tumors. However, ERK inhibition rapidly relieves feedback and sensitizes the cell to ligand-dependent signaling, leading to a rebound in Ras activity and ERK signaling. The degree of rebound is variable and predicted to determine the sensitivity of the tumor to the inhibitor. Inhibiting RAF-inhibitor-induced pathway reactivation with MEK inhibitors or inhibitors of the relevant ligand-activated receptors will be required for maximal antitumor activity.

mutation are sensitive to MEK inhibitors (Sebolt-Leopold et al., 1999; Leboeuf et al., 2008; Pratilas et al., 2008; Solit et al., 2006). However, these drugs inhibit ERK signaling in all cells, and toxicity to normal tissue limits their dosing and their therapeutic effects (Kirkwood et al., 2012).

ATP-competitive RAF inhibitors have also been developed (Bollag et al., 2010). The biologic effects of MEK inhibitors and RAF inhibitors in $BRAF^{V600E}$ melanomas are similar. However, RAF inhibitors effectively inhibit ERK signaling only in tumors with mutant BRAF (Hatzivassiliou et al., 2010; Heidorn et al., 2010; Joseph et al., 2010; Poulikakos et al., 2010). In cells with wild-type (WT) BRAF, Ras activation supports the formation of Ras-dependent RAF dimers. Binding of RAF inhibitors to one protomer in the dimer allosterically transactivates the other and causes activation of ERK signaling in these cells (Poulikakos et al., 2010). We hypothesized that, in $BRAF^{V600E}$ tumors, levels of Ras activity are too low to support the formation of functional dimers, so that $BRAF^{V600E}$ is primarily monomeric and inhibited by the drug. This mutation-specific pathway inhibition by the drug gives it a broad therapeutic index and likely accounts for its remarkable antitumor effects in melanomas with BRAF mutation (Chapman et al., 2011; Sosman et al., 2012). In support of this model, acquired resistance to RAF inhibitors is due to lesions that increase Ras activity, e.g., NRAS mutation or RTK activation (Nazarian et al., 2010), and to aberrantly spliced forms of $BRAF^{V600E}$ that dimerize in a Ras-independent manner (Poulikakos et al., 2011).

We have now endeavored to test the hypothesis that the levels of Ras activity in $BRAF^{V600E}$ melanomas are too low to support significant expression of active RAF dimers and to elucidate the mechanism underlying this phenomenon and its biologic and therapeutic consequences.

RESULTS

In $BRAF^{V600E}$ Melanomas, Ras Activation Is Suppressed by ERK-Dependent Feedback

Assessment of $BRAF^{V600E}$ melanoma cells confirmed that they have low levels of GTP-bound Ras (Figure 1A; Figure S1A available online). As expected, Ras-GTP levels were most elevated in tumor cells with mutant Ras and were lower in cells in which ERK signaling is driven by RTKs. Ras-GTP levels were significantly lower in melanoma cell lines harboring $BRAF^{V600E}$ and could be detected only when immunoblots were overexposed (Figure 1A).

We investigated whether low Ras activity is due to high levels of ERK signaling. We have shown that ERK-dependent transcriptional output is markedly elevated in $BRAF^{V600E}$ melanomas (Joseph et al., 2010; Pratilas et al., 2009) and includes Spry proteins, which suppress the activation of Ras by various RTKs. This suggests that ERK-dependent feedback inhibition of receptor signaling causes suppression of Ras activation in these tumors. Pharmacologic inhibition of RAF or MEK led to induction of Ras-GTP to varying degrees in $BRAF^{V600E}$ tumors (Figures 1B, 1C, and S1B), with induction beginning 4–8 hr after drug addition and reaching a steady state 24 hr after pathway inhibition (Figure 1B). Although marked induction of Ras-GTP occurred, levels remained significantly lower than those observed in tumor cells with EGFR activation (Figure S1C). These findings show that ERK-dependent feedback suppresses Ras activity in $BRAF^{V600E}$ melanomas and are consistent with the idea that $BRAF^{V600E}$ signals in a Ras-independent manner.

Induction of Ras-GTP correlated with decreasing levels of Spry proteins and the ERK phosphatase DUSP6 (Figures 1B and S1C). Spry proteins inhibit RTK signaling, in part by binding to Grb2 and sequestering the Grb2:SOS complex so it cannot bind RTKs (Kim and Bar-Sagi, 2004; Mason et al., 2006). In $BRAF^{V600E}$ melanomas, Spry1, 2, and 4 are overexpressed in an ERK-dependent manner (Figure S1D). To determine whether Spry overexpression contributes to feedback inhibition of Ras, we knocked down the expression of Spry1, 2, and 4 with small interfering RNA (siRNAs), and Ras-GTP was assessed 48 hr later. Downregulation of either Spry1 or Spry2 increased total (pan) Ras-GTP levels, whereas knockdown of Spry 4 had no effect. Spry2 knockdown resulted in induction of HRas, NRas, and KRas-GTP, while Spry1 and 4 downregulation appeared to induce HRas-GTP alone (Figures 1D and S1E; data not shown). Knockdown of all three isoforms did not result in greater induction of Ras-GTP than knockdown of Spry2 alone (Figures 1D and S1E). Induction of Ras-GTP in these cells was associated with increased phosphorylation of $CRAF^{S338}$, a modification associated with CRAF activation. These data suggest that ERK-dependent feedback inhibition of Ras activation is mediated, in part, by expression of Spry proteins.

We hypothesized that Spry proteins block activation of Ras by interfering with RTK signaling. Since A375 melanoma cells express EGFR and respond to its ligands (see below), we tested whether the effect of Spry2 knockdown was reversed by neratinib, an irreversible inhibitor of EGFR/HER kinases. Neratinib had no effect on Ras-GTP in A375 cells, but reduced the Ras-GTP increase induced by Spry2 knockdown (Figure 1E). This supports the idea that ERK-dependent expression of Spry2 blocks RTK-dependent activation of Ras.

Induction of Ras-GTP by RAF Inhibitors Is Accompanied by a Rebound in Phospho-ERK

Increased Ras-GTP should be accompanied by an increase in RAF-inhibitor-resistant RAF dimers and a concomitant increase in pERK and ERK signaling. After initial inhibition of ERK phosphorylation in seven $BRAF^{V600E}$ melanomas treated with the RAF inhibitor, we observed a pronounced rebound in four cell lines, and a more marginal rebound in two others (Figure 1F). The pERK rebound was also elicited by dabrafenib, a more potent RAF inhibitor (Figure S1F). The rebound was preceded by loss of ERK-dependent inhibitory phosphorylation of CRAF at S289, S298, and S301 and was associated with an induction of the CRAF S338 activating phosphorylation and a slight induction of pMEK, detected in A375 cells (Figures S1F and S1G) but not in all the cell lines.

The rebound in pERK was accompanied by increased expression of genes previously shown to be ERK-dependent in $BRAF^{V600E}$ melanomas (Figures S1H–S1L). The magnitude of pERK reactivation varied across the melanomas examined, but pERK levels reached a steady state that was maintained for at least 7 days (data not shown). The magnitude of ERK reactivation was less pronounced in melanomas than in colorectal and thyroid carcinomas harboring $BRAF^{V600E}$ (J.A.F., unpublished data).

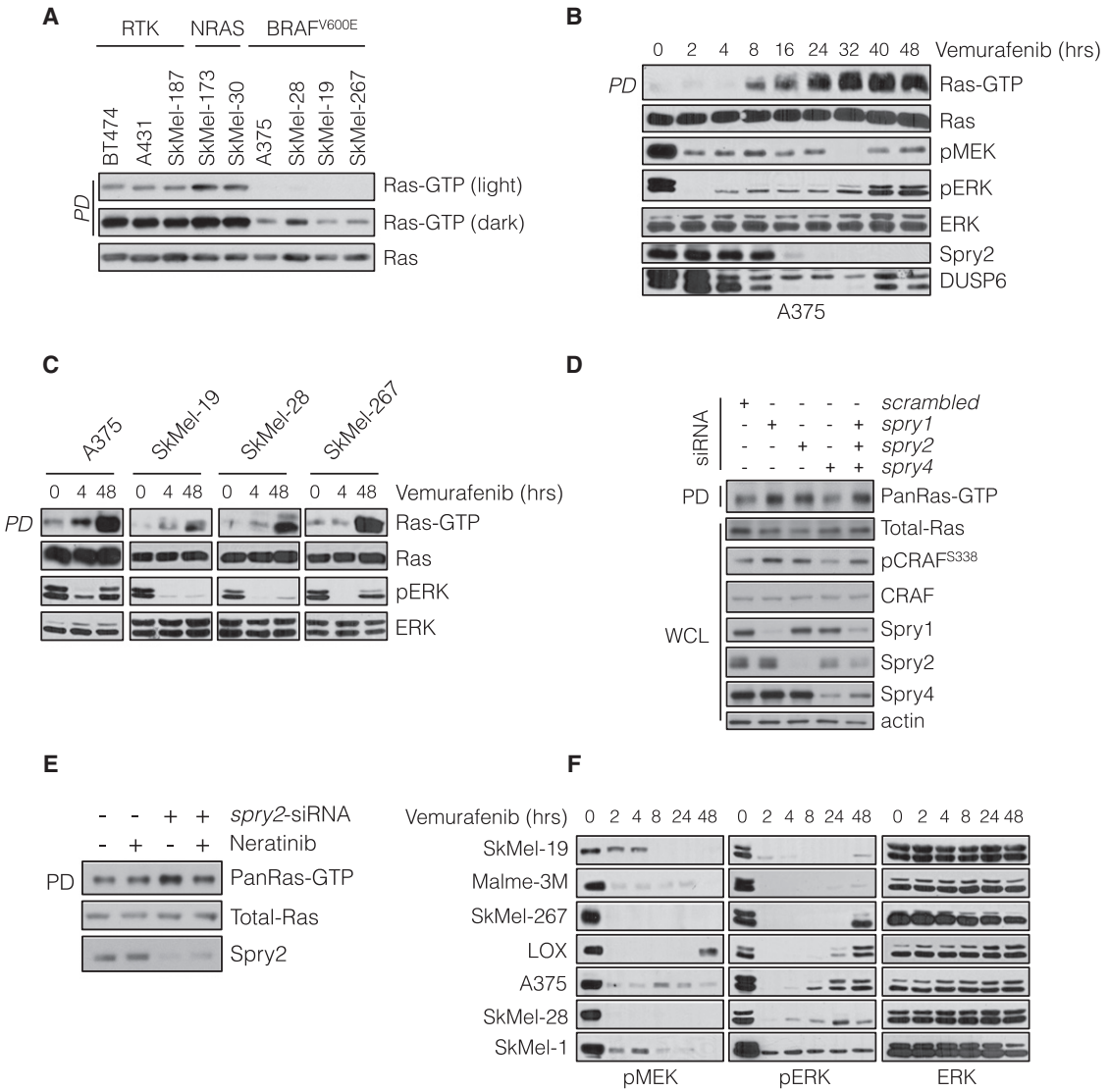

Figure 1. BRAF^{V600E} Melanomas Maintain a State of Low Ras-GTP through Negative-Feedback Regulation

(A) Whole-cell lysates (WCLs) from the indicated cell lines were subjected to pull-down (PD) assays with GST-bound CRAF Ras-binding domain (RBD). WCL and PD products were immunoblotted (IB) with a pan-Ras antibody.

(B and C) BRAF-mutated melanoma cell lines were treated with vemurafenib (2 μM) for the indicated times. Ras-GTP was detected as in (A). Phospho and total levels of ERK pathway components were assayed by IB.

(D) A375 cells (BRAF^{V600E}) were transfected with siRNA pools targeting the indicated Spry isoforms or scrambled oligonucleotides. WCLs were subjected to GST-RBD PD and analyzed by IB for the indicated proteins.

(E) A375 cells were transfected with *spry2* siRNA and 48 hr after transfection they were treated with neratinib (1 μM) for 1 hr. Ras-GTP levels were determined as above.

(F) BRAF^{V600E} melanoma cell lines were treated with vemurafenib (2 μM) for various times. The effect on ERK signaling is shown.

See also Figure S1.

We examined whether pERK rebound required Ras activation. Knockdown of Ras isoforms by siRNA had little effect on baseline pERK, but decreased the residual pERK in A375 and SkMel-28 cells treated with vemurafenib (Figure 2A). These results confirm that ERK signaling is Ras independent in BRAF-mutated melanomas, but that ERK rebound after RAF inhibition is Ras dependent. Since activation of WT Ras requires exchange factor activity, we asked whether rebound required SOS1, a Ras-specific guanine nucleotide exchange factor that is inhibited by Spry (Nimnual and Bar-Sagi, 2002). Downregulation of SOS1 in A375 cells diminished pERK rebound after inhibition with vemurafenib without affecting baseline pERK (Figure 2B).

ERK Rebound Is Dependent on Expression of CRAF-Containing Dimers that Are Resistant to RAF Inhibition

Our data suggest that relief of ERK-dependent feedback inhibition of Ras activity diminishes the effect of RAF inhibitors. To

support this idea, we asked whether MEK inhibitors increase Ras activation and cause resistance to RAF inhibitors. The MEK inhibitor (PD0325901) inhibited ERK phosphorylation and induced Ras-GTP levels within 24 hr of addition (Figures 2C and S1B). With this in mind, we asked if relief of feedback by MEK inhibitors affected vemurafenib inhibition of MEK phosphorylation. Vemurafenib treatment for 1 hr potently inhibited pMEK in untreated $BRAF^{V600E}$ melanomas and in those cells exposed to the MEK inhibitor for up to 12 hr, at which time Ras-GTP had not increased appreciably (Figure 2C). After 24 and 48 hr of exposure, however, Ras-GTP was induced and inhibition of pMEK by the RAF inhibitor was much less effective (Figures 2C and S2A–S2C). Similar results were achieved with different MEK (trametinib) and RAF (dabrafenib) inhibitors (Figure S2B).

These data support the idea that relief of ERK-dependent feedback increases the level of Ras-dependent RAF dimers. This turned out to be the case. As measured by coimmunoprecipitation of endogenous proteins, the MEK inhibitor increased CRAF:BRAF dimers at times that correlated with induction of Ras-GTP and RAF inhibitor resistance (12–48 hr, Figures 2D and S2C).

Spry proteins suppressed RTK-induced Ras activation in $BRAF^{V600E}$ melanomas. We asked if Spry expression was required for maximal inhibition of RAF. In A375 melanoma cells, knockdown of Spry1–4 reduced the degree of acute inhibition of MEK phosphorylation by vemurafenib (Figure 2E). A similar result was obtained when Spry2 was knocked down alone (Figure S2D). These findings suggest that Spry overexpression contributes to maximal RAF inhibition in BRAF melanomas.

If formation of RAF dimers is responsible for rebound in ERK phosphorylation in tumors treated with RAF inhibitors, ERK rebound should be CRAF dependent. As previously shown (Hingorani et al., 2003; Wellbrock et al., 2004b), knockdown of CRAF expression had no effect on ERK signaling in A375 cells (Figure 2F). In contrast, in tumors treated with RAF inhibitors, residual pERK was significantly reduced when CRAF expression was reduced by siRNA (Figure 2F).

Together, these data suggest that relief of ERK-dependent feedback by MEK or RAF inhibitors induces Ras-GTP and the formation of CRAF-containing dimers that are insensitive to the RAF inhibitor. If ERK-rebound is driven by these dimers, it should be sensitive to MEK inhibitors, but not to RAF inhibitors (Poulikakos et al., 2010). We tested this assertion in $BRAF^{V600E}$ melanoma cell lines treated with vemurafenib (Figure 2G). In these cell lines, vemurafenib caused maximal inhibition of pERK within 2 hours of inhibition, and rebound occurred within 8 hours. ERK-rebound was insensitive to retreatment with vemurafenib, 24 hr after the initial treatment, but was sensitive to MEK inhibition. Similar findings were observed when the experiment was repeated with the other MEK and RAF inhibitors (Figure S2E). These data support the idea that relief of ERK-dependent feedback leads to a rebound in pERK and a new steady state in which the pathway is driven by RAF dimers that are insensitive to RAF inhibition.

Our data show that relief of feedback inhibition of Ras is necessary for induction of ERK rebound. Overexpression of the ERK phosphatase DUSP6 is a property of $BRAF^{V600E}$ melanomas and rapidly decreases after RAF inhibition. We asked whether downregulation of DUSP6 also contributed to ERK rebound. A375 cells were transfected with DUSP6-specific siRNAs and then treated with vemurafenib. Knocking down DUSP6 resulted in increased residual pERK following RAF inhibition, without significant differences in residual pMEK (Figure S2F). This suggests the decrease in DUSP6 expression plays a permissive role in pERK rebound following RAF inhibition.

We asked if relief of PI3K or mTOR pathway feedback also affected inhibition of MEK phosphorylation by vemurafenib. A375 cells were treated with selective inhibitors of MEK, ERK, mTOR kinase, AKT, or PI3K for 48 hr, followed by treatment with vemurafenib to assess inhibition of MEK phosphorylation by RAF. Inhibiting MEK or ERK, prevented inhibition of MEK phosphorylation by vemurafenib. This was associated with loss of Spry2 expression and induction of $CRAF^{S338}$ (Figure 2H). Inhibition of PI3K, AKT, or mTOR kinase did not affect sensitivity to vemurafenib, Spry2 expression, or pCRAF. The mTOR kinase inhibitor did not affect vemurafenib inhibition even though it relieved feedback inhibition of signaling to $pAKT^{T308}$. Thus, maximal effectiveness of RAF inhibitors specifically requires intact ERK-dependent feedback.

Inhibition of ERK Rebound with MEK Inhibitors Enhances the Suppression of ERK Output and Tumor Growth by RAF Inhibitors

Since ERK phosphorylation and output were reactivated in a MEK-dependent manner in tumors exposed to RAF inhibitors, we examined whether concurrent RAF and MEK inhibition resulted in better inhibition of the pathway and tumor growth. As compared to treatment with either agent alone (Figure S3A), ERK phosphorylation was inhibited to greater degree in $BRAF^{V600E}$ melanomas exposed to vemurafenib and a low concentration of PD0325901 (5 nM). The combination of dabrafenib and trametinib also inhibited the growth of A375 cells in culture better than either drug alone (Figure S3B).

We tested the effectiveness of combining RAF and MEK inhibitors in vivo in four $BRAF^{V600E}$ melanoma mouse xenograft models (Figure 3A). These experiments were done with an effective dose (12.5 mg/kg) of PLX4720, which is closely related to vemurafenib but easier to formulate (Tsai et al., 2008), and a low dose (2 mg/kg) of PD0325901. Each inhibitor was effective alone (Figure 3A), with regression observed in approximately 50% of animals in either arm. In contrast, combined therapy caused regression of all but one tumor (25/26). Figures S3C–S3F show tumor responses over 4 weeks of treatment. The combination of RAF and MEK inhibitors was effective in SkMel-28 and SkMel-267 xenografts (Figures S3C and S3D). In A375 and LOX xenografts (Figures S3E and S3F), the addition of MEK inhibitor did not significantly improve tumor growth inhibition initially, but did delay tumor regrowth following prolonged treatment.

We repeated the experiment with a higher dose of PLX4720 (50 mg/kg) in SkMel-267 and SkMel-28 xenografts and found that the combination of RAF and MEK inhibition was still superior to either drug alone (Figures 3B and 3C). Flow-cytometric analysis of tumor-derived cells from SkMel-28 xenografts revealed that more than 50% of ERK remained phosphorylated after single agent inhibition of RAF or MEK alone (Figure 3D). The combination, however, resulted in a near complete ERK inhibition. Taken together, these results suggest that combined

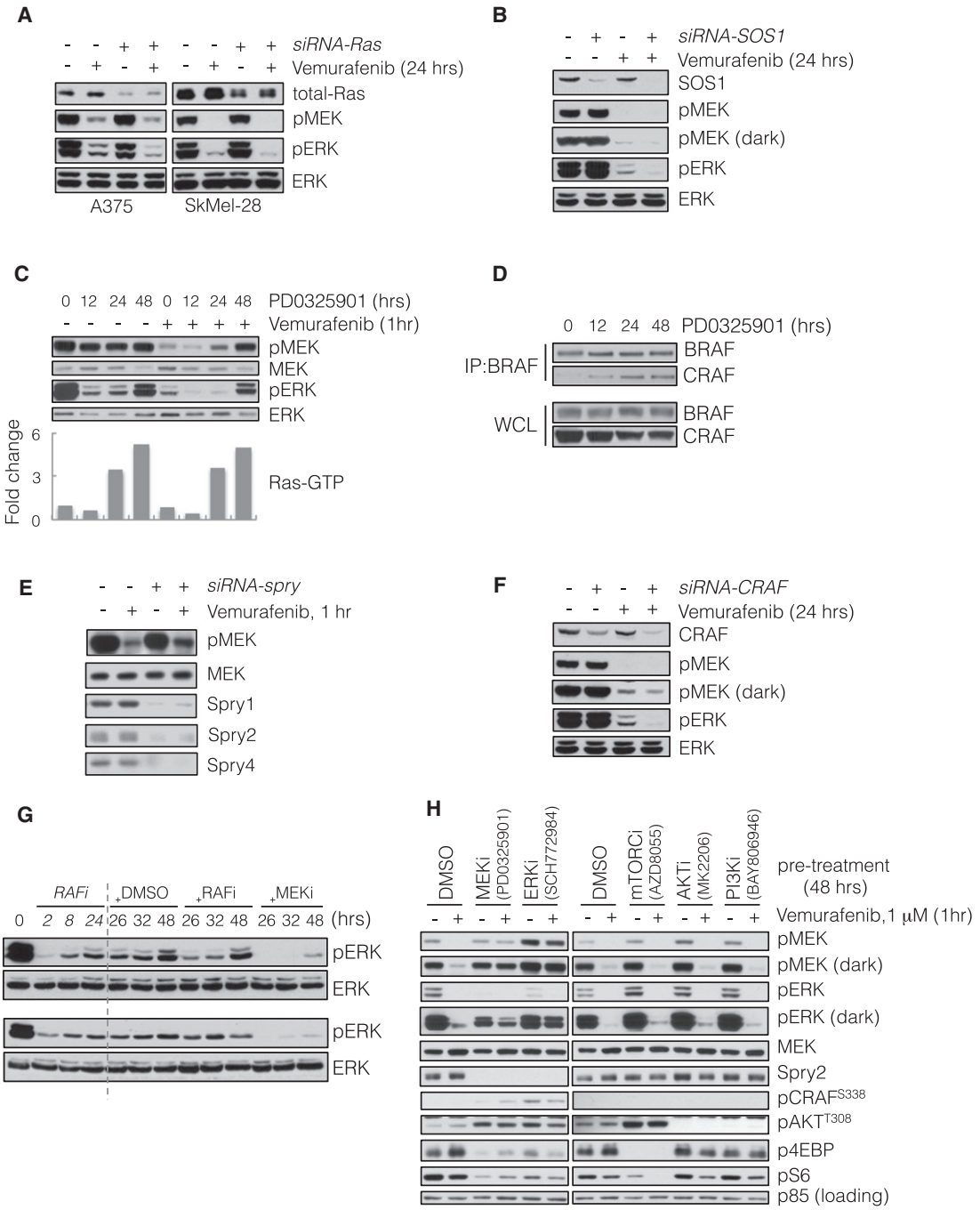

Figure 2. ERK Rebound Is Dependent on Formation of CRAF-Containing Dimers that Are Resistant to RAF Inhibition

(A) $BRAF^{V600E}$-expressing A375 and SkMel-28 cells were transfected with siRNA pools targeting all three Ras isoforms (+) or scrambled oligonucleotides (–). Forty-eight hours after transfection, the cells were treated with vemurafenib (2 μM) for 24 hr and analyzed by immunoblotting (IB) to detect the indicated proteins.

(B) A375 cells were transfected with siRNA pools targeting SOS1. Forty-eight hours after transfection, the cells were treated with vemurafenib (2 μM) for 24 hr and analyzed by IB as above.

(C) A375 cells were untreated or initially pretreated with MEK inhibitor PD0325901 (50 nM) for the times shown. Subsequently, vemurafenib (1 μM) was added for 1 hr. WCLs were assayed to determine changes in pMEK and pERK. WCLs were also analyzed with a GST-RBD Elisa assay. The fold change in the amount of GTP-bound Ras, as compared to untreated cells, is shown.

(D) $BRAF^{V600E}$ expressing Malme-3M cells were treated with PD0325901 (50 nM) for various times. To assess BRAF-CRAF dimerization, WCLs were subjected to immunoprecipitation (IP) with a BRAF-specific antibody and then IB for CRAF.

(E) A375 cells were transfected with siRNA pools targeting *spry1-4* genes. After 48 hr, they were treated with vemurafenib (1 μM) for 1 hr. WCLs were analyzed to determine changes in inhibition of MEK phosphorylation.

(F) A375 cells were transfected with *CRAF* siRNAs and subsequently treated with vemurafenib for 24 hr. Changes in phospho and total ERK are shown.

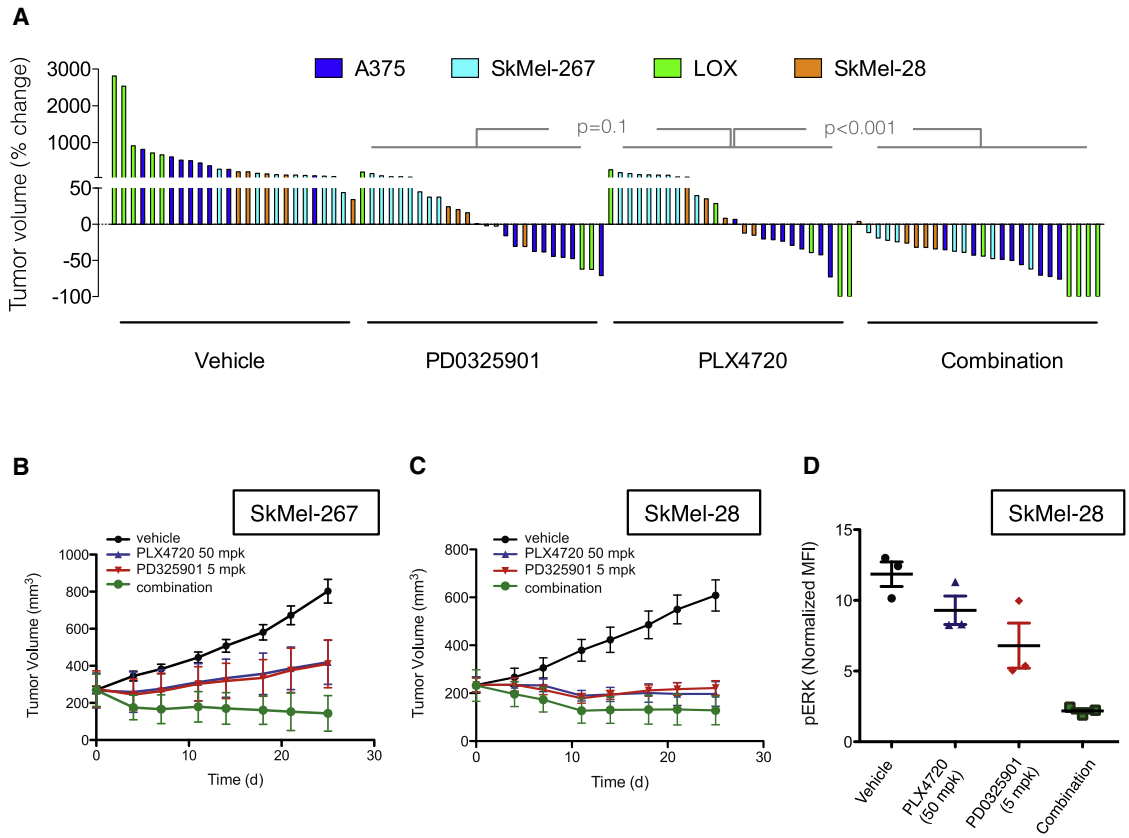

Figure 3. Combination of RAF and MEK Inhibitors Results in Improved Tumor Growth Inhibition In Vivo

(A) Mice bearing xenografts from four different $BRAF^{V600E}$ melanoma cell lines were treated with vehicle, PD0325901 (2 mg/kg), PLX4720 (12.5 mg/kg), or their combination for 4 weeks. A waterfall representation of the best response for each tumor is shown.

(B and C) Mice bearing SkMel-267 (B) and SkMel-28 (C) xenografts were treated with PLX4720 (50 mg/kg) alone or in combination with PD0325901 (5 mg/kg) for the indicated times. The tumor volumes (and SEM) are shown as a function of time after treatment.

(D) Cells derived from SkMel-28 xenografts treated as shown for 48 hr were subjected to flow-cytometric analysis to measure levels of pERK in isolated human melanoma cells.

See also Figure S3.

inhibition of RAF and MEK has enhanced tumor activity and that this is due to more complete inhibition of ERK signaling.

Relief of ERK-Dependent Feedback Potentiates Receptor Signaling

We hypothesized that elevated ERK-dependent feedback in these cells suppresses mitogenic signaling and causes these cells to be poorly responsive to growth factors. If this is the case, relief of ERK-dependent feedback by inhibitors of ERK signaling should result in increased transduction of the ligand-activated signal. In order to test this hypothesis, we assessed the ability of exogenous ligands to activate signaling in $BRAF^{V600E}$ cells before and after inhibition of ERK signaling with vemurafenib (Figures 4A–4D).

$BRAF^{V600E}$ melanoma cells have high levels of pMEK and pERK and high levels of expression of DUSP6 and Spry2 (Figure 4A, lane 1). After 24 hr of exposure to vemurafenib (lane 2), pMEK and pERK are quite low, with residual levels of pERK due to rebound. DUSP6 and Spry2 levels are markedly diminished 4–8 hr after drug exposure (lanes 7–10). To assess the ability of an exogenous ligand to activate signaling, we added EGF or Neuregulin (NRG) at various times after vemurafenib treatment and evaluated signaling 10 min after ligand addition (Figures 4A and 4B, respectively, lanes 3–10). Vemurafenib completely suppressed pMEK and pERK within 30 min of treatment and neither ligand appreciably induced pMEK, pERK, pCRAF, or pAKT after 1 hr of RAF inhibition (lane 5). After 2 hr of RAF inhibition, however, EGF significantly stimulated pMEK

(G) $BRAF^{V600E}$-expressing cell lines were initially treated with vemurafenib (1 μM) for 2, 8, and 24 hr. After 24 hr of treatment, DMSO, vemurafenib (1 μM, RAFi), or PD0325901 (5 nM, MEKi) was added for an additional 2, 8, and 24 hr, respectively. The total treatment time is indicated. The effect on ERK signaling is shown.

(H) A375 cells were pretreated with inhibitors targeting the indicated kinases for 48 hr, followed by treatment with vemurafenib for 1 hr. WCLs were analyzed to detect the ability of vemurafenib to inhibit MEK phosphorylation by RAF, as well as the ability of the indicated compounds to inhibit their targets. Their effects on Spry2 and pCRAF are also shown.

See also Figure S2.

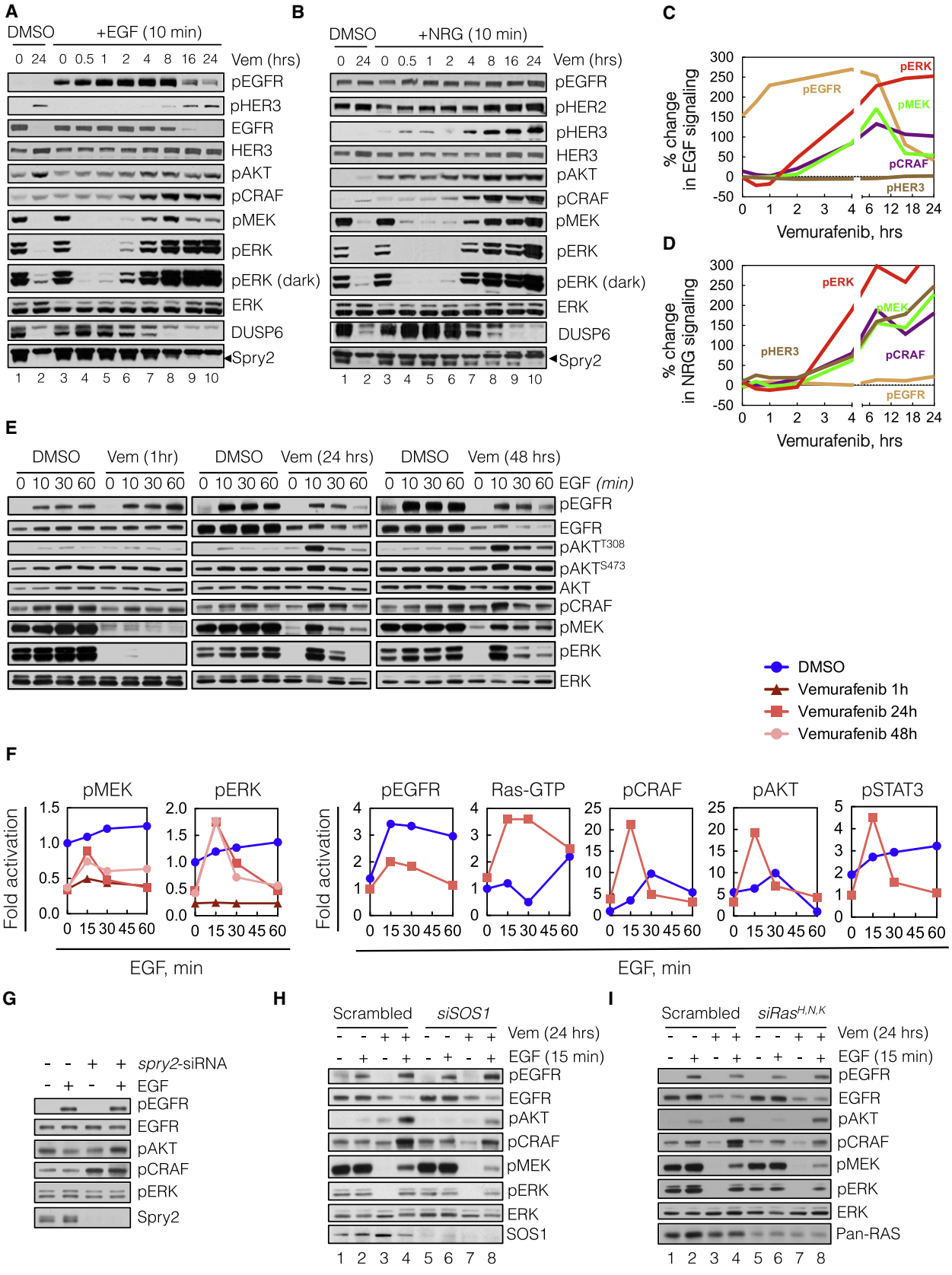
A
DMSO
+EGF (10 min)
0 24 0 0.5 1 2 4 8 16 24 Vem (hrs)
pEGFR
pHER3
EGFR
HER3
pAKT
pCRAF
pMEK
pERK
pERK (dark)
ERK
DUSP6
Spry2
1 2 3 4 5 6 7 8 9 10
B
DMSO
+NRG (10 min)
0 24 0 0.5 1 2 4 8 16 24 Vem (hrs)
pEGFR
pHER2
pHER3
HER3
pAKT
pCRAF
pMEK
pERK
pERK (dark)
ERK
DUSP6
Spry2
1 2 3 4 5 6 7 8 9 10
C
% change in EGF signaling
pERK
pEGFR
pMEK
pCRAF
pHER3
Vemurafenib, hrs
D
% change in NRG signaling
pERK
pMEK
pHER3
pCRAF
pEGFR
Vemurafenib, hrs
E
DMSO
Vem (1hr)
DMSO
Vem (24 hrs)
DMSO
Vem (48 hrs)
0 10 30 60 0 10 30 60 0 10 30 60 0 10 30 60 0 10 30 60 0 10 30 60 EGF (min)
pEGFR
EGFR
pAKTT308
pAKTS473
AKT
pCRAF
pMEK
pERK
ERK
DMSO
Vemurafenib 1h
Vemurafenib 24h
Vemurafenib 48h
F
pMEK
pERK
Fold activation
EGF, min
pEGFR
Ras-GTP
pCRAF
pAKT
pSTAT3
Fold activation
EGF, min
G
spry2-siRNA
EGF
pEGFR
EGFR
pAKT
pCRAF
pERK
Spry2
H
Scrambled
siSOS1
Vem (24 hrs)
EGF (15 min)
pEGFR
EGFR
pAKT
pCRAF
pMEK
pERK
ERK
SOS1
1 2 3 4 5 6 7 8
I
Scrambled
siRasH,N,K
Vem (24 hrs)
EGF (15 min)
pEGFR
EGFR
pAKT
pCRAF
pMEK
pERK
ERK
Pan-RAS
1 2 3 4 5 6 7 8

and pERK (lane 6). Ligand stimulation of signaling, which we term "signalability," rose markedly after 4–8 hr of RAF inhibition (Figure 4A, lanes 7–8; Figure 4C), and was maintained after 24 hr of exposure to the inhibitor (lanes 9 and 10). A similar profile of ligand-induced signaling was observed when the cells were stimulated with NRG (Figure 4B, lanes 3–10; Figure 4D). The ability of ligands to induce pMEK and pERK was accompanied by an increase in their induction of CRAF and AKT phosphorylation.

These data show that ligand stimulation of ERK and PI3K signaling in $BRAF^{V600E}$ melanomas is low (i.e., suppressed signalability), but, hours after the ERK pathway is inhibited, the transduction of the signal is markedly potentiated (i.e., restored signalability). This could be due to enhanced activation of receptors, enhanced signaling downstream of the activated receptor, or both. Induction of EGFR phosphorylation after exposure to EGF for 10 min increased slightly 1 hr after RAF inhibition, at which time downstream signaling was not activated, and remained essentially constant from 2 to 8 hr after RAF inhibition (Figures 4A and 4C). EGFR expression did not change over this time. These findings suggest that enhancement of EGF signalability is due to relief of feedback inhibition of intracellular transduction of the ligand-induced signal. Of note, phospho- and total EGFR decreased significantly 16–24 hr after RAF inhibition, but induction of signaling by EGF was undiminished (Figure 4A, lanes 9 and 10).

The ability of NRG to induce phosphorylation of HER3 was enhanced 4 hr after RAF inhibition, while a minimal increase was noted in the levels of HER3 protein expression (Figures 4B and 4D). These results suggest that loss of ERK-dependent feedback potentiates NRG activation of HER3, an event that includes heterodimerization and phosphorylation by other HER kinases.

To test the generality of the phenomenon of increased signalability following RAF inhibition, A375 and SkMel-28 cells were treated with vemurafenib for 24 hr and then stimulated for 10 min with EGF, NRG, epiregulin (ERG), hepatocyte growth factor (HGF), insulin-like growth factor (IGF1), or platelet-derived growth factor (PDGF) (Figure S4A). With the exception of IGF1 and PDGF, the ability of all of other ligands to activate ERK was enhanced by pretreatment with vemurafenib. The effect of RAF inhibition on receptor phosphorylation was complex (Figure S4B). Ligand-induced phosphorylation of EGFR and IGF1R were not appreciably changed after 24 hr of ERK inhibition, whereas phosphorylation of Met was enhanced in SkMel-28 but not in A375 cells. These data show that activation of $BRAF^{V600E}$ suppresses the transduction of signaling from multiple receptors and demonstrate the complexity of the details of this suppression in different tumors.

We characterized in more detail the kinetics of EGF stimulation of signaling in vemurafenib-treated A375 cells (Figures 4E and 4F). ERK is maximally inhibited after 1 hr of vemurafenib treatment but EGF activation of EGFR did not activate downstream effectors at this time. After 24 and 48 hr of vemurafenib treatment, however, EGF activates MEK, ERK, AKT, and STAT3 phosphorylation. Induction of effector phosphorylation could be blocked by HER kinase inhibitors or in the case of AKT by inhibition of PI3K (data not shown).

Our data suggest that overexpression of Spry proteins plays a role in suppressing signalability. To test this hypothesis, we determined if knocking down Spry2 in A375 melanomas enabled EGFR signaling. Downregulation of Spry2 induced pCRAF and increased EGF induction of pAKT (Figure 4G). Spry knockdown, however, did not affect EGFR-induced pERK, consistent with the idea that loss of DUSP6 expression is permissive for this effect. Knockdown of either SOS1 or Ras isoforms decreased the EGF-induced activation of pCRAF, pMEK, and pERK after 24 hr of vemurafenib treatment in A375 cells, suggesting that reactivation of ERK signaling requires these proteins (Figures 4H and 4I, respectively, lane 8 versus 4). These data support our conclusion that Spry proteins contribute to suppression of signalability by ERK-dependent feedback.

Diverse Exogenous Ligands Reduce the Effectiveness of RAF Inhibitors

Our data suggest that the response of $BRAF^{V600E}$ melanoma cells to growth factors is limited. In contrast, after RAF inhibitor treatment, the restoration of signalability enables signal transduction from extracellular ligands, a process that is likely to diminish RAF inhibition. To determine which growth factors were capable of attenuating the antiproliferative effects of vemurafenib, we expressed a library of 317 cDNA constructs, encoding 220 unique secreted or single-pass transmembrane proteins in 293T cells (Figure 5A). The media derived from these cultures were added to $BRAF^{V600E}$ melanomas in combination with vemurafenib and the effect on proliferation was assessed. We identified more than five different ligand families (including EGF, HGF, NRG, and FGF) that antagonized the vemurafenib sensitivity in one or more of eight $BRAF^{V600E}$ melanomas tested (Figures 5B and S5A). In contrast, other growth factors, such as PDGF and IGF, had a minimal effect, and some, such as transforming growth factor-β, accentuated vemurafenib-induced growth inhibition. A detailed presentation of the assay for the

Figure 4. Relief of ERK-Dependent Feedback Potentiates Receptor Signaling

(A–D) $BRAF^{V600E}$-expressing A375 cells were treated with vemurafenib (vem, 2 μM) for various times. At the indicated times, the cells were stimulated with either EGF (100 ng/ml, A) or NRG (100 ng/ml, B) for 10 min. WCLs were analyzed by immunoblotting (IB) to assay downstream signaling. The percentage change in ligand induced signaling (C and D) was determined by densitometric analysis of the bands in (A) and (B), respectively.

(E and F) A375 cells were untreated (DMSO) or treated with vemurafenib for 1, 24, or 48 hr in serum-free media and then stimulated with EGF for the indicated times. EGF-induced changes in phosphorylation of signaling intermediates were determined by IB (E) and quantified by densitometry (F). Changes in Ras-GTP were measured with an ELISA based GST-RBD assay (shown) and confirmed with a traditional pull-down assay (data not shown).

(G) A375 cells were transfected with *spry2* siRNAs, followed by serum starvation for 24 hr and EGF stimulation for 10 min. WCLs were IB with the indicated antibodies.

(H and I) A375 cells were transfected with siRNAs targeting either SOS1 (H) or the three Ras isoforms (I) or scrambled siRNAs. Then, the cells were treated with vemurafenib for 24 hr in serum-free media, followed by stimulation with EGF for 10 min. The phosphorylation of various signaling intermediates is shown.

See also Figure S4.

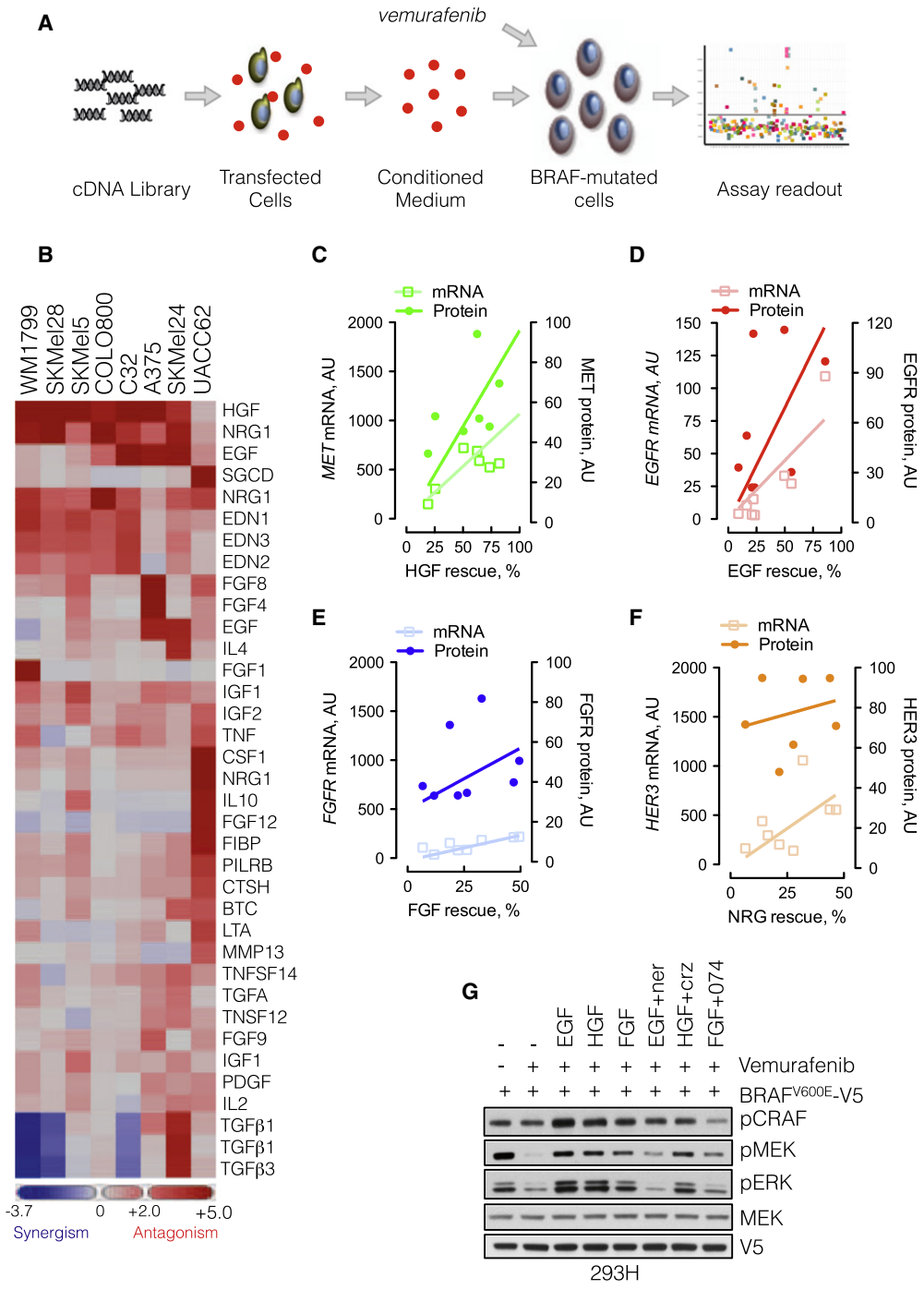

Figure 5. Secreted Exogenous Ligands Reduce the Effectiveness of RAF Inhibitors

(A) Schematic representation of the secretome assay. 293T cells grown in 384-well plates were transfected with a cDNA library encoding 220 unique secreted and single-pass transmembrane proteins. Secreted ligands were collected in the conditioned medium, which was combined with vemurafenib (1 μM) and added to melanoma cell lines to assay the effect on proliferation.

(B) Heatmap representation of the effect of secreted ligands in the ability of vemurafenib to inhibit growth in a panel of eight $BRAF^{V600E}$ melanomas (some ligands were encoded by multiple cDNAs). Ligands with most potent effects are shown.

(C–F) The percentage rescue by the indicated growth factors was plotted as a function of the mRNA and protein level of the respective RTK. The mRNA level was obtained from expression profiling of the indicated lines, whereas the protein level was quantified by immunoblotting (shown in Figure S5C) and densitometry.

(G) 293H cells were transfected with V5-tagged $BRAF^{V600E}$, followed by treatment with vemurafenib (1 μM, 15 min), alone, and in combination with the indicated ligands and inhibitors (1 μM each) of HER kinases (neratinib), MET (crizotinib), or FGFR (PD173074). The ability of vemurafenib to inhibit MEK phosphorylation is shown.

See also Figure S5.

effects of ligands on the proliferation of SkMel-28 cells exposed to vemurafenib is shown in Figure S5B.

The ability of several ligands to reduce sensitivity to vemurafenib was further validated in A375, SkMel-19, and SkMel-267, in which growth factors increased the vemurafenib IC_{50} (from less than 2-fold to greater than 5-fold, Figure S5C). In contrast, in SkMel-28 cells, the IC_{50} increased to greater than 5 μM in the presence of EGF, NRG, or HGF.

We attempted to identify factors that determined whether specific ligands (EGF, NRG, FGF, HGF) affected the vemurafenib-response in these cell lines. The attenuation of vemurafenib effect by these growth factors correlated with the level of mRNA and protein expression of their cognate receptors (Figures 5C–5F and S5D).

The data in Figure 4 suggest that RTK ligands will decrease RAF inhibition by vemurafenib. To test whether this is the case in a single cellular background, we treated 293H cells expressing $BRAF^{V600E}$ with vemurafenib, in the presence or absence of EGF, HGF, and FGF. These growth factors reduced the ability of vemurafenib to inhibit pMEK (Figure 5G), an effect that was reversed by inhibition of the respective RTKs, although the effect of MET inhibitor crizotinib was modest.

HER Kinase Activity Is Upstream of ERK Rebound

In vivo, $BRAF^{V600E}$ melanomas may be exposed to autocrine, paracrine, and endocrine RTK ligands. Our model suggests that reactivation of signalability when ERK feedback is inhibited will enable signaling from mitogenic growth factors. Since ERK rebound occurred in A375 cells exposed to vemurafenib under serum-free conditions (data not shown), we hypothesized that secreted ligands were involved. To test this possibility, we collected conditioned medium from serum-deprived A375 cells and found that it induced ERK signaling in 293H cells, as did EGF stimulation (Figure 6A, lanes 2 and 3). This induction was blocked by the HER kinase inhibitor neratinib (lane 4), suggesting that A375 cells secrete a HER kinase ligand. Furthermore, whereas vemurafenib effectively inhibited pERK in $BRAF^{V600E}$-transfected 293H cells (lanes 5 and 6), its ability to inhibit was reduced by A375-conditioned medium (lane 7). Under these conditions, maximal inhibition by vemurafenib was restored when neratinib was also added (lane 8).

To determine whether activated HER kinases support pERK rebound in $BRAF^{V600E}$ cells, cells were treated for 48 hr with vemurafenib, alone or in combination with neratinib. We found that cotreatment with neratinib decreased ERK reactivation in vemurafenib-treated cells but had no detectable effect on pERK in the absence of vemurafenib (Figure 6B). Of note, neratinib inhibited pEGFR without affecting pERK in the absence of vemurafenib treatment. This confirms that while upstream receptor activation may be required for ERK rebound, it is not sufficient. Relief of ERK-dependent upstream feedback is the primary cause of ERK reactivation. The receptor may be activated, but the signal is transduced effectively only when vemurafenib blocks ERK feedback.

In Figure 2, we show that MEK inhibition relieved feedback inhibition of Ras, induced RAF dimerization, and decreased the ability of vemurafenib to inhibit MEK phosphorylation. We asked if inhibition of HER kinase signaling in this setting restored the activity of vemurafenib. A375 and Malme-3M cells were pretreated with a MEK inhibitor (PD0325901) and/or a HER kinase inhibitor (neratinib) for 48 hr, followed by treatment with vemurafenib for 1 hr. Pretreatment with the MEK inhibitor alone attenuated the inhibition of MEK phosphorylation by vemurafenib (Figure 6C, lane 2 versus 6). Neratinib had no effect on ERK signaling when given alone, but restored the ability of vemurafenib to inhibit its target in cells pretreated with the MEK inhibitor (lane 6 versus 8). This restoration was associated with a decrease in the amount of BRAF-CRAF dimers induced by MEK inhibitor treatment, although dimerization was not completely abolished (Figure 6D). This suggests that while signals originating from HER kinases attenuate the effect of RAF inhibitors, other RTK-dependent pathways likely contribute as well. Indeed, the attenuation of vemurafenib's effect caused by pretreatment with a MEK inhibitor was also reversed by inhibition of FGFR. The MET inhibitor crizotinib did not affect the ability of vemurafenib to inhibit RAF in this system, but it did inhibit feedback-mediated activation of AKT (Figure 6E). Finally, the inhibition of RAF by vemurafenib in combination with HER kinase inhibitors neratinib or lapatinib caused more growth inhibition in vivo than RAF inhibition alone (Figure 6F). These findings together with those in Figure 3 suggest that maximizing inhibition of ERK output by combining RAF inhibitors with inhibitors of ERK rebound may be required for full therapeutic benefit.

DISCUSSION

Activation of BRAF by mutation occurs in approximately 8% of human cancers including the majority of melanomas (Davies et al., 2002; Badalian-Very et al., 2010; Brose et al., 2002; Nikiforova et al., 2003; Schiffman et al., 2010; Tiacci et al., 2011). Recently, ATP-competitive inhibitors of RAF kinase have been shown to be extremely effective in the treatment of melanomas with mutant BRAF (Chapman et al., 2011). This is thought to occur because these drugs inhibit ERK signaling only in tumors with mutant BRAF, whereas they induce ERK in other tumors and normal cells (Hatzivassiliou et al., 2010; Heidorn et al., 2010; Joseph et al., 2010; Poulikakos et al., 2010).

Induction occurs because RAF inhibitors cause transactivation of Ras-dependent RAF dimers (Poulikakos et al., 2010). However, $BRAF^{V600E}$ signals as a functional monomer and RAF inhibitors inhibit ERK signaling in this setting. We now show that Ras activity is extremely low in $BRAF^{V600E}$ melanomas. This finding confirms that $BRAF^{V600E}$ functions in a Ras-independent fashion in these cells. The questions arising now are why Ras activity is low, and whether there a causal relationship that explains why a RAF mutant that signals as a monomer is prevalent in tumor cells with low Ras activity? It is possible that physiologic levels of Ras-GTP are low in the normal precursor cells from which melanomas develop. RAF mutants that require Ras dependent dimerization would have low activity in these cells and there would be a strong selection for a RAF mutant capable of signaling as a monomer. Alternatively, ERK activation induces feedback inhibition of upstream signaling, which may be sufficient to potently suppress Ras activation. Here, we have demonstrated the latter to be the case. Inhibition of ERK signaling with either RAF or MEK inhibitors significantly induced Ras activation in these tumors.

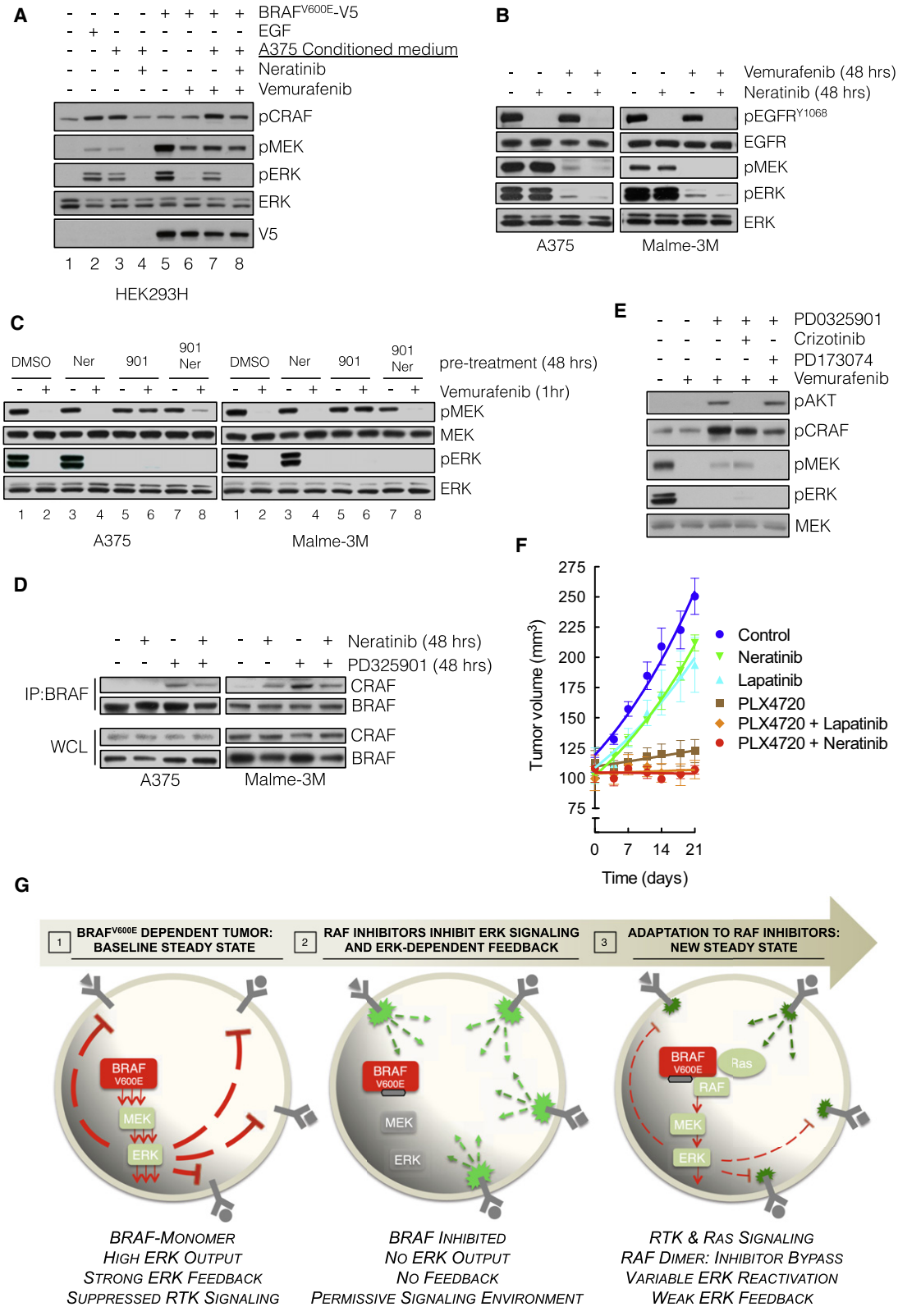

Figure 6. Targeting HER Receptor Signaling Restores Sensitivity to RAF Inhibition

(A) BRAF^{V600E}-expressing A375 cells were grown in serum-free medium for 24 hr and the medium was collected. This conditioned medium (CM) was added to 293H cells (lanes 1–4) or to 293H cells expressing exogenous V5 tagged BRAF^{V600E} (lanes 5–8). The cells were also treated with the indicated combinations of CM, vemurafenib, and neratinib in order to assay the effect on ERK signaling.

This induction is likely multifactorial with contributions from the various components of ERK feedback, such as direct phosphorylation of SOS and EGFR, as well as overexpression of Spry. Here, we show that knockdown of Spry in $BRAF^{V600E}$ cells increased Ras and RAF activation, and decreased the sensitivity of the pathway to RAF inhibitors. Spry proteins, however, do not affect the direct inhibition of SOS and CRAF by ERK, and therefore, even though Spry knockdown enables signaling from RTKs to SOS, loss of Spry alone cannot account for the full effect of ERK-dependent feedback.

Because physiologic activation of ERK is self-limited in extent and duration (Courtois-Cox et al., 2006), one may ask how oncoproteins cause sufficient activation of ERK output at all? We believe that activation of ERK output requires selection of oncoproteins that have decreased sensitivity to feedback, or second mutations that inactivate the feedback apparatus. In fact, we have previously shown that whereas ERK transcriptional output is quite elevated in tumors with mutant BRAF or mutant Ras, it is only marginally elevated in tumor cells with mutant EGFR or amplified HER2 (Pratilas et al., 2009). In these tumors, ERK pathway feedback is intact and levels of Ras activation are low. In contrast, the mutant Ras protein is constitutively activated (McCormick, 1993) and it is thus refractory to feedback inhibition of upstream signaling.

We propose that there is a powerful selection for the $BRAF^{V600E}$ mutation because it signals as a Ras-independent monomer that is insensitive to feedback. This results in marked elevation of ERK output, with consequent feedback inhibition of Ras-GTP. In agreement with this idea, inhibition of ERK signaling relieves this feedback, and causes induction of Ras activation. Ras activation is associated with a rebound in ERK phosphorylation and output. This rebound is Ras and SOS dependent, and more importantly, is CRAF dependent. Therefore, while the rebound may be potentiated by the loss of ERK phosphatases following RAF inhibition, these findings are consistent with the idea that rebound requires reactivation of upstream signaling and induction of RAF dimers that are refractory to RAF inhibitors but sensitive to MEK inhibition.

If RAF inhibitors cause the Ras-dependent formation of active RAF dimers that are refractory to RAF inhibition, why do these drugs work at all? The induction of Ras-GTP is variable in different melanoma cell lines. It tends to be modest, however, reaching levels that are still significantly below those found in RTK-driven tumor cells. This results in a concomitant modest increase in ERK phosphorylation and in ERK output. In most melanomas, this reactivation is not sufficient to cause resistance. We believe, however, that it can attenuate the effects of therapy, as we find that combining RAF inhibitor with a low-dose MEK inhibitor causes greater inhibition of pERK and ERK output than either drug alone, and enhanced antitumor activity in vivo in melanoma xenograft models. Thus, the variability observed in the degree of $BRAF^{V600E}$ melanoma response in patients treated with RAF inhibitors may be due in part to variable relief of feedback. This suggests that combined inhibition could increase the degree or duration of response obtained with RAF inhibition alone.

Others have noted that ERK rebound is greater in $BRAF^{V600E}$ thyroid (J.A.F., unpublished data) and colon (Corcoran et al., 2012) carcinomas and is associated with resistance to the RAF inhibitor. Recent studies show that rebound in colorectal tumors may be associated with feedback reactivation of EGFR function (Corcoran et al., 2012; Prahallad et al., 2012). This may explain why RAF inhibitors have been much less effective in the treatment of $BRAF^{V600E}$ colorectal cancer than they are in melanoma.

Prahallad et al. (2012) report that RAF inhibitors induce EGFR activation by inhibiting the ERK-dependent CDC25C phosphatase and thus activating EGFR signaling in colorectal cancer cells. Our data suggest that ERK-dependent feedback is complex and that relief of feedback and rebound in ERK activity is due to multiple mechanisms. In melanomas, we did not observe an association between ERK rebound and sustained induction of EGFR phosphorylation. Corcoran et al. (2012) also demonstrated that ERK phosphorylation rapidly rebounds after initial inhibition by RAF inhibitors in colorectal cancer. They also find that this rebound is EGFR dependent and associated with Ras activation, but not with induction of EGFR phosphorylation. Here, we demonstrate that relief of ERK-dependent feedback by RAF inhibitors results in Ras activation, induction of CRAF-containing dimers, and RAF-inhibitor-resistant ERK rebound. In contrast to our findings, Corcoran et al. do not observe Ras reactivation or ERK rebound in melanomas. This is probably because the degree of rebound is greater in colorectal cancer than it is in melanoma, in which it is more difficult to appreciate. We believe that potent ERK-dependent feedback inhibition of signaling is a general phenomenon in tumors with $BRAF^{V600E}$ and that the antitumor effects of drugs that inhibit ERK signaling will be diminished by relief of this feedback.

It is clear that the degree of rebound varies among individual tumors within lineages and that the rebound is greater on average in some lineages (e.g., colorectal), than in others (e.g., melanoma). Although it is unlikely that this is a simple process dependent on reactivation of a single receptor, it appears that the process may be preferentially dependent on activation of a particular receptor in some lineages (e.g., EGFR in colorectal

(B) A375 and Malme3M cells were treated with vemurafenib (1 μM) alone or in combination with neratinib (1 μM) for 48 hr, and the effect on EGFR and downstream signaling was analyzed.
(C) The cells were pretreated with MEK inhibitor PD0325901 (901, 50 nM), and HER-kinase inhibitor neratinib (Ner, 1 μM), alone or in combination for 48 hr, followed by vemurafenib (1 μM) for 1 hr. Phospho- and total MEK and ERK are determined by IB.
(D) The indicated cell lines were treated with PD0325901 and/or neratinib. WCLs were subjected to IP with a BRAF-specific antibody and IB for CRAF. The level of BRAF and CRAF in the WCLs is shown.
(E) A375 cells were treated as in (C) but PD0325901 was combined with crizotinib and PD173074 (1 μM each), targeting MET and FGFR, respectively.
(F) SkMel-28-derived xenografts were treated with combinations of PLX4720 (50 mg/kg), neratinib (20 mg/kg), and lapatinib (150 mg/kg). Tumor growth (and SEM) as a function of time is shown.
(G) Graphical representation of $BRAF^{V600E}$ melanomas adapting to RAF inhibitors. High levels of ERK-dependent feedback suppress RTK signaling and maintain mutant BRAF in a monomeric, drug-sensitive state. Inhibition of ERK signaling inactivates feedback and restores RTK signaling to Ras. The resulting RAF dimers are resistant to RAF inhibitors, leading to bypass of inhibition and reactivation of ERK signaling.

carcinoma; Corcoran et al., 2012; Prahallad et al., 2012). Our findings show that signaling from many receptors is suppressed by ERK-dependent feedback in melanomas and reactivated when feedback is relieved by ERK inhibition. It must be kept in mind that as receptor activation of ERK increases, feedback increases and receptor signaling declines. Each tumor reaches a new steady state of ERK activity after RAF inhibition that must be dependent on the level of ERK output required to induce feedback. If feedback mechanisms are sensitive to induction by low levels of ERK output, rebound will be modest. If high levels of ERK output are required to reinitiate feedback, marked ERK rebound will occur and the tumor will be resistant. Future progress will depend on determining the lineage-dependent and tumor-specific factors responsible for the new steady state.

Our data show that $BRAF^{V600E}$ melanomas are characterized by high levels of ERK-dependent feedback that operates globally to regulate oncogenic signaling. These cells have markedly decreased sensitivity to extracellular ligands. Indeed, the transduction of signals from activated RTKs, a cellular property that we have termed signalability, is markedly suppressed in $BRAF^{V600E}$ melanomas. After ERK inhibition, however, the ERK-dependent negative feedback is lost, and the ability of ligands to activate signaling is markedly enhanced. This is our key finding: at baseline these tumors are relatively insensitive to the effects of secreted growth factors, because the ability of such ligands to induce signaling is disabled. After administration of drugs that effectively inhibit ERK signaling, feedback is reduced and growth factors can signal. Thus, they may attenuate or prevent the antitumor effects of the inhibitor. The signaling network is radically changed and reactivated as an adaptation to inhibition of ERK signaling (Figure 6G).

Recently, several reports have shown that ligands, particularly HGF, can cause resistance to RAF inhibitors (Straussman et al., 2012; Wilson et al., 2012). Induction of signalability when ERK-dependent feedback is relieved requires the presence of active RTKs. We show here that multiple ligands contribute to ERK rebound in melanomas exposed to RAF inhibitors. However, receptor activation is permissive for induction of signalability, i.e., necessary, but not sufficient. Rebound in ERK signaling is due to relief of feedback inhibition of signal transduction when ERK activation is inhibited.

In order to understand how the tumor adapts to pathway inhibition and design more effective therapies, it will be necessary to identify the pathways that become reactivated in patients, as it is not clear that preclinical models are useful in this regard. This will require comparison of pretreatment biopsies with biopsies obtained hours after treatment and the development of new technologies to determine which ligands are present and which pathways have become reactivated. This will allow the development of rational combination therapies aimed at inhibiting the adaptation of the tumor to the targeted therapy.

EXPERIMENTAL PROCEDURES

Cell Lines, Antibodies, and Reagents

Cell lines were maintained as previously described (Solit et al., 2006). Antibodies against phospho and total ERK, MEK, AKT, CRAF, HER1-3, IGF1R, and PDGFRβ were obtained from Cell Signaling; DUSP6, Spry and Ras from Santa Cruz Biotechnology. PD0325901 was synthesized at MSKCC organic synthesis core facility by O. Ouerfelli. Vemurafenib and PLX4720 were provided by Plexxikon. Trametinib and dabrafenib were obtained from GlaxoSmithKline. Neratinib was obtained from Selleckem. Drugs for in vitro studies were dissolved in dimethyl sulfoxide (DMSO) to yield 10 or 1 mM stock solutions and stored at −20°C.

Transfections, Immunoblotting, and Ras-GTP Assays

siRNA pools were obtained from Dharmacon and transfected into cells by using Lipofectamine RNAiMAX, according to manufacturer's instructions. Cell lysis and immunoblotting were performed as described (Basso et al., 2002). GTP-bound Ras was measured using the CRAF Ras-binding domain (RBD) pull-down and Detection Kit (Thermo Scientific) or an ELISA-based RBD pull-down assay (Millipore), as instructed by the manufacturers.

RT-PCR Analysis

RNA was extracted using the RNeasy Mini Kit (QIAGEN), reverse transcribed, and used for quantitative RT-PCR, as previously described (Pratilas et al., 2009). Relative expression of target genes was calculated using the delta-delta Ct method and normalized to the mRNA content of three housekeeping genes.

Animal Studies

Nu/nu athymic mice were obtained from the Harlan Laboratories and maintained in compliance with IACUC guidelines. Subcutaneous xenografts and tumor measurements were performed as described (Solit et al., 2006). All studies were performed in compliance with institutional guidelines under an IACUC approved protocol (Memorial Sloan-Kettering Cancer Center No. 09-05-009).

Tumor Phospho-Flow Analysis

Tumors excised after 48 hr of drug exposure were homogenized and stained with the Live/Dead Fixable Aqua Dead Cell Stain (Invitrogen) according to manufacturer's instructions, followed by fixation and permeabilization and then analysis by flow cytometry with antibodies detecting HLA-ABC (eBioscience), pERK1/2 (Cell Signaling), and APC (Southern Biotech).

Secretome Screen

A collection of 317 cDNA constructs, representing 220 unique secreted and single-pass transmembrane proteins, were reverse transfected individually into 293T cells using Fugene HD (Promega) in a 384-well plate format (Harbinski et al., 2012). After 4 days of incubation, to allow accumulation of secreted proteins, conditioned media from each well was transferred to the assay cells, to which vemurafenib (1 μM) was also added. Proliferation was measured 96 hr later by using CellTiter-Glo. For each individual experiment (performed in triplicate for each cell line) the relative light units (RLUs) were plotted as a function of the various ligand-expressing constructs. Cell growth in the absence of vemurafenib or conditioned media (i.e., DMSO only), and in the presence of vemurafenib alone, were used as controls. The effect (e.g., rescue) of each ligand in the ability of vemurafenib to inhibit growth was calculated by the formula: (median RLU for the construct − median RLU vemurafenib alone)/median RLU DMSO. The rescue values were then used to create a heatmap with the TIBCO Spotfire software. The relative mRNA levels were obtained from expression analysis of the indicated cell lines (Barretina et al., 2012). The relative protein level was determined by immunoblotting (Figure S5D) and densitometric analysis.

SUPPLEMENTAL INFORMATION

Supplemental Information includes five figures and can be found with this article online at http://dx.doi.org/10.1016/j.ccr.2012.10.009.

ACKNOWLEDGMENTS

This work has been funded by the National Institutes of Health (P01-CA129243 to N.R. and K08-CA127350 to C.A.P.), Melanoma Research Alliance (to N.R. and C.A.P.), STARR Cancer Consortium (to N.R.), the Experimental Therapeutics Center of MSKCC (to N.R.), Harry J. Lloyd Charitable Trust (to P.I.P.), the Charles A. Dana Foundation (to P.L.), and Mr. William H. Goodwin and Mrs. Alice Goodwin and the Commonwealth Foundation for Cancer Research (to N.R.). The authors are grateful to Gideon Bollag for providing vemurafenib

and PLX4720, Bart Lutterbach and Giordano Caponigro for insightful discussions, and Christopher Wilson and Fred Harbinski for their assistance with secretome screen.

Received: May 5, 2012
Revised: August 31, 2012
Accepted: October 19, 2012
Published: November 12, 2012

REFERENCES

Avraham, R., and Yarden, Y. (2011). Feedback regulation of EGFR signalling: decision making by early and delayed loops. Nat. Rev. Mol. Cell Biol. *12*, 104–117.

Badalian-Very, G., Vergilio, J.A., Degar, B.A., MacConaill, L.E., Brandner, B., Calicchio, M.L., Kuo, F.C., Ligon, A.H., Stevenson, K.E., Kehoe, S.M., et al. (2010). Recurrent BRAF mutations in Langerhans cell histiocytosis. Blood *116*, 1919–1923.

Barretina, J., Caponigro, G., Stransky, N., Venkatesan, K., Margolin, A.A., Kim, S., Wilson, C.J., Lehár, J., Kryukov, G.V., Sonkin, D., et al. (2012). The Cancer Cell Line Encyclopedia enables predictive modelling of anticancer drug sensitivity. Nature *483*, 603–607.

Basso, A.D., Solit, D.B., Chiosis, G., Giri, B., Tsichlis, P., and Rosen, N. (2002). Akt forms an intracellular complex with heat shock protein 90 (Hsp90) and Cdc37 and is destabilized by inhibitors of Hsp90 function. J. Biol. Chem. *277*, 39858–39866.

Bollag, G., Hirth, P., Tsai, J., Zhang, J., Ibrahim, P.N., Cho, H., Spevak, W., Zhang, C., Zhang, Y., Habets, G., et al. (2010). Clinical efficacy of a RAF inhibitor needs broad target blockade in BRAF-mutant melanoma. Nature *467*, 596–599.

Brose, M.S., Volpe, P., Feldman, M., Kumar, M., Rishi, I., Gerrero, R., Einhorn, E., Herlyn, M., Minna, J., Nicholson, A., et al. (2002). BRAF and RAS mutations in human lung cancer and melanoma. Cancer Res. *62*, 6997–7000.

Chapman, P.B., Hauschild, A., Robert, C., Haanen, J.B., Ascierto, P., Larkin, J., Dummer, R., Garbe, C., Testori, A., Maio, M., et al.; BRIM-3 Study Group. (2011). Improved survival with vemurafenib in melanoma with BRAF V600E mutation. N. Engl. J. Med. *364*, 2507–2516.

Corcoran, R.B., Ebi, H., Turke, A.B., Coffee, E.M., Nishino, M., Cogdill, A.P., Brown, R.D., Della Pelle, P., Dias-Santagata, D., Hung, K.E., et al. (2012). EGFR-mediated re-activation of MAPK signaling contributes to insensitivity of BRAF mutant colorectal cancers to RAF inhibition with vemurafenib. Cancer Discov. *2*, 227–235.

Courtois-Cox, S., Genther Williams, S.M., Reczek, E.E., Johnson, B.W., McGillicuddy, L.T., Johannessen, C.M., Hollstein, P.E., MacCollin, M., and Cichowski, K. (2006). A negative feedback signaling network underlies oncogene-induced senescence. Cancer Cell *10*, 459–472.

Davies, H., Bignell, G.R., Cox, C., Stephens, P., Edkins, S., Clegg, S., Teague, J., Woffendin, H., Garnett, M.J., Bottomley, W., et al. (2002). Mutations of the BRAF gene in human cancer. Nature *417*, 949–954.

Dougherty, M.K., Müller, J., Ritt, D.A., Zhou, M., Zhou, X.Z., Copeland, T.D., Conrads, T.P., Veenstra, T.D., Lu, K.P., and Morrison, D.K. (2005). Regulation of Raf-1 by direct feedback phosphorylation. Mol. Cell *17*, 215–224.

Douville, E., and Downward, J. (1997). EGF induced SOS phosphorylation in PC12 cells involves P90 RSK-2. Oncogene *15*, 373–383.

Downward, J. (2003). Targeting RAS signalling pathways in cancer therapy. Nat. Rev. Cancer *3*, 11–22.

Eblaghie, M.C., Lunn, J.S., Dickinson, R.J., Münsterberg, A.E., Sanz-Ezquerro, J.J., Farrell, E.R., Mathers, J., Keyse, S.M., Storey, K., and Tickle, C. (2003). Negative feedback regulation of FGF signaling levels by Pyst1/MKP3 in chick embryos. Curr. Biol. *13*, 1009–1018.

Hanafusa, H., Torii, S., Yasunaga, T., and Nishida, E. (2002). Sprouty1 and Sprouty2 provide a control mechanism for the Ras/MAPK signalling pathway. Nat. Cell Biol. *4*, 850–858.

Harbinski, F., Craig, V.J., Sanghavi, S., Jeffery, D., Liu, L., Sheppard, K.A., Wagner, S., Stamm, C., Buness, A., Chatenay-Rivauday, C., et al. (2012). Rescue screens with secreted proteins reveal compensatory potential of receptor tyrosine kinases in driving cancer growth. Cancer Discov. *2*, 948–959.

Hatzivassiliou, G., Song, K., Yen, I., Brandhuber, B.J., Anderson, D.J., Alvarado, R., Ludlam, M.J., Stokoe, D., Gloor, S.L., Vigers, G., et al. (2010). RAF inhibitors prime wild-type RAF to activate the MAPK pathway and enhance growth. Nature *464*, 431–435.

Heidorn, S.J., Milagre, C., Whittaker, S., Nourry, A., Niculescu-Duvas, I., Dhomen, N., Hussain, J., Reis-Filho, J.S., Springer, C.J., Pritchard, C., and Marais, R. (2010). Kinase-dead BRAF and oncogenic RAS cooperate to drive tumor progression through CRAF. Cell *140*, 209–221.

Hingorani, S.R., Jacobetz, M.A., Robertson, G.P., Herlyn, M., and Tuveson, D.A. (2003). Suppression of BRAF(V599E) in human melanoma abrogates transformation. Cancer Res. *63*, 5198–5202.

Joseph, E.W., Pratilas, C.A., Poulikakos, P.I., Tadi, M., Wang, W., Taylor, B.S., Halilovic, E., Persaud, Y., Xing, F., Viale, A., et al. (2010). The RAF inhibitor PLX4032 inhibits ERK signaling and tumor cell proliferation in a V600E BRAF-selective manner. Proc. Natl. Acad. Sci. USA *107*, 14903–14908.

Kim, H.J., and Bar-Sagi, D. (2004). Modulation of signalling by Sprouty: a developing story. Nat. Rev. Mol. Cell Biol. *5*, 441–450.

Kirkwood, J.M., Bastholt, L., Robert, C., Sosman, J., Larkin, J., Hersey, P., Middleton, M., Cantarini, M., Zazulina, V., Kemsley, K., and Dummer, R. (2012). Phase II, open-label, randomized trial of the MEK1/2 inhibitor selumetinib as monotherapy versus temozolomide in patients with advanced melanoma. Clin. Cancer Res. *18*, 555–567.

Leboeuf, R., Baumgartner, J.E., Benezra, M., Malaguarnera, R., Solit, D., Pratilas, C.A., Rosen, N., Knauf, J.A., and Fagin, J.A. (2008). BRAFV600E mutation is associated with preferential sensitivity to mitogen-activated protein kinase kinase inhibition in thyroid cancer cell lines. J. Clin. Endocrinol. Metab. *93*, 2194–2201.

Mason, J.M., Morrison, D.J., Basson, M.A., and Licht, J.D. (2006). Sprouty proteins: multifaceted negative-feedback regulators of receptor tyrosine kinase signaling. Trends Cell Biol. *16*, 45–54.

McCormick, F. (1993). Signal transduction. How receptors turn Ras on. Nature *363*, 15–16.

Nazarian, R., Shi, H., Wang, Q., Kong, X., Koya, R.C., Lee, H., Chen, Z., Lee, M.K., Attar, N., Sazegar, H., et al. (2010). Melanomas acquire resistance to B-RAF(V600E) inhibition by RTK or N-RAS upregulation. Nature *468*, 973–977.

Nikiforova, M.N., Kimura, E.T., Gandhi, M., Biddinger, P.W., Knauf, J.A., Basolo, F., Zhu, Z., Giannini, R., Salvatore, G., Fusco, A., et al. (2003). BRAF mutations in thyroid tumors are restricted to papillary carcinomas and anaplastic or poorly differentiated carcinomas arising from papillary carcinomas. J. Clin. Endocrinol. Metab. *88*, 5399–5404.

Nimnual, A., and Bar-Sagi, D. (2002). The two hats of SOS. Sci. STKE *2002*, pe36.

Poulikakos, P.I., Persaud, Y., Janakiraman, M., Kong, X., Ng, C., Moriceau, G., Shi, H., Atefi, M., Titz, B., Gabay, M.T., et al. (2011). RAF inhibitor resistance is mediated by dimerization of aberrantly spliced BRAF(V600E). Nature *480*, 387–390.

Poulikakos, P.I., Zhang, C., Bollag, G., Shokat, K.M., and Rosen, N. (2010). RAF inhibitors transactivate RAF dimers and ERK signalling in cells with wild-type BRAF. Nature *464*, 427–430.

Prahallad, A., Sun, C., Huang, S., Di Nicolantonio, F., Salazar, R., Zecchin, D., Beijersbergen, R.L., Bardelli, A., and Bernards, R. (2012). Unresponsiveness of colon cancer to BRAF(V600E) inhibition through feedback activation of EGFR. Nature *483*, 100–103.

Pratilas, C.A., Hanrahan, A.J., Halilovic, E., Persaud, Y., Soh, J., Chitale, D., Shigematsu, H., Yamamoto, H., Sawai, A., Janakiraman, M., et al. (2008). Genetic predictors of MEK dependence in non-small cell lung cancer. Cancer Res. *68*, 9375–9383.

Pratilas, C.A., Taylor, B.S., Ye, Q., Viale, A., Sander, C., Solit, D.B., and Rosen, N. (2009). (V600E)BRAF is associated with disabled feedback inhibition of

RAF-MEK signaling and elevated transcriptional output of the pathway. Proc. Natl. Acad. Sci. USA *106*, 4519–4524.

Schiffman, J.D., Hodgson, J.G., VandenBerg, S.R., Flaherty, P., Polley, M.Y., Yu, M., Fisher, P.G., Rowitch, D.H., Ford, J.M., Berger, M.S., et al. (2010). Oncogenic BRAF mutation with CDKN2A inactivation is characteristic of a subset of pediatric malignant astrocytomas. Cancer Res. *70*, 512–519.

Sebolt-Leopold, J.S., Dudley, D.T., Herrera, R., Van Becelaere, K., Wiland, A., Gowan, R.C., Tecle, H., Barrett, S.D., Bridges, A., Przybranowski, S., et al. (1999). Blockade of the MAP kinase pathway suppresses growth of colon tumors in vivo. Nat. Med. *5*, 810–816.

Solit, D.B., and Rosen, N. (2011). Resistance to BRAF inhibition in melanomas. N. Engl. J. Med. *364*, 772–774.

Solit, D.B., Garraway, L.A., Pratilas, C.A., Sawai, A., Getz, G., Basso, A., Ye, Q., Lobo, J.M., She, Y., Osman, I., et al. (2006). BRAF mutation predicts sensitivity to MEK inhibition. Nature *439*, 358–362.

Sosman, J.A., Kim, K.B., Schuchter, L., Gonzalez, R., Pavlick, A.C., Weber, J.S., McArthur, G.A., Hutson, T.E., Moschos, S.J., Flaherty, K.T., et al. (2012). Survival in BRAF V600-mutant advanced melanoma treated with vemurafenib. N. Engl. J. Med. *366*, 707–714.

Straussman, R., Morikawa, T., Shee, K., Barzily-Rokni, M., Qian, Z.R., Du, J., Davis, A., Mongare, M.M., Gould, J., Frederick, D.T., et al. (2012). Tumour micro-environment elicits innate resistance to RAF inhibitors through HGF secretion. Nature *487*, 500–504.

Tiacci, E., Trifonov, V., Schiavoni, G., Holmes, A., Kern, W., Martelli, M.P., Pucciarini, A., Bigerna, B., Pacini, R., Wells, V.A., et al. (2011). BRAF mutations in hairy-cell leukemia. N. Engl. J. Med. *364*, 2305–2315.

Tsai, J., Lee, J.T., Wang, W., Zhang, J., Cho, H., Mamo, S., Bremer, R., Gillette, S., Kong, J., Haass, N.K., et al. (2008). Discovery of a selective inhibitor of oncogenic B-Raf kinase with potent antimelanoma activity. Proc. Natl. Acad. Sci. USA *105*, 3041–3046.

Wellbrock, C., Karasarides, M., and Marais, R. (2004a). The RAF proteins take centre stage. Nat. Rev. Mol. Cell Biol. *5*, 875–885.

Wellbrock, C., Ogilvie, L., Hedley, D., Karasarides, M., Martin, J., Niculescu-Duvaz, D., Springer, C.J., and Marais, R. (2004b). V599EB-RAF is an oncogene in melanocytes. Cancer Res. *64*, 2338–2342.

Wilson, T.R., Fridlyand, J., Yan, Y., Penuel, E., Burton, L., Chan, E., Peng, J., Lin, E., Wang, Y., Sosman, J., et al. (2012). Widespread potential for growth-factor-driven resistance to anticancer kinase inhibitors. Nature *487*, 505–509.

Metastatic Ability: Adapting to a Tissue Site Unseen

Neil A. Bhowmick[1,2,3,*]
[1]Department of Medicine, Cedars-Sinai Medical Center, Los Angeles, CA 90048, USA
[2]Greater Los Angeles Veterans Administration, Los Angeles, CA 90073, USA
[3]Samuel Oschin Comprehensive Cancer Institute, 8750 Beverly Boulevard, Atrium 103, Los Angeles, CA 90048, USA
*Correspondence: bhowmickn@cshs.org
http://dx.doi.org/10.1016/j.ccr.2012.10.011

The microenvironment of the primary as well as the metastatic tumor sites can determine the ability for a disseminated tumor to progress. In this issue of *Cancer Cell*, Calon and colleagues find that systemic TGF-β can facilitate colon cancer metastatic engraftment and expansion.

Preventing the metastatic progression of tumors is a prevailing issue in cancer biology. In liquid tumors, like multiple myeloma, which colonizes the bone, we can imagine the cancer cells have pre-existing equipment required to survive and thrive in the bone microenvironment. For ovarian serous carcinoma dissemination and expansion within the peritoneal cavity, cell autonomous mechanisms of tumor proliferation, epithelial-to-mesenchymal transdifferentiation, and anti-apoptotic signaling may be predominant requirements for metastasis. However, the non-random metastatic tropism of solid tumors, such as that of the breast, colon, and prostate, often need to adapt to more than one distant site, including lymph nodes, bone, and soft tissue. In these examples, tumor size at the primary site and the number of circulating tumor cells are relatively less significant determinants of adaptation at the secondary site.

The extensive global sequencing efforts of the primary tumor epithelia have not helped to predict colon cancer metastatic potential (Jones et al., 2008). In contrast, profiling the microenvironment of the primary tumor seems to be predictive for liver and prostate cancer metastatic progression (Blum et al., 2008; Budhu et al., 2006). In this issue of *Cancer Cell*, Calon et al. (2012) report that measuring reciprocating signals by the tumor and host are likely going to be more predictive of colon cancer growth at the metastatic site. Specifically, the authors found that elevated levels of transforming growth factor-beta (TGF-β) expression was a superior predictor of metastatic growth of colon cancer rather than pathologic staging. They present a study addressing the apparent paradox characterized by high TGF-β levels in the tumor and mutational inactivation of TGF-β signaling observed in colon cancer epithelia. As such, the elevated TGF-β would be affecting the cells of the host, in particular, endothelia and fibroblasts, at the distant metastatic site. Calon et al. (2012) suggest that a stromal TGF-β response, involving IL-11, potentiates colon cancer engraftment and growth at liver and lung metastatic sites. The immune regulatory effects of TGF-β could not be specifically examined as the observations were made in immune-compromised xenograft mouse models. However, the work suggests a novel mechanism of colon cancer metastatic progression following the initial steps of tumor cell dissemination.

Multiple mechanisms of metastatic progression are possible. One such possibility is that tumor cells possessing stem-like features may have a growth advantage in a secondary site; their pluripotent potential could presumably facilitate adaptation to a new environment (Figure 1A). A tumor cell cannot evolve to adapt to an environment to which it has not been exposed. In this case, the success of the metastasis is reliant on the plasticity of the stem-like tumor cell. A recent report suggested that expression of the extracellular matrix component periostin in mammary tumors can support stem-like features to favor metastatic progression (Malanchi et al., 2012). In the process of prostate cancer and stromal coevolution in the primary tumor site, paracrine cytokines expressed by prostatic fibroblasts that lose TGF-β responsiveness alter the interactions of tumor epithelia, with its matrix enabling significant expansion in secondary bone tissue (Li et al., 2012). Another recent report supports the idea that specific changes in the matrix and its integrin interaction with primary lung tumor cells are critical determinants of metastatic progression (Reticker-Flynn et al., 2012). Figure 1B illustrates that an alternative means of successful metastatic progression can be a result of a disseminated tumor cell having the ability to survive in the secondary site until it can express factors that enable it to thrive (Stoecklein et al., 2008). The secondary tissue microenvironment can reciprocally respond to the disseminated tumor cell, such that a collaborative effort enables metastatic progression. Tumor dormancy, which is associated with micrometastases that are not visibly progressing, can involve the coevolutionary process at the metastatic site, which includes cell autonomous changes as well as those of the host vasculature and immune system. It has been clear for some time that TGF-β mediates processes associated with tumor cell extravasation in terms of increased motility and cell survival. However, these cell-autonomous TGF-β activities cannot be attributed to elevated metastatic potential, because TGF-β signaling is increasingly found to be impaired or completely absent in multiple cancer types, including colon cancer epithelia. Figure 1C illustrates changes that can occur in the primary and metastatic tumor microenvironment as a result of elevated systemic TGF-β. These changes may normalize the microenvironment of the two sites such that the metastatic niche is primed for tumor growth, as suggested in the study by Calon et al.

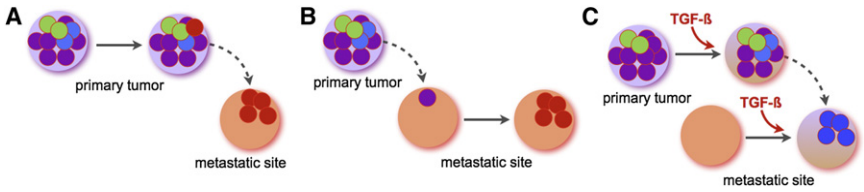

Figure 1. Scenarios for Metastatic Expansion

There are multiple possible mechanisms for metastatic progression. It is assumed that the rate limiting steps of metastasis do not necessarily involve the processes of tumor cell dissemination, but rather compatibility of tumor cells with their metastatic site.

(A) A primary tumor cell can acquire traits within the primary tumor that enable its progression in the metastatic site.

(B) Alternatively, the disseminated tumor cells that lodge in the metastatic site can lie 'dormant' until the new microenvironment potentiates the acquisition of traits that enable tumor progression.

(C) The work by Calon et al. (2012) suggests that elevated TGF-β and its downstream products induce changes in the microenvironment of the primary tumor and the metastatic site to facilitate metastatic progression. There are other possibilities mediating metastatic progression including variations and combinations of these three scenarios. The role of the immune system is not accounted for in this assessment.

(2012). The role of the innate immune system in the development of a pre-metastatic niche has been described (Kaplan et al., 2005). However, the detection of TGF-β in circulation in colon cancer metastatic progression in patients supports the role of tumor-derived cytokines in the primary site having long range effects in altering the microenvironment of the metastatic site (Calon et al., 2012). The role of TGF-β in altering the microenvironment of the primary and metastatic sites can be therapeutically leveraged. For example, TGF-β blockade increases chemotherapeutic penetration into tumors by causing perivascular cell activation, leading to increased tumor perfusion and reduced extracellular matrix formation (Liu et al., 2012).

Translational opportunities for the application of these results are dependent on further understanding of the host response to TGF-β signaling. The inhibition of TGF-β signaling at the level of the ligand, receptor-ligand complex, and intracellular signaling molecules are being studied. However, the targeting of downstream paracrine factors, initially thought to be a fools-game of chasing the numerous TGF-β responsive genes, is starting to come down to fewer examples of viable candidates to support greater tumor specificity. Nevertheless, there is an even greater need to understand the metastatic site in order to appropriately determine the TGF-β induced factor(s). Metastatic tropism is reliant on the dynamics of the tumor cell as it attempts to convert its microenvironment to its advantage (Figure 1). Thus, to time the therapeutic window for pharmacological intervention of a metastatic mechanism would be challenging. However, addressing metastasis methods collectively used by heterogeneous tumors may require a multipronged approach that would include targeting the microenvironment at both primary and metastatic sites through a cell type-directed manner.

REFERENCES

Blum, D.L., Koyama, T., M'Koma, A.E., Iturregui, J.M., Martinez-Ferrer, M., Uwamariya, C., Smith, J.A., Jr., Clark, P.E., and Bhowmick, N.A. (2008). Clin. Cancer Res. *14*, 7790–7797.

Budhu, A., Forgues, M., Ye, Q.H., Jia, H.L., He, P., Zanetti, K.A., Kammula, U.S., Chen, Y., Qin, L.X., Tang, Z.Y., and Wang, X.W. (2006). Cancer Cell *10*, 99–111.

Calon, A., Espinet, E., Palomo-Ponce, S., Tauriello, D.V.F., Iglesias, M., Céspedes, M.V., Sevillano, M., Nadal, C., Jung, P., Zhang, X.H.-F., et al. (2012). Cancer Cell *22*, this issue, 571–584.

Jones, S., Chen, W.D., Parmigiani, G., Diehl, F., Beerenwinkel, N., Antal, T., Traulsen, A., Nowak, M.A., Siegel, C., Velculescu, V.E., et al. (2008). Proc. Natl. Acad. Sci. USA *105*, 4283–4288.

Kaplan, R.N., Riba, R.D., Zacharoulis, S., Bramley, A.H., Vincent, L., Costa, C., MacDonald, D.D., Jin, D.K., Shido, K., Kerns, S.A., et al. (2005). Nature *438*, 820–827.

Li, X., Sterling, J.A., Fan, K.H., Vessella, R.L., Shyr, Y., Hayward, S.W., Matrisian, L.M., and Bhowmick, N.A. (2012). Mol. Cancer Res. *10*, 494–503.

Liu, J., Liao, S., Diop-Frimpong, B., Chen, W., Goel, S., Naxerova, K., Ancukiewicz, M., Boucher, Y., Jain, R.K., and Xu, L. (2012). Proc. Natl. Acad. Sci. USA *109*, 16618–16623.

Malanchi, I., Santamaria-Martínez, A., Susanto, E., Peng, H., Lehr, H.A., Delaloye, J.F., and Huelsken, J. (2012). Nature *481*, 85–89.

Reticker-Flynn, N.E., Malta, D.F., Winslow, M.M., Lamar, J.M., Xu, M.J., Underhill, G.H., Hynes, R.O., Jacks, T.E., and Bhatia, S.N. (2012). Nat Commun. *3*, 1122.

Stoecklein, N.H., Hosch, S.B., Bezler, M., Stern, F., Hartmann, C.H., Vay, C., Siegmund, A., Scheunemann, P., Schurr, P., Knoefel, W.T., et al. (2008). Cancer Cell *13*, 441–453.

PGAMgnam Style: A Glycolytic Switch Controls Biosynthesis

Barbara Chaneton[1] and Eyal Gottlieb[1,*]
[1]Cancer Research UK, The Beatson Institute for Cancer Research, Switchback Road, Glasgow G61 1BD, UK
*Correspondence: e.gottlieb@beatson.gla.ac.uk
http://dx.doi.org/10.1016/j.ccr.2012.10.014

Therapeutic strategies that target glycolysis and biosynthetic pathways in cancer cells are currently the main focus of research in the field of cancer metabolism. In this issue of *Cancer Cell*, Hitosugi and colleagues show that targeting PGAM1 could be a way of "killing two birds with one stone".

The metabolism of cancer cells differs from that of many normal cells and is mostly characterized by higher rates of glucose metabolism under normal oxygen levels. This trait enables cancer cells to satisfy their demand for both energy and biosynthetic building blocks required for proliferation. For that reason, it is not surprising that many glycolytic enzymes are commonly overexpressed in tumors (Tennant et al., 2009). Phosphoglycerate mutase (PGAM1) catalyzes the conversion of 3-phosphoglycerate (3PG) into 2-phosphoglycerate (2PG) as part of the glycolytic pathway using a phospho-histidine residue at the enzyme's catalytic domain (His11) as a phosphate donor/acceptor and 2,3-bisphosphoglycerate as an intermediate metabolite (Fothergill-Gilmore and Watson, 1989). In humans, PGAM1 is widely expressed at levels that vary among different tissues as well as during differentiation and transformation. PGAM1 is overexpressed in several types of cancer (Fothergill-Gilmore and Watson, 1989; Ren et al., 2010). Because PGAM1 expression is negatively regulated by the tumor suppressor TP53, the loss of the latter may cause increased expression of PGAM1 in cancer. This portrays PGAM1 as a potential therapeutic target, and indeed, pharmacological inhibition of PGAM1 reduced proliferation of breast cancer cells (Evans et al., 2005). Furthermore, in cancer cells that overexpress the tightly-regulated isoform of pyruvate kinase PKM2, PGAM1 phosphorylation on His11, and hence PGAM1's activity, are induced by phosphoenolpyruvate, the substrate of pyruvate kinase (Vander Heiden et al., 2010).

The notion that metabolites can act as signaling molecules in distant metabolic pathways is gaining significant attention and support (Figure 1A). Some of the best known examples are the activation of PKM2, which catalyzes the last step of glycolysis, by fructose 1,6-bisphosphate (an upstream glycolytic intermediate) and the inhibition of phosphofructokinase-1 (another key regulated glycolytic enzyme) by phosphoenolpyruvate, citrate, and ATP (Ashizawa et al., 1991; Evans et al., 1981). These regulatory loops ensure that glycolytic intermediates are optimally utilized and channeled into the appropriate metabolic pathway to balance energetic and anabolic demands. Recently, the amino acid serine was demonstrated to bind and directly activate PKM2 in order to control the bifurcation point from glycolysis to serine biosynthesis (Chaneton et al., 2012). In line with this concept, this issue of *Cancer Cell* features the work by Hitosugi et al. (2012), which demonstrates that, in addition to their involvement in glycolysis, both the substrate and product of PGAM1 (3PG and 2PG, respectively) modulate two other biosynthetic pathways derived from glycolysis: the oxidative branch of the pentose phosphate pathway (PPP) and the serine biosynthesis pathway (Figure 1A).

Hitosugi et al. (2012) studied the prospective therapeutic approach of PGAM1 inhibition in cancer cells and the associated metabolic consequences. Silencing the expression of PGAM1 with short-hairpin RNA caused an increase in the intracellular levels of 3PG and a decrease in 2PG levels, which is associated with a block in the glycolytic flow. Surprisingly, the downregulation of PGAM1 levels also inhibited the entry of glucose 6-phosphate into the oxidative PPP, a process which supports de novo nucleotide biosynthesis. Hitosugi et al. (2012) demonstrated that the increase in 3PG directly causes the inactivation of the PPP enzyme 6-phosphogluconate dehydrogenase (6PGD) by competing with its substrate 6-phosphogluconate. What's more, the decrease in 2PG levels upon PGAM1 downregulation was accompanied by a reduction in phosphoglycerate dehydrogenase (PHGDH) activity, which utilizes 3PG as a substrate and carries out the first regulated step in the serine biosynthesis pathway (Figure 1B). Interestingly, the cell permeable analog of 2PG (methyl-2-PG) rescued PGAM1-silenced cells by increasing the flux of 3PG into the serine biosynthesis pathway through PHGDH and, with that, alleviated the inhibition of the PPP by 3PG while also rescuing glycolysis. Furthermore, a screen for small molecule inhibitors of PGAM1 identified an allosteric inhibitor that affected cell metabolism and growth of xenografted tumors in vivo in a manner similar to PGAM1 silencing. These observations strengthen the concept that targeting PGAM1 pharmacologically may be beneficial for cancer therapy not only by reducing an important energy source of cancer cells, but also by preventing anabolic processes required for cell growth and proliferation.

The work by Hitosugi et al. (2012) not only provides new insights into the complex mechanism of metabolic regulation (by identifying 2PG and 3PG as signaling molecules that regulate biosynthetic pathways), but also emphasizes the potential effectiveness of exploiting such complexity, which allows for the targeting of both energetic and anabolic processes with a single drug. However, one of the main challenges in targeting cancer metabolism is the robustness

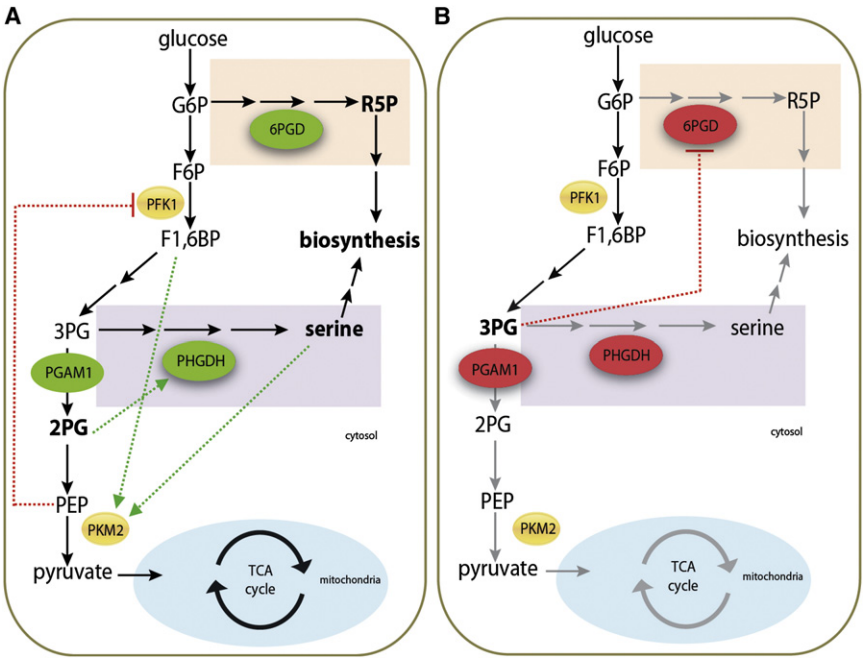

Figure 1. The Dual Catabolic and Anabolic Roles of PGAM1 that Make It a Useful Target for Cancer Treatment

(A) Glycolysis and biosynthetic processes that "branch" from glucose metabolism are required to support growth and proliferation of cells. These processes must be tightly controlled and adjusted to meet cellular needs. Intricate regulatory loop signals exist to enable such control. These include phosphofructokinase-1 (PFK1) inhibition by phosphoenolpyruvate (PEP) and the activation of pyruvate kinase (PK) M2 isoform (PKM2) (the predominant isoform expressed in proliferating cells) by fructose 1,6-bisphosphate (F1,6BP) and serine. PGAM1 is overexpressed in many cancer cells supporting energetic demands by enabling increased glycolytic flux. At the same time, its product 2-phosphoglycerate (2PG) stimulates phosphoglycerate dehydrogenase (PHGDH), which catalyzes the first and rate-limiting step in the serine biosynthesis pathway (purple rectangle).

(B) Upon inhibition of PGAM1, an increase in 3-phosphoglycerate (3PG) and a decrease in 2PG occur. This leads to a decrease in glycolytic flow and energy production by PK as well as the tricarboxylic acid (TCA) cycle in the mitochondria. In addition, the reduction in 2PG due to PGAM1 inhibition prevents the channeling of 3PG into the serine biosynthetic pathway, leading to further accumulation of 3PG. Accumulated 3PG, in turn, inhibits 6-phosphogluconate dehydrogenase (6PGD) in the pentose phosphate pathway (brown rectangle) and ribosome 5-phosphate (R5P) production. In effect, the inhibition of PGAM1, a glycolytic enzyme, not only limits glycolysis, but also two important anabolic processes required for cell proliferation.

Green or red dotted lines indicate direct positive or negative regulatory effects and green or red ovals represent active or inactive enzymes, respectively. Black or gray arrows represent active or inhibited reactions, respectively.

and plasticity of metabolic networks that allow cancer cells to adapt and overcome impediments. In addition, a consideration for long- and short-term toxicity to metabolically active normal tissues must be taken into account when a core glucose metabolic pathway is being targeted. Encouragingly, the in vivo work reported by Hitosugi et al. (2012) demonstrated a good therapeutic index for such a strategy.

REFERENCES

Ashizawa, K., Willingham, M.C., Liang, C.M., and Cheng, S.Y. (1991). J. Biol. Chem. *266*, 16842–16846.

Chaneton, B., Hillmann, P., Zheng, L., Martin, A.C., Maddocks, O.D., Chokkathukalam, A., Coyle, J.E., Jankevics, A., Holding, F.P., Vousden, K.H., et al. (2012). Nature. Published online October 14, 2012. http://dx.doi.org/10.1038/nature11540.

Evans, M.J., Saghatelian, A., Sorensen, E.J., and Cravatt, B.F. (2005). Nat. Biotechnol. *23*, 1303–1307.

Evans, P.R., Farrants, G.W., and Hudson, P.J. (1981). Philos. Trans. R. Soc. Lond. B Biol. Sci. *293*, 53–62.

Fothergill-Gilmore, L.A., and Watson, H.C. (1989). Adv. Enzymol. Relat. Areas Mol. Biol. *62*, 227–313.

Hitosugi, T., Zhou, L., Elf, S., Fan, J., Kang, H.-B., Seo, J.H., Shan, C., Dai, Q., Zhang, L., Xie, J., et al. (2012). Cancer Cell *22*, this issue, 585–600.

Ren, F., Wu, H., Lei, Y., Zhang, H., Liu, R., Zhao, Y., Chen, X., Zeng, D., Tong, A., Chen, L., et al. (2010). Mol. Cancer *9*, 81.

Tennant, D.A., Durán, R.V., Boulahbel, H., and Gottlieb, E. (2009). Carcinogenesis *30*, 1269–1280.

Vander Heiden, M.G., Locasale, J.W., Swanson, K.D., Sharfi, H., Heffron, G.J., Amador-Noguez, D., Christofk, H.R., Wagner, G., Rabinowitz, J.D., Asara, J.M., and Cantley, L.C. (2010). Science *329*, 1492–1499.

Epigenetic Therapy Leaps Ahead with Specific Targeting of EZH2

Ari Melnick[1,*]
[1]Departments of Medicine and Pharmacology, Weill Cornell Medical College, 1300 York Avenue, New York, NY 10065, USA
*Correspondence: amm2014@med.cornell.edu
http://dx.doi.org/10.1016/j.ccr.2012.10.016

The Polycomb epigenetic silencing protein EZH2 is affected by gain-of-function somatic mutations in B cell lymphomas. Two recent reports describe the development of highly selective EZH2 inhibitors and reveal mutant EZH2 as playing an essential role in maintaining lymphoma proliferation. EZH2 inhibitors are thus a promising new targeted therapy for lymphoma.

Aberrant patterning of epigenetic marks is a fundamental hallmark of human cancer. Studies exploring genome-wide distribution of DNA methylation and histone modifications consistently reveal profound perturbations in primary human tumor specimens (Baylin and Jones, 2011). Such findings have contributed to the increasing enthusiasm for ''epigenetic therapy'' to reprogram the epigenome of tumor cells. Two recent reports have extended this paradigm to an exciting new therapeutic target, EZH2.

EZH2 is the core enzymatic subunit of an epigenetic gene-silencing complex called polycomb repressive complex 2 (PRC2). EZH2 is a SET domain histone methyltransferase that preferentially catalyzes histone 3 lysine 27 (H3K27) methylation, a repressive mark that maintains epigenetic silencing of genes (Chase and Cross, 2011). EZH2 is active only when associated with other PRC2 core components EED, SUZ12, and RbAp48 (Chase and Cross, 2011). During lymphopoiesis, EZH2 is required for developing pre-B cells to acquire a full spectrum of immunoglobulin VDJ recombinants (Su et al., 2003). However, EZH2 expression reaches its peak when mature B cells are stimulated to form germinal centers (GCs) and undergo immunoglobulin affinity maturation (Velichutina et al., 2010). GC B cells are uniquely adapted to tolerate rapid proliferation and simultaneous genotoxic stress, which enables them to generate high-affinity antibodies. GC B cells give rise to the most common types of B cell lymphomas including diffuse large B cell lymphomas (DLBCLs) and follicular lymphomas (FLs).

Remarkably, 20% of DLBCLs and 10% of FLs display heterozygous somatic mutations of EZH2 involving Y641 or A677 (Morin et al., 2010). These mutations enable EZH2 to more efficiently add a third methyl group to H3K27 (Sneeringer et al., 2010). EZH2 mutant DLBCL cells exhibit increased abundance of H3K27me3 and reduction of H3K27me1 (Morin et al., 2010). The significance of this change is unknown, but presumably would facilitate more stable or potent repression of EZH2 target genes. Until now, it has been unclear whether the relatively subtle change in the stoichiometry of methylated H3K27 in EZH2 mutant DLBCLs would exert significant influence on the malignant phenotype. Regardless of the mutation status, a majority of DLBCLs feature high expression of EZH2, likely reflecting their GC origin (Velichutina et al., 2010). Moreover, genomics studies in primary human GC B cells showed that EZH2 represses numerous proliferation checkpoint genes, suggesting a role in facilitating proliferation (Velichutina et al., 2010). Hence, it is of great interest to address whether mutations in EZH2 contribute significantly to maintain the survival of lymphoma cells or just represent subtle ''tuning'' of an epigenetic silencing mechanism that is already present.

Some of these questions can now be addressed thanks to the development of highly selective EZH2 inhibitors, an achievement with important scientific and clinical implications. Using high-throughput screening for inhibitors of the PRC2 complex followed by medicinal chemistry optimization, two research groups generated low nanomolar potency small molecule EZH2 inhibitors (Knutson et al., 2012; McCabe et al., 2012). These small molecules displayed remarkable selectivity for EZH2 and showed similar efficacy against wild-type and mutant forms of EZH2. Notably, when applied to a large panel of B cell lymphoma cell lines, EZH2 inhibitors were most effective against DLBCLs, especially those with EZH2 point mutations. The compound induced apoptotic cell death in addition to proliferation arrest in the most sensitive cell lines. EZH2 mutant DLBCL cells are therefore exquisitely dependent on EZH2 to maintain their growth and survival. Nononcogene addiction to EZH2 may also occur in at least a subset of EZH2 wild-type DLBCLs, perhaps reflecting a potential biological role for EZH2 in normal GC B cells.

In an attempt to link the biologic actions of EZH2 inhibitor to gene expression and H3k27 methylation, a series of profiling experiments were performed (McCabe et al., 2012). The most EZH2-dependent cell lines showed predominant gene upregulation after exposure to GSK126, one of the EZH2 inhibitors, associated with a heavier pretreatment burden of H3K27me3 (McCabe et al., 2012). Transcriptional response was stronger in EZH2 mutant versus wild-type cell lines. However, the logic of these associations seems to break down when comparing differentially regulated genes among the most GSK126-responsive cell lines. It would not be unreasonable to expect EZH2 mutant cell lines to display a strong signature of GSK126-induced genes given their shared biological dependence on EZH2. Yet, only 35 genes overlapped in four out of the five cell lines profiled. Independent of experimental questions, such as whether heterogeneity is a product of cell line epigenetic diversification in vitro or whether gene expression

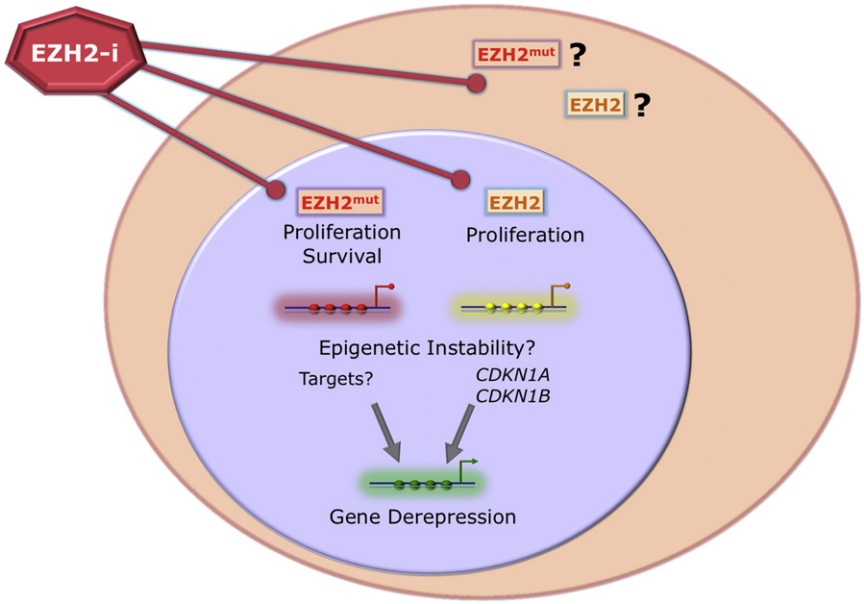

Figure 1. EZH2 Inhibitors Target Mutant and Wild-type EZH2 in DLBCL Cells with Equal Potency

EZH2 may form an active PRC2 complex in both nucleus and cytoplasm, although its cytoplasmic function in B cells is unknown. Mutant EZH2 mediates both survival and proliferation, whereas wild-type might be mostly linked to proliferation. Mutant EZH2 more strongly represses chromatin (red) than wild-type EZH2 (yellow) by inducing greater levels of H3K27me3. Wild-type EZH2 represses proliferation-associated genes such as *CDKN1A* and *CDKN1B*, whereas the target genes of mutant EZH2 may be different or more variable. Mutant EZH2, and perhaps wild-type EZH2 to a lesser extent, may contribute to epigenetic instability such as more heterogeneous distribution of H3K27me3. Newly-described EZH2 inhibitors (EZH-i) epigenetically reprogram DLBCL cells with mutant or wild-type EZH2 (green), leading to the derepression of target genes and perhaps alleviation of epigenetic instability manifested as proliferation arrest and cell death.

microarrays have the necessary dynamic range to robustly capture changes in low abundance transcripts, it is interesting to consider the implications of these results. For example, might it be possible that EZH2 mutation enables a state of "epigenetic instability" whereby H3K27 patterning evolves stochastically such that tumors in individual patients may silence different sets of genes, any combination of which might have similar effects in facilitating transformation? There is a precedent for such a notion in that proliferating GC B cells display a greater degree of cytosine methylation heterogeneity than resting B cells (Shaknovich et al., 2011). Likewise, it is conceivable that proliferation in GC B cells could also drive H3K27 methylation heterogeneity. Alternatively, it is possible that only a small number of genes contribute in a meaningful way to the oncogenic effects of mutant EZH2, in which case, the nonoverlapping genes may represent mostly noise. It is also intriguing to consider whether gene expression and/or H3K27 methylation changes might be a red herring. For example, PRC2 complex is also localized to cytoplasm, and in T cells, may regulate processes such as actin polymerization (Su et al., 2005). Might the effect of EZH2 inhibitors be related to nonepigenetic mechanisms? These provocative results challenge the field to perform functional assays and modeling to resolve these questions (Figure 1).

Regardless of these deeper mechanistic questions, the report by McCabe et al. (2012) has major translational implications. Even though EZH2 is an essential protein during development, mice tolerated the drug without apparent toxicity. Most importantly, GSK126 displayed an extremely powerful anti-lymphoma effect on human DLBCL cell line xenografts, with complete growth inhibition at lower doses and tumor eradication at higher doses of drug (McCabe et al., 2012). Tumor eradication is not easily achievable in DLBCL xenograft studies, raising the possibility that mutant EZH2 might play a role in self-renewal of putative lymphoma propagating cells. EZH2 is known to play a key role in the self-renewal of stem cells (Chase and Cross, 2011), so it is conceivable that, in addition to growth arrest and apoptosis, EZH2 inhibitors might promote the extinction of EZH2-dependent lymphomagenic clones. These data provide a compelling case for testing EZH2 inhibitors in clinical trials for patients with DLBCL harboring mutant EZH2 and/or high H3K27 methylation levels. Finally, in addition to DLBCL, EZH2 is also mutated in FL and is overexpressed in solid tumors including prostate and breast cancer (Chase and Cross, 2011). Therefore, the rational translation of EZH2 inhibitor therapy holds great promise toward improved efficacy and reduced toxicity for patients with these diseases.

REFERENCES

Baylin, S.B., and Jones, P.A. (2011). Nat. Rev. Cancer *11*, 726–734.

Chase, A., and Cross, N.C. (2011). Clin. Cancer Res. *17*, 2613–2618.

Knutson, S.K., Wigle, T.J., Warholic, N.M., Sneeringer, C.J., Allain, C.J., Klaus, C.R., Sacks, J.D., Raimondi, A., Majer, C.R., Song, J., et al. (2012). Nat. Chem. Biol. *8*, 890–896.

McCabe, M.T., Ott, H.M., Ganji, G., Korenchuk, S., Thompson, C., Van Aller, G.S., Liu, Y., Graves, A.P., Iii, A.D., Diaz, E., et al. (2012). Nature. Published online October 10, 2012. http://dx.doi.org/10.1038/nature11606.

Morin, R.D., Johnson, N.A., Severson, T.M., Mungall, A.J., An, J., Goya, R., Paul, J.E., Boyle, M., Woolcock, B.W., Kuchenbauer, F., et al. (2010). Nat. Genet. *42*, 181–185.

Shaknovich, R., Cerchietti, L., Tsikitas, L., Kormaksson, M., De, S., Figueroa, M.E., Ballon, G., Yang, S.N., Weinhold, N., Reimers, M., et al. (2011). Blood *118*, 3559–3569.

Sneeringer, C.J., Scott, M.P., Kuntz, K.W., Knutson, S.K., Pollock, R.M., Richon, V.M., and Copeland, R.A. (2010). Proc. Natl. Acad. Sci. USA *107*, 20980–20985.

Su, I.H., Basavaraj, A., Krutchinsky, A.N., Hobert, O., Ullrich, A., Chait, B.T., and Tarakhovsky, A. (2003). Nat. Immunol. *4*, 124–131.

Su, I.H., Dobenecker, M.W., Dickinson, E., Oser, M., Basavaraj, A., Marqueron, R., Viale, A., Reinberg, D., Wülfing, C., and Tarakhovsky, A. (2005). Cell *121*, 425–436.

Velichutina, I., Shaknovich, R., Geng, H., Johnson, N.A., Gascoyne, R.D., Melnick, A.M., and Elemento, O. (2010). Blood *116*, 5247–5255.

SnapShot: Acute Myeloid Leukemia

Bernd B. Zeisig, Austin G. Kulasekararaj, Ghulam J. Mufti, and Chi Wai Eric So
Department of Haematological Medicine, King's College London, London SE5 9NU, UK

Cancer Cell

Clinical Features and Risk Stratification of AML

Prognostic category	Favorable risk (5 yr OS: 45%-80%)		Intermediate risk (5 yr OS: 20%-40%)		Adverse risk (5 yr OS: 5%-20%)	
	40%-45% of AML cases		25%-35% of AML cases		25%-30% of AML cases	
	Aberration	Frequency (%)	Aberration	Frequency (%)	Aberration	Frequency (%)
	• t(15:17)	7-12	• NK with *FLT3*-ITD	15-20	• 11q23,	3-5
	• t(8:21)	5-8	• NK with *NPM*^{WT} & no *FLT3*-ITD	10-17	• inv(3)/t(3;3)/*EVI-1*	~1
	• inv(16)	5-8	• t(9:11)	2-3	• t(6;9)/*DEK-NUP214*	~1
	• NK with *NPM*^{mut} & no *FLT3*-ITD	18-25	• Other cytogenetic abnormalities not included elsewhere	5-8	• -7/7q-	3-5
	• NK with biallelic *CEBPA*^{mut}	6-12			• -5/5q-	2-3
					• 17p deletions	~2
					• CK	10-12
Current therapies	Standard induction cytotoxic therapy ("3+7"), followed by postremission therapy with high dose cytarabine ATRA as a differentiating agent with anthracycline based chemotherapy in t(15;17)		Standard induction cytotoxic therapy ("3+7"), followed by postremission consolidation Allogeneic HSCT should be considered as main modality of consolidation, especially in patients with *FLT3*-ITD		Standard induction cytotoxic therapy ("3+7"), although dismal outcome with chemotherapy alone Allogeneic HSCT should be offered in clinical remission 1 Consider use of investigational and novel agents	

Cytogenetic Aberrations in AML

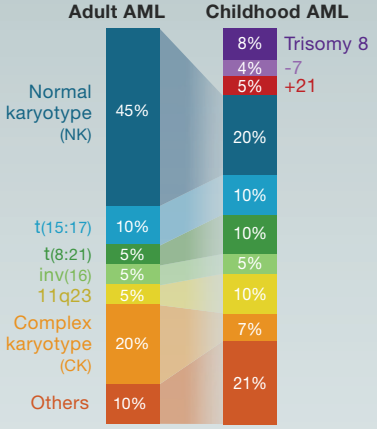

Molecular Mechanisms, Recurrent Gene Mutations, and Emerging Targeted Therapies in AML

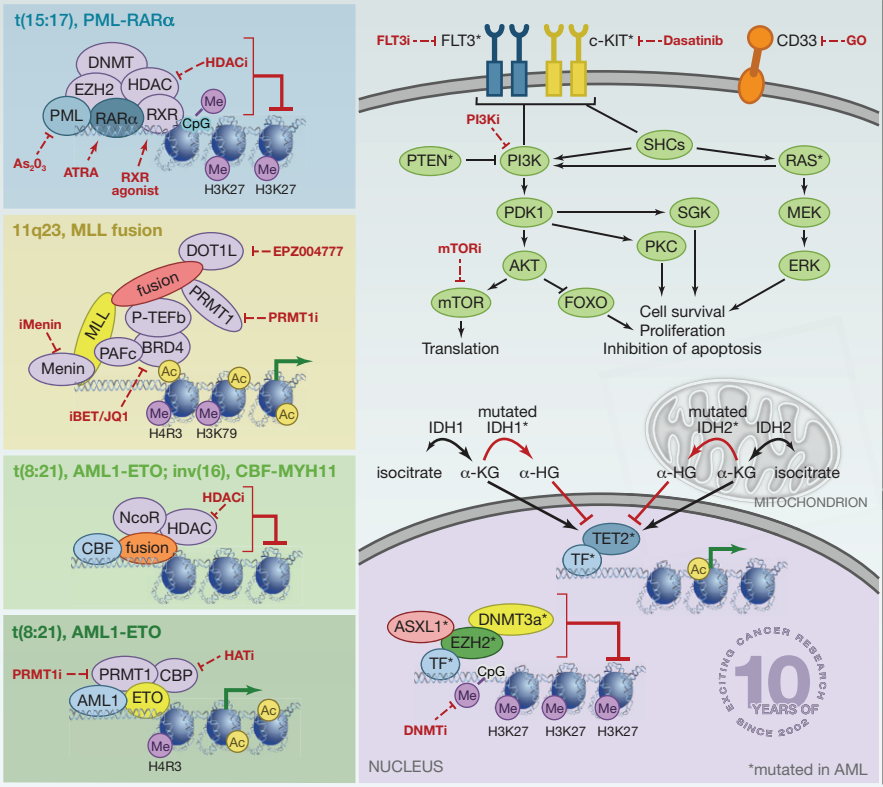

	Gene	Frequency (in NK-AML) and comments
Signalling	*FLT3*-ITD	20%-25% (28%-35%); High blast count; Poor prognosis especially in cases with high mutant to WT allelic ratio
	FLT3-TKD	5%-7% (10%-14%); Prognostic impact remains controversial
	NRAS	10% (9%-14%); Enriched in CBF AML; Prognosis unknown
	C-KIT	<5% (<5%); 25-30% in CBF leukaemia
	PTEN	<2% (2%); Prognosis unknown
Transcription factors (TF)	*NPM1*	25%-30% (40%-65%); M4 blast morphology lacks CD34 expression; Hox gene upregulation; Favorable prognosis in the presence of *FLT3*^{WT}; Female preponderance
	CEBPA	5%-10% (10-19%); Favorable prognosis if biallelic mutation
	RUNX1	5%-13% (6-25%); Enriched in trisomy 13 and FAB M0; Poor prognosis
	WT1	10% (10%-13%); Associated with M0 FAB type; Poor prognosis
	TP53	2%-4% (<2%); Predominantly in CK-AML; Very poor prognosis
Epigenetic modifiers	*DNMT3A*	20%-25% (32%-35%); Heterozygous R882 mutations account for 40%-60% of mutations; Poor prognosis in NK-AML
	IDH1/IDH2	12%-22% (25%-30%); Mutant *IDH1 & 2* are mutually exclusive; *IDH1* mutations enriched in patients with *NPM1*^{mut}; IDH1 is localized in cytoplasm and peroxisomes
	TET2	7%-15% (15%-23%); Mutually exclusive to *IDH1/2* mutations; More prevalent in secondary AML especially MPN
	ASXL1	3% (3%-5%); Poor prognosis
	EZH2	<2% (<1%); Enriched in MDS/MPN; Prognosis unknown
	MLL-PTD	<2% (2%-5%); Enriched in trisomy 11
Overexpressed	*EVI-1*	Deregulated in inv(3)(q21q26); Poor prognosis
	MN1	Poor response to chemotherapy; Correlated with *NPM*^{WT} and high BAALC expression
	BAALC	High expression in NK and +8; Poor prognosis
	ERG	Poor prognosis in CK and NK AML
	miR-181	Increased in FAB M1/M2, *CEBPA*^{mut}; Favorable prognosis

Cell of Origin and Clonal Evolution Model of Leukemic Stem Cells

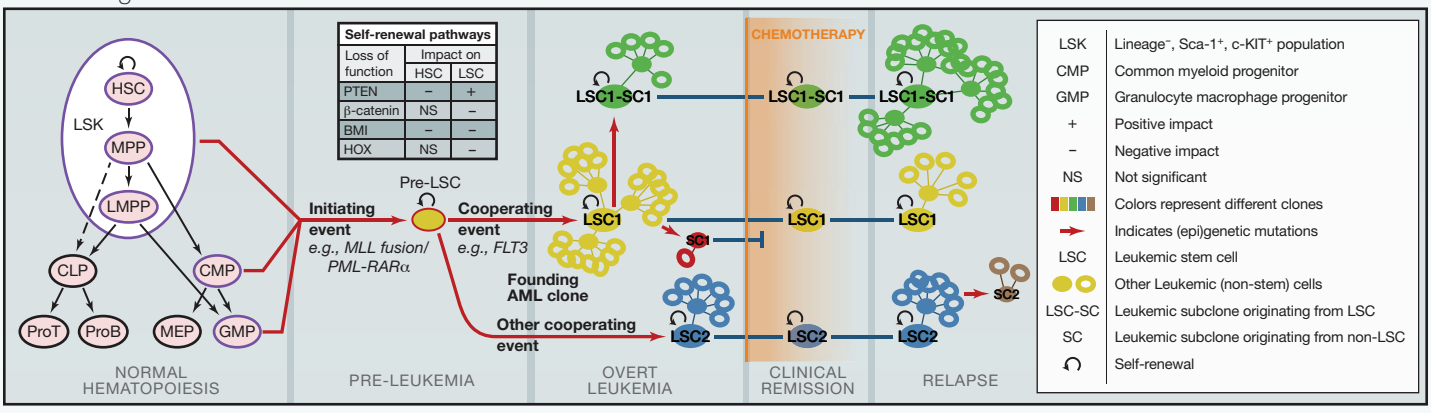

See online version for legend and references.

SnapShot: Acute Myeloid Leukemia

Bernd B. Zeisig, Austin G. Kulasekararaj, Ghulam J. Mufti, and Chi Wai Eric So
Department of Haematological Medicine, King's College London, London SE5 9NU, UK

Cancer Cell

Clinical Features and Risk Classification of AML

Acute myeloid leukemia (AML) is a heterogeneous clonal disorder of hematopoietic stem/progenitor cells characterized by the rapid growth of abnormal white blood cells (blasts) that accumulate in the bone marrow and interfere with the production of normal blood cells. In contrast to the classical French-American-British (FAB) classification based on morphological appearance of blasts and their cytochemistry, the 2008 revised WHO classification of AML incorporates cytogenetic/genetic data that help to define biologically homogenous entities with prognostic and therapeutic relevance. Based on (cyto)genetic features of the AML, patients can be broadly classified into three risk groups, although patient-specific factors (age, performance status, comorbidity, etc.) are also key predictors of outcome. The "3+7" combination of daunorubicin and cytarabine is routinely used as induction chemotherapy for adult patients with AML, except PML-RARα leukemia, whereas molecular profiling is currently guiding postinduction therapeutic strategies. Comparison between adult and childhood AML shows that children have a higher incidence of chromosomal translocation, whereas normal (NK) and complex karyotype (CK)—the latter includes monosomal karyotype (MK) and is associated with dismal prognosis—are more prevalent in adults. While risk classification has advanced in the last decades, treatment of AML, except for t(15;17) leukemia, is only marginally improved, mainly by better supportive care, highlighting the need for novel therapies.

Molecular Mechanisms, Recurrent Gene Mutations, and Emerging Targeted Therapies in AML

PML-RARα from t(15;17) that exclusively associates with FAB-M3 (acute promyelocytic leukemia, APL) forms transcriptionally repressive complexes with retinoic X receptor (RXR), histone deacetylases (HDACs), enhancer of zeste (EZH2), and DNA methyltransferase (DNMT). All-trans retinoic acid (ATRA), which dissociates repressor complexes from PML-RARα and mediates its subsequent degradation, can effectively induce differentiation of APL cells. In combination with chemotherapy, ATRA achieves a 5 year overall survival of approximately 80%. While As_2O_3, which degrades PML-RARα, is commonly employed to treat relapsed patients, other targeted therapeutic agents, including HDAC inhibitors and RXR agonists, are being developed.

The MLL gene located at 11q23 has over 60 different fusion partners in AML. Wild-type MLL encodes a SET domain containing H3K4 histone methyltransferase but the SET domain is invariably replaced by the partner proteins in MLL fusions. All MLL fusions retain MLL's N terminus that recruits Menin and the polymerase associated factor complex (PAFc), which are critical for DNA binding, gene expression, and cellular transformation. Importantly, the fusion partners themselves recruit a variety of protein complexes involved in transcriptional elongation (p-TEFb) and/or histone methylation, e.g., DOT1L (H3K79) or PRMT1 (H4R3), resulting in aberrant transcriptional activation. Several novel targeted strategies are emerging for 11q23 AML, including inhibition of Menin, DOT1L, PRMT1, the histone acetylation reader BRD4, and LSD1 (although the mechanisms underlying the efficacy of LSD1 inhibition remain unclear).

Genes encoding core binding factors including AML1/RUNX1 and CBFβ are the most frequently rearranged ones in AML. Both core binding factor fusions complex with transcriptional repressors, such as HDACs and NCoR, to suppress expression of downstream targets, thus prompting HDAC inhibitors as potential therapeutic agents. AML1-ETO fusions may also recruit transcriptional coactivators such as PRMT1 and histone acetyltransferase (HAT) CBP that are critical for transformation.

Going beyond microarray analyses, next-generation sequencing has been unravelling the vast genetic heterogeneity in AML and improving risk stratification, especially for NK-AML. This has led to the discovery of not only several candidate genes that could be classified under the conventional two-hit model (e.g., signaling and transcription factors) of myeloid leukemogeneis but also those involved in epigenetic regulation, spliceosome machinery, and the cohesin complex. Interestingly, some of the mutations identified in NK-AML such as those in FLT3 and c-KIT are also recurrent in AML with translocations. Several kinase inhibitors (e.g., FLT3i and dasatinib), anti-CD33 antibody conjugate gemtuzumab ozogamicin (GO), and hypomethylating agents are currently in clinical trials. The role of epigenetic modulation in AML has only started to be unraveled, even though the therapeutic benefit of hypomethylating agents in low blast AML predates our knowledge of the existence of these epigenetic regulator mutations.

Cell of Origin and Clonal Evolution Model of Leukemic Stem Cells

The cell of origin for AML stem cells is still unclear. However, studies using mouse models have shown that both hematopoietic stem cells (HSCs) and progenitor cells can be targeted by initiating events, such as MLL fusions and PML-RARα, to generate preleukemic stem cells (pre-LSCs) and, subsequently, LSCs with acquisition of additional cooperative events (e.g., FLT3). The origin of LSCs can influence the leukemia type and lineage, although the cellular origin's role in treatment response remains to be determined. LSCs possess self-renewal ability and can give rise to short-lived progenies, which form the bulk of the leukemic population in the patient. LSCs and leukemic progenies can further evolve into different subclones by acquiring additional mutations, leading to multiple (epi)genetically different leukemic clones with various clone sizes in the patient at the time of diagnosis. After chemotherapy, the bulk of leukemic cells is eradicated, leading to clinical remission; however, chemoresistant LSCs persist in the patient at low levels. With time, LSCs, which may be shaped by the treatment, can give rise to different progenies again, reinitiating the disease. Thus, the dominant clone at the time of relapse may not necessarily be the same as the one at diagnosis. Self-renewal is a common feature shared by LSCs and HSCs. Pathways such as β-catenin and PTEN, which have differential effects on LSCs versus normal HSCs, may be key targets to eradicate LSCs.

ACKNOWLEDGMENTS

We thank Prof. Mel Greaves and Prof. David Grimwade for critical comments and constructive advice. Studies in the author's lab are supported by the Leukaemia and Lymphoma Research (LLR) UK, Kay Kendall Leukaemia Fund (KKLF), Medical Research Council (MRC), and the Association for International Cancer Research (AICR).

REFERENCES

Cheung, N., and So, C.W. (2011). Transcriptional and epigenetic networks in haematological malignancy. FEBS Lett. *585*, 2100–2111.

Ding, L., Ley, T.J., Larson, D.E., Miller, C.A., Koboldt, D.C., Welch, J.S., Ritchey, J.K., Young, M.A., Lamprecht, T., McLellan, M.D., et al. (2012). Clonal evolution in relapsed acute myeloid leukaemia revealed by whole-genome sequencing. Nature *481*, 506–510.

Döhner, H., Estey, E.H., Amadori, S., Appelbaum, F.R., Büchner, T., Burnett, A.K., Dombret, H., Fenaux, P., Grimwade, D., Larson, R.A., et al.; European LeukemiaNet (2010). Diagnosis and management of acute myeloid leukemia in adults: recommendations from an international expert panel, on behalf of the European LeukemiaNet. Blood *115*, 453–474.

Greaves, M., and Maley, C.C. (2012). Clonal evolution in cancer. Nature *481*, 306–313.

Grimwade, D., Hills, R.K., Moorman, A.V., Walker, H., Chatters, S., Goldstone, A.H., Wheatley, K., Harrison, C.J., and Burnett, A.K.; National Cancer Research Institute Adult Leukaemia Working Group (2010). Refinement of cytogenetic classification in acute myeloid leukemia: determination of prognostic significance of rare recurring chromosomal abnormalities among 5876 younger adult patients treated in the United Kingdom Medical Research Council trials. Blood *116*, 354–365.

Ley, T.J., Mardis, E.R., Ding, L., Fulton, B., McLellan, M.D., Chen, K., Dooling, D., Dunford-Shore, B.H., McGrath, S., Hickenbotham, M., et al. (2008). DNA sequencing of a cytogenetically normal acute myeloid leukaemia genome. Nature *456*, 66–72.

Shih, A.H., Abdel-Wahab, O., Patel, J.P., and Levine, R.L. (2012). The role of mutations in epigenetic regulators in myeloid malignancies. Nat. Rev. Cancer *12*, 599–612.

Swerdlow, S.H., Campo, E., Harris, N.L., Jaffe, E.S., Pileri, S.A., Stein, H., Thiele, J., and Vardiman, J.W. (2008). WHO Classification of Tumours of Haematopoietic and Lymphoid Tissues, Fourth Edition (Lyon, France: IARC Press).

Visvader, J.E., and Lindeman, G.J. (2012). Cancer stem cells: current status and evolving complexities. Cell Stem Cell *10*, 717–728.

Wang, L., Gural, A., Sun, X.-J., Zhao, X., Perna, F., Huang, G., Hatlen, M.A., Vu, L., Liu, F., Xu, H., et al. (2011). The leukemogenicity of AML1-ETO is dependent on site-specific lysine acetylation. Science *333*, 765–769.